P

Paired Electrosynthesis

Nicola Aust and Axel Kirste
BASF SE, Ludwigshafen, Germany

Introduction

Organic electrochemistry can be a very powerful synthetic tool [1–3]. Anodic oxidation as well as cathodic reduction processes are utilized [4]. If one wants to carry out a synthesis based on an anodic oxidation, the cathodic process is normally not of synthetic interest and vice versa. Nevertheless in some cases the counter-electrode process can be used also. An example is the cathodic evolution of hydrogen in protic solvents like water or methanol, while the anodic process renders the desired product. The evolving hydrogen can be utilized as fuel material. In these cases the counter-electrode reaction is of economical and not of synthetic use. But electrochemists dream of a paired electrosynthesis using cathodic and anodic process for synthesis to achieve the ultimate goal: a 200 % electrosynthesis.

There are several ways possible to perform such a paired electrosynthesis, e.g., in a parallel, convergent, divergent, or linear assembly [5, 6] (Fig. 1).

In a parallel electrosynthesis the products generated at anode and cathode do not interfere or react. In contrast stands the convergent paired electrosynthesis where the generated products react to one final product or where by anodic and cathodic process the same product is synthesized. Using one substrate and creating an oxidized and a reduced product is the main feature of a divergent paired electrosynthesis. The linear assembly has in common that also only one substrate is employed. But in the linear paired electrosynthesis, one product is synthesized from the substrate by one- or two-mediated electrode processes sometimes in a cascade-like path. All different forms of a paired electrosynthesis have in common that they are highly efficient and therefore resources preserving and waste/emissions minimizing. This is also summarized under the term "green synthesis" [6].

The benefit is high, but it is obvious that to conduct a successful paired electrosynthesis is not an easy task. Both electrode processes have to be compatible. Yield losses at the counter-electrode or a high effort to separate the electrode processes stand against a paired electrolysis. Product separation and isolation is an important factor especially in a parallel or divergent electrosynthesis [7]. The following electrolyses shall illustrate the important features of a paired electrosynthesis and show the broad range of application.

Example of a Parallel Paired Electrosynthesis

A successful industrial example of a parallel paired electrosynthesis is BASF's electrolysis of 4-*tert*-butylbenzaldehyde dimethylacetal and
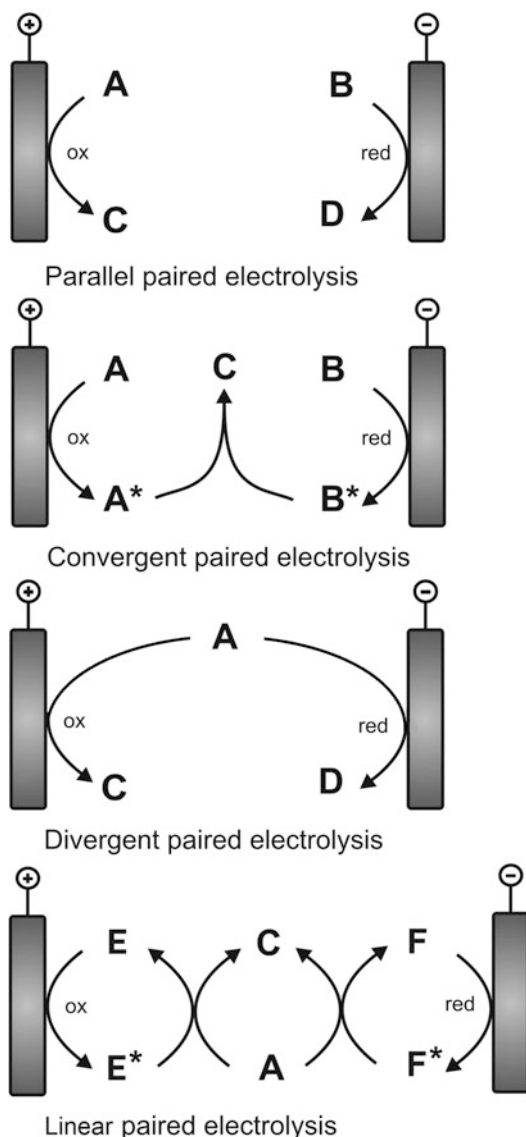
Paired Electrosynthesis, Fig. 1 Different forms of a paired electrosynthesis (*A*, *B* = substrate; *C*, *D* = product; *E*, *F* = mediator)

phthalide simultaneously in an undivided cell [8] (Fig. 2).

Already in the 1980s the electrosynthesis of acetals of aromatic aldehydes has been established at BASF. Employing the anodic substitution with methanol as nucleophile on methyl-substituted aromatic compounds, one generates by double methoxylation first the intermediate

ether and then the corresponding acetal [9, 10]. At the cathode hydrogen is generated (Fig. 3).

After the electrolysis the acetals can be hydrolyzed to their aldehydes and methanol is recovered. By this elegant way to avoid overoxidation to the acids, aromatic aldehydes are synthesized from toluene derivatives [11]. The electrosynthesis takes place in good yields for toluene derivatives with electron pushing para-substituents like the *tert*-butyl group. It is carried out in an undivided cell developed by BASF: the capillary gap cell which contains a stack of bipolar round graphite electrodes. The electrodes are separated by spacers and connected in series [12].

More than 10 years after the establishment of the acetalization process, electrochemists at BASF have searched for a compatible reductive process that can be run instead of the hydrogen evolution. What they have found is the reduction of phthalic acid dimethylester to phthalide [8] (Fig. 2). Phthalide is a compound that was up till then generated by classical catalytic hydrogenation from phthalic acid anhydride [7]. Part of the process development has been to fit the paired electrosynthesis in the same capillary gap cell like the acetalization of the toluene derivatives.

The methanol balance as well as the proton balance is remarkable: two moles of methanol that get released in the cathodic process are used for the acetalization at the anode and four protons used for the cathodic reduction are generated in the anodic acetalization. The electric energy consumption of the paired electrosynthesis is not increased compared to the non-paired process. Because hydrogen is avoided completely, the energy/fossil fuel to generate the hydrogen for the reduction step is economized [7].

But without the development of a skillful work-up, the paired electrosynthesis would not have become a successful industrial process up till now. In the non-paired electrosynthesis, 4-*tert*-butylbenzaldehyde dimethylacetal gets distilled for purification and this procedure has been retained. The main challenge has been to purify the rest of the electrolysis solution containing the phthalide. The BASF electrochemists have found a way to isolate

Paired Electrosynthesis, Fig. 2 Parallel electrosynthesis of 4-*tert*-butylbenzaldehyde dimethylacetal and phthalide

anode reaction

cathode reaction

anode reaction

cathode reaction

$$4H^+ + 4e^- \longrightarrow 2\,H_2$$
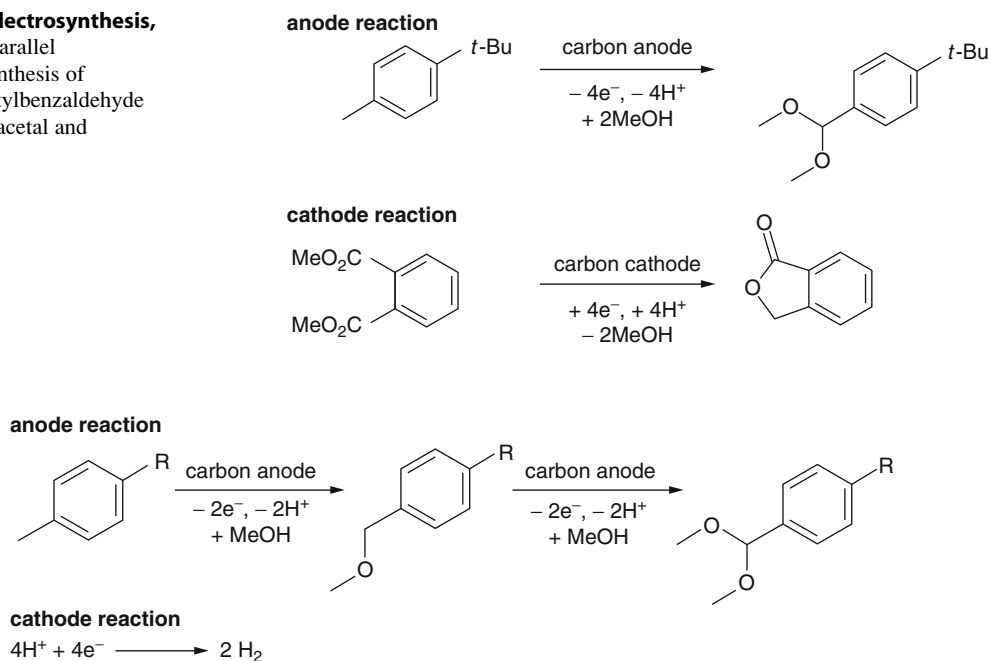
Paired Electrosynthesis, Fig. 3 Electrosynthesis of acetals of aromatic aldehydes

and to purify phthalide with a skillful layer crystallization process [7].
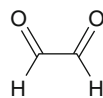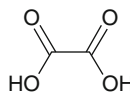
Example of a Convergent Paired Electrosynthesis

The anodic and cathodic production of glyoxylic acid in aqueous solution is an interesting example of a convergent paired electrosynthesis [13, 14] (Fig. 4).

Industrially the main chemical route to glyoxylic acid is the oxidation of glyoxal with nitric acid [15]. A challenge in this synthesis is to prevent overoxidation to oxalic acid and CO_2. Electrochemically the anodic oxidation of glyoxal is possible as well as the cathodic reduction of oxalic acid. Both electrolyses have been investigated thoroughly.

An important aspect in the anodic oxidation of glyoxal that has been discovered is the clear improvement of the oxidation by hydrochloric acid as mediator [16] (Fig. 5).

First reports about the reduction of oxalic acid have already been published around 1900. In an acidic electrolyte the reduction of oxalic acid at

anode reaction

cathode reaction

Paired Electrosynthesis, Fig. 4 Convergent electrosynthesis of glyoxylic acid

a mercury or lead cathode is described [17]. Decades later, the reduction has been studied intensively [18, 19]. Preferred cathodes are still high overpotential cathodes like lead electrodes [18]. The reduction at graphite electrodes has also been of interest. To improve the reduction at graphite, the addition of metal salts which have a high hydrogen overpotential has been found [20]. This emphasizes the obvious: in aqueous solution it is crucial to oppress the

Paired Electrosynthesis, Fig. 5 Mediated anodic oxidation of glyoxal to glyoxylic acid
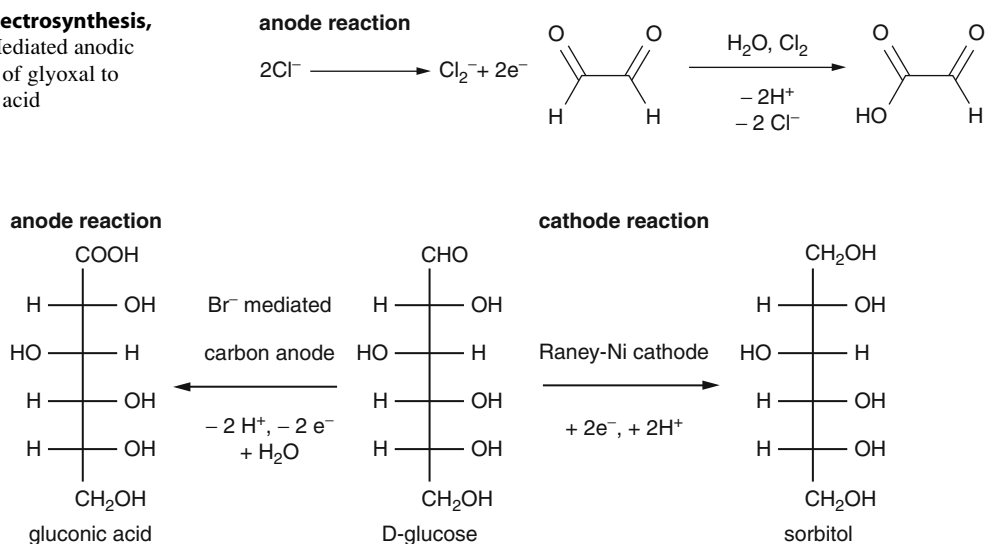
Paired Electrosynthesis, Fig. 6 Divergent electrosynthesis of gluconic acid and sorbitol from glucose

evolution of hydrogen as reductive process in order to be able to reduce the oxalic acid.

The combination of both processes to a paired synthesis bears the next improvement in the electrochemical synthesis of glyoxylic acid first in an undivided cell [13] and later in a divided cell [14]. In the example of the divided cell, the compartments are separated by a cationic exchange membrane. The use of hydrochloric acid renders also in the paired process a good selectivity for the anodic glyoxylic acid generation and guarantees a sufficient conductivity of the aqueous glyoxal solution. The cathodic reduction of oxalic acid takes place as well in an aqueous solution containing hydrochloric acid as supporting electrolyte. Graphite is used as anode and lead as cathode. The choice of temperature and pH is decisive. But also under optimized parameter, overoxidation of glyoxylic acid to oxalic acid and CO_2 is found. By precipitation of the glyoxylic acid, a pure product in good yields is obtained [14].

Example of a Divergent Paired Electrosynthesis

An established divergent paired electrosynthesis is the production of gluconic acid and sorbitol from glucose [21] (Fig. 6).

For the oxidation of glucose to gluconic acid, it is obviously important to avoid overoxidation to glucaric acid. The oxidation is halogenide mediated. In this case bromide is the mediator of choice. To control the selectivity to gluconic acid by the applied charge is an advantage of organic electrochemistry that is used in this case. pH and temperature are also crucial parameters for a sufficient selectivity. The sensitivity of a carbohydrate oxidation in general to these parameters is also shown later by Marsais [22] and Schäfer [23] who have investigated the (TEMPO)-mediated oxidation of carbohydrates (in non-paired processes). The cathodic reduction is improved by the choice of a Raney Nickel powder catalyst instead of a Zn(Hg) cathode. The paired process is carried out in aqueous solution in an undivided flow reactor that was adapted for this electrosynthesis [21].

Example of a Linear Paired Electrosynthesis

The synthesis of methyl ethyl ketone from 2,3-butanediol is a remarkable example of a linear paired electrosynthesis [24] (Fig. 7).

In a bromide-mediated reaction, acetoin is generated from 2,3-butanediol. Afterwards acetoin

Paired Electrosynthesis, Fig. 7 Linear electrosynthesis of methyl ethyl ketone from 2,3-butanediol

anode reaction   cathode reaction
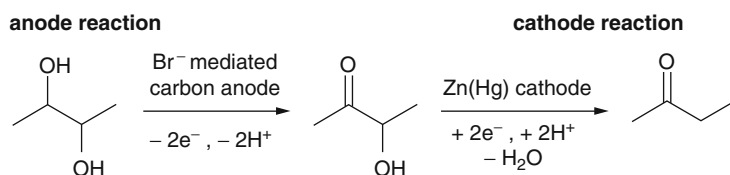
is reduced at a Hg/Zn cathode to methyl ethyl ketone. The use of an undivided cell is inevitable in this case. The reaction control is very important because the oxidation of 2,3-butanediol with the oxidized mediator is slow. To avoid a reduction of this species, a special flow cell has been developed. A reaction tube after the graphite anode renders sufficient time to oxidize 2,3-butanediol. This example emphasizes how crucial electrolysis conditions and setup is to avoid the undesired reaction at the counter-electrode. In this case the oxidized mediator has to be protected from reduction, and of course the formed methyl ethyl ketone should not be mediated oxidized at the anode to acetoin.

Summary and Future Directions

The examples illustrate the diversity as well as the common features of a paired electrosynthesis. One can start with one or two substrates to generate one or two products. Electrode processes can be mediated or direct. Undivided and divided cells are employed in paired electrosyntheses. But as in the BASF phthalide example, it is crucial for the synthesis of glyoxylic acid, sorbitol, and methyl ethyl ketone that the cathodic process is the reduction of the substrate and not the reduction of protons because in these cases protons are generated at the anode and the electrolysis takes place in a protic solvent. Therefore effects that minimize the overpotential of hydrogen have to be omitted. Reaction control is important in all described examples, and consequently the cell and the setup have to fit for each case. Work-up and product isolation are significant for a successful synthesis and can be even more challenging in a paired synthesis.

A skillful solution is demonstrated by the BASF process.

Future directions, respectively, particular processes, are hard to foresee though the development of more paired electrosynthesis examples is being expected because the essence of such an electrolysis is very attractive: it uses the mole of charge moved in the cell in the most efficient way. The work can be based on the knowledge about successful paired electrosyntheses that is generated for decades as it is partly reflected by the presented examples.

Cross-References

▶ Anodic Substitutions
▶ Electrochemical Functional Transformation
▶ Electrosynthesis Using Mediator
▶ Green Electrochemistry
▶ Organic Electrochemistry, Industrial Aspects

P

References

1. Lund H, Hammerich O (2001) Organic electrochemistry. Marcel Dekker, New York
2. Schäfer HJ, Bard AJ, Stratmann M (2004) Organic electrochemistry. In: Encyclopedia of electrochemistry, vol 8. Wiley-VCH, Weinheim
3. Eberson L, Nyberg K (1976) Synthetic uses of anodic substitution reactions. Tetrahedron 32:2185–2206
4. Schäfer HJ (1981) Anodic and cathodic CC-bond formation. Angew Chem Int Ed 20:911–934
5. Paddon CA, Atobe M, Fuchigami T, He P, Watts P, Haswell SJ, Pritchard GJ, Bull SD, Marken F (2006) Towards paired and coupled electrode reactions for clean organic microreactor electrosyntheses. J Appl Electrochem 36:617–634
6. Frontana-Uribe BA, Little RD, Ibanez JG, Palma A, Vasquez-Medrano R (2010) Organic

electrosynthesis: a promising green methodology in organic chemistry. Green Chem 12:2099–2119

7. Hannebaum H, Pütter H (1999) Elektrosynthesen Strom doppelt genutzt: Erste technische "Paired Electrosynthesis". Chemie in unserer Zeit 33:373–374

8. Hannebaum H, Pütter H (BASF) DE19618854

9. Wendt H, Bitterlich S (1992) Anodic synthesis of benzaldehydes – 1. Voltammetry of the anodic oxidation of toluene in non-aqueous solutions. Electrochim acta 37:1951–1958

10. Wendt H, Bitterlich S, Lodowicks E, Liu Z (1992) Anodic synthesis of benzaldehydes – 2. Optimization of the direct anodic oxidation of toluenes in methanol and ethanol. Electrochim Acta 37:1959–1969

11. Degner D (BASF) DE2848397. Degner D, Barl M, Siegel H (BASF) DE2848397

12. Beck F, Guthke H (1969) Entwicklung neuer Zellen für electro-organische Synthesen. Chem-Ing-Tech 41:943–950

13. Scott K (1991) A preliminary investigation of the simultaneous anodic and cathodic production of glyoxylic acid. Electrochim Acta 36:1447–1452

14. Jalbout AF, Zhang S (2002) New paired electrosynthesis route for glyoxalic acid. Acta Chim Slov 49:917–923

15. Mattioda G, Christidis Y (2000) Glyoxylic acid. In: Ullmann's encyclopedia of industrial chemistry, vol 17. Wiley-VCH, Weinheim, pp 89–92

16. Pierre G, El Kordi M, Cauquis G, Mattioda G, Christidis Y (1985) Electrochemical synthesis of glyoxylic acid from glyoxal. Part 1. Role of the electrolyte, temperature and electrode material. J Electroanal Chem 186:167–177

17. Tafel J, Friedrichs G (1904) Elektrolytische Reduction von Carbonsäuren und Carbonsäureestern in schwefelsaurer Lösung. Chem Ber 37:3187–3191

18. Goodridge F, Lister K, Plimley RE, Scott K (1980) Scale-up studies of the electrolytic recuction of oxalic to glyoxalic acid. J Appl Electrochem 10:55–60

19. Picket DJ, Yap KS (1974) A study of the production of glyoxylic acid by the electrochemical reduction of oxalic acid solution. J Appl Electrochem 4:17–23

20. Scharbert B, Dapperheld S, Babusiaux P (Hoechst) DE4205423

21. Park K, Pintauro PN, Baizer MM, Nobe K (1985) Flow rate studies of the paired electro-oxidation and electroreduction of glucose. J Electrochem Soc 132:1850–1855

22. Ibert M, Fuertès P, Merbouh N, Fiol-Petit C, Feasson C, Marsais F (2010) Improved preparative electrochemical oxidation of D-glucose to D-glucaric acid. Electrochim Acta 55:3589–3594

23. Schnatbaum K, Schäfer HJ (1999) Electroorganic Synthesis 66: Selective anodic oxidation of carbohydrates mediated by TEMPO. Synthesis 864–872

24. Li W, Nonaka T, Chou T-C (1999) Paired electrosynthesis of organic compounds. Electrochemistry 67:4–10

Permanent Electrochemical Promotion for Environmental Applications

Leonardo Lizarraga and Philippe Vernoux
Université Lyon 1, CNRS, UMR 5256, IRCELYON, Institut de recherches sur la catalyse et l'environnement de Lyon, Villeurbanne, France

Introduction

Electrochemical Promotion of Catalysis (EPOC), or Non-Faradaic Electrochemical Modification of Catalytic Activity (NEMCA) effect, is a promising concept for boosting catalytic processes and advancing the frontiers of catalysis. This innovative field aims to modify both the activity and the selectivity of catalysts in a controlled manner. EPOC utilizes solid electrolyte materials as catalytic carriers. Ions contained in these electrolytes are electrochemically supplied to the catalyst surface and act as promoting agents to modify the catalyst electronic properties in order to achieve optimal catalytic performance. EPOC can be considered as an electrically controlled catalyst-support interaction in which promoting ionic agents are accurately supplied onto the catalytic surface by electrical potential control. The main advantage of EPOC is that the electrochemical activation magnitude is much higher than that predicted by Faraday's law. Therefore, EPOC requires low currents or potentials. Moreover, promoting species such as O^{2-} and H^+ cannot be formed via gaseous adsorption and cannot be easily dosed by chemical means. EPOC has been investigated thoroughly for more than 70 catalytic reactions [1, 2] and is reversible, since the catalyst restores its initial activity, typically within a few minutes after current interruption. Recently, however, some studies have shown that, for specific operating conditions and catalyst-electrodes, the reversibility of this phenomenon strongly depends on the duration of the polarization.

For prolonged polarization times, the catalytic reaction rate after current interruption can remain higher than the value before current application [3]. This behavior has been reported as "permanent-electrochemical promotion of catalysis" (P-EPOC). This phenomenon was mainly observed over catalysts which have multiple valence states and the ability to form oxides, i.e., Pt/PtO_x or Rh/Rh_2O_3.

State-of-the-Art

The phenomenon of P-EPOC has been mainly observed on yttria-stabilized zirconia (YSZ), an O^{2-} conducting electrolyte, interfaced with different catalysts: IrO_2 [4], RuO_2 [5], Rh [6–9], Pt [3, 10–12], and Pd [13]. Two recent studies have reported P-EPOC on Pt films interfaced with $K-\beta''Al_2O_3$, a K^+ conducting ceramic [14], or $Ba_3Ca_{1.18}Nb_{1.82}O_{9-a}$, a H^+ conductor [15]. Two parameters are commonly used to quantify the magnitude of the EPOC effect [2]: the rate enhancement ratio, r, defined as $r = r/r_0$, where r is the electropromoted catalytic rate and r_0 the open-circuit, i.e. non-promoted, catalytic rate; and the apparent Faradaic efficiency, Λ, defined as $\Lambda = (r - r_0)/(I/nF)$. P-EPOC effect is quantified using a "permanent" rate enhancement ratio [3], y, which has been defined as $y = r_{P-EPOC}/r_0$, where r_{P-EPOC} is the catalytic rate in an open-circuit state after current interruption.

A typical EPOC experiment setup consists of an electrochemical cell based on a dense pellet or tube of a solid electrolyte (YSZ, $K-\beta''Al_2O_3$, etc.). The pellet or tube is covered on both sides by three electrodes: working, counter and reference [2]. The catalytic activity of catalyst layers, used as working electrodes, can be modified by applying small potentials or currents between the working and the counter electrodes. Figure 1 shows two typical transients, i.e. variation of the catalytic rate versus time, for two different polarization times. At t = 0, a small positive current (300 μA) is applied across the IrO_2/YSZ interface exposed to a C_2H_4/O_2 atmosphere. Upon current application, the rate of ethylene catalytic
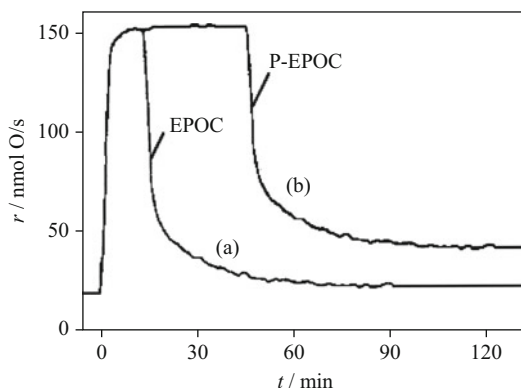
Permanent Electrochemical Promotion for Environmental Applications, Fig. 1 Polarization and relaxation transients of the rate of C_2H_4 combustion on IrO_2/YSZ catalyst due to an anodic current application (300 mA) for two different times: (**a**) short polarization to give reversible EPOC and (**b**) long polarization time to give P-EPOC. T = 380 °C, P_{O2} = 17 kPa, P_{C2H4} = 0.14 kPa (Reprint ref 3)

combustion on IrO_2, expressed in moles of O consumed per second, drastically increases by around a factor of 3.5 and reaches a plateau after a few minutes. This enhancement is non-Faradaic, with a Faradaic efficiency larger than 100. The reversibility of this NEMCA effect depends on the polarization time. For short current applications (a few minutes), the catalytic rate gradually decreases down to its initial value after the current interruption. For prolonged polarizations (1 h), the catalytic rate also slowly decreases when the current stops, but more than 1 h after this interruption, it reaches a stable value, called the P-EPOC state, higher that its initial one.

Table 1 lists all reactions and catalysts where the P-EPOC phenomenon was observed, along with operating conditions. The P-EPOC phenomenon was mainly observed (Fig. 1 and Table 1) when long anodic polarizations, i.e. high anodic charges, were applied at the catalyst/electrolyte interfaces. In addition, most of these studies, especially those using Pt, were performed in oxygen excess conditions in the temperature range where PtO_x species are stable. Recent studies have shown that the y values have a $t^{1/2}$ dependence in respect to polarization time at constant
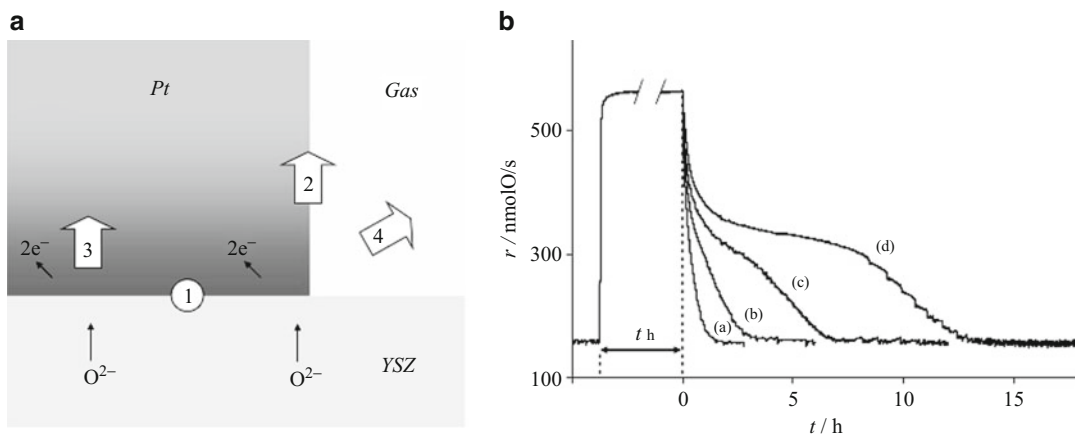
Permanent Electrochemical Promotion for Environmental Applications, Table 1 Exhaustive list of P-EPOC studies

Reactions	Catalyst (preparation method)	Solid electrolyte	T/°C	Preagent/kPa	PO_2/kPa	Polarization time/min	γmax	Ref
NO reduction by C_3H_6	Rh (paste calcination)	YSZ	300–380	$P_{C3H6} = 0.1$ $P_{NO} = 0.1$	0.5	60–180	6	6–8
C_2H_4 deep oxidation	IrO$_2$ (thermal decomposition)	YSZ	380	$P_{C2H4} = 0.14$	17	120	3	4
	RuO$_2$	YSZ	360	$P_{C2H4} = 0.14$	12	180	1.3	5
	Pt (paste calcination)	YSZ	550	$P_{C2H4} = 0.25$	1	60–6,600	2	3
	Pt (sputtering)	YSZ	375	$P_{C2H4} = 0.2$	8.5	10–600	2.2	10
	Pt/FeOx (pulsed laser deposition)	YSZ	375-425	$P_{C2H4} = 0.19$	8.2	40–60	10	11
	Pt (paste calcination)	$Ba_3Ca_{1.18}Nb_{1.82}O_{9-\alpha}$	350	$P_{C2H4} = 1$	2-8	100	4	15
C_3H_8 deep oxidation	Pt (sputtering)	YSZ	350	$P_{C3H8} = 0.2$	4.5	15	1.3	12
C_3H_6 deep oxidation	Pt (wet impregnation)	$K-\beta''Al_2O_3$	310	$P_{C3H6} = 0.2$	1	300	1.35	14
CH_4 deep oxidation	Pd (wet impregnation)	YSZ CeO$_2$/YSZ	470-600	$P_{CH4} = 0.4$	1	150	2	13
CH_4 partial oxidation	Rh (paste impregnation)	TiO$_2$/YSZ	550	$P_{CH4} = 0.5$–1	0.5	15–55	11	9

current, indicating a diffusion controlled process [10, 12]. Besides, the Comninellis research group has performed different electrochemical investigations (cyclic voltammetry, double step chronopotentiometry, etc.) for the system O_2 (g), Pt/YSZ, which evidences the possible electrochemical formation of PtO_x at long polarization time, with a kinetic dependence of $t^{1/2}$ [3, 16–18]. All of these facts are indicative of the importance of the formation of oxide species, such as PtOx or Rh_2O_3 in the P-EPOC effect. Comninellis and collaborators (Fig. 2a) have proposed a mechanism for the P-EPOC phenomenon as a function of the three different locations of oxygen species when an anodic polarization is applied (O^{2-} ions pumped from YSZ to Pt) [3]. When starting anodic polarizations, oxygen species first generate a monolayer at the catalyst/YSZ interface (1) and then rapidly spillover to the catalyst surface in the form of promoting ionic species (2), i.e. partially discharged ions ($O^{\delta-}$), which are at the origin of the reversible EPOC phenomenon. The coverage of these promoting species is maximal after a few minutes of polarization when reaching the plateau of catalytic activity. The third type of stored oxygen is attributed to the growth of an oxide layer starting at the Pt/YSZ interface (3). After current interruption, the promoters stored at the gas-exposed surface are consumed by the reaction, and the catalytic activity decreases. The oxide layer at the Pt/YSZ interface could then act as a tank of promoting ions which can spillover to the catalyst surface via solid state diffusion and enhance the catalytic rate (P-EPOC state).

The mechanism proposed by Comninellis and collaborators is well supported by the transients shown in Fig. 2b on thick Pt films, where the P-EPOC state disappears after some hours, depending on the anodic charge supplied (polarization time). After the release of all stored oxygen promoting species, the catalytic rate returns to its initial value. Therefore, the phenomenon is more persistent than permanent. However, long-term stable P-EPOC states were observed on thin Pt films (sputtering) interfaced

Permanent Electrochemical Promotion for Environmental Applications, Fig. 2 (**a**) Oxygen species produced electrochemically under anodic polarization. Storage at three different locations: (1) at the Pt/YSZ interface, (2) at the gas-exposed catalyst surface via backspillover and (3) in the bulk platinum at the vicinity of the Pt/YSZ interface. Leaving (via O_2 evolution and/or chemical reaction) toward the gas phase is indicated (4). (**b**) Dependence of the rate transients observed during open-circuit relaxation on the anodic polarization time: (a) 1 h, (b) 2 h, (c) 4 h, (d) 11 h. T = 525 °C. Feed composition: P_{C2H4} = 0.25 kPa, P_{O2} = 1 kPa. Reprinted from reference 3

on YSZ upon short anodic polarization times (a few minutes) [10, 12]. This interesting result can be explained through the electrochemical formation of a thermodynamically stable interfacial PtO_x species at the Pt/YSZ interface, in which it is not in contact with the reactive gas mixture. The P-EPOC effect, in this case, was only removed by applying cathodic currents that decompose PtO_x species. This interfacial PtO_x layer increases the oxygen chemical potential gradient across the Pt/YSZ interface and then promotes the thermal migration of $O^{\delta-}$ promoting species from the electrolyte to the metal/gas interface. This effect can be analyzed as a self-driven EPOC mechanism as permanent effects observed in wireless NEMCA transients [19].

Future Environmental Applications

Air pollution originating from automotive traffic and industries is an increasing problem, especially in urban areas. Major challenges are the treatment of gaseous streams from automobiles and plants, such as the abatement of NOx, soot, unburned CO and hydrocarbons, as well as low temperature catalytic combustion of traces such as volatile organic compounds (VOCs). VOCs present in buildings or cars are wide-ranging classes of chemicals, and currently over 300 compounds are considered as VOCs by the US Environmental Protection Agency (EPA). Their release has widespread environmental implications. The EPA has validated that indoor air pollution is one of the top human health risks. The studies on indoor air quality (IAQ) have been transited gradually to indoor volatile organic compounds. The removal of formaldehyde is vital for improving IAQ and human health due to a carcinogenic risk. The challenge addressed to the scientific catalysis community is to find smart, stable, efficient and selective catalysts with limited loadings of noble metals. EPOC is one of the ways to improve and control in-situ catalyst performance and stability. In addition, P-EPOC is particularly suitable for oxidation reactions occurring in oxygen excess (Table 1), for which noble metals are the most effective catalysts. Short pulse electrical polarizations could be sufficient to obtain high and long-term catalytic activity enhancements of noble metal-based catalysts (Pt, Pd, Rh), allowing use of

extremely low loadings and electricity. In particular, P-EPOC is a promising and energy-saving solution for catalytic oxidation of VOCs and light hydrocarbon combustion. Nevertheless, additional fundamental and experimental studies are necessary to improve the understanding of the P-EPOC phenomena in order to optimize their efficiency, most particularly at low temperatures.

Cross-References

▶ Electrochemical Promotion for the Abatement of Gaseous Pollutants

▶ Non-Faradaic Electrochemical Modification of Catalytic Activity (NEMCA)

▶ Solid Electrolytes

References

1. Vayenas CG, Bebelis S, Ladas S (1990) Dependence of catalytic rates on catalyst work function. Nature 343:625–627
2. Vayenas CG, Bebelis S, Pliangos C, Brosda S, Tsiplakides D (2001) Electrochemical activation of catalysis: promotion, electrochemical promotion and metal–support interactions. Kluwer Academic/Plenum Publishers, New York
3. Falgairete C, Jaccoud A, Foti G, Comninellis C (2008) The phenomenon of "permanent" electrochemical promotion of catalysis (P-EPOC). J Appl Electrochem 38:1075–1082
4. Nicole J, Tsiplakides D, Wodiunig S, Comninellis C (1997) Activation of catalyst for gas-phase combustion by electrochemical pretreatment. J Electrochem Soc 144:L312–L314
5. Wodiunig S, Patsis V, Comninellis C (2000) Electrochemical promotion of RuO_2-catalysts for the gas phase combustion of C_2H_4. Solid State Ionics 136:813–817
6. Foti G, Lavanchy O, Comninellis C (2000) Electrochemical promotion of Rh catalyst in gas-phase reduction of NO by propylene. J Appl Electrochem 30:1223–1228
7. Pliangos C, Raptis C, Badas T, Vayenas CG (2000) Electrochemical promotion of NO reduction by C_3H_6 on Rh/YSZ catalyst-electrodes. Ionics 6:119–126
8. Pliangos C, Raptis C, Badas T, Vayenas CG (2000) Electrochemical promotion of NO reduction by C_3H_6 on Rh/YSZ catalyst-electrodes. Solid State Ionics 136:767–773
9. Baranova EA, Fóti G, Comnillis C (2004) Current-assisted activation of Rh/TiO$_2$/YSZ catalyst. Electrochem Commun 6:389–394
10. Souentie S, Xia C, Falgairete C, Li YD, Comninellis C (2010) Investigation of the "permanent" electrochemical promotion of catalysis (P-EPOC) by electrochemical mass spectrometry (EMS) measurements. Electrochem Commun 12:323–326
11. Mutoro E, Koutsodontis C, Luerssen B, Brosda S, Vayenas CG, Janek J (2010) Electrochemical promotion of Pt (111)/YSZ (111) and Pt-FeO$_x$/YSZ (111) thin catalyst films: Electrocatalytic, catalytic and morphological studies. Appl Catal B Environ 100:328–337
12. Souentie S, Lizarraga L, Papaioannou EI, Vayenas CG, Vernoux P (2010) Permanent electrochemical promotion of C_3H_8 oxidation over thin sputtered Pt films. Electrochem Commun 12:1133–1135
13. Jiménez-Borja C, Dorado F, Lucas-Consuegra A, García-Vargas JM, Valverde JL (2009) Complete oxidation of methane on Pd/YSZ and Pd/CeO$_2$/YSZ by electrochemical promotion. Catal Today 146:326–329
14. de Lucas-Consuegra A, Dorado F, Valverde JL, Karoum R, Vernoux P (2007) Low-Temperature propene combustion over Pt/K-bAl$_2$O$_3$ electrochemical catalys: Characterization, catalytic activity measurements, and investigation of the NEMCA effect. J Catal 251:474–484
15. Thursfield A, Brosda S, Pliangos C, Schober T, Vayenas CG (2003) Electrochemical Promotion of an oxidation reaction using a proton conductor. Electrochim Acta 48:3779–3788
16. Falgairete C, Fóti G (2009) Oxygen storage in O$_2$/Pt/YSZ cell. Catal Today 146:274–278
17. Fóti G, Jaccoud A, Falgairete C, Comninellis C (2009) Charge storage Pt/YSZ interface. J Electroceram 23:175–179
18. Falgairete C, Xia C, Li YD, Harbich W, Fóti G, Comninellis C (2010) Investigation of the Pt/YSz interface at low oxygen partial pressure by solid electrochemical mass spectroscopy under high vacuum conditions. J Appl Electrochem 40:1901–1907
19. Poulidi D, Rivas ME, Metcalfe IS (2011) Controlled spillover in a single catalyst pellet: rate modification, mechanism and relationship with electrochemical promotion. J Catal 281:188–197
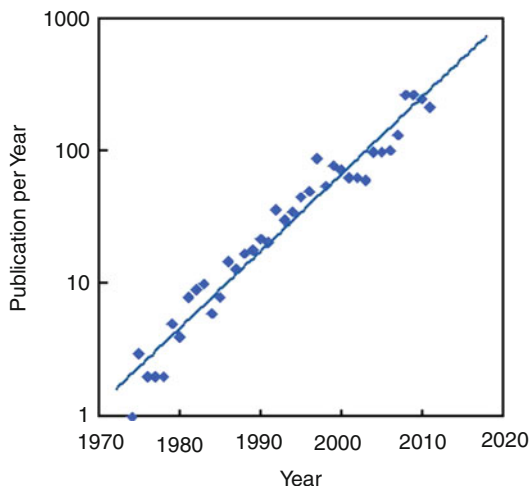
Perovskite Proton Conductor

Nikolaos Bonanos
Department of Energy Conversion and Storage, Technical University of Denmark, Roskilde, DK

Introduction

Perovskite proton conductors belong to the class of high temperature proton conductors (HTPCs),

solids that conduct electricity by transporting H^+ ions (protons) at temperatures above ambient, typically 400–1,000 °C. Unlike more common proton conductors, such as ice or $KHSO_4$, in which hydrogen is part of the chemical structure, in HTPCs, it is taken up from traces of water vapor in the atmosphere via gas-solid equilibrium. Accordingly, the hydrogen does not normally appear in the chemical formulae of the compounds. Typical high temperature proton conductors are $SrCeO_3$, $SrZrO_3$, $BaCeO_3$, $BaZrO_3$, $KTaO_3$, $LaNbO_4$, suitably doped, and La_6WO_{12} without a dopant; of these compounds, the first five are perovskites. Perovskite proton conductors are of interest as electrolytes in fuel cells, water vapor electrolysis cells, electrochemical hydrogen pumps, and hydrogen sensors. When they display electronic conduction in addition to the protonic, these materials can function as hydrogen semipermeable membranes of very high selectivity. In this article, perovskite proton conductors are describe with the non-specialist reader in mind. Detailed discussions of perovskite proton conductors and their applications can be found in review articles [1–5].

Since the 1960s, hydrogen has been known to exist in oxides, but only in trace amounts, and was not believed to alter the physical properties of the oxide significantly. In the early 1970s, it became clear that the role of hydrogen was important, and sometimes dominant. In the year 1981, in which the first international conference on Solid State Proton Conductors [6] was held in Paris, a landmark paper was published by H. Iwahara and coworkers [7] demonstrating proton conductivity in Sc-doped $SrCeO_3$ and operating a prototype water vapor electrolyzer at 900 °C. During the 30 years that have elapsed since then, the subject has moved from the marginal to the mainstream, and features strongly in the International Conferences on Solid State Ionics (SSI) and Solid State Proton Conductors (SSPC). Figure 1 shows the number of publications per year that include the words *proton* and *conduction* and *oxides* in their title or keywords. If the present trend were to continue, by 2020, the subject would attract about 1,000 publications per year!

Perovskite Proton Conductor, Fig. 1 Number of scientific publications per year that include the words *proton*, *conduction*, and *oxides* in their title or keywords. The idea for this graph comes from ref. [3]

Generation of Protonic Carriers in Perovskite Proton Conductors

The chemical reaction that describes the incorporation of water molecules into an oxide is given in (Eq. 1), using Kröger-Vink notation:

$$H_2O(g) + O_O^{\times} + V_O^{\cdot\cdot} \leftrightarrow 2OH_O^{\cdot} \qquad (1)$$
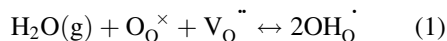
This means that a water molecule reacts with an oxygen ion on a normal site ($O_O\times$) and an oxygen vacancy ($V_O^{\cdot\cdot}$) to produce two hydroxyl ions occupying oxygen sites; in other words, the protonic species. The oxygen vacancies are created by doping or, less commonly, are part of the structure. In the case where the host is tetravalent and the dopant trivalent, the dopant would be denoted as [M′]. Reaction (1) is characterized by an equilibrium constant K_W defined by the equation:

$$K_W = \frac{\left[OH_O^{\cdot}\right]^2}{\left[V_O^{\cdot\cdot}\right]P_{H_2O}} \qquad (2)$$

where

$$\left[V_O^{\cdot\cdot}\right] = \frac{1}{2}\left([M'] - \left[OH_O^{\cdot}\right]\right) \qquad (3)$$

In its "rest state," the protonic species resides on an oxygen ion, to be precise *within* the oxygen ion, since the ionic radius of O^{2-} is 1.40 Å, while that of OH^- is 1.37 Å (both values refer to sixfold coordination of these species). To enable ionic conduction, the hydrogen must be able to hop from one oxygen ion to another.

The requirements for a solid to be an HTPC can be summarized as follows:

- It must be an oxide (all systems known so far are oxides).
- It must contain oxygen vacancies, by nature or by doping.
- It must have the right chemical properties to favor the incorporation of water molecules.
- It must permit the momentary breaking of O–H bonds, if the protons are going to be mobile.
- If it is to be used as an electrolyte, it should not have predominant electronic conductivity.

The requirement for oxygen vacancies is strong, since without the reaction described by (Eq. 1), the $OH_O^{\cdot}$ species cannot form. Usually, the vacancies are created by doping with an element of valence lower than that of the host element. Perovskites (Fig. 2) are a structure type in which high temperature protonic conduction is commonly observed. Perovskites have two types of cation site: a larger 12-coordinated site (A) and a smaller 6-coordinated site (B). An example of a perovskite doped on the B-site would be $BaZr_{1-y}Y_yO_{-y/2}$. If the oxygen vacancies can be hydrated, as described above, the first three criteria for an HTPC will have been fulfilled.

Perovskites such as $BaZrO_3$ and $SrCeO_3$, doped as above, are able to absorb a quantity of water vapor, while others such as $CaTiO_3$ and $SrTiO_3$, are less able to do so. The difference in the ease of hydration has been linked to the basicity of the elements constituting the oxide [1]. Alternatively, the electronegativity has been implicated. More specifically, a correlation has been found between the standard enthalpy of hydration and the difference in electronegativity between the A-site and B-site elements in the perovskite (Fig. 3) [8]. The open points are from reference [8]; the solid points are for $BaCe_{0.9-x}Zr_xY_{0.1}O_{3-\delta}$ (BCZY) [9].
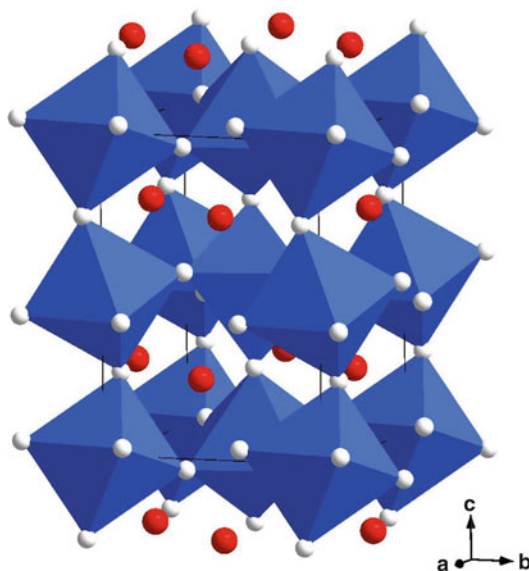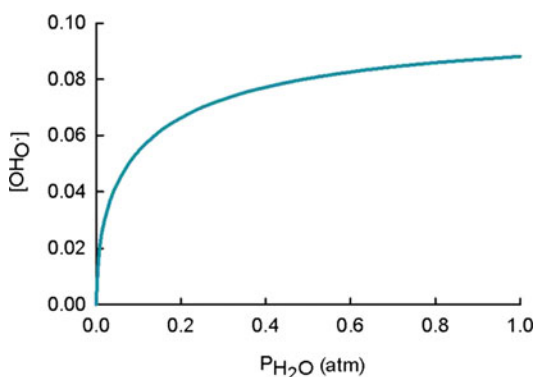

Perovskite Proton Conductor, Fig. 2 Structure of $SrCeO_3$, a typical perovskite proton conductor when doped with a trivalent element on the Ce site. The spheres represent the A-cation, Sr, while the octahedra have the B-cation, Ce at the center, and oxygen at the apices. A strong distortion from the cubic structure is visible the structure is shown in the *Pbnm* setting
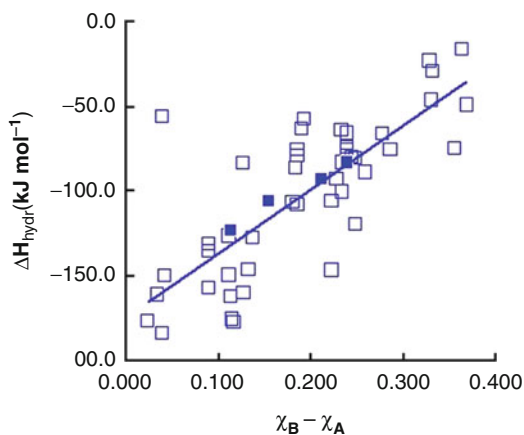
Perovskite Proton Conductor, Fig. 3 Correlation between standard enthalpy of hydration and the electronegativity difference of the A- and B-site elements in the perovskite (Fig. 3). The open points are tabulated by Norby et al. [8], while the solid points are for $BaCe_{0.9-x}Zr_xY_{0.1}O_{3-\delta}$ (BCZY) [9]

A corresponding plot of the standard entropy (not shown) displays no clear trend, suggesting that the entropy is determined by the conversion of the gaseous water molecules to solid species, rather than by which solid they enter into. The enthalpy and entropy of hydration, together with the temperature, determine the equilibrium constant of the reaction. For $\chi_{B}-\chi_{A} = 0.2$, midway in the plot, values of $\Delta H = -100 \, kJ \cdot mol^{-1}$ and $\Delta S = -110 \, J \cdot mol^{-1} \cdot K^{-1}$ are interpolated, giving an equilibrium constant K_W of 1.31 for 873 K. Figure 4 shows the hydration isotherm for this value of K_W.


Perovskite Proton Conductor, Fig. 4 Concentration of protonic carriers as a function of partial pressure of water vapor for an oxide with an equilibrium constant K_W of 1.31 (Eq. 2). The plot is also called a hydration isotherm

It is an unfortunate fact of chemistry that greater basicity implies greater affinity for CO_2, and this is one of the main disadvantages of the perovskite class of proton conductors. The problem is particularly acute at lower temperatures, which, ironically, is the range that can benefit most from perovskite proton conductors (the temperature range of 700 °C and above is already well served by oxide ion conductors). For this reason, researchers, especially at University of Oslo, believe that alternatives to perovskite systems are a *sine qua non* for cells that operate reliably in the presence of hydrocarbons. Forgoing the highly electropositive elements Sr and Ba and opting for La, compounds such as $LaNbO_4$ and $LaTaO_4$ are obtained, which are fully stable to CO_2 [10] These compounds require doping (usually Ca) and have low protonic conductivity (Fig. 5), while another, La_6WO_{12} does not require doping and has higher conductivity [11]. On the downside, the tungstate's reactivity with NiO presents problems for the fabrication of fuel cell anodes in the conventional way.

Mechanism of Transport

The transport of protons occurs, as stated earlier, by a hopping mechanism. This can be modelled using large collections of atoms and applying

Perovskite Proton Conductor, Fig. 5 Ionic conductivity (predominantly protonic) of selected HTPCs at 800 °C (various sources)
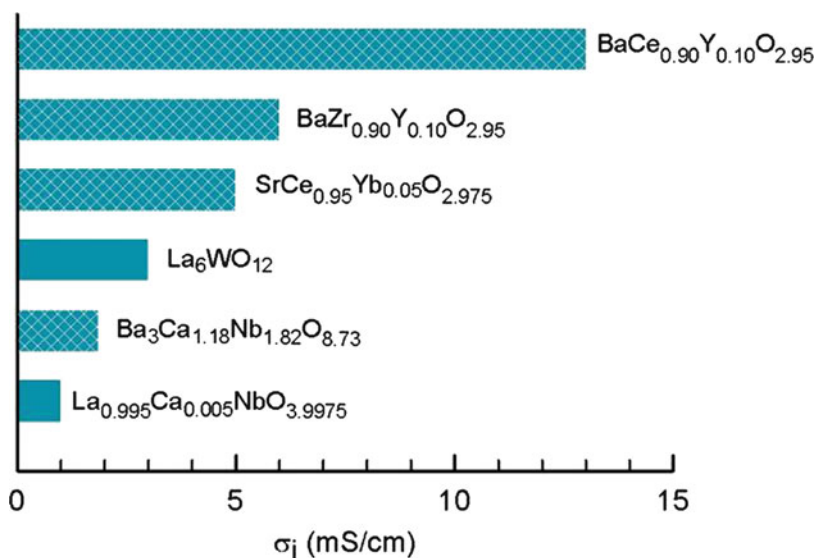
experimentally determined interatomic potentials. Alternatively, the lattice can be modelled by quantum mechanical techniques, which do not require interatomic potentials as inputs, but are computationally more demanding. Simulations of this type demonstrate that the proton hopping is facilitated by vibrations of the oxygen ions; this leads to the counterintuitive conclusion that longer B-cation oxygen bonds lead to lower activation energies for transport – in line with experimental results. Molecular dynamics studies have followed the path of a single proton in the lattice of $BaCeO_3$ for a duration of *ca.* 100 ps, revealing two kinds of motion: fast rotation and slower transport from one oxygen to another [12].

Density Functional Theory (DFT) methods allow the ab initio calculation [13] of the energy of both molecules and lattices. By minimizing the energy, the positions of all atoms can be obtained and the paths of ions can be traced. These methods have opened a new window onto the process of proton transport in oxides. For example, a recent study has shown that, for $SrTiO_3$, when a proton is introduced into a lattice already containing another proton, it experiences an energy minimum at a short distance from the original species [14]. In other words, an attractive force arises that leads to defect pairing, despite the existing electrostatic repulsion between the two species. The experimental test of this prediction and its implications for hydration thermodynamics and conduction mechanisms would be promising areas of research.

Minority Conduction Processes

Considering (Eq. 1), it is apparent that the concentrations of oxide ion vacancies and hydroxyls are in competition and that the concentration of $OH_O^\bullet$ cannot exceed that of the dopant. When other point defects, namely, electrons (e') and holes ($h_i^\bullet$), are allowed, the following electroneutrality condition is obtained:

$$2\left[V_O^{\bullet\bullet}\right] + \left[OH_O^\bullet\right] + \left[h_i^\bullet\right] - [e'] - [M'_B] = 0 \quad (4)$$
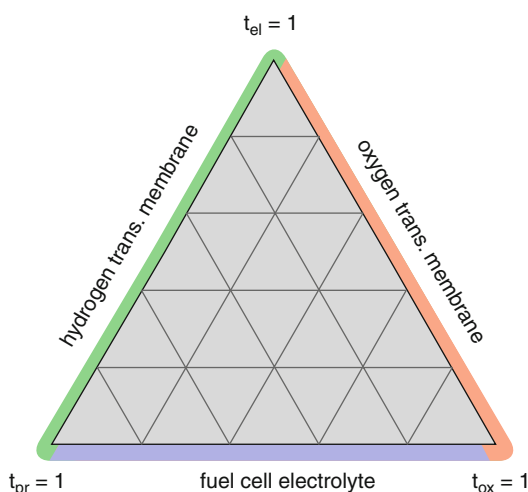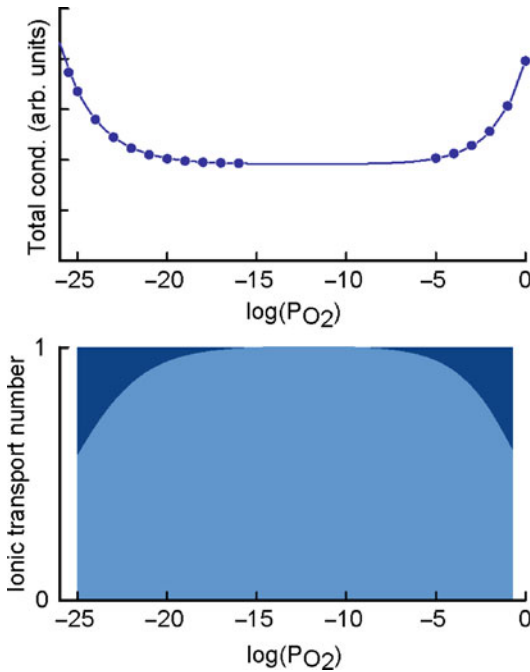

Perovskite Proton Conductor, Fig. 6 Diagram showing the possible ionic transport numbers for oxide ions, protons, and electron holes in a HTPC, following the relation: $t_{ox} + t_H + t_h = 1$. The preferred regimes for three types of function are shown in the figure

The conductivities due to each of these defects are determined by their concentrations multiplied by their mobilities. As a result of the electron–hole equilibrium, these defects cannot both be present in high concentration at the same time. Therefore, perovskite proton conductors normally display protonic, oxide ion and one type of electronic conductivity. For an HTPC in oxidizing conditions the main defects are $V_O^{\bullet\bullet}$, $OH_O^\bullet$, and $h_i^\bullet$. The situation can be visualized in the diagram of Fig. 6, which indicates the domains favorable for applications in fuel cell electrolytes and hydrogen transport membranes. The domain for oxygen transport membranes (i.e., no proton conduction) is included for the sake of completeness.

Even though perovskite proton conductors are selected for their protonic conductivity, possessing a minority electronic conductivity component is not necessarily a disadvantage. Figure 7a shows a plot of the total conductivity versus the oxygen partial pressure (P_{O2}) on a logarithmic scale. The curve follows an equation of the type:

$$\sigma_{tot} = \sigma_i + \sigma_p^\circ \cdot P_{O_2}{}^n + \sigma_n^\circ \cdot P_{O_2}{}^n \quad (5)$$
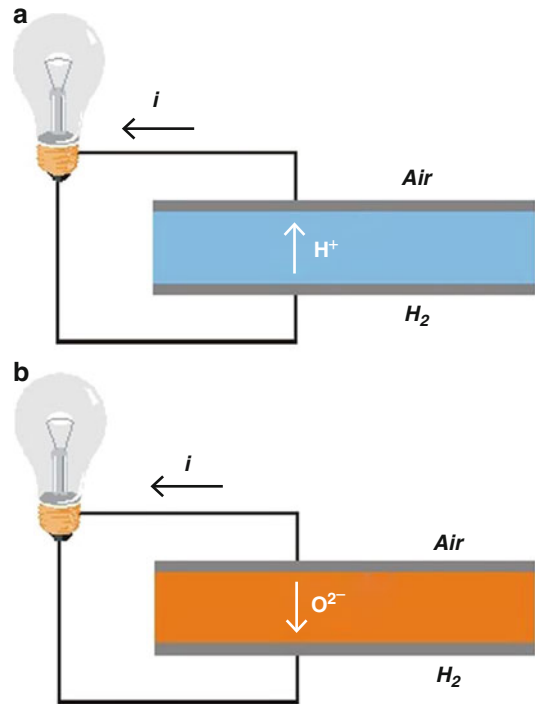
Perovskite Proton Conductor, Fig. 7 Two transport properties for a typical HTPC, plotted versus the logarithm of oxygen partial pressure (P_{O2}). (**a**) Total conductivity (**b**) Ionic transport number

Perovskite Proton Conductor, Fig. 8 Schematic diagram of two types of H_2/O_2 fuel cells: (**a**) PCFC based on high temperature proton conductor (**b**) SOFC, based on an oxide ion conductor

In this equation, σ_i is the ionic conductivity, assumed to be independent of P_{O2}, while σ_p° and σ_n° are parameters describing the other conductivity components at a P_{O2} of 1 atm [15]. In Fig. 7b, the ionic transport number σ_i/σ_{tot} is plotted on the same logarithmic scale. In a fuel cell, for example, an H_2/O_2 cell, the emf is dependent on the mean ionic transport number. In Fig. 7b, the mean ionic transport number is the area ratio of the light colored block to the whole block. As a result, partial electronic conductivity limited to the high and low P_{O2} regions is not a problem. This is also observed in practice, where H_2/O_2 or H_2/air cells based on perovskite proton conductors give open circuit voltages within a few percent of the theoretical values [16].

Future Directions

In the above, we have not specified whether the ionic conduction was via a protonic or an oxide ion mechanism – both allow the operation of a fuel cell. There is, however, a crucial difference between the two types of cell, illustrated in Fig. 8. In the proton conducting fuel cell (PCFC), the water vapor is evolved at the cathode, while in the solid-oxide fuel cell (SOFC) with oxide ion-conducting electrolyte, it is evolved at the anode. For a PCFC, the water vapor can be easily diluted by an excess of air, which also removes waste heat. In an SOFC, the fuel is recirculated to condense the water vapor, leading to a more complex auxiliary plant.

In the first years of work on perovskite proton conductors, many researchers, including the author, assumed that PCFCs would be useful only in connection with hydrogen fuel cells, while with hydrocarbon fuels, SOFCs would be the only choice. However, work by Coors and coworkers has demonstrated that perovskite proton conductors with minority oxide ion conduction can sustain stable currents for long

periods with dry hydrocarbon fuels [17]. It appears that such cells work by internal reforming the hydrocarbon, mediated by oxygen transport. This is an interesting and promising area for future research, both applied and theoretical. Another area of interest is the PCFC cathode, for which there are unanswered questions concerning reaction mechanisms, for example, the role – if any – of oxide ion conduction in the cathode material. Cathodes for PCFCs also present material challenges in terms of transport properties and stability to high partial pressures of water vapor [18, 19].

The range of transport properties and the applications are likely to keep the subject of perovskite proton conductors in the spotlight for many years to come.

Cross-References

References

1. Kreuer K-D (2003) Proton-conducting oxides. Annu Rev Mater Res 33:33–359
2. Malavasi L, Fischer CAJ, Islam MS (2010) Oxide-ion and proton conducting electrolyte materials for clean energy applications: structural and mechanistic features. Chem Soc Rev 39:4370–4387
3. Fabbri E, Pergolesi D, Traversa E (2010) Materials challenges toward proton-conducting oxide fuel cells: a critical review. Chem Soc Rev 39:4366–4369
4. Athanassiou C, Pekridis G, Kaklidis N, Kalimeri K, Vartzoka S, Marnellos G (2007) Hydrogen production in solid electrolyte membrane reactors (SEMRs). Int J Hydrog Energy 32(1):38–54
5. Iwahara H (1996) Proton conducting ceramics and their applications. Solid State Ion 86–88(1):9–15
6. Jensen J, Kleitz M (eds) (1982) Solid state protonic conductors I: Danish-French workshop on solid state materials for low to medium temperature fuel cells and monitors, with emphasis on proton conductors, Paris, France, 8–11 Dec 1981. Odense, Denmark
7. Iwahara H, Esaka T, Uchida H, Maeda N (1981) Proton conduction in sintered oxides and its application to steam electrolysis for hydrogen production. Solid State Ion 3/4:359
8. Norby T, Widerøe M, Glöckner R, Larring Y (2004) Hydrogen in oxides. Dalton Trans 2004:3012–3018
9. Ricote S, Bonanos N, Caboche G (2009) Water vapor solubility and conductivity study of the proton conductor $BaCe_{0.9-x}Zr_xY_{0.1}O_{3-\delta}$. Solid State Ion 180(14–16):990–997
10. Norby T, Haugsrud R (2006) Proton conduction in rare-earth ortho-niobates and ortho-tantalates. Nat Mater 5:193–196
11. Haugsrud R, Kjølseth C (2008) Effects of protons and acceptor substitution on the electrical conductivity of La_6WO_{12}. J Phys Chem Solids 69(7):1758–1765
12. Münch W, Seifert G, Kreuer K-D, Maier J (1996) A quantum molecular dynamics study of proton conduction phenomena in $BaCeO_3$. Solid State Ion 86–88:647–652
13. See for example Wikipedia, "Ab initio quantum chemistry methods"
14. Bork N, Bonanos N, Rossmeisl J, Vegge T (2011) Thermodynamic and kinetic properties of H defect pairs in $SrTiO_3$ from density functional theory. Phys Chem Chem Phys 13:15256–15263
15. Bonanos N (2001) Oxide-based protonic conductors, point defects and transport properties. Solid State Ion 145:265–274
16. Bonanos N, Knight KS, Ellis B (1995) Perovskite solid electrolytes: structure, transport properties and fuel cell applications. Solid State Ion 79:161–170
17. Coors WG (2004) Steam reforming and water-gas shift by steam permeation in a protonic ceramic fuel cell. J Electrochem Soc 51(7):A994
18. He F, Wu T, Peng R, Xia C (2009) Cathode reaction models and performance analysis of $Sm_{0.5}Sr_{0.5}CoO_{3-\delta}$–$BaCe_{0.8}Sm_{0.2}O_{3-\delta}$ composite cathode for solid oxide fuel cells with proton conducting electrolyte. J Power Sources 194:263–268
19. Ricote S, Bonanos N, Rørvik PM, Haavik C (2012) Microstr./perform. of $La_{0.58}Sr_{0.4}Co_{0.2}Fe_{0.8}O_{3-\delta}$ cathodes deposited on $BaCe_{0.2}Zr_{0.7}Y_{0.1}O_{3-\delta}$ by infiltration and spray pyrolysis. J Power Sources 209:172–179

pH Electrodes - Industrial, Medical, and Other Applications

Winfried Vonau
Kurt-Schwabe-Institut fuer Mess- und Sensortechnik e.V. Meinsberg, Waldheim, Germany

Introduction

The pH value of a solution is a measure of the activity of hydronium ions ($H_3O^+ \rightleftharpoons H^+ + H_2O$) in the solution and as such it is a measure of the acidity or basicity of that medium. On the one hand pH stands for power of hydrogen (H); on the other hand, the term pH is derived from p, the mathematical symbol of the negative logarithm. The pH value is often simply referred to as concentration of hydrogen ions. Acids and bases are connected with free hydronium and hydroxyl ions, respectively. The relationship between hydronium and hydroxyl ions in a given solution is constant for a given set of conditions and one can be determined by knowing the other. The usual range of pH values encountered is between 0 and 14, with 0 being the value for concentrated acids, 7 being the value for pure water, and 14 being the value for concentrated lyes. It is possible to get pH values <0 (e.g., 10 M HCl) and >14 (e.g., 10 M NaOH). In Fig. 1 examples of pH values of a selection of substances are given.

There is a wide variety of applications for pH measurement. For example, pH measurement and control is the key to the successful purification of drinking water, manufacturing of sugar, sewage treatment, food processing, electroplating, the effectiveness and safety of medicines, cosmetics, etc. Plants require the soil to be within a certain pH range in order to grow properly; animals or humans can sicken or die if their blood pH level is not within the correct limits.

Important Mathematical Correlations and Calculations

Definitions:

$$pH = -lg\ a_{H_3O^+} \qquad (1)$$

$a_{H_3O^+} \cdots$ activity of hydronium ions

$$pOH = pK_w - pH \qquad (2)$$

$K_w \cdots$ water ion product ($10^{-14} mol^2\ L^{-2}$) at 25 °C

For the calculation of pH values, it must be distinguished between strong and weak acid [HA(nion)] and base [C(ation)OH] solutions. Strong acids and bases are almost completely dissociated in water. Hydrochloric acid (HCl) is a good example of a strong acid and sodium hydroxide (NaOH) of a strong base.

For instance, for a 0.01 M solution of HCl, the activity of hydronium ions can be taken as 0.01 M and according to Eq. 1 the pH = 2.

For weak acids and bases, the situation is more complicated. Here, the acid and base dissociation constants ($K_{a(b)}$ or $pK_{a(b)}$ values) have to be considered. For such media there is no complete dissociation, but its degree is given by the equilibrium, Eq. 3. In the following, for reasons of simplification H_3O^+ is replaced by H^+ and [i] stands for the activity of a component i:

$$K_a = \frac{[H^+][A^-]}{[HA]} \qquad (3)$$

Using the nominal concentration of the acid, C_a, which is equivalent to the amount of acid that is initially added to a solution
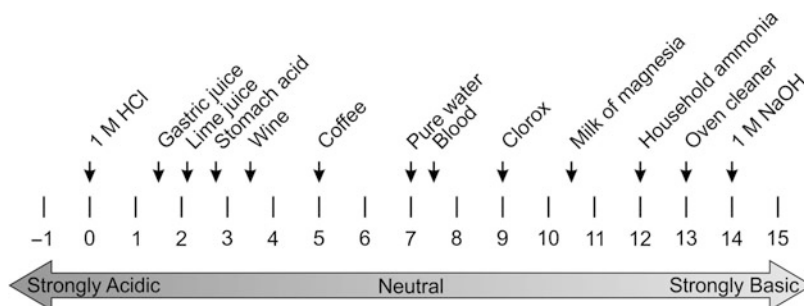
$$C_a = [HA] + [A^-] \qquad (4)$$

for a strong acid which is completely dissociated the term [HA] can be neglected:

$$C_a = [A^-] \qquad (5)$$

In the case of a weak acid, HA is not completely dissociated, and thus the assumption

pH Electrodes - Industrial, Medical, and Other Applications, Fig. 1 pH values of different substances at 25 °C [1]

$[A^-] >> [HA]$ is not valid. Therefore the full mass balance Eq. 4 must be taken.

If the acid is not very diluted and not extremely weak, ions from water dissociation can be neglected; Eq. 6 can be formulated:

$$[H^+] \approx [A^-] \qquad (6)$$

There are three equations with three unknowns, ($[H^+]$, $[A^-]$, and $[HA]$), which need to be solved for $[H^+]$. The mass balance equation allows to solve it for $[HA]$ in terms of $[H^+]$.

Rearrangements of above equations lead to Eqs. 7 and 8 resulting finally in Eq. 9 (with the positive square root) giving the expression for the H$^+$ activity in weak acidic solutions:

$$K_a = \frac{[H^+]^2}{C_a - [H^+]} \qquad (7)$$

$$[H^+]^2 + K_a[H^+] - K_a C_a = 0 \qquad (8)$$

$$[H^+] = \frac{-K_a + \sqrt{K_a^2 + 4K_a C_a}}{2} \qquad (9)$$

pH calculations in real media require a lot of knowledge of the composition of these systems and the ambient conditions (temperature, pressure, additional components, etc.). Unfortunately, this task is solvable only with additional effort in mathematics, where to a lot of literature is available, e.g., [2]. In most cases, a simple arithmetic determination of pH values of complex systems is not possible. For this reason it is necessary to have practicable measuring methods at one's disposal.

pH Measurement

In Fig. 2 the current procedures for pH determination are shown. As to be seen, electrochemical methods, which following solely will be reported in greater detail, dominate.

The measurement is executed potentiometrically using several pH and reference electrodes. The relation is based on the idealized Eq. 10:

$$E \cdots E^\ominus - (RT/F)\ln [H^+] \qquad (10)$$

$E^\ominus \ldots$ standard electrochemical cell potential (voltage)

$R \ldots$ gas constant

$T \ldots$ temperature in Kelvins

$F \ldots$ Faraday constant

Depending on the measurement task, indicator and reference electrode are chosen. For a long time, the utilization of hydrogen electrodes is known as a possibility to measure pH values. A hydrogen electrode can be made by coating a platinum electrode with a fresh layer of platinum black and passing a flow of hydrogen gas over it. The platinum-black coating allows the adsorption of hydrogen species onto the electrode. When dipped into a solution containing hydronium ions, according to Eq. 11 at $pH_2 = 101.3$ kPa in the hydrogen electrode turns up a potential which is proportional to the H$^+$ activity. Hydrogen electrodes are mainly used under standard conditions as reference electrodes (see also subchapters Potentiometry and Reference electrodes) and in combination with these or with any other reference electrodes as indicator electrodes for the pH measurement:
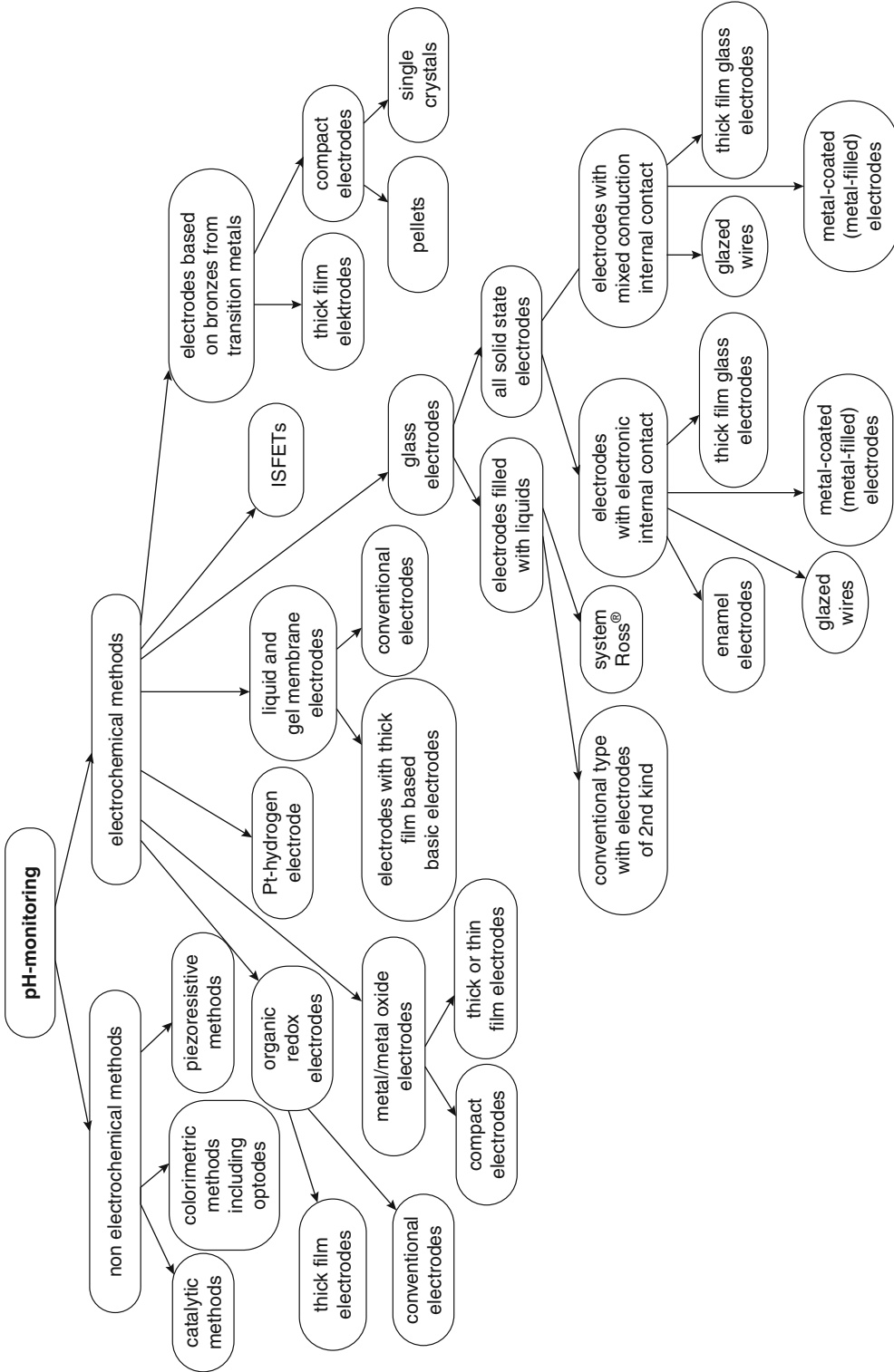
pH Electrodes - Industrial, Medical, and Other Applications, Fig. 2 Experimental methods to measure pH values
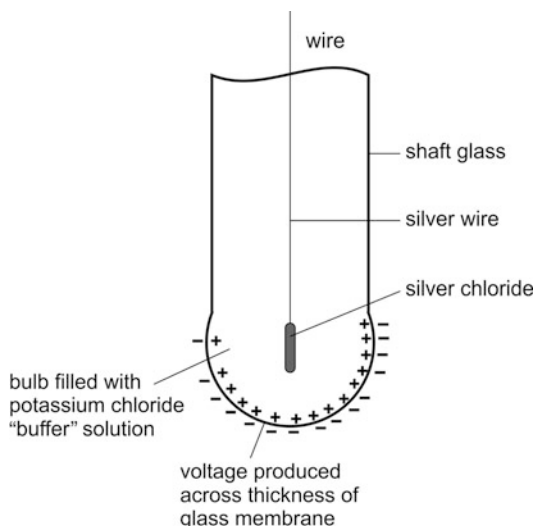
pH Electrodes - Industrial, Medical, and Other Applications, Fig. 3 Scheme of a glass electrode

$$E = E^{\ominus} + (RT/F)\ln [H^+] \\ - (RT/2F)\ln pH_2 \qquad (11)$$

Due to their ungainliness, today hydrogen electrodes are only seldom in use, e.g., for the calibration of precision buffers. New concepts are focused on the use of miniaturized hydrogen electrodes with internal hydrogen source and gas-diffusion electrodes consisting of Pd and Pt to be applied for food quality control and for measurements in fluoride-containing solutions [3].

In most cases, pH glass electrodes serve as pH selective half-cell. This kind of electrode was introduced by Cremer [4] and is shown in principle in Fig. 3.

Main components are electrode glass, internal electrolytic solution, and internal reference electrode. Electrode glasses normally have a thickness of about 0.1–0.2 mm and their composition often is among the best-kept secrets of the manufacturers of the electrodes. However, the main components, e.g., SiO_2, Li_2O, Na_2O, or CaO, are known [5]. In most cases and in correspondence with the pH meter, the internal solution is a buffer of pH = 7 into which a silver/silver chloride electrode is immersed. A special type of pH glass electrodes uses homogeneous redox systems instead of electrodes of second kind as internal reference. Such electrodes deliver a better response behavior during temperature changes. As redox system is to be used for this purpose, $I_3^-/3I^-$ has been recommended in [6]. At $c_{I_3^-}/c_{I^-}^3 \approx 5*10^{-5}$ the potential between 0 and 70 °C changes by a maximum of 1 mV.

While in the past glass electrodes have been used only in a limited temperature range, an extensive development work had been done to enhance the working temperature range of the electrodes from −25 to 130 °C. However, there are no such glass electrodes, which cover the entire range of temperature. The traditional glass electrode with an internal liquid reference system, as all other electrodes of this kind, exhibits some drawbacks: position dependence when the electrodes are stored or used, pressure and temperature dependence, mechanical fragility, and several limitations concerning the miniaturization.

For these reasons, it is a goal to develop all-solid-state electrodes for pH measurement. A main problem to be solved was to connect the ionically conducting glass with an electronic conductor. Although the current flow is very low due to the high resistance of the glass, a reversible electrochemical reaction should take place at the phase boundary by transferring cations between the phases. The possibility to fabricate all-solid-state glass electrodes is in principle already mentioned by Kratz [7]. According to the electrochemical requirements, it is not sufficient to use metals instead of buffer solutions as internal reference electrodes. So, e.g., it was tried to coat bright platinum wires with pH-electrode glass. In the resulting system the electrochemical reaction was blocked. Improved approaches were carried out by arranging a silver plate on the inside of glass membranes, by filling of glass electrode bodies with mercury or several amalgams or by solidifying melts of alloys with low melting points within glass electrode bodies. Due to the solution of sodium or lithium and cadmium in the mercury or in the metal layer, the electrode reactions can become reversible. It was also practiced to use materials having both electronic and ionic

conductivity as an internal reference system (interlayer of glass with mixed conductivity, tungsten bronze as a mixed conducting material, modified carbon fleeces, sandwich of pH-sensitive glass, and mixed conducting glass). It has been shown that the measuring behavior of such electrodes (a summarizing report is given in [8]), due to an enhanced reversibility, is much better than that of electrodes with directly metallized pH glass membranes.

Beside the functional optimization of the electrodes, also a further development of manufacturing technology for their production is a continuous challenge. Corresponding to the new knowledge about all-solid-state electrodes planar glass electrodes in thick film technology were

pH Electrodes - Industrial, Medical, and Other Applications, Fig. 4 Thick film pH glass electrode

developed, which e.g., are applicable as insertion electrode in meat or other solid foods (see Fig. 4).

Because of the good correlation of the coefficients of thermal expansion between pH-electrode glasses and steel, the last mentioned substance is a predestinated substrate material for thick film glass electrodes. This fact also causes the availability of pH enamel electrodes [9], which among others were developed for use in the severe, highly corrosive operating environments of agitated glassed steel reactors. It can be placed inside the chemical reactor and withstands the rigors of heat, pressure, and dynamic agitation to provide continuous pH measurement. No protective cage is needed or used. The pH probe is suited to situations where slurries are encountered, providing years of service with minimum maintenance. Typical applications include agitated reactors, pipelines with high flow rates, erosive and highly corrosive slurries, limestone recirculation lines, pulp and paper applications, pharmaceutical production, paint pigment manufacturing, fermentation, and neutralization processes. Sometimes, a constant concentration of one ionic component in the analyzed medium is given (e.g., Na^+). Then a second Na^+-sensitive enamel electrode can be used as external reference electrode as shown in Fig. 5.

There are a lot of other, partly niche applications where glass electrodes according to the national and international standards are not perfectly suited. Planar technologies open up opportunities for new multisensor arrays including pH electrodes. Depending on the special application, besides glass membrane electrodes, also other types of pH electrodes play a role as separate probe and as well as a part of multisensor systems.

Especially for medical and biotechnological applications miniaturized planar pH electrodes are needed. Here metal/metal oxide electrodes and electrodes based on ion-selective field effect

pH Electrodes - Industrial, Medical, and Other Applications, Fig. 5 All-solid-state enamel pH combination electrode

reference enamel   pH enamel   connector
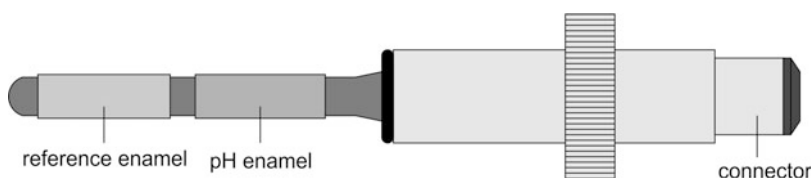
transistors (ISFET) are used. An example for the first mentioned type is Ru/RuO$_2$-electrodes that can be fabricated in thin as well as in thick film technology. They can for instance be used for the

pH Electrodes - Industrial, Medical, and Other Applications, Fig. 6 ISFET pH probes for measurements in stomatology (**a**) and gynecology (**b**)

simultaneous in vitro measurement of metabolic, morphologic, and electrophysiologic parameters of living cells and tissue. pH-ISFET electrodes for the first time were mentioned by Bergveld [10]. In Fig. 6 an example for the usage of such type of electrodes as single probe is given. Figure 7 shows the layout of a multielectrode array including ISFETs for the pH determination.

For several applications in pH measurement older electrode concepts are still in use. For reasons of cost probes for the determination of pH values in gastroenterology (see Fig. 8) often consist of antimony electrodes with diameters <3 mm [12]. Their pH function as an electrode of the second kind is given by Eq. 12 which is formulated for a temperature of 25 °C:
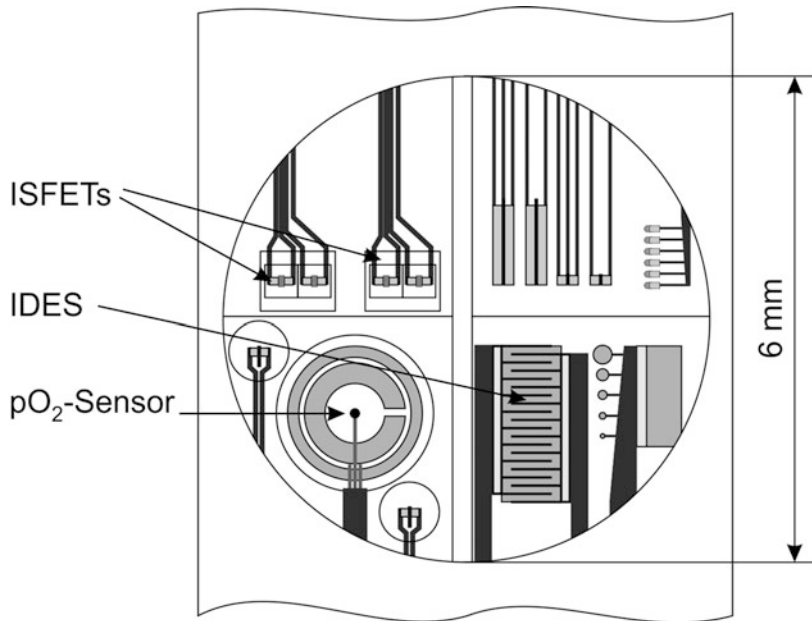
pH Electrodes - Industrial, Medical, and Other Applications, Fig. 7 Layout of a multiparametric silicon sensor chip including pH ISFETs [11]
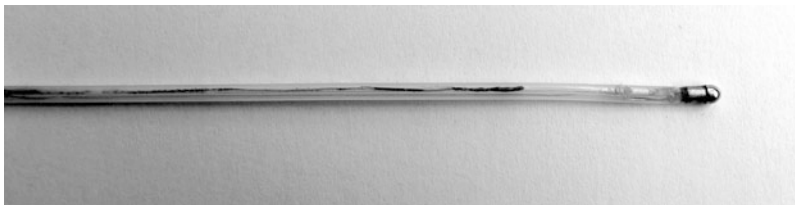
pH Electrodes - Industrial, Medical, and Other Applications, Fig. 8 Antimony combination electrode with silver chloride reference electrode for pH measurements in the gastroenterology

$$E = E_{(Sb)}^{\ominus} + \frac{0.059}{3}\ln K_{L_{Sb(OH)_3}} + 0.059*14 - 0.059\ pH \tag{12}$$

The equilibrium of redox reactions where hydronium ions are taking part is dependent on the pH value. A favored redox system for pH measurements is the equilibrium between quinone and hydroquinone. The quinhydrone electrode based thereon [13] was the most commonly used device for the electrochemical pH deter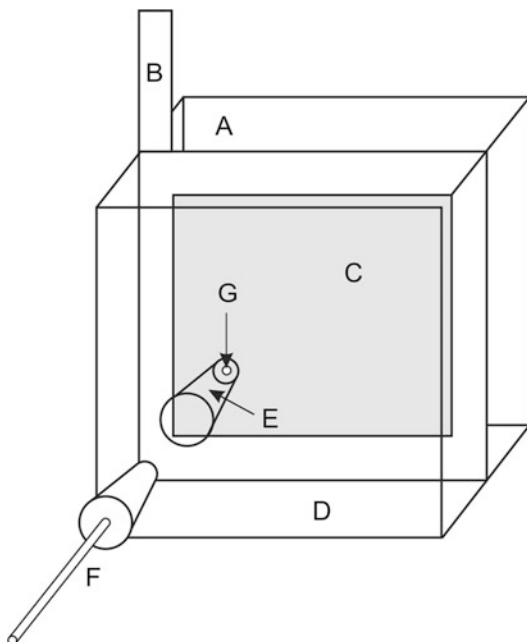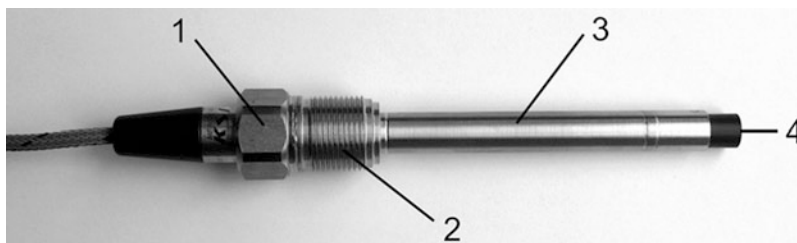mination in the laboratory until the introduction of the glass electrode. Here, the redox voltage is measured with a conventional reference and a blank platinum electrode. Due to the rapid and reproducible establishment of its chain voltage, this electrode possesses importance for several applications, e.g., for measurements in fluoride-containing media. They were advanced in recent years as pH thick film electrodes, too and among others, qualified for a usage in flow-through mode (see Fig. 9).

For measurements in emulsions, alkaline solutions, and solutions with only moderate concentrations of oxidizing or reducing agents, the well-known quinhydrone electrode was further developed as solid composite electrode.

An electrode based on this conception is also available for flow injection potentiometry [13].

Independent of the kind of the used pH electrode, especially under extreme operational conditions, high demands are placed on the stability of the selective membranes, reinforcing materials and tightness of the electrode housing. In Fig. 10 in this connection, a pressure and temperature stable antimony electrode is shown for the use in geothermal applications or in water steam circle of power stations. In Fig. 11 a glass electrode for precision measurement in the deep sea is presented establishing a corresponding internal pressure in the inner core of the pH electrode.

pH Electrodes - Industrial, Medical, and Other Applications, Fig. 9 Scheme of the detector cell: *A* and *D* poly (methyl methacrylate) plates, *B* copper spacer frame, *C* pH-sensitive layer, *E* hole for FIA fitting, *F* FIA tube fittings, *G* hole through the sensitive material [14]

pH Electrodes - Industrial, Medical, and Other Applications, Fig. 10 pH electrode to be used under extreme application conditions. *1* ... electrode head, *2* ... thread M 22 × 1.5 mm, *3* ... stainless steel (or titanium) bushing (inner diameter: 12 mm), *4* ... antimony electrode

pH Electrodes - Industrial, Medical, and Other Applications, Fig. 11 Pressure stable pH glass electrode in the deep sea
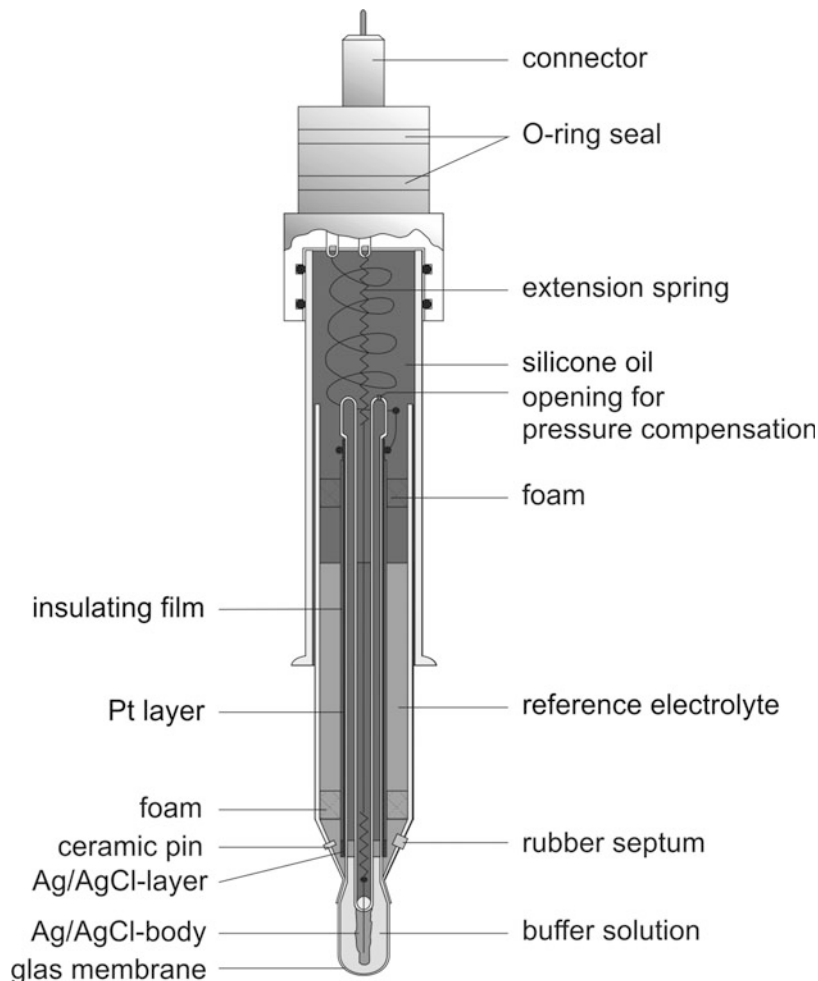
Future Directions

Because of the higher-than-average importance of pH electrodes in measurement technology, R&D in this field will be necessary also in the future. Major tasks will be improving selectivity and reducing cross sensitivities, respectively; further miniaturization while maintaining electrode performance of common electrodes; expansion of the area of application concerning pressure and temperature; reducing calibration efforts in connection with increasing the lifetime; inexpensive production using new fabrication methods; and further integration in multisensor systems.

Cross-References

▶ Potentiometry
▶ Reference Electrodes
▶ Sensors

References

1. Shipman J, Wilson J (1990) An introduction to physical science. D. C. Heath, Boston
2. Schwabe K (1969) pH-Fibel. Deutscher Verlag für Grundstoffindustrie, Leipzig
3. Vonau W, Oelßner W, Schwarz J, Hörig A, Kohnke HJ, Heller G, Kurzenknabe (2011) German Patent DE 10 2011 113 941

4. Cremer M (1906) Über die Ursachen der elektromagnetischen Eigenschaften der Gewebe, zugleich ein Beitrag zur Lehre von den polyphasischen Elektrolytketten. Z Biol 46:562–608
5. Solokow AI, Passinski AH (1932) Über Glaselektroden. Z Phys Chem A 160:366–377
6. Ross JW (1982) Potentiometrische Elektrode. German Patent, DE 146 066
7. Kratz L (1950) Die Glaselektrode und ihre Anwendungen. Dietrich Steinkopff, Frankfurt
8. Vonau W, Guth U (2006) pH monitoring: a review. J Solid State Electrochem 10(9):746–752
9. Emmerich B (1978) Die Emailelektrode, eine neue Lösung zur pH-Messung im Betrieb. Regelungstechn. Praxis 20:313
10. Bergveld P (1972) Development, operation and application of the ion-selective field-effect transistor as a tool for electrophysiology. IEEE Trans Biomed Eng 19:340–351
11. Brischwein M, Motrescu ER, Otto AM, Cabala E, Grothe H, Wolf B (2003) Functional cellular assays with multiparametric silicon sensor chips. Lab Chip 3(4):234–240
12. Vandenplas Y, Badriul H, Verghote M, Hauser B, Kaufman L (2004) Glass and antimony electrodes for oesophageal pH monitoring in distressed infants: how different are they? Eur J Gastroenterol Hepatol 16:1325–1330
13. Biilmann ME (1921) Sur l′hydrogenation des quinhydrones. Ann Chim 15:109–157
14. Kahlert H, Pörksen JR, Behnert J, Scholz F (2005) FIA acid-base titration with a new flow-through PH detector. Anal Bioanal Chem 382:1981–1986

Photocatalyst

Bunsho Ohtani
Catalysis Research Center, Hokkaido University, Sapporo, Hokkaido, Japan

Definition

Photocatalysts are materials that induce photocatalytic reaction under photoirradiation. A general definition of photocatalysis, a conceptual name of photocatalytic reactions, is a chemical reaction induced by photoabsorption of a solid material, or "photocatalyst," which remains unchanged during the reaction. Therefore, "photocatalyst" should act catalytically, i.e., without change, under light. Although molecules or metal complexes dissolved in solution or in the gas phase, not solid materials, can drive such photoinduced reactions without change during the reactions, they are called "photosensitizer" but not "photocatalyst." photoinduced reactions are, in principle, initiated by photoabsorption, i.e., excitation of electrons in a material, followed by electron transfer from/to a reaction substrate. The photoexcited electrons can reduce a substrate adsorbed on the surface of a photocatalyst, and positive holes, electron deficiencies, can oxidize an adsorbed substrate, if the electronic levels of photoexcited electrons and positive holes are higher and lower than the redox levels of substrates, respectively. This is one of the necessary conditions for photocatalysis and will be discussed later.

For photocatalysts, there are several modes of photoexcitation as shown below.

Band-Gap Excitation

For conventional photocatalysts such as titanium (IV) oxide (TiO_2; titania), band-gap excitation occurs when irradiated. In a schematic representation of the electronic structures of semiconducting (or insulating) materials, a band model, an electron in an electron-filled valence band (VB) is excited by photoabsorption to a vacant conduction band (CB), which is separated by a band gap (a forbidden band), from the VB, leaving a positive hole in the VB. An important point is that photoabsorption and electron-positive hole generation are inextricably linked; a VB electron is not excited after photoabsorption. These electrons and positive holes can induce reduction and oxidation, respectively, of chemical species adsorbed on the surface of a photocatalyst, unless they recombine with each other so as not to induce a redox reaction but to produce heat and/or photoemission. Such a mechanism accounts for the photocatalytic reactions of semiconducting (or insulating) materials absorbing photons by the bulk of materials.

Since light of energy greater than band gap can excite electrons in VB to CB, light of wavelength shorter than that corresponds to the band gap,

i.e., longer-wavelength limit for photoabsorption (photoexcitation) is fixed by the band structure of a photocatalyst. For metal oxides, it has been known that VB is mainly composed of O_{2p} orbitals and thereby the position (top) of VB is independent of the kind of metal, i.e., only the CB (bottom) position is changed depending on the kind of metal. Therefore, in order to narrow the band gap, i.e., to use light of longer wavelength, metal oxides having lower CB level should be used. Considering the VB top level seems enough low to oxidize most of organic/inorganic compounds, the band-gap narrowing for metal oxides leads to disadvantageous lowering of the CB bottom level.

Transition Between an Electronic Level and a Band

Photocatalysts that can use visible light included in sunlight and indoor light have been looked for since the conventional photocatalysts such as titania can absorb, i.e., be excited only by ultraviolet light. The strategy to utilize visible light in photocatalysis can be roughly divided into three categories. The first one is to use the semiconductor with a narrow band gap. Metal nitride or sulfides often have colors and are expected to work as photocatalysts under visible-light irradiation when used. However, they tend to be oxidized and possibly lose their photocatalytic activity. Then, it was proposed to raise the top of VB of stable metal oxides to reduce the band-gap energy by doping various elements as the second strategy. Many papers have reported the band-gap narrowing by doping nitrogen, carbon or sulfur, etc., to titania and the introduction of visible-light responsibility. Actually, shift of the photoabsorption spectrum to the longer-wavelength side is observed by doing a variety of elements. It has been suggested in the recent studies, however, that the electronic structure of such doped material was not an expected one; levels of doped elements are separated from the VB to form an independent sub-bands.

In recent studies, clusters of ions such as copper or iron and their oxide were deposited (grafted) to induce photoexcitation of electrons in VB of base metal oxide such as titania to the electronic level of these loaded clusters or electrons in the electronic level to CB, i.e., interfacial charge transfer. When the electronic states of the grafted clusters are located between the CB bottom and the VB top of titania, the interfacial charge transfer can be driven under visible-light irradiation, and a new photoabsorption band appears in a wavelength region longer than that for band-gap excitation.

Excitation Through Surface-Plasmon Resonance Absorption

Another example of visible light-driven reaction through non-band-gap excitation is a photocatalytic reaction that uses surface-plasmon resonance (SPR) absorption of small metal particles loaded on base metal oxides. For example, gold particles of the size of ten to several ten nanometers, presenting purplish red color by the SPR absorption, loaded on titania particles have been used for photocatalytic reactions under visible-light irradiation at the wavelength of ca. 600 nm. Based on the results that titania or a related material is necessary for this visible light-driven reaction and that SPR absorption cannot induce electronic excitation of electrons, the mechanism of this kind of reaction seems complicated and is now under discussion.

Thermodynamics

As thermodynamics says, if ΔG is negative ($\Delta G < 0$ as in the case, e.g., in oxidative decomposition of organic compounds under aerated conditions) and if ΔG is positive (D$G > 0$, as in the case, e.g., in splitting of water into hydrogen and oxygen), energy is released and stored, respectively. Therefore, if the standard electrode potential of the compound to be reduced by electrons is higher, i.e., more negative (cathodic), than that of the compound to be oxidized by positive holes, ΔG is positive, i.e., the reaction stores energy and vice versa. A notable point is that both situations, energy release and storage, are possible in photocatalysis, while thermal catalyses are limited to only reactions of negative ΔG, i.e., spontaneous reactions. The reason why photocatalysts can drive even

a reaction of positive ΔG, which does not proceed spontaneously, is that an overall redox reaction can proceed, even if its ΔG is positive, in a system in which reduction and oxidation steps are spatially or chemically separated; otherwise, the reaction between reduction and oxidation products proceeds to give no net products. Under these conditions, both partial Gibbs energy change for reactions of photoexcited electrons with oxidant (ΔG_e) and positive holes with reductant (ΔG_h) are required to be negative, i.e., reactions by photoexcited electrons and positive holes proceed spontaneously by photoexcitation. In other words, for the reaction through band-gap excitation, the CB bottom and VB top positions must be higher (more cathodic) and lower (more anodic) than standard electrode potentials of an electron acceptor (oxidant) and an electron donor (reductant), respectively, to make Gibbs energy change of both half reactions negative, as has often been pointed out as a necessary condition for photocatalysis.

Photocatalytic Activity

The widely used scientific term "activity" often appears in papers on photocatalysis as "photocatalytic activity." Although the author does not know who first started using this term in the field of photocatalysis, researchers in the field of conventional catalysis were using this term even before the 1980s, when photocatalysis studies had begun to be promoted by the famous work of the so-called Honda–Fujishima effect on photoelectrochemical decomposition of water into oxygen and hydrogen using a single-crystal titania electrode, as mentioned above. Most authors, including the present author, prefer to use the term "photocatalytic activity," but in almost all cases, the meaning seems to be the same as that of absolute or relative reaction rate. A possible reason why the term "photocatalytic activity" is preferably used is that the term may make readers think of "photocatalytic reaction rate" as a property or ability of a photocatalyst, i.e., photocatalysts have their own activity. On the other hand, "reaction rate" seems to be controlled by given reaction conditions including

a photocatalyst. In the field of conventional catalysis, "catalytic activity" has been used to show a property or performance of a catalyst, since an "active site," substantial or virtual, on a catalyst accounts for the catalytic reaction. The estimated reaction rate per active site can be called "catalytic activity." In a similar sense, the term "turnover frequency," i.e., number of turnovers per unit time of reaction, is sometimes used to show how many times one active site produces a reaction product(s) within unit time. On the contrary, it is clear that there are no active sites, as in the meaning used for conventional catalysis, in which rate of catalytic reaction is predominantly governed by the number or density of active sites, on a photocatalyst. The term "active site" is sometimes used for a photocatalytic reaction system with dispersed chemical species, e.g., metal complexes and atomically adsorbed species, on support materials. However, even in these cases, a photocatalytic reaction occurs only when the species absorb light, and therefore, species not irradiated cannot be active sites. A possible mechanism of photo induced reaction is that photoirradiation induces production of stable "active sites" that work as reaction centers of conventional catalytic reactions, though this is different from the common mechanism of photocatalysis by electron–positive hole pairs. Anyway, photocatalytic reaction rate strongly depends on various factors such as the irradiance of irradiated light that initiates a photocatalytic reaction. Considering that the dark (nonirradiated) side of a photocatalyst or suspension does not work for the photocatalytic reaction, the use of the term "active site" seems inappropriate.

Design of Active Photocatalysts

Since an ordinary photocatalysis is induced by photoexcited electrons and positive holes, rate of photocatalytic reaction must depend on photoirradiation irradiance (light flux) and efficiencies of both photoabsorption and electron–positive hole utilization. The efficiency of electron–positive hole utilization is called

quantum efficiency, i.e., the number (or rate) ratio of product(s) and absorbed photons, and even if quantum efficiency is high, the overall rate should be negligible when the photocatalyst does not absorb incident light. This is schematically represented as

$$[\text{Rate}/\text{mol s}^{-1}] = [\text{Irradiance}/\text{mol s}^{-1}] \\ \times [\text{Photoabsorption efficiency}] \\ \times [\text{Quantum efficiency}].$$

Since all of the parameters in this equation must be functions of light wavelength, the overall rate can be estimated by integration of a product of spectra of photoirradiation, photoabsorption, and quantum efficiencies. When we discuss activity of a photocatalyst, it seems reasonable to evaluate a product of photoabsorption and quantum efficiencies, i.e., apparent quantum efficiency. Assuming that quantum efficiency does not depend on the irradiation (absorption) irradiance, the actual reaction rate can be estimated by multiplying with the irradiance. On the basis of these considerations, enhancement of photocatalytic activity can be achieved by increase in both efficiencies. For example, preparing visible-light absorbing photocatalysts, as a recent trend in the field of photocatalysis, and depositing noble metal particles onto the surface of photocatalysts lead to the improvement of these efficiencies, respectively. In this sense, the design of active photocatalysts seems simple and feasible, but we encounter the problem that both efficiencies are related to each other, and we do not know how we can improve the quantum efficiency since correlations between physical/structural properties and photocatalytic activity have only partly been clarified.

Future Perspectives

Since most of researchers in the field of photocatalysis came from different fields of chemistry, catalysis chemistry, electrochemistry, materials chemistry, photochemistry, etc., there seemed no common concepts shared by them. It is necessary to understand photocatalysis appropriately considering thermodynamics and kinetics of photocatalysis introduced in this section.

Cross-References

▶ TiO$_2$ Photocatalyst

References

1. Ohtani B (2008) Preparing articles on photocatalysis—beyond the illusions, misconceptions and speculation. Chem Lett 37(3):216–229
2. Ohtani B (2010) Photocatalysis A to Z—what we know and what we don't know. J Photochem Photobiol C Photochem Rev 11(4):157–178
3. Ohtani B (2011) Photocatalysis by inorganic solid materials: revisiting its definition, concepts, and experimental procedures. Adv Inorg Chem 63:395–430

Photochromizm and Imaging

Tetsu Tatsuma
Institute of Industrial Science, University of Tokyo, Tokyo, Japan

Introduction

Photochromism is the reversible color changes of a material, one way or both ways of which are induced by light irradiation. In relation to electrochemistry, photoinduced charge separation gives positive and negative charges, and the former and/or the latter cause redox reactions accompanied by color changes. There are three types of electrochemical photochromism (i.e., photoelectrochromism). (1) A material absorbs light and gives rise to charge separation. It reduces (or oxidizes) itself by separated charges, resulting in a color change. It is electrochemically or chemically reoxidized (or re-reduced) (single material systems). (2) Material A absorbs light and gives charge separation. It reduces (or oxidizes) material B by separated charges and
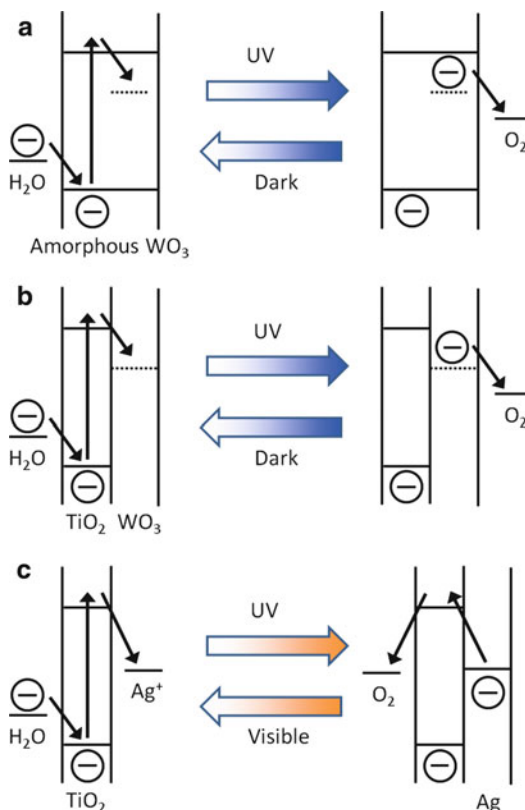
changes its color. Reduced (or oxidized) material B is electrochemically or chemically reoxidized (or re-reduced) (composite material systems). (3) Material A absorbs light of wavelength λ_1 and gives charge separation. It reduces (or oxidizes) material B by separated charges and changes its color. Reduced (or oxidized) material B now absorbs light of wavelength λ_2 and gives charge separation. It reoxidizes (or re-reduces) itself to original material B (composite material systems with reversible photoinduced processes). Some examples are described in the following sections.

Single Material Systems

MoO_3, WO_3, and V_2O_5 films (amorphous in many cases) irradiated with UV light changes their color from colorless to blue [1, 2]. Electrons in the valence band of the metal oxide are excited to the conduction band and used for self-reduction of the film (Fig. 1a). The film is bleached gradually in dark by reoxidation in the presence of ambient oxygen. Slightly reduced MoO_3 are colored even by visible light [3].

Photochromizm and Imaging, Fig. 1 Mechanisms of some typical photochromic materials. (**a**) Single material system. (**b**) Composite material system. (**c**) Composite material systems with reversible photoinduced processes

Composite Material Systems

A semiconductor photocatalyst such as TiO_2 or ZnO (Chapter 309535, 310654) is coupled with an electrochromic system. As electrochromic systems, metal ion/metal oxide systems (Tl^+/Tl_2O_3, Pb^{2+}/PbO_2, Mn^{2+}/MnO_2, and Co^{2+}/CoO_2) and metal ion/metal systems (Ag^+/Ag) can be used [4]. In the former system, metal ions are oxidized to colored metal oxides by holes generated in the valence band of the photo-irradiated semiconductor and bleached by electrochemical reduction of the oxide. In the latter, metal ions are reduced to colored metal particles by photoexcited electrons in the conduction band. A system with Prussian white/Prussian blue is also used. Prussian white on TiO_2 is oxidized to Prussian blue by UV irradiation [5]. Redox reactions of conducting polymers such as

polypyrrole derivatives are also employed [6, 7]. Methylene blue can also be combined with polyaniline as a photocatalyst, and methylene blue is photoelectrochemically reduced to a colorless form [8]. WO_3 can be coupled with TiO_2, as a mixed suspension [9, 10], or a photoelectrochromic cell with a TiO_2 photoanode and a WO_3 electrochromic cathode [11]. A WO_3-TiO_2 composite film also works not only in an electrolyte [12] but also in air [13]. The blue film colored by photoelectrochemical reduction under UV irradiation can be bleached due to reoxidation by dissolved or ambient oxygen (Fig. 1b). In the coloration process in air, adsorbed water works as electrolyte so that a photoanodic reaction at TiO_2 and cathodic reaction at WO_3 can take place separately.

Composite Material Systems with Reversible Photoinduced Processes

In this type of photochromic materials, reversed processes are driven by light of different wavelengths. When TiO_2 with adsorbed Ag^+ ions is irradiated with UV light in air, electrons in the TiO_2 valence band are excited to the conduction band, and Ag^+ ions are reduced by the electrons to Ag nanoparticles that exhibit localized surface plasmon resonance (LSPR) (Fig. 1c) (Chapter 309533). The deposited Ag nanoparticles are different in size, so that they exhibit different colors since the LSPR wavelength redshifts as the particle size increases. If the Ag nanoparticle ensemble, which has absorption over the visible range, is irradiated with a monochromatic green light, for instance, particles resonant with green light are selectively excited and oxidized to Ag^+ ions due to plasmon-induced charge separation (Chapter 309533) [14]. After sufficient irradiation, there are no Ag particles that absorb green light, and the sample reflects green light [15]. As a result, the sample shows green color. Likewise, the material exhibits blue, red, or white color after irradiation with light of the corresponding color [16–18].

The multicolor photochromic material can be initialized by UV irradiation. A drawn image is gradually bleached under room light on the basis of its principle. To retain a drawn image, the Ag nanoparticles may be protected by an alkylthiol [19].

The multicolor photochromism can be extended to near-infrared region by using Ag nanorods so that invisible images, which are viewable with infrared cameras, can be drawn and overlaid with a visible image [20]. Polarization-selective imaging is also possible with nanorods.

Future Directions

Photochromic materials can be applied to smart windows and sunglasses. In view of thermal control, photochromism in the infrared region would be more important. Additional potential applications of photochromism are simple and inexpensive display materials for rewritable papers and book readers. Further development of multicolor photochromism would therefore be of significance. In particular, reproducibility of colors and drawing time for images would be important issues. It would also be applied to nanophotonic devices [21] exhibiting reversible responses.

Cross-References

► Photocatalyst
► Plasmonic Electrochemistry (Surface Plasmon Effect)
► TiO_2 Photocatalyst

References

1. Deb SK, Chopoorian JA (1966) J Appl Phys 37:4818
2. Colton RJ, Guzman AM, Rabalais JW (1978) Acc Chem Res 11:170
3. Yao JN, Hashimoto K, Fujishima A (1992) Nature 355:624
4. Inoue T, Fujishima A, Honda K (1980) J Electrochem Soc 127:1582
5. DeBerry DW, Viehbeck A (1983) J Electrochem Soc 130:249
6. Inganäs O, Lundström I (1984) J Electrochem Soc 131:1129
7. Yoneyama H, Wakamoto K, Tamura H (1985) J Electrochem Soc 132:2414
8. Kuwabata S, Mitsui K, Yoneyama H (1992) J Electrochem Soc 139:1824
9. Ohtani B, Atsumi T, Nishimoto S, Kagiya T (1988) Chem Lett 1988:295
10. Tennakone K, Ileperuma OA, Bandara JMS, Kiridena WCB (1992) Semicond Sci Technol 7:423
11. Bechinger C, Ferrere S, Zaban A, Sprague J, Gregg BA (1996) Nature 383:608
12. Tatsuma T, Saitoh S, Ohko Y, Fujishima A (2001) Chem Mater 13:2838
13. Tatsuma T, Saitoh S, Ngaotrakanwiwat P, Ohko Y, Fujishima A (2002) Langmuir 18:7777
14. Tian Y, Tatsuma T (2005) J Am Chem Soc 127:7632
15. Matsubara K, Tatsuma T (2007) Adv Mater 19:2802
16. Ohko Y, Tatsuma T, Fujii T, Naoi K, Niwa C, Kubota Y, Fujishima A (2003) Nat Mater 2:29
17. Naoi K, Ohko Y, Tatsuma T (2004) J Am Chem Soc 126:3664
18. Tatsuma T (2013) Bull Chem Soc Jpn 86:1

19. Naoi K, Ohko Y, Tatsuma T (2005) Chem Commun 1988:1288
20. Kazuma E, Tatsuma T (2012) Chem Commun 48:1733
21. Tanabe I, Tatsuma, T (2012) Nano Lett 12:5418

Photoelectrochemical CO$_2$ Reduction

Shunsuke Sato
Toyota Central Research and Development Laboratories, Inc., Nagakute, Aichi, Japan

Introduction

The development of a photocatalytic system to produce useful organic chemicals by reducing CO$_2$ under sunlight is an increasingly important research area addressing global warming and fossil fuel shortages. If CO$_2$ can be reduced by utilizing water as an electron donor, such a reaction would mimic photosynthesis in plants. Development of the water oxidation catalysts and CO$_2$ reduction catalysts are important to achieve it. There are several methods to achieve CO$_2$ reduction using catalysts such as electrocatalysts, photoelectro-catalysts, and photocatalysts.

Electrocatalytic CO$_2$ reduction can be conducted by metal catalysts, semiconductor catalysts, and molecular catalysts (metal complexes) under electrical biases. The electrocatalyst requires a great electrical potential in order to achieve a catalytic CO$_2$ reduction, which may be regarded as activation energy for the reaction. Potentials for CO$_2$ reduction to various products are given in Table 1. Single-electron reduction of CO$_2$ to CO$_2$ radical anion occurs at -1.9 V versus NHE. The unfavorably high negative potential for the single-electron reduction of CO$_2$ is caused by the large reorganization energy between the linear CO$_2$ molecule and bent-bonded CO$_2$ radical anion. Therefore, it is difficult to reduce CO$_2$ molecule using an electrical energy only. The electrocatalysts are able to facilitate proton-coupled multi-electron reactions which require

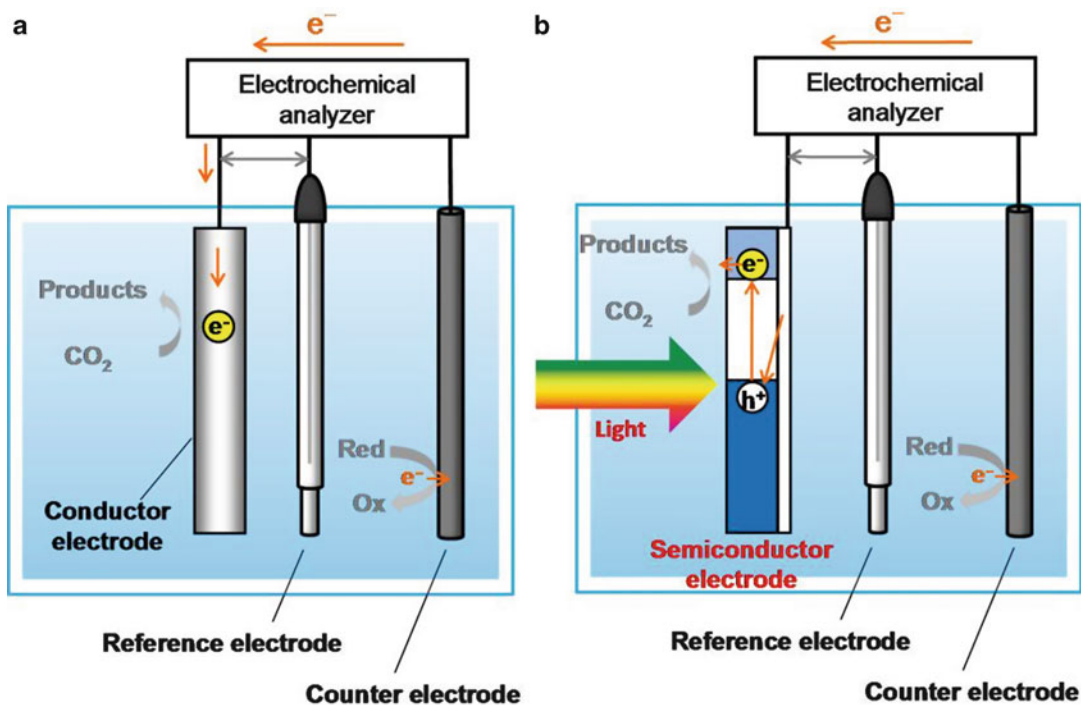**Photoelectrochemical CO$_2$ Reduction, Table 1** CO$_2$ reduction potentials

	E^0/V vs. NHE
$CO_2 + e^- \longrightarrow CO_2^{-}$	< -1.9
$CO_2 + 2e^- + 2H^+ \longrightarrow HCOOH$	-0.61
$CO_2 + 2e^- + 2H^+ \longrightarrow CO + H_2O$	-0.53
$CO_2 + 4e^- + 4H^+ \longrightarrow HCHO + H_2O$	-0.48
$CO_2 + 6e^- + 6H^+ \longrightarrow CH_3OH + H_2O$	-0.38
$CO_2 + 8e^- + 8H^+ \longrightarrow CH_4 + 2H_2O$	-0.24

lower potentials than those for the single-electron reactions. The potentials for reduction of CO$_2$ to various organics show that the potentials required for reactions are lowered with increasing numbers of electrons and protons involved in the reactions. However, many electrocatalysts require much higher electrical energy (overpotential) than the theoretical values. Thus, developing electrocatalysts which can reduce the overpotential is necessary.

Advantages and Disadvantages of Photoelectrochemical Reaction

Photoelectrochemical (PEC) reaction is a similar to electrochemical reaction in regard to an experimental setup. However, PEC reaction uses semiconductor electrodes instead of conductor electrodes used in electrochemistry (Fig. 1). Semiconductors (electrodes) possess a band gap where no electron states can exist and generate pairs of electrons and holes upon absorption of light whose photon energy is larger than the band gap energy. Semiconductors have been used to convert solar photon energy into electrical energy by photovoltaic devices. Thus, there have been attempts to utilize semiconductor electrodes for PEC CO$_2$ reduction.

Advantage of the PEC reaction is the lower overpotential required for it than that for the electrochemical reaction, because photoexcitation of the semiconductor improves energy of electrons up to a level of conduction band from valence band in the semiconductor (Fig. 2). Here, reaction rate and catalytic ability depends on light

Photoelectrochemical CO_2 Reduction, Fig. 1 Reaction mechanism of electrochemical reaction (**a**) and PEC reaction (**b**)
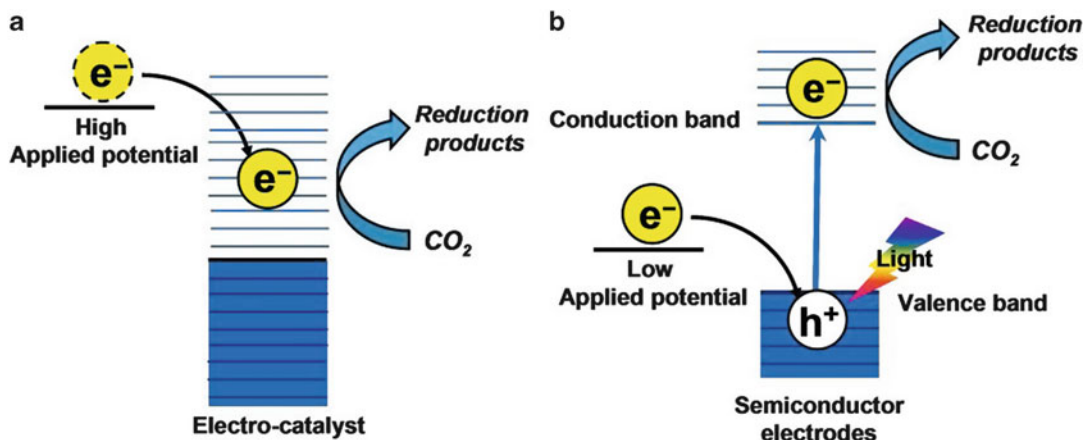
Photoelectrochemical CO_2 Reduction, Fig. 2 Schematic energy diagram of electrochemical reaction (**a**) and PEC reaction (**b**)

intensity and quality of semiconductor surface as a catalyst, respectively. When activity at a semiconductor surface for a specific reaction is poor, the corresponding PEC reaction rate is very slow, irrespective of a level of applied potential. Therefore, controlling surface chemistry of the semiconductor appropriate for each specific reaction is crucial for high-efficiency PEC reaction. The same is true of electrochemical reaction.

PEC CO₂ Reduction

In 1972, Honda and Fujishima reported first PEC hydrogen production reaction by water-splitting using Pt electrode (cathode) and TiO_2 semiconductor photoanode under ultraviolet light irradiation [1]. On the contrary, the first PEC reduction of CO_2 by InP photocathode was reported by Halmann in 1978 [2]. Then PEC CO_2 reduction was reported in many papers. However, the efficiency of the PEC CO_2 reduction was low even under irradiation, more intense than sunlight, and with a high electrical bias. Furthermore, most of the results suffer from low selectivity of products from CO_2 reduction, because semiconductor electrodes prefer to produce hydrogen, which is due to the catalytic nature of surface of semiconductors or co-catalysts deposited on the semiconductors. Therefore, majority of PEC reaction reported to date have been the solar hydrogen production [3–6].

Recently, there appeared reports on successful PEC CO_2 reduction reaction, which consists of combinations of semiconductor electrodes and molecular catalysts [7–9].

In 2008, Bocarsly et al. developed a CO_2 reduction system consisting of a GaP photocathode and a pyridinium ion dissolved in aqueous solution [7]. They insist that pyridinium ions which receive electron from visible-light-excited GaP acts as a catalyst for successive six-electron reduction of carbon dioxide to methanol in 0.1 M acetate buffer under an electrical bias. Reduction product selectivity ranges from 90 % to 51 % under an electric bias from -0.3 V to -0.7 V (vs. SCE).

In 2010, Arai et al. have developed a photocathode for CO_2 reduction in water which consists of a combination of Ru-complex catalyst and InP [8]. This system produces formic acid from CO_2 and H_2O under visible-light irradiation with a selectivity of ca. 62 % with an electrical bias of -0.6 V (vs. SCE). In this entry, by isotope tracer analyses using $^{13}CO_2$ and D_2O, it was verified that carbon and proton sources for formate formation were CO_2 and H_2O, respectively.

Future Directions

PEC CO_2 reduction technique can reduce electrical bias and overpotential compared to electrical CO_2 reduction. Development of semiconductor electrodes is very important in this research area, because PEC catalytic ability depends on the semiconductor electrodes in regard to

photoabsorption and energy of photoexcited electrons. Development of co-catalysts such as molecule catalysts which can control selectivity for CO_2 reduction products is also necessary. The goal of the PEC reaction is to develop PEC-based system for selective CO_2 reduction that makes use of water molecules as both proton and electron sources under solar irradiation like the photosynthetic process in plant. Recently, it was reported that a tandem-type CO_2 photo-recycling cell was successfully constructed by combining the Ru-complex/InP photocathode for CO_2 reduction with a TiO_2 photoanode catalyst capable of for water oxidation and that the system utilized H_2O as both an electron donor and a proton source under simulated sunlight with no electrical bias (Fig. 3) [10]. Selectivity for formate formation was about 70 % and solar conversion efficiency for CO_2 reduction to formate was about 0.04 %. This is the first report of photocatalytic CO_2 reduction with high selectivity utilizing H_2O as both an electron donor and a proton source using sunlight as an only energy input, where the reaction pathway was completely proven by isotope tracer analyses. The future trend toward a significant and useful PEC CO_2 reduction would be the conjugation of the CO_2 reduction and the water oxidation.

Cross-References

▶ Photocatalyst
▶ Photoelectrochemistry, Fundamentals and Applications

References

1. Fujishima KH (1972) Electrochemical photolysis of water at a semiconductor electrode. Nature 238:37
2. Halmann M (1978) Photoelectrochemical reduction of aqueous carbon-dioxide on p-type gallium-phosphide in liquid junction solar-cells. Nature 275:115
3. Khaselev O, Turner JA (1998) A monolithic photo-voltaic-photoelectrochemical device for hydrogen production via water splitting. Science 280:425
4. Licht S (2001) Multiple band gap semiconductor/electrolyte solar energy conversion. J Phys Chem B 105:6281
5. Ingler WB Jr, Khan SUM (2006) A self-driven p/n-Fe_2O_3 tandem photoelectrochemical cell for water splitting. Electrochem Solid-State Lett 9:G144
6. Alexander BD, Kulesza PJ, Rutkowska I, Solarska R, Augustynski J (2008) Metal oxide photoanodes for solar hydrogen production. J Mater Chem 18:2298
7. Barton EE, Rampulla DM, Bocarsly AB (2008) ive solar-driven reduction of CO_2 to methanol using a catalyzed p-GaP based photoelectrochemical cell. J Am Chem Soc 130:6342
8. Arai T, Sato S, Uemura K, Morikawa T, Kajino T, Motohiro T (2010) Photoelectrochemical reduction of CO_2 in water under visible-light irradiation by a p-type InP photocathode modified with an electropolymerized ruthenium complex. Chem Commun 46:6944
9. Kumar B, Smieja JM, Kubiak CP (2010) Photoreduction of CO_2 on p-type Silicon using Re(bipy-Bu_t)(CO)$_3$Cl: photovoltages exceeding 600 mV for the selective reduction of CO_2 to CO. J Phys Chem C 114:14220
10. Sato S, Arai T, Morikawa T, Uemura K, Suzuki TM, Tanaka H, Kajino T (2011) Selective CO_2 conversion to formate conjugated with H_2O oxidation utilizing semiconductor/complex hybrid photocatalysts. J Am Chem Soc 133:15240

Photoelectrochemical Disinfection

Danae Venieri
Department of Environmental Engineering,
Technical University of Crete, Chania, Greece

Introduction

Maintenance of the microbiological quality and safety of water systems is imperative, as their fecal contamination may exact high risks to human health and result in significant economic losses. Disinfection of water and wastewater is important in the control of waterborne diseases, as it is the final barrier against human exposure to pathogenic microorganisms [1]. Waterborne diseases, which are transmitted through the ingestion of contaminated water that serves as the passive carrier of the infectious agent, illustrate the importance of effective inactivation of pathogens contained in water and wastewater [2]. Common disinfectants used in the drinking and wastewater industries include chlorine,
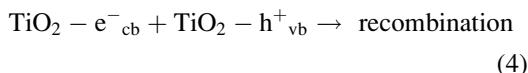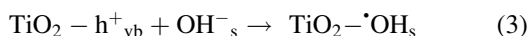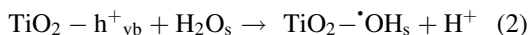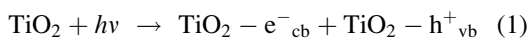
chlorine dioxide, ozone and ultraviolet light, which may act by many different means to kill organisms or prevent their growth (i.e. destruction of cellular components and inhibition of nucleic acid replication) [1, 3].

Over the last decades, there have been intensive efforts toward the development of efficient technologies for microbial inactivation in various aqueous matrices. In this perspective, advanced oxidation processes (AOPs) have been recognized as an emerging group of techniques, demonstrating high disinfection efficiency in aqueous samples [4]. These methods are based primarily on the in situ generation of highly reactive intermediate chemical species, like hydroxyl radicals, offering a simple and effective process for inactivating pathogenic bacteria and destroying organic compounds [3, 5, 6]. TiO_2 photocatalysis is an important member of AOPs, and its benefits regarding water and wastewater disinfection have been demonstrated with respect to *Escherichia coli*, *Staphylococcus aureus* and *Enterococcus faecalis* [2, 7–9]. In most photocatalytic applications, the catalyst is employed as a slurry of fine particles in a photochemical reactor, resulting in certain difficulties such as post-reaction catalyst recovery and low quantum efficiencies [10, 11]. These problems may be addressed by immobilization of TiO_2 on a conducting support and application of a potential bias, so as to reduce the recombination of charge carriers, which is the main limitation of the process photonic efficiency [12, 13]. These modifications have led to the development of photoelectrocatalysis (PEC), in which a small positive potential is applied to a TiO_2-based thin film in the form of a photoanode. The constant current density or bias potential applied to the semiconductor electrode promotes the efficient separation of electron–hole pairs from electron transfer by an external circuit and accelerates the production of photogenerated oxidizing chemical species on the catalyst surface [14].

According to the literature [15], illumination of a semiconductor-electrolyte interface with photons having energy greater than its band gap energy generates electron–hole pairs at the anode electrode surface. The simultaneous application of a bias positive to the flat-band potential produces a bending of the conduction and valence bands which, in turn, causes a more effective separation of the photogenerated carriers within the space charge layer. In other words, the potential gradient forces the electrons towards the cathode, thus leaving the photogenerated holes to react at the anode with H_2O and/or OH^- to yield hydroxyl radicals, i.e.:

Anode (working electrode):

$$TiO_2 + h\nu \rightarrow TiO_2 - e^-_{cb} + TiO_2 - h^+_{vb} \quad (1)$$

$$TiO_2 - h^+_{vb} + H_2O_s \rightarrow TiO_2 - {}^\bullet OH_s + H^+ \quad (2)$$

$$TiO_2 - h^+_{vb} + OH^-_s \rightarrow TiO_2 - {}^\bullet OH_s \quad (3)$$

$$TiO_2 - e^-_{cb} + TiO_2 - h^+_{vb} \rightarrow \text{recombination} \quad (4)$$

Cathode (counter electrode):

$$2H_2O + 2e^- \rightarrow H_2 + 2OH^- \quad (5)$$
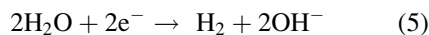
where the subscripts cb and vb denote the conduction and valence bands, respectively, h^+ and e^- denote the photogenerated holes and electrons, respectively, and the subscript s refers to species adsorbed onto the photoanode surface.

Microbial Inactivation During PEC

Given the importance of effective inactivation of pathogens contained in water and wastewater so as to control waterborne diseases, PEC seems to be a promising and efficient tool. Inactivation of microorganisms is a gradual process that involves a number of physicochemical and biochemical processes. The bactericidal function of this technique can be attributed to the oxidation properties of photocatalytically generated active oxygen species (AOS), which cause damage to cellular membranes and further destruction of bacterial structures [16]. The most commonly accepted photocatalytic inactivation mechanism is based on the attack of ROS to the bacterial cell wall,

where the bacteria-catalyst contact takes place [17]. Furthermore, radiation during PEC is equally important, as it induces DNA lesions, damaging nucleic acids and making them functionless. The hydroxyl radical (and other AOS), directly generated by this process, is the main cause of DNA destruction, which in turn leads to cell death. Most studies dealing with UV irradiation of microbial cells have concluded that the extremely reactive hydroxyl radical, for which no defense exists, is able to damage DNA [18].

Factors Affecting Disinfection During PEC

The studies refer to PEC as means of disinfection, highlighting the importance of certain parameters like type of microorganism, applied voltage, bacterial concentration, treatment time, and the aqueous matrix, which are considered determining factors of microbial inactivation [14].

Type of Microorganism

Generally, most studies dealing with the evaluation of PEC as a disinfection method have mainly focused on *Escherichia coli* inactivation with the application of conventional culture techniques, while other pathogens have not been considered [2, 12, 16, 19]. The importance of the tested bacterial strain should be underlined when disinfection occurs, especially considering that the bactericidal effect of PEC involves loss of membrane integrity and peroxidation of its phospholipids. In this sense, bacteria other than coliforms with different resistance rates should be taken into account. Gram-negative bacteria possess an additional outer membrane containing two lipid bilayers, which provide them higher complexity. However, since it is strongly believed that the attack occurs on the bacteria outer cell wall, certain attention is paid to the differences of wall structure. In this sense, Gram-positive bacteria, which possess a thick peptidoglycan cell wall, have been reported to be photocatalytically more resistant than Gram-negative, and according to the literature, a higher number of ROS are needed for their complete inactivation [20]. On the other hand, several authors have suggested different inactivation mechanisms, showing that Gram-negative bacteria are more resistant to the photocatalytic process, due to their more complex structure given by the additional outer membrane [17]. Apart from bacterial species, certain considerations should be given to other microorganisms like protozoan parasites and viruses, whose presence in water and wastewater poses great risks for public health. Although these microorganisms have been recognized as highly resistant during disinfection treatments, they have been merely reported in studies dealing with PEC.

Applied Voltage

It is presumed that raising the anodic potential increases the depth of the space charge region and suppresses the extent of electron–hole recombination, thus enhancing photocatalytic rates [21]. The beneficial effect of increasing the applied potential on PEC bacteria killing has already been reported in studies dealing mainly with the inactivation of *E. coli* [12, 19]. However, it should been pointed out that increasing the anodic potential above a certain value will not result in an increased inactivation rate, depending on the microorganism tested and the experimental conditions [21].

Bacterial Concentration

PEC disinfection rate is inversely proportional to bacterial concentration in water samples. Total inactivation may be achieved in relatively short treatment time (i.e. within approximately 15 min) when bacterial inoculum contains 10^3 – 10^5 CFU/mL, depending on the bacterial strain. At higher concentrations, residual bacterial cells may reach a plateau, implying a threshold, under which no further inactivation occurs. It is important

to note here that the overall effect of initial concentration on the disinfection process is highly dependent on the type of microorganism used. Gram-positive bacteria require longer treatment time than Gram-negative with equal cellular density, while even longer times have been recorded when dealing with protozoan parasites [22].

Aqueous Matrix

Disinfection efficiency of treatment methods should be performed in real conditions, i.e. using samples of complex composition that contain multiple bacterial populations. Very few studies have been performed applying PEC for the inactivation of microorganisms in wastewater samples. Generally, treatment of wastewater samples shows a lower degree of disinfection compared to water. When processing wastewater samples, the viability and culturability of bacteria is affected by the presence of other competitive microorganisms and the interaction amongst them. According to Hong et al. [23], samples containing multiple bacterial populations or biofilms show great resistance against conventional disinfection methods, requiring long treatment time or more stressed conditions [23]. Although PEC is capable of inactivating bacteria to a certain extent in real wastewater, the residual cells do not indicate a sample free of microbial indicators and, therefore, safe for public health. In addition, another parameter under consideration is the particulate matter present in wastewater, which aids in the resistance of microorganisms to disinfection, as it may interfere by physically shielding bacterial cells and protecting the integrity of the contained DNA. Furthermore, part of the photogenerated AOS may be wasted to attack the organic carbon of the wastewater (about 8 mg/L, which typically consists of highly resistant humic-type compounds and biomass-associated products) and/or scavenged by bicarbonates, sulfates and chlorides, rather than inactivate pathogens. This could be overcome by increasing AOS concentration through raising the applied potential [21].

Future Directions

PEC has been acknowledged as an emerging disinfection technique, as it shows satisfactory inactivation rates of microorganisms. However, challenges still remain for further improvement, considering the extended microbial variety and the different response of each microorganism during PEC treatment. Up to now, most studies have dealt with the common fecal indicator *Escherichia coli*, while other microbes/pathogens have been merely mentioned. Future directions regarding photoelectrocatalytic disinfection are referred to thorough study of multiple microorganisms, including protozoan parasites and viruses and determination of the disinfection mechanism which occurs during water and wastewater treatment. According to the results obtained, PEC has the potential to be applied for effective microbial inactivation in aqueous matrices, with the view of protecting public health.

Cross-References

▶ Disinfection of Water, Electrochemical
▶ Electrodisinfection of Urban Wastewater for Reuse
▶ Photoelectrochemical Disinfection of Air (TiO_2)

References

1. Maier RM, Pepper IL, Gerba CP (2009) Environmental microbiology. Academic Press/Elsevier, USA
2. Chen CY, Wu LC, Chen HY, Chung YC (2010) Inactivation of *Staphylococcus aureus* and *Escherichia coli* in water using photocatalysis with fixed TiO_2. Water Air Soil Pollut 212:231–238
3. Malato S, Fernández-Ibáñez P, Maldonado MI, Blanco J, Gernjak W (2009) Decontamination and disinfection of water by solar photocatalysis: recent overview and trends. Catal Today 147:1–59
4. Frontistis Z, Daskalaki VM, Katsaounis A, Poulios I, Mantzavinos D (2011) Electrochemical enhancement of solar photocatalysis: degradation of endocrine disruptor bisphenol-A on Ti/TiO2 films. Water Res 45:2996–3004

5. Chong MN, Jin B, Chow CWK, Saint C (2010) Recent developments in photocatalytic water treatment technology: a review. Water Res 44:2997–3027

6. Nissen S, Alexander BD, Dawood I, Tillotson M, Wells RP, Macphee DE, Killham K (2009) Remediation of a chlorinated aromatic hydrocarbon in water by photoelectrocatalysis. Environ Pollut 157:72–76

7. Chatzisymeon E, Droumpali A, Mantzavinos D, Venieri D (2011) Disinfection of water and wastewater by UV-A and UV-C irradiation: application of real-time PCR method. Photochem Photobiol Sci 10:389–395

8. Rémy SP, Simonet F, Cerda EE, Lazzaroni JC, Atlan D, Guillard C (2011) Photocatalysis and disinfection of water: identification of potential bacterial targets. Appl Catal B Environ 104:390–398

9. Venieri D, Chatzisymeon E, Gonzalo MS, Rosal R, Mantzavinos D (2011) Inactivation of *Enterococcus faecalis* by TiO$_2$-mediated UV and solar irradiation in water and wastewater: culture techniques never say the whole truth. Photochem Photobiol Sci 10:1744–1750

10. Egerton TA, Kosa SAM, Christensen PA (2006) Photoelectrocatalytic disinfection of *E. coli* suspensions by iron doped TiO$_2$. Phys Chem Chem Phys 8:398–406

11. Marugán J, Hufschmidt D, Sagawe G, Selzer V, Bahnemann D (2006) Optical density and photonic efficiency of silica-supported TiO$_2$ photocatalysts. Water Res 40:833–839

12. Egerton TA (2011) Does photoelectrocatalysis by TiO2 work? J Chem Technol Biotechnol 86:1024–1031

13. Marugán J, Christensen P, Egerton T, Purnama H (2009) Synthesis, characterization and activity of photocatalytic sol–gel TiO$_2$ powders and electrodes. Appl Catal B Environ 89:273–283

14. Martínez-Huitle CA, Brillas E (2009) Decontamination of wastewaters containing synthetic organic dyes by electrochemical methods: a general review. Appl Catal B Environ 87:105–145

15. Morrison SR (1980) Electrochemistry at semiconductors and oxidized metal electrodes. Plenum Press, New York

16. Li G, Liu X, Zhang H, An T, Zhang S, Carroll AR, Zhao H (2011) In situ photoelectrocatalytic generation of bactericide for instant inactivation and rapid decomposition of Gram-negative bacteria. J Catal 277:88–94

17. Pal A, Pehkonen SO, Yu LE, Ray MB (2007) Photocatalytic inactivation of Gram-positive and Gram-negative bacteria using fluorescent light. J Photochem Photobiol A Chem 186:335–341

18. Gogniat G, Dukan S (2007) TiO$_2$ Photocatalysis causes DNA damage via fenton reaction-generated hydroxyl radicals during the recovery period. Appl Environ Microbiol 73:7740–7743

19. Philippidis N, Nikolakaki E, Sotiropoulos S, Poulios I (2010) Photoelectrocatalytic inactivation of *E. coli* XL-1 blue colonies in water. J Chem Technol Biotechnol 85:1054–1060

20. Van Grieken R, Marugán J, Pablos C, Furones L, López A (2010) Comparison between the photocatalytic inactivation of Gram-positive E. faecalis and Gram-negative E. coli faecal contamination indicator microorganisms. Appl Catal B Environ 100:212–220

21. Baram N, Starosvetsky D, Starosvetsky J, Epshtein M, Armon R, Ein-Eli Y (2009) Enhanced inactivation of E. coli bacteria using immobilized porous TiO2 photoelectrocatalysis. Electrochim Acta 54:3381–3386

22. Cho M, Cates EL, Kim JH (2011) Inactivation and surface interactions of MS-2 bacteriophage in a TiO2 photoelectrocatalytic reactor. Water Res 45:2104–2110

23. Hong SH, Jeong J, Shim S, Kang H, Kwon S, Ahn KH, Yoon J (2008) Effect of electric currents on bacterial detachment and inactivation. Biotechnol Bioeng 100:379–386

Photoelectrochemical Disinfection of Air (TiO$_2$)

Tsuyoshi Ochiai and Akira Fujishima
Kanagawa Academy of Science and Technology, Takatsu–ku, Kawasaki, Kanagawa, Japan
Photocatalysis International Research Center, Tokyo University of Science, Noda, Chiba, Japan

Historical Overview

In the late 1960s, one of the present authors (AF) began to investigate the photoelectrolysis of water, using a single crystal TiO$_2$ electrode. Then, the first report on the efficient production of hydrogen from water by TiO$_2$ photocatalysis was published in Nature in 1972, at the time of the "oil crisis" [1]. Thus, TiO$_2$ photocatalysis drew the attention of many people as one of the promising methods to obtain this new energy source. However, even though the reaction efficiency is very high, TiO$_2$ can absorb only the UV light contained in solar light, which is only about 3 %. Therefore, from the viewpoint of hydrogen

production technology, TiO_2 photocatalysis is not very attractive. Instead, research shifted in the 1980s to the utilization of the strong photoproduced oxidation power of TiO_2 for the decomposition of various contaminants in both water and air. In this case, the holes (h^+) generated in TiO_2 were highly oxidizing, and most contaminants were essentially oxidized completely. In addition, various forms of active oxygen, such as $O_2^{\bullet-}$, $^{\bullet}OH$, $HO_2^{\bullet}$, and $O^{\bullet}$, produced by the following processes, may be responsible for the decomposition reactions:

$$e^- + O_2 \rightarrow O_2^{\bullet-}(ad)$$

$$O_2^-(ad) + H^+ \rightarrow HO_2^{\bullet}(ad)$$

$$h^+ + H_2O \rightarrow {}^{\bullet}OH(ad) + H^+$$

$$h^+ + O_2^{\bullet-}(ad) \rightarrow 2O^{\bullet}(ad)$$
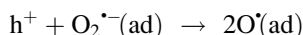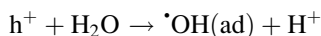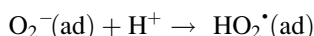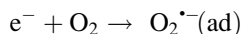
For the purpose of easy handling of photocatalysts, the immobilization of TiO_2 powders on supports was carried out in the late 1980s. Then, the novel concept of light cleaning materials coated with a TiO_2 film photocatalyst under UV light was investigated. In 1997, the marked change in water wettability of the TiO_2 surface before and after UV light irradiation was also reported in Nature as a novel phenomenon of TiO_2 photocatalysis [2]. With the discovery of this phenomenon, the application range of TiO_2 coatings has been largely widened, as mentioned in Fig. 1 and in the literature [3–5].

Figure 2 shows the market transition of industries related to photocatalysis, based on a survey by the Photocatalysis Industry Association of Japan. This data represents the sales volume for companies that are members of the Photocatalysis Industry Association of Japan. The sales volume greatly increased during the past decade, especially for the "cleanup" application involved in photocatalytic water and/or air purifiers. This trend indicates the increasing number of people who are interested in environmental issues such as food poisoning and sick house syndrome. Moreover, the swine influenza
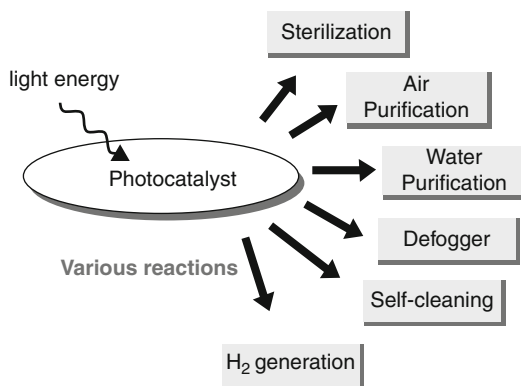
Photoelectrochemical Disinfection of Air (TiO₂), Fig.1 Schematic illustration of applications of photocatalysis

outbreak of 2009 raised serious fears of a global pandemic, suddenly increasing the sales volume of photocatalytic air purifiers. Therefore, photoelectrochemical disinfection of air is currently one of the most important applications of TiO_2 photocatalysis.

Mechanism of Photocatalytic Disinfection

Sunada et al. studied the photocatalytic disinfection process of *Escherichia coli* on TiO_2 film [6]. A typical experiment involves placing an *E. coli* suspension containing $\sim 2 \times 10^5$ colony forming units (CFU)/ml on an illuminated TiO_2-coated glass plate (1.0 mW cm^{-2} UV light). Under these conditions, there were no surviving cells after only 90 min of illumination. In contrast, no obvious changes in survival were observed when the TiO_2-coated glass plate was stored in the dark or when a glass plate was used as the substrate under UV illumination. Figure 3 shows AFM photographs of *E. coli* cells on a TiO_2-coated glass plate after different UV illumination times (Fig. 3a–c), along with a schematic illustration of the process (Fig. 3d–f). After illumination for 1 day, the outermost layer clearly seen in Fig. 3a disappeared (Fig. 3b). After illumination for 6 days, the cylindrical shape of the cells disappeared completely (Fig. 3c), suggesting the

Photoelectrochemical Disinfection of Air (TiO₂), Fig. 2 Market transition of industries related to photocatalysis (Source: Photocatalysis Industry Association of Japan)
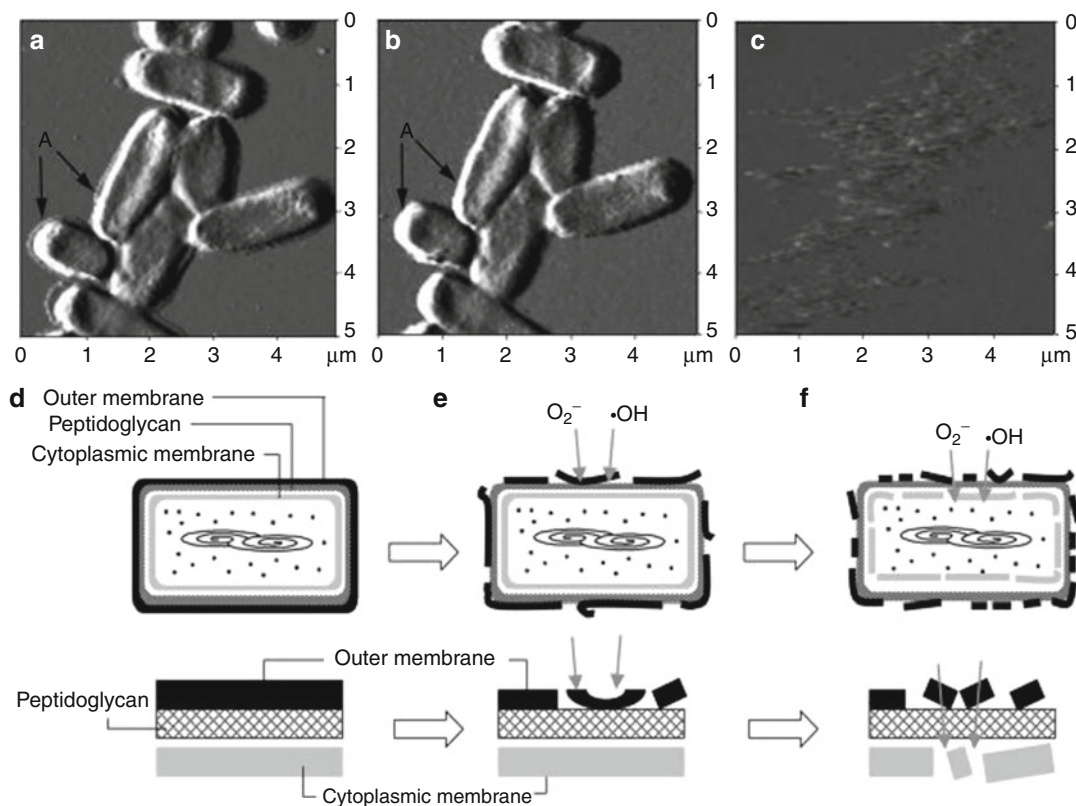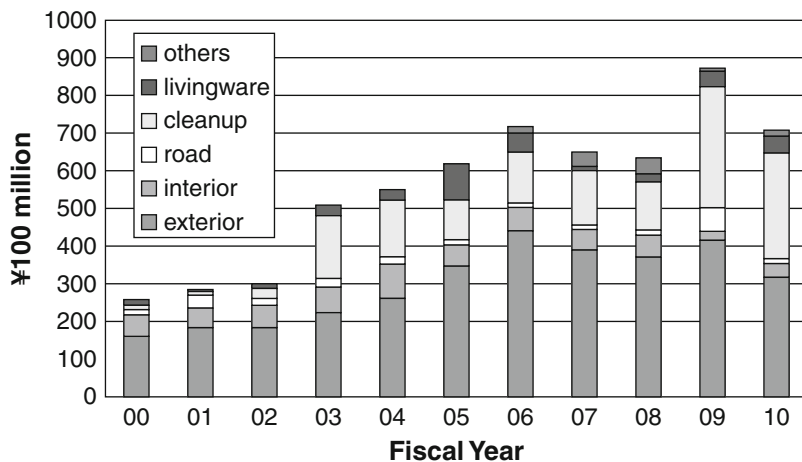
Photoelectrochemical Disinfection of Air (TiO₂), Fig. 3 AFM photographs of *E. coli* cells on TiO₂-coated glass plate after different UV illumination times (**a–c**) and a schematic illustration of the process (**d–f**) (Reprinted from Journal of Photochemistry and Photobiology A: Chemistry, 156, K. Sunada, T. Watanabe, K. Hashimoto, Studies on photokilling of bacteria on TiO₂ thin film, 227–233, 2003, with permission from Elsevier)

Photoelectrochemical Disinfection of Air (TiO$_2$), Fig. 4 The overview and the SEM image of TMiP

complete decomposition of dead cells. Taken together, they concluded that the photokilling of bacteria on the illuminated TiO$_2$ surface could occur by a two-step reaction mechanism (Fig. 3d–f): (1) the disordering of the outer membrane of cells on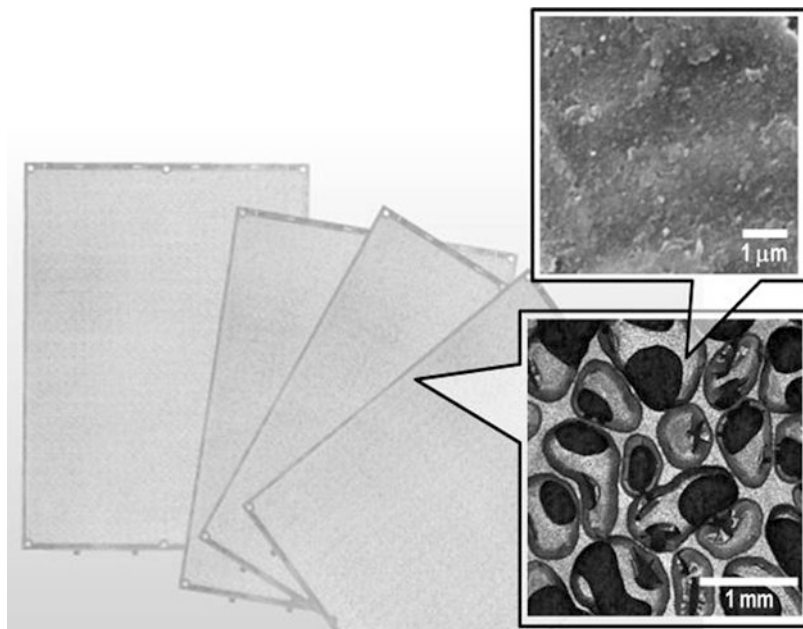 the illuminated TiO$_2$ surface and (2) disordering of the inner membrane (the cytoplasmic membrane) and killing of the cell. In the first stage, the outer cell membranes were decomposed partially by the reactive species ($\cdot$OH, H$_2$O$_2$, O$_2^{\cdot-}$) produced by the TiO$_2$ photocatalyst (Fig. 3e). During this stage, cell viability was not lost very efficiently. However, the permeability of reactive species will be increased. Consequently, reactive species easily reach and attack the inner membrane (Fig. 3f). The structural and functional disordering of the cytoplasmic membrane due to lipid peroxidation led to the loss of cell viability and to cell death. If the illumination continued for a sufficiently long time, the dead cells were found to be decomposed completely (Fig. 3c). Moreover, Kikuchi et al. reported that the *E. coli* could be killed even when the cells were separated from the TiO$_2$ surface by a 50 μm PTFE spacer under similar experimental conditions [7]. This result indicates that photocatalytic disinfection of

bacteria can occur remotely. This results in important applications in the disinfection of air with TiO$_2$ photocatalysis and suggests that a combination of TiO$_2$ photocatalysts with antibacterial reagents that can permeate the outer membrane could show a far superior photokilling activity.

Future Directions

There are many approaches for solving the above mentioned problems. For the first problem, we have fabricated the easy-to-handle photocatalytic filter material, TiO$_2$ nanoparticles impregnated on titanium mesh (TMiP^{TM}), by collaboration with involved companies [8]. Figure 4 shows the overview and the SEM image of TMiP. The Ti mesh, obtained by controlled chemical etching of titanium foil of 0.2 mm thickness, was anodized in an acid solution. Then the Ti mesh was heated to make a TiO$_2$ layer on the surface. Heated Ti mesh was dip-coated with TiO$_2$ anatase sol and was then heated again to sinter TiO$_2$ nanoparticles onto the anodized Ti mesh surface. Because of its highly ordered three-dimensional structure with modified TiO$_2$ nanoparticles,

TMiP provides excellent air pass through while maintaining a high level of surface contact. In addition, TMiP is flexible and lightweight enough to design various air purification units with UV sources [9–11]. For solving the second problem, The Project to Create Photocatalyst Industry for Recycling-oriented Society (NEDO project) was conducted from 2007 to 2012 with an investment of ¥5.1 billion. This has given particular impetus to the research and development of highly sensitive visible light-responsive photocatalysts. The project team found that the visible light activity of a WO_3 photocatalyst with co-catalysts such as Pt, Pd, WC, CuO, or Cu(II) clusters was drastically enhanced via the efficient oxygen reduction process [12, 13] – in particular, Cu-modified WO_3-based photocatalyst, with a visible light reactivity 10 times higher than that of existing products made from N-doped TiO_2. This project is expected to lead to the development of photocatalyst effects of a magnitude sufficient for deodorization, VOC elimination, and sterilization and antibacterial scenarios for interior applications. Lastly, to eliminate "phony products," the standardization process in the photocatalyst industry is proceeding by the Japanese Industrial Standards Committee. At the same time, ISO standardization is also being introduced. Furthermore, the New Energy and Industrial Technology Development Organization (NEDO) has taken the lead in promoting standardization of performance evaluation methods for visible light-responsive photocatalysts since 2007. In addition, the Photocatalysis Industry Association of Japan is formulating standards for photocatalyst products tested by the standardized methods.

In conclusion, we can expect a large number of applications in the photoelectrochemical disinfection of air by using TiO_2 photocatalysts because of the expansion to new fields of research and development. In particular, we feel that achieving a healthy and comfortable living environment is becoming an important issue, and TiO_2 photocatalysis can fulfill an important role in the disinfection of air.

Cross-References

▶ Disinfection of Water, Electrochemical
▶ Organic Pollutants, Direct Electrochemical Oxidation
▶ Photocatalyst
▶ Photoelectrochemical Disinfection
▶ TiO₂ Photocatalyst

References

1. Fujishima A, Honda K (1972) Electrochemical photolysis of water at a semiconductor electrode. Nature 238:37–38
2. Wang R, Hashimoto K, Fujishima A, Chikuni M, Kojima E, Kitamura A, Shimohigoshi M, Watanabe T (1997) Light-induced amphiphilic surfaces. Nature 388:431–432
3. Fujishima A, Rao TN, Tryk DA (2000) Titanium dioxide photocatalysis. J Photochem Photobiol C Photochem Rev 1:1–21
4. Hashimoto K, Irie H, Fujishima A (2005) TiO₂ photocatalysis: a historical overview and future prospects. Jpn J Appl Phys 44:8269–8285
5. Fujishima A, Zhang X, Tryk DA (2008) TiO₂ photocatalysis and related surface phenomena. Surf Sci Rep 63:515–582
6. Sunada K, Watanabe T, Hashimoto K (2003) Studies on photokilling of bacteria on TiO₂ thin film. J Photochem Photobiol A Chem 156:227–233
7. Kikuchi Y, Sunada K, Iyoda T, Hashimoto K, Fujishima A (1997) Photocatalytic bactericidal effect of TiO₂ thin films: dynamic view of the active oxygen species responsible for the effect. J Photochem Photobiol A Chem 106:51–56
8. Ochiai T, Hoshi T, Slimen H, Nakata K, Murakami T, Tatejima H, Koide Y, Houas A, Horie T, Morito Y, Fujishima A (2011) Fabrication of TiO₂ nanoparticles impregnated titanium mesh filter and its application for environmental purification unit. Catal Sci Technol 1:1324–1327
9. Ochiai T, Niitsu Y, Kobayashi G, Kurano M, Serizawa I, Horio K, Nakata K, Murakami T, Morito Y, Fujishima A (2011) Compact and effective photocatalytic air-purification unit by using of mercury-free excimer lamps with TiO₂ coated titanium mesh filter. Catal Sci Technol 1:1328–1330
10. Slimen H, Ochiai T, Nakata K, Murakami T, Houas A, Morito Y, Fujishima A (2012) Photocatalytic decomposition of cigarette smoke by using TiO₂ impregnated titanium mesh filter. Ind Eng Chem Res 51:587–590
11. Ochiai T, Nakata K, Murakami T, Morito Y, Hosokawa S, Fujishima A (2011) Development of an air-purification unit using a photocatalysis-plasma hybrid reactor. Electrochemistry 79:838–841

12. Arai T, Horiguchi M, Yanagida M, Gunji T, Sugihara H, Sayama K (2008) Complete oxidation of acetaldehyde and toluene over a Pd/WO$_3$ photocatalyst under fluorescent- or visible-light irradiation. Chem Commun 2008:5565–5567

13. Abe R, Takami H, Murakami N, Ohtani B (2008) Pristine simple oxides as visible light driven photocatalysts: highly efficient decomposition of organic compounds over platinum-loaded tungsten oxide. J Am Chem Soc 130:7780–7781

Photoelectrochemical Processes, Electro-Fenton Approach for the Treatment of Contaminated Water

Luis Godinez[1] and Francisco J. Rodriguez Valadez[1,2]
[1]Centro de Investigación y Desarrollo Tecnológico en Electroquímica S.C., Querétaro, Mexico
[2]S. C. Sanfandila, Research Branch, Center for Research and Technological Development in Electrochemistry, Querétaro, Mexico

Introduction

Advanced Oxidation Processes (AOPs) are characterized by the generation and use of the •OH radical species for treating wastewaters, and among the different AOPs, the Fenton reaction is probably the most popular approach. The Fenton reaction was discovered in 1894 by H. J. Fenton, who reported that low concentrations of iron ions in H$_2$O$_2$ aqueous solutions could effectively promote the oxidation of tartaric acid. Later, in 1934, Haber & Weiss suggested that the ferrous ion was actually promoting the decomposition of H$_2$O$_2$ and thus the formation of the •OH radical species, whose presence was, in fact, the reason for the observed oxidation power of the Fenton mixture [1, 2].

The •OH radical species has many advantages over other common chemicals for the elimination of a wide variety of pollutants in water effluents. As can be seen in Table 1, its oxidation potential is very high (2.8 V), larger than ozone (2.42 V)

and than H$_2$O$_2$ (1.78 V) itself. The oxidation kinetics of the ·OH radical species is also large, and, due to its inherent reactivity and molecular size, it is conveniently nondiscriminating for treating complex mixtures of organic pollutants in water. In addition, the oxidation by-products are hydroxylated compounds which, as opposed to the toxic by-products that may result from halogen-based oxidation processes, make these water treatment technologies environmentally friendly [3, 4].

The Fenton Process

The Fenton process involves the reaction of ferrous ions with hydrogen peroxide molecules in aqueous solution to generate a series of oxidizing species of which the hydroxyl radical is the most powerful and reactive. In this way, it is widely accepted that the •OH species is formed as described by Eq. 1 [5–8]:

$$Fe^{2+} + H_2O_2 \ \rightarrow \ Fe^{3+} + OH^- + \bullet OH$$
$$k_1 = 70 \ M^{-1}s^{-1} \tag{1}$$
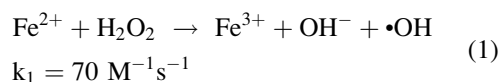
However, different studies have also suggested the presence of other oxidizing species that result from the coupled reactions 2–6 [8, 9]:

$$Fe^{3+} + H_2O_2 \rightarrow \ Fe - OOH^{2+} + H^+$$
$$k_2 = 0.001 - 0.01 \ M^{-1}s^{-1} \tag{2}$$

$$Fe - OOH^{2+} + H^+ \rightarrow \ HO_2^\cdot + Fe^{2+} + H^+ \tag{3}$$

$$\bullet OH + H_2O_2 \rightarrow \ HO_2^\cdot + H_2O \tag{4}$$

$$Fe^{2+} + HO_2^\cdot + H^+ \rightarrow \ Fe^{3+} + H_2O_2 \tag{5}$$

$$Fe^{3+} + HO_2^\cdot \rightarrow Fe^{2+} + O_2 + H^+ \tag{6}$$
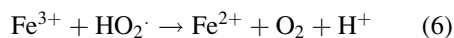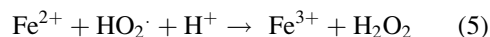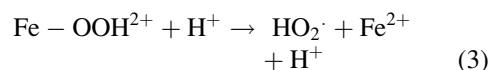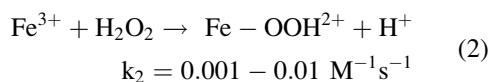
The Fenton process is therefore an attractive approach to treat a wide variety of contaminated effluents, in particular those that require fast kinetics, contain persistent pollutants, or impose limitations in terms of space requirements.

Photoelectrochemical Processes, Electro-Fenton Approach for the Treatment of Contaminated Water, Table 1 Oxidation potential of some chemicals commonly used in water treatment processes

Oxidant	Oxidation potential (V vs NHE)
Fluoride	3.0
•OH radical	2.8
Atomic oxygen	2.42
Ozone	2.42
Hydrogen peroxide	1.78
Permanganate	1.68
Chlorine dioxide	1.57
Hypochlorous acid	1.45
Chlorine	1.36
Bromine	1.09
Iodine	0.54

The Fenton mixture, however, has rarely been taken to industrial scale due to some inherent problems that result in its nonpractical application. Since the Fenton mixture requires a fixed concentration of H_2O_2, it is necessary to constantly dilute and control the amount of peroxide that needs to be fed into the reactor. The commercial H_2O_2 solutions needed for this process are expensive and require careful handling due to their reactive nature. The ferrous ions, on the other hand, need to be removed from the treated effluent, adding an additional operation that carries an associated cost. In order to solve these problems, some variations on the classical Fenton approach have been explored.

The Electro-Fenton Approach

Among these variations, the Electro-Fenton approach has recently gained much attention due to its potential advantages. As its name suggests, the Electro-Fenton approach is an electrochemical methodology in which one or more of the reagents needed for the Fenton mixture is formed through electrochemical reactions. The main advantage consists in the possibility to control their generation using electrical variables, i.e., current and potential, which are easily implemented and controlled [10, 11].

There are two main types of Electro-Fenton processes [1, 12]:

- Cathodic Electro-Fenton process
- Anodic Electro-Fenton process.

The main difference between these two methodologies is related to the way in which the iron ions are incorporated into the system. While in the cathodic Electro-Fenton process an Fe^{2+} or Fe^{3+} electrolyte is added to the reaction mixture, in the anodic Electro-Fenton system, an iron anode is employed as the source of the ferrous ions. In both processes, however, there is a continuous production of H_2O_2 which is formed from the electrochemical reduction of dissolved oxygen at the cathode surface as described by Eq. 7 [2, 12]:

$$O_{2(g)} + 2H^+ + 2e^- \rightarrow H_2O_2 \qquad (7)$$
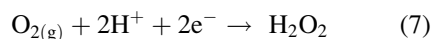
As it was previously mentioned, the electro-generated H_2O_2 reacts with the ferrous ions to produce the radical species •OH. As described in Eq. 8, at the cathode surface, the reduction of ferric ions to their active ferrous form also takes place:

$$Fe^{3+} + e^- \rightarrow Fe^{2+} \qquad (8)$$
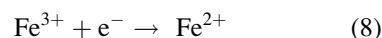
In this way, the Fe^{2+} species becomes available for further reaction with more electro-generated H_2O_2, thus sustaining the •OH electrochemical generation process.

In an anodic Electro-Fenton process, an iron anode is employed to electrochemically generate the Fe^{2+} ions, as described by Eq. 9:

$$Fe^0 \rightarrow Fe^{2+} + 2e^- \qquad (9)$$
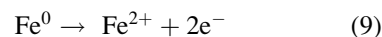
In Fig. 1, a simplified scheme of the reactions that take place in an Electro-Fenton cell is presented.

As can be inferred by inspection of Fig. 1, the electrochemical generation of the Fenton mixture depends on a series of variables that must be properly defined and controlled. Among these, the saturation of oxygen must be maintained; the value of applied current, the conductivity of the solution, the pH, the material of the

Photoelectrochemical Processes, Electro-Fenton Approach for the Treatment of Contaminated Water, Fig. 1 Reactions in an Electro-Fenton cell [10]
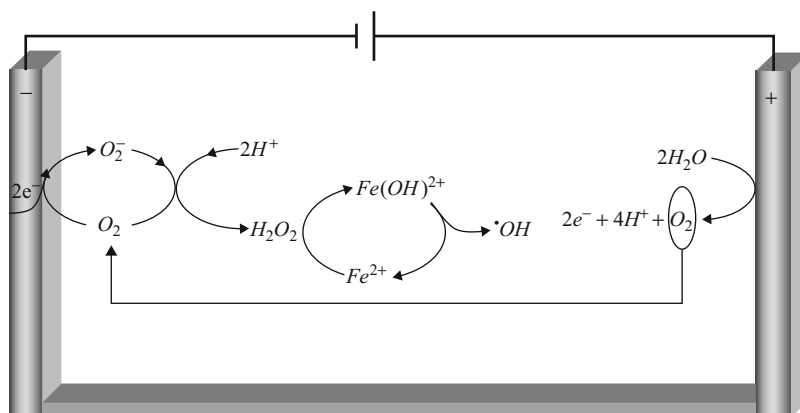
electrodes, and the proper mixing of the electro-generated reagents that must react with the pollutant species after being prepared are all of paramount importance.

Future Directions

As has been discussed in this brief presentation, the Electro-Fenton approach is characterized by a high potential for its practical application in water treatment processes. However, there still are a series of problems that must be dealt with before these systems can become widely used technologies in the field of water treatment. Among these, there is the need to properly understand and develop heterogeneous processes in which the iron is supported in the reactor so that the subsequent separation process can be avoided [13–16]. In this regard, it is also important to study and optimize the use of the Fenton mixture employing other transition metals which, as some reports suggest, may be more efficient than iron itself [17–19]. On the other hand, it is important to explore and incorporate the use of electromagnetic radiation in photo-assisted processes (in particular, the use of solar radiation, which would be a relatively cheap energy input to assist in the treatment process). It is well known that light-activated processes foster the regeneration of the Fe^{2+} species from its oxidized form and that the use of semiconductor anodes can trigger the electrochemical formation of •OH radicals by hole injection at the anode surface. In this regard,

it is also important to point out that there are intensive research efforts preparing and studying semiconductor-doped materials for photo-assisted Electro-Fenton processes (thus defining another potentially important area of technology development called the Photo-Electro-Fenton approach) [20–22]. Depending on the specific nature of the technology to be developed for specific applications, it is also important to study the combination of the Fenton-based processes with traditional technologies such as biological and physicochemical reactors in order to fully optimize and take advantage of the full potential of the Fenton mixture [23].

Cross-References

▶ Electrochemical Bioremediation
▶ Electrochemical Treatment of Landfill Leachates
▶ Electro-Fenton Process for the Degradation of Organic Pollutants in Water
▶ Organic Pollutants, Direct Electrochemical Oxidation
▶ Photoelectrochemical Disinfection
▶ TiO$_2$ Photocatalyst

References

1. Parsons S (2004) Advanced oxidation process for water and wastewater treatment. IWA publishing, London
2. Goldstein G, Meyerstein D, Czapski G (1993) The Fenton reagents. Free Radic Biol Med 15:435–445

3. Bandala E, Corona B, Guisar R, Uscanga M (2007) Aplicación de procesos Avanzados de Oxidación en la desactivación secuencial de microorganismos Resistentes en Agua. Ciencia... Ahora 20:52–63

4. Kim JK, Metcalfe IS (2007) Investigation of the generation of hydroxyl radicals and their oxidative role in the presence of heterogeneous copper catalysts. Chemosphere 69:689–696

5. Peralta-Hernández JM, Meas-Vong Y, Rodríguez F, Chapman T, Maldonado I, Godínez LA (2006) In situ electrochemical and photo-electrochemical generation of the fenton reagent: a potentially important new water treatment technology. Water Res 40:1754–1762

6. Lucas MS, Peres JA (2006) Decolorization of the azo dye Reactive Black 5 by Fenton and photo-Fenton oxidation. Dye Pigment 71:236–244

7. Deng Y, Englehard JD (2009) Kinetics and oxidative mechanism for H_2O_2-enchanced iron-mediated aeration (IMA) treatment of recalcitrant organic compounds in mature landfill leachate. J Hazard Mater 169:370–375

8. Qiang Z, Chang J-H, Huang C-P (2003) Electrochemical regeneration of Fe_{2p} in Fenton oxidation processes. Water Res 37:1308–1319

9. Lu MC, Lin C-J, Liao C-H, Ting WP, Huang R-Y (2001) Influence of pH on the dewatering of activated sludge by Fenton's reagent. Water Sci Technol 44:327–332

10. Liou RM, Chen SH, Hung MY, Hsu CS (2004) Catalytic oxidation of pentachlorophenol in contaminated soil suspensions by Fe^{+3}- Resin/H_2O_2. Chemosphere 55:1271–1280

11. Duarte F, Maldonado-Hódar FJ, Pérez-Cardenas AF, Madeira LM (2009) Fenton-like degradation of azo-dye Orange II catalyzed by transition metal son carbón aerogels. Appl Catal B Environ 85:139–147

12. Pignatello JJ, Oliveros E, MacKay A (2006) Advanced oxidation processes for organic contaminant destruction based on the Fenton reaction and related chemistry. Crit Rev Environ Sci Technol 36:1–84

13. Qiuqiang Chen, Pingxiao Wu, Yuanyuan Li, Nengwu Zhu, Zhi Dang (2009) Heterogeneous photo-Fenton photodegradation of reactive brilliant orange X-GN over iron-pillared montmorillonite under visible irradiation. J Hazard Mater 168:901–908

14. Kasiri MB, Aleboyeh H, Aleboyeh A (2008) Degradation of Acid Blue 74 using Fe-ZSM5 zeolite as a heterogeneous photo-Fenton catalyst. Appl Catal Environ 84:9–15

15. Rey-May Liou, Shih-Hsiung Chen, Mu-Ya Hung, Chin-Shan Hsu a, Juin-Yih Lai (2005) Fe (III) supported on resin as effective catalyst for the heterogeneous oxidation of phenol in aqueous solution. Chemosphere 59:117–125

16. Balanosky E, Fernández J, Kiwi J, López A (1999) Degradation of membrane concentrates of the textile industry by Fenton like reactions in iron-free solutions at biocompatible pH values (pH $\approx$ 7–8). Water Sci Technol 40(4–5):417–424

17. Verma P, Baldrian P, Gabriel J, Trnka T, Nerud F (2004) Copper-ligand complex for the decolorization of synthetic dyes. Chemosphere 57:107–1211

18. Bali U, Karagözoglu B (2007) Performance comparison of Fenton process ferric coagulation and H2O2/pyridine/Cu(II) system for Decolorization of Remazol Turquoise Blue G-133. Dye Pigment 74:73–80

19. Fathima N, Aravindhan R, Rao J, Nair B (2008) Dye house wastewater treatment through advanced oxidation process using Cu-exchanged Y Zeolite: a heterogeneous catalytic approach. Chemosphere 70:146–1151

20. Esquivel K, García MG, Rodríguez F, Ortiz-Frade L, Godínez L (2013) Study of the photo-electrochemical activity of cobalt- and nickel doped TiO2 photoanodes for the treatment of a dye-contaminated aqueous solution. Journal of Applied Electrochemistry 43:433–440

21. Zhao B, Meleb G, Piob I, Li J, Palmisano L, Vasapollob G (2010) Degradation of 4-nitrophenol (4-NP) using Fe-TiO2 as a heterogeneous photo-Fenton catalyst. Journal of Hazardous Materials 176:569–574

22. Zarei M, Khataee A, Fathinia M, Seyyednajafi F, Ranjbar H (2012) Combination of nanophotocatalysis with electro-Fenton-like process in the removal of phenol from aqueous solution: GC analysis and response surface approach. International Journal of Industrial Chemistry 3:1–11

23. Sheng H Lin, Chih C Chang (2000) Treatment of landfill leachate by combined electro-Fenton oxidation and sequencing batch reactor method. Water Res 34(17):4243–4249

Photoelectrochemistry, Fundamentals and Applications

Krishnan Rajeshwar
The University of Texas at Arlington,
Arlington, TX, USA

Introduction

Light can influence an electrochemical system in variant ways. The basis for the photoeffect is *photoexcitation* either of a molecule located in the electrolyte phase or of the electrode material itself. The former constitutes the basis of either

a *photogalvanic cell* or a *dye-sensitized solar cell* as discussed later. In the latter case of electrode photoexcitation a metal electrode can absorb the incident light and if the energy exceeds its work function threshold, can cause *photoemission* of electrons from the metal into the electrolyte phase where they become solvated and thus stabilized. On the other hand, if the electrode material is a semiconductor, photons can be absorbed in a quantized fashion if their incident energy is equal to or greater than the semiconductor band-gap energy. In these cases we have *photoelectrochemical cells*. Yet another situation may be distinguished where *colloidal* nanoparticles of an inorganic semiconductor are suspended in solutions and irradiated with photons to drive *photocatalytic* processes of interest. Finally a hybrid approach involves using a nanocrystalline semiconductor film as an electrode in a *photoelectrocatalytic* cell. The field of *photoelectrochemistry* encompasses all of the above variant scenarios, each one of which is examined in turn next. *Photosplitting* (*photoelectrolysis*) and *photocatalytic* systems are also discussed in what follows. The impetus for studies of these systems has been both fundamental (for example, to test electron transfer theories) and applied, with the applications largely directed toward solar energy conversion (specifically *storage*) and environmental remediation [1].

Approaches

Photogalvanic Cells

A homogeneous redox component, i.e., one that is dissolved in an electrolyte phase can be photochemically excited to yield excited state species that can undergo redox reactions. The prototypical molecule here is the metal complex, [Ru (bpy)$_3$]$^{2+}$ where bpy = 2,2'-bipyridine ligand. Thus the excited state of this molecule is a fairly powerful reductant:

$$[\text{Ru(bpy)}_3^{2+}]^* + \text{Fe}^{3+} \rightarrow \text{Fe}^{2+} + \text{Ru(bpy)}_3^{3+}$$
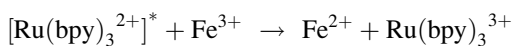
The back reaction constitutes the back-reaction regenerating the original reactants:

$$\text{Fe}^{2+} + \text{Ru(bpy)}_3^{3+} \rightarrow \text{Ru(bpy)}_3^{2+} + \text{Fe}^{3+}$$
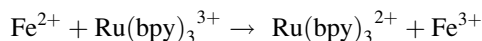
Thus the light energy simply is thermalized. However the kinetics of this reaction can be made slower (e.g., by manipulating local microenvironments) such that appreciable concentrations of the photoreaction products can be accumulated. By immersing electrodes into the solution one can force a Faradaic (photo)current to flow in response to the second step above with each electrode being made selective to one of the half-reactions. Since the original excitation energy can be harnessed (at least partially), these devices called *photogalvanic cells*, are relevant to applications related to solar energy conversion [2–4].

Much of the interest that was centered on these devices in the early 1970s have since largely subsided because of practical difficulties in designing electrode interfaces that are selective and have fast kinetics for the desired half-reaction.

Dye-sensitized Solar Cells (DSSCs)

These are conceptually very similar to the photogalvanic devices in that the initial photoexcitation occurs on a dye molecule that is either anchored or strongly adsorbed on an oxide semiconductor support (nominally TiO$_2$). Again using [Ru(bpy)$_3$]$^{2+}$ as an example, the photoexcited species, [Ru(bpy)$_3^{2+}$], inject a photoelectron into (acceptor) states in the oxide support thus getting oxidized. Regeneration of the oxidized state of the dye (using a redox shuttle such as iodide/polyiodide) accompanied by redox conversion of the resultant species at the countereelctrode completes the electrical circuit and results in a photocurrent flow in the external circuit of the cell. The result is light energy → electricity conversion in the device.

The breakthrough in the DSSC technology occurred in 1990 when strategies were developed (using corresponding developments in nanotechnology) to prepare *mesoporous* TiO$_2$ films so

that appreciable amounts of dye could be sequestered on the oxide support phase thus enhancing the incident photon-to-electron conversion efficiency (IPCE) and the photocurrent yields [5–7]. These developments in turn had a marked influence on the health and viability of the field of photoelectrochemistry itself [8], and DSSCs continue to be an intensely studied research topic.

Recent developments in DSSC have turned toward adapting these devices to incorporate a solar energy storage component. Replacement of the liquid electrolyte with a *solid electrolyte* or a gel has also been an important area of research activity as are efforts directed to improving the long- term (several years!) stability of the DSSC components.

Photoelectrochemicalcells

Consider a metal working electrode first. The ejected electrons from a metal electrode surface will travel a few A into the electrolyte phase and then become solvated. These solvated species display interesting chemistry and electrochemistry if suitable electron scavengers are available to interact with them. The resultant *free radical species* can be probed spectroscopically in these photoelectrochemical or *spectrophotoelectrochemical* experiments. The irradiation can be either continuous or pulsed and with the advent of powerful laser sources a whole slew of experimental strategies open up [9, 10]. Of course with continuous irradiation the spectroscopic probe will have to be orthogonally placed to avoid interference with the incoming radiation [11].

On the other hand, solid-state physics principles teach that semiconductors are characterized by filled and empty states that are more appropriately termed as *bands*, specifically *valence* and *conduction bands* (VB and CB) respectively [12]. These are the solid states analogues of the corresponding energy levels in molecules called highest occupied molecular orbital (HOMO) and lowest unoccupied molecular orbital (LUMO) respectively; i.e., the E_g becomes the solid- state analog of the molecular HOMO-LUMO energy gap. While in a *metal*, the bands are half- filled (giving rise to its electrical conductivity when an electric field is applied), the VB and CB in a *semiconductor* are separated by an energy gap (E_g) that may range from $\sim$0.1 eV to $\sim$3.5 eV. In an *insulator* this gap is usually much larger. Now when photons are incident such that their energy, hu $> E_g$, electron–hole pairs are excited in the semiconductor, and in the presence of a built-in field at the interface (discussed in detail in other chapters in this encyclopedia), the *excitons* are dissociated into electrons and holes. Depending on whether the semiconductor is n- type or p-type, the minority carriers (holes for n-type, electrons for p-type) are driven to the semiconductor/electrolyte interface. Thus *photooxidation* and*photoreduction* reactions occur respectively between these carriers and redox species in the electrolyte phase.

Thus *semiconductor working electrode* materials and their interfaces with electrolytes form the basis for a very important class of *photoelectrochemical* cells [12]. In principle both *organic* and *inorganic* semiconductor materials may be utilized although we shall mainly focus on inorganic semiconductors for our present discussion.

If either an n-type photoanode or a p-type photocathode is used in conjunction with a metal counterelectrode and a reversible redox electrolyte (e.g., Fe(CN)$6^{3-/4-}$), we have the basis for a *regenerative* photoelectrochemical cell. Alternately both an n-type and a p-type semiconductor may be used in tandem in a twin-photoelectrode geometry for the cell, much like what plants do in photosynthesis (For example [13]). Note that in these case there is no *net chemistry occurring in the electrolyte phase in response tophotoexcitation*, i.e., what is photooxized (or photoreduced) at one terminal is re-reduced (or re-oxidized) back at the other. The result is conversion or transduction of photon energy to electrical energy.

One can well argue that there is no real advantage to be accrued from the use of such an energy conversion device relative to a *solid-state photovoltaic* device that is much more robust and simpler to implement. Who would want to put a (potentially toxic) liquid on a roof top, even in a sealed device with attendant risk of leakage?! Indeed aside from furnishing important fundamental insights into charge transfer at

semiconductor-electrolyte interfaces, *liquid junction regenerative solar cells* have drawn little practical interest. Much more important (from a solar energy storage perspective) are the so-called *photoelectrolytic* cells; these are discussed next.

Photoelectrolytic Cells

Consider an n-type (oxide) semiconductor in contact with a liquid electrolyte for specificity. If a reversible redox system is not present, then the photogenerated holes will attack the electrolyte species (or the solid lattice) instead. In an aqueous electrolyte adsorbed water molecules or hydroxide ions are always present. Photooxidation of these species will generate dioxygen if the energetics at the interface are satisfied [14]. At the counterelectrode the electrons will reduce protons in the electrolyte, assuming again that the interfacial energetics are optimal. The net result is the photosplitting of water into dioxygen and hydrogen in a *photoelectrolytic* cell. Note that unlike in the liquid-junction regenerative cell discussed above, there is next chemical change in the electrolyte phase.

As can be imagined, the implications in terms of solar energy storage are tremendously important and it is no wonder that the original paper on this topic [15] continues to be one of the most widely cited in the chemical literature. It is worth pointing out that in the original work a pH gradient was imposed in the electrochemical cell to serve as an additional "bias" to the insufficient energy of the conduction band electrons in rutile to photoreduce protons.

It is somewhat sobering that three decades have elapsed since the original study on the feasibility of solar water splitting and we are no closer to a satisfactory solution to this challenge [8] that has been aptly termed as the "Holy Grail" [16]. Issues such as process efficiency, photoelectrode stability, and potential materials cost continue to dog efforts aimed at overcoming this challenge. A detailed discussion of these issues is prohibited by space constraints here; instead, the reader is referred to review articles on this topic [14, 17]. Intense effort also has gone into the design and development of schemes that

require no *external bias* voltage (over and above what is generated by the light) to sustain the water splitting process. That is, the entire process is then *spontaneous* under photoexcitation of the semiconductor and a photocurrent continues to flow as long as the light is on. Obviously this entails an (open-circuit) photovoltage in excess of ∼1.5 V (assuming operation at ambient temperature) to be generated in the system with no deleterious consequences in terms of electrode corrosion etc.!

Figure 1 provides a schematic illustration of the three types of devices, namely, regenerative, photoelectrolytic and DSSC.

Photocatalysis

An entirely related field of research, underpinned by very similar photophysics principles as those detailed above for photoelectrochemical cells, evolved around the same time as the first demonstration of solar water splitting using TiO_2 [18]. This involved the possibility of utilizing the (very energetic) holes available in a low-lying valence band in TiO_2 to photoxidize (organic) pollutants confined in the electrolyte phase [1, 19]. In this instance, unlike with the water photosplitting reaction above, the photooxidation of organics in thermodynamically *downhill* (negative free energy change) such that the terminology: *photocatalysis* is entirely appropriate. That is, light merely serves to speed up a sluggish electrochemical process in the dark [20]. By contrast the photogeneration of H_2 and O_2 from water represents a *photoelectrosynthetic* process.

This field of activity has enjoyed exponential growth since the 1970s spurred by environmental remediation applications and many semiconductors beyond TiO_2 have been examined as well as an astounding range of solution substrates [1, 19, 21]. It is worth noting that unlike advanced oxidation processes (AOPs) for combating environmental pollution, the semiconductor-based *heterogeneous photocatalysis* approach is compatible with both oxidizable and reducible solution species or even a combination of both [22]. For example AOPs clearly cannot be used to treat a waste stream consisting of phenols and toxic metal ions (e.g., Cd^{2+}, Hg^{2+}) unlike
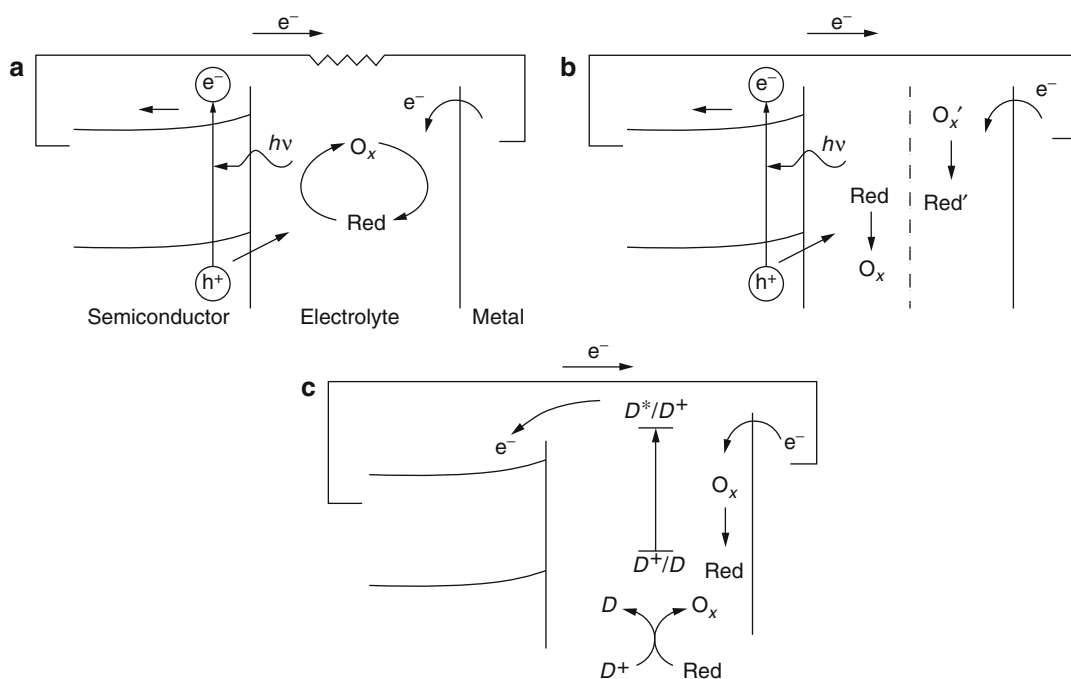
Photoelectrochemistry, Fundamentals and Applications, Fig. 1 Types of photoelectochemical devices for solar energy conversion (**a**), (**b**) and (**c**) depict regenerative, photoelectrolytic and dye-sentisitized configurations, respectively. As in the remainder of the chapter, and *n*-type semi-conductor is assumed in these cases for specificity

a remediation scheme based on the use of TiO_2 or another semiconductor. This is simply because both photogenerated holes and electrons can be utilized to oxidize and reduce the target pollutant respectively in the latter case. Incidentally many mechanism-oriented studies have been directed at the questions surrounding what the interfacial reactions involve: for example, direct oxidation by photogenerated holes or one mediated by hydroxyl radicals (or other reactive oxygen species, ROS), role of semiconductor surface states or traps etc. [19].

Finally the heterogeneous photocatalysis technique has been extended in scope to include the treatment of contaminated air and gas-phase pollutants. Photocatalyst suspensions, while they offer several advantages associated with huge surface area and consequently large reaction cross- sections, simplicity of reactor etc., are also limited in that a bias potential cannot be applied to further accelerate the photoprocess. Further, photocatalyst recovery after use is complicated. In contrast the use of *nanocrystalline photocatalyst* films affords effective solutions to both these issues in a*photoelectrocatalysis* cell geometry [21].

Note that the slurry-based approach can be used for water photosplitting purposes as well and has been a popular configuration by many researchers in Japan and elsewhere. In this scenario there is a crucial factor in a suspension-based vis-a-vis an electrode-based photoelectrolytic cell geometry that is worthy of attention. In the former a potential explosive mixture of H_2 and O_2 are photoegenrated in close proximity. Back-reactions involving the photoproducts (leading to a *photostationary state*) are also an issue in the former case. More simply one of the half-reactions (say the oxygen evolution reaction or OEC) is substituted with a (sacrificial) redox half-reaction such that the net reaction is thermodynamically down-hill and the reaction now becomes *photocatalytic* rather than*photosynthetic* [20].

Active Material Aspects

Early in the evolution of the field of photoelectrochemistry, the semiconductors were mostly used in single crystal form. While this configuration furnished a rich library of fundamental data in the 1970s and 1980s on the nature of semiconductor/electrolyte interfaces in the dark and under illumination, the use of single crystals is not compatible with practical deployment of photoelectrochemical devices. This then paved the way to the use of semiconductor *thin films* (usually polycrystalline but sometimes even amorphous) supported on metals or transparent conducting glass. More recently, the advent of nanotechnology has opened the door to the use of *nanocrystalline* semiconductor films. Currently considerable attention is focused on the photoelectrochemical behavior of inorganic semiconductors in the form of quantum (or Q) dots, either directly in suspended form in solution or in thin film form [22]. Their unique optical and electronic properties considerably expand the scope of photoelectrochemical devices that use Q- dots as the active material. The other aspect of the search for new families of semiconductor materials for photoelectrochemical applications has been to focus on compounds that contain earth-abundant and non-toxic elements such as Cu, Fe, W, Ti etc. instead of precious and toxic elements such as Ga, In, Se, Cd etc. This in turn has the added bonus of potentially lowering the cost associated with the ultimate device. In solar conversion devices, the active materials component(s) (i.e., semiconductors) constitute a healthy fraction of the overall device cost [23].

Further Application Possibilities

We close this discussion with the note that water splitting is not the only reaction of interest in solar energy conversion and environmental remediation. Splitting of CO_2 (to a fuel product such as methanol or methane) constitutes a value-added approach to combating the accumulation of this greenhouse gas molecule [24]. However the kinetic bottlenecks to CO_2 splitting pose steep technical challenges in coming up with solutions that are being actively pursued in laboraties worldwide. Combining this value-added approach with the use of semiconductors such as CuO and Cu_2O are attractive from a translational perspective [25, 26]. Photoassisted water splitting to generate hydrogen from p-type semiconductors such as Cu_2O can also be combined with a (dark) oxidation reaction at the counterelectrode that is designed to break down an environmental pollutant (e.g., organic dye) thus adding value to the hydrogen photogeneration step [27].

Concluding Remarks

The field of photoelectrochemistry continues to make strides during its ca. 40 year lifespan. While our current knowledge of the fundamental aspects of charge transfer at semiconductor-electrolyte interfaces can be regarded as fairly mature, there are still unresolved aspects related to the specific *chemical* and *electrochemical* nature of traps and surface states at these interfaces. Much remains to be done in further development of experimental tools for studying the dynamic role of these charge transfer-mediating sites *under conditions typical of an operating solar cell*. On the applications side, the many challenges remaining for the development of stable, efficient, and cost-effective systems for solar water and CO_2 splitting will continue to keep future generations of researchers busily engaged for years to come. In particular solar conversion efficiencies routinely exceeding the $\sim$10 % threshold will be required to trigger the interest of the chemical engineering community and engage it in further concerted efforts aimed at designs of photoelectrolytic reactors and the like.

Cross-References

▶ Photocatalyst
▶ Photoelectrochemical CO_2 Reduction

References

1. Rajeshwar K (1997) Environmental electrochemistry. Academic, San Diego
2. Archer MD (1975) J Appl Electrochem 5:17
3. Lin CT, Sutin N (1976) J Phys Chem 80:97
4. Albery WJ, Archer MD (1978) J Electroanal Chem 86:1
5. Gratzel M (ed) (1983) Energy resources through photochemistry and catalysis. Academic, New York
6. O'Regan B, Gratzel M (1991) Nature 353:737
7. Gratzel M (2005) Inorg Chem 44:6841
8. Rajeshwar K (2011) J Phys Chem Lett 2:1301
9. Barker GC (1971) Ber Bunsenges Phys Chem 75:728
10. Kissinger PT, Heineman WR (eds) (1996) Laboratory techniques in electrochemistry, 2nd edn. Marcel Dekker, New York
11. Rajeshwar K, Lezna RO, de Tacconi NR (1992) Anal Chem 64:429A
12. Rajeshwar K (2001) In: Licht S (ed) Encyclopedia of electrochemistry, Chap. 1. Wiley-VCH, Weinheim, p 3–53
13. Nocera DG (2012) Acc Chem Res, 45:767 and references therein
14. Rajeshwar K (2007) J Appl Electrochem 37:765
15. Fujishima A, Honda K (1972) Nature 238:37
16. Bard AJ, Fox MA (1995) Acc Chem Res 28:141
17. Rajeshwar K (1985) J Appl Electrochem 15:1
18. Carey JH, Lawrence J, Tosine HM (1976) Bull Environ Contam Toxicol 16:897
19. Rajeshwar K (1995) J Appl Electrochem 25:1067
20. Rajeshwar K, Ibanez JG (1995) J Chem Educ 72:1044
21. Rajeshwar K, Osugi ME, Chanmanee W, Chenthamarakshan CR, Zanoni MVB, Kajitvichyanukul P, Krishnan-Ayer R (2008) J Photochem Photobiol C Photochem Rev 9:15
22. For example, Kamat PV (2008) J Phys Chem B 113:18737
23. Weaver N, Singh R, Rajeshwar K, Singh P, DuBow J (1981) Sol Cell 3:221
24. Boston DJ, Huang KL, de Tacconi NR, MacDonnell FM, Rajeshwar K (2013) In: Lewerenz HJ, Peter LM (eds) Photoelectrochemical water splitting: challenges and new perspectives. RSC Press (in press), UK
25. Ghadimkhani G, de Tacconi NR, Chanmanee W, Janaky C, Rajeshwar K (2013) Chem Commun 49: 1297–1299
26. Rajeshwar K, de Tacconi NR, Ghadimkhani G, Chanmanee W, Janaky C (2013) Chem Phys Chem 14:2251–2259
27. Somasundaram S, Chenthamarakshan CR, de Tacconi NR, Rajeshwar K (2007) Int J Hydrogen Energ 32:4661

Photogalvanic Cells, Principles and Perspectives

Jonathan E. Halls[1] and Jay D. Wadhawan[2]
[1]Department of Chemistry, The University of Bath, Bath, UK
[2]Department of Chemistry, The University of Hull, Hull, UK

Introduction

In modern society, it is common knowledge that the levels of fossil fuels and the stored energy they provide are rapidly decreasing – as a finite resource, it is imperative that new methods of delivering energy to the global population are sought. Due to the abundance of radiant energy provided by the Sun – the solar energy falling on the surface of the Earth in two weeks is equivalent to the energy contained in the initial global supply of fossil fuels – and the environmental uncertainty surrounding nuclear power, much attention has been paid to the development of different systems for harnessing solar energy [1]. In particular, this area of interest has led to numerous investigations into photoelectrochemical (PEC) cells, due to their possible rôle as transducers of solar to electrical energy [2].

Photoelectrochemical Energy Conversion

A PEC cell can be defined as one in which one or both half cells exhibit a PEC effect – which can in turn be described as one in which the irradiation of an electrode or electrolyte system produces a change in the electrode potential (on open circuit) or in the current flowing (on closed circuit) [1].

Becquerel [3, 4] first proposed this theory when, in 1839, he observed the flow of current between two unsymmetrical illuminated metal electrodes in sunlight [5].

PEC effects, and therefore cells, can exist in two forms – photovoltaic (PV) and photogalvanic (PG) – the latter of which shall be discussed extensively within this review. A third type of PEC cell has been proposed by Tien et al. [6] which combines the effects of the photogalvanic and photovoltaic processes and is subsequently named the photogalvanovoltaic effect. However, the feasibility of using this process as a commercial application is questionable, and research into photogalvanovoltaic cells is extremely limited [7, 8].

A PV effect can be characterized as an effect due to photoreduction of electrons and holes, along with no accompanying chemical change. The PV cell absorbs photons from solar energy (sunlight), the energy of which is then transferred to electrons in the system, which consequently leave their respective positions to become part of the electrical current – forming holes [1]. PV cells are purely solid-state devices and have been found to have suitable properties for use as industrial and commercial solar cells – however, they are incredibly complex in terms of production due to the need for extensive purification of the silicon used within the semiconductor cells, which in turn leads to increased manufacturing costs. In contrast to PV systems, cells that exhibit a PEC effect such as the PG cells described in Table 6 further on exhibit a storage capacity and can consequently achieve in one "stage" what a combination of a PV cell with a storage battery achieves in two. This is a fundamental reason behind the extensive research into modifications of PG cells to increase their efficiency. While the abundance of solar radiation received by Earth is relatively constant over time, the exposure of a given surface at a given time to solar energy varies daily and seasonally – consequently, having a solar energy conversion device with an incorporated storage capability is extremely beneficial [1]. The values for mean total solar radiation received by Earth over a 24-h day are given in Fig. 1.

This review will focus solely on the characteristics, analysis, and developments of photogalvanic cells, which in contrast to PV cells are relatively cheap to construct – however, current research proves inconclusive as to whether they can exhibit efficiency and reliability properties as favorable as those found in PV devices.

The Photogalvanic Effect

The PG effect is described by Rabinowitch as "the change in the electrode potential of a galvanic system, produced by illumination and traceable to a photochemical process in the body of the electrolyte" [9, 10]. Cells exhibiting a PG effect have a higher storage capacity than PV cells, but a lower conversion efficiency (theoretically $\sim$18 % but observed values are much lower) [5, 11]. Consequently, extensive research has been carried out concerning the manipulation of substances used in PG cells (i.e., reductants and photosensitizers) in order to maximize electrical output [5].

A typical PG cell is made up of two parallel electrodes (an illuminated and a dark) between which a thin layer of electrolyte solution is contained; see Fig. 2. A photochemical reaction is induced within the electrolyte as a result of solar energy entering through the semitransparent or transparent (illuminated) electrode – the resulting high energy products react, driving electrons around an external circuit [12, 13]. Two redox couples are dissolved within the electrolyte, and the reaction scheme is given in Eq. 1.

Absorption of solar radiation is undertaken by component A, a dye. A subsequent electron-transfer reaction between the excited $A*$ and Z yields energetic products B and Y [13]:

$$\frac{A + Zk}{\rightleftharpoons B + Y} \tag{1}$$

Photochemistry:

$$\frac{Ah\nu}{\longrightarrow A^*} \tag{2}$$
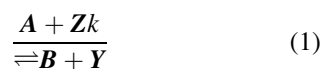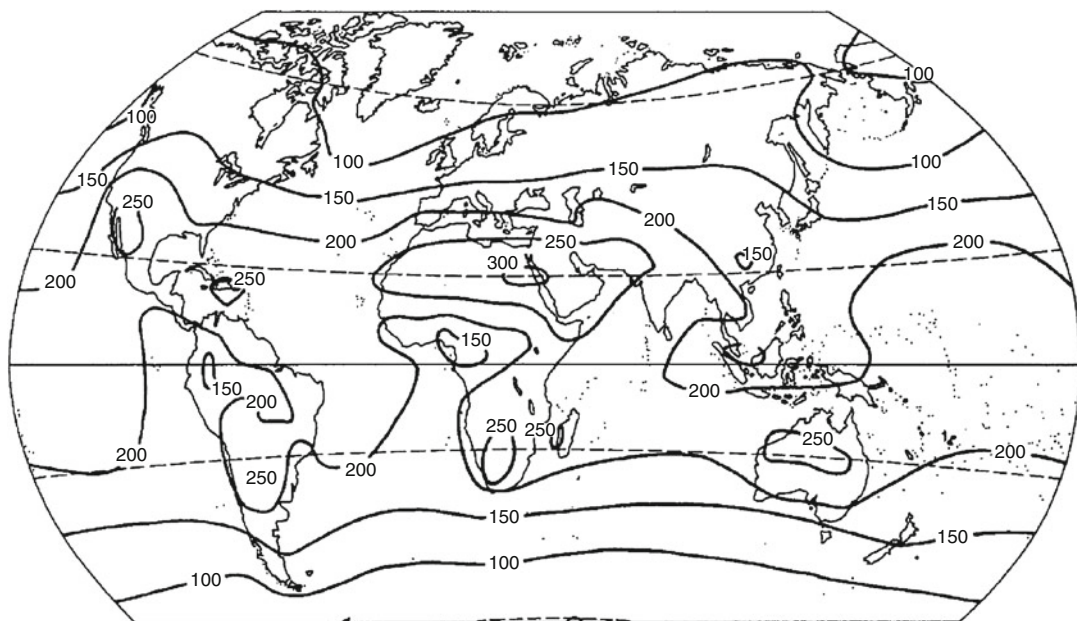
Photogalvanic Cells, Principles and Perspectives, Fig. 1 Mean annual intensity of solar radiation on a horizontal plane at the surface of the Earth. Numbers represent solar irradiance in W m^{-2} averaged over a 24 h day (Reproduced from reference Springer Science+Business Media, Journal of Applied Electrochemistry, 5, 1975, 17, Electrochemical aspects of solar energy conversion, M. D. Archer, Figure. With kind permission from Springer Science and Business Media)
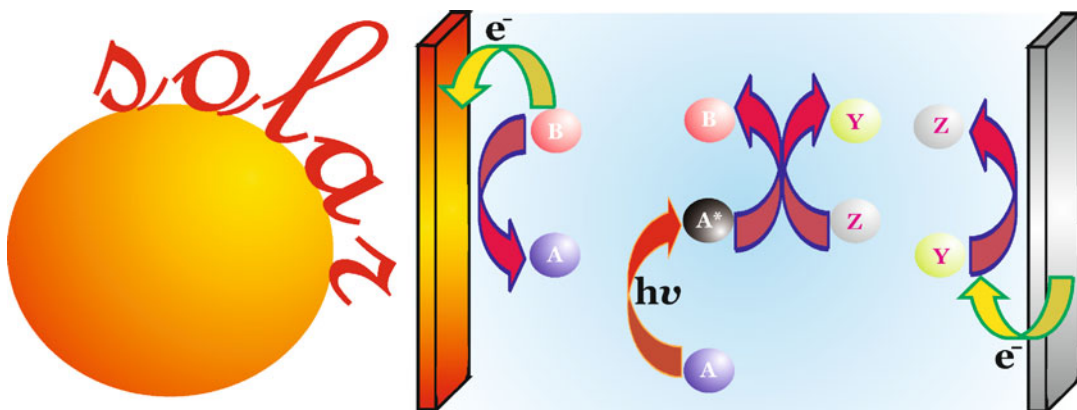
Photogalvanic Cells, Principles and Perspectives, Fig. 2 Schematic representation of a thin-layer photogalvanic cell. The illuminated electrode (*left-hand side*) is constructed from a semitransparent/transparent material (such as SnO$_2$, In$_2$O$_3$, or ZnO), with a photogalvanic electrode filling the space between the illuminated and dark (*right-hand side*) electrodes

$$\xrightarrow{A^* + ZK_q} B + Y \qquad (3)$$

A back reaction between **B** and **Y** yields original components **A** and **Z**:

$$\xrightarrow{B + Yk} A + Z \qquad (4)$$

Discussed in further detail later on, the rapidity of this reaction is of great hindrance to the

performance of the cell. Component B must locate the illuminated electrode (where solar radiation permeates the cell) and react there before the back reaction occurs [13].

Electrode reactions:

$$B \pm e \longrightarrow A \qquad (5)$$

$$Y \pm e \longrightarrow Z \qquad (6)$$

Following on from Becquerel's aforementioned discovery [3], the PG effect was initially recognized by Rideal and Williams [14] before Rabinowitch [9, 10] subsequently examined the photochemical and photogalvanic properties of a thionine (Th)-iron system. The scheme is described below, while the mechanism and kinetics are described later.

$$\frac{1}{2}Th + Fe^{2+} \underset{\text{dark}}{\overset{hv}{\rightleftharpoons}} \frac{1}{2}Leu - Th + Fe^{3+} \qquad (7)$$
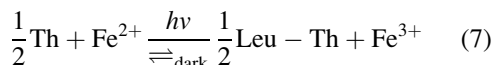
Rabinowitch discovered this redox equilibrium was the most light-sensitive known – thionine dyes absorb at 500–700 nm, comparable with values of maximal solar radiation – and as a result would possess a high level of PG sensitivity. As explained in the later sections, the thionine-iron (a dye and reductant, respectively) redox cell yielded a low energy conversion efficiency (<1 %), but the results were somewhat promising due to the ability to manipulate the dye and/or reductant – and subsequently established much research into optimization of the necessary components within the system [9, 15].

Photogalvanic Cell Overview

The Ideal Photogalvanic Cell

Albery and Archer analyzed the various factors which affect the ability of a PG cell to deliver the optimum power conversion efficiency (theoretically $\sim$18 %) [16, 17]. These authors discovered that the processes occurring within a PG cell were dependent on the system's photochemistry, homogeneous kinetics, mass transfer, and electrode kinetics – and therefore, the energy

converted depended on species concentration, hv intensity, the electrode kinetics, and their spacing and diffusion lengths [17].

Over a series of articles, Albery and Archer calculated the optimum length characteristics for an efficient PG cell [1, 12, 13, 16–20]. It should be noted that while Albery and Archer's work is perspicacious and seminal, it is imperative to realize that their considerations were only undertaken under the assumption of minimal electrical migration within the PG cell. Of course this is not true in many cases, and the generality of their results in conditions of low supporting electrolyte concentration must therefore be considered with caution.

To enhance solar energy conversion, it was discovered that the following conditions be obeyed:

$$10X_\varepsilon < X_g, X_k, X_l \qquad (8)$$

Although to produce the maximum theoretical power yield, the following PG cell conditions have been established – however, in practice this is unfeasible, as explained later:

$$10X_\varepsilon \cong X_G \cong \frac{1}{2}X_G < X_l \qquad (9)$$

Table 1 provides the definitions of these four X parameters (Fig. 3).

Equation 8 denotes that X_ε must be bigger than the three other length parameters controlling the efficiency of a PG cell. Initially, the absorbance length must be smaller than the generating length in order to ensure there is sufficient amounts of component A available to absorb the incoming photons of solar radiation and to inhibit the bleaching of the solution at the semitransparent electrode. In order for B to be able to diffuse to this electrode before it is broken down via the back reaction, the absorbance length must also be smaller than the reaction length. Finally, to ensure B reacts on the electrode interacting with hv, the absorbance length must be smaller than the cell length. The value of X_k is known to be approximately 10^{-3} cm; therefore by use of Eq. 8 and the equations described in Table 1,

Photogalvanic Cells, Principles and Perspectives, Table 1 Definition of characteristic lengths for a PG cell (Adapted from reference [12])

Name	Symbol and equation	Description
Cell length	X_l	The distance between electrodes
Absorbance length	$X_\varepsilon = (\varepsilon[A])^{-1}$	The distance over which light is absorbed
Generating length	$X_g = \left(\frac{D}{\phi I_0 \varepsilon}\right)^{\frac{1}{2}}$	The distance A diffuses in light of irradiance I_0 before being converted to B
Reaction length	$X_k = \left(\frac{D}{k[Y]}\right)^{\frac{1}{2}}$	The distance over which B diffuses before being broken down in reaction with Y

where D = diffusion coefficient of B, ϕ = quantum efficiency for generation of B and is tantamount to the ratio of photons absorbed to the amount produced, I = molar flux of photons, and ε = molar extinction coefficient of A (units $cm^2\ mol^{-1}$)

Photogalvanic Cells, Principles and Perspectives, Fig. 3 Schematic definition of the characteristic lengths for a PG cell (Reprinted with permission from W. John Albery (1982) Development of photogalvanic cells for solar energy conservation. Accounts of Chemical Research 15: 142. Copyright (1982) American Chemical Society)
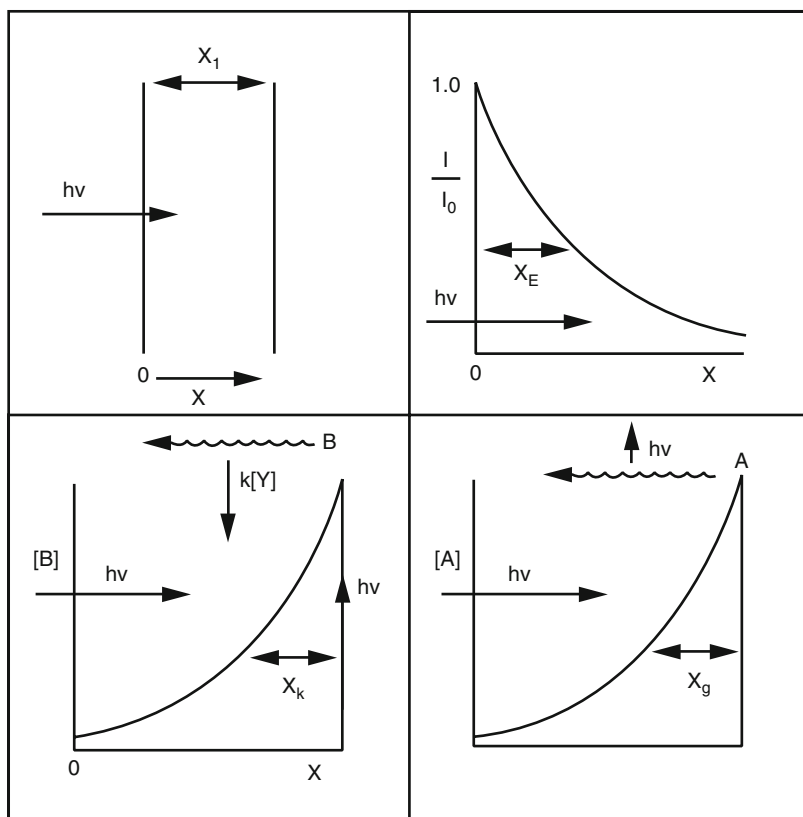
Albery and Archer were able to calculate the values of the four parameters for an ideal cell [12, 13].

Electrode Selectivity and Kinetics

The selectivity of the electrodes and their kinetics are an essential consideration for the design of a practical PG cell. The B and Y components of the PG cell reaction must react at the illuminated and dark electrodes, respectively, in order to generate a current. If the illuminated electrode is not selective, the back reaction ($B + Y \rightarrow A + Z$) is catalyzed due to Y reacting at the site instead of B – however, a selective electrode facilitates diffusion of Y across to the dark electrode, allowing B to react at the necessary position.

Photogalvanic Cells, Principles and Perspectives, Table 2 Ideal electrochemical rate constants (Adapted from reference [12])

Couple	Illuminated electrode	Dark electrode
A, B	$k'_B > \dfrac{D}{X_k} \approx$ 5×10^{-3} cm s^{-1}	$k'_B[B] << k'_Y[Y]$
Y, Z	$k'_Y[Y] << k'_B[B]$	$k'_Y > \dfrac{D}{X_l} \approx$ 5×10^{-3} cm s^{-1}

Table 2 gives the electrochemical rate constants for an ideal PG cell. For a species to react at a specified electrode within an electrochemical reaction, the ratio D/X (where X is one of the length parameters outlined in Table 1) must be smaller than the rate constant k'. The opposite is true for a species to be lost via reaction in the electrolyte or diffusion to the opposite electrode. As **B** is required at the illuminated electrode, and as shown by Eq. 8, for an ideal PG cell it is necessary for reaction length to be smaller than cell length, **B** is less likely to diffuse to the dark electrode than it is to be destroyed by reaction with **Y**. Consequently, for component **B** the characteristic length is X_k. As explained further down, the concentration of **Y** and **Z** is assumed to be larger due to the diffusion distance, so for component **Y** the characteristic length is X_l [12].

Overall, it can be seen that if the electrode kinetics of the **A**,**B** and **Y**,**Z** couples are fast on the two electrodes (illuminated and dark, respectively) than the potentials of the respective electrodes will be similar to the standard electrode potentials of the two couples. Thus, the voltage generated by the PG system can be approximated by Eq. 10, and relies on differential electrode kinetics [12, 13].

$$E_\Delta \cong \left| E^\Theta_{A,\,B} - E^\Theta_{Y,\,Z} \right| \qquad (10)$$

If identical electrodes are selected for use in a PG cell, or if the **A, B** couple reacts via the dark electrode, then the system becomes a concentration cell – a severely inefficient solar energy conversion device, as explained later.

Effect of Species Concentration

Along with the optimization of electrode properties, the other major factor influencing the efficiency of a PG cell is the varying concentrations of the four components within the basic PEC reaction – **A, B, Y,** and **Z**. For the fundamental diffusion of components **Y** and **Z** across a PG cell in contrasting directions, the diffusive concentration gradient of **B** at the illuminated electrode is required to be in equality with **Y** and **Z** [12]. In addition, Eq. 8 denotes that the ideal distance between electrodes must be bigger than the absorbance length; thus, the variance in concentration across the system for components **Y** and **Z** must be greater than that of **B** [12]. Given that for an efficient PG cell, the flux of electrons of **Y** and **Z** should approximately equal I_0, the aforementioned variance in concentration (Δc) can be calculated as follows:

$$I_0 = \frac{D\Delta c}{X_l} \qquad (11)$$

where $\Delta c = [Y]_0 - [Y]_{X_l} = [Z]_{X_l} - [Z]_0$, with $[Y]$ and $[Z]$ at the midpoint of the cell being equal to their respective concentrations $[Y]_D$ and $[Z]_D$ in the absence of light [12].

For the diffusive transport of components **Y** and **Z** to the desired electrodes (dark and illuminated, respectively), the concentrations of the two need to be greater than $\frac{1}{2}\Delta c$ in the absence of light, which ensures their presence – and therefore their subsequent reaction – at the two electrodes. The presence of **Y** on the dark electrode ensures minimization of the back reaction, increases the electrochemical kinetics via inhibition of the **Y, Z** couple on the illuminated electrode, and produces a flow of current with **B** reacting on the opposite electrode [13, 17, 19, 20]. With **Z** located at the illuminated electrode, the excited **A*** component (the dye) can be trapped, enabling formation of **B**. The following set of equations, established by Albery and Foulds, allow the calculation of optimum concentrations of **Z, Y,** and **A** [12].

For the formation of **B**, the quantum efficiency for production can only be maximized if

Photogalvanic Cells, Principles and Perspectives, Fig. 4 Graphical illustration of the polarization (*red*) and power (*blue*) characteristics of an ideal photogalvanic cell. Note that the fill factor as defined by Eq. 17 is 25 % for an ideal galvanic cell under discharge
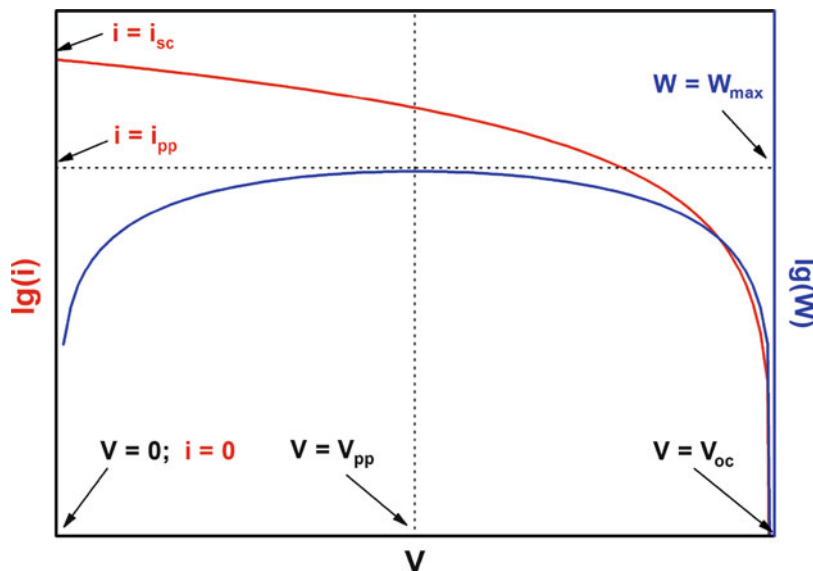
$$k_q[Z]_0\tau > 10 \tag{12}$$

where τ = lifetime of excited state A^* if Z is not present.

As mentioned above, the presence of the Y, Z couple on the illuminated electrode must be as low as possible – therefore, by increasing $[Y]$ and minimizing $[Z]$, the potential difference produced by the cell improves via the resulting effects on the potential of the Y, Z half cell [17]. Taking into account these requirements, and the above equation, the subsequent condition for Z results

$$[Z]_D \approx \Delta c + \frac{10}{k_q\tau} \tag{13}$$

As stated, the concentration of Y must be increased to a value large enough to produce a beneficial voltage from the cell and to prevent concentration polarization, but not so large as to aid destruction of B via the back reaction [12, 17]:

$$[Y]_D > \frac{1}{2}\Delta c \tag{14}$$

From Table 1, we can therefore obtain

$$[Y]_D = \frac{40}{k} - \frac{1}{2}\Delta c \tag{15}$$

Finally, to shorten the absorbance length, $[A]$ should be maximized, ensuring photons of solar energy are retained in close proximity to the electrode undergoing irradiation of solar light, facilitating the PEC reaction [12].

Solar Energy Conversion and Practical Power Output

Following the manipulation of the above parameters within a PG cell, the practicality of the system as a solar energy converter can be assessed by calculating the values of conversion efficiency and fill factor (a measure of the device quality). Conversion efficiency indicates the amount of incoming solar irradiation converted to electrical energy, while the fill factor describes the ratio of the (actual) maximum obtainable power to the theoretical. Both can be expressed as percentages. Figure 4 gives a graphical illustration of fill factor.

Conversion efficiency:

$$\eta = \frac{V_{pp}i_{pp}}{AE} \times 100 \tag{16}$$

Fill factor:

$$F_f = \frac{V_{pp}i_{pp}}{V_{oc}i_{sc}} \tag{17}$$

where A = area of each electrode, E = input light irradiance, V_{pp} = value of the cell voltage at power point, i_{pp} = value of the current at power point, V_{oc} = open circuit voltage, and i_{sc} = current at short circuit.

To determine η, E is calculated as

$$E = \frac{W_{max}}{A} \qquad (18)$$

where W_{max} is the maximum power produced by the cell and, for a cell with differential electrode kinetics (i.e., the ideal cell explained earlier), can be calculated as follows:

$$W_{max} = 0.8AF\phi I_0 \Delta E \qquad (19)$$

where ΔE = difference in standard electrode potentials for the A, B and Y, Z couples.

For standard solar radiation with Sun elevation angle of 30° (AM 2.0), I_0 can be estimated to have a value of $\sim 1.6 \times 10^{-3}$ mol photons m^{-2} s^{-1}.[17] If $\phi = 1$ and $\Delta E = 1.1$ V [1] (the optimum value), Eq. 19 establishes W_{max} as having a value of 140 W m^{-2}, which corresponds to a power conversion efficiency of 18 % [12, 17, 19]. Albery and Archer demonstrated however that this theoretical conversion efficiency is, in practice, unrealistic due to the impossibility of optimizing all the available parameters [19].

If typical values of D and ε are taken, 10^{-5} cm^2 s^{-1} and 10^8 cm^2 mol^{-1}, respectively, the generating length is found to be

$$X_g \sim 10^{-3} \text{ cm} \qquad (20)$$

The ideal cell requires the generating length to be ten times larger than the optical absorbance length, so

$$X_\varepsilon \sim 10^{-4} \text{ cm} \qquad (21)$$

Therefore it follows that

$$[A] \sim 10^{-1} \text{ M} \qquad (22)$$

Consequently, the dye must prove to be relatively soluble in order to absorb the solar radiation as close to the illuminated electrode as possible. Taking the value of X_g above, along with Eq. 9, the following condition must be obeyed for the kinetics of the reaction B with Y:

$$k[Y] \sim 40 \text{s}^{-1} \qquad (23)$$

To ensure the inhibition of concentration polarization (keeping the dark electrode unpolarized), $[Y]$ must be twice as large as $[B]$:

$$[Y] > 2[B] \sim 10^{-2}[A] \sim 10^{-3} \text{M} \qquad (24)$$

From Eqs. 8 and 9 it can be seen that the absorbance length must be smaller than the distance between electrodes, and as a result the rate constant, k', of the reaction of A and B at the illuminated electrode must be very fast:

$$k' > \frac{D}{X_\varepsilon} \sim 10^{-1} \text{cm s}^{-1} \qquad (25)$$

The required value of this rate constant proves a major disadvantage in obtaining the maximum theoretical conversion efficiency from a PG cell, as it is highly unusual for a redox couple to exhibit electrode kinetics as fast as the above value [19, 20].

It can be seen that obtaining maximum efficiency from a cell relies on the solubility of the dye (A), an extremely rapid rate constant for the A, B couple, and relatively slow kinetics for the electron-transfer reaction of B and Y. It is inconceivable that electron-transfer reactions obeying the above conditions while at the same time satisfying the Marcus theory could occur [16, 21–23].

As explained earlier, a PG system acting as a concentration cell proves to be severely inefficient as a solar energy converter, due to ΔE not having any bearing on the maximum obtainable power – both electrodes are identical. Therefore, W_{max} for a concentration cell is calculated as follows:

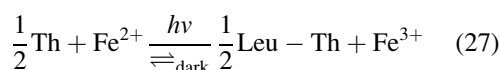$$W_{max} = 0.28ART\phi I_0 \qquad (26)$$

Photogalvanic Cells, Principles and Perspectives, Fig. 5 The three structures of the thionine dye within the iron-thionine PG system

Taking the same values of I_0 and ϕ as above, W_{max} is ~1.1 W m^{-2}, which corresponds to a maximum cell conversion efficiency of 0.15 %, i.e., practically useless [19, 20].
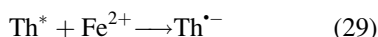
Early Developments of Molecular Systems for Photogalvanic Cells
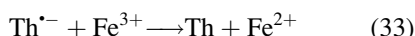
Early Photogalvanic Systems

Hatchard and Parker [24] further investigated the kinetics of the initial iron-thionine system discovered by Rabinowitch and derived the following mechanism for the collection and conversion of solar energy within this system:

$$\frac{1}{2}\text{Th} + \text{Fe}^{2+} \underset{\text{dark}}{\overset{hv}{\rightleftharpoons}} \frac{1}{2}\text{Leu} - \text{Th} + \text{Fe}^{3+} \quad (27)$$

Forward reactions:

$$\text{Th} + hv + \text{Th}^* \quad (28)$$

$$\text{Th}^* + \text{Fe}^{2+} \longrightarrow \text{Th}^{\bullet -} \quad (29)$$

$$2\text{Th}^{\bullet -} \longrightarrow \text{Th} + \text{Leu} - \text{Th} \quad (30)$$

Back reactions:

$$\text{Leu} - \text{Th} + \text{Fe}^3 \longrightarrow \text{Th}^{\bullet -} + Fe^{2+} \quad (31)$$

$$2\text{Th}^{\bullet -} \longrightarrow \text{Th} + \text{Leu} - \text{Th} \quad (32)$$

$$\text{Th}^{\bullet -} + \text{Fe}^{3+} \longrightarrow \text{Th} + \text{Fe}^{2+} \quad (33)$$

where Th^* = triplet state of thionine dye, $\text{Th}^{\bullet -}$ = semithionine half-reduced form, and Leu = leucothionine (Fig. 5).

The overall reaction for this type of PG cell differs from the basic reaction considered earlier, in that the thionine (photosensitive dye) couple is a two-electron redox system, and can be given by the following reaction:

$$2Z + A \underset{k_{-1}}{\overset{g}{\rightleftharpoons}} Z + B + Y \underset{k_{-2}}{\overset{k_2}{\rightleftharpoons}} C + 2Y \quad (34)$$
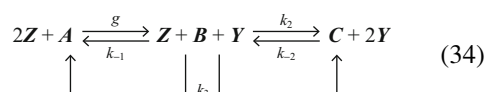
This two-electron thionine couple (A, C) and the one-electron outer sphere iron (reductant) couple (Y, Z) manifests itself as an ability to obtain the required electrode selectivity of B and Y on the illuminated and dark electrode, respectively. However, this mechanism also complicates the method of establishing the system's homogeneous kinetics, as explained further on.

Variations in Cell Parameters for an *A*, *B*, *C* System

Hatchard and Parker [24] and Ferreira and Harriman [25] established that the leucothionine product was formed via the disproportionation reaction of $B + B$, as opposed to the reaction with Z as seen earlier for an A, B cell [1]. B is therefore an intermediary product, the stability of which is not sufficient to reach the illuminated electrode. The quantum efficiency of leucothionine is consequently a deciding factor in determining ideal conditions for a cell of this type and is incorporated into efficiency calculations as follows:

$$\text{Flux producing } C = g\phi_c \quad (35)$$

where

$$\phi_c = \frac{1}{\left(\frac{2+k_{-1}[Y]}{k_3[B]}\right)} \qquad (36)$$

$$g = \phi I_\varepsilon [A] \qquad (37)$$

In order to realize the optimum value for the quantum efficiency of C (in this case, ½), B must be broken down by the aforementioned disproportionation reaction and half of the photogenerated B must react to form C. Thus, it follows that $k_3[B] \gg k_{-1}[Y]$ is an essential condition. If $k_3[B] \ll k_{-1}[Y]$, an inefficient system results, as the majority of the photogenerated B reacts with Y, forming the original reactant A (the back reaction).

An efficient cell therefore requires

$$\frac{2k_3[B]}{k_{-1}[Y]} > \frac{2k_3 g}{k_{-1}^2 [Y]^2} > 1 \qquad (38)$$

Subsequent substitution with Eq. 37 results in the conditions for the concentration of Y:

$$[Y] < \left(\frac{2\phi I_0}{X_\varepsilon} \times \frac{k_3}{k_{-1}^2}\right)^{\frac{1}{2}} \qquad (39)$$

Referring back to Eq. 8, the above equation agrees with the requirement of a small absorbance length for an efficient cell – in this case, it increases the likelihood of B to disproportionate. In addition to this, in a similar fashion to the $[Y]_D$ parameters for the ideal A, B cell denoted earlier, $[Y]_D$ for this A, B, C cell can now be defined as

$$[Y]_D = \left(\frac{\phi I_0}{5 X_\varepsilon} \times \frac{k_3}{k_{-1}^2}\right)^{\frac{1}{2}} - \left(\frac{1}{2}\Delta c\right) \qquad (40)$$

Analysis of practical A, B, C photogalvanic cells has shown that the concentration of Y and Z (the inorganic iron couple) helps induce the required homogeneous kinetics [12, 23, 24]. The concentrations of the iron redox couple aid the prevention of concentration polarization at the dark electrode, while trapping A^* at the illuminated electrode ($[Fe^{2+}]$) and inhibiting destruction of B or C in the electrolyte ($[Fe^{3+}]$).

Photogalvanic Cells, Principles and Perspectives, Table 3 Conditions for an ideal PG cell (Adapted from references [12, 13])

Characteristic length	Approximate value for an ideal photogalvanic cell
X_l	10^{-2} cm, giving $[Y] \sim 10^{-2}$ M
X_ε	10^{-4} cm, giving $[A] \sim 10^{-1}$ M
X_k	10^{-3} cm, giving $k[Y] \sim 10$ s^{-1} and $k < 10^3$ M^{-1} s^{-1}

As explained in Table 3, for an ideal cell the absorbance length is approximately 10^{-4} cm, which corresponds to dominance of the k_{-2} parameter. However, thionine dye has a low solubility – meaning the absorbance length can be as long as 10^{-1} cm – and thus the k_{-1}^2/k_3 parameter becomes equally important. This is a considerable factor in the relative inefficiencies of iron-thionine PG cells – a high absorbance length means B struggles to disproportionate and C fails to reach the illuminated electrode [12].

Various modifications have been attempted in order to increase the solar energy conversion efficiency of the iron-thionine PG cell, including adding sulfonate groups onto the thionine dye in order to increase solubility [13] and irreversibly coating a thionine electrode with up to twenty thionine monolayers to increase absorbance of solar radiation and thus decrease ε [26]. However, research has broadened since early innovations by Rabinowitch, Albery, Archer, and Foulds, and the common approach is now motivated towards improvisations of the dye and reductant to induce wholesale changes in the efficiencies of PG cells.

Modern Approaches for Photogalvanic Cell Advancement

Modification of Photosensitizing Dye
Photosensitizing dyes, which in PG cells are almost always organometallic or heterocompounds, exhibit both the redox characteristics similar to the irreversible inorganic (Y, Z) couple and the ability to absorb light

intensity of a certain wavelength. To aid the conversion of solar energy to electrical energy, a chosen dye in a PG cell must therefore absorb light at a wavelength of approximately 500–700 nm – while also having a relatively soluble structure and a suitable reduction potential [26–28]. A variety of dye structures have been used to investigate their suitability for use in PG cells, several of which are listed in Table 4 below.

Modification of Reductant

A survey of current literature indicates that the photosensitizing dye has been the subject of much modification in investigations to optimize PG cell efficiency. In a similar fashion, manipulation of the reductant has also received close attention, following on from the early realization that the use of sacrificial electron donors such as triethanolamine (TEA) and ethylenediaminetetraacetic acid (EDTA) with suitable dyes produces higher photopotentials and photocurrents than their early counterparts, e.g., iron and hydroquinone. Table 5 gives an illustration of this [2, 28]. However, EDTA and TEA are unable to produce higher photopotentials and photocurrents in cells with proflavin, rhodamine B, and rose Bengal due to these dyes having high negative potentials. One method of restricting this problem is by adding methyl viologen (MV^{2+}) to the system, which acts as a mediator – catalyzing the photoredox reduction (MV^{2+} is reduced – the process of which oxidizes the dye – thus forming a cation of the dye which reacts with the EDTA or TEA) [28].

Literature Results for a Variety of Molecular Photogalvanic Systems

Table 6 describes a selection of PG systems that have been investigated within current literature. The following table, Table 7, depicts the experimental results obtained from the systems listed. In terms of storage capacity, this is $t_{1/2}$ and is calculated by applying light radiation of a suitable (i.e., solar) wavelength until the potential reaches a constant value, at which point a load is applied to the cell to induce a current at power point. The time taken for the output of

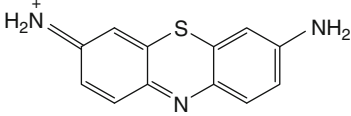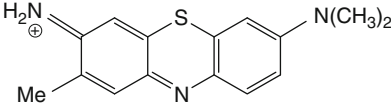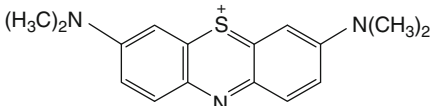the cell to fall, in the dark, to its half at power point is $t_{1/2}$ [15].
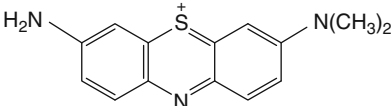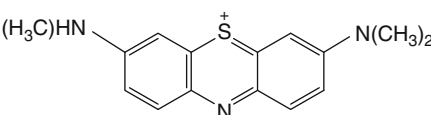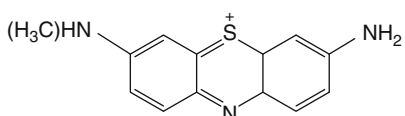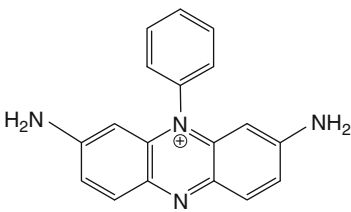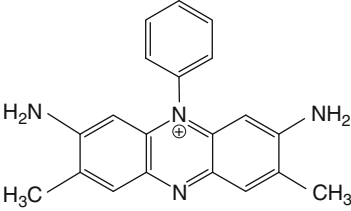
Tables 6 and 7 give an illustration of the variance within research to optimize PG cells. Given are systems with varying groups of dyes – thiazines (azure B, toluidine blue, methylene blue, azure A), phenazines (safranine, safranin-O), a xanthene (rhodamine 6G), and a triphenyl methyl derivative (malachite green), as well as differing reductants, including the aforementioned sacrificial electron donors EDTA and TEA. Much investigation has been undertaken concerning thiazine and phenazine dyes due to their suitable absorption wavelength maxima, solubility, and the ease in which different substituents can be modified on the basic structure of the compound, i.e., adding sulfonate groups to thiazine compounds to increase solubility [13].

However, the power produced, the fill factor, and the conversion efficiency of many engineered PG cells are all somewhat disappointing – a level has not yet been reached where PG cells could be considered a feasible replacement for the more costly PV cell. A number of factors contribute to this, many of which have been discussed within this review and can be related back to Eqs. 8 and 9 for an optimum PG cell, originally formulated by Albery and Archer [17, 18]. Without careful manipulation of electrode spacing, kinetics, and diffusion lengths at the electrodes – in conjunction with mass transfer, the photochemistry, and the homogeneous kinetics of the system – the power developed by a PG cell cannot be optimized and may consequently be a crucial determinant for current literature displaying disappointing results relative to the optimum theorized by the pioneering work of Albery and Archer [1, 12, 13, 16–20].

Effects of System Conditions
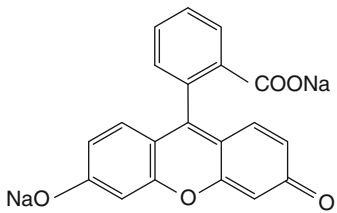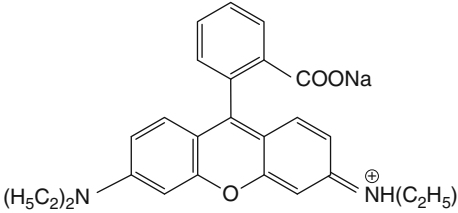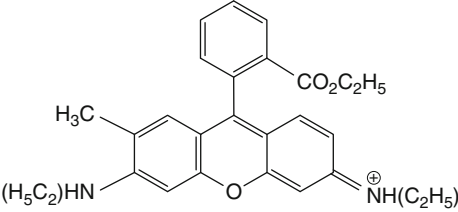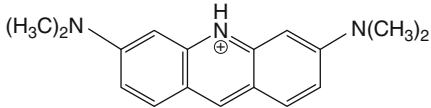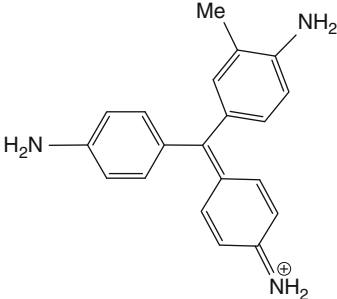
Lal [36] and Dube and Sharma [37] have shown it is possible to use a mixture of two dyes within the PG system in an attempt to maximize the use of the broad solar spectrum. Using EDTA as a reductant, Lal used a mixture of thionine and Azure B as a photosensitizing dye, which contributed to a solar energy conversion efficiency of 0.18 %. Dube and Sharma witnessed conversion

Photogalvanic Cells, Principles and Perspectives, Table 4 A list of potential dyes for PG cells (Adapted from reference [2])

Dye	Class	Structure	λ_{max}/nm
Thionine	Thiazine		596
Toluidine blue	Thiazine		630
Methylene blue	Thiazine		665
Azure A	Thiazine		635
Azure B	Thiazine		647
Azure C	Thiazine		620
Phenosafranine	Phenazine		520
Safranin-O	Phenazine		520

Photogalvanic Cells, Principles and Perspectives, Table 4   (continued)

Dye	Class	Structure	λ_{max}/nm
Fluorescein	Xanthene		490
Rhodamine B	Xanthene		551
Rhodamine 6G	Xanthene		524
Acridine orange	Acridine		492
Fuchsine	Triphenylmethane		545

efficiencies of 0.17 %, 0.18 %, and 0.19 % when using dye mixtures of Azure A and Azure B, Azure B and Azure C, and Azure A and Azure C, respectively, with mannitol as a reductant. In general, as can be seen by referral to Tables 6 and 7, the conversion efficiencies seen by Lal and Dube and Sharma do not correspond to a particularly efficient system, an analysis which is supported by the relatively low photocurrents and photopotentials also seen for these mixed dye systems. This and the additional complexity issue raised by using more than one dye are

Photogalvanic Cells, Principles and Perspectives, Table 5 The photocurrent and photovoltage of a selection of PG cells upon variation of the reductant (Adapted from references [2] and [28])

Dye	Reductant	Photocurrent/$\mu A\ cm^{-2}$	Photopotential/mV
Thionine	Fe^{2+}	3.30	140
	Hydroquinone	2.80	20.0
	EDTA	12.0	190
	TEA	18.0	250
	TEA + MV^{2+}	18.0	210
Riboflavine	Hydroquinone	0.830	20.0
	EDTA	58.0	720
	TEA	35.0	500
	TEA + MV^{2+}	37.0	430
Proflavin	Hydroquinone	0.430	1.90
	Hydroquinone + MV^{2+}	0.410	2.40
	EDTA	0.790	140
	EDTA + MV^{2+}	25.0	350
	TEA	0.250	60.0
	TEA + MV^{2+}	6.25	320
	MV^{2+}	0.038	5.00
Rhodamine B	EDTA	0.092	28.0
	EDTA + MV^{2+}	0.092	10.0
Rose bengal	EDTA	0.025	19.0
	EDTA + MV^{2+}	0.017	20.0

Photogalvanic Cells, Principles and Perspectives, Table 6 A selection of PG systems that have been investigated. Research is listed in chronological order

Reference	Dye	Reductant	Surfactant
[29]	Azure B	Nitrilotriacetic acid (NTA)	N/A
[30]	Safranine	EDTA	N/A
		Glucose	N/A
		NTA	N/A
[11]	Toluidine blue	Glucose	CTAB
[31]	Methylene blue	Oxalic acid	N/A
[32]	Azure A	Ascorbic acid	NaLS
[33]	Bromophenol red	EDTA	N/A
[5]	Rhodamine 6G	Oxalic acid	DSS
			CTAB
			TX-100
[15]	Safranine O	EDTA	Tween-80
[34]	Toluidine blue	Arabinose	NaLS
	Malachite green	Arabinose	NaLS
[35]	Safranine	DTPA	Brij 35
	Bismarck brown	DTPA	Brij 35
	Methyl orange	DTPA	Brij 35

Photogalvanic Cells, Principles and Perspectives, Table 7 Experimental results for selection of PG cells listed in Table 6

Reference	Photocurrent/μA	Photopotential/mV	Fill factor	Conversion efficiency/%	Storage capacity/min
[29]	60.0	340	0.290	0.180	50.0
[30]	50.0	760	0.580	0.262	19.0
	35.0	373	0.180	0.036	85.0
	35.0	415	0.370	0.084	8.00
[11]	51.0	268	0.410	0.058	6.00
[31]	110	312	0.280	0.121	35.0
[32]	160	770	0.340	0.546	110
[33]	45.0	581	0.270	0.036	35.0
[5]	425	1936	0.410	0.860	131
	215	1145	0.450	0.240	68.0
	310	1478	0.380	0.550	96.0
[15]	300	785	0.340	0.977	60.0
[34]	60	813	0.259	0.145	123
	36	348	0.024	0.059	32.0
[35]	155	842	0.410	0.644	122
	115	786	0.480	0.519	117
	95	625	0.400	0.207	94.0

possible reasons for the relatively small amount of research into mixed dye PG cells, with most engineered towards suitable selection and/or modification of a single photosensitizing dye [38].

It can be seen from Tables 6 and 7 that, in general, PG systems containing a surfactant produced higher relative values for photocurrent, photopotential, and conversion efficiency than systems studied in which a surfactant was absent. Fendler and Fendler [39] and Atwood and Florence [40] have attributed this to the ability of a surfactant to solubilize certain molecules (i.e., the photosensitizing dye) and the catalytic effect that carefully chosen surfactants induce on particular chemical reactions. Furthermore, Rohatgi-Mukherjee et al. theorized that addition of a surfactant into a PG system increases conversion efficiency via facilitating the separation of photogenerated products by hydrophobic-hydrophilic interaction of the products with the surfactant interface [27].

Genwa and Genwa provided a thorough example of the benefit of micellar PG systems, by analyzing the electrical output and efficiency of the same cell with three different surfactants – anionic, cationic, and nonionic (DSS, CTAB, and TX-100, respectively) [5]. The results are tabulated in Table 7, showing that the use of an anionic surfactant is more beneficial than nonionic, followed by cationic. Results for the same system containing no surfactant resulted in a photocurrent, photopotential, fill factor, and conversion efficiency of 152 μA, 985 mV, 0.39, and 0.22 %, respectively – thus illustrating the possibility of increasing the electrical output of a PG cell by more than double via the addition of a suitable surfactant.

Finally, in terms of pH of the PG system, it has been found that photopotential and photocurrent increase with increase in pH up to a certain maximum, after which it decreases at a similar rate. Several research articles, including Gangotri and Gangotri [15], Genwa and Chouhan [32], and Dube et al. [29], have observed that the pH for the optimum condition is related to the pK_a of the reductant, with the pH being equal to or slightly higher than the pK_a of the reductant. The aforementioned authors cite a possible reason for this as the availability of the reductant in its neutral or anionic form – a superior electron donor.
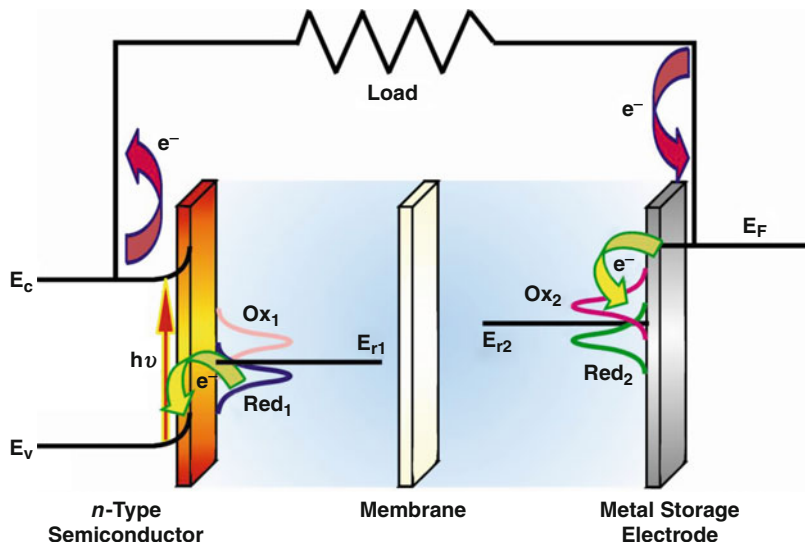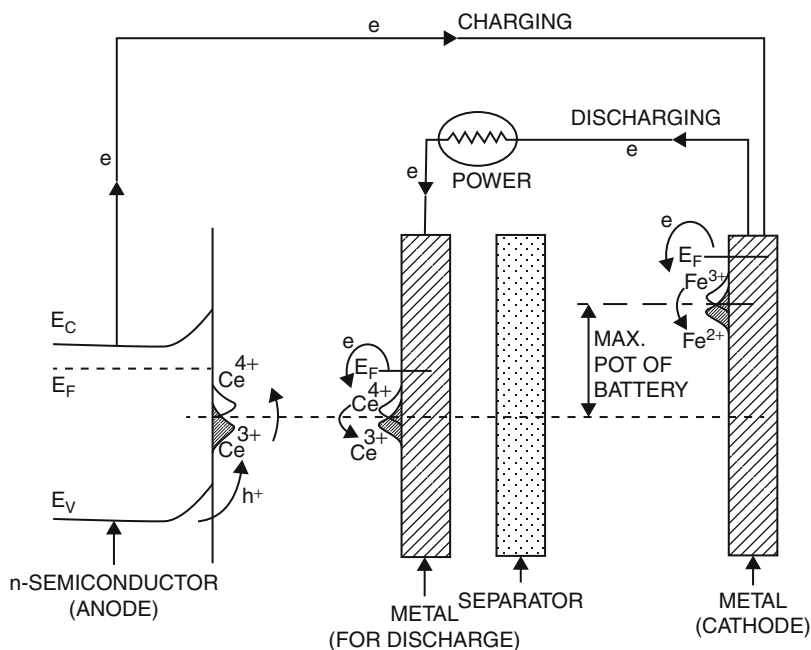
Semiconductor-Based Photogalvanic Cells

In semiconductor photogalvanic cells, the semiconductor acts as the light energy harvester, allowing the formation of either weakly bound (Wannier) or strongly bound (Frenkel) excitons provided the incident photon energy is larger than the bandgap separation. For *n*-type semiconductors in contact with a redox electrolyte at open

circuit, the band bending at the interface (tantamount to the formation of a Schottky barrier) allows for oxidation processes to take place via the valence band, causing the photoanode to acquire a negative potential. This in turn causes a shift in the Fermi level with consequent reduction in the band bending until the flatband potential is reached (at high illumination intensities).

Photogalvanic Cells, Principles and Perspectives, Table 8 Semiconductor-based PG systems (Reprinted from Electrochimica Acta, 36(7), Maheshwar Sharon, P. Veluchamy, C. Natarajan, Dhananjay Kumar, Solar rechargeable battery–principle and materials, 1107–1126, Copyright (1991), with permission from Elsevier)

System	V_{oc}/mV	Discharge current/μA
Three-electrode systems		
$BaTiO_3$ | Ce^{3+},Ce^{4+} || Fe^{3+},Fe^{2+} | Pt	825	38
n-CdSe | S^{2-},S || C || storage electrode HO^-	430	N/A
$MoSe_2$ | Br^-,Br_3^- || I_3^-,I^- | Pt	400	4,000
GaAs | S^{2-},Se_2^{2-} | Cd	250	8,000
CdSe | S^{2-},S_x^{2-} || Se_2^{2-},Se,Se^{2-} | Pt	50–200	8,000
CdSe | S^{2-},S_x^{2-} |Cd	300–400	10,000
n-$MoSe_2$ | HBr,Br_2 | Nafion®-315 | I_3^-,HI | Pt	490	15,000
n-MX_2 | I^-,I_3^- || AQ,AQH_2 | C	260	1,000
$MX_2 = WSe_2$,MoS_2; $AQ =$ anthraquinone-2,6-disodium disulfonate		
n-Pb_3O_4 | Fe^{2+},Fe^{3+}|| IO_3^-,I^- | Pt	840	410
n-Cd(Se,Te) | S_x^{2-} | CoS | membrane | CsOH,CsSH | SnS | Sn	510	1,500
n-CdS | Na_2S,S,NaOH || NaOH | SbO_2^- | Sb	60	N/A
Four-electrode systems		
p-WSe_2 | MV^{2+} || I^- | n-WSe_2	800	12,000
p-InP | PEO,NaSCN,Na_2S,S | n-CdS	540	1
p-InP | porphyrin | Nafion-117 | $Ru(bpy)_3^{2+}$ | n-CdS	380	1
Without a membrane		
n-CdSe | $CdSO_4$ | p-CdTe	100	1

Photogalvanic Cells, Principles and Perspectives, Fig. 8 Schematic illustration of the requirements of the various energy levels for the Sharon-Schottky PG cell (Reprinted from Electrochimica Acta, 36(7), Maheshwar Sharon, P. Veluchamy, C. Natarajan, Dhananjay Kumar, Solar rechargeable battery–principle and materials, 1107–1126, Copyright (1991), with permission from Elsevier)

$$\Delta V \approx E_g \geq V_{fb}$$

This system allows for light to electrical energy conversion, as illustrated in Fig. 6.

It follows that if a two-electrode configuration is used with a "storage electrode" acting as a dark electrode process and the illuminated electrode allowing for a redox transformation, Fig. 6, then the system may operate as a PG cell. However, this configuration holds the disadvantage that the dark reaction at the semiconductor (the reverse of the light-driven process) is necessarily sluggish

| Ag | Ag$_2$SO$_4$ | Li$_2$SO$_4$ 0.01 M Na$_4$ZnTPPS 10^{-4} M Tosylate$_4$ZnTMPP 10^{-4} M (aq) | BTPPATPBCl 0.01 M quencher 10^{-3} M (DCE) | BTPPACl 0.001 M LiCl 0.01 M (aq) | AgCl | Ag′ |

Photogalvanic Cells, Principles and Perspectives, Fig. 9 Cell diagram for a liquid | liquid solar cell. The organic supporting electrolyte is bis(triphenyl-phosphoranyilidene)ammonium tetrakis(4-chlorophenyl)borate, BTPPATPBCl (Reprinted from Electrochemistry Communications, David J Fermín, Hong D Duong, Zhifeng Ding, Pierre F Brevet, Hubert H Girault, Solar energy conversion using dye-sensitised liquid|liquid interfaces, 29–32, Copyright (1999), with permission from Elsevier)

Photogalvanic Cells, Principles and Perspectives, Fig. 10 Schematic representation of the light energy conversion process based on the heterogeneous quenching of a sensitizer S by an electron acceptor Q at a liquid|liquid interface in the presence of a supersensitizer O$_{ss}$/R$_{ss}$ (Reprinted from Electrochemistry Communications, David J Fermín, Hong D Duong, Zhifeng Ding, Pierre F Brevet, Hubert H Girault, Solar energy conversion using dye-sensitised liquid|liquid interfaces, 29–32, Copyright (1999), with permission from Elsevier)
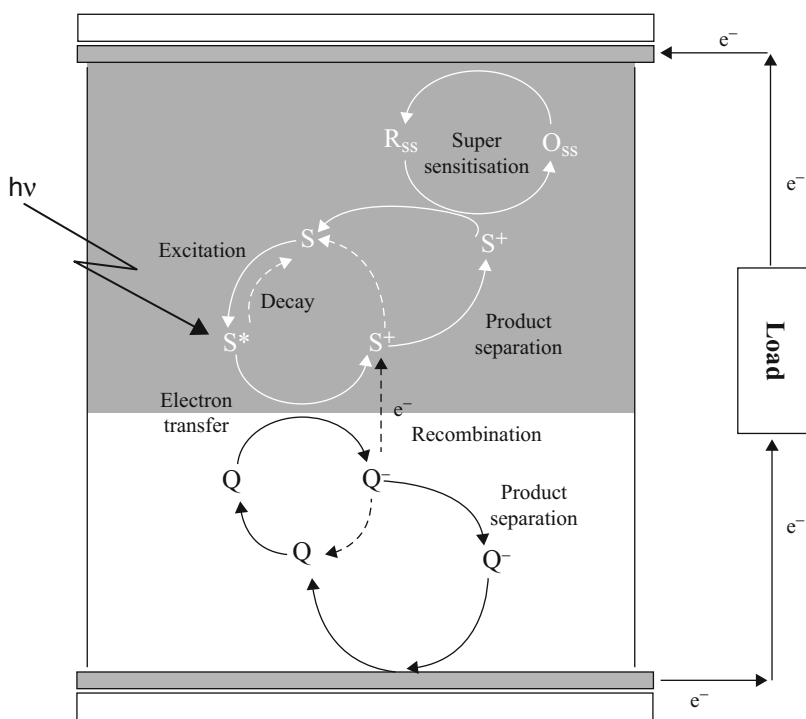
for efficient photoelectrochemistry; the formation of a barrier at the semiconductor | electrolyte interface opposes the dark reaction because of the depletion layer. This causes the need to use a semiconductor electrode for light-powered charging, but a third electrode made from a metal for the discharge process, Fig. 7 [41–43]. An example of this type of cell is the CdSe | polysulfide (S$_x^{2-}$) system, based on the cell diagram [42], CdSe | HS$^-$, HO$^-$, S$_x^{2-}$ | Membrane | HS$^-$, and HO$^-$ | SnS | Sn. Under illumination, holes (h$^+$) in the n-type CdSe electrode are able to oxidize HS$^-$ to sulfur:

$$HS^- + HO^- - 2h^+ \longrightarrow S + H_2O \qquad (41)$$
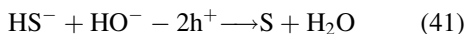
The sulfur engages in further reaction within the electrolyte to form polysulfide complexes,

$$S + S_X^{2-} \longrightarrow S_{X+1}^{2-} \qquad (42)$$
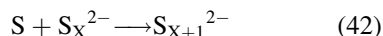
so that the bisulfide/sulfur equilibrium occurs (at open circuit) at the counter electrode,

$$S + H_2O + 2e^- \underset{}{\overset{}{\rightleftarrows}} HS^- + HO^- \qquad (43)$$

and tin sulfide/sulfur equilibrium occurs (at open circuit) at the storage electrode,

$$SnS + H_2O + 2e^- \underset{}{\overset{}{\rightleftarrows}} Sn + HS^- + HO^- \quad (44)$$

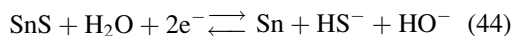Such cells can be readily extended to afford a four-electrode system containing an *n*-type anode and a *p*-type cathode for light-driven charging, with two metal electrodes for discharge [41], with the two compartments separated by a membrane. Consider the reaction

$$Fe^{3+} + Ce^{3+} \underset{dark}{\overset{light}{\rightleftarrows}} Ce^{4+} + Fe^{2+} \qquad (45)$$
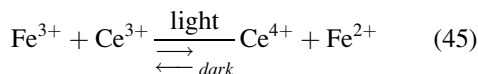
During charge, light-generated holes in the *n*-type semiconductor oxidize Ce^{3+} to Ce^{4+} with electrons passing through Ohmic contact with the semiconductor from the conduction band to the conduction band of a *p*-type semiconductor, where Fe^{3+} is reduced to Fe^{2+}, either in the dark or via a light-driven reaction. Under discharge, the continuum of electronic energy levels in the metal allows for the reverse processes

$$Ce^{4+} + e^- \longrightarrow Ce^{3+} \qquad (46)$$

$$Fe^{2+} - e^- \longrightarrow Fe^{3+} \qquad (47)$$
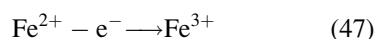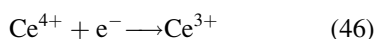
Several examples of successful cells of this type have been developed (Table 8), including all-solid-state devices [41–45].

A particularly exciting cell that has been developed is the Sharon-Schottky cell, Fig. 8 [41]. Here, the semiconductor light harvester is employed as a *membrane* between two redox electrolytes. One of these forms a Schottky barrier in front of the electrode and a second electrolyte is employed as an Ohmic contact. This allows complementary processes to occur at
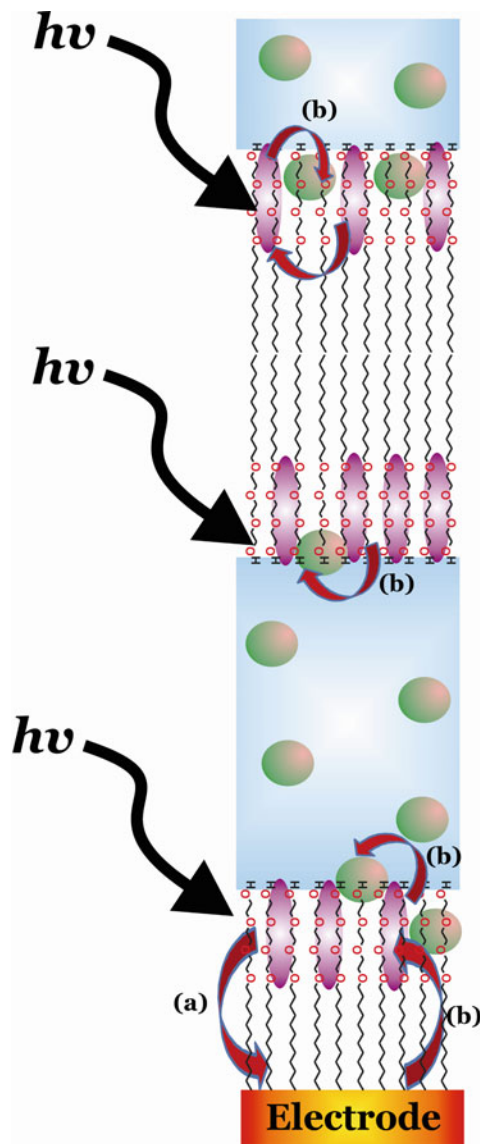
Photogalvanic Cells, Principles and Perspectives, Fig. 11 Cartoon illustrations of the development of a photo-Dember voltage (**a**) and a photogalvanic voltage (**b**) at the illuminated electrode. The aqueous subphase (23.1 Å) is *smaller* than the lipid bilayer (37.8 Å); the photoactive dye is indicated by the burgundy bananas, and redox species from the aqueous subphase are indicated by *green spheres*. The *arrows* representing *light* have been purposely drawn out of place to emphasize the photochemical electron-transfer nature of the process; the *red arrows* indicate the electron flow pathways (Reproduced with permission from reference [52]. Copyright (2012) Royal Society of Chemistry)

Photogalvanic Cells, Principles and Perspectives, Table 9 Performance of various galvanic cells constructed using the L_a phase of Brij 30/H_2O under 350 nm light (center band, bandwidth 30 nm, intensity of 1.8 mW cm^{-2}). Data presented were averaged over at least three different constructed cells (Copyright (2012) Royal Society of Chemistry)

Conditions	[a]E_{oc}/V	[b]j_{sc}/μA cm^{-2}	[c]E_m/V	[d]P_m/μW cm^{-2}	Fill factor/%	Maximum power conversion/%
Zn ∣ L_α (0.7 mmol PMe, 98 μmol $ZnCl_2$, ∣ ITO Not degassed[e]	1.11	17.2	0.31	2.73	14.2	0.15
Zn ∣ L_α (0.1 mmol PMe, 0.1 mmol $ZnCl_2$, KCl[f]) ∣ ITO Not degassed[e]	0.99	48.6	0.26	6.90	14.3	0.37
Zn ∣ L_α (0.7 mmol PMe, 95 μmol $ZnCl_2$, KCl[f]) ∣ ITO Degassed[g]	0.99	118.7	0.67	20.81	17.6	1.11
Zn ∣ L_α (0.4 mmol PMe, 0.4 mmol PMeCl, 40 μmol $ZnCl_2$, KCl[f]) ∣ ITO Degassed[g]	1.19	172.3	0.61	34.4	16.3	1.83
Al ∣ L_α (0.5 mmol PMe, 3.0 mmol $AlCl_3$, KCl[f]) ∣ ITO Degassed[g]	0.85	264.8	0.26	18.5	8.21	0.99

[a]Cell emf
[b]Current density of cell at short circuit
[c]Cell potential difference at maximum power
[d]Maximum power density
[e]*Not degassed* refers to the non-exclusion of molecular oxygen from the experiment
[f]*KCl* refers to the doping of the aqueous subphase with 0.1 M KCl
[g]*Degassed* refers to the rigorous exclusion of oxygen from the experiment

metal electrodes located a short distance from the semiconductor and essentially reduces the Ohmic loss within the device, since the semiconductor acts as an electrode for the majority carriers and a photoelectrode for the minority carriers. The advantage here is that the full bandgap of the semiconductor is used for energy conversion. An example of this system is [46] the cell diagram, Ag ∣ Ag(CN)$_2^-$ ∣ α-Fe$_2$O$_3$ (E$_{CB}$ = −4.14 eV; E$_{VB}$ = −6.14 eV) ∣ Fe(CN)$_6^{4-}$, Fe(CN)$_6^{3-}$ ∣ Pt in which Ohmic contact exits between the α-Fe$_2$O$_3$ and Ag(CN)$_2^-$, with a Schottky junction between α-Fe$_2$O$_3$ and ferri-/ferrocyanide. This cell generated 5.8 mA cm^{-2} at 0.9 V, with light-induced oxidation of ferrocyanide. It is important that, for efficient operation, the Fermi level of silver matches the conduction band energy of the semiconductor. The advantage of this system is that it is easy to fabricate and a large number of cells can be connected in series without using any conducting wire [41].

Future Directions

The use of the liquid ∣ liquid interface as a means for charge separation after photochemically induced interfacial redox reaction is an exciting and relatively recent development for exploitation in PG cell systems [47–50], not least as a result of the similarity between electron transfer at the liquid ∣ liquid interface and semiconductor ∣ electrolyte junctions [22].

Fermín and Girault [51] developed the PG cell depicted in Fig. 9, employing Ru(bpy)$_3^{2+}$ as a supersensitizer (S) between a nonpolarized

water | 1,2-dichloroethane interface, with a proposed reaction scheme illustrated in Fig. 10. The cell was found to provide an electron-to-photon ratio on the order of 0.1 % under green light (543 nm) and steady-state conditions. Analysis of the polarization and power characteristics for the experimental cell gave 0.7 nW cm^{-2} at 25 mV, which under linear extrapolation permits solar to electrical energy conversion on the order of 0.05 % under AM 1.0 illumination.

Our laboratory [52] extended this approach for the use of lyotropic liquid crystals ("liquid nanotechnology") doped with photoredox active materials in considering the cell Zn | Zn^{2+}(aq)/ N-methylphenothiazine (Brij 30) | ITO, where the dark reaction involves the use of a sacrificial electrode to keep the open circuit voltage high. The concept is illustrated in Fig. 11 and exploits the nanometric space and thus diffusion lengths available. Typical cell performance data are given in Table 9, illustrating that under violet (350 nm) light, approximately 2 % power conversion efficiency is possible with a 15 % fill factor. The cell was observed to behave as an electrochemical capacitor (voltage efficiency ~85 %; power efficiency ~80 %), with estimated maximum energy density of ~1 W h kg^{-1} at a power density of ~1 kW kg^{-1}, clearly demonstrating this approach to be of potential pragmatic use.

Conclusion

While it can be seen from Table 7 that the conversion efficiencies for many formulated PG cells are some way off the ~18 % optimum theorized by Albery and Archer [17], the ability to vary a number of parameters within the system, and the relative ease of doing so, affords a customizable property that the PV cell cannot compete with. Providing a compromise can be made regarding the effects of the system photochemistry, mass transport and the homogeneous kinetics, illumination intensity, and species concentration, PG cells hold promise for a commercially and environmentally viable alternative to the common PV devices (e.g., solar panels) used today.

Lord Porter said that "I have no doubt that we will be successful in harnessing the Sun's energy... If sunbeams were weapons of war, we would have had solar energy centuries ago" [53]. Although unfortunate, it is perhaps human nature that matters concerning society are disregarded until they become distinctly personal – with the realization in the last five decades that Earth's finite energy resources are rapidly diminishing, the subject of discovering renewable, viable energy sources has become an increasingly important research area, the success of which can only increase as levels of understanding and modern technological advancement continue to grow.

Cross-References

▶ Conductivity of Electrolytes
▶ Dye-Sensitization
▶ Dye-Sensitized Electrode, Photoanode
▶ Electrical Double-Layer Capacitors (EDLC)
▶ Electrode
▶ Membrane Processes, Electrodialysis
▶ Membrane Technology
▶ Photocatalyst
▶ Photoelectrochemistry, Fundamentals and Applications
▶ Polymer Electrolyte Fuel Cells, Mass Transport
▶ Quantum Dot Sensitization
▶ Semiconductor Electrode
▶ Solid State Dye-Sensitized Solar Cell

References

1. Archer MD (1975) Electrochemical aspects of solar-energy conversion. J Appl Electrochem 5:17
2. Jana AK (2000) Solar cells based on dyes. J Photochem Photobiol A 132:1
3. Becquerel E (1839) Recherches sur les effets de la radiation chimique de la lumiére solaire au moyen des courants électriques. C R Acad Sci Paris 9:145

4. Becquerel E (1839) Mémoire sur les effets électriques produits sous l'influence des rayons solaires. C R Acad Sci Paris 9:561

5. Genwa KR, Genwa M (2008) Photogalvanic cell: A new approach for green and sustainable chemistry. Sol Energy Mater Sol Cells 92:522

6. Mountz JM, Tien HT (1978) Photogalvanovoltaic cell. Sol Energy 21:291

7. Tien HT, Mountz JM (1978) Photo-galvano-voltaic cell - new approach to use of solar-energy. Int J Energy Res 2:197

8. Tien HT, Higgen J, Mountz JM (1979) Solar energy: chemical conversion and storage. Humana Press, Clifton, p 203

9. Rabinowitch E (1940) The photogalvanic effect I. The photochemical properties of the thionine-iron system. J Chem Phys 8:551

10. Rabinowitch E (1940) The photogalvanic effect II. The photogalvanic properties of the thionine-iron system. J Chem Phys 8:560

11. Gangotri KM, Meena RC, Meena R (1999) Use of micelles in photogalvanic cells for solar energy conversion and storage: cetyl trimethyl ammonium bromide-glucose-toluidine blue system. Photochem Photobiol A 123:93

12. Albery WJ, Foulds AW (1979) Photogalvanic cells. J Photochem 10:41

13. Albery WJ (1982) Development of photogalvanic cells for solar-energy conversion. Acc Chem Res 15:142

14. Rideal EK, Williams DC (1925) The action of light on the ferrous ferric iodine iodide equilibrium. J Chem Soc 127:258

15. Gangotri P, Gangotri KM (2009) Studies of the micellar effect on photogalvanics: solar energy conversion and storage in EDTA-safranine O-Tween-80 system. Energy Fuel 23:2767

16. Albery WJ, Archer MD (1976) Photogalvanic cells .1. potential of zero current. Electrochim Acta 21:1155

17. Albery WJ, Archer MD (1977) Optimum efficiency of photogalvanic cells for solar-energy conversion. Nature 270:399

18. Albery WJ, Archer MD (1977) Photogalvanic cells .2. current-voltage and power characteristics. J Electrochem Soc 124:688

19. Albery WJ, Archer MD (1978) Photogalvanic cells .3. maximum power obtainable from a thin-layer photogalvanic concentration cell with identical electrodes. J Electroanal Chem 86:1

20. Albery WJ, Archer MD (1978) Photogalvanic cells .4. maximum power from a thin-layer cell with differential electrode-kinetics. J Electroanal Chem 86:19

21. Marcus RA (1965) On the theory of electron-transfer reactions. VI. Unified treatment of homogeneous and electrode reactions. J Chem Phys 43:679

22. Smith BB, Halley JW, Nozik AJ (1996) On the Marcus model of electron transfer at immiscible liquid interfaces and its application to the semiconductor liquid interface. Chem Phys 205:245

23. Royea WJ, Fajardo AM, Lewis NS (1997) Fermi golden rule approach to evaluating outer-sphere electron-transfer rate constants at semiconductor/liquid interfaces. J Phys Chem B 101:11152

24. Hatchard CG, Parker CA (1961) The photoreduction of thionine by ferrous sulphate. Trans Faraday Soc 57:1093

25. Ferreira MIC, Harriman A (1977) Photoredox reactions of thionine. J Chem Soc Faraday Trans 1 73:1085

26. Hall DE, Eckert JA, Lichtin NN, Wildes PD (1976) Multilayer iron-thionine photogalvanic cell. J Electrochem Soc 123:1705

27. Rohatgi-Mukherjee KK, Choudhary R, Bhowmik BB (1985) Molecular interaction of phenosafranin with surfactants and its photogalvanic effect. J Colloid Interface Sci 106:45

28. Tsubomura H, Shimoura Y, Fujiwara S (1979) Chemical processes and electric-power in photogalvanic cells containing reversible or irreversible reducing agents. J Phys Chem 83:210

29. Dube S, Sharma SL, Ameta SC (1997) Photogalvanic effect in azur B-NTA system. Energy Convers Manage 38:101

30. Gangotri KM, Regar OP (1997) Use of azine dye as a photosensitizer in solar cells: Different reductants - Safranine systems. Int J Energy Res 21:1345

31. Gangotri KM, Meena RC (2001) Use of reductant and photosensitizer in photogalvanic cells for solar energy conversion and storage: oxalic acid-methylene blue system. J Photochem Photobiol A 141:175

32. Genwa KR, Chouhan A (2006) Role of heterocyclic dye (Azur A) as a photosensitizer in photogalvanic cell for solar energy conversion and storage: NaLS-ascorbic acid system. Sol Energy 80:1213

33. Ameta SC, Punjabi PB, Vardia J, Madhwani S, Chaudhary S (2006) Use of bromophenol red-EDTA system for generation of electricity in a photogalvanic cell. J Power Sources 159:747

34. Genwa KR, Kumar A, Sonel A (2009) Photogalvanic solar energy conversion: Study with photosensitizers toluidine blue and malachite green in presence of NaLS. Appl Energy 86:1431

35. Genwa KR, Khatri NC (2009) Comparative study of photosensitizing dyes in photogalvanic cells for solar energy conversion and storage: Brij-35-Diethylene-triamine Pentaacetic Acid (DTPA) system. Energy Fuel 23:1024

36. Lal C (2007) Use of mixed dyes in a photogalvanic cell for solar energy conversion and storage: EDTA-thionine-azur-B system. J Power Sources 164:926

37. Dube S, Sharma SL (1994) Studies in photochemical conversion of solar-energy - simultaneous use of 2 dyes with mannitol in photogalvanic cell. Energy Convers Manage 35:709

38. Jana AK, Bhowmik BB (1999) Enhancement in power output of solar cells consisting of mixed dyes. J Photochem Photobiol A 122:53
39. Fendler JH, Fendler EJ (1975) Catalysis in micellar and macromolecular systems. Academic Press, New York
40. Atwood D, Florence AT (1983) Surfactant systems. Chapman and Hall, New York
41. Sharon M, Veluchamy P, Natarajan C, Kumar D (1991) Solar rechargeable battery - principle and materials. Electrochim Acta 36:1107
42. Licht S (2002) Photoelectrochemical solar energy storage cells. In: Licht S, Bard AJ, Stratmann M (eds) Encyclopædia of electrochemistry, vol 6. Wiley-VCH, Weinheim, p 317
43. Licht S, Hodes G (2008) Photoelectrochemical storage cells. In: Archer MD, Nozik AJ (eds) Nano-structured and photoelectrochemical systems for solar photon conversion. Imperial College Press, London, p 591
44. Hada H, Takaoka K, Saikawa M, Yonezawa Y (1981) Energy-conversion and storage in solid-state photogalvanic cells. Bull Chem Soc Jpn 54:1640
45. Yonezawa Y, Okai M, Ishino M, Hada H (1983) A photochemical storage battery with an n-gap photo-electrode. Bull Chem Soc Jpn 56:2873
46. Sharon M, Rao GR (1986) Photoelectrochemical cell with liquid (ohmic) semiconductor liquid (schottky-barrier) system. Indian J Chem 25A:170
47. Volkov AG (1995) Energy-conversion at liquid/liquid interfaces - artificial photosynthetic systems. Electrochim Acta 40:2849
48. Mareček V, Armond AHD, Armond MKD (1989) Photochemical electron transfer in liquid/liquid solvent systems. J Am Chem Soc 111:2561
49. Brown AR, Yellowlees LJ, Girault HH (1993) Photoinitiated electron-transfer reactions across the interface between two immiscible electrolyte-solutions. J Chem Soc Faraday Trans 89:207
50. Fedoseeva M, Grilj J, Kel O, Koch M, Letrun R, Markovic V, Petkova I, Richert S, Rosspeintner A, Sherin PS, Villamaina D, Lang B, Vauthey E (2011) Photoinduced electron transfer reactions: From the elucidation of old problems in bulk solutions towards the exploration of interfaces. Chimia 65:350
51. Fermín DJ, Duong HD, Ding Z, Brevet PF, Girault HH (1999) Solar energy conversion using dye-sensitised liquid vertical bar liquid interfaces. Electrochem Commun 1:29
52. Halls JE, Wadhawan JD (2012) Photogalvanic cells based on lyotropic nanosystems: towards the use of liquid nanotechnology for personalised energy sources. Energy Environ Sci 5:6541
53. Rhodes BK, Odell R (1992) A dictionary of environmental quotations. John Hopkins University Press, Baltimore, p 265

Photography, Silver Halides

Tadaaki Tani
Society of Photography and Imaging of Japan, Tokyo, Japan

## Introduction and Characteristics

Photography with silver halide (AgX) is based on the photodecomposition reaction of AgX under illumination and was invented by L. J. M. Daguerre in 1839. The sensitivity of a photographic material with AgX depends on the absorption spectrum of AgX, which extends from ultraviolet to blue region. Dye sensitization, which was invented by H. Vogel in 1873, makes photographic materials with AgX sensitive to light that sensitizing dyes on its surface absorb and thus to light in green, red, and near-infrared region [1]. Photographic materials are diversified to meet various uses and include color negative films, color reversal films, color papers, photographic films for medical examination, and printing.

Photographic materials are manufactured by coating aqueous gelatin suspensions of AgX grains and additives (i.e., photographic emulsions) on substrates and record images of light and high-energy irradiation through photographic processes of exposure, development, and fix. On exposure, an electron appears in the conduction band of an AgX grain as a result of the light absorption of the grain or a sensitizing dye molecule on it. An electron in the conduction band migrates and is captured by one of shallow traps on the grain surface (i.e., the electronic processes for photographic sensitivity). An electron at a trap attracts an interstitial silver ion and reacts with it to form an Ag atom (i.e., the ionic process). The repetition of the electronic and ionic processes at the same site leads to the formation of an Ag cluster and becomes to be a latent image center, which is composed of four or more Ag atoms and can initiate photographic development [1].

A latent image center that acts as a deep electron trap on an AgX grain receives an electron from a developing agent molecule in a developer and then attracts and reacts with an interstitial silver ion to add an Ag atom to a latent image center during the development process. The repetition of these processes results in the conversion of an AgX grain with a latent image center on it to an Ag grain. Silver halide grains that remain after the development process are dissolved during the fix process. Since only the AgX grains with latent image centers on their surfaces are converted to black Ag grains, a latent image is developed to give a negative black-and-white image after these processes. For color photography, a developing agent molecule gives an electron to a latent image center and becomes to be an oxidation product, which then reacts with a coupler molecule in a photographic material to form a dye molecule for a color image. Then, Ag and AgX grains are removed after color development [1].

Reactions associated with photographic development are based on electrochemistry [1]. The redox potential of a developer with respect to its silver potential is the driving force for photographic development and used for the examination of the development process, which it causes. The oxidation potential of a compound is used to examine its ability as a developing agent on the basis of the relationship between oxidation potentials and rates of development among a series of compounds [2]. Although the oxidation potential of a developing agent molecule is based on the oxidation reaction, in which two electrons are involved in the oxidation of one molecule, a latent image center is too small to receive two electrons at the same time. The potentials for one-electron oxidation of developing agents have been evaluated by use of their semiquinone formation constants and are in closer relationship with their development rates than those for two-electron oxidation as were measured by polarography [3].

Since a visible light image can be reproduced by the combination of three primary lights (i.e., blue, green, red), color films and papers are composed of a layered photo-sensor, which is
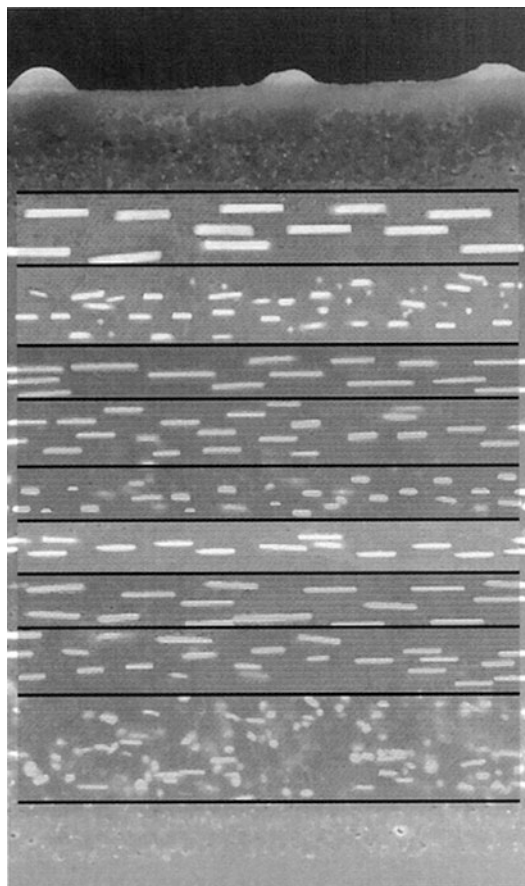
Photography, Silver Halides, Fig. 1 A scanning electron micrograph of the section of a layered photo-sensor in a color negative film, where white lines and spots are the sections of AgX grains. The photo-sensor is composed of 14 layers with different functions and ∼20 μm thick in total

sensitive to light in blue, green, and red regions separately owing to the light absorption of AgX grains and/or sensitizing dyes on the grains. A color negative film is composed of a layered photo-sensor coated on a TAC film base with thickness of ∼100 μm. Fig. 1 shows a scanning electron micrograph of the section of a layered photo-sensor in a color negative film, where white lines and spots are the sections of AgX grains. The photo-sensor in this figure is composed of 14 layers with different functions and ∼20 μm in total. Major layers are blue-, green-, and red-sensitive, while each major layer is
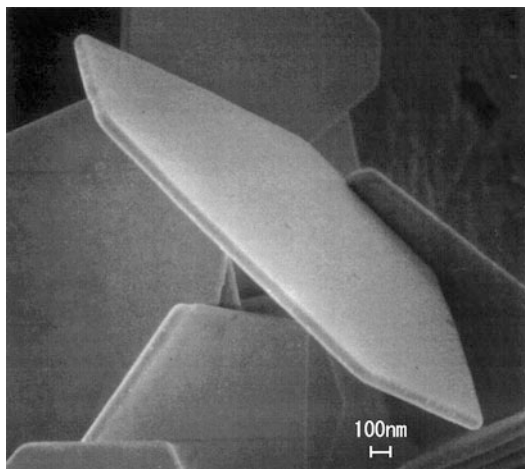
Photography, Silver Halides, Fig. 2 A scanning electron micrograph of tabular AgX grains developed for highly sensitive layers in a color negative film

composed of sub-layers with high, medium, and low sensitivities. Namely, a color negative film is designed to capture a light image in whole visible region with wide dynamic range of exposure [1].

As described above, photographic materials as represented by a color negative film are finely constructed hybrid systems composed of inorganic materials such as AgX grains that are well designed in nanoscale and more than 100 kinds of functional organic compounds. For example, monodispersed ultrathin tabular AgX grains as shown in Fig. 2 are designed from viewpoints of their structure, physical property, and photographic sensitivity, produced on a large scale and arranged with their main surfaces in parallel with the surface of a film base as seen in Fig. 1. The photo-sensor with 14 different layers in Fig. 1 is precisely coated all together on a large scale and at high speed. The coefficient of variation in thickness among arbitrary points in each layer is less than 2 %.

For the development of color films, extensive studies have been made on dye sensitization. After the electron transfer mechanism and the energy transfer one were proposed for it and examined extensively for many years from various viewpoints, the former has been accepted. Namely, a sensitizing dye molecule on an AgX grain is excited by an incident photon and injects an excited electron into the conduction band of the grain. An injected electron takes part in the formation of a latent image center on the grain. This model demands that the LUMO level of a sensitizing dye molecule should be higher than the bottom of the conduction band of AgX [1].

Thus, the height of LUMO of a dye with respect to that of the bottom of the conduction band of AgX together with the height of HOMO of a dye with respect to that of the top of the valence band of AgX is one of the most important properties for understanding and designing the dye sensitization of photographic materials and evaluated by organic electrochemistry in addition to ultraviolet photoelectron spectroscopy and molecular orbital method. The reduction and oxidation potentials (E_R and E_{OX}, respectively) are related to the heights of LUMO and HOMO (ε_{LU} and ε_{HO}, respectively), respectively, as follows [1].

$$\varepsilon_{LU} = E_R + C \tag{1}$$

$$\varepsilon_{HO} = E_{OX} + C' \tag{2}$$

where C and C' are constants. The values of E_R and E_{OX} of dyes could be measured by polarography, cyclic voltammetry, and phase-selective second-harmonic (PSSH) voltammetry. The values of E_R and E_{OX}, which were measured by means of PSSH voltammetry, could be free from the errors owing to the secondary reactions of reduced and oxidized dyes formed as results of electrode reactions [4]. Tremendous number of sensitizing dyes have been synthesized and subjected to the measurement of polarography and then PSSH voltammetry for precise evaluation of their ε_{LU} and ε_{HO}.

The electron transfer mechanism has enhanced the achievement of dye sensitization with high efficiency and the accumulation of the knowledge on the electron transfer process. The efficiency and rate of the electron transfer in dye sensitization have been analyzed in the framework of Marcus theory with respect to the value

of E_R of a dye that is in linear relationship with the electronic energy gap between ε_{LU} of the dye and the bottom of the conduction band of AgX according to Eq. 1 [5]. The degree of the recombination between an injected electron and a positive hole remaining at HOMO of a dye has been analyzed with respect to the values of E_{OX} of the dye that is in linear relationship with ε_{HO} according to Eq. 2 [1]. The electron transfer mechanism for dye sensitization has been applied to dye-sensitized solar cells on the basis of electrochemistry [6]. J-aggregates with sharp and intense absorption bands have been indispensable for color films and have attracted wide interests owing to their unique characteristics [1]. The vacuum level shift as observed for the first time at interfaces between AgX and sensitizing dyes has become to be important knowledge for the electronic structure at interfaces between substrates and organic semiconductors in various devices [1].

Recently, digital still cameras with solid state devices (i.e., CCD and CMOS) as photo-sensors have achieved such sensitivity and image quality as to meet the demand of most consumers and overwhelmed color films owing to their convenience. Other photographic films have been similarly overwhelmed by electronic imaging technologies.

However, AgX photographic materials are characterized by high image quality with large frame area, natural image reproduction, durability for a very long period, and three-dimentional imaging with high resolution, being used in the future as color films with natural image reproduction, black-and-white films with high image information and durability for achives, and new nuclear films that are composed of nanoparticles of AgX and being developed for the detection of dark matters [1].

Cross-References

▶ Dye-Sensitization
▶ Polarography
▶ Solid State Dye-Sensitized Solar Cell

References

1. Tani T (2011) Photographic science advances in nanoparticles, J-aggregates, dye sensitization, and organic materials. Oxford University Press, Oxford
2. Bent RL, Dessloch JC, Duennebier FC, Fassett DW, Glass DB, James TH, Julian DB, Ruby WR, Smell JM, Sterner JH, Thirtle JR, Vittum PW, Weissberger A (1951) Chemical constitution, electrochemical, photographic and allergenic properties of *p*-amino-*N*-dialkylamines. J Am Chem Soc 73:3100–3125
3. Tong LKJ, Bishop CA, Glesmann MC (1964) Correlation between oxidation potentials and development rates of some hydroquinones and *p*-phenylenediamines. Photogr Sci Eng 8:326–328
4. Lenhard J (1986) Measurement of reversible electrode potentials for cyanine dyes by use of phase-selective second-harmonic AC voltammetry. J Imag Sci 30:27–35
5. Tani T, Suzumoto T, Ohzeki K (1990) Energy gap dependence of efficiency of photoinduced electron transfer from cyanine dyes to silver bromide microcrystals in spectral sensitization. J Phys Chem 94:1298–1301
6. Graetzel M (2007) Nanocrystalline injection solar cells. In: Poortmans J, Arkhipov V (eds) Thin film solar cells: fabrication, characterization and application. Wiley, West Sussex

Photolysis of Water

Akihiko Kudo
Tokyo University of Science, Tokyo, Japan

Introduction

Photocatalytic and photoelectrochemical water splitting are important from the viewpoint of energy and environmental issues in a global level because it enables an ideal hydrogen production from water using a renewable energy such as a solar energy. Once solar hydrogen is obtained, carbon dioxide can be converted to various organic compounds by the reaction with the hydrogen. Artificial photosynthesis is achieved through the hydrogenation of carbon dioxide using the solar hydrogen. The artificial photosynthesis is an attractive reaction as an ultimate green sustainable chemistry and will

contribute to solving energy and environmental issues resulting in bringing an energy revolution.

The Honda-Fujishima effect of water splitting using a TiO_2 electrode was reported in the early stage of 1970s. When TiO_2 is irradiated with UV light, electrons and holes are generated as shown in Fig. 1 [1]. The photogenerated electrons reduce water to form H_2 on a Pt counter electrode while holes oxidize water to form O_2 on the TiO_2 electrode with some external bias by a power supply or pH difference between a catholyte and an anolyte. New photoelectrode and powdered photocatalyst materials for water splitting have been discovered one after another since this pioneer work.

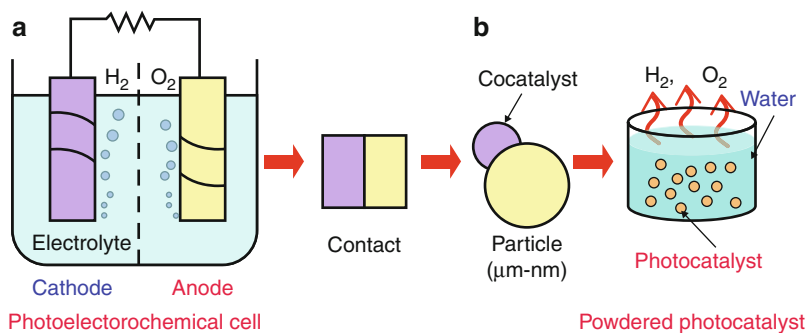## Bases of Photocatalytic Water Splitting

Photoelectrochemical Cells and Powdered Photocatalysts

There are two methods for water splitting using photon energy as shown in Fig. 2. There are
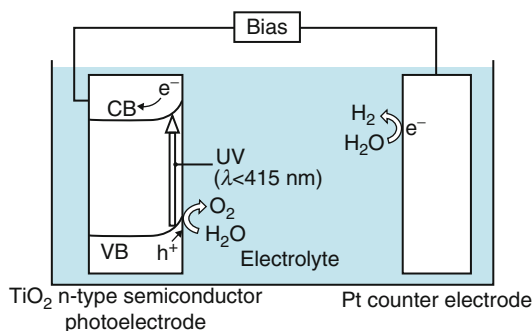
Photolysis of Water, Fig. 1 Honda-Fujishima effect for water splitting using an n-type TiO_2 photoelectrode

advantageous and disadvantageous points for each method. In photoelectrochemical cells represented by Honda-Fujishima effect shown in Fig. 1, n- and p-type photoelectrode materials can be use as an anode and cathode, respectively. Major advantageous point of this system is that H_2 can be obtained separately from O_2. Even if a material does not possess the suitable potential that is determined with the electronic band structure for water splitting, the water splitting may be possible with assistance of an external bias. Moreover, charge separation to suppress recombination between photogenerated electrons and holes is assisted by the external bias. However, materials for the photoelectrochemical cells are limited, because electrodes should be fabricated and possess an electric conductivity. In powdered photocatalysts, various kinds of materials can be used. The system is simple, because photocatalyst powder is just dispersed or dipped in water. So, it is advantageous for applying to a large-scale process.

Processes in Powdered Photocatalysts

Many heterogeneous photocatalysts have semiconductor properties. Figure 3 shows main processes in a photocatalytic reaction using a powdered system.

The first step is absorption of photons to form electron-hole pairs. Semiconductors have the band structure in which the conduction band is separated from the valence band by a band gap with a suitable width. When the energy of incident light is larger than that of a band gap, electrons and holes are generated in the conduction and valence bands, respectively.

Photolysis of Water, Fig. 2 Comparison of photoelectrochemical cell with powdered photocatalyst for water splitting

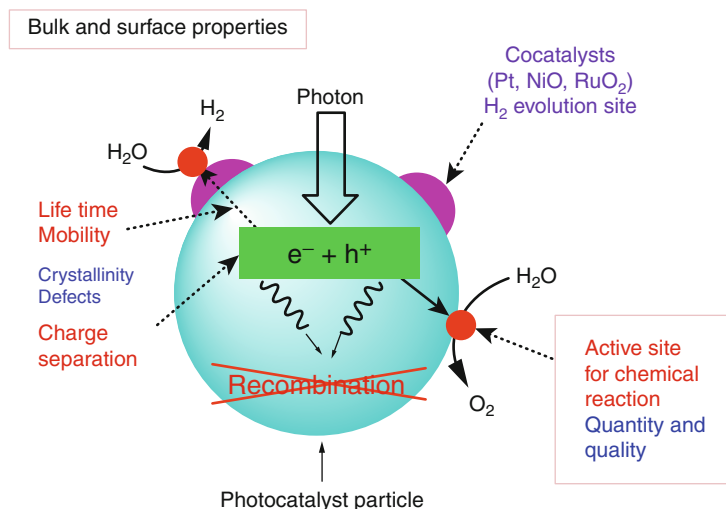**Photolysis of Water, Fig. 3** Processes of photocatalytic water splitting

The photogenerated electrons and holes cause redox reactions similarly to electrolysis. Water molecules are reduced by the electrons to form H_2 and are oxidized by the holes to form O_2 for overall water splitting. Important points in the semiconductor photocatalyst materials are a width of the band gap and levels of the conduction and valence bands. The bottom level of the conduction band has to be more negative than the redox potential of H^+/H_2 (0 V vs. NHE), while the top level of the valence band be more positive than the redox potential of O_2/H_2O (1.23 V). Therefore, the theoretical minimum band gap for water splitting is 1.23 eV that corresponds to light of about 1,100 nm.

The second step consists of charge separation and migration of photogenerated carriers. Crystal structure, crystallinity, and particle size strongly affect the step. The higher the crystalline quality is, the smaller the amount of defects is. The defects operate as trapping and recombination centers between photogenerated electrons and holes, resulting in a decrease in the photocatalytic activity.

The final step involves the surface chemical reactions. The important points for this step are surface character (active sites) and quantity (surface area). Even if the photogenerated electrons and holes possess thermodynamically sufficient potentials for water splitting, they will have to recombine with each other if the active sites for redox reactions do not exist on the surface. Cocatalysts such as Pt, NiO, RuO_2, and Cr-Rh oxide are usually loaded to introduce active sites for H_2 evolution because the conduction band levels of many oxide photocatalysts are not high enough to reduce water to produce H_2 without catalytic assistance.

Water Splitting and Sacrificial H_2 or O_2 Evolution Using Powdered Photocatalysts

"Water splitting" means to split H_2O simultaneously giving H_2 and O_2 in a 2:1 ratio. On the other hand, there are sacrificial H_2 and O_2 evolution reactions as shown in Fig. 4. When the photocatalytic reaction is carried out in an aqueous solution including a reducing reagent, in other words, electron donors or hole scavengers, such as alcohol and a sulfide ion, photogenerated holes irreversibly oxidize the reducing reagent instead of water. It enriches electrons in a photocatalyst, and an H_2 evolution reaction is enhanced. This reaction will be meaningful for realistic hydrogen production if biomass and abundant compounds in nature and industries are used as the reducing reagents. On the other hand, photogenerated electrons in the conduction band are consumed by oxidizing reagents (electron acceptors or electron scavengers) such as Ag^+ and Fe^{3+} resulting in that an O_2

Photolysis of Water, Fig. 4 Sacrificial H_2 and O_2 evolution over photocatalysts
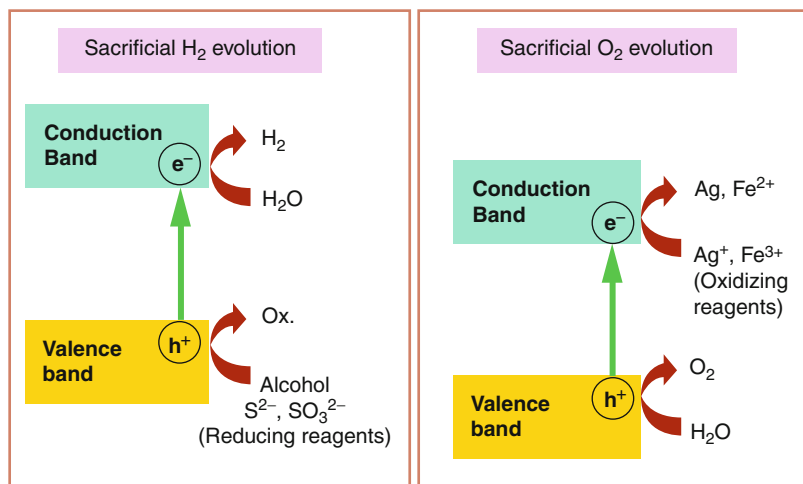

evolution reaction is enhanced. These reactions using sacrificial reagents are studied to evaluate if a certain photocatalyst satisfies the thermodynamic and kinetic potentials for H_2 and O_2 evolution. These reactions are regarded as half reactions of water splitting and are often employed as test reactions of photocatalytic H_2 or O_2 evolution. Even if a photocatalyst is active for these half reactions, the results do not guarantee a photocatalyst to be active for overall water splitting into H_2 and O_2 in the absence of sacrificial reagents.

Water splitting is an uphill reaction in which a light energy is converted to a chemical energy as shown in Fig. 5. In contrast, the sacrificial H_2 evolution is usually a downhill reaction. In this sense, the term of "water splitting" in the absence of sacrificial reagents should be distinguishably used toward H_2 or O_2 evolution from aqueous solutions in the presence of sacrificial reagents.

Water Splitting by Powdered Photocatalysts with Wide Band Gaps

Many metal oxide photocatalysts with wide band gaps can split water into H_2 and O_2 efficiently in a stoichiometric ratio under UV light irradiation
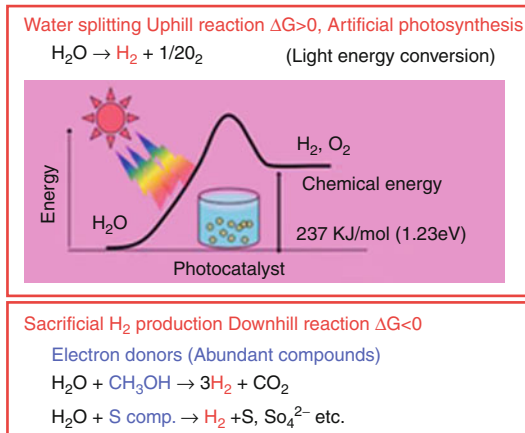
Photolysis of Water, Fig. 5 Photocatalytic water splitting and sacrificial H_2 evolution

as shown in Table 1 [2, 3]. These photocatalysts consist of metal cations with d^0 or d^{10} configuration. Representative photocatalysts with wide band gaps that respond to only UV are TiO_2 and $SrTiO_3$. ZrO_2, Ta_2O_5, and tantalates such as $NaTaO_3$ are also active for photocatalytic water splitting. $K_4Nb_6O_{17}$ and $K_2La_2Ti_3O_{10}$ with layered structures are unique photocatalysts. Ge_3N_4 and GaN: Zn are non-oxide photocatalysts [4]. NiO/$NaTaO_3$: La and $RhyCr_{2-y}O_3$/Ga_2O_3:

Photolysis of Water, Table 1 Wide band gap oxide photocatalysts consisting of metal cations with d^0 or d^{10} configuration for water splitting

Photocatalyst	Band gap/eV	Cocatalyst	Year
TiO_2	3.2	Rh	1985
$CaTiO_3$	3.5	NiO_x	2002
$SrTiO_3$	3.2	NiO_x	1980
$Rb_2La_2Ti_3O_{10}$	3.4–3.5	NiO_x	1997
$La_2Ti_2O_7$	3.8	NiO_x	1999
$La_2Ti_2O_7$:Ba		NiO_x	2005
$KLaZr_{0.3}Ti_{0.7}O_4$	3.91	NiO_x	2003
$La_4CaTi_5O_{17}$	3.8	NiO_x	1999
$KTiNbO_5$	3.6	NiO_x	1999
$Na_2Ti_6O_{13}$		RuO_2	1990
$Gd_2Ti_2O_7$	3.5	NiO_x	2006
$Y_2Ti_2O_7$	3.5	NiO_x	2004
ZrO_2	5	None	1993
$K_4Nb_6O_{17}$	3.4	NiO_x	1986
$Ca_2Nb_2O_7$	4.3	NiO_x	1999
$Sr_2Nb_2O_7$	4	NiO_x	1999
$Ba_5Nb_4O_{15}$	3.85	NiO_x	2006
$ZnNb_2O_6$	4	NiO_x	1999
$Cs_2Nb_4O_{11}$	3.7	NiO_x	2005
La_3NbO_7	3.9	NiO_x	2004
Ta_2O_5	4	NiO_x	1994
$K_3Ta_3Si_2O_{13}$	4.1	NiO	1997
$K_3Ta_3B_2O_{12}$	4	None	2006
$LiTaO_3$	4.7	None	1998
$NaTaO_3$	4	NiO	1998
$KTaO_3$	3.6	Ni	1996
$AgTaO_3$	3.4	NiO_x	2002
$NaTaO_3$:La	4.1	NiO	2000
$SrTa_2O_6$	4.4	NiO	1999
$Sr_2Ta_2O_7$	4.6	NiO	2000
$KBa_2Ta_3O_{10}$	3.5	NiO_x	1999
$PbWO_4$	3.9	RuO_2	2004
$RbWTaO_6$	3.8	NiO_x	2004
CeO_2:Sr		RuO_2	2007
$NaInO_2$	3.9	RuO_2	2003
$CaIn_2O_4$		RuO_2	2001
$SrIn_2O_4$	3.6	RuO_2	2001
$CaSb_2O_6$	3.6	RuO_2	2002
Ga_2O_3:Zn	4.6	Ni	2008

Zn photocatalysts have recently proven that highly efficient water splitting is possible using a powdered photocatalyst under UV light irradiation.

Water Splitting by Powdered Photocatalysts with Visible-Light Response

The goal of this research field is to produce hydrogen by usage of solar energy, the so-called solar hydrogen production. In order to utilize solar energy efficiently, it is indispensable to develop visible-light-driven photocatalysts [3].

There are two types of photocatalyst systems accompanied with one photon process and Z-schematic two-photon process for water splitting under visible-light irradiation as shown in Fig. 6. Some oxynitrides are active for water splitting as photocatalysts accompanied with one photon process [4]. Two-photon systems, as seen in photosynthesis by green plants (Z-scheme), are another way to achieve overall water splitting [5]. The Z-scheme is composed of an H_2-evolving photocatalyst, an O_2-evolving photocatalyst, and an electron mediator as shown in Table 2. Some Z-scheme photocatalysts work without electron mediators. Photocatalysts that are active only for half reactions of water splitting can be employed for the construction of the Z-scheme, that is, the merit of the Z-scheme.

Water Splitting by Photoelectrochemical Cells

It is important to see the stability of photocurrent and to determine the amounts of evolved H_2 and O_2 for photoelectrochemical water splitting, because we cannot always guarantee that obtained photocurrent is due to water splitting. Even if photocurrent is observed, it is sometimes due to some redox reactions rather than water reduction and oxidation. As mentioned above, an external bias can be applied to enhance photoelectrochemical water splitting. However, the applied external bias versus not a reference electrode but a counter electrode must be smaller than 1.23 V that was a theoretical voltage required for electrolysis of water, if one thinks of light energy conversion. Of course, non-bias is an ideal condition. WO_3, Fe_2O_3, and $BiVO_4$ have been extensively studied as photoanodes for O_2

Photolysis of Water, Fig. 6 Water splitting using single and Z-schematic photocatalysts

One photon process   Two photon process
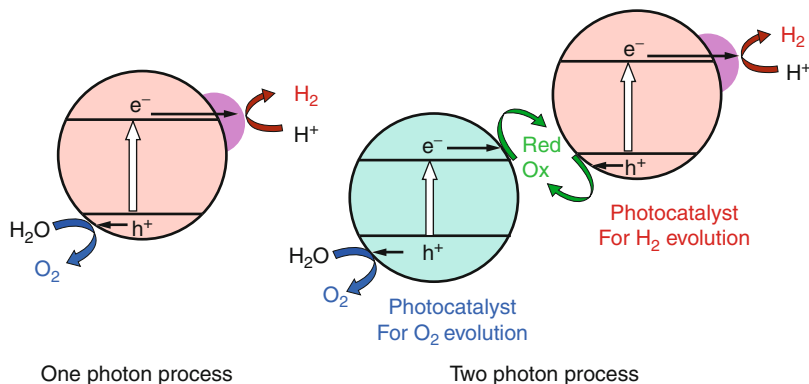
Photolysis of Water, Table 2 Z-scheme type photocatalyst systems working under VIS irradiation

H_2-evolving photocatalysts	H_2-evolving photocatalysts	Electron mediator
Pt/SrTiO$_3$:Cr,Ta	Pt/WO$_3$	IO$_3^-$/I$^-$
Pt/TaON	Pt/WO$_3$	IO$_3^-$/I$^-$
Pt/TaON	RuO$_2$/TaON	IO$_3^-$/I$^-$
Pt/CaTaO$_2$N	Pt/WO$_3$	IO$_3^-$/I$^-$
Pt/BaTaO$_2$N	Pt/WO$_3$	IO$_3^-$/I$^-$
Pt/ZrO$_2$/TaON	Pt/WO$_3$	IO$_3^-$/I$^-$
Coumarin/ K$_4$Nb$_6$O$_{17}$	IrO$_2$-Pt/WO$_3$	IO$_3^-$/I$^-$
Pt/ZrO$_2$/TaON	Ir/R-TiO$_2$/Ta$_3$N$_5$	IO$_3^-$/I$^-$
Pt/ZrO$_2$/TaON	RuO$_2$/TaON	IO$_3^-$/I$^-$
Pt/SrTiO$_3$:Rh	BiVO$_4$	Fe$^{3+/2+}$
Pt/SrTiO$_3$:Rh	Bi$_2$MoO$_6$	Fe$^{3+/2+}$
Pt/SrTiO$_3$:Rh	WO$_3$	Fe$^{3+/2+}$
Ru/SrTiO$_3$:Rh	BiVO$_4$	Fe$^{3+/2+}$
Ru/SrTiO$_3$:Rh	PbWO$_4$:Cr	Fe$^{3+/2+}$
Ru/SrTiO$_3$:Rh	BiVO$_4$	[Co(bpy)$_3$]$^{3+/2+}$
Ru/BaTa$_2$O$_6$:Ir,La	BiVO$_4$	[Co(bpy)$_3$]$^{3+/2+}$
Pt/SrTiO$_3$:Rh	BiVO$_4$	None
Ru/SrTiO$_3$:Rh	BiVO$_4$	None
Ru/SrTiO$_3$:Rh	AgNO$_3$	None
Ru/SrTiO$_3$:Rh	Bi$_2$MoO$_6$	None
Ru/SrTiO$_3$:Rh	TiO$_2$:Cr,Sb	None
Ru/SrTiO$_3$:Rh	TiO$_2$:Rh,Sb	None
Ru/SrTiO$_3$:Rh	WO$_3$	None

evolution to combine an ordinary metal electrodes, dye sensitized solar cells, and p-type semiconductor photoelectrodes for H_2 evolution.

Summary

At the present stage, the materials with which solar water splitting can be carried out are limited and the efficiencies are not satisfying us. Various kinds of efficiencies have been reported to evaluate the performances of photoelectrochemical cells and powdered photocatalysts. A quantum efficiency is scientifically important. Moreover, energy conversion efficiency of solar to hydrogen (STH) will be a standard value to evaluate the efficiency of an artificial photosynthesis system. It is indicated on roadmaps in the world that the construction of solar fuel production systems by artificial photosynthesis is a conclusive solution for energy and environmental issues. Solar water splitting is the core reaction of the artificial photosynthesis. If we can produce abundant hydrogen by the artificial photosynthesis, we can use it for not only a clean energy but also a raw material in chemical industries. CO_2 and N_2 can be converted to useful compounds using the solar hydrogen. Of course, there are several processes to utilize solar energy. There are merits and demerits for each process. Characteristic point of photocatalytic water splitting is the simplicity. Therefore, it is advantageous to a large-scale application harvesting a wide area of sunlight. The final goal of this research area is to construct an artificial photosynthesis resulting in revolution for energy.

Cross-References

▶ Photocatalyst
▶ Photoelectrochemistry, Fundamentals and Applications

References

1. Fujishima A, Honda K (1972) Electrochemical photolysis of water at a semiconductor electrode. Nature 238:37
2. Osterloh FE (2008) Inorganic materials as catalysts for photochemical splitting of water. Chem Mater 20:35
3. Kudo A, Miseki Y (2009) Heterogeneous photocatalyst materials for water splitting. Chem Soc Rev 38:253
4. Maeda K, Domen K (2007) New non-oxide photocatalysts designed for overall water splitting under visible light. J Phys Chem C 111:7851
5. Kudo A (2011) Z-scheme photocatalyst systems for water splitting under visible light irradiation. MRS Bull 36:32

Photorechargeable Cell

Tsutomu Miyasaka
Graduate School of Engineering,
Toin University of Yokohama,
Yokohama, Kanagawa, Japan

Introduction

All kinds of existing devices for storage and charge–discharge of electric power (condensers, capacitor, secondary batteries, etc.) utilize electrochemical interfaces. On the other hand, electric power can be produced from light by photoelectrochemical cells which also use electrochemical interfaces bearing photosensitive materials (semiconductors and dyes). Combination of these phenomena into a single hybrid cell makes it possible to convert light energy into power and store it in the cell structure at the same time. Such kind of cell capable of reversible photo-charge and dark discharge is called photorechargeable cell, which is a type of solar cell endowed with power storage ability. The merit of this cell is its function of stabilizing and sustaining the output electric power against variation of light intensity and cutoff of light.

There have been many trials to combine a photovoltaic electrode and rechargeable materials for invention of photorechargeable cells [1–7]. The methods of power storage so far proposed are classified into two types. One is the cell incorporating charge–discharge reactions of redox materials that have been employed in the study of secondary batteries. The other is the cell employing electrostatic capacitance change for power storage and release.

Materials and Structures for Rechargeable Half Cell

Photorechargeable cells can be devised by electrochemical combination of photoelectrochemical half cell and rechargeable half cell. Because photovoltaic power generation, either by dye-sensitized photocells or conventional solid-state solar cells (Si, CIS, etc.), is characterized to produce low output voltage less than 1 V, it is desired that the function of power storage can realize high capacity and energy density within the low voltage range. Conductive polymer materials that perform charge–discharge reactions at low voltages with relatively high coulombic capacity meet the above requirements. Among these polymers are polypyrrole [4, 5, 7], polyaniline [6], and polythiophene [7]. In a typical cell structure, counter electrode of a dye-sensitized solar cell is loaded with a layer of polypyrrole [4]. Polypyrrole undergoes a charge–discharge reaction due to doping and undoping of anion such as ClO_4^- and BF_4^- at a potential around -0.3–0.4 V versus SCE. This doping reaction is also crucial for endowing the conductivity to the polymer. To construct

photoanode of the photovoltaic half cell, metal oxide or compound semiconductor electrodes or dye-sensitized semiconductor electrodes have been employed. It is necessary for practical use that the photoanode has good sensitivity to visible light and performs rapid photo-charging with high photocurrent density. In addition, photoanode is desired to generate voltage as high as possible to drive charging of the storage materials. Dye-sensitized mesoporous semiconductors, sensitive to visible light (wavelengths up to 800–900 nm), meet these requirements. Photoexcitation of a dye-sensitized TiO_2 photoanode causes electron flow to the polypyrrole-loaded counter electrode where electrons are stored by reducing the polymer. In the optimum conditions for polymer structure and electrolyte composition, charging capacity can reach 90 mAh/g. A desired structure of the cell to operate efficient charge–discharge at high energy density is a three-electrode construction in which a middle electrode (inserted) separates electrolytes compositions for photovoltaic generation and charge storage. While counter electrode bears polypyrrole for the storage of photoexcited electrons, the middle electrode that is set opposed to the dye-sensitized anode bears a material for the storage of holes so that it is positively charged, i.e., oxidized, during light excitation of the anode. Polythiophene has been employed for a hole storage material [7]. The polymer-based photorechargeable cells achieve cyclic charge–discharge in the voltage range of 0.5–0.7 V [5, 7] with coulombic densities more than 50mAh g^{-1} [5]. Besides polymer materials, inorganic compounds such as MnO_2 and WO_3 [3, 8] also work as high-capacity storage materials to compose the rechargeable half cell. Carbonaceous materials are also considered to be useful for power storage materials. Especially, high energy density is achieved by lithium ion intercalation at charging voltages <4.2 V, which is however out of the range that photovoltaic generation concern. Soft carbonaceous materials have been successfully applied to various types of photoelectrochemical cells [9]. They can also be applied to the photorechargeable cell in the other way as they also serve as excellent materials for capacitor electrodes that work in a wide range of voltage.

Photocapacitor

Besides the use of redox materials, the other type of photorechargeable cell is devised by using carbon materials for power storage half cell. Here, the charge–discharge mechanism differs from the above method and is based on the principle of capacitor that electrostatically stores electric power in terms of electric double layer capacitance. Activated carbon (AC) of large surface areas (>100 m g^{-1}) has been adopted for commercial capacitors of high charge–discharge capacity. In comparison with redox-type storage materials, these carbon-based capacitors are more stable against charge–discharge cycles and perform rapid charging reactions to photocurrent change (light variation). The photorechargeable capacitor is known as photocapacitor [10]. The device has been fabricated as a simple sandwich-type cell consisting of a dye-sensitized semiconductor photoanode, a redox-free liquid electrolyte, and a counter electrode in which two electrodes bear porous AC layers. In principle, charging proceeds by dye-sensitized electron injection to semiconductor (TiO_2) and simultaneous hole injection to the AC layer that is in junction with dye/TiO_2. The injected electron flows to the counter electrode and charges the AC layer. Figure 1 shows the structure and charge–discharge mechanism. The cell, which is free of redox reactions, is capable of charging up to 0.45 V [10]. The charging voltage, however, is lower than the expected range corresponding to the photovoltage of dye-sensitized solar cell, >0.7 V, which is due to the absence of redox system in electrolyte to favor the photovoltaic generation. Three-electrode type photocapacitor with a structure of separated electrolytes has been designed to overcome this subject [11]. Its structure is basically similar to those used in the above redox-type cells except for AC layers that replace polymers. Figure 2 illustrates the cell structure, in which the middle electrode can be a thin metal foil. Preparation of dye-sensitized

Photorechargeable Cell,
Fig. 1 Two-electrode
sandwich-type structure of
photocapacitor and charge-
transfer mechanism in the
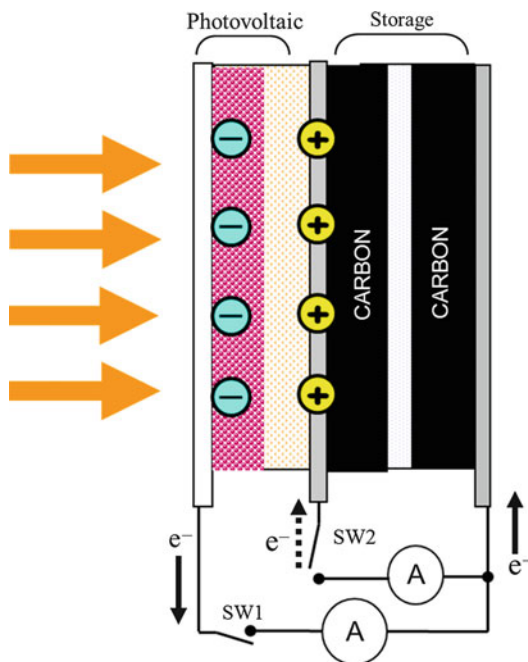processes of photo-charge
and dark discharge
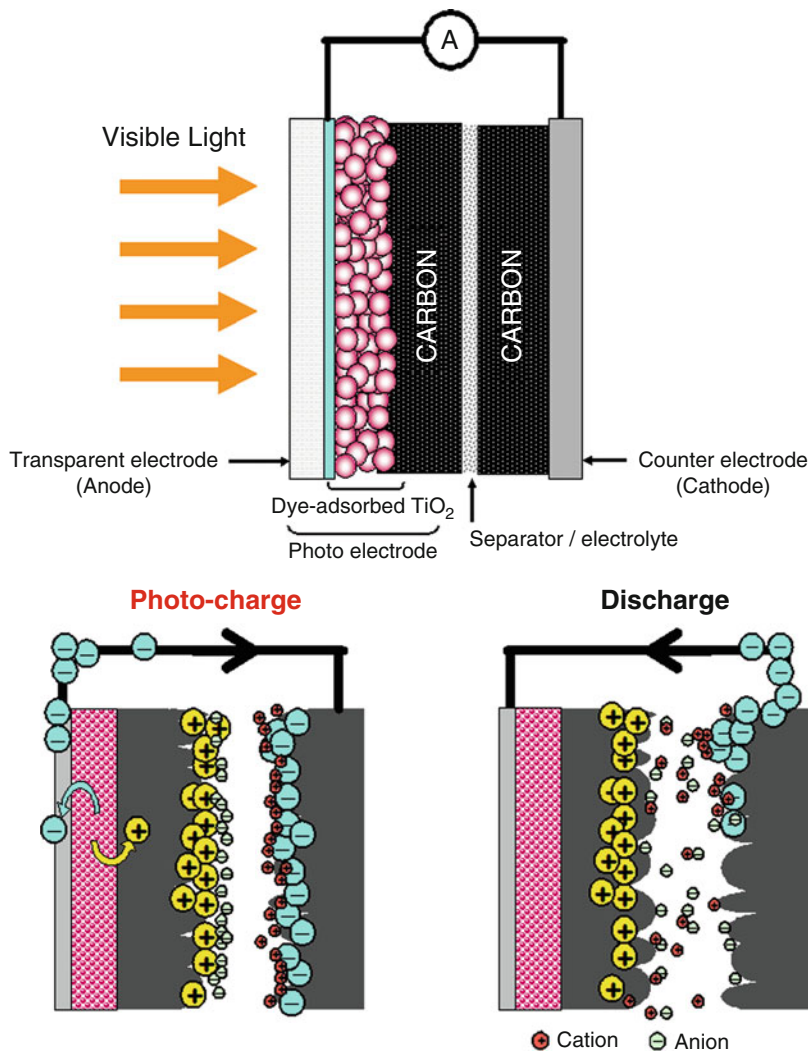
photoanode follows the conventional method of fabricating a mesoporous TiO_2 electrode on a transparent conductive substrate (see keyword, dye-sensitized photoanode). The electrolyte of the photovoltaic unit consisting photoanode and middle electrode is an iodine-/triiodide-containing organic solution and that of the AC-coated capacitor unit is 1 M tetraethylamine BF_4-containing propylene carbonate. Various kinds of sensitizers (dyes, quantum dots) and semiconductors can be applied to the construction of photoanode.

To operate the photocapacitor, charging is done by visible light irradiation to the photoanode in the condition of short-circuiting the external circuit, and discharge is done by connecting the middle and counter electrodes in the circuit. Rate of charging is fully dependent on the light intensity and tends to decrease with time until charging is saturated. In discharge, current density can be regulated as constant by galvanostatic circuitry. Figure 3 shows a photo-charge and dark-discharge characteristics of the photocapacitor. Illuminated with white light of $100 \ mW \ cm^{-2}$, charging voltage reaches as high as 0.8 V. On discharge in the dark, cell voltage exhibited a constant decrease with time under constant current. This linear decrease is

a characteristic of the electric double layer capacitor, and the cell capacitance is determined by the reciprocal of the slope, Idt/dV, where I and t represent current and discharging time, respectively. Using a Ru complex-sensitized TiO_2 photoanode, three-electrode photocapacitor fabricated in optimized conditions shows a charging voltage of 0.85 V yielding a maximum capacitance per the amount of AC of 200 F g^{-1}, specific capacitance per electrode area of 6 F cm^{-2}, and energy density per area of 230 mWh cm^{-2}. This performance corresponds to 4 % as a global solar energy storage efficiency starting from the conversion of incident energy and ending with energy storage in the cell. Following the method of carbon-based photocapacitors, polythiophene derivatives have been applied to replace the AC layers as redox active materials. It gives an energy density of 21.3 μ Wh cm^{-2} with charging voltage of 0.75 V [12]. The photocapacitors are fairly stable against more than thousands of repeated charge–discharge cycles.

Photorechargeable cells work as the solar cell endowed with power-stabilizing function against light variation, the function being incorporated at the material level in a single sandwich-type device. Figure 3 displays data demonstrating that the photocapacitor stabilizes the output power under exposure to random fluctuation of outdoor sunlight [9] (Fig. 4).

Photorechargeable Cell, Fig. 2 Three-electrode type photocapacitor. Photo-charge (*solid arrow*) and discharge (*dashed arrow*) processes are controlled on external circuit by switching (SW1, SW2)

Future Perspectives

Because photorechargeable devices have a flat shape, similar to solar cells, to receive light, the amount of charge storage material loaded on the electrode area is limited. In a single flat device, storage capacity and energy density can only be increased by

Photorechargeable Cell, Fig. 3 Photo-charge (*left*) and discharge (*right*) characteristics of photocapacitor in function of voltage with charge–discharge time
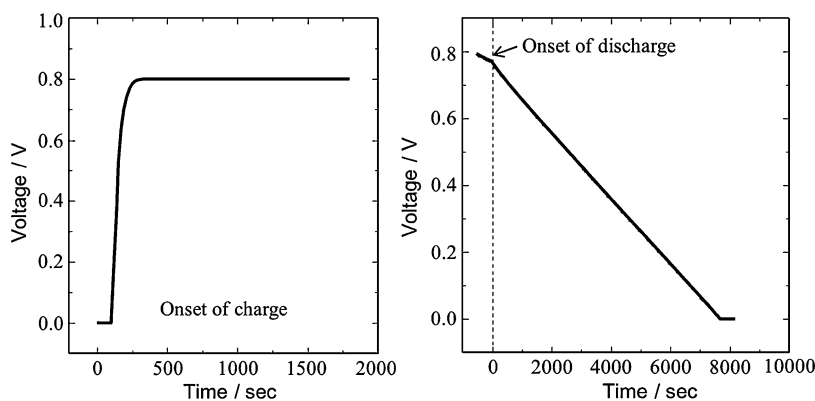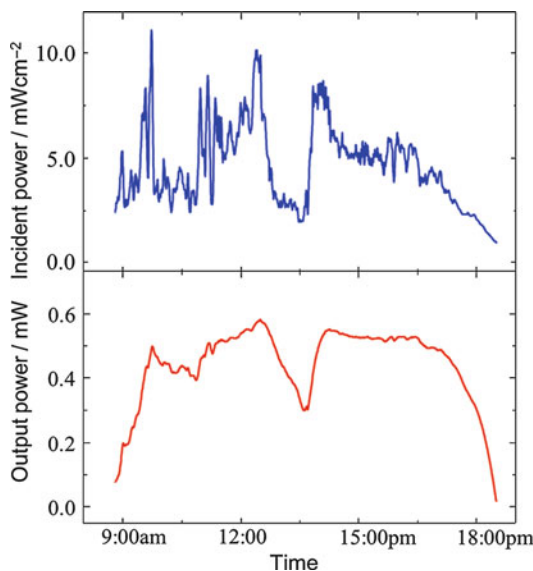
Photorechargeable Cell, Fig. 4 Output power of the photocapacitor in comparison with the change of incident solar irradiation power during a day

increasing the thickness of the material. For large power storage, conventional capacitors such as cylinder types are more useful by way of electrically connecting a solar cell module and a storage cell. In this case, however, circuitry of stabilizing the solar cell output is prerequisite to connection. Replacement of solar cell with photorechargeable cell may save such load of circuitry. For small power industry, which is related to consumer electronic devices, photorechargeable device is a more useful tool for continuous supply of photo-generated power to secondary batteries such as lithium ion batteries. High sensitivity of dye-sensitized power generation to weak indoor light is especially advantageous for versatile applications in power storage and supply to small power electronic devices such as computers and other IT equipment.

Cross-References

▶ Photocatalyst

▶ Photoelectrochemistry, Fundamentals and Applications

▶ TiO$_2$ Photocatalyst

References

1. Licht S, Hodes G, Tenne R, Manassen J (1987) A light-variation insensitive high efficiency solar cell. Nature 326:863–864
2. Kaneko M, Okada T, Minoura H, Sugiura T, Ueno Y (1990) Photochargeable multilayer membrane device composed of CdS film and prussian blue battery. Electrochim Acta 35:291–293
3. Hauch A, Georg A, Krasovec UO, Orel B (2002) Photovoltaically self-charging battery. J Electrochem Soc 149:A1208–A1211
4. Nagai H, Segawa H (2004) Energy-storable dye-sensitized solar cell with a polypyrrole electrode. Chem Commun 8:974–975
5. Saito Y, Ogawa A, Uchida S, Kubo T, Segawa H (2010) Energy-storable dye-sensitized solar cells with interdigitated nafion/polypyrrole-Pt comb-like electrodes. Chem Lett 39:488–489
6. Karami H, Mousavi MF, Shamsipur M (2003) New design for dry polyaniline rechargeable batteries. J Power Sources 117:255–259
7. Liu P, Yang HX, Ai XP, Li GR, Gao XP (2012) A solar rechargeable battery based on polymer charge storage electrodes. Electrochem Commun 16:69–72
8. Saito Y, Uchida S, Kubo T, Segawa H (2010) Surface-oxidized tungsten for energy-storable dye-sensitized solar cells. Thin Solid Films 518:3033–3036
9. Miyasaka T, Ikeda N, Murakami TN, Teshima K (2007) Light energy conversion and charge storage with soft carbonaceous materials that solidify mesoscopic electrochemical interfaces. Chem Lett 36:480–487
10. Miyasaka T, Murakami TN (2004) The photocapacitor: an efficient self-charging capacitor for direct storage of solar energy. Appl Phys Lett 85:3932–3934
11. Murakami TN, Kawashima N, Miyasaka T (2005) A high-voltage dye-sensitized photocapacitor of three-electrode system. Chem Commun 26:3346–3348
12. Hsu CY, Chen HW, Lee KM, Hu CW, Ho KC (2010) A dye-sensitized photo-supercapacitor based on PProDOT-Et2 thick films. J Power Sources 195:6232–6238

Plasmonic Electrochemistry (Surface Plasmon Effect)

Tetsu Tatsuma
Institute of Industrial Science, University of Tokyo, Tokyo, Japan

Introduction

Photoelectrochemistry has been applied to photocatalysis (see the entries ▶ Photocatalyst,

Plasmonic Electrochemistry (Surface Plasmon Effect), Fig. 1 Possible mechanisms for (**a**) plasmonic excitation of dye or semiconductor and (**b**) plasmon-induced charge separation
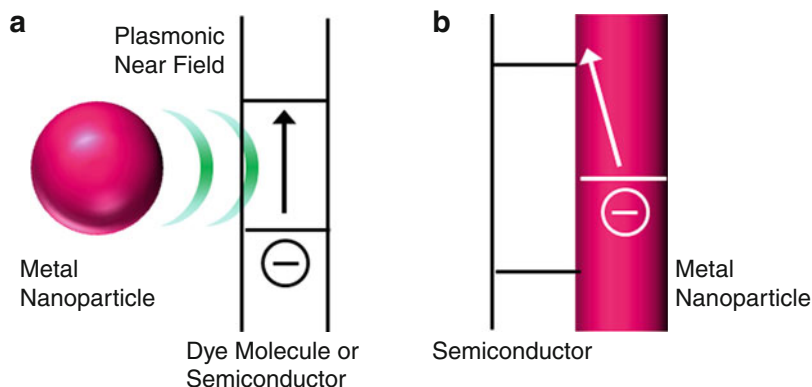
▶ TiO$_2$ Photocatalyst) and redox reaction-based solar cells such as dye-sensitized solar cells (see the entries ▶ Dye-Sensitized Electrode, Photoanode). In photoelectrochemistry, semiconductors such as TiO$_2$ or dye molecules such as Ru-complexes are used for light harvesting elements. Those elements are often used as thick deposits so that incident photons are absorbed extensively. An alternative approach to sufficient light absorption is the use of plasmonic metal nanoparticles. Nanoparticles of noble metal such as Au, Ag, and Cu absorb and scatter light due to localized surface plasmon resonance (LSPR), which is collective oscillation of conduction electrons at the metal surface by coupling with an incident electromagnetic field. LSPR is of interest for the following three aspects:

(1) strong light absorption, which is roughly proportional to particle volume;
(2) tunable optical properties, e.g., resonance intensity and wavelength dependent on particle size and shape, interparticle spacing, and dielectric environment; and
(3) non-propagating, oscillating electric field (optical near field) strongly localized in close proximity to the particle surface, beyond the diffraction limit.

There are two approaches to light harvesting based on LSPR:
(i) excitation of dye or semiconductor by plasmonic near field (Fig. 1a) and
(ii) charge separation at the interface between a plasmonic metal nanoparticle and a semiconductor (plasmon-induced charge separation) (Fig. 1b).

Plasmonic Excitation of Dye and Semiconductor

Plasmonic excitation of dye molecules and semiconductors has been used for surface-enhanced Raman scattering (SERS) and enhancement of fluorescence. It is also used for photoelectrochemistry such as dye-sensitized solar cells [1, 2] and photocatalysis [3, 4]. The LSPR band of metal nanoparticle antennae must overlap the absorption band of the dye or semiconductor used, so that the plasmonic near field around the metal nanoparticle can excite the dye or semiconductor. Since lifetime of LSPR is much longer than the time for which a photon passes by the metal nanoparticle, the excitation by near field can be more efficient than direct excitation by incident photons. The enhancement factor is defined by "photocurrent (or reaction rate) in the presence of the nanoparticles"/"photocurrent (or reaction rate) in the absence of the nanoparticles." Its value is typically from 2 to 20. The optimum spacing between the metal nanoparticle and the dye molecule or semiconductor is normally a few nm to a few tens nm [5, 6]. In the case of too small spacing or direct contact, energy transfer from the dye molecule or semiconductor to the metal nanoparticle may be so high that photoelectrochemical processes are suppressed. For the same reason, the use of plasmonic nanoparticles could have negative effect on systems with strong light absorption, whereas it is effective for enhancement of systems with weak light absorption.

Plasmon-Induced Charge Separation

Visible or near infrared light-induced charge separation [7] is observed for semiconductors (TiO_2, $SrTiO_3$, ZnO, CeO_2) in contact with plasmonic nanoparticles of Au, Ag, or Cu. The action spectra of the charge separation are close to LSPR-based absorption spectra of the corresponding metal nanoparticles. A possible mechanism is electron transfer from resonant metal nanoparticles to semiconductor due to an external photoelectric effect or hot electron injection. Actually, TiO_2 electrodes modified with plasmonic metal nanoparticles exhibit negative photopotential shifts and anodic photocurrents [8], whereas electrodes with metal nanoparticles coated with TiO_2 exhibit opposite responses, i.e., positive photopotential shifts and cathodic photocurrents [9]. On the other hand, the charge separation takes place preferentially at sites where the plasmonic electric field is localized [10].

In the case of Au, nanoparticles are stable both under light irradiation and in the dark. Therefore, the charge separation system is applied to photovoltaic cells and photocatalysis. Photovoltaic cells may be a wet type or solid state. In the wet-type cell, a photoanode such as electrode/nSC/MNP (nSC = n-type semiconductor; MNP = metal nanoparticle) [8] or a photocathode such as electrode/MNP/nSC [9] is used with an electrolyte containing a redox couple. Structures of solid-state cells are electrode/nSC/MNP/HTM/electrode (HTM = hole transport material or p-type semiconductor) [11] and electrode/nSC/MNP/electrode [12].

Photocatalytic systems based on the plasmon-induced charge separation can be used for oxidation of alcohols, aldehydes, and phenol [8, 13]; mineralization of carboxylic acids [14]; oxidation of benzene to phenol [15]; release of hydrogen from alcohols and ammonia [16]; and oxidation and reduction of water (but not water splitting) [17]. The photocatalytic system can also be applied to hydrophilic/hydrophobic patterning based on photocatalytic removal of a hydrophobic thiol adsorbed on metal nanoparticles [18].

In the case of Ag, nanoparticles are oxidized to Ag^+ ions by the charge separation [7, 19, 20]. The Ag^+ ions are reduced back to Ag nanoparticles by photocatalytic effects of photoexcited semiconductor (e.g., UV-irradiated TiO_2). This pseudo-reversible process is exploited for photochromism (see entry ▶ Photochromizm and Imaging) including multicolor photochromism [19], infrared and polarized photochromism, and fast photochromism. Holographic data storage [21] and photomorphing gels [20] are additional applications. Ag nanoparticles can be stabilized by chemical modification with a hydrophobic thiol. The electrode/MNP/TiO_2 system mentioned above can also protect Ag nanoparticles from oxidation so that it can be used for wet-type photovoltaic cells and photocatalysis.

In the case of Cu, nanoparticles are ready to be oxidized even in the absence of light. However, Cu nanoparticles coated with a thin protective layer (e.g., poly(vinyl alcohol)) are stable even under resonant light and exhibit plasmon-induced charge separation [22].

Future Directions

An increased number of papers have been published in recent years regarding electrochemistry based on the plasmonic excitation and the plasmon-induced charge separation. For further developments and practical applications, mechanisms and characteristics of those phenomena must be studied in further detail. These systems would make photovoltaic devices less expensive and simpler on the basis of efficient light absorption.

Cross-References

▶ Photocatalyst
▶ TiO_2 Photocatalyst
▶ Dye-Sensitized Electrode, Photoanode
▶ Photochromizm and Imaging

References

1. Wen C, Ishikawa K, Kishima M, Yamada K (2000) Effects of silver particles on the photovoltaic properties of dye-sensitized TiO_2 thin films. Sol Energ Mater Sol C 61:339

2. Standridge SD, Schatz GC, Hupp JT (2009) Distance dependence of plasmon-enhanced photocurrent in dye-sensitized solar cells. J Am Chem Soc 131:8407

3. Ingram DB, Linic S, (2011) Water splitting on composite plasmonic-metal/semiconductor photoelectrodes: evidence for selective plasmon-induced formation of charge carriers near the semiconductor Surface. J Am Chem Soc 133:5202

4. Gao H, Liu C, Jeong HE, Yang P (2012) Plasmon-enhanced photocatalytic activity of iron oxide on gold nanopillar. ACS Nano 6:234

5. Kawawaki T, Takahashi Y, Tatsuma T (2011) Enhancement of dye-sensitized photocurrents by gold nanoparticles: Effects of dye-particle spacing. nanoscale 3:2865

6. Torimoto T, Horibe H, Kameyama T, Okazaki K, Ikeda S, Matsumura M, Ishikawa A, Ishihara H, (2011) Plasmon-enhanced photocatalytic activity of cadmium sulfide nanoparticle immobilized on silica-coated gold particles. J Phys Chem Lett 2:2057

7. Tatsuma T, (2013) Plasmonic photoelectrochemistry: Functional materials based on photoinduced reversible Redox Reactions of Metal Nanoparticles. Bull Chem Soc Jpn 86:1

8. Tian Y, Tatsuma T (2005) Mechanisms and applications of plasmon-induced charge separation at TiO_2 films loaded with gold nanoparticles. J Am Chem Soc 127:7632

9. Sakai N, Fujiwara Y, Takahashi Y, Tatsuma T (2009) Plasmon resonance-based generation of cathodic photocurrent at electrodeposited gold nanoparticles coated with TiO_2 films. Chemphyschem 10:766

10. Kazuma E, Sakai N, Tatsuma T (2011) Nanoimaging of localized plasmon-induced charge separation. Chem Commun 47:5777

11. Yu K, Sakai N, Tatsuma T (2008) Plasmon resonance-based solid-state photovoltaic devices. Electrochemistry 76:161

12. Takahashi Y, Tatsuma T (2011) Solid state photovoltaic cells based on localized surface plasmon-induced charge separation. Appl Phys Lett 99:182110

13. Kowalska E, Abe R, Ohtani B (2009) Visible light-induced photocatalytic reaction of gold-modified titanium(IV) oxide particles: action spectrum analysis. Chem Commun 2009:241

14. Kominami H, Tanaka A, Hashimoto K (2010) Mineralization of organic acids in aqueous suspensions of gold nanoparticles supported on cerium(IV) oxide powder under visible light irradiation. Chem Commun 46:1287

15. Ide Y, Matsuoka M, Ogawa M (2010) Efficient visible-light-induced photocatalytic activity on gold-nanoparticle-supported layered titanate. J Am Chem Soc 132:16762

16. Tanaka A, Sakaguchi S, Hashimoto K, Kominami H (2012) Preparation of Au/TiO_2 exhibiting strong surface plasmon resonance effective for photoinduced hydrogen formation from organic and inorganic compounds under irradiation of visible light. Catal Sci Technol 2:907

17. Silva CG, Juarez R, Marino T, Molinari R, García H (2011) Influence of excitation wavelength (UV or Visible Light) on the photocatalytic activity of titania containing gold nanoparticles for the generation of hydrogen or oxygen from water. J Am Chem Soc 133:595

18. Tian Y, Notsu H, Tatsuma T (2005) Visible-light-induced patterning of Au- and Ag-TiO_2 nanocomposite film surfaces on the basis of plasmon photoelectrochemistry. Photochem Photobiol Sci 4:598

19. Ohko Y, Tatsuma T, Fujii T, Naoi K, Niwa C, Kubota Y, Fujishima A (2003) Multicolor photochromism of TiO_2 films loaded with Ag nanoparticles. Nat Mater 2:29

20. Tatsuma T, Takada K, Miyazaki T (2007) UV light-induced swelling and visible light-induced shrinking of a TiO2-containing redox gel. Adv Mater 19:1249

21. Qiao Q, Zhang X, Lu Z, Wang L, Liu Y, Zhu X, Li J (2009) Formation of holographic fringes on photochromic Ag/TiO_2 nanocomposite films. Appl Phys Lett 94:074104

22. Yamaguchi T, Kazuma E, Sakai N, Tatsuma T (2012) Photoelectrochemical responses from polymer-coated plasmonic copper nanoparticles on TiO_2. Chem Lett 41:1340–1342

Platinum Monolayer Electrocatalysts

Radoslav R. Adzic[1] and Yun Cai[2]
[1]Chemistry Department, Brookhaven National Laboratory, Upton, NY, USA
[2]Material Science, Joint Center for Artificial Photosynthesis, Lawrence Berkeley National Laboratory, Berkeley, CA, USA

Introduction

Fuel cells are expected to be one of major sources of clean energy given their uniquely high energy

conversion efficiency and low or zero emissions. Particularly important will be the application of proton exchange membrane fuel cell (PEMFC) in transportation. It will cause a substantial decrease of adverse effects of using fossil fuels on the environment. However, the slow kinetics of oxygen-reduction reaction (ORR) at fuel-cell cathodes cause a significant loss of the cell voltage even with the best Pt-based catalysts, which lowers the energy conversion efficiency. This drawback and the problem of Pt dissolution during long-term fuel-cell operations demand high Pt content at the cathode [1, 2]. The costs associated with high Pt contents hinder the commercialization of fuel-cell technology. Platinum monolayer electrocatalysts [3, 4] were developed to answer the challenges of slow kinetics of oxygen-reduction reaction (ORR) at fuel-cell cathodes, insufficient stability of Pt, and low CO tolerance Pt-based anode electrocatalysts [5].

Platinum monolayer electrocatalysts have a core–shell structure with a monolayer of Pt as the shell supported by various conductive nanostructures with single or multiple metal components as the core. This class of electrocatalysts possesses the following unique properties: (1) ultimately low Pt content, containing only one monolayer amount of Pt; (2) complete utilization of Pt since all Pt atoms are on the surface and directly participate in the reaction; and (3) tunable activity and stability from the modification of the structural and electronic properties of Pt_{ML} induced by substrate [3, 4, 6]. Based on the composition and structure of the substrates, the Pt_{ML} electrocatalysts can be divided into the following categories:

1. Pt_{ML} on metal or alloys
2. Pt_{ML} on core–shell cores

From the shape of substrates, in addition to the traditional 0D nanoparticles, 1D nanowires and 3D nanocrystals have also been used as substrates for Pt_{ML}. The unique features of Pt_{ML} electrocatalysts open various possibilities for designing electrocatalysts with specific catalytic properties by choosing appropriate substrates.
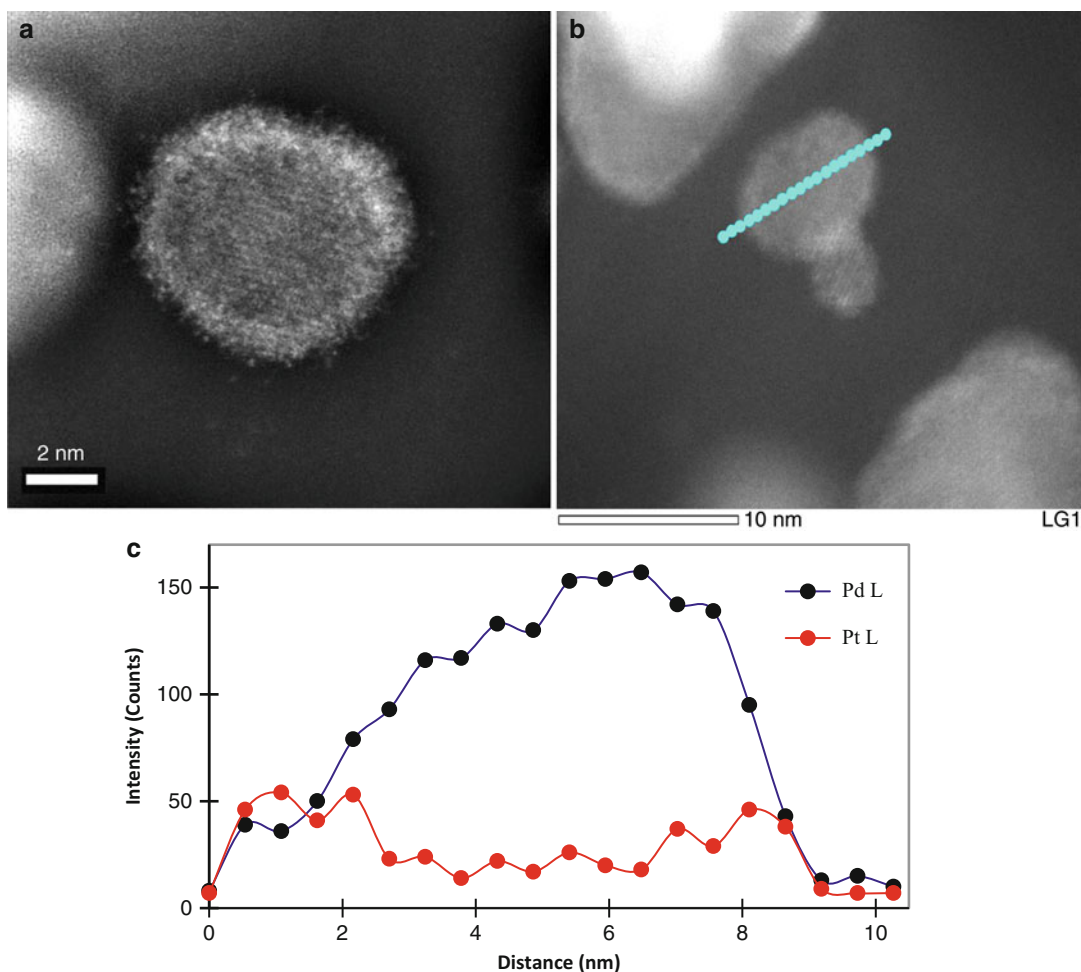
Synthesis of Pt_{ML} Electrocatalysts

A typical Pt_{ML} electrocatalyst is prepared by placing a monolayer of Pt atoms on metal nanoparticles using galvanic displacement of an underpotentially deposited (UPD) Cu monolayer by a Pt monolayer [3, 7]. Underpotential deposition describes the formation of a submonolayer or monolayer of a metal on a foreign metallic substrate at potentials positive to the reversible Nernst potential, that is, before bulk deposition can occur [8]. The experimental setup for Pt_{ML} deposition on an electrode consists of a cell with several compartments; one used for Cu UPD, one for rinsing the electrode after emersion from $CuSO_4$ solution, and one for displacement of a Cu monolayer upon electrode immersion in Pt^{2+} solution. The cell is under an inert gas (Ar or N_2) and facilitates all operations in an O_2-free environment.

The deposition of Pt_{ML} is a two-step process. First, a Cu UPD layer is deposited in a $CuSO_4$ solution via holding the potential positive to the bulk deposition for Cu. Then, after removing potential control, the electrode is transferred in a Pt^{2+} solution. Pt replaces the underpotentially deposited Cu by a simple redox exchange. A schematic diagram of the entire process is shown in Fig. 1.

$$Cu_{upd}/Pd + Pt^{2+} \longrightarrow Pt/Pd + Cu^{2+}$$
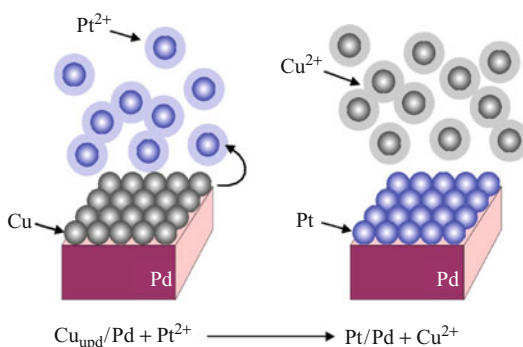
Platinum Monolayer Electrocatalysts, Fig. 1 Schematics of the galvanic displacement of a Cu UPD monolayer by Pt. *Blue* and *gray balls* represent Pt and Cu atoms, respectively. The *clouds* around balls indicate ions [9]

Platinum Monolayer Electrocatalysts, Fig. 2 $Pt_{ML}/Pd/C$: (**a**) HAADF-STEM image; line profile analysis (**b**) STEM image (**c**) the corresponding scanning EDS [10]

Scale-up synthesis of these electrocatalysts to produce kilogram quantities can be carried out in cells with larger cathode areas and cell volumes. A convenient cell consists of a Ti cylinder container (more than 10 cm in diameter) that also serves as the working electrode; the inside wall is coated with RuO_2, which is corrosion resistant, and the UPD of Cu is not taking place on this surface. A Pt black sheet used as counter electrode is in a separate compartment.

Structural and Electronic Characterizations of Pt_{ML} Electrocatalysts

The morphology and structure of Pt_{ML} electrocatalysts were characterized by high-angle annular dark-field (HAADF) imaging using scanning transmission electron microscopy (STEM). Figure 2a shows a typical HAADF-STEM Z-contrast image of $Pt_{ML}/Pd/C$ nanoparticle, bright shell and relatively darker core, suggesting
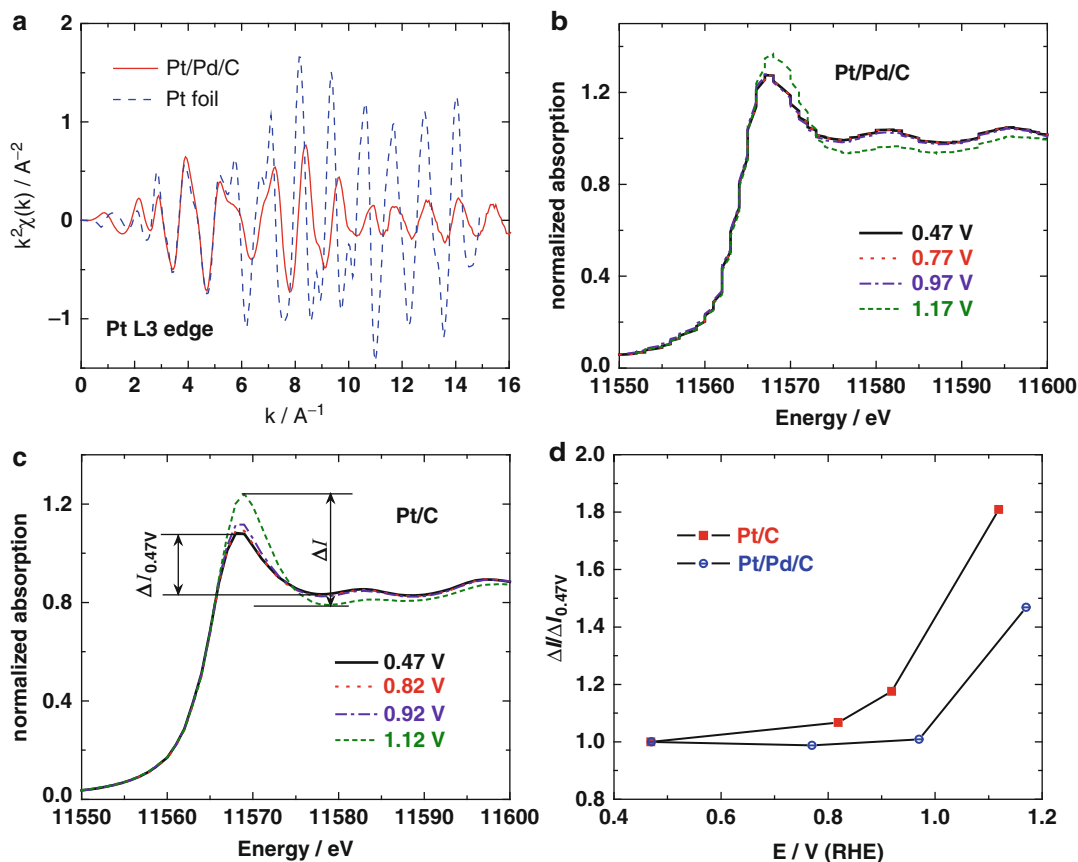
Platinum Monolayer Electrocatalysts, Fig. 3 (**a**) In situ EXAFS (k^2-weighted) k-space spectra of Pt L3 edge obtained from Pt_{ML}/Pd/C and Pt foil in 1 M $HClO_4$ at a potential of 0.41 V/RHE. XANES spectra obtained with Pt_{ML}/Pd/C (**b**) and Pt/C (**c**) electrocatalysts at four different potentials in 1 M $HClO_4$. (**d**) A comparison of the change of the absorption peak as a function of potential for Pt_{ML}/Pd/C and Pt/C

the formation of a core–shell structure, i.e., a Pt ($Z = 78$) shell on a Pd ($Z = 46$) nanoparticle [10]. Figure 2b, c illustrates the line profile analysis by STEM/energy-dispersive X-ray spectrometry (EDS), showing the distribution of Pt and Pd component in a single nanoparticle. The analysis of Pt and Pd distribution exhibits the following three marked features:

1. Pt atoms fully cover the Pd nanoparticle surface,
2. The Pt intensity is fairly constant along the center of Pd nanoparticle.
3. At the both edges of Pd nanoparticle, the Pt intensity is approximately doubled compared with that at center.

These features demonstrate the formation of a core (Pd)–shell (Pt) structure. The elemental distribution of the catalysts can also be obtained from the chemical mapping from the EELS signal as discussed in ref [11].

The element-specific electronic properties, e.g., Pt 5d-band state, of Pt_{ML} electrocatalysts and the local environment, such as bond distance and coordination number of individual component, were obtained using X-ray absorption near-edge structure (XANES), and extended X-ray absorption fine structure (EXAFS) spectroscopies, respectively.

Figure 3 shows the in situ EXAFS of Pt L3 edge from the Pt_{ML}/Pd/C electrocatalyst in 1 M $HClO_4$

at various potentials together with those from the reference foil [10]. Drastic difference between Pt_{ML}/Pd and the Pt foil was observed, especially the oscillatory behavior in k-space (Fig. 3a). The Pt–Pt and Pt–Pd bond lengths are determined to be 2.729 ± 0.005 Å and 2.724 ± 0.007 Å, respectively, which are smaller than that of bulk Pt (2.775 Å). The coordination numbers (CN) of Pt–Pt and Pt–Pd are 5.8 ± 0.8 and 2.7 ± 0.7, respectively. In the case of a complete Pt monolayer on a Pd(111), the CN of Pt–Pt is 6, while for Pt–Pd, it is 3. The slightly different CN for monolayers on nanoparticles, the CN of Pt–Pt and Pt–Pd from the fitting results, verify the Pt monolayer formation on Pd nanoparticle surfaces.

Strong evidence of delayed oxidation of a Pt monolayer on Pd nanoparticles in comparison with the oxidation of Pt nanoparticles was obtained from in situ XANES measurements as a function of potential. Figure 3a shows the Pt L3 edge spectra obtained on the Pt_{ML}/Pd/C electrocatalysts at four different potentials. Only at the highest potentials is there an increase in the intensity of white line as a consequence of the PtOH formation causing a depletion of Pt's d-band. The increase in the intensity of the white line for the Pt/C electrocatalyst commences at considerably less positive potentials (Fig. 3b, c). This indicates that the oxidation of a Pt monolayer on palladium substrate requires higher potentials than that of platinum nanoparticles on a carbon substrate, which is in accord with the voltammetry data [3].

Factors Affecting the Activity of Pt Monolayer

Core–Shell Interaction

Monolayer of Pt atoms on a foreign metal will undergo compressive or tensile strain, depending on the difference in atomic radii of Pt and the other metal [4]. Thus, Pt atoms deposited on a Ru substrate would have a large compressive strain, but they would have only a small compressive strain on Pd and a tensile strain when deposited on Au. In addition to the strain effect, the electronic couplings between Pt_{ML} and its supporting substrates also affect the electronic property of surface Pt atoms. Both the surface strain and electronic modification generate a d-band center shift of the Pt monolayer [12, 13].

O/OH Binding

The studies of Pt monolayer electrocatalysts confirmed and elucidated the role of OH or O adsorption on the ORR kinetics [3]. This is in agreement with the density functional theory (DFT) calculations showing a strong correlation between the position of d-band center and binding energies of small adsorbates on strained surfaces and metal overlayers; the latter has a direct impact on the catalytic activity of the reactions [13]. For Pt_{ML} electrocatalysts, there is a volcano-type dependence of the ORR activity on the position of d-band center [6]. Figure 4 shows the experimentally determined activity (kinetic current) and the DFT calculation of binding energy of oxygen as functions of calculated d-band center (ε_d–ε_F) on various single-crystal substrates. The highest activity was observed on Pt_{ML}/Pd(111) which has a slight upshift of d-band center and a weaker binding of O than that on Pt(111).

OH Coverage/OH–OH Repulsion Energy

The work on Pt_{ML} electrocatalysts revealed a new factor playing a role in determining activity for the ORR, which involves the OH–OH repulsion between OHs on Pt and other metals in the surface layer. In addition to the strength of O/OH binding with Pt, the coverage of OH is another important factor that affects the activity of Pt_{ML} electrocatalysts; the high OH coverage on Pt is known to inhibit ORR. The data for Pt_{ML} electrocatalysts, with an additional metal mixing with Pt to form a mixed monolayer, shows that the interaction between the Pt and the other metal in the shell induces a change of lateral repulsion energy of adsorbed OH or O and thus change the OH coverage on Pt [14].

Figure 5 depicts an experiment on a Pt–M mixed layer [14]. The lateral repulsion energy between adsorbed OH or between adsorbed OH and O changes when different M is used. A very

Platinum Monolayer Electrocatalysts, Fig. 4 Kinetic currents (j_K; *square symbols*) at 0.8 V for O_2 reduction on the platinum monolayers supported on different single-crystal surfaces in a 0.1 M $HClO_4$ solution and calculated binding energies of atomic oxygen (BE_O; *filled circles*) as functions of calculated d-band center (ε_d–ε_F); relative to the Fermi level of the respective clean platinum monolayersLabels. *1* Pt_{ML}/Ru(0001), *2* Pt_{ML}/Ir(111), *3* Pt_{ML}/Rh(111), *4* Pt_{ML}/Au(111), *5* Pt(111), *6* Pt_{ML}/Pd(111) [6]
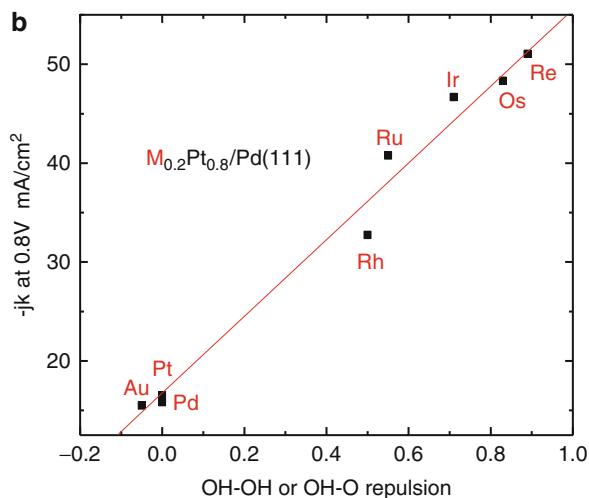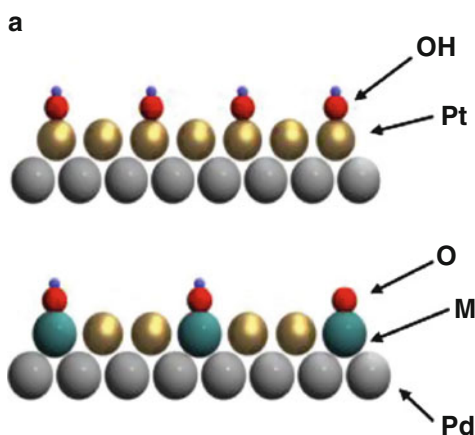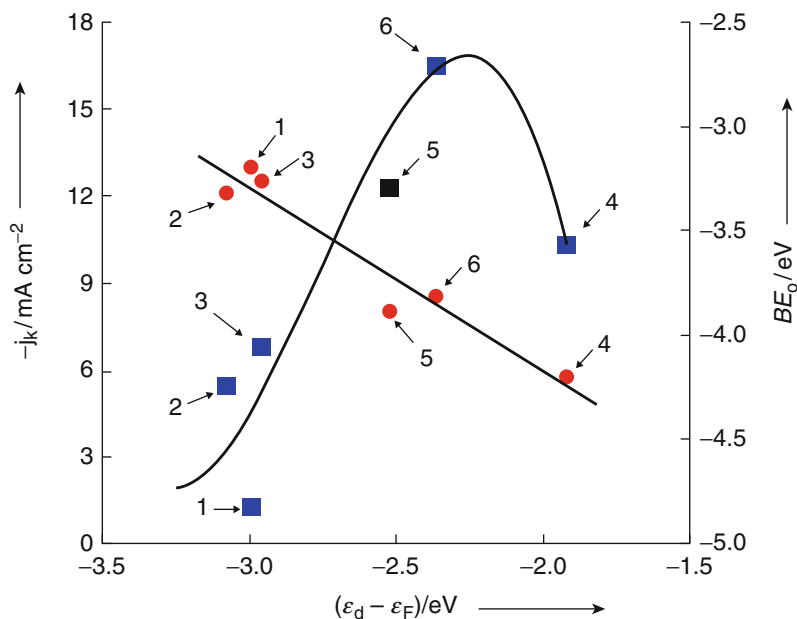
Platinum Monolayer Electrocatalysts, Fig. 5 (**a**) Model for the reduced OH adsorption on Pt atoms caused by a lateral repulsion with OH on another metal making a mixed monolayer. (**b**) Kinetic current at 0.80 V as a function of the calculated interaction energy between two OHs or OH and O on a $M_{0.2}Pt_{0.8}$ monolayer. *Positive energies* indicate more repulsive interaction compared to Pt_{ML}/Pd(111) [14]

good linear correlation is found between the measured kinetic current densities and the effective repulsion energy between two OH(a)s or an O(a) and an OH(a) calculated from first principles. The strong repulsion between these two adsorbates destabilizes the OH adsorption on Pt and accordingly reduces the OH coverage. Such good linear correlation suggests that the destabilization of OH on Pt and the resulted reduced OH coverage, due to the influence from the second metal, are responsible for the enhanced ORR kinetics.

a

b
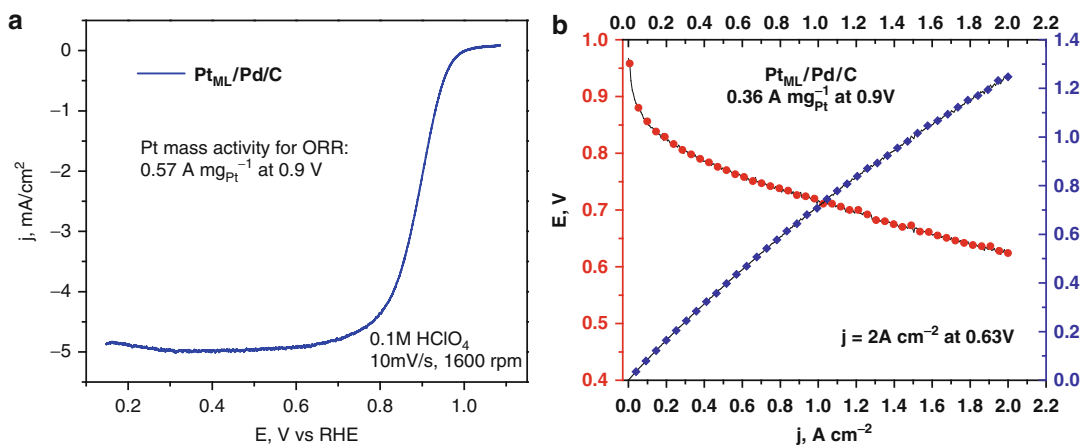
Platinum Monolayer Electrocatalysts, Fig. 6 Polarization curves for Pt_{ML}/Pd/C measured on RDE (**a**) and MEA (**b**). Other data are indicated in the graph

Rotating Disk Electrode and Fuel-Cell Measurements

Performance of Pt_{ML} electrocatalysts has been determined using single-crystal surfaces [15], thin-film rotating disk electrode (RDE), and in fuel-cell membrane electrode assembly (MEA). Higher activities observed with rotating electrodes are ascribed to a better Pt utilization of Pt. Figure 6 displays the data on RDE and MEA prepared from Pt_{ML}/Pd/C nanoparticles: 0.57 and 0.36 A/mg_{Pt} in Pt mass activities at 0.9 V were obtained from the measurements on RDE and MEA, respectively.

The Rational Design of Pt_{ML} Electrocatalysts

The unique features of Pt_{ML} electrocatalysts enable a wide selection of substrates to attain an electrocatalyst having low noble-metal content with enhanced catalytic activity and stability. A desired substrate should be able to affect the Pt monolayer by causing a weakening of the Pt–OH bond, a reduction of the OH coverage, and a delay of PtOH formation to more positive potentials than on pure Pt. The followings are some examples of the design of substrates to achieve the above goals.

Varying the Composition and Structure

Composition of the substrate has a significant impact on the catalytic activity of Pt_{ML}, through strain effect and electronic coupling. Pd has been found the most active metal as the substrate. To further reduce the content of noble metal and/or to enhance the catalytic activity and stability, non-noble metal, e.g., Co, Ni, and Fe, can be incorporated into the core as well as the components with higher dissolution potential, Au, Ir, for example. In addition to the random mix, a core–shell structure, with stable shell, is another effective way layer to preclude the dissolution of non-noble-metal core and/or to mediate the activity over a less reactive core.

For example, the addition of a small content of Au to Pd, e.g., a Pd_9Au_1 alloy core achieves remarkable enhancement of the stability while retaining the ORR activity as high as that on Pt_{ML}/Pd/C [16]. MEA fuel-cell tests showed that Pt_{ML}/Pd_9Au/C remains active even after 200,000 potential cycles. In addition to alloys, highly stable, inexpensive intermetallic compounds can also be attractive candidates as the supports for Pt_{ML}. Pt_{ML} electrocatalyst with intermetallic Pd–Pb core exhibits an ORR activity superior to Pt/C [17].

Multimetallic alloy nanoparticle cores, obtained by in situ decomposition of a Prussian blue analogue, e.g., Pt_{ML}/AuNi0.5Fe, show a remarkable Pt mass activity as 1.38 A/mg_{Pt}

and all-noble-metal activity as 0.18 A/mg$_{Pt+Au}$ [18]. The interaction of Pt$_{ML}$ with the stratified structure of the core containing 3–5 atomic layers of Au – plays an essential role in determining the activity and stability of the catalyst (insignificant loss after 15,000 triangular-potential cycles) and the high electrochemical stability of the gold shell that precludes the exposure of the relatively active inner-core materials to the electrolyte.

The high-temperature-annealed Pd$_3$Fe(111) alloy core, i.e., Pd/Pd$_3$Fe, has a top layer with the structure same as Pd(111) but different electronic properties (i.e., a −0.25 eV downshift of the d-band center compared to Pd(111)) [19]. It is considerably more active than Pd(111), and the observed enhancement of ORR activity of Pt$_{ML}$/Pd/Pd$_3$Fe originates mainly from the destabilization of OH binding, leading to a decreased Pt–OH coverage on the Pt surface.

The IrNi core–shell nanoparticle core has a two-layer Ir shell around inner Ni core fabricated via thermally induced segregation [20]. The Ir shell completely protects the Ni atoms in the core from oxidation or dissolution under elevated potentials after 5,000 potential cycles. It is evident that Ir shell completely protects Ni core from oxidation or dissolution in acid electrolyte under elevated potentials. DFT calculations using a sphere-like model for the nanoparticle demonstrated that mixing Ni with Ir (Pt$_{ML}$/IrNi/C) induces geometric, electronic, and segregation effects, thus weakening the binding energy of oxygen and so resulting in higher activity than in Pt/C and Pt$_{ML}$/Ir/C electrocatalysts.

Iridium, given its stability, could be a good candidate as the substrate for Pt$_{ML}$. However, Ir as a core causes the Pt lattice to contract too much, significantly decreasing the d-band center, and it thus entails a very weak adsorption of O$_2$ on Pt, resulting in slow ORR kinetics. An addition of a Pd monolayer (interlayer), placed between the Pt monolayer and the Ir core, i.e., Pt$_{ML}$/Pd$_{ML}$/Ir/C, lowers the excessive effect of Ir as corroborated by DFT calculation and consequently ameliorates the ORR kinetics [21]. Xing et al. used the PdAu alloy as the interlayer to

mediate the Pt$_{ML}$ catalytic properties [22]. Besides an enhanced activity, this catalyst showed an excellent stability that may be due to the stabilizing effect of Au [23].

Induced Lattice Contraction by Hollow Core
The study on Pt hollow nanoparticles shows that the hollow structure induces a lattice contraction in the Pt shell and exhibits higher activity and better stability than solid Pt nanoparticles for ORR [24]. The lattice contraction not only enhances the ORR kinetics but also prevents the instability caused by dissolution of core materials. Placing a Pt$_{ML}$ on Pd and Pd–Au hollow cores, obtained using Ni nanoparticles as sacrificial templates, improved its properties for the ORR. The hollow architecture results from the combination of galvanic replacement and the Kirkendall effect [25]. The larger ORR-active surface area and the significant savings of noble metal brought about by the hollow structure accordingly enhanced up to 0.57 A/mg of the total-metal mass activity of the electrocatalyst for the ORR.

The Effects of Facets and Shapes
Atoms at low-coordination sites, i.e., edges, kinks, and defects, have been shown to have a stronger binding with OH than those at 2D terrace sites and thus inhibit the oxygen reduction [11]. Those non-registered atoms are also prone to stronger binding with adsorbates and thus prone to dissolution [26]. On the other hand, it has been shown that nanoparticles with a higher ratio of (111) facets have higher activity for the oxygen-reduction reaction [11]. Therefore, a desired nanoparticle core for Pt$_{ML}$ should possess a high ratio of atoms at (111) facets and less atoms at low-coordination sites. The following paragraphs show three examples to achieve this goal.

Reduction of Low-Coordination Sites
The removal of low-coordination sites via Br treatment on Pd/C core engenders nanoparticles with a smooth surface and increased content of (111) facets. As a result, 1.5 fold enhancement of the ORR activity is achieved on Pt$_{ML}$ catalyst with such core [27].

Platinum Monolayer Electrocatalysts, Table 1 Comparison of specific Pt mass and PGM mass activities of PtML electrocatalysts on different core nanoparticles for the ORR measured by the kinetic currents at 0.9 V. The values for conventional Pt/C electrocatalyst are given for comparison

Cores	Specific activity ($mA\ cm^{-2}$)	Pt mass activity ($A\ mg^{-1}$)	Noble-metal mass activity ($A\ mg^{-1}$)
Pt/C	0.3	0.2	0.2
Pd	0.7	1.64	0.25
Pd_{Hollow}	0.9	1.5	0.45
$Pd_{20}Au_{Hollow}$	0.85	1.62	0.61
$Pd/Ir_{sublayer}$	0.94	2.17	0.13
Pd_{NWe}	0.85	1.85	0.22
PdAu	1.5	3.5	
Pd_{NW}	0.77	1.83	0.55
$Pd_{tetrahedral}$	0.64	0.92	0.14

Pd_{NWe} Electrodeposited NW, Pd_{NW} wet chemistry synthesis. Other data are given in the graph

Pd Tetrahedron Core

The production of active facets can also be achieved by using nanocrystals with well-defined facets as substrates. The concave Pd tetrahedron (TH Pd) is a good example, which has a small number of low-coordination sites and defects and high content of the shape-determined high-coordinated facets [28, 29]. The ORR kinetics of Pt_{ML}/TH Pd/C is improved significantly.

Pd Nanowire Core

As it is generally observed, Pd nanowires (NW) have smooth surfaces with fewer low-coordination sites and edges and less surface imperfections than nanoparticles. Such surfaces are suitable for the ORR and make a good support for a Pt-ML since OH adsorption on them is shifted positively with reduced coverage. The power density of this catalyst is close to 1 W/cm^2 with only 40 $\mu gPt/cm^2$ (0.1 mg/cm^2 PGM) content, which compares favorably with reported data for other catalysts [30].

Table 1 displays a comparison of activities of several Pt_{ML} electrocatalysts having different cores from the above rational designs. A considerable difference between some core–shell couples indicates a remarkable possibility for tuning the activity of these catalysts and the flexibility of this approach.

Pt Submonolayer Anode Electrocatalysts with High CO Tolerance

The presence of small concentration of CO is enough to strongly impair the performance of Pt-based catalysts. To increase CO tolerance, Ru is introduced to Pt to form a PtRu alloy for the anode. One of the roles played by Ru is to provide RuOH species for the oxidation of CO to CO_2, leaving Pt sites free for adsorption and oxidation of H_2 or MeOH (bifunctional mechanism [31]). Electroless (spontaneous) deposition of Pt submonolayer on Ru(0001) surface [32] and Ru nanoparticles [33] was used to synthesize such electrocatalyst with excellent CO tolerance for the oxidation of reformate H_2 [34]. The DFT calculation from Koper et al. found that CO binds most weakly on Pt_{ML}/Ru among various PtRu combinations in their study [35]. The example in Fig. 7a compares the CO tolerance in an accelerated test of the Pt submonolayer catalyst $PtRu_{20}$ with that of one commercial PtRu alloy catalyst in the oxidation of H_2 containing 1,000 ppm CO: the commercial PtRu lost almost all the activity after 100 min, while $PtRu_{20}$ remains active even after 350 min. The long-term fuel-cell performance stability test of the $PtRu_{20}$ electrocatalyst (Fig. 7b) shows no detectable loss in performance over 870 h with the Pt loading approximately 1/10th of the stand loading.

With the Pt monolayer or submonolayer concept, the DFT calculation from Nilekar et al. found a promising new category of electrocatalysts for anode with high CO–CO repulsion energy which leaves to low CO binding energy: mixed-metal Pt monolayer electrocatalysts [36]. Their results suggest that in addition to Ru, Ir, Os, and Re could also be good candidates for mixed-metal Pt monolayer.

Activity and Stability of Pt_{ML} Electrocatalysts in Fuel-Cell Tests

Figure 8a displays the TEM image of the cross-section of MEA after 100,000 potential cycles from 0.6 to 1.0 V, and the corresponding distribution of Pt, Au, and Pd in the catalytic
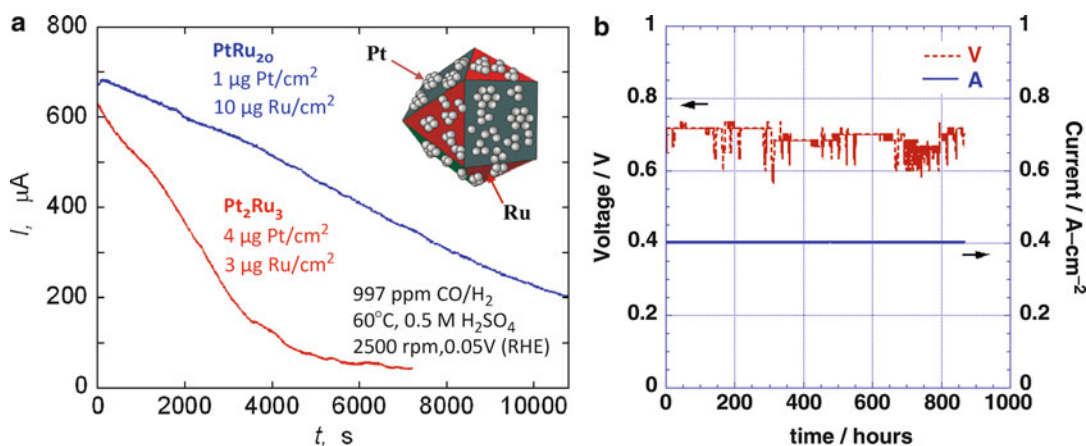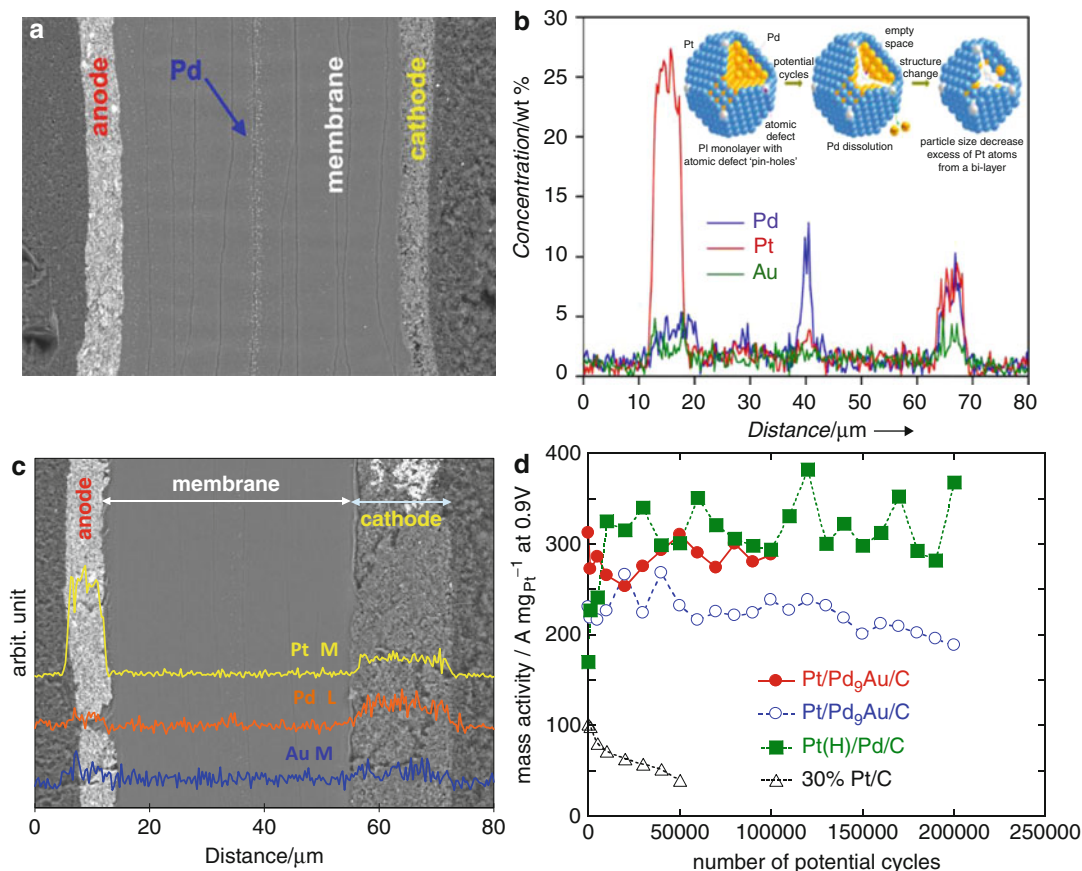
Platinum Monolayer Electrocatalysts, Fig. 7 (**a**) Accelerated CO tolerance tests of the $PtRu_{20}$ and of a commercial electrocatalyst for the oxidation of H_2 with 997 ppm of CO at 60 °C at 0.05 V on a rotating disk electrode (2,500 rpm) with the loadings indicated in the graph. The $PtRu_{20}$ (1 % Pt, 10 % Ru on C) electrocatalyst exhibits considerably higher CO tolerance. (**b**) Long-term performance stability test of the $PtRu_{20}$ electrocatalyst in an operating fuel cell. The fuel cell's voltage at constant current of 0.4 A/cm^2 is given as a function of time for the electrode of 50 cm^2 with an anode containing 180 µg/cm^2 of Ru, and 18 µg/cm^2 of Pt (or 0.063 g/kW of Pt that is approximately 1/10 of the standard Pt loading) and a standard air cathode with a Pt/C electrocatalyst. The fuel was clean H_2 or H_2 with 50 ppm of CO and 3 % air; temperature 80 °C. A change of fuel from the CO + H^2 mixture to H^2 caused an intermittent spike in the current trace

nanoparticles after the stability test is displayed in Fig. 8b [16]. A Pd band forms in the middle due to Pd dissolution and Pd^{2+} reduction by H_2 diffusing from the anode; Pt and Au remain in the cathode. Pd is a slightly more reactive metal than Pt and so dissolves at slightly lower potentials (0.92 (Pd) vs. 1.19 (Pt) V). The small dissolution limits the excursions of potential in an operating fuel cell, or at least minimizes it. Such partial dissolution of Pd entails a small contraction of the Pt_{ML} shell, giving rise to a more stable structure with increased dissolution resistance and specific activity. This is the self-healing effect observed with this core–shell system as depicted in the model insert in Fig. 8b: the slow dissolution of Pd causes the decrease in the particle size, leading to some contraction of the Pt layer. The excess of Pt atoms from a monolayer shell can form a partial bilayered structure, or hollow particles may be formed due to the Kirkendall effect.

The distribution of Au in PdAu alloy has a great impact on the stabilization of Pd under potential cycling in the acid media. Figure 8c displays the cross-section of MEA and the posttest distribution of Pt, Au, and Pd in the Pt_{ML}/Pd_9Au catalyst based on highly uniform PdAu alloy. Such a uniform alloy causes a positive shift of Pd oxidation, in accord with its stabilization potential and reduced PdOH formation, as evidenced from voltammetry and in situ EXAFS studies, in particular confirming the changes in coordination number of Pd–O. Potential cycling did not entail any decrease in Pd, Pt, or Au. The Pt mass activity of the $Pt/Pd_9Au/C$ electrocatalyst in a test involving 200,000 potential cycles decreased negligibly (Fig. 8d, red circles). The DOE's target for 30,000 potential cycles under the same protocol is a loss of 40 %. For comparison, the mass activity of a commercial Pt/C catalyst shows a terminal loss below 50,000 cycles (Fig. 8d, open triangles). The preparation of a highly compact Pt-ML, using the combined processes of H absorption and H adsorption on Pd to reduce Pt^{2+}, leads to the production of a new generation of $Pt_{ML}/Pd/C$ catalysts with outstanding, unprecedented stability: there was no loss of activity over 200,000 potential

Platinum Monolayer Electrocatalysts, Fig. 8 (**a**) Cross-section of the MEA of $Pt_{ML}/Pd_9Au/C$ after 100,000 potential cycles from 0.6 to 1.0 V. (**b**) Corresponding distribution of Pt, Au, and Pd, vs. distance after the test. The insert shows the model for the slow dissolution of Pd and the decrease in the particle's size, leading to some contraction of the Pt layer. (**c**) The cross-section of the MEA and overlaid posttest distribution of Pt, Au, and Pd in the $Pt_{ML}/Pd_9Au/C$ catalyst based on a highly uniform PdAu alloy after 200,000 potential cycles. (**d**) Comparison of the Pt mass activity for Pt/Pd_9Au/C (*open circles*), Pt_{ML}/Pd_9Au catalyst based on highly uniform PdAu alloy (*red circles*) $Pt_{ML}/Pd/C$ electrocatalyst with highly compact Pt-ML (*green squares*) and of a commercial Pt/C catalyst (*open triangles*) [16]

cycles (Fig. 8d green squares). Furthermore, under more severe conditions with a potential range of 0.6 –1.4 V, there were no significant losses of Pt and Au, although the dissolution of Pd was apparent.

Summary and Future Directions

Although Pt monolayer electrocatalysts are at early stage of development, significant improvements in their activity and stability have been achieved, and the accelerated stability tests in fuel cells established them as a viable practical concept. Moreover the well-established scaled-up synthesis has made Pt_{ML} electrocatalysts ready for applications including the automotive one. In contrast to the content of platinum in the cathode catalysts currently being tested in fuel-cell vehicles, viz., 400 $\mu gPt/cm^2$, Pt_{ML} electrocatalysts require only 40–80 $\mu gPt/cm^2$ and 60–100 $\mu gPd/cm^2$. Thus, the requirement for a 100 KW fuel cell in a medium-sized electric car, with the catalyst's performance of 1 W/cm^2, is 4–8 g of Pt and about 10 g of Pd. Currently, catalytic converters use 5 g of Pt per vehicle.

Therefore, there would be no need for considerable increase of the present rate of supply of Pt.

Owing to the unique features of Pt monolayer electrocatalysts, there is a broad range of possibilities for further improving the activity and stability and reducing the costs. The design of future Pt_{ML} electrocatalysts includes the change of composition, shape, and size of cores to optimize the core–shell interaction. In detail, the research can be performed from the following aspects: (1) Further reduction of the noble-metal (e.g., Pd) content by alloying it with non-noble metals, using its hollow nanoparticle counterparts, or by designing new inexpensive supports, such as IrNi described above. (2) Modification of the properties of the Pt-ML by selecting the appropriate top atomic layer of the cores to enable the employment of a variety of core materials. (3) Design and synthesis of core materials with defined facets, preferably (111) facets, like nanowires and nanorods which have their high resistance to surface oxidation and possess large fraction of (111) facets. Electrodeposition of nanowires is particularly promising since by its nature, this technique is capable of positioning the catalyst optimally in MEA, thus facilitating its highest utilization. (4) Incorporation of the synthesis of Pt_{ML} electrocatalysts with the fuel-cell setup to further reduce the production cost and better accommodation of the catalysts on the electrode. These studies would substantially reduce the technical barriers to produce durable, economical fuel cells. Given the limited resources of Pt, the concepts Pt_{ML} catalysts will have a broad impact on future catalysis research and technology.

Cross-References

▶ Electrocatalysts for the Oxygen Reaction, Core-Shell Electrocatalysts

▶ Hydrogen Oxidation and Evolution on Platinum in Acids

▶ Oxygen Reduction Reaction in Acid Solution

▶ Oxygen Reduction Reaction in Alkaline Solution

▶ Platinum-Based Anode Catalysts for Polymer Electrolyte Fuel Cells

▶ Platinum-Based Cathode Catalysts for Polymer Electrolyte Fuel Cells

▶ Polymer Electrolyte Fuel Cells (PEFCs), Introduction

References

1. Adžić RR (1998) Recent advances in the kinetics of oxygen reduction. In: Lipkowski J, Ross PN (eds) Electrocatal. Wiley-VCH, Weinheim, p 197
2. Gottesfeld S, Zawodzinski TA (2008) Polymer electrolyte fuel cells. In: Alkire RC, Gerischer H, Kolb DM, Tobias CW (eds) Advances in electrochemical science and engineering. Wiley-VCH, Weinham, pp 195–301
3. Zhang J, Mo Y, Vukmirovic MB, Klie R, Sasaki K, Adzic RR (2004) Platinum monolayer electrocatalysts for O_2 reduction: Pt Monolayer on Pd(111) and on carbon supported Pd nanoparticles. J Phys Chem B 108:10955–10964
4. Adzic R, Zhang J, Sasaki K, Vukmirovic M, Shao M, Wang J, Nilekar A, Mavrikakis M, Valerio J, Uribe F (2007) Platinum monolayer fuel cell electrocatalysts. Top Catal 46:249–262
5. Markovic NM (2003) Fuel cell electrocatalysis. In: Vielstich W, Lamm A, Gasteiger HA (eds) Handbook of fuel cells: fundamentals, technology applications. Wiley, Hoboken, pp 368–393
6. Zhang J, Vukmirovic MB, Xu Y, Mavrikakis M, Adzic RR (2005) Controlling the catalytic activity of platinum-monolayer electrocatalysts for oxygen reduction with different substrates. Angew Chem Int Ed 44:2132–2135
7. Brankovic SR, Wang JX, Adzic RR (2001) Metal monolayer deposition by replacement of metal adlayers on electrode surfaces. Surf Sci 474:L173–L179
8. Kolb DM (1978) In: Gerischer H, Tobias CW (eds) Advances in electrochemistry and electrochemical engineering. Wiley, New York, p 125
9. Vukmirović MB, Bliznakov ST, Sasaki K, Wang JX, Adzic RR (2011) Electrodeposition of metals in catalyst synthesis: the case of platinum monolayer electrocatalysts. Electrochem Soc Int 20:33–40
10. Sasaki K, Wang JX, Naohara H, Marinkovic N, More K, Inada H, Adzic RR (2010) Recent advances in platinum monolayer electrocatalysts for oxygen reduction reaction: scale-up synthesis, structure and activity of Pt shells on Pd cores. Electrochim Acta 55:2645–2652
11. Wang JX, Inada H, Wu L, Zhu Y, Choi Y, Liu P, Zhou W-P, Adzic RR (2009) Oxygen reduction on well-defined core − shell nanocatalysts: particle size, facet, and Pt shell thickness effects. J Am Chem Soc 131:17298–17302
12. Hammer B, Nørskov JK (2000) Theoretical surface science and catalysis – calculations and concepts. In: Bruce CG, Helmut K (eds) Advances in catalysis. Academic, New York, pp 71–129

13. Greeley J, Nørskov JK, Mavrikakis M (2002) Electronic structure and catalysis on metal surfaces. Annu Rev Phys Chem 53:319–348
14. Zhang J, Vukmirovic MB, Sasaki K, Nilekar AU, Mavrikakis M, Adzic RR (2005) Mixed-metal Pt monolayer electrocatalysts for enhanced oxygen reduction kinetics. J Am Chem Soc 127:12480–12481
15. Zhang J, Vukmirović MB, Sasaki K, Uribe F, Adžić RR (2005) Platinum monolayer electrocatalysts for oxygen reduction: effect of substrates, and long-term stability. J Serb Chem Soc 70:513–525
16. Sasaki K, Naohara H, Cai Y, Choi YM, Liu P, Vukmirovic MB, Wang JX, Adzic RR (2010) Core-protected platinum monolayer shell high-stability electrocatalysts for fuel-cell cathodes. Angew Chem Int Ed 49:8602–8607
17. Ghosh T, Vukmirovic MB, DiSalvo FJ, Adzic RR (2009) Intermetallics as Novel supports for Pt monolayer O2 reduction electrocatalysts: potential for significantly improving properties. J Am Chem Soc 132:906–907
18. Gong K, Su D, Adzic RR (2010) Platinum-monolayer shell on AuNi0.5Fe nanoparticle core electrocatalyst with high activity and stability for the oxygen reduction reaction. J Am Chem Soc 132:14364–14366
19. Zhou W-P, Yang X, Vukmirovic MB, Koel BE, Jiao J, Peng G, Mavrikakis M, Adzic RR (2009) Improving electrocatalysts for O_2 reduction by fine-tuning the Pt − support interaction: Pt monolayer on the surfaces of a Pd3Fe(111) single-crystal alloy. J Am Chem Soc 131:12755–12762
20. Sasaki K, Kuttiyiel KA, Barrio L, Su D, Frenkel AI, Marinkovic N, Mahajan D, Adzic RR (2011) Carbon-supported IrNi core–shell nanoparticles: synthesis, characterization, and catalytic activity. J Phys Chem C 115:9894–9902
21. Knupp S, Vukmirovic M, Haldar P, Herron J, Mavrikakis M, Adzic R (2010) Platinum monolayer electrocatalysts for oxygen reduction: Pt monolayer on carbon-supported PdIr nanoparticles. Electrocatal 1:213–223
22. Xing Y, Cai Y, Vukmirovic MB, Zhou W-P, Karan H, Wang JX, Adzic RR (2010) Enhancing oxygen reduction reaction activity via Pd − Au alloy sublayer mediation of Pt monolayer electrocatalysts. J Phys Chem Lett 1:3238–3242
23. Zhang J, Sasaki K, Sutter E, Adzic RR (2007) Stabilization of platinum oxygen-reduction electrocatalysts using gold clusters. Science 315:220–222
24. Wang JX, Ma C, Choi Y, Su D, Zhu Y, Liu P, Si R, Vukmirovic MB, Zhang Y, Adzic RR (2011) Kirkendall effect and lattice contraction in nanocatalysts: a new strategy to enhance sustainable activity. J Am Chem Soc 133:13551–13557
25. Yin Y, Rioux RM, Erdonmez CK, Hughes S, Somorjai GA, Alivisatos AP (2004) Formation of hollow nanocrystals through the nanoscale Kirkendall effect. Science 304:711–714
26. Budevski E, Staikov G, Lorenz WJ (1996) Electrochemical phase formation and growth – an introduction to the initial stages of metal deposition. VCH, Weinheim
27. Cai Y, Ma C, Zhu Y, Wang JX, Adzic RR (2011) Low-coordination sites in oxygen-reduction electrocatalysis: their roles and methods for removal. Langmuir 27:8540–8547
28. Gong K, Vukmirovic MB, Ma C, Zhu Y, Adzic RR (2011) Synthesis and catalytic activity of Pt monolayer on Pd tetrahedral nanocrystals with CO-adsorption-induced removal of surfactants. J Electroanal Chem 662:213–218
29. Huang X, Tang S, Zhang H, Zhou Z, Zheng N (2009) Controlled formation of concave tetrahedral/trigonal bipyramidal palladium nanocrystals. J Am Chem Soc 131:13916–13917
30. Wagner FT, Lakshmanan B, Mathias MF (2010) Electrochemistry and the future of the automobile. J Phys Chem Lett 1:2204–2219
31. Wang JX, Marinković NS, Zajonz H, Ocko BM, Adžić RR (2001) In situ x-ray reflectivity and voltammetry study of Ru(0001) surface oxidation in electrolyte solutions. J Phys Chem B 105:2809–2814
32. Brankovic SR, McBreen J, Adžić RR (2001) Spontaneous deposition of Pt on the Ru(0001) surface. J Electroanal Chem 503:99–104
33. Brankovic SR, Wang JX, Adzic RR (2001) Pt submonolayers on Ru nanoparticles: a novel low Pt loading, high CO tolerance fuel cell electrocatalyst. Electrochem Solid-State Lett 4:A217–A220
34. Sasaki K, Wang JX, Balasubramanian M, McBreen J, Uribe F, Adzic RR (2004) Ultra-low platinum content fuel cell anode electrocatalyst with a long-term performance stability. Electrochim Acta 49:3873–3877
35. Koper MTM, Shubina TE, van Santen RA (2002) Periodic density functional study of CO and OH adsorption on Pt − Ru alloy surfaces: implications for CO tolerant fuel cell catalysts. J Phys Chem B 106:686–692
36. Nilekar AU, Sasaki K, Farberow CA, Adzic RR, Mavrikakis M (2011) Mixed-metal Pt monolayer electrocatalysts with improved CO tolerance. J Am Chem Soc 133:18574–18576

Platinum-Based Anode Catalysts for Polymer Electrolyte Fuel Cells

Paramaconi Rodriguez[1] and Thomas J. Schmidt[2]
[1]School of Chemistry, The University of Birmingham, Birmingham, UK
[2]Electrochemistry Laboratory, Paul Scherrer Institut, Villigen, Switzerland

Introduction

Polymer electrolyte fuel cells (PEFCs) are considered to be a promising electric power source

Platinum-Based Anode Catalysts for Polymer Electrolyte Fuel Cells, Fig. 1 Contribution of anode-, cathode-, and electrolyte-related performance losses in a DMFC (Modified from [13, 27])
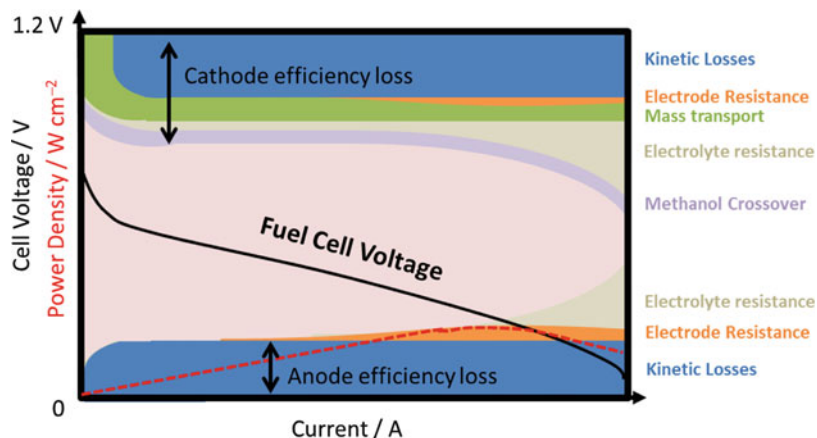
for stationary and automotive applications due to their potentially high energy density combined with exhaust-free operation. However, before the effective commercialization, several technical problems related specifically to durability issues must be resolved [1, 2]. The oxygen reduction reaction (ORR) is one of the main causes of the polarization loss in the cathodes and accounts for 80 % of the total loss [1–3]. The performance of a PEFC, hence, is limited by the ORR on the cathode side. Other significant challenges can be found on the anode side especially when operated with impure hydrogen derived from reformation reactions, which typically contain low levels of carbon monoxide, i.e., between 10 and 100 ppm of CO. Carbon monoxide is known to be a catalyst poison which strongly adsorbs on the commonly used Pt catalysts and can result in significant anodic polarization losses [4–8].

When operated with hydrogen feed gas, anode durability typically is not an issue provided that no starvation of hydrogen occurs, e.g., due to insufficient distribution of hydrogen inside the stack (so-called H_2 gross starvation). Under these undesired conditions, the anode potential is increased from below typically 0.1 V to values exceeding more than 1.5 V, resulting in instantaneous corrosion of the anode catalyst and support [9, 10].

Besides hydrogen as a fuel, also methanol or other organic liquid energy carriers can be oxidized in so-called direct oxidation fuel cells, e.g., direct methanol fuel cells (DMFC) [11–15] or direct alcohol fuel cells (DAFC) [16–18]. Methanol, however, is volatile and a toxic compound. As a replacement, other organic fuels, such as ethanol, ethylene glycol, propanol, and dimethyl oxalate, are being considered as fuels for DAFC [16, 17]. The most extensively studied alternative fuel is ethanol, considering that it is safer and has a higher energy density compared to methanol (8.01 kWh kg^{-1} versus 6.09 kWh kg^{-1}) [19–26].

Considering only the thermodynamics of the DMFC (used here as a representative of direct alcohol fuel cells), methanol should be oxidized spontaneously when the potential of the anode is above 0.05 V/SHE. Similarly, oxygen should be reduced spontaneously when the cathode potential is below 1.23 V/SHE, identical to a H_2–O_2 fuel cell. However, kinetic losses due to side reactions cause a deviation of ideal thermodynamic values and decrease the efficiency of the DMFC. This is presented in Fig. 1b, which includes various limiting effects as kinetics, ohmic resistance, alcohol crossover, and mass transport. The anode and cathode overpotentials for alcohol oxidation and oxygen reduction reduce the cell potential and together are responsible for the decay in efficiency of approximately 50 % in DMFCs [13, 27].

This essay briefly will summarize the different catalyst approaches for the underlying anode reactions for the oxidation of pure H_2, H_2-rich reformates including CO, and alcohols such as methanol and ethanol.

Anode Electrocatalysts for Hydrogen Oxidation Reaction (HOR)

The most effective catalyst for HOR at the anode in PEFCs are Pt nanoparticles supported on carbon-type supports. Since the HOR on Pt in acidic environment is very fast with values of the exchange current density of several hundreds of mA/cm$^2_{Pt}$ (80 °C, 100 kPa H$_2$ [28]) as compared to below 10^{-5} mA/cm$^2_{Pt}$ for the ORR at 80 °C and 100 kPa O$_2$ [29]. it is possible to reduce the anodic Pt loading to values of below 0.1 mg$_{Pt}$/cm^2 without increasing the polarization overpotential [30].

However, as was mentioned above that even small traces of CO can cause significant decrease in fuel cell performance. It was reported that only 5 ppm CO in the hydrogen stream leads to a drop of the maximum power density to less than half the value obtained for pure hydrogen [31]. The preparation of an efficient electrocatalyst with high activity for the HOR with good CO tolerance is related to the understanding of reaction mechanisms on its surface.

Several studies on platinum electrodes showed that the CO poisoning mechanism occurs because of strong adsorption of CO on the catalyst surface, which blocks the HOR [6, 32, 33]. Generally, in order to improve the CO tolerance of fuel cell anodes, several strategies can be employed [34]: (1) alloying of platinum with a second metal which either helps to reduce the adsorption energy of CO and therefore may help to reduce the effective CO coverage through a so-called ligand or electronic effect or which offers adsorption sites for oxygenated species in a bifunctional mechanism [7, 35–40]; (2) the use of catalysts which do not adsorb CO at all; or (3) the increase of the temperature in order to reduce the effective CO coverage (cf. Fig. 2, entry "▶ High-Temperature Polymer Electrolyte Fuel Cells", this volume).

Starting with the first approach, bimetallic PtM (M = Fe, Ru, Mo, Sn, or W) catalysts have been proposed [4, 7, 37–39, 41–51]. This first class has a (pseudo-)bifunctional mechanism of action, as in the case of Pt–Ru, where CO is adsorbed on both the Pt and Ru sites. The second metal does not
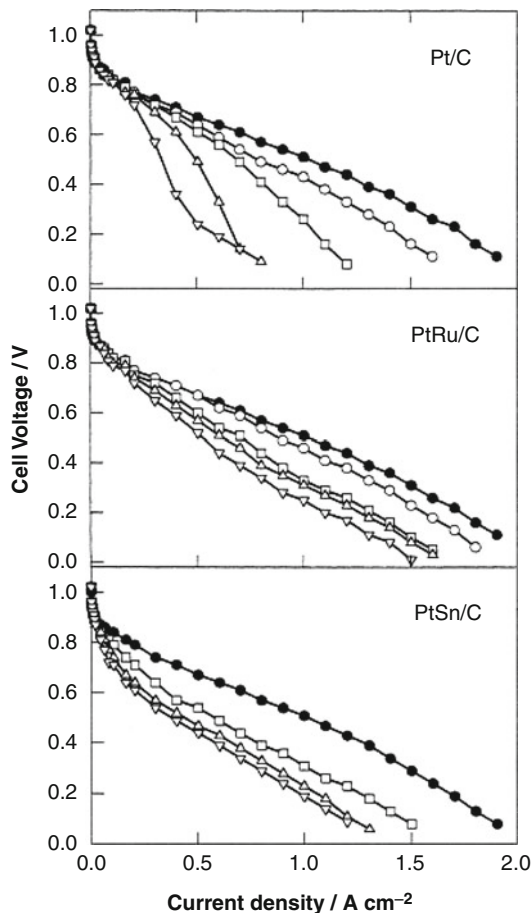
Platinum-Based Anode Catalysts for Polymer Electrolyte Fuel Cells, Fig. 2 Single cell performance plots for Pt/C, PtRu/C, and PtSn/C at 85 °C at several CO concentrations: (•) 0 ppm; () 5 ppm; (□) 20 ppm; (Δ) 50 ppm; and (∇) 100 ppm (Reproduced by permission from [8])

serve exclusively to adsorb OH$_{ad}$. The surface reaction for Pt–Ru can be formulated as

$$Pt(Ru) - CO_{ad} + Ru - OH_{ad} \rightarrow CO_2 + H^+ + e^-. \tag{1}$$
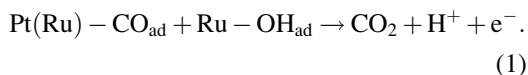
In the bifunctional mechanism, the presence of a second metal (normally oxophilic) favors the formation of the OH species promoting the early electrooxidation of the CO. As every oxidized CO opens up two sites for the hydrogen oxidation, Eq. 2,

$$H_2 \rightarrow 2H + 2e^-, \tag{2}$$
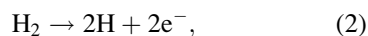
the strategy is clear that shifting the CO oxidation reaction to potentials as low as possible will significantly increase the rates for HOR.

The electronic effect claims that the second metal in the alloy modifies the H_2 and CO adsorption energies, reducing the CO coverage and by then creating Pt sites available for the H_2 oxidation. Quite significant efforts have been carried out to developing a CO-tolerant anode electrocatalyst at levels of 50 ppm of CO (with a noble metal loading lower than 0.1 mgcm^{-2} or less). Among the several binary alloy systems, PtRu and PtSn have shown promising performance for the HOR in the presence of CO, but the origin of this effect (bifunctional or electronic or both) remains under discussion [4, 37–39, 42–44, 46, 47]. Previous results on carbon-supported nanocrystalline PtRu and PtSn alloys, under in situ electrochemical conditions and using X-ray absorption spectroscopy, have shown changes in the electronic structure (Pt $5d$ band vacancy) but also a short-range atomic order (Pt–Pt bond distance and coordination number, the so-called lattice strain). Alloying Pt with Sn causes lowering of the Pt $5d$ band center and increase the Pt–Pt interatomic distance. On the other hand, the effect when alloying Ru with Pt is exactly opposite. Both effects induce a change in the CO poisoning characteristics in their systems, resulting in different activation energies, surface coverage, reaction orders, etc.

Figure 2 shows the single-cell polarization characteristics of CO-tolerant PtRu/C and PtSn/C relative to Pt/C for the HOR in PEFCs at 85 °C and different CO concentration.

Based on a simple kinetic model, Springer et al. [52] suggested that the polarization of the hydrogen electrode at low current density is limited essentially by the maximum rate of hydrogen dissociative chemisorption on a small fraction of the catalyst surface free of CO. It was also found that a rate of CO oxidation on Pt as low as 10 nAcm^{-2} could have a significant effect in lowering the CO steady-state coverage and thus in increasing the magnitude of the hydrogen electrooxidation current.

Other catalysts have shown similar properties, as it is the case of PtFe and PtMo. Watanabe and co-workers demonstrate that PtFe shows an excellent CO tolerance for the H_2 oxidation, similar to the PtRu catalyst [35, 50]. According to the authors, this effect is associated to a positive shift in the binding energy of the Pt $4f$ or $4d$ orbitals. The positive shift of the binding energies indicates an increase of the valence band ($5d$ orbital), resulting in a lower electron back-donation to the CO molecules and therefore a decrease in the CO coverage. Several investigations on PtMo report a good CO tolerance that it was ascribed to a bifunctional mechanism where oxygenated species on the molybdenum atoms react efficiently with the CO adsorbed on the Pt [53, 54].

The Pt/WO$_x$ system has also been subject of several studies although catalytic activity is not as strong as that for ruthenium. In this case, the catalytic activity was associated to the rapid change of the oxidation state of W, involving the redox couples $W^{(VI)}/W^{(IV)}$ or $W^{(VI)}/W^{(V)}$, which again promote the formation of hydrous oxide and therefore the oxidation of the CO [55–57].

The catalytic activity of a PtRu alloy catalyst, which is the most active system for oxidation of CO-contaminated H_2 fuel, can be further improved by using ternary alloy catalyst. In this regard, Chen et al. [58] reported a superior performance of a PtRuWO$_3$/C against CO poisoning in a stream of H_2/100 ppm CO at 80 °C at 220 mA cm^{-2} after a test period of 6 h. Other studies performed by Götz et al. demonstrated that under operation conditions of H_2/150 ppm CO (75 °C), the system PtRuW shows the highest activity at low current densities, while PtRuSn is the best catalyst at current densities higher than 300 mAcm^{-2} [51]. In addition, the activity of both catalysts at higher current densities exceeded the activity of the PtRu (E-TEK) commercial catalyst. Papageorgopoulos et al. [51] have reported that the addition of 10 at %Mo showed a significant improve in performance toward the H_2 oxidation in the presence of CO compared to PtRu/C. On the other hand, addition of Nb in a PtRu/C catalysts had a negative effect in PtRu by promoting CO poisoning [51].

As a result of a DFT calculations of a variety of model ternary PtRuM alloy catalysts yielded detailed adsorption energies and activation

barriers and a combinatorial experimental electrocatalysis performed over 64-element electrode array with composition PtRuM (M = Co, Ni, and W), it is reported that PtRuCo ternary catalysts clearly outperformed the standard PtRu catalyst, followed by PtRuNi ternary catalysts [59].

In addition to the above mentioned catalyst, Schmidt et al. [60] reported the superior activity and CO tolerance of PdAu/C (Vulcan XC-72) (platinum-free electrocatalysts) at 60 °C compared to PtRu/C. This enhanced CO tolerance was explained by the significantly reduced CO adsorption energy on the PdAu surface, resulting in very low effective CO coverage and therefore in high HOR rates [60, 61].

Hydrogen Starvation

One of the main challenges for the commercialization of PEFCs is the long-term stability. As was explained above, under fuel cell operation, hydrogen is oxidized at the anode while oxygen is reduced at cathode catalyst layer.

$$2H^+ + 2e^- \rightarrow H_2 \qquad\qquad E° = 0 \text{ V} \qquad (3)$$

$$O_2 + 4H^+ + 4e^- \rightarrow 2H_2O \quad E° = 1.23 \text{ V} \quad (4)$$
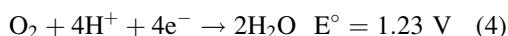
In total, electric energy, water, and heat are produced. However, additional and undesired reactions can produce catalyst layer degradation and consequently can limit the lifetime of the fuel cell. Carbon corrosion and dissolution of the active metal catalyst are the main undesired side reactions in PEFCs [62–66].

Localized hydrogen starvation at a PEFCs anode can lead to the formation of local cells as presented on the Fig. 3a and takes place mainly during the start–stop cycling when a H_2/O_2 front is moving through the anode compartment of the cell [65]. In short, due to the presence of both H_2 and O_2 in the anode of a fuel cell, the cell becomes internally shorted with the result of a cathodic potential excursion to approx. 1.5 V [67].
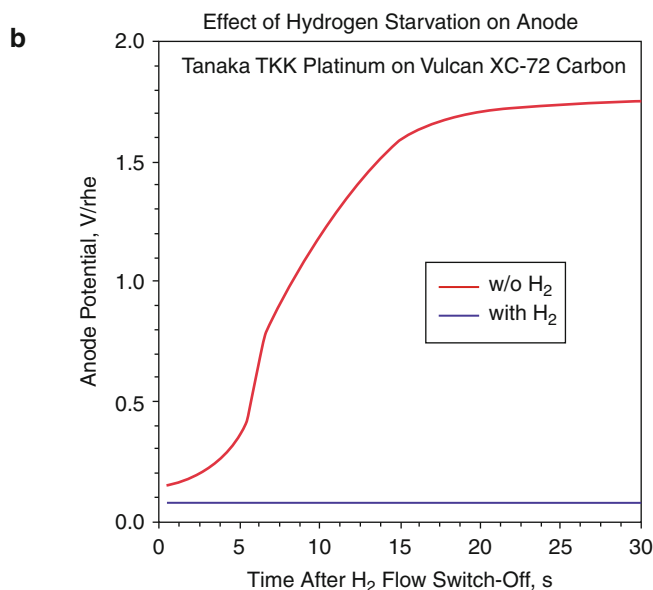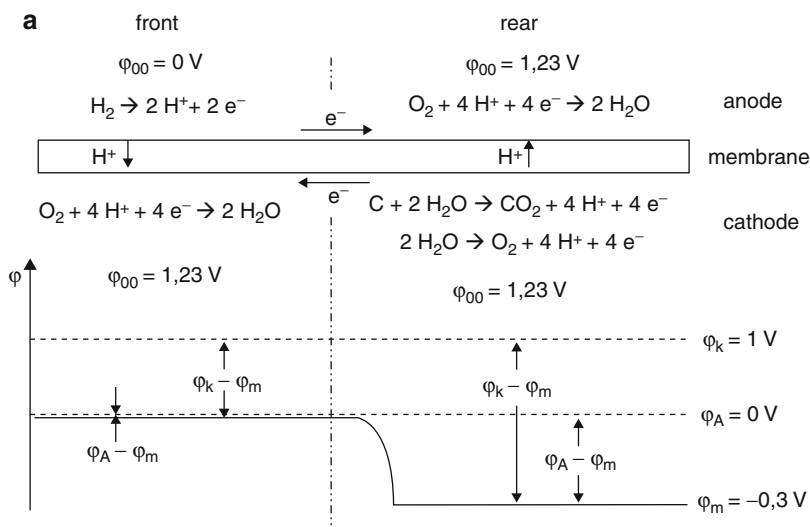
The consequences of carbon corrosion at the *cathode* due to local hydrogen starvation have been confirmed with start–stop experiments and with experiments involving the deliberate blocking of hydrogen flow field channels. The main cause for local hydrogen starvation in real PEFCs is associated to water droplet formation inside flow field channels.

Gross hydrogen starvation occurs when the complete anode compartment of the PEFC is free of hydrogen. This situation occurs, e.g., when individual flow fields inside a fuel cell stack are not supplied by H_2 due to inhomogeneous hydrogen distribution when gas inlets of cells are blocked due to liquid water. Under operating conditions, i.e., when a current is drawn off the PEFC in the absence of fuel, the anode potential is increasing to a value where some other oxidation reactions can occur, typically to potentials when the carbon support of the anode catalyst is oxidized. In Fig. 3b, the effect of the hydrogen starvation mechanism on the cell potential of a PEFC anode is shown under a constant current of 20 mA/cm^2. In this model experiment, the anode potential increases as a function of time when the fuel gas is switched from hydrogen to Argon flow. In the presence of H_2, the potential exhibits a constant value of less than 0.1 V/ RHE (Eq. 3). However, when the H_2 flow is replaced by Ar, the potential gradually increases, at a rate that depends on the pseudocapacitance of the electrode material, to higher potentials than 1.6 V/RHE. This potential excursion leads to severe, rapid, and irreversible carbon corrosion [65, 66, 68–71].

Besides engineering solutions such as continuous H_2 flow in the anode to avoid accumulation of liquid water and/or nitrogen, different material mitigation strategies have been proposed in order to minimize effects of local hydrogen starvation which include the following: (1) the use of an oxygen evolution reaction (OER) catalyst in the cathode catalyst layer opening up an energetically more favorable reaction pathway during internal shorting as compared to carbon

Platinum-Based Anode Catalysts for Polymer Electrolyte Fuel Cells, Fig. 3 (**a**) Reverse current decay mechanism at *local* hydrogen starvation in the rear part of a PEM cell (Reproduced by permission from [9]). (**b**) Effect of *gross* hydrogen starvation on the half-cell potential at the anode side (Reproduced by permission from [10])

a

front

rear

$\varphi_{00} = 0\ V$ $\varphi_{00} = 1,23\ V$

$H_2 \rightarrow 2\ H^+ + 2\ e^-$ e^- $O_2 + 4\ H^+ + 4\ e^- \rightarrow 2\ H_2O$ anode

$H^+ \downarrow$ $H^+ \uparrow$ membrane

$O_2 + 4\ H^+ + 4\ e^- \rightarrow 2\ H_2O$ e^- $C + 2\ H_2O \rightarrow CO_2 + 4\ H^+ + 4\ e^-$ cathode

$2\ H_2O \rightarrow O_2 + 4\ H^+ + 4\ e^-$

φ $\varphi_{00} = 1,23\ V$ $\varphi_{00} = 1,23\ V$

$\varphi_k = 1\ V$

$\varphi_k - \varphi_m$ $\varphi_k - \varphi_m$

$\varphi_A = 0\ V$

$\varphi_A - \varphi_m$ $\varphi_A - \varphi_m$

$\varphi_m = -0,3\ V$

b

Effect of Hydrogen Starvation on Anode

Tanaka TKK Platinum on Vulcan XC-72 Carbon

w/o H_2
with H_2

Anode Potential, V/rhe

Time After H_2 Flow Switch-Off, s

oxidation; (2) the use of non-carbon supports which cannot be oxidized under local starvation conditions; and (3) the use of a highly selective anode catalyst which cannot reduce oxygen in the anode compartment [72], therefore avoiding the internal cell shorting.

More information regarding carbon corrosion and the use of novel support materials can be found in [3] and references therein.

Anode Electrocatalyst for Alcohol Oxidation

As in many other systems, the nature and the structure of the electrode material play an important role in the adsorption and electrooxidation of most organic fuels commonly used in DAFC. Many groups attempted to develop Pt-free electrocatalysts as anode materials for alcohol

a

b

c
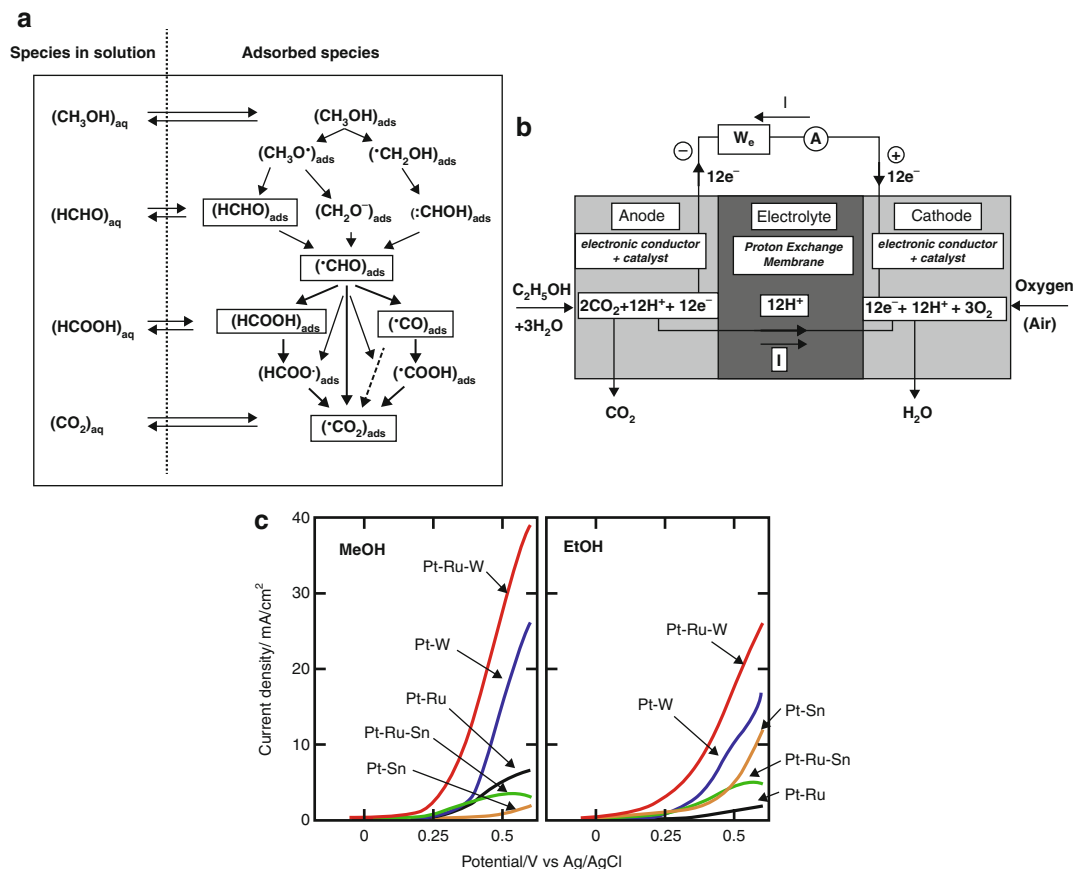
Platinum-Based Anode Catalysts for Polymer Electrolyte Fuel Cells, Fig. 4 (**a**) Reaction mechanism for the methanol electrochemical oxidation proposed by Lamy et al. (**b**) Schematic representation of a DEFC (Reproduced by permission from [16]). (**c**)

Voltammograms of $Pt_{80}Ru_{20}$; $Pt_{80}Sn_{20}$; $Pt_{85}W_{15}$; $Pt_{60}Ru_{15}Sn_{25}$; $Pt_{65}Ru_{20}W_{15}$ supported nanoparticles electrodes in 0.5 M H_2SO_4 + 1 M methanol or ethanol solution at 30 °C; $v = 10$ mVs^{-1} (Reproduced by permission from [83])

oxidation, but only platinum seems to be able to adsorb alcohols and to break the C–H bonds efficiently. However, the dissociative chemisorption of an alcohol leads to the formation of strongly poisoning intermediate species (mainly adsorbed CO or COH), which block the electroactive sites of the catalysts, see discussion of CO tolerance above. During alcohol oxidation, many other intermediates species are formed, and different reaction mechanisms and poisoning species have been proposed. A temptative reaction mechanism proposed by Lamy et al. [16] is presented in Fig. 4a and is discussed in this volume, chapter "▶ Direct Alcohol Fuel Cells (DAFCs)".

As in the development of CO-tolerant catalysts for PEFC anodes, the main challenge for the development of catalysts for the oxidation of alcohols is to reduce or to avoid the formation of strongly adsorbed poisoning species (i.e., CO) or to favor their oxidation at low overpotentials.

As described before, a route to improve the electrocatalytic properties of platinum, and to decrease the poisoning of its surface by adsorbed CO or CO containing species, is to prepare alloys with a second metal (or third metal). Many different binary and ternary platinum-based anode catalysts, such as PtRu, PtSn, PtMo, PtRuMo, PtRh/SnO$_2$, or PtRuW, have been examined
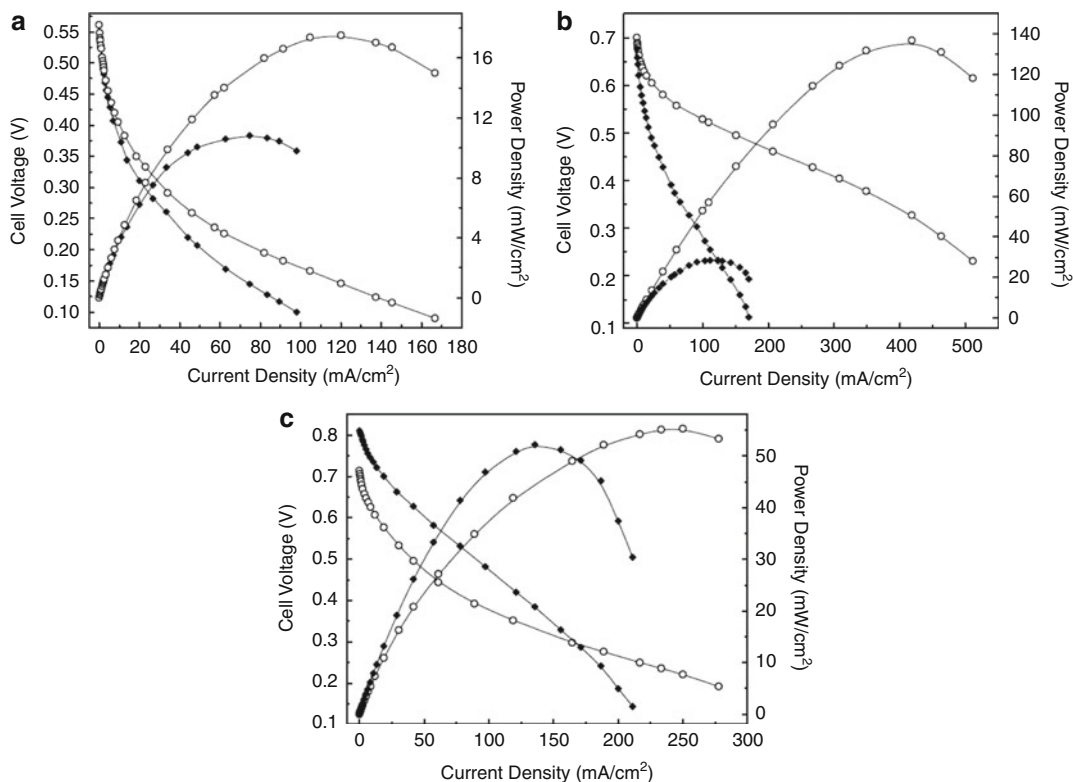
Platinum-Based Anode Catalysts for Polymer Electrolyte Fuel Cells, Fig. 5 The performance of single DAFC with (**a**) Pt/C; (**b**) PtRu/C (20–10 %), 1.33 mg_{Pt}/cm^2; and (**c**) PtSn/C, 1.33 mg_{Pt}/cm^2 as anode catalysts. Cathode: 1.0 mg_{Pt}/cm^2 (20 wt.% Pt/C, Johnson Matthey Co.). p_{O2}: 0.2 MPa (abs.); 90 °C; MeOH (or EtOH): 1 M and 1.0 ml/min. Nafion®-115 was used as electrolyte. (○) DMFC (◆) DEFC (Reproduced by permission from [91])

toward the methanol and ethanol electrooxidation [19, 20, 73–82].

Among all the alcohols, ethanol has being subject of extensive studies because it is a green fuel and can be easily obtained as biofuel. The schematic of direct ethanol fuel cell is presented in Fig. 4b, while Fig. 4c shows the onset on the oxidation potential of methanol and ethanol for different alloy catalyst.

Regarding the ethanol oxidation mechanism, adsorbed CO and CH_x fragments have been identified as the main poisoning reaction intermediates [77, 84–90].

The cell performances reported by Zhou et al. for DMFCs and DEFCs with Pt/C, PtRu/C, and PtSn/C employed as anode catalyst are summarized in Fig. 5. The performances of single cells are significantly different when anode catalyst composition is the variable parameter to be considered, keeping the other parameter constant. In this evaluation, even though the Pt loading on anode catalyst layer is higher than that of other bimetallic anode catalysts (2.0 mg_{Pt}/cm^2 for Pt/C vs. 1.3 mg_{Pt}/cm^2 for PtRu/C and PtSn/C), the performance of the respective single cells is still poor. It can also be concluded that the performance of single DMFC with Pt/C and PtRu/C as anode catalyst is higher than that of single DEFC, due to the fact that methanol is more reactive than ethanol. On the other hand, PtSn/C catalyst has shown a better performance on a single DEFC than on a single cell of DMFC in the current density range from 0 to 168 mA/cm^2 [91].

Conclusions

Whereas the oxidation of pure hydrogen in H_2-PEFC is not challenging from the electrocatalytic point of view (the only challenge actually remaining is how much the Pt loading can be reduced), the oxidation of H_2-rich reformates obtained from hydrocarbon or alcohol reforming with even ppm levels of CO remains one of the biggest challenges for reformate-driven PEFC development. Although some Pt alloys, e.g., PtRu, show very high CO tolerance, from an operational system point of view, there is not a large range of CO levels which can be tolerated, and fuel processing to the desired level is a PEFC systems challenge. Although the many progresses have been made over the last years in the direct oxidation of hydrocarbons and alcohols in DAFCs, only hydrogen (both pure or reformate) fuelled systems offer the high power densities, e.g., necessary for stationary fuel cell systems. Direct alcohol systems may find a place in some applications in the portable electronics market, where power density requirements are not as high.

Cross-References

▶ Direct Alcohol Fuel Cells (DAFCs)
▶ Electrocatalysis - Basic Concepts, Theoretical Treatments in Electrocatalysis via DFT-Based Simulations
▶ Electrocatalysis of Anodic Reactions
▶ High-Temperature Polymer Electrolyte Fuel Cells
▶ Hydrogen Oxidation and Evolution on Platinum in Acids
▶ Platinum-Based Cathode Catalysts for Polymer Electrolyte Fuel Cells
▶ Polymer Electrolyte Fuel Cells (PEFCs), Introduction

References

1. Gasteiger HA et al (eds) (2011) Polymer electrolyte fuel cells 11. ECS transactions 41(1). The Electrochemical Society, Pennington
2. Vielstich W, Gasteiger HA, Yokokawa H (eds) Handbook of fuel cells – advances in electrocatalysis, materials, diagnostics and durability, vols 5 and 6. Wiley-VCH, Chichester
3. Rabis A, Rodriguez P, Schmidt TJ (2012) Electrocatalysis for polymer electrolyte fuel cells: recent advances and future challenges. ACS Catal 2:864–890
4. Pereira LGS, Paganin VA, Ticianelli EA (2009) Investigation of the CO tolerance mechanism at several Pt-based bimetallic anode electrocatalysts in a PEM fuel cell. Electrochim Acta 54(7):1992–1998
5. Wee J-H, Lee K-Y (2006) Overview of the development of CO-tolerant anode electrocatalysts for proton-exchange membrane fuel cells. J Power Sources 157(1):128–135
6. Chu HS et al (2006) Transient behavior of CO poisoning of the anode catalyst layer of a PEM fuel cell. J Power Sources 159(2):1071–1077
7. Arenz M et al (2005) Carbon-supported Pt-Sn electrocatalysts for the anodic oxidation of H_2, CO, and H_2/CO mixtures. Part II: the structure-activity relationship. J Catal 232(2):402–410
8. Lee SJ et al (1999) Electrocatalysis of CO tolerance in hydrogen oxidation reaction in PEM fuel cells. Electrochim Acta 44(19):3283–3293
9. Ohs JH et al (2011) Modeling hydrogen starvation conditions in proton-exchange membrane fuel cells. J Power Sources 196(1):255–263
10. Halalay IC et al (2011) Anode materials for mitigating hydrogen starvation effects in PEM fuel cells. J Electrochem Soc 158(3):B313–B321
11. Yan L et al (2007) Transition metal oxides as DMFC cathodes without platinum. J Electrochem Soc 154(7):B664–B669
12. Coutanceau C et al (2004) Preparation of Pt-Ru bimetallic anodes by galvanostatic pulse electrodeposition: characterization and application to the direct methanol fuel cell. J Appl Electrochem 34(1):61–66
13. Zainoodin AM, Kamarudin SK, Daud WRW (2010) Electrode in direct methanol fuel cells. Int J Hydrogen Energy 35(10):4606–4621
14. Ren X et al (2000) Recent advances in direct methanol fuel cells at Los Alamos National Laboratory. J Power Sources 86(1–2):111–116
15. Oedegaard A, Hentschel C (2006) Characterisation of a portable DMFC stack and a methanol-feeding concept. J Power Sources 158(1):177–187
16. Lamy C et al (2002) Recent advances in the development of direct alcohol fuel cells (DAFC). J Power Sources 105(2):283–296
17. Lamy C, Belgsir EM, Leger JM (2001) Electrocatalytic oxidation of aliphatic alcohols: application

to the direct alcohol fuel cell (DAFC). J Appl Electrochem 31(7):799–809

18. Braunchweig B et al (2013) Electrocatalysis: a direct alcohol fuel cell and surface science perspective. Catal Today 202:197–209

19. Kowal A et al (2009) Ternary Pt/Rh/SnO$_{(2)}$ electrocatalysts for oxidizing ethanol to CO$_{(2)}$. Nat Mater 8(4):325–330

20. Wang Z-B, Yin G-P, Lin Y-G (2007) Synthesis and characterization of PtRuMo/C nanoparticle electrocatalyst for direct ethanol fuel cell. J Power Sources 170(2):242–250

21. Rousseau S et al (2006) Direct ethanol fuel cell (DEFC): electrical performances and reaction products distribution under operating conditions with different platinum-based anodes. J Power Sources 158(1):18–24

22. Zhou WJ et al (2005) Direct ethanol fuel cells based on PtSn anodes: the effect of Sn content on the fuel cell performance. J Power Sources 140(1):50–58

23. Song SQ et al (2005) Direct ethanol PEM fuel cells: the case of platinum based anodes. Int J Hydrogen Energy 30(9):995–1001

24. Leger JM et al (2005) How bimetallic electrocatalysts does work for reactions involved in fuel cells? Example of ethanol oxidation and comparison to methanol. Electrochim Acta 50(25–26):5118–5125

25. Vigier F et al (2004) Development of anode catalysts for a direct ethanol fuel cell. J Appl Electrochem 34(4):439–446

26. Lamy C et al (2004) Recent progress in the direct ethanol fuel cell: development of new platinum-tin electrocatalysts. Electrochim Acta 49(22–23):3901–3908

27. Hogarth MP, Ralph TR (2002) Catalysis for low temperature fuel cells – Part III: challenges for the direct methanol fuel cell. Platinum Metals Rev 46(4):146–164

28. Neyerlin KC et al (2007) Study of the exchange current density for the hydrogen oxidation and evolution reactions. J Electrochem Soc 154(7):B631–B635

29. Neyerlin KC et al (2005) Effect of relative humidity on oxygen reduction kinetics in a PEMFC. J Electrochem Soc 152(6):A1073–A1080

30. Schwanitz B et al (2011) Stability of ultra-low Pt anodes for polymer electrolyte fuel cells prepared by magnetron sputtering. Electrocatalysis 2:35–41

31. Schmidt TJ, Gasteiger HA, Behm RJ (1999) Rotating disk electrode measurements on the CO tolerance of a high-surface area Pt/Vulcan carbon fuel cell catalyst. J Electrochem Soc 146(4):1296–1304

32. Camara GA, Ticianelli EA, Mukerjee S, Lee SJ, McBreen J (June 2002) CO poisoning of hydrogen oxidation reaction in PEMFCs. J Electrochem Soc 149(6) A748–753

33. Lemons RA (1990) Fuel cells for transportation. J Power Sources 29(1–2):251–264

34. Schmidt TJ, Markovic NM (2006) Electrocatalysis of inorganic reactions: bimetallic surfaces.

In: Somasundaran P (ed) Encyclopedia of surface and colloid science. Taylor and Francis, New York, pp 2017–2031

35. Igarashi H et al (2001) CO tolerance of Pt alloy electrocatalysts for polymer electrolyte fuel cells and the detoxification mechanism. Phys Chem Chem Phys 3(3):306–314

36. Hajbolouri F et al (2004) CO tolerance of commercial Pt and PtRu gas diffusion electrodes in polymer electrolyte fuel cells. Fuel Cells 4(3):160–168

37. Yajima T, Uchida H, Watanabe M (2004) In-situ ATR-FTIR spectroscopic study of electro-oxidation of methanol and adsorbed CO at Pt-Ru alloy. J Phys Chem B 108(8):2654–2659

38. Camara GA et al (2002) Correlation of electrochemical and physical properties of PtRu alloy electrocatalysts for PEM fuel cells. J Electroanal Chem 537(1–2):21–29

39. Lucas CA, Markovic NM, Ross PN (2000) Structural effects during CO adsorption on Pt-bimetallic surfaces. II. The Pt(111) electrode. Surf Sci 448(2–3):77–86

40. Nilekar AU et al (2011) Mixed-metal Pt mono layer electrocatalysts with improved CO tolerance. J Am Chem Soc 133(46):18574–18576

41. Zhang L et al (2011) A novel CO-tolerant PtRu core–shell structured electrocatalyst with Ru rich in core and Pt rich in shell for hydrogen oxidation reaction and its implication in proton exchange membrane fuel cell. J Power Sources 196(22):9117–9123

42. Yamanaka T et al (2010) Particle size dependence of CO tolerance of anode PtRu catalysts for polymer electrolyte fuel cells. J Power Sources 195(19):6398–6404

43. Lopes PP, Ticianelli EA (2010) The CO tolerance pathways on the Pt–Ru electrocatalytic system. J Electroanal Chem 644(2):110–116

44. Stolbov S et al (2009) High CO tolerance of Pt/Ru nanocatalyst: insight from first principles calculations. J Chem Phys 130(12):124714

45. Takeguchi T et al (2007) Preparation and characterization of CO-tolerant Pt and Pd anodes modified with SnO$_2$ nanoparticles for PEFC. J Electrochem Soc 154(11):B1132–B1137

46. Russell AE et al (2007) Unravelling the complexities of CO$_2$ tolerance at PtRu/C and PtMo/C. J Power Sources 171(1):72–78

47. Okanishi T et al (2006) Chemical interaction between Pt and SnO$_2$ and influence on adsorptive properties of carbon monoxide. Appl Catal A Gen 298:181–187

48. Stamenkovic V et al (2005) In situ CO oxidation on well characterized Pt$_3$Sn(hkl) surfaces: a selective review. Surf Sci 576(1–3):145–157

49. Ioroi T et al (2003) Enhanced CO-tolerance of carbon-supported platinum and molybdenum oxide anode catalyst. J Electrochem Soc 150(9): A1225–A1230

50. Watanabe M, Zhu Y, Uchida H (2000) Oxidation of CO on a Pt–Fe alloy electrode studied by surface

enhanced infrared reflection-absorption spectroscopy. J Phys Chem B 104(8):1762–1768

51. Papageorgopoulos DC, Keijzer M, de Bruijn FA (2002) The inclusion of Mo, Nb and Ta in Pt and PtRu carbon supported 3 electrocatalysts in the quest for improved CO tolerant PEMFC anodes. Electrochim Acta 48(2):197–204

52. Springer T, Zawodzinski T, Gottesfeld S (1997) Modelling of polymer electrolyte fuel cell performance with reformate feed streams: effects of low levels of CO in hydrogen. The Electrochemical Society, Pennington

53. Grgur BN, Markovic NM, Ross PN Jr (1998) Electrooxidation of H_2, CO, and H_2/CO mixtures on a well-characterized Pt 70 Mo 30 bulk alloy electrode. J Phys Chem B 102(14):2494–2501

54. Mukerjee S et al (1999) Investigation of enhanced CO tolerance in proton exchange membrane fuel cells by carbon supported PtMo alloy catalyst. Electrochem Solid State Lett 2(1):12–15

55. Micoud F et al (2009) Unique CO-tolerance of Pt–WO_x materials. Electrochem Commun 11(3):651–654

56. Micoud F et al (2010) The role of the support in COads monolayer electrooxidation on Pt nanoparticles: Pt/WOxvs. Pt/C. Phys Chem Chem Phys 12(5):1182–1193

57. Nagel T et al (2003) On the effect of tungsten on CO oxidation at Pt electrodes. J Solid State Electrochem 7(9):614–618

58. Chen KY, Shen PK, Tseung ACC (1995) Anodic oxidation of impure H_2 on teflon-bonded Pt-Ru/WO_3/C electrodes. J Electrochem Soc 142(10): L185–L187

59. Strasser P et al (2003) High throughput experimental and theoretical predictive screening of materials – a comparative study of search strategies for new fuel cell anode catalysts. J Phys Chem B 107(40):11013–11021

60. Schmidt TJ et al (2001) On the CO tolerance of novel colloidal PdAu/carbon electrocatalysts. J Electroanal Chem 501:132–140

61. Schmidt TJ et al (2003) Electrooxidation of H_2, CO, and CO/H_2 on well characterized Au(111)Pd surface alloys. Electrochim Acta 48:3823–3828

62. Ishigami Y et al (2012) Real-time visualization of CO_2 generated by corrosion of the carbon support in a PEFC cathode. Electrochem Solid State Lett 15(4):B51–B53

63. Kulikovsky AA (2011) A simple model for carbon corrosion in PEM fuel cell. J Electrochem Soc 158(8): B957–B962

64. Kim J, Lee J, Tak Y (2009) Relationship between carbon corrosion and positive electrode potential in a proton-exchange membrane fuel cell during start/stop operation. J Power Sources 192(2):674–678

65. Linse N et al (2012) Quantitative analysis of carbon corrosion during fuel cell start-up and shut-down by anode purging. J Power Sources 219:240–248

66. Linse N et al (2010) Start/stop induced carbon corrosion in polymer electrolyte fuel cells. In: Proceedings of the ASME 8th international conference on fuel cell

science, engineering, and technology, Brooklyn vol 22010. pp 357–362

67. Fuller T, Gray G (2006) Carbon corrosion induced by partial hydrogen coverage. ECS Trans 1(8):345–353

68. Tang H et al (2006) PEM fuel cell cathode carbon corrosion due to the formation of air/fuel boundary at the anode. J Power Sources 158(2):1306–1312

69. Schulenburg H et al (2011) 3D imaging of catalyst support corrosion in polymer electrolyte fuel cells. J Phys Chem C 115(29):14236–14243

70. Perry ML, Patterson TW, Reiser CA (2006) Systems strategies to mitigate carbon corrosion in fuel cells. ECS Trans 3(1):783–795

71. Liu ZY et al (2008) Characterization of carbon corrosion-induced structural damage of PEM fuel cell cathode electrodes caused by local fuel starvation. J Electrochem Soc 155(10):B979–B984

72. Genorio B et al (2011) Tailoring the selectivity and stability of chemically modified platinum nanocatalysts to design highly durable anodes for PEM fuel cells. Angew Chem Int Ed 50(24):5468–5472

73. García G, Tsiouvaras N, Pastor E, Peña MA, Fierro JLG, Martínez-Huerta MV (2012) Ethanol oxidation on PtRuMo/C catalysts: in situ FTIR spectroscopy and DEMS studies. Int J Hydrogen Energy 37(8):7131–7140

74. Li M et al (2010) Ethanol oxidation on the ternary Pt-Rh-$SnO_{(2)}$/C electrocatalysts with varied Pt:Rh:Sn ratios. Electrochim Acta 55(14):4331–4338

75. Lee E, Murthy A, Manthiram A (2010) Effect of Mo addition on the electrocatalytic activity of Pt-Sn-Mo/C for direct ethanol fuel cells. Electrochim Acta 56(3):1611–1618

76. Jian X-H et al (2009) Pt-Ru and Pt-Mo electrodeposited onto Ir-IrO_2 nanorods and their catalytic activities in methanol and ethanol oxidation. J Mater Chem 19(11):1601–1607

77. Giz MJ, Camara GA, Maia G (2009) The ethanol electrooxidation reaction at rough PtRu electrodeposits: a FTIRS study. Electrochem Commun 11(8):1586–1589

78. Li H et al (2007) Comparison of different promotion effect of PtRu/C and PtSn/C electrocatalysts for ethanol electro-oxidation. Electrochim Acta 52(24):6622–6629

79. Wang H, Jusys Z, Behm RJ (2006) Ethanol electrooxidation on carbon-supported Pt, PtRu and Pt3Sn catalysts: a quantitative DEMS study. J Power Sources 154(2):351–359

80. Colmati F, Antolini E, Gonzalez ER (2006) Effect of temperature on the mechanism of ethanol oxidation on carbon supported Pt, PtRu and Pt3Sn electrocatalysts. J Power Sources 157(1):98–103

81. Li M, Cullen DA, Sasaki K, Marinkovic NS, More K, Adzic RR (2013) Ternary electrocatalysts for oxidizing ethanol to carbon dioxide: making Ir capable of splitting C–C bond. J Am Chem Soc 135(1):132–141

82. Ammam M, Easton EB (2013) PtCu/C and Pt(Cu)/C catalysts: synthesis, characterization and catalytic activity towards ethanol electrooxidation. J Power Sources 222:79–87

83. Tanaka S et al (2005) Preparation and evaluation of a multi-component catalyst by using a co-sputtering system for anodic oxidation of ethanol. J Power Sources 152:34–39

84. Lai SCS, Koper MTM (2010) The influence of surface structure on selectivity in the ethanol electro-oxidation reaction on platinum. J Phys Chem Lett 1(7):1122–1125

85. Lai SCS et al (2008) Mechanism of the dissociation and electrooxidation of ethanol and acetaldehyde on platinum as studied by SERS. J Phys Chem C 112(48):19080–19087

86. Shao MH, Adzic RR (2005) Electrooxidation of ethanol on a Pt electrode in acid solutions: in situ ATR-SEIRAS study. Electrochim Acta 50(12):2415–2422

87. Vigier F et al (2004) On the mechanism of ethanol electro-oxidation on Pt and PtSn catalysts: electrochemical and in situ IR reflectance spectroscopy studies. J Electroanal Chem 563(1):81–89

88. de Souza JPI et al (2002) Electro-oxidation of ethanol on Pt, Rh, and PtRh electrodes. A study using DEMS and in-situ FTIR techniques. J Phys Chem B 106(38):9825–9830

89. Cantane DA et al (2012) Electro-oxidation of ethanol on Pt/C, Rh/C, and Pt/Rh/C-based electrocatalysts investigated by on-line DEMS. J Electroanal Chem 681:56–65

90. Detacconi NR et al (1994) In-situ FTIR study of the electrocatalytic oxidation of ethanol at iridium and rhodium electrodes. J Electroanal Chem 379(1–2):329–337

91. Zhou WJ et al (2004) Performance comparison of low-temperature direct alcohol fuel cells with different anode catalysts. J Power Sources 126(1–2):16–22

Platinum-Based Cathode Catalysts for Polymer Electrolyte Fuel Cells

Emiliana Fabbri and Thomas J. Schmidt
Electrochemistry Laboratory, Paul Scherrer
Institute, Villigen, Switzerland

Introduction

Polymer electrolyte fuel cells (PEFCs) are electrochemical devices converting chemical energy of fuels into electrical energy with relatively high efficiencies and low emissions. For these reasons they have attracted great attention as promising power sources for small stationary, mobile, and portable applications. The heart of a PEFC is the membrane electrode assembly (MEA), which is composed of anodic and cathodic catalytic layers (CLs), where electrochemical reactions occur, gas diffusion layers (GDLs), and a proton-conducting membrane. For the CLs in hydrogen driven PEFCs, Pt has been early recognized and still remains the catalyst of choice. The development of Pt-based CLs has gone through a number of different stages in the last three decades. In the early days of PEFC development, the CLs relied on vey high loadings of Pt (about 4 mg cm^{-2}) to achieve reasonable fuel cell performance [1]. The CLs were made of unsupported Pt-black powders, with very low surface areas (10–30 m^2 g^{-1}) and thereby requiring high Pt loadings per unit area in order to attain reasonable performance. In the late 1980's and early 1990's, by developing CLs based on Pt supported on porous carbon and incorporating in the CL a proton-conducting phase, it was possible to achieve the same performance for the cathodic and anodic reactions reducing the noble metal loading down to 0.35 mg cm^{-2} [2, 3]. The introduction of a proton-conducting phase such as Nafion led to an extended reaction zone and, thereby, to a larger catalyst utilization. Supporting Pt particles on porous carbon allowed higher Pt dispersion and hence larger catalyst surface area compared to unsupported Pt-black. The carbon support not only provides high dispersion of Pt nanoparticles, but it also possess high electronic conductivity to minimize ohmic losses and adequate porosity to ensure efficient mass transport of reactants and products from and to the CLs. Table 1 provides a list of the most widely used carbon supports and their surface area. After the breakthrough of CLs based on carbon-supported Pt catalysts, the new generation of PEFCs emerged and the Pt loading could be progressively reduced. However, while at present the Pt anode loading can be as low as 0.05 mg cm^{-2} without measurable kinetic losses [5] (in the case of operation with pure H$_2$), the Pt
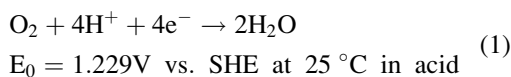
Platinum-Based Cathode Catalysts for Polymer Electrolyte Fuel Cells, Table 1 Brunauer–Emmett–Teller (BET) surface area of the most used carbon supports in Pt/C catalysts [4]

Carbon	BET surface area/$m^2 g^{-1}_C$
Black pearl	1,600
Ketjenblack	800
Vulcan XC-72C	240
Black pearls graphitized	240
Ketjenblack graphitized	160
Vulcan XC-72C graphitized	80

Platinum-Based Cathode Catalysts for Polymer Electrolyte Fuel Cells, Fig. 1 Possible reaction scheme for the ORR on Pt-based catalysts (Ref. [8])
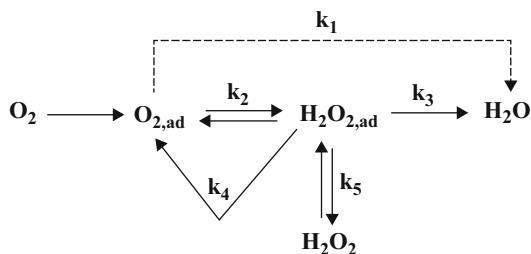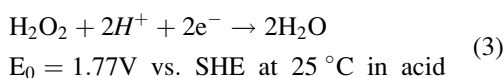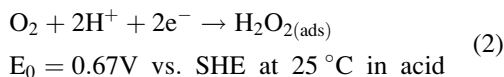
loading required at the cathode is still about 0.4 mg cm^{-2} [6]. Besides the large Pt cathode loading, the slow ORR kinetics at the positive electrode are responsible for about two thirds of the overall voltage losses of a PEFC at high current density, and therefore large efforts are currently devoted to search for more active catalysts and reducing the Pt loading.

Performance: ORR Kinetics

As already mentioned above, the oxygen reduction reaction (ORR) at the PEFC cathode suffers from poor kinetics, resulting in overpotentials of about 0.3–0.4 V. In acidic environment, Pt-based catalysts are still recognized the materials of choice for the ORR which leads to water formation according to the following equation:

$$O_2 + 4H^+ + 4e^- \rightarrow 2H_2O$$
$$E_0 = 1.229V \text{ vs. SHE at } 25\,^\circ C \text{ in acid} \tag{1}$$

Besides direct 4e^- reduction of adsorbed oxygen to water, ORR can also proceed by 2e^- reduction of O_2 to adsorbed H_2O_2, which then either desorbs or undergoes a second 2e^- reduction to water [7]:

$$O_2 + 2H^+ + 2e^- \rightarrow H_2O_{2(ads)}$$
$$E_0 = 0.67V \text{ vs. SHE at } 25\,^\circ C \text{ in acid} \tag{2}$$

$$H_2O_2 + 2H^+ + 2e^- \rightarrow 2H_2O$$
$$E_0 = 1.77V \text{ vs. SHE at } 25\,^\circ C \text{ in acid} \tag{3}$$

Figure 1 presents a simplified reaction scheme for the oxygen reduction reaction [8]: direct 4e^- reduction of adsorbed oxygen to water (k1), 2e^- reduction to adsorbed H_2O_2 as an intermediate (k2) which can be then further reduced to water (k3), chemically decompose to water and O_2 (k4), or desorbs from the surface (k5).

It was firstly reported that in absence of adsorbed impurities, the ORR on Pt proceeds principally through the direct pathway, both in acid and alkaline electrolytes [9]. However, it was later suggested that the 2e^- + 2e^- pathway more reasonably applies to Pt-based catalysts [8]. Besides a chemical intuition, which would rather suggest a molecular than dissociative adsorption of O_2 in liquid environment (where strong adsorbates are generally present), rotating ring-disk (RRDE) measurements have also given experimental evidence of this assumption [8]. ORR on Pt-based catalysts involves several reaction steps, which include both chemical and electrochemical reactions. Among them, the rate determining step (rds) is considered the addition of the first electron to the adsorbed oxygen in a proton-coupled process [8, 10]. The number of electrons transferred in the rds can be determined by the Tafel slope obtained plotting the IR-corrected potential vs the logarithm of the kinetic current. In acidic environments, polycrystalline Pt catalysts exhibit a Tafel slope of about 60 mV dec^{-1} at potentials above ∼0.85 V_{RHE}, while at more negative potentials a slope of 120 mV dec^{-1} is observed [11, 12]. The change in the Tafel slope has been ascribed to surface

Platinum-Based Cathode Catalysts for Polymer Electrolyte Fuel Cells, Fig. 2 DFT activities as a function of the oxygen binding energy derived by density functional theory (DFT) calculations. The volcano is in good agreement with experiment, showing that Pt is the best catalysts for oxygen reduction (Ref. [16])
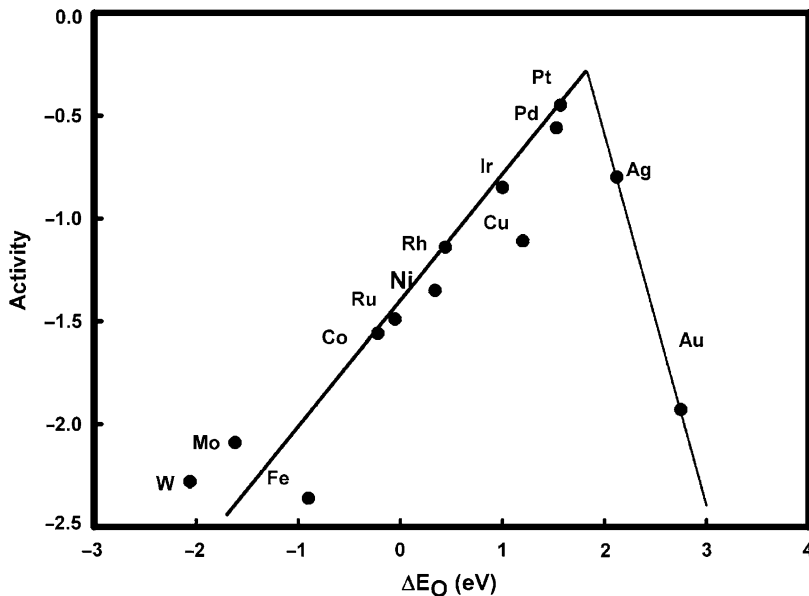
coverage by irreversible adsorption of HO_{ad}, which starts at 0.8–0.85 V and increases rapidly at more positive potentials. The Tafel slope of $60\ mV\ dec^{-1}$ is consistent with the first electron charge transfer as the rds under Temkin conditions of adsorption of oxygen-containing species, while the slope of $120\ mV\ dec^{-1}$ is characteristic for the same rds under Langmuirian conditions [13]. Adsorbed OH not only blocks active Pt site for the ORR but also alters the adsorption energy of ORR intermediates [14]. Given the first electron transfer to the adsorbed oxygen as rds and for a first-order dependence of the kinetics of ORR, the current density (i) has been proposed [8] to be determined either by the free Pt sites available for the adsorption of O_2, $(1 - \Theta_{ads})$, or by the change of Gibbs energy of adsorption of reactive intermediates (ΔG_{ads}):

$$i = nFKc_{O_2}(1 - \Theta_{ads})^x \exp(-\beta FE/RT) \\ \times \exp(-\gamma\ r\Theta_{ads}/RT) \quad (4)$$

where F, x, β, γ, and R are constants, n is the number of electrons, c_{O2} is the oxygen concentration in the solution, K is the chemical rate constant, E is the applied potential, $r\Theta_{ads}$ is a parameter characterizing the rate of change of ΔG_{ads} with surface coverage, and Θ_{ads} is the

fraction of electrode surface sites covered by all the adsorbed species [8]. The sensitivity of the Pt catalytic activity to other adsorbed species which block Pt-active sites also meant that great care must be taken to avoid trace impurities during measurements [15]. Modification of the Pt surface atomic or electronic structure leading to a reduced adsorption of hydroxyls (i.e., increasing the $(1 - \Theta_{ads})$ term in Eq. 4) without changing the overall mechanism will result in higher catalyst activity. Besides the influence of the adsorbated species, the ORR activity of Pt-based catalysts is also affected by the oxygen binding energy to the metal surface. Theoretically calculated oxygen binding energy as a function of the ORR activity for several metals shows a volcano plot (Fig. 2) indicating that too strong and too weak O_2 binding energy are both not favorable for ORR, according to the well-known Sabatier principle [16]. It has been later shown that the strength of the oxygen–metal bond interaction and the interaction of Pt with adsorbed species both strongly depend on the Pt d-band center and on the Pt–Pt interatomic distance [17].

As mentioned above, to minimize the amount of Pt required for a given level of activity, Pt catalyst is generally dispersed as small

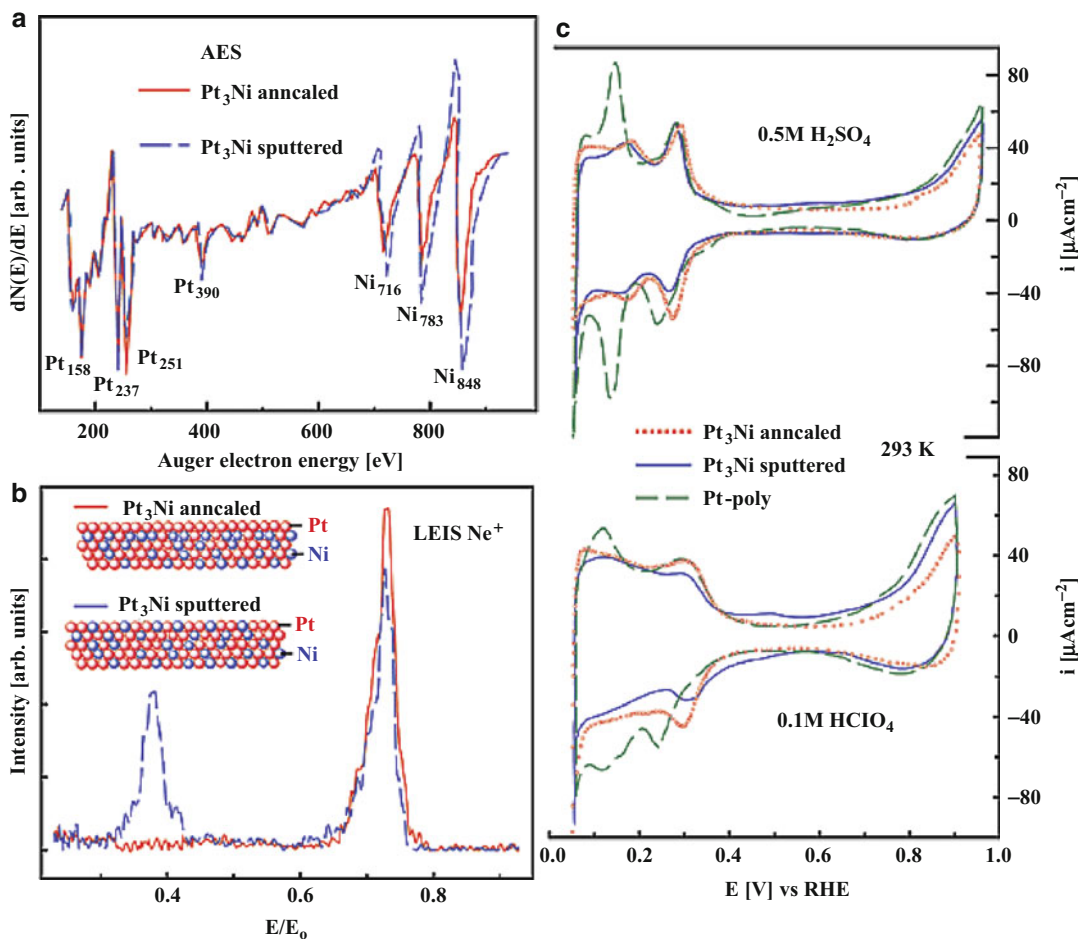**Platinum-Based Cathode Catalysts for Polymer Electrolyte Fuel Cells, Fig. 3** Oxygen reduction on Pt(hkl) in 0.05 M H_2SO_4 *lower part*, disk currents; *upper part*, ring currents. *Top view* of the surface structure of Pt(111), Pt(100), and Pt(110) (Ref. [8])
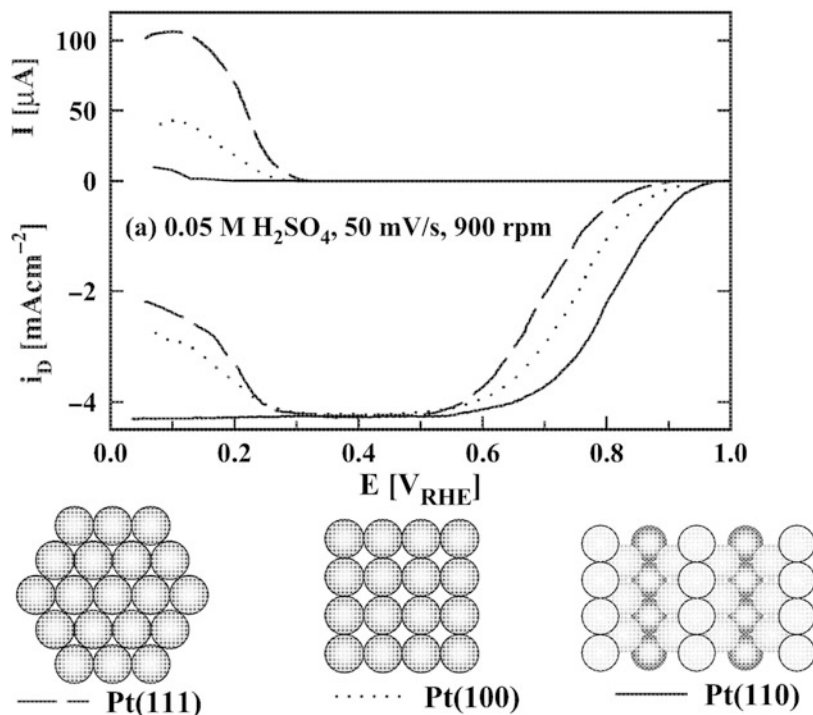
particles on high surface area carbon supports (Pt/C). It was proposed from the very beginning a modification of the Pt/C activity with the variation of the Pt particle size, i.e., for Pt particles in the range of 1–12 nm, the highest mass activity is obtained for Pt particles of about 3 nm [18]. Kinoshita [19] suggested that the maximum in mass activity observed at about 3 nm particle size is correlated with the large surface fraction of Pt atoms on the (100) and (110) crystal faces, while for smaller particles size the (111) crystal facets start to predominate and correlations to Pt single-crystal ORR activities have been drawn (Fig. 3). Newer results cannot necessarily confirm the maximum of mass activity at a specific particle size, showing a constant increase in mass activity with decreasing particle size, while the specific activity is constantly dropping in the same direction. This effect was correlated to the increase of potential of total zero charge (*pztc*) with increasing particle size towards large particles and bulk and as a consequence to the higher oxidation probability of small particles [20, 21].

Recent Advances in Pt-Based Catalyst Activity

In the last decades the fundamental understanding of the factors controlling the ORR has dramatically improved and is now guiding next-generation catalyst development. Although significant advances have been made in the area of non-Pt cathode catalysts, Pt-based catalysts are currently the most promising option to provide high catalytic activity towards ORR. Most emerging approaches focus on controlling the surface structure and composition of catalytic nanoparticles to achieve higher ORR activity with less amount of Pt. Improved ORR-specific activities have been reported alloying Pt with non-noble metals [22] or producing Pt core–shell nanoparticles (i.e., Pt layers supported on non-noble metal nanoparticles) [23, 24]. Typically, Pt-alloy catalysts consist of either binary or ternary systems containing different transition metals such as Co, Fe, or Ni. Compared to pure Pt, ORR activities of these catalysts are up to a factor of 4 higher [22], thus allowing the

Platinum-Based Cathode Catalysts for Polymer Electrolyte Fuel Cells, Fig. 4 (**a**) Auger electron spectroscopy of as-sputtered and annealed Pt_3Ni. (**b**) Low-energy ion-scattering spectra of the same two surfaces, also shown is a schematic picture. (**c**) Cyclic voltammetry of Pt and two Pt_3Ni surfaces at 293 K in 0.5 M H_2SO_4 and 0.1 M $HClO_4$ (Ref. [28])

reduction of catalyst loading without loss of PEFC performance. The commercially available PtCo/C system provides MEA measurement values of specific and mass activity close to the targets set by the US Department of Energy for automotive applications, for example, 1.2 mA cm^{-2}_{Pt} and 0.39 Am g^{-2}_{Pt} at 0.9 V_{SHE} [25]. Studies on the electrochemical stability of Pt alloys under PEFC operation show contradictory results. Some groups found an improved durability [26] whereas others reported accelerated catalyst degradation [27]. Contrasting results in the literature arise from the strong influence of several variable parameters

(composition, particle size, and shape), which make it difficult to draw a definitive conclusion on the performance of Pt-alloy supported nanoparticles. As described above, thin-film single-crystal electrodes can serve as valuable model systems to understand the effect of structural aspects such as single-crystal facet orientation, size, and composition on the ORR activity. Studies on model electrodes have shown that while as-sputtered Pt-alloy catalysts present randomly distributed Pt atoms on the surface, annealed samples exhibit a coordinated pure "Pt skin" (see Fig. 4) [28, 29]. On the surface of these Pt-skin alloys, ORR proceeds via the same

reaction mechanism described above for pure Pt, but the cyclic voltammetry in acid electrolytes shows a shift in the onset of oxide formation towards more positive potentials (up to 50 mV). This finding indicates that Pt-alloying leads to a fundamental change in the adsorption coverage of OH spectator species (i.e., the $(1 - \Theta_{ads})$ term in Eq. 4) [28].

Compared to pure Pt, the Pt-skin alloys show a shift in the d-band center which influences both the metal bond strength and the adsorption of the oxygenated spectators [17, 29]. For the Pt-skin alloys, the increase in the 5d vacancies results in an increase of the 2p electron donation from O_2 to the catalyst, leading to a weakening of the O–O bond compared to pure Pt. Given also the structure sensitivity of Pt to adsorbed anions, the synergy between the optimum in the surface crystal structure and electronic properties led to the highest catalytic activity ever reported to the best of our knowledge [29]. The ORR activity at 0.9 V_{RHE} for $Pt_3Ni(111)$ skin is about 1 order of magnitude higher than Pt(111) single crystal and about 90 times higher than a standard commercial dispersed Pt/C in comparative RDE measurements [29]. On the basis of these findings, a breakthrough in catalyst development would be the development of nanocatalysts able to reproduce the $Pt_3Ni(111)$ skin structure. Recently, truncated-octahedral Pt_3Ni particles with predominantly (111) facets were synthesized, showing activity values up to four times those of commercial Pt/C [30]. New results from Carpenter et al. demonstrated the synthesis and also high activity of PtNi-octaeder catalysts matching the aforementioned DOE targets by increasing the specific activity by a factor of 5 [31]. To mimic the Pt-alloy skin structure, electrochemical surface dealloying concept has been also proposed. The latter consists in a selective electrodissolution of non-noble metal atoms from bimetallic precursors in order to achieve a core–shell structure with a Pt-rich shell and a poor alloy particle core [24]. Increase in ORR activity (about three to sixfold) has been reported after Cu or Co dealloying from PtCu/C and PtCo/C, respectively, compared to Pt/C.
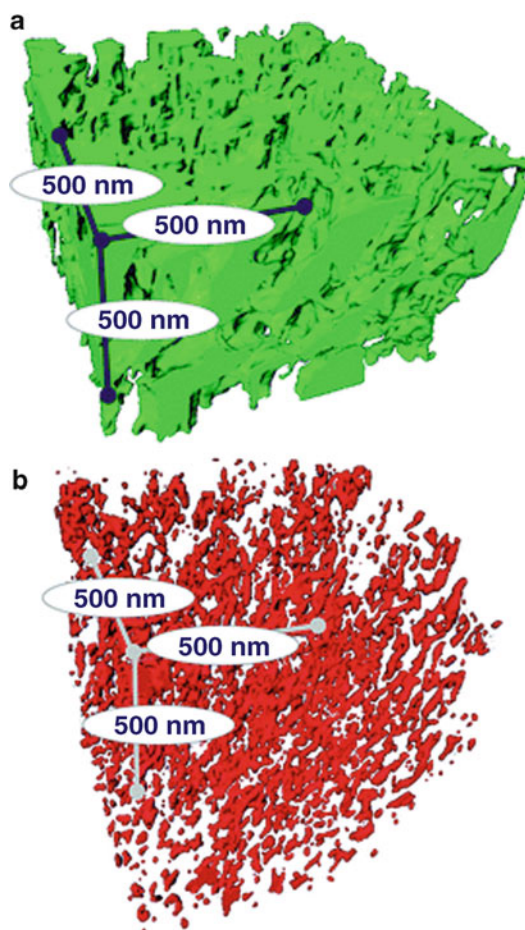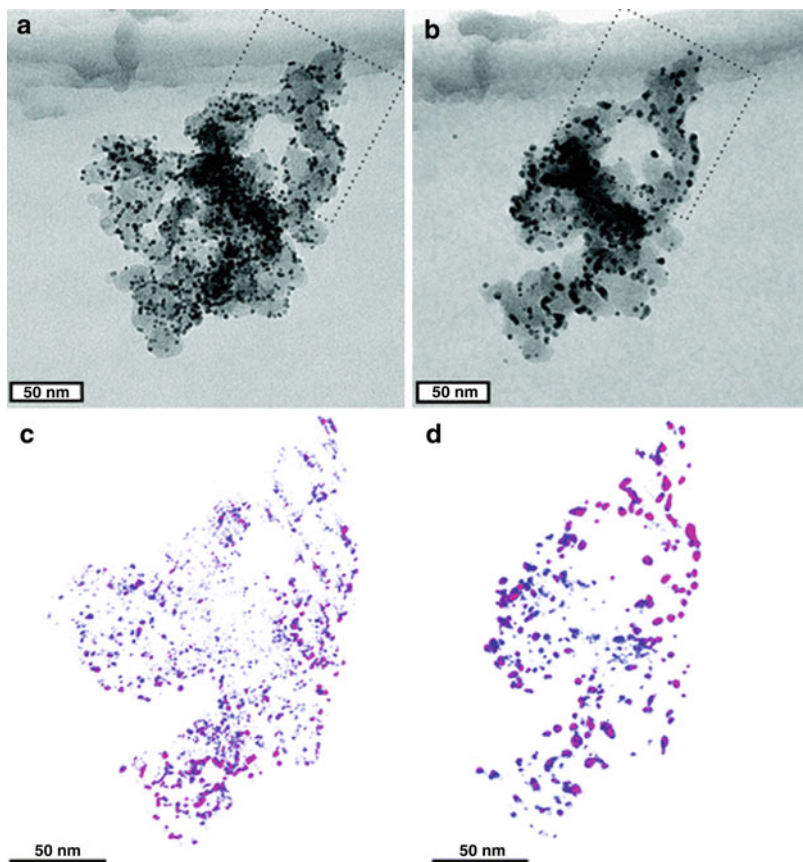
Platinum-Based Cathode Catalysts for Polymer Electrolyte Fuel Cells, Fig. 5 3D pore structure of the pristine cathode catalyst layer (**a**) and after 1,000 start/stop cycling (**b**). The *colored phase* represents the pore structure (Ref. [32])

Corrosion Issues

To reach the requirements of performance and durability for both automotive and stationary PEFC applications [20], catalyst durability has become an important issue both for of academic and industrial R&D. Cathode degradation in operating PEFCs mainly occurs under transient conditions, leading both to Pt dissolution/degradation and carbon-support corrosion. At typical operational pH conditions and above ~0.9 V, two main mechanisms lead to Pt degradation: (i) diffusion of dissolved Pt species

towards the electrolyte membrane where they are chemically reduced by crossover hydrogen and then precipitated, leading to a loss of electrically connected Pt particles, and (ii) Ostwald ripening of Pt inside the cathode electrode leading to a loss of Pt surface area due to nanoparticle growth. Regarding the durability of carbon support, even though carbon oxidation reaction can thermodynamically occur at potential as low as 0.206 V_{SHE}, due the sluggish kinetic of this reaction, carbon corrosion represents only a minor contribution to the cell degradation under steady-state operation. However, the corrosion becomes significantly accelerated during start/stop cycling due to the propagation of a hydrogen/air front through the anode compartment which leads to elevated potentials at the cathode (up to 1.5 V). Carbon-support corrosion leads to the so-called cathode thinning caused by

loss of carbon void volume, which results in an increased oxygen diffusion resistance and loss of Pt surface area. Figure 5 shows morphology changes visualized by 3D-rendering SEM micrographs of Pt/C catalyst slices before and after 1,000 start/stop cycling [32]. The effect of start/stop cycling (3,600 cycles between 0.4 and 1.4 V_{SHE}) on the surface area of Pt catalyst is shown in Fig. 6 [33].

To improve the PEFC cathode durability, both materials and system approaches have been proposed in the last years. From the system point of view, improvements in cathode durability can be achieved by minimizing the residence time of the hydrogen–air front in the anode compartment. On the materials side, Pt alloys have shown higher durability compared relative to Pt-based electrodes [34]. However, since transition metal reduction potential is below that of hydrogen,

once dissolved they will remain in the electrolyte membrane, leading to H^+ exchange and reduction of the fuel cell performance. To reduce start/stop degradation of the catalyst support, graphitized carbon particles have been proposed as alternative to carbon-black, showing improved durability compared to the latter but also smaller surface area than carbon-black (Table 1) [4]. Furthermore, since the support is still based on carbon materials, the oxidation reaction is only delayed but not completely avoided. A more straightforward approach to completely prevent carbon corrosion consists in replacing carbon-based supports with more stable supports or in using unsupported Pt catalysts. In the last years, a growing number of publications report the use of carbides, nitrides, or conductive oxides as alternative Pt supports. Improved durability has been obtained for WC compared to Vulcan XC-72R over 100 cycles between 0 and 1.4 V [35]. However, carbides as well as nitrides compounds are still thermodynamically unstable under the oxidative conditions of a PEFC cathode. Therefore, their oxidation is expected after long cycling leading to a loss of their electronic conductivity and surface area. Differently, doping binary oxides and using advanced synthesis methods can lead to stable materials under the most relevant PEFC cathode conditions with high electronic conductivity and high surface area. Pt supported on $Mo_{0.3}Ti_{0.7}O_2$ have shown improved durability as well as activity towards ORR compared to commercial Pt/C [36]. After 5,000 potential cycling at room temperature between 0 and 1.1 V, $Pt/Mo_{0.3}Ti_{0.7}O_2$ showed a decrease of activity at 0.9 V of 8 %, while the activity of Pt/C and PtCo/C decreased of 50.6 % and 25.8 %, respectively, under in the same experimental conditions. Under long stability test (10,000 potential cycling between 0.3 and 1.3 V_{RHE}), Pt/SnO_2 have showed only a slight decrease of the electrochemical surface area, while strong degradation was observed for Pt/C catalyst prepared and tested with the same procedure [37]. Furthermore, under fuel cell tests Pt/SnO_2 showed similar performance than Pt/C catalyst. A different non-carbon catalyst support developed by 3M is based on an oriented array of
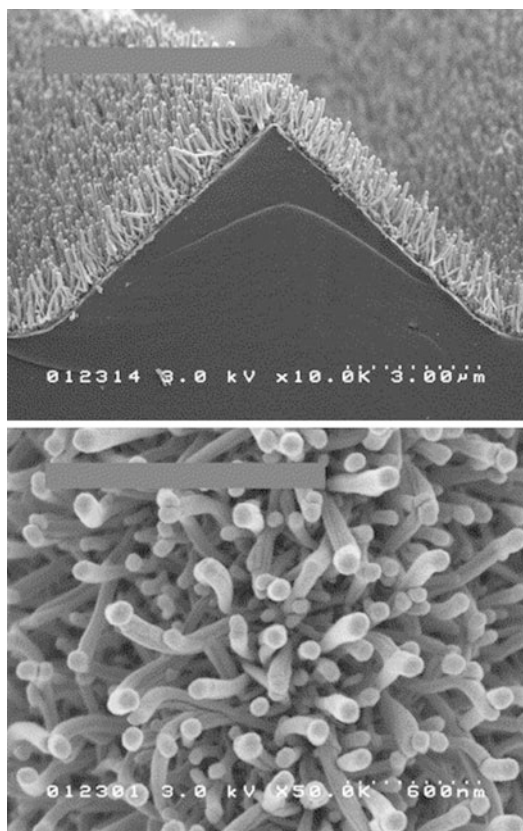
Platinum-Based Cathode Catalysts for Polymer Electrolyte Fuel Cells, Fig. 7 Scanning electron micrographs of typical NSTF catalysts as fabricated on a microstructured catalyst transfer substrate, seen (*top*) in cross section with original magnification of ×10,000, and (*bottom*) in plain view with original magnification of ×50,000 (Ref. [38])

organic whiskers, with a length below 1 mm, a diameter of about 50 nm, and a number density of about 30–40 whiskers mm^{-2} [25]. The complete catalyst is achieved by coating the whisker structure with the desired catalyst thin film by physical vapor deposition or magnetron sputtering (see Fig. 7) [38]. These nanostructured thin-film (NSTF) catalysts present for the same catalyst loading significantly lower electrochemical surface area compared to conventional Pt/C catalysts; but the high catalyst utilization of almost 100 % and negligible losses within the catalyst layer lead to ten times higher area-specific activity and 50 % higher mass activity

than conventional Pt/C. Furthermore, NSTF catalysts are much more resistant to loss of surface area from high voltage cycling than Pt/C. It was reported that while Pt/C loses 90 % of the initial surface area in 2,000 cycles between, a NSTF-Pt catalyst asymptotically approached a maximum of 33 % surface area loss in 9,000 cycles between [38].

Conclusions and Future Directions

In the view of a sustainable energy system, more and more attention has been directed towards the development of efficient energy conversion systems such as PEFCs. However, in order to achieve a widespread commercialization, still cost and durability issues must be solved. In the last decades, system optimization and fundamental understanding of the ORR mechanism at the PEFC cathode have led to a drastic reduction of the Pt loading and thus of the cost system. On the basis of the findings achieved so far, a breakthrough in catalyst development would be the production of nanocatalysts able to reproduce the structure and electronic properties of the $Pt_3Ni(111)$ model electrodes. On the durability side, carbon-support replacement represents an urgent target to achieve. Promising results have been obtained using oxide-based supports; in addition this strategy can open new possibilities also in the search for more active catalysts because the establishment of a metal-support interaction may lead to a further activity enhancement.

Cross-References

▶ Electrocatalysis - Basic Concepts, Theoretical Treatments in Electrocatalysis via DFT-Based Simulations
▶ Oxygen Reduction Reaction in Acid Solution
▶ Platinum-Based Anode Catalysts for Polymer Electrolyte Fuel Cells
▶ Polymer Electrolyte Fuel Cells (PEFCs), Introduction

References

1. Srinivasan S, Manko DJ, Koch H, Enayetullah MA, Appleby AJ (1990) Recent advances in solid polymer electrolyte fuel cell technology with low platinum loading electrodes. J Power Sources 29:367–387
2. Raistrick ID (1986) Diaphragms, separators, and ion exchange membranes. In: Van Zee JW, White RE, Kinoshita K, Burney HS (eds) The Electrochemical Society softbound proceeding series, Pennington
3. Taylor EJ, Anderson EB, Vilambi NRK (1992) Preparation of high-platinum-utilization gas diffusion electrodes for proton-exchange-membrane fuel cells. J Electrochem Soc 139:L45–L46
4. Yu PT, Gu W, Zhang J, Makharia R, Wagner FT, Gasteiger HA (2009) Carbon support requirements for highly durable fuel cell operation. In: Büchi FN, Inaba M, Schmidt TJ (eds) Polymer electrolyte fuel cell durability. Springer, New York
5. Neyerlin KC, Gu WB, Jorne J, Gasteiger H (2007) A study of the exchange current density for the hydrogen oxidation and evolution reactions. J Electrochem Soc 154:B631–B635
6. Wagner FT, Lakshmanan B, Mathias M (2010) Electrochemistry and the future of the automobile. J Phys Chem Lett 1:2204–2209
7. Sepa DB, Vojnovic MV, Damjanovic A (1981) Reaction intermediates as a controlling factor in the kinetics and mechanism of oxygen reduction at platinum electrodes. Electrochim Acta 26:781–793
8. Markovic NM, Schmidt TJ, Stamenkovic V, Ross PN (2001) Oxygen reduction reaction on Pt and Pt bimetallic surfaces: a selective review. Fuel Cells 1:105–115
9. Yeager E (1984) Electrocatalysts for O_2 reduction. Electrochim Acta 29:1527–1537
10. Sidik RA, Anderson AB (2002) Density functional theory study of O_2 electroreduction when bonded to a Pt dual site. J Electroanal Chem 528:69–76
11. Paulus UA, Schmidt TJ, Gasteiger HA, Behm RJ (2001) Oxygen reduction on high-surface area Pt/Vulcan carbon catalyst: a thin-film rotating ring-disk electrode study. J Electroanal Chem 495:134–145
12. Subramanian NP, Greszler TA, Zhang J, Gu W, Makharia R (2012) Pt-oxide coverage-dependent oxygen reduction reaction (ORR) kinetics. J Electrochem Soc 159:B531–B540
13. Grgur BN, Markovic NM, Ross PN (1997) Temperature-dependent oxygen electrochemistry on platinum low-index single crystal surfaces in acid solutions. Can J Chem 75:1465–1471
14. Markovic NM, Gasteiger HA, Grgur BN, Ross PN (1999) Oxygen reduction reaction on Pt(111): effects of bromide. J Electroanal Chem 467:157–163
15. Paulus UA, Schmidt TJ, Gasteiger HA (2003) Poisons for the oxygen reduction. In: Vielstich W, Gasteiger HA, Lamm A (eds) Handbook of fuel cells, vol 2. Wiley, Chichester

16. Norskov JK et al (2004) Origin of the overpotential for oxygen reduction in fuel cell cathode. J Phys Chem B 108:17886–17892

17. Stamenkovic V et al (2006) Changing the activity of electrocatalysts for oxygen reduction by tuning the surface electronic structure. Angew Chem Int Ed 45:2897–2901

18. Peuckert M, Yoneda T, Dalla Betta RA, Boudart M (1986) Oxygen reduction on small supported platinum particles. J Electrochem Soc 133:944–947

19. Kinoshita K (1990) Particle size effects for oxygen reduction on highly dispersed platinum in acid electrolytes. J Electrochem Soc 137:845–848

20. Rabis A, Rodriguez P, Schmidt TJ (2012) Electrocatalysis for polymer electrolyte fuel cells: recent achievements and future challenges. ACS Catal 2:864–890

21. Mayrhofer KJJ, Blizanac BB, Arenz M, Stamenkovic V, Ross PN, Markovic NM (2005) The impact of geometric and surface electronic properties of Pt-catalysts on the particle size effect in electrocatalysis. J Phys Chem B 109:14433–14440

22. Gasteiger HA, Kocha SS, Sompalli B, Wagner FT (2005) Activity benchmarks and requirements for Pt, Pt-alloy, and non-Pt oxygen reduction catalysts for PEMFCs. Appl Catal Environ 56:9–35

23. Wei ZD et al (2008) Electrochemically synthesized Cu/Pt core-shell catalysts on a porous carbon electrode for polymer electrolyte membrane fuel cells. J Power Sources 180:84–91

24. Koh S, Strasser P (2007) Electrocatalysis on bimetallic surfaces: modifying catalytic reactivity for oxygen reduction by voltammetric surface dealloying. J Am Chem Soc 129:12624–12625

25. Debe MK (2012) Electrocatalyst approaches and challenges for automotive fuel cells. Nature 7:43–51

26. Yu P, Pemberton M, Plasse P (2005) PtCo/C cathode catalyst for improved durability in PEMFCs. J Power Sources 144:11–20

27. Zignani C, Antolini E, Gonzalez ER (2008) Evaluation of the stability and durability of Pt and Pt-Co/C catalysts for polymer electrolyte membrane fuel cells. J Power Sources 182:83–90

28. Stamenkovic V, Schmidt TJ, Ross PN, Markovic NM (2002) Surface composition effects in electrocatalysis: kinetics of oxygen reduction on well-defined Pt_3Ni and Pt_3Co alloy surfaces. J Phys Chem B 106:11970–11979

29. Stamenkovic VR et al (2007) Improved oxygen reduction activity on $Pt_3Ni(111)$ via increased surface site availability. Science 315:493–497

30. Wu JB et al (2010) Truncated octahedral Pt_3Ni ORR electrocatalysts. J Am Chem Soc 132:4984–4985

31. Carpenter MK, Moylan TE, Kukreja RS, Atwan MH, Tessema MM (2012) Solvothermal synthesis of platinum alloy nanoparticles for oxygen reduction electrocatalysis. J Am Chem Soc 134:8535–8542

32. Schulenburg H, Schwanitz B, Linse N, Scherer GG, Wokaun A (2011) 3D imaging of catalyst support corrosion in polymer electrolyte fuel cell. J Phys Chem C 115:14236–14243

33. Meier JC et al (2012) Degradation mechanisms of Pt/C fuel cell catalysts under simulated start–stop conditions. ACS Catal 2:832–843

34. Hartnig C, Schmidt TJ (2011) Simulated start–stop as a rapid aging tool for polymer electrolyte fuel cell electrodes. J Power Sources 196:5564–5572

35. Chhina H, Campbell S, Kesler O (2007) Thermal and electrochemical stability of tungsten carbide catalyst supports. J Power Sources 164:431–440

36. Ho VTT et al (2011) Nanostructured $Ti_{0.7}Mo_{0.3}O_2$ support enhances electron transfer to Pt: high-performance catalyst for oxygen reduction reaction. J Am Chem Soc 133:11716–11724

37. Masao A, Noda S, Takasaki F, Ito K, Sasaki K (2009) Carbon-Free Pt electrocatalysts supported on SnO_2 for polymer electrolyte fuel cells. Electrochem Solid State Lett 12:B119–B122

38. Debe MK, Schmoeckel AK, Vernstrom GD, Atanasoski R (2006) High voltage stability of nanostructured thin film catalysts for PEM fuel cells. J Power Sources 161:1002–1011

Polarography

Michael Heyrovsky
J. Heyrovsky Institute of Physical Chemistry of the ASCR, Prague, Czech Republic

In its primary meaning, polarography is the method of potential-controlled *electrolysis with dropping mercury electrode*, usually of drop time 3–5 s, as working electrode. The physicochemical properties of mercury are specially advantageous in electrochemistry. As liquid element it can be prepared in the highest purity by repeated distillation, its surface is homogeneous and isotropic on atomic scale. The dropping renews spontaneously the electrode surface irrespective of processes that could have occurred on it, which makes the results of measurements highly reproducible. Mercury has a high surface tension, and in contact with a solution, many dissolved species have the tendency to adsorb on its surface, depending on its potential. In electrochemistry mercury has of all metals the highest hydrogen overvoltage which gives mercury electrodes wide potential range for following electrode reactions

in negative direction. On the other hand, in a relatively narrow range of positive potentials, metallic mercury dissolves into ions which may interact with components of the solution thus enabling their determination. In general, polarography is better suited for following cathodic than anodic processes. In order to keep the resistance of the polarographic cell as low as possible, the electrolyzed solutions should contain a supporting electrolyte, usually of 0.1–1 M/l concentration. In the simple *"classical" polarography* the mean current flowing through the cell with dropping mercury electrode is recorded as function of direct potential applied to the dropping electrode with respect to an electrode maintaining constant potential, the reference electrode. The presence of an electroactive substance shows on the polarographic curve usually in the form of a concentration-dependent current increase to a limiting value, or "wave," in a definite potential range.

Systematic experimental research resulted in distinction of several basic kinds of polarographic currents which theoreticians formulated by quantitative equations for their instantaneous time course and then for their mean time course during the drop life:

- *Charging current* given by charging electrical double layer of the dropping electrode by ions from the solution
- *Diffusion current* given by the rate of diffusion of the electroactive species from solution to the surface of the dropping electrode
- *Kinetic current* given by the rate of a chemical reaction producing the electroactive species in the vicinity of the electrode
- *Catalytic current* given by the rate of a catalytic process generating the electroactive species near or at the electrode surface
- *Adsorption current* given by the rate and extent of adsorption of electroactive and surface active species from the solution at the surface of the electrode.

Besides the mentioned basic currents on polarographic curves, *current maxima can occur*, according to experimental conditions either "of the first kind"(tapering shape) or "of the second kind"(rounded shape). "Classical" polarography

has been used for experimental research in electrochemistry or for qualitative and quantitative electroanalytical determinations, its advantage being simple operations and a relatively cheap apparatus. It allows to analyze electroactive species down to 10^{-6} M/l concentration, in case of catalytic currents even lower. In analytical practice after recording polarographic curves, the *"polarometric" (*or *"amperometric")* *titrations* can be introduced with dropping mercury electrode maintained at constant potential of the limiting current, indicating actual concentration of the electroactive substance.

The "classical" polarography has been fully developed and internationally widely utilized by the nineteen forties. The technical progress in the middle of twentieth century led to various modifications of the primary simple method. In *"alternating current polarography"* on the direct voltage applied to the cell is superimposed alternating voltage of small amplitude, and instead of direct current the resulting alternating current is recorded, producing current peaks instead of "waves" on the current-voltage curves; the peaks apart of being the measure of concentration indicate the occurrence of possible adsorption/desorption processes at the electrode surface. In *"square-wave polarography"* the small alternating voltage superimposed on the polarizing voltage is of rectangular shape and the instantaneous current is measured at the end of each individual voltage pulse, i.e., with lowered charging current component – this considerably increases the sensitivity of the method. The fact that the instantaneous charging current at the dropping mercury electrode decreases with time of the drop life has been also utilized in *"tast polarography"* where the total polarographic current is recorded before the drop falls off, i.e., when the charging current component of the total current is minimized and the sensitivity for diffusion current is thus increased. In *"pulse polarography"* the individual drops of the dropping mercury electrode are polarized by gradually increasing pulses of constant voltage, while the current is measured at the end of the drop life when the charging current component is negligible, the result being again increased sensitivity. *"Differential pulse*

polarography" records differences between instantaneous currents at the ends of subsequent drops which produces polarographic curves with current peaks in place of waves, also with high sensitivity. Besides the abovementioned methods, many other modifications of polarography have been described.

In order to speed up the method of classical polarography instead of recording current-voltage curves graphically, the cathode ray oscilloscope was used providing their optical display. Because in the *"oscillographic polarography"* the time scale is different than in the classical method, the shape of the current-voltage curves is different and hence the theory of classical polarography cannot be directly applied. It is more so in the *"alternating current oscillographic polarography,"* a method belonging to chronopotentiometry, where the dropping electrode is polarized by alternating current and the curves of potential versus time and of the derivative of potential/time dependence versus potential are followed; as the experimental conditions are different, the results considerably differ, qualitatively and quantitatively, from those of classical polarography.

When the dropping of the mercury electrode is stopped and the current-potential curve is recorded with one stable hanging mercury drop, the method formally belongs to *voltammetry* – according to accepted terminology polarography is voltammetry with dropping mercury electrode. However, as long as the hanging mercury drop is maintained as working electrode, that particular voltammetry can be considered as polarography in wider sense because of similar background conditions. If the potential scan is applied to the electrode in one direction, it is **linear voltammetry**, and if it is applied in one direction and back, it is **cyclic voltammetry**. Cyclic voltammetry offers a simple check of reversibility of an electrode process – a direct comparison of the cathodic and anodic reaction. In analytical applications the voltammetry with hanging mercury drop has the advantage over classical polarography in that an active species can be accumulated at the electrode under constant potential for some time and then electrochemically determined during a following

voltage scan – by that *voltammetric "stripping"* method an electroactive species can be determined in nanomolar and lower concentrations.

If the cell with hanging mercury drop electrode is polarized by constant current and the time changes of the electrode potential are recorded, the thus introduced *chronopotentiometric method* provides effects which can be interpreted on the basis of experience with polarography and which extend polarographic results further. That is, for example, the case with catalytic evolution of hydrogen. In current-controlled electrolysis the electrode potential changes at the rate given by the intensity of the polarizing current – in this way at mercury electrode the negative potentials are reached in general faster in chronopotentiometry than in voltammetry and the catalysis of hydrogen evolution occurs at less negative potentials. A particularly well-developed signal of hydrogen catalysis, called *"peak H,"* is produced in *constant current derivative stripping chronopotentiometry* (or chronopotentiometric stripping analysis, CPSA). This "peak H" is used in bioelectrochemistry to study and determine biomacromolecules such as peptides, proteins, nucleic acids, or polysaccharides.

After decades of development in science and technology, polarography is being generally understood not as a single research method but rather as a field of electrochemistry based on the unique properties of mercury electrodes.

Cross-References

▶ Mercury Drop Electrodes
▶ Polarography
▶ Potentiometry
▶ Voltammetry of Adsorbed Proteins

References

1. Schmidt H, Stackelberg M v (1964) Modern polarographic methods. Academic, New York
2. Meites L (1965) Polarographic techniques, 2nd edn. Wiley, Interscience, New York
3. Kalvoda R (1965) Techniques of oscillographic polarography, 2nd edn. Elsevier, SNTL, Amsterdam

4. Heyrovský J, Kůta J (1966) Principles of polarography. Academic, New York
5. Heyrovský J, Zuman P (1968) Practical polarography. Academic, London/New York
6. Bond AM (1980) Modern polarographic methods in analytical chemistry. Marcel Dekker, New York
7. Baizer MM, Lund H (1983) Organic electrochemistry. Marcel Dekker, New York
8. Meites L, Zuman P, Rupp EB, Fenner TL, Narayanan A (1983) Handbook series in organic electrochemistry, vol I-VI. CRC, Boca Raton
9. Meites L, Zuman P, Rupp EB, Fenner TL, Narayanan A (1986) Handbook series in inorganic chemistry, vol I-VII. CRC, Boca Raton
10. Brainina KZ, Neyman E (1993) Electroanalytical stripping methods. Wiley-Interscience, New York
11. Crow DR (1994) Principles and applications of electrochemistry, 4th edn. Blackie Academic Professional, London
12. Galus Z (1994) Fundamentals of electroanalysis, 2nd edn. Elis Horwood/Polish Scientific Publishers PWN, New York/Warsaw
13. Kissinger PT, Heineman WR (1996) Laboratory techniques in electroanalytical chemistry. Marcel Dekker, New York
14. Vanýsek P (1996) Modern techniques in electroanalysis. Wiley, New York
15. Bard AJ, Faulkner LR (2001) Electrochemical methods, 2nd edn. Wiley, New York
16. Scholz F (2002) Electroanalytical methods. Springer, Berlin
17. Paleček E, Scheller F, Wang J (eds) (2005) Electrochemistry of nucleic acids and proteins. Elsevier, Amsterdam
18. Wang J (2006) Analytical electrochemistry, 3rd edn. Wiley, New York

Pollutants in Water - Electrochemical Remediation Using Ebonex Electrodes

Nigel J. Bunce and Dorin Bejan
Department of Chemistry, Electrochemical Technology Centre, University of Guelph, Guelph, ON, Canada

Introduction

Ebonex$^{®}$ is the trade name for an electrically conductive ceramic suboxide of titanium, having the approximate composition Ti_4O_7 and conductivity comparable to that of carbon.

Early research on Ebonex, including its discovery in 1981, has been described by Hayfield, who noted that an impetus for its development was to find an electrode material that would be resistant to highly corrosive environments [1]. As a ceramic material, Ebonex powder can be sintered into a variety of shapes and also porosities [2].

Ti_4O_7 is one of a wide range of defined compositions TiO_x ($0.5 < \times < 2$); those between that of Ebonex ($\times = 1.75$) and $\times = 1.9$ have a triclinic crystal structure and are known as Magnéli phases Ti_nO_{2n-1}. Titanium dioxide cannot be reduced to the metal with hydrogen, carbon, or carbon monoxide but is reduced to TiO_x suboxides at $\sim$1,200–1,300 °C, usually with hydrogen.

To date, the most frequent application of Ebonex (named for its black color) has been in cathodic protection, especially of the steel rods used to reinforce concrete [1]. There is an extensive literature on Ebonex coated with various other materials (noble metals, carbon, lead dioxide), whose deposition is favored by Ebonex's high overpotential for hydrogen and oxygen evolution. Applications for coated Ebonex include batteries, fuel cells, and dechlorination of chlorinated pollutants [2], but the focus of this article is the use of uncoated Ebonex as an electrode material for electrolysis of pollutant substances, most often for electrochemical oxidation.

Concepts

Ebonex has many of the properties of a nonactive anode, at which reactive hydroxyl species are produced upon oxidation of water. Most nonactive anodes are based on main group elements, such as PbO_2, SnO_2, and boron-doped diamond (BDD), whereas Ebonex is based on titanium, a first-row transition metal.

The mechanistic distinction between active and non-active anodes is considered elsewhere in this encyclopedia [3]. Both types of anodes act indirectly, by electrochemical oxidation of water to reactive anode-bound species that can bring about chemical oxidation of a substrate.

At an anode **A**, the relevant reactions are given by Eqs. (1) and (2):

$$A + H_2O \rightarrow A{\sim}{}^{\bullet}OH + H^+ + e^- \qquad (1)$$

$$A{\sim}{}^{\bullet}OH \rightarrow A = O + H^+ + e^- \qquad (2)$$
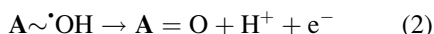
At a non-active anode, the sorbed hydroxyl radicals ("physisorbed active oxygen") from Reaction (1) can initiate free radical (one-electron) reactions of oxidizable substrates. Often, this leads to complete mineralization of organic materials (also called electrochemical combustion).

Active anodes are dimensionally stable anodes based on noble metal oxides such as RuO_2, IrO_2, and Pt ($=PtO_x$ under anodic polarization), at which the initially formed $A \sim {}^{\bullet}OH$ is readily oxidized further to give chemisorbed active oxygen (Eq. 2). Oxidations at active anodes rarely give efficient mineralization of the substrate. At both types of anode, the parasitic production of molecular O_2 lowers the current efficiency for substrate oxidation.

Ebonex has a wide range of potentials over which water is stable (approximately -1 V to $+ 2.7$ V vs. Ag/AgCl in aqueous sulfuric acid) [2], but shifted significantly in the expected negative direction in base [4]. Most relevant to the present perspective is the similarity of the anodic range to that of boron-doped diamond, for which values of the overpotential for the OER are ${\sim}1.3$ V [3].

Typical evidence that Ebonex functions as a non-active anode is that when Ebonex was compared with different anodes for oxidations of acetaminophen (AP) and p-benzoquinone (BQ), Ebonex behaved much more like BDD (non-active) than like Ti/IrO_2-Ta_2O_5 (active) in terms of the low yield of BQ formed from AP, and in the rates of transformation versus complete mineralization [5, 6]. The oxidation of coumarin to the fluorescent product, 7-hydroxycoumarin, is also a useful qualitative probe for the presence of hydroxyl species in these oxidations [7, 8]. The activity of Ebonex is consistently less than that of BDD, suggesting a lower concentration of hydroxyl species. In competition experiments involving substrates that are resistant to direct oxidation but susceptible to hydroxyl radical attack, substrate loss was slower at Ebonex anodes than at BDD under similar conditions but with less discrimination between substrates, suggesting that at Ebonex the hydroxyl radicals are bound less tightly to the anode [7].

The behavior of Ebonex is more complicated than that of the conventional non-active anodes PbO_2, SnO_2-Sb_2O_5, and BDD. Passivation towards oxygen evolution occurs at high current density, because the surface becomes oxidized to less conductive Magnéli phases or even to TiO_2 [9]. Bejan et al. [6] found that when a pair of Ebonex electrodes was polarized for a period of time and then the current was interrupted, depolarization occurred with evolution of gases, indicating oxidation or reduction of the Ebonex surface upon anodic or cathodic polarization, respectively. This is consistent with the working paradigm that the non-active behavior of an Ebonex anode is accompanied by oxidation of the Magnéli phase towards the composition TiO_2. The gradual loss of anode activity occurs because the $A = O$ species from Ebonex fails to oxidize added substrates, making the surface oxidation essentially irreversible, contrasting typical active anodes such as Ti/RuO_2. Recovery of the anode performance can be achieved by reducing the inactive deposit back to an active form. This paradigm may parallel observations by Beck and Gabriel [10] that Ti/TiO_2 ceramic materials can be made conducting under cathodic polarization, suggesting the possible electrochemical formation of the Magnéli phase. The resulting surface can catalyze the reduction of other substrates.

Consistent with this explanation for anode passivation, when an Ebonex anode was used for repeated oxidations of p-nitrosodimethylaniline, the rate constant for loss of the substrate gradually decreased; partial anodic activity was restored by cathodic polarization of the deactivated anode [6]. In the oxidation of sulfide ion, a constituent of geothermal sour brines, the gradual loss of activity of an Ebonex anode was overcome by employing periodic polarity reversal in order to reduce the over-oxidized surface layer back to the Magnéli phase [11]. Sulfide was

oxidized to sulfate with high chemical yield but with current efficiency ~50 % compared with a quantitative current efficiency at BDD.

Results

Initial voltammetric studies had seemed to suggest that Ebonex is inert towards both oxidation and reduction of added substrates. The well-known ferrocyanide/ferricyanide couple shows smaller currents at Ebonex than at, e.g., platinum, with the oxidation and reduction currents shifted to more positive and more negative potentials, respectively. This evidence for slow electron transfer indicates that high overpotentials are needed to drive electrolysis at Ebonex [9]. Based on voltammetry, Grimm et al. [12] concluded that Ebonex was inert towards the oxidation of phenol, because the addition of 5 mM phenol to supporting electrolyte caused only a small current increase in the potential range of water stability. Likewise, Scott and Cheng [13] reported no voltammetric oxidation current for oxidation of oxalic acid at an Ebonex anode; however, they did observe an increase in the cell voltage upon prolonged polarization, consistent with gradual oxidative inactivation of the Ebonex anode.

Smith et al. [14] had reported that the porosities of porous and hardened Ebonex were 12–15 % and <2 %, respectively, and that the voltammetric behavior of Ebonex in terms, for example, of the potential range of water stability is highly dependent on porosity [9]. Recently, Kitada et al. [15] reported selective preparation of macroporous monoliths of Magnéli phases having widely different porosities and bulk densities.

The idea that porous Ebonex might be used as a flow-through permeable electrode, originally suggested by Chen et al. [16], was exploited by Zaky and Chaplin [17], who used a porous, cylindrical Ebonex anode as a reactive electrochemical membrane for the oxidation of several model compounds. These included oxalic acid and p-.methoxyphenol that might have been expected to be inert to oxidation based on the

previous voltammetry studies [12, 13] – for example, well-defined oxidation currents were obtained with p-methoxyphenol at slow sweep rates [17]. Under electrolysis conditions, contaminated influent water was passed through the cylinder, while a current was passed between the cylinder (anode) and a central stainless steel rod (cathode). With oxalic acid as substrate, the concentration of substrate in the effluent from the cylinder and in the permeate both decreased with the applied current, essentially to zero in the permeate. p-Methoxyphenol could also be remediated, in terms of both the substrate concentration and the COD. At low current densities (=low anode potential), a significant proportion of the COD removed was associated with material adsorbed to the anode, which is typical of anode fouling by phenolic compounds upon electrochemical oxidation. Fouling was eliminated at an anode potential >2 V versus SHE, consistent with an indirect oxidation mechanism, corresponding to the production of hydroxyl radicals under these conditions.

Scialdone et al. [18] compared Ebonex with several other anodes for the mineralization of 1,2-dichloroethane at pH 2. In this application, Ebonex performed poorly in comparison with BDD (CE ~12 % vs. ~50 %) and no better than active anodes such as Pt and $Ti/IrO_2\text{-}Ta_2O_5$. Whether the current yield could be improved by periodic polarity reversal was not studied.

Nowack et al. [19] used Magnéli phase TiO_x for the oxidation of cyanide ion to cyanate (which hydrolyzed to ammonia and carbonate) at pH ~13. From initial cyanide concentrations in the range 0.5–2.0 g L^{-1}, the specific energy ranged from 12 to 260 kWh per kg cyanide, depending on the extent of remediation of cyanide.

Chen et al. [16] achieved complete mineralization of trichloroethylene at an Ebonex anode, the chief products being CO_2 (and about 10 % CO), chloride, and chlorate. The authors determined the fractions of the anodic current carried out to form O_2, carbon oxides, and ClO_3^- and observed the expected relationship that the current efficiency for TCE oxidation decreased at the expense of that for O_2 with increasing anode potential. Spin trapping experiments were

carried out to search for hydroxyl radical intermediates, although the identity of the spin adduct was later challenged as not definitive for HO$^\bullet$ [7].

Considering the activity of Ebonex as a cathode, it was found [20, 21] that the resistance of Ebonex was so great towards the reduction of sulfite ions that sulfite could be oxidized to sulfate using combinations of Ebonex cathode with various anodes even in undivided cells. Chen et al. [22] likewise reported that uncoated Ebonex was inactive towards the reductive dechlorination of trichloroethylene.

When Ebonex cathodes were used for the reduction of aqueous nitrate ion, comparable amounts of ammonia and elemental nitrogen were formed, as at many other cathodes [23]. Complete denitrification was achieved by coupling the electrochemical reduction to oxidation of ammonia in the presence of chloride ion, which was oxidized to hypochlorite at the anode. The chemical oxidation of ammonia to nitrogen by hypochlorite corresponds to breakpoint chlorination in water treatment. The advantage of Ebonex in this application is its ability to undergo periodic polarity reversal, in order to avoid fouling of the cathode by carbonate deposits in hard water. The optimum experimental arrangement comprised a pair of Ebonex electrodes whose polarity was periodically reversed, along with a "full time" anode (e.g., Ti/IrO$_2$-Ta$_2$O$_5$) to optimize the oxidation of chloride to hypochlorite. This procedure parallels an early application of Ebonex electrodes for swimming pool electrochlorinators, which also involve electrochemical hypochlorination, with polarity reversal to avoid the accumulation of hard water scale [1].

Advantages and Future Directions

Ebonex electrodes have been used for electrolysis of both organic and inorganic pollutants, as anodes or as cathodes. Ebonex is produced from inexpensive starting materials (titania and hydrogen) and has excellent corrosion resistance and the ability, as a conductive ceramic, to be fabricated into a variety of shapes. Mechanistically, Ebonex has characteristics of both active and non-active anodes – it furnishes reactive hydroxyl radicals but also undergoes surface oxidation. However, the "higher oxides" produced from Ebonex are more oxidized Magnéli phases than Ti$_4$O$_7$ and have little or no oxidizing power towards added substrates. In comparison with BDD as a non-active anode, Ebonex exhibits similar mineralization ability but with lower current efficiency, and its activity must be maintained by employing periodic polarity reversal with the combination Ebonex anode–Ebonex cathode in order to reduce the over-oxidized Ti$_4$O$_7$ phase back to its reactive form. Polarity reversal appears to be a promising application for the remediation of aqueous wastes that contain hardness cations. Unlike BDD, which tends to be degraded at high pH, Ebonex electrodes can be used in both acidic and alkaline solutions. However, there has been relatively little comparison of Ebonex with other non-active anodes, and its full range of applications is probably yet to be discovered.

References

1. Hayfield PCS (2002) Development of a new material – Monolithic Ti$_4$O$_7$ Ebonex$^®$ Ceramic. Royal Society of Chemistry/Metal Finishing Information Services, Cambridge, UK/Herts
2. Walsh FC, Wills RGA (2010) The continuing development of Magnéli phase titanium sub-oxides and Ebonex$^®$ electrodes. Electrochim Acta 55:6342–6351
3. Bunce NJ, Bejan D (2013) Oxidation of organic pollutants on active and non active anodes. In: Savinell RF, Ota K, Kreysa G (eds) Encyclopedia of applied electrochemistry. Springer
4. Pollock RJ, Houlihan JF, Bain AN, Coryea BS (1984) Electrochemical properties of a new electrode material Ti$_4$O$_7$. Mater Res Bull 19:17–24
5. Waterston K, Wang JW, Bejan D, Bunce NJ (2006) Electrochemical waste water treatment: electrooxidation of acetaminophen. J Appl Electrochem 36:227–232
6. Bejan D, Malcolm JD, Morrison L, Bunce NJ (2009) Mechanistic investigation of the conductive ceramic Ebonex as an anode material. Electrochim Acta 54:5548–5556
7. Bejan D, Guinea E, Bunce NJ (2012) On the nature of the hydroxyl radicals produced at boron-doped diamond and Ebonex anodes. Electrochim Acta 69:275–281

8. Kisacik I, Stefanova A, Ernst S, Baltruschat H (2013) Oxidation of carbon monoxide, hydrogen peroxide and water at a boron doped diamond electrode: the competition for hydroxyl radicals. Phys Chem Chem Phys 15:4616–4624

9. Smith JR, Walsh FC, Clarke RL (1998) Electrodes based on Magnéli phase titanium oxides: the properties and application of Ebonex® materials. J Appl Electrochem 28:1021–1033

10. Beck F, Gabriel W (1985) Heterogeneous redox catalysis at titanium/titanium dioxide cathodes. Reduction of nitrobenzene. Angew Chem 97:765–767

11. El-Sherif S, Bejan D, Bunce NJ (2010) Electrochemical oxidation of sulfide ion in synthetic sour brines using periodic polarity reversal at Ebonex electrodes. Can J Chem 88:928–936

12. Grimm J, Bessarabov D, Maier W, Storck S, Sanderson RD (1998) Sol–gel film-preparation of novel electrodes for the electrocatalytic oxidation of organic pollutants in water. Desalin 115:295–302

13. Scott K, Cheng H (2002) The anodic behaviour of Ebonex® in oxalic acid solutions. J Appl Electrochem 32:583–589

14. Smith JR, Nahle AH, Walsh FC (1997) Scanning probe microscopy studies of Ebonex® electrodes. J Appl Electrochem 27:815–820

15. Kitada A, Hasegawa G, Kobayashi Y, Kanamori K, Nakanishi K, Kageyama H (2012) Selective preparation of macroporous monoliths of conductive Titanium Oxides Ti_nO_{2n-1} (n = 2, 3, 4, 6). J Am Chem Soc 134:10894–10898

16. Chen G, Betterton EA, Arnold RG (1999) Electrolytic oxidation of trichloroethylene using a ceramic anode. J Appl Electrochem 29:961–970

17. Zaky AM, Chaplin BP (2013) Porous substoichiometric TiO_2 anodes as reactive electrochemical membranes for water treatment. Environ Sci Technol 47:6554–6563

18. Scialdone O, Galia A, Filardo G (2008) Electrochemical incineration of 1,2-dichloroethane: effect of the electrode material. Electrochim Acta 53:7220–7225

19. Nowack N, Heger K, Korneli D, Rheindorf A (2005) Oxidation of cyanides in wastewaters (low-concentration region) by fixed-bed electrolysis. Chem Ing Tech 77:1927–1936

20. Scott K, Taama WM (1997) Electrolysis of simulated flue gas solutions in an undivided cell. J Chem Technol Biotechnol 70:51–56

21. Scott K, Cheng H, Taama W (1999) Zirconium and Ebonex® as cathodes for sulphite ion oxidation in sulphuric acid. J Appl Electrochem 29:1329–1338

22. Chen G, Betterton EA, Arnold RG, Ela WP (2003) Electrolytic reduction of trichloroethylene and chloroform at a Pt- or Pd-coated ceramic cathode. J Appl Electrochem 33:161–169

23. Kearney D, Bejan D, Bunce NJ (2012) The use of Ebonex electrodes for the electrochemical removal of nitrate ion from water. Can J Chem 90:666–674

Polyelectrolytes, Films-Specific Ion Effects in Thin Films

Natascha Schelero and Regine von Klitzing
Stranski-Laboratorium, Institut für Chemie, Fakultät II, Technical University Berlin, Berlin, Germany

Introduction

This entry addresses specific ion effects in thin films with thicknesses in the nano- to micrometer range and focuses on the effect of monovalent cations and anions on the structure of thin films. First, thin organic adsorbed films, so-called polyelectrolyte multilayers (PEMs) which are prepared by sequential adsorption of polyanions and polycations on a charged surface [10], are presented. Second, thin liquid (aqueous) films are discussed. These are thin layers of a continuous phase through which the dispersed phase (bubbles, droplets, solid particles) of colloidal dispersions such as foams, emulsions, and suspensions interacts. Both PEMs and liquid films have one thing in common: The amount as well as the type of ions plays a central role in determining the properties of such thin films.
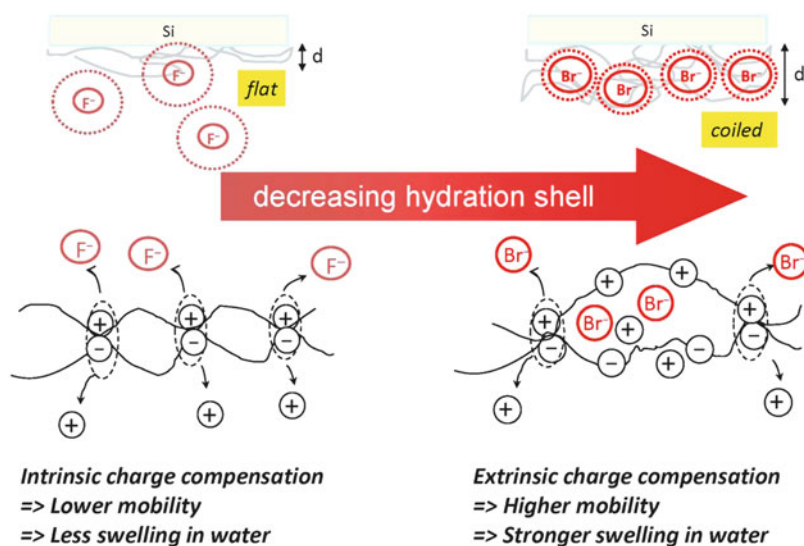
Specific Ion Effects on the Properties of Polyelectrolyte Multilayers

Polyelectrolyte multilayers (PEMs) are prepared by layer-by-layer (LbL) technique, where polycations and polyanions are alternately adsorbed from aqueous solutions [10]. The impact of the amount and type of salt on the structural properties, mobility, and the swelling behavior of polyelectrolyte multilayers has been investigated for more than 10 years [11, 12, 15, 18, 22–24, 28–30, 37, 40].

Dubas and Schlenoff [12] reported for the first time a tendency of increasing PEM thickness with increasing size of monovalent ions, which has been confirmed by several other studies in the meanwhile

Polyelectrolytes, Films-Specific Ion Effects in Thin Films,
Fig. 1 Scheme of the ion-specific effect on the complexation of polyanions and polycations

Intrinsic charge compensation
=> Lower mobility
=> Less swelling in water

Extrinsic charge compensation
=> Higher mobility
=> Stronger swelling in water

[11, 29, 30, 37, 40]. The observed ion-specific effects were associated with the hydrophobicity of the ions and the ions' affinity to the polyelectrolyte. Later, Klitzing et al. explained this effect by the difference between cosmotropic and chaotropic ions [37]. The influence of specific anions on certain properties of PEMs has been investigated extensively by Salomäki et al. [28–30]. The anions tested within this work followed the famous Hofmeister series and gave an increasing storage shear modulus with increasing ion size. The latter result is in contradiction to the increase in chain mobility found later by Nazaran et al. [24].

Wong et al. showed that the specific ion effects on building up polyelectrolyte multilayers become important above a certain ionic strength, namely, 0.1 M for anions and 0.25 M for cations [40].

Recently, Liu et al. have broadened the field of ion-specific effects on polyelectrolyte multilayers by investigation of the deposition of PSS/PDADMAC multilayers in mixed electrolyte solutions (PDADMAC: poly(diallyldimethylammonium chloride)) [22]. It appeared that the effects of anions of a mixed electrolyte solution on the deposition of PEMs are nonadditive. Moreover, in a mixed electrolyte solution containing both chaotropic and cosmotropic anions, the multilayer buildup is dominated by chaotropic anions.

The PSS/PDADMAC multilayer growth in a single electrolyte solution containing one type of chaotropic anions (e.g., Br^-, ClO_3^-) is nonlinear (increasing increment with increasing number of deposited layers). In contrast to this, in the presence of cosmotropic anions like F^-, CH_3COO^-, $H_2PO_4^{4-}$, and SO_2^{4-}, a linear growth is observed: The multilayer buildup is determined by the conformation of PDADMAC chains [11, 30, 36, 37, 40]. An overview of the ion-specific effect is shown in Fig. 1.

The effects of monovalent anions and cations on the properties can be understood as following [37]: Cosmotropic ions have a well-ordered large hydration shell. Chaotropic ions are large with a significant polarizability, a weak electric field, and their hydration water can be easily removed. That makes it easier for chaotropic ions to adapt to the environment, e.g., the polyion. This might lead to a stronger attraction between them, which could be a kind of "bridging" and/or overlap of hydration shells of ions and the oppositely charged groups of the polyions. This leads to a stronger screening and chain coiling followed by increase in thickness and roughness [30, 37, 40], comparable to the effect of increasing ionic strength or decreasing charge density. The effect of anions is much larger than the effect of cations, since

anions have a much larger difference in polarizability than typical cations due to their larger variety of their diameter [40]. Also theoretical calculations predict an effect of the ion type on their distribution around a polyelectrolyte [8]. Short-range dispersion forces have to be added to DLVO forces to describe this effect.

The stronger attraction between polyion and oppositely charged chaotropic ions explains the dominating effect of chaotropic ions in comparison to cosmotropic ones [22]. A further consequence is extrinsic compensation of the polyion charge. In contrast to this, in the presence of cosmotropic ions, the polyion charge is rather compensated by oppositely charged polyions, i.e., intrinsic charge compensation [36]. Since the mobility of polymer chains in the multilayer depends on the density of complexation sites between polyanions and polycations, extrinsic charge compensation leads to a higher chain mobility (liquefied system) than intrinsic one (glassy system) [24]. The degree of chain mobility determines also the type of growth. More mobile PEMs show a tendency for a nonlinear growth, while intrinsically charge compensated chains show a rather linear growth [11, 30, 36, 37, 40]. PEMs can be also liquefied after preparation, by adding chaotropic ions [24]. At high ion concentration, the PEMs can be even erased, which is more efficient with chaotropic ions than with cosmotropic ones: chaotropic ions can easily destroy the complexation sites. Another consequence of extrinsic charge compensation is that PEMs which are built up in the presence of chaotropic ions can swell stronger in water than PEMs which are formed in the presence of cosmotropic ions [11, 15, 28]. The lower density of complexation sites leads to a kind of sponge-like swelling of the PEM. This explains the higher permeability in case of chaotropic ions [15]. In contrast to this, the density of a dry PEM is higher, when they were prepared with chaotropic ions. This is due to the higher flexibility of the individual polymer chains caused by stronger electrostatic screening along the polyelectrolyte chains [11].

Specific Ion Effects on Thin Liquid Films

Interactions between the opposing film surfaces are important for the stability of a liquid film like foam films, emulsion films, etc. Related to this, the adsorption of ions at the film interfaces plays a decisive role.

Many experimental and theoretical results contradict each other concerning the ion adsorption at the air/water interface, since they are sensitive for different length scales. Some methods are only sensitive for the surface layer and not for subsurface layers, others are sensitive for both. For the stability of colloidal systems, interfacial forces over a range of several tens of nanometers are important and related to an average surface charge across the complete interfacial region.

This surface interaction causes an excess pressure normal to the film interfaces, called disjoining pressure, which is the sum of repulsive electrostatic (π_{el}), attractive van der Waals (π_{vdW}), and repulsive steric pressures (π_{st}). Adapted from these interactions, two different types of thin films can be distinguished: common black films (CBFs), stabilized by π_{el} and Newton black films (NBFs), stabilized by π_{st}.

Wetting Films

Solely, in an asymmetric film (e.g., wetting film), one can determine the sign and precise value of the overall charge of the free air/water surface. This technique has successfully been used by the authors to probe the existence of negative surface charges at the air/water interface [9, 16].

A simple system to study ion-specific effects is a water film on a substrate, e.g., Silicon. Schelero and Klitzing studied water films at different ionic strengths and in the presence of different types of salts [33] (see Fig. 2).

At a fixed concentration of 10^{-4} M sodium salts, the film thickness increases in the order of $F^- < Cl^- < I^-$, i.e., with increasing ion size (Fig. 2a). After the addition of iodide salts (qualitatively the same for other halides) to the water wetting film, the film thickness increases in the order of $Cs^+ < K^+ < Na^+$, i.e., with decreasing
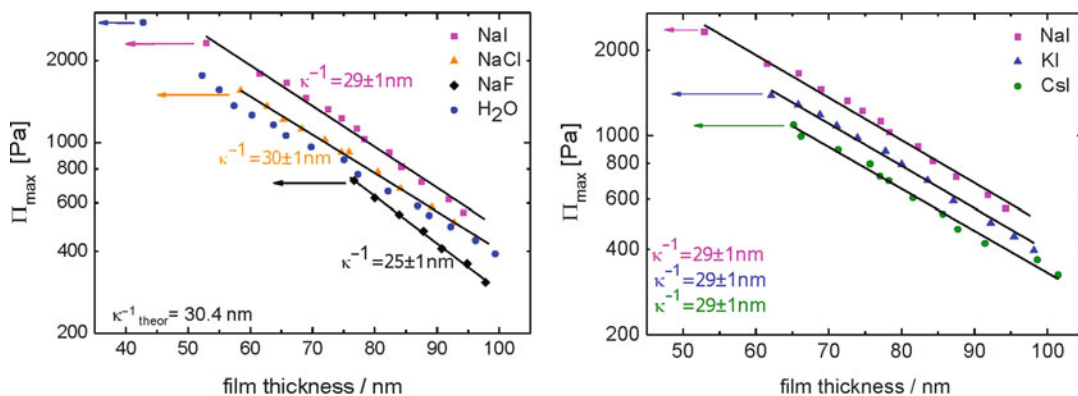
Polyelectrolytes, Films-Specific Ion Effects in Thin Films, Fig. 2 Disjoining pressure isotherms of aqueous wetting films on Si wafers

ion size (Fig. 2b). Under the assumption that the air/water interface is negatively charged, this result clearly shows that with increasing ion size, i.e., decreasing charge density, ions show a stronger tendency to adsorb at the surface. Enhancement of anions at the air/water interface leads to an increase of stability and film thickness due to an increase of the surface potential. The same adsorption effect is found for cations, but with the reversed effect on the surface potential and thus on the film thickness and stability. This is a clear further indication for an excess of negative charges at the air/water interface. It is worth to note that anions have such a drastic effect at the air/water interface although the surface is negatively charged. This demonstrates the dominating effect of the hydration shell of ions over electrostatics on their adsorption at the air/water interface.

Foam Films

Foams and emulsions are achieved due to adsorption of foam stabilizing agents like surfactants at the interface between the dispersed and continuous phases. The foam stability is often related to the stability of thin liquid films formed between two air bubbles. All considered foam films are stabilized by ionic surfactant.

Independent of the salt type, the addition of salt leads to several counteracting stabilization mechanisms in foam films [5–7, 13, 34]: The first mechanism originates from the electrostatic screening between the opposing equally charged film interfaces, leading to thinner films and often to a lower film stability. The second mechanism is due to lateral screening of the charges of adjacent surfactant head groups within the adsorption layer. This leads to the formation of more condensed films which promote foam film stability. Another mechanism affecting the stability of foam films is that electrolyte influences the surface activity of the surfactant. With the addition of salt, the dielectric constant of the solvent is reduced [27]. The dielectric properties of the medium where the head groups are located are directly linked with the degree of dissociation of the surfactant [5, 14, 19, 34]. Furthermore, the degree of dissociation changes due to different ion binding to the surfactant. The concentration of surfactant at the air/water interface can be either enhanced or reduced by adding electrolytes. For example, the adsorption of SDS at the air/water interface increases with increasing salt concentration due to electrostatic screening [20, 35].

Sentenac and Benattar were the first who observed ion-specific effects in foam films. They investigated the influence of LiCl and CsCl on aerosol-OT (AOT) films at a fixed surfactant concentration close to the cmc [35]. The addition of LiCl leads to about 10-nm thicker films than in case of CsCl. The disjoining pressure isotherms of the AOT/CsCl systems can be described by the classical DLVO approach
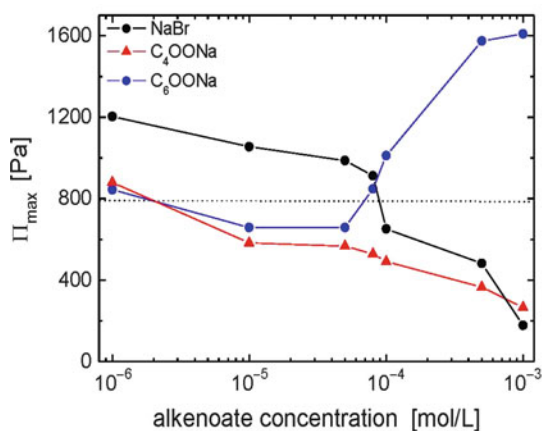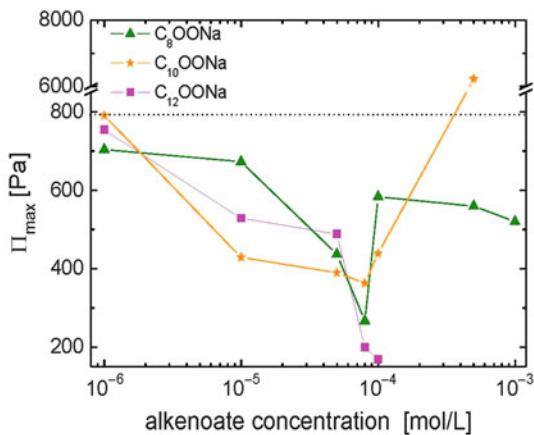
Polyelectrolytes, Films-Specific Ion Effects in Thin Films, Fig. 3 Disjoining pressure isotherms of LiDS (*filled circles*), SDS (*open squares*), and CsDS (*filled triangles*) at a surfactant concentration of 10–4 M. The solid line refers to the results from PB calculation

while it fails in case of LiCl. Apparently, an additional repulsion arises in the LiCl containing $\pi(h)$ isotherm. The authors argue that it is a consequence of the reduced screening due to the large hydration shell of Li$^+$. Another explanation could be that the adsorption of Li$^+$ at the surface is weaker because of its hydrated radius.

Recently, a detailed study of specific ion effects on SDS foam films showed that chaotropic anions show a strong adsorption at the negatively charged surfaces of foam films [32] in analogy to the negatively charged air/water interface in wetting films. Again, especially the pronounced anion effects at a negatively charged surface imply that the adsorption of ions to the film surfaces is governed rather by ion-specific than electrostatic interactions. The order of the effect of halides and alkalis is the same as that detected for aqueous wetting films on Si of the pure salt solutions [33].

It is important to realize that the addition of ions which differ from the original counterion of the surfactant molecules leads to competitive ion adsorption. This could result in an exchange of the native counterion of the surfactant. Generally, ion-specific effects on foam films can be investigated in two ways: (i) due to the addition of salt as already discussed before and (ii) by variation of the counterion of the surfactant. The latter approach has the advantage of having only one type of counterion present in the solution.

A lot of work has been published concerning the effect and nature of counterions on the properties of surfactants (e.g., cmc, aggregation number, cloud point and ionization number) [1–4, 21, 31, 38, 39, 41], but only few publications deal with the counterion effect on the properties of foam or foam films. Interestingly, the counterion size has an opposite effect on foaming and foam stability. Pandey et al. found decreasing foamability of dodecyl sulfate surfactants with the order Li$^+$ > Na$^+$ > Cs$^+$ > Mg^{2+} as counterion. This has been explained by differences in micellar stability and diffusion of monomers. Due to the larger hydration shell of Li$^+$, Li$^+$ binds less strongly to the SD$^-$ headgroups which leads to stronger repulsion between the SD$^-$ headgroups than in case of CsDS. This leads to higher cmc of SDS and higher monomer to micelle ratio. Obviously, for the highly dynamic process of foaming, the fast adsorption of monomers to the film interfaces is much more efficient than the slow one of micelles followed by the required breakage of micelles.

While there is no significant ion effect on foam stability below the surfactant's cmc, above cmc, the foam stability in the presence of CsDS and Mg(DS)$_2$ is much larger than for LiDS and NaDS. This indicates that the presence of stable micelles is essential for high foam stability. Surface viscosity measurements correlated well with the foam stability trends and gave the following order

LiDS < NaDS < CsDS, indicating that the molecules of CsDS are more tightly packed at the air/water interface, which is also supported by surface tension measurements [26].

In opposite to macroscopic foams, the type of counterion affects the thickness and stability of single foam films, already below the cmc [32]. By keeping the headgroup constant, a decrease in film thickness and stability with increasing size of the counterion is found (Fig. 3). This result is independent of the charge of the headgroup and is explained by a decreasing surface charge due to decreasing degree of dissociation. It indicates that below surface saturation concentration, surface charges play an important role for stabilization and above the cmc (i.e., surface saturation), the packing density of the surfactant is dominating.

Future Directions

So far, for PEMs mainly the effects of monovalent ions are reported, which follow more or less the Hofmeister series. It is still unclear if this simple image as illustrated in Fig. 1 can be generalized to other ion types. Another open question is: If the polarizability [25] or rather the ion hydrophobicity [17] presents the decisive parameter.

Ion-specific effects on wetting films and foam films are mainly dominated by the affinity of ions to adsorb at the air/solution interface. This has a pronounced influence on the film thickness and stability. Additionally, foam film properties are affected by the propensity of ions to interact with the headgroups of the foam stabilizer. The open question is: If these findings can be generalized to other surfaces.

Cross-References

References

1. Bales BL, Benrraou M, Zana R (2002) Characterization of micelles of quaternary ammonium surfactants as reaction media I: Dodeclytrimethylammonium bromide and chloride. J Phys Chem B 106:1926–1939
2. Bales BL, Benrraou M, Zana R (2002) Krafft temperature and micelle ionization of aqueous solutions of cesium dodecyl sulfate. J Phys Chem B 106:9033–9035
3. Bales BL, Shahin A, Lindblad C, Almgren MJ (2000). Timeresolved fluorescence quenching and electron paramagnetic resonance studies of the hydration of lithium dodecyl sulfate micelles. J Phys Chem B 104: 256–263 and references therein
4. Benrraou M, Bales BL, Zana R (2003) Effect of the nature of the counterion on the properties of anionic surfactants. 1. cmc, ionization degree at the cmc and aggregation number of micelles of sodium, cesium, tetramethylammonium, tetraethylammonium, tetrapropylammonium, and tetrabutylammonium dodecyl sulfates. J Phys Chem B 107:13432–13440
5. Bergeron V (1997) Disjoining pressures and film stability of alkyltrimethylammonium bromide foam films. Langmuir 13:3474–3482
6. Bergeron V, Radke C (1992) Equilibrium measurements of oscillatory disjoining pressures in aqueous foam films. Langmuir 8:3020–3026
7. Black IJ, Herrington TM (1995) Determination of thickness and rupture pressure for aqueous foam part 1.- films stabilized by anionic surfactantsfilms. J Chem Soc Faraday Trans 91:4251–4260
8. Boström M, Williams D, Ninham B (2002) The influence of ionic dispersion potentials on counterion condensation on polyelectrolytes. J Phys Chem B 106:7908–7912
9. Ciunel K, Armelin M, Findenegg GH, von Klitzing R (2005) Evidence of surface charge at the air/water interface from thin-film studies on polyelectrolyte-coated substrates. Langmuir 21:4790–4793
10. Decher G (1997) Fuzzy nanoassemblies: toward layered polymeric multicomposites. Science 277:1232–1237
11. Dodoo S, Steitz R, Laschewsky A, von Klitzing R (2011) Effect of ionic strength and type of ions on the structure of water swollen polyelectrolyte multilayers. Phys Chem Chem Phys 13:10318–10325
12. Dubas ST, Schlenoff JB (1999) Factors controlling the growth of polyelectrolyte multilayers. Macromolecules 32:8153–8160
13. Exerowa D, Kolarov T, Khristov K (1987) Direct measurement of disjoining pressure in black foam films. Colloids Surf 22:161–169
14. Fainerman V, Lucassen-Reynders E (2002) Adsorption of single and mixed ionic surfactants at fluid interfaces. Adv Colloid Interface Sci 96:295–323
15. Haitami AE, Martel D, Ball V, Nguyen HC, Gonthier E, Labbé P, Voegel JC, Schaaf P, Senger B, Boulmedais F (2009) Effect of the supporting

electrolyte anion on the thickness of pss/pah multilayer films and on their permeability to an electroactive probe. Langmuir 25:2282–2289

16. Hänni-Ciunel K, Schelero N, von Klitzing R (2009) Negative charges at the air/water interface and their consequences for aqueous wetting films containing surfactants. Faraday Discuss 141:41–53

17. Horinek D, Serr A, Bonthius D, Bostroem M, Kunz W, Netz R (2008) Molecular hydrophobic attraction and ion-specific effects studied by molecular dynamics. Langmuir 24:1271–1283

18. Kharlampieva R, Pristinski D, Sukhishvili S (2007) Hydrogenbonded multilayers of poly(carboxybetaine)s. Macromolecules 40:6967–6972

19. Kralchevsky PA, Danov KD, Broze G, Mehreteab A (1999) Thermodynamics of ionic surfactant adsorption with account for the counterion binding: effect of salts of various valency. Langmuir 15:2351–2365

20. Kumar MK, Ghosh P (2006) Coalescence of air bubbles in aqueous solutions of ionic surfactants in presence of inorganic salt. Chem Eng Res Des 84:703–710

21. Kumar MK, Sharma D, Khan ZA (2001) Cloud point phenomenon in ionic micellar solutions: a SANS study. Langmuir 17:2549–2551

22. Liu G, Hou Y, Xiao X, Zhang G (2010) Specific anion effects on the growth of a polyelectrolyte multilayer in single and mixed electrolyte solutions investigated with quartz crystal microbalance. J Phys Chem B 114:9987–9993

23. Mermut O, Barret C (2003) Effects of charge density and counterions on the assembly of polyelectrolyte multilayers. J Phys Chem B 107:2525–2530

24. Nazaran P, Bosio V, Jaeger W, Anghel D, von Klitzing R (2007) Lateral mobility of polyelectrolyte chains in multilayers. J Phys Chem B 111:8572–8581

25. Ninham BW, Yaminsky V (1997) Ion binding and ion specificity: the hofmeister effect and onsager and lifshitz theories. Langmuir 13:2097–2108

26. Pandey S, Bagwe RP, Shah DO (2003) Effect of counterions on surface and foaming properties of dodecyl sulfate. J Colloid Interface Sci 267:160–166

27. Sack H (1927) Über die Dielektrizitätskonstanten von Elektrolytlösungen bei geringen Konzentrationen. Ph. D. thesis, Eidgenössischen Technischen Hochschule in Zürich

28. Salomäki M, Kankare J (2008) Specific anion effect in swelling of polyelectrolyte multilayers. Macromolecules 41:4423–4428

29. Salomäki M, Laiho M, Kankare J (2004) Counteranion-controlled properties of polyelectrolyte multilayers. Macromolecules 37:9585–9590

30. Salomäki M, Tervasmäki P, Areva S, Kankare J (2004) The hofmeister anion effect and the growth of polyelectrolyte multilayers. Langmuir 20:3679–3683

31. Satake I, Iwamatsu I, Hosokawa S, Matuura R (1963) The surface activities of bivalent metal alkyl sulfates. i. On the micelles of some metal alkyl sulfates. Bull Chem Soc Japan 36:204–209

32. Schelero N, Hedicke G, Linse P, Klitzing RV (2010) Effects of counterions and co-ions on foam films stabilized by anionic dodecyl sulfate. J Phys Chem B 114:15523–15529

33. Schelero N, Klitzing RV (2011) Ion specific effects on thin aqueous wetting films. Soft Matter 7:2936–2942

34. Schulze-Schlarmann J, Buchavzov N, Stubenrauch C (2006) A disjoining pressure study of foam films stabilized by tetradecyl trimethyl ammonium bromide c14tab. Soft Matter 2:584–594

35. Sentenac D, Benattar JJ (1998) Long range hydration effects in electrolytic free suspended black films. Phys Rev Lett 81:160–163

36. Klitzing RV (2006) Internal structure of polyelectrolyte multilayer assemblies. Chem Phys Phys Chem 8:5012–5033

37. Klitzing RV, Wong J, Jaeger W, Steitz R (2004) Short range interactions in polyelectrolyte multilayers. Curr Opin Colloid Interface Sci 9:158–162

38. Wen W-Y, Saito S (1964) Apparent and partial molal volumes of five symmetrical tetraalkylammonium bromides in aqueous solutions. J Phys Chem 68:2639–2644

39. Wirth HE, LoSurdo AJ (1972) Proton magnetic resonance in concentrated aqueous solutions of tetraalkylammonium bromides and inorganic halides at 25 and 65.deg. J Phys Chem 76:130–132

40. Wong J, Zastrow H, Jaeger W, Klitzing RV (2009) Specific ion versus electrostatic effects on the construction of polyelectrolyte multilayer. Langmuir 25:14061–14070

41. Yu Z-Y, Zhang X, Zhou Z, Xu G (1990) Physicochemical properties of aqueous mixtures of tetrabutylammonium bromide and anionic surfactants. Effects of surfactant chain length and salinity. J Phys Chem 94:3675–3681

P

Polyelectrolytes, Properties

Yoav D. Livney
Faculty of Biotechnology and Food Engineering, The Technion, Israel Institute of Technology, Haifa, Israel

Introduction

Polyelectrolytes are polymers with ionizable groups [1–9]. In polar solvents, such as water, these groups ionize by either dissociation (e.g., carboxyl: $-COOH <=> -COO^- +H^+$), or proton-association (e.g., amine: $-NH_2 + H^+ <=> -NH_3^+$), which also produces counterions in the surrounding solution. The ionization in aqueous solution,

which is pH and ionic strength dependent, confers unique properties to the polyelectrolytes, dominated by strong long-range electrostatic interactions [10], and by entropic effects of counterions [6, 11–13]. Both living organisms and human technology make many various uses of the versatility of polyelectrolyte behavior [8]. Examples of polyelectrolytes include polyanions (or polyacids), like DNA, polyacrylic acid [6]; polycations (or polybases), like chitosan [14, 15], polylysine [16, 17]; and polyampholytes, i.e., polymers carrying both positive and negative charges [18], like most proteins.

The presence of charged groups leads to several important differences in solution behavior of polyelectrolytes, compared to uncharged polymers [6]: (i) the crossover concentration from dilute to semidilute is much lower; (ii) a pronounced peak (whose wave-vector magnitude increases with $c^{1/2}$) appears in the scattering function of homogeneous polyelectrolyte solutions, not in that of nonionic polymer solutions; (iii) the osmotic pressure of polyelectrolyte solutions in pure water is several orders of magnitude higher than that of uncharged polymers (at same concentration), and it increases almost linearly with polymer concentration, independently of molecular weight. These facts, along with the strong dependence of the osmotic pressure of the polyelectrolyte solutions on added salt, show it is mainly due to counterion contribution; (iv) the viscosity of polyelectrolyte solutions varies linearly with $c^{1/2}$ (Fuoss' law [19]), while for uncharged polymers, it varies linearly with c; (v) compared to solutions of uncharged polymers, polyelectrolytes in semidilute solutions follow unentangled dynamics over a much wider concentration range [6]. While the vast majority of the studies on polyelectrolytes were focused on aqueous solutions, a few studies considered nonaqueous polyelectrolyte solutions [20, 21].

The properties of polyelectrolytes in solutions and at charged surfaces depend on the fraction of ionized groups, solvent quality for the polymer, dielectric constant of the medium, salt concentration, and polymer–substrate interactions [5–7].

Properties of Polyelectrolytes and Their Solutions

Structural Properties

Similarly to nonionic polymers, polyelectrolytes are macromolecules made of covalently linked repeating units (mers, or monomers), which may be identical, forming a homopolymer, or different, forming a heteropolymer or copolymer. The monomers of different types may be randomly distributed along the chain, grouped into blocks of same type, forming a block-copolymer (e.g., an A_nB_m diblock copolymer is made of two blocks, one of n A monomers, and the other of m B monomers), or specifically ordered in a particular sequence, as in DNA, RNA, and proteins. The linear sequence of monomers of different types has dramatic impact on the properties of the copolymer. In particular, being polyelectrolytes, the distribution of positive and negative charges along the chain defines the charge distribution and charge density (local and global), properties which intensely affect chain conformation in solution, and interactions between molecules of the same polymer, as well as with other species in solution [22]. Additionally, polyelectrolytes, like other polymers, may have various architectural structures. They may be linear, linear with side groups, branched, hyperbranched (i.e., with branched-branches), star-shaped, dendritic (i.e., formed in "generations" of branching points, from a central point outward), and more. Polyelectrolytes may also be cross-linked to form polyelectrolyte gels, notably polyelectrolyte hydrogels, some of which have super-absorbent capabilities (e.g., polyacrylic acid hydrogels used in diapers). The backbone configuration, which describes the stereochemical positioning of side groups, or tacticity, may either be isotactic (all consecutive side groups are oriented the same way), syndiotactic (alternating sides), or atactic (random orientations (e.g., as in polystyrene sulfonate [23]).

Typical anionic groups occurring in bio-polyelectrolytes include carboxyl (–COO$^-$, e.g., in pectin, alginate, and proteins), phosphate ($>PO_4^-$, e.g., in DNA), sulfate ($-SO_4^-$, e.g., in carrageenan). The typical cationic group in

bio-polyelectrolytes is amine ($-NH_3^+$, e.g., in chitosan and in proteins).

Electrochemical Properties

Aqueous polyelectrolyte solutions are electrically conductive, due to the presence of both the polyions and the counterions [24]. Strongly acidic groups (e.g., phosphate and sulfonate) ionize in solution over a very wide pH range. Strongly acidic groups have an acid-dissociation constant (K_a) for which pK_a is typically <2, while weakly acidic groups typically have a pK_a >2. Organic bases (e.g., amines) are weak bases and thus basic side groups have an association constant for protonation (K_b) for which pK_b is typically <10. This means that weak acidic and basic groups are only partially ionized at intermediate pH conditions, and so the fractional ionization and the consequent charge-related properties of weak polyelectrolytes are thus strongly pH dependent. Additionally, according to the theory of weak polyacids by Katchalsky (1954), due to interaction between the charged groups along a polymer chain, the dissociation constant will depend on both ionic strength in the solution (degree of shielding) and the distance between adjacent charged groups on the polymer. Katchalsky developed the following relationship: $pH = pK_0 - \log[(1-\alpha/)\alpha] + 0.4343e\Psi/kT$, where pK_0 is the intrinsic pK_a, α is the degree of dissociation, e is the elementary charge, and Ψ is the electrostatic potential around the polyelectrolyte. The last term is the contribution of the polyelectrolyte field to the standard free energy of ionization of a single group, above the free energy of ionization where no such field is acting (pK_0). According to Katchalsky, the dissociation constant, when half of the carboxylic groups are protonated, $pKa(\alpha = 0.5)$, may be determined by plotting pH as function of $\log[(1-\alpha/)\alpha]$. By plotting the apparent dissociation constant, $pK_a(app) \equiv pH\text{-}\log[(1-\alpha/)\alpha]$, as function of α, the intrinsic dissociation constant (the dissociation constant of a single acidic group when all neighboring acidic groups are uncharged) is obtainable by extrapolation to $\alpha = 0$. For example, the pK_0 and $pK_a(\alpha = 0.5)$ have been determined [25] by potentiometric titration using NMR spectroscopy (in D_2O) for hyaluronan (a linear polysaccharide abundant in mammalian tissues consisting of alternating monosaccharide units, N-acetyl glucosamine, and glucuronic acid, connected by β-(1-3) and β-(1-4) glycosidic bonds, respectively). As NaCl concentration increased (10, 50, 100 mM) and the consequent Debye-screening length decreased (3.04, 1.36, 0.96 nm), the pK_a ($\alpha = 0.5$) remained expectedly unchanged (3.14, 3.16, 3.15) but the pK_0 decreased (3.05, 2.82, 2.81) until the Debye-screening length approached the length of the repeating disaccharide unit of hyaluronic acid (∼1 nm) [25].

The electrostatic attraction between polyelectrolyte chains and counterions in solutions can result in condensation of counterions on polyelectrolytes. The counterion condensation [26] appears to be due to a fine interplay between the electrostatic attraction of a counterion to a polymer chain and the loss of the translational entropy by counterions due to their localization in the vicinity of the polymer chain [6]. The attraction of added ions to fixed charges on the polyelectrolyte chain and the ability to reduce this attraction by screening of competing small ions is the basis for ion exchange technologies, including water purification and ion exchange chromatography [27].

Another important aspect of the screening effect is commonly known as the "electric double layer" (EDL), a concept which simplistically describes the fact that near a charged surface in solution, a layer of oppositely charged ions is formed, to maintain electroneutrality [28]. The region containing the strongly bound counterions is often called the Stern Layer, while the adjacent region where ions move freely influenced by the electric and thermal forces is called the diffuse layer, or the Gouy–Chapman layer [28, 29]. The effective thickness of the EDL in the linearized Poisson–Boltzmann theory may be described by the Debye length, k^{-1} [28, 30], $\kappa^{-1} = \sqrt{\frac{\varepsilon_r \varepsilon_0 k_B T}{2N_A e^2 I}}$, where ε_r is the relative permittivity of the electrolyte solution, ε_0 is the electric permittivity of vacuum, k_B is the Boltzmann constant, T is the absolute temperature, N_A is Avogadro's number, e is the elementary charge, and I is the ionic strength.

Because the electrical potential at the surface of a colloidal particle in solution cannot be directly and unambiguously measured, the potential at the hydrodynamic slip-plane, called the zeta potential (ζ), is commonly studied, based on measurements of electrophoretic mobility, i.e., the terminal velocity of a colloidal particle, e.g., a polyelectrolyte molecule, under a constant electric field, divided by field intensity [29]. For polyampholytes, the pH where the electrophoretic mobility is zero is the isoelectric point, i.e., the pH where the numbers of positive and negative charges on the particle are equal [29]. There are several theories relating electrophoretic mobility to ζ, each based on specific assumptions; hence, the choice of a proper theory must be based on assuring the validity of these assumptions for the system studied. The most commonly cited in this respect is the Smoluchowski theory [31]. Smoluchowski's theory is valid for particles of any shape, provided the (local) curvature radius, a, largely exceeds the Debye length κ^{-1}, i.e., $\kappa a \gg 1$. According to Smoluchowski, the electrophoretic mobility, u_e, is related to ζ by $u_e = \varepsilon_r \varepsilon_0 \zeta / \eta$, known as the Helmholtz–Smoluchowski equation, where η is the dynamic viscosity of the liquid [29, 31]. For $\kappa a < 1$, the Hückel–Onsager equation applies: $u_e = 2\varepsilon_r \varepsilon_0 \zeta / 3\eta$ [29]. Additional situations and the relevant theories available are detailed by Delgado et al. [29].

Lyotropic Properties (Hofmeister Series: Ion-Specific Effects)

Ion-specific effects are universal in biology, biochemistry, chemistry, and chemical engineering [32]. They were first systematically studied by Franz Hofmeister [32–34], who observed the different protein precipitating effects ("salting-out") of various salts, and described them in terms of the "water withdrawing power of salts." Hofmeister effects, or series, refer to the relative effect of anions or cations on a wide range of phenomena, not only related to proteins or to polyelectrolytes [35–38]. Advances in experimental and computational methodologies have led to insights into the underlying molecular mechanisms, although a deeper molecular understanding still seems to be elusive. The principal

reason appears to be that the Hofmeister series emerges from a combination of a general effect of cosolutes (salts, etc.) on solvent structure, and of specific interactions between the cosolutes and the solute (protein or other biopolymer) [39]. Originally, it was thought that an ion's influence on macromolecular properties was caused at least in part by "making" or "breaking" bulk water structure. Recent time-resolved and thermodynamic studies of water molecules in salt solutions, however, demonstrate that bulk water structure is not central to the Hofmeister effect. Instead, models are being developed that depend upon direct ion–macromolecule interactions as well as interactions with water molecules in the first hydration shell of the macromolecule [40], and in the first couple of hydration layers of the ion [41, 42]. Small ions of high charge density (kosmotropes) bind water molecules strongly, whereas large monovalent ions of low charge density (chaotropes) bind water molecules weakly relative to the strength of water–water interactions in bulk solution [43, 44]. Kosmotropic anions tend to cause "salting-out" of polyelectrolytes, nonionic polymers, and other colloids and cosolutes. Chaotropic anions and kosmotropic cations tend to cause "salting in" (although at high concentrations most salts cause salting-out) [38, 45–49]. Positively charged macromolecular systems may show inverse Hofmeister behavior only at relatively low-salt concentrations, but revert to a direct Hofmeister series as the salt concentration is increased [50]. The topic of ion-specific effects is also dealt with in other sections of this encyclopedia.

Rheological Properties of Polyelectrolyte Solutions

Dobrynin and coworkers [6, 51] have extended and generalized the scaling theory of de Gennes [52] and Pfeuty [53] to both unentangled and entangled regimes of intrinsically flexible polyelectrolyte solutions. In semidilute solutions, the electrostatic persistence length of a polyelectrolyte is assumed to be proportional to the Debye-screening length. If the salt concentration is low, the unentangled semidilute concentration

regime spans three to four decades in polymer concentration. When comparing the rheological properties of polyelectrolytes to those of neutral polymers, it can be generalized that the viscosity of polyelectrolyte solutions is proportional to the square root of polymer concentration $\eta \sim c^{1/2}$ (Fuoss' law [54]), while for solutions of uncharged polymers at the same concentration, the viscosity is proportional to polymer concentration [6]. Moreover, there is no concentration regime where reduced viscosity η/c of solutions of neutral polymers decreases with polymer concentration ($\eta/c \sim c^{-1/2}$ for polyelectrolytes in the Fuoss regime) [6]. Polyelectrolytes should form entanglements at the same relative viscosity as neutral polymer solutions ($\eta \approx 50\eta(s)$) (s=solvent), and in the entangled regime of salt-free polyelectrolyte solutions $\eta \sim c^{3/2}$ [51]. While the viscosity of a hydrophilic polyelectrolyte (e.g., poly(acrylic acid) (PAA)) increases smoothly with increasing neutralization as pH is raised, the viscosity of a hydrophobic polyelectrolyte (e.g., poly(methacrylic acid) (PMA) remains almost constant at low pH, and increases abruptly as pH reaches a critical value, indicating a globule-to-coil transition upon charging, because water is a poor solvent for the uncharged PMA, but good for the charged polyelectrolyte [6, 55].

Intermolecular and Surface Properties

Intermolecular interactions between different polyelectrolytes have a plethora of implications and applications in science and technology. In principle, different polyelectrolytes may present either repulsive or attractive intermolecular interactions [56]. Similar charge sign favors repulsion, which, at low concentrations, tends to lead to co-solubility, but at high concentrations, may lead to segregative phase separation, due to thermodynamic incompatibility [57]. Opposite charge signs on polyelectrolytes may lead to association driven by attractive Coulombic interactions [58], resulting in electrostatic-complex formation, and possibly, to associative phase separation, also termed complex coacervation [56, 59, 60]. This phenomenon was first observed for proteins by Kossel in 1896 [61]

and for protein–polysaccharide coacervation in 1911 by Tiebackx [62] who observed the appearance of opacity or precipitation upon mixing of gelatin and gum arabic in acid conditions. It was first systematically studied for protein–polysaccharide complexes by Bungenberg de Jong and Kruyt [63], and for synthetic polyelectrolytes by Michaels & Miekka [64]. Protein–polysaccharide interactions have since been extensively studied and reviewed [59, 60, 65–70], and so were polyelectrolyte complexes in general [71–75]. Intermolecular polyelectrolyte interactions are mainly dependent on pH (which affects ionization), ionic strength (causing screening), and the stoichiometric ratio of the macroions involved and the total concentration. Insoluble complex coacervates become progressively more soluble with increasing salt concentration [75]. Other important factors are the molecular characteristics of the polyelectrolytes (molecular weight, charge density, conformation, etc.), solvent quality (including presence of cosolvents, and cosolutes, ion-specific effects), mixing procedures, and conditions (temperature, pressure, shear, etc.) [56, 59, 65, 67, 70]. Recently, computer simulations are helping in gaining new insights into polyelectrolyte complexation [74, 76–79]. The net charge of two macroions might be of same sign, and yet association may be favorable, thanks to local "patches" of high charge density, e.g., as in case of a protein slightly above its isoelectric pH (but with densely positive charge patches) associating with an anionic polyelectrolyte [80, 81]. By carefully controlling the ratio of the oppositely charged polyelectrolytes, either precipitated coacervates (mutual charge neutralization) or soluble complexes (excess charge due to surplus of one of the polyelectrolytes) may be formed, which may be applied, e.g., for the formation of nanocomplexes useful as protective vehicles for bioactive compounds in clear solutions [82, 83].

An important application of electrostatic complexation of oppositely charged polyelectrolytes is known as the "layer-by-layer deposition" or electrostatic self-assembly [84–87], which is the alternating deposition of positively and negatively charged polyelectrolytes onto

a charged surface. The surface could be that of a solid or of another liquid phase, and may have any shape. Various materials have been used with this technique, e.g., synthetic polyelectrolytes, biopolymers (proteins, DNA, polysaccharides) and more, mainly for delivery and controlled release applications [88, 89]. A typical example is the nanocoating of emulsion droplets, emulsified with a low molecular weight ionic surfactant (e.g., SDS), by several alternating layers of oppositely charged polyelectrolytes (e.g., chitosan and pectin) [90], as a way to form a microcapsule. Sometimes the core particle is later dissolved to leave a hollow multilayered shell [91]. From a fundamental viewpoint, the adsorption of a polyelectrolyte on a surface is an intriguing process, which questionably reached equilibrium, and whose kinetics has only been scarcely studied and reviewed [92].

Block-copolymer polyelectrolytes, with at least one hydrophobic block (in the main chain or a grafted side chain), may demonstrate self-assembly behavior in aqueous solution [93], and may adsorb onto hydrophobic surfaces, which may be facilitated by increasing ionic strength [94]. Moreover, such block-copolymeric amphiphiles typically have a much lower critical micellization concentration (CMC) [95] and a much longer micelle life time (by several orders of magnitude) compared to low molecular weight surfactants [96]. Emulsions stabilized by block-copolymeric polyelectrolytes are generally much more stable than their counterparts stabilized by low molecular weight surfactants of similar hydrophilic–lipophilic balance (HLB) [97]. Micelle formation and micellar structure depends on various parameters like block lengths, salt concentration, pH, and solvent quality, and their stability depends on electro-steric stabilization forces [98]. Certain proteins, like β-casein, are natural examples of such "block-copolymeric amphiphiles" [99, 100]. These properties of amphiphilic polyelectrolytes are useful for various applications, including encapsulation and delivery of hydrophobic bioactives [101], like drugs [102, 103] and nutraceuticals [104, 105], formation of self-assembled nanoreactors [106], and more.

Similarly charged polyelectrolytes may interact attractively by bridging action of mediating counterions. The higher the charge density of the polyelectrolytes, the higher the required charge density of the mediating counterion. An example is the preferred potassium-induced gelation of k-carrageenan (one sulfate group per disaccharide repeating unit) vs. the preferred calcium-induced gelation of i-carrageenan (two sulfate groups per disaccharide repeating unit) [107]. An important additional example includes calcium-induced gelation of alginate, particularly block-wise guluronic rich type, for which the egg-box model for cooperative calcium-assisted cross-link zones was proposed [108]. This type of quick ion-induced gelation has found important applications, notably in gel-bead formation by dripping of alginate solution into calcium-ion containing solution, e.g., for encapsulation purposes [109].

Osmotic Pressure and Gel Swelling of Polyelectrolyte Systems

In dilute polyelectrolyte solutions without added salt, the Poisson–Boltzmann cylindrical cell model accounts fairly well for thermodynamic and some transport properties observed [110–112]. Accordingly, the osmotic pressure in such solutions may be expressed in a virial expansion as commonly used with only two terms [110]:

$$\Pi = CRT(1/M + A_2 C)$$

where M is the molecular weight, C the polymer concentration (g/mL), and A_2, the second virial coefficient, is:

$$A_2 = 4\pi^{3/2}\rho(z)N_A R_F / M^2$$

where $\rho(z)$ is the penetration function, which is constant (0.21) in good solvents [113], N_A is Avogadro's number, and R_F is the Flory radius (for a single chain in a good solvent; $R_F \sim M^{3/5}$) [110].

Above the overlap-onset concentration, c*, according to the Scaling Theory of de Gennes [52], the osmotic pressure (Π_{os}) of a semidilute neutral polymer solution is principally the thermal energy κT per correlation volume:

$$\Pi_{os} \approx kT/\xi^3 \quad c > c*$$

where ξ is the correlation length. In polyelectrolyte solutions, there is an important additional contribution of ions to the total osmotic pressure ($\Pi_{os} = \Pi_p + \Pi_i$) [51]. Even though ions may pass through the membrane (used for measuring the osmotic pressure) which separates the polyelectrolyte from the pure solvent, Donnan equilibrium requires that charge neutrality would be maintained on both sides of the membrane [114–117]. When salt ions concentration is much lower than polyelectrolyte counterions concentration ($c > > 2Ac_s$; A is the number of monomers between uncondensed charges, and c_s is the number-density salt concentration, assuming monovalent ions), then $\Pi_i \approx kTc/A$ (c is the monomer number-density concentration). On the other extreme, at high salt concentration, the counterions are distributed almost uniformly on both sides of the membrane, and salt redistributes to maintain charge neutrality, which also contributes to the osmotic pressure [51, 117]: $\Pi_i \approx kTc^2/4A^2c_s$ ($c<<2Ac_s$). Combining these two expressions to extrapolate the two extremes, one obtains: $\Pi_i \approx kTc^2/(4A^2c_s + Ac)$. Hence, the total osmotic pressure, which is the sum of all these polymer and ionic contributions, is [51]:

$$\Pi_i \approx kT\left[c^2/\left(4A^2c_s + Ac\right) + 1/\xi^3\right]$$

At low-salt concentrations, the ionic (c/A) contribution generally dominates over the semidilute polymer contribution ($1/\xi^3$), while at high salt concentrations, both the ionic ($c^2/4A^2c_s$) and polymer contributions to the osmotic pressure are much smaller than in low-salt solutions. For the vast majority of polyelectrolyte systems studied, the ionic contribution dominates both at low and at high salt concentrations, and the polymer contribution term may be negligible [51].

Polyelectrolyte gels are capable of swelling to much greater extents than their uncharged counterparts, because of high osmotic pressure due to dissociated counterions. Gel swelling, according to the widely accepted Flory-Rehner [118] conception, is governed by the additive contributions of the osmotic pressure, Π_{os}, acting to swell the gel, and the elastic pressure of the network, which at swelling equilibrium counteracts and balances the osmotic pressure, i.e., the swelling pressure Π_{sw} (which equals zero at swelling equilibrium), is:

$$\Pi_{sw} = \Pi_{os} - \Pi_{net}$$

Theories of rubber elasticity [119], such as the "affine network theory" [120] or the "phantom network theory" [121], provide expressions for the network pressure, depending on cross-link functionality and network topology. For a perfect tetrafunctional network without trapped entanglements, the elastic network pressure is given by [120]:

$$\Pi_{net} = k_B TA \frac{\phi R^2}{NR_0^2}$$

where N is the number of statistical segments between cross-links, and R and R_0 are the mean square end-to-end distances of a network strand at a concentration Φ and in its reference state, respectively. The prefactor, A, according to the phantom network theory, predicts $A = 0.5$, while the affine network theory predicts $A = 1$ [120, 122]. Additional theoretical treatments of this intriguing problem may be found, e.g., in [123–125], and in recent years, computer simulations [9, 74, 126–129] are contributing significantly to advance our understanding and gain new insights of polyelectrolytes and their networks. Polyelectrolyte gels have numerous applications, such as superabsorbents [130, 131] (in diapers, hygienic and wound dressing products, and in agriculture [132] – "water-holding" for soil improvement), in sensor technologies [133], in ion exchange resins [134, 135], in food technology [136] (gel-textured products), in biomedical applications [137, 138] environmentally responsive hydrogels [139] have applications in implants, in drug targeting, and many more.

Future Directions

While much progress has been made over the years in our understanding of polyelectrolytes,

which enabled numerous important applications, much work remains to be done, particularly in terms of the effects of solvent and cosolutes, including Hofmeister series and water-structure effects on polyelectrolytes, dynamics of gel swelling, adsorption on surfaces, formation of multilayered films, and self-assembly of amphiphilic macroions. The advancements in computer capabilities will continue to facilitate simulations, which are becoming progressively more explicit in the ability to model atomistic structure and dynamics of macromolecules and surrounding solvent components. Improvement of organic synthesis capabilities, along with better thermodynamic understanding and more powerful computerization tools, will enable design of new polymeric architectures, including protein-like sequence-based polyampholytes for programmed conformational and functional behaviors, enabling novel nanotechnologies for advanced applications.

Cross-References

▶ Ion Properties
▶ Ions at Solid-Liquid Interfaces
▶ Polyelectrolytes, Films-Specific Ion Effects in Thin Films
▶ Polyelectrolytes, Simulation
▶ Specific Ion Effects, Evidences
▶ Specific Ion Effects, Theory

References

1. Barrat JL, Joanny JF (1996) Theory of polyelectrolyte solutions. J Adv Chem Phys 94:1–66
2. Forster S, Schmidt M, Antonietti M (1992) Experimental and theoretical investigation of the electrostatic persistence length of flexible polyelectrolytes at various ionic strengths. J Phys Chem 96:4008–4014
3. Forster S, Schmidt M (1995) Polyelectrolytes in solution. Adv Polym Sci 120:51–133
4. Tanford C (1961) Physical chemistry of macromolecules. Wiley, New York/London
5. Hara M (ed) (1993) Polyelectrolytes, science and technology. Marcel Dekker, New York
6. Dobrynin A, Rubinstein M (2005) Theory of polyelectrolytes in solutions and at surfaces. Prog Polym Sci 30:1049–1118. doi:10.1016/j.progpolymsci.2005.07.006
7. Mandel M (1988) Polyelectrolytes. In: Mark HF, Bikales N, Overberger CG, Menges G (eds) Polyelectrolytes, 2nd edn. Wiley, New York
8. Katchalsky A (1954) Problems in the physical chemistry of polyelectrolytes. J Polym Sci 12:159–184. doi:10.1002/pol.1954.120120114
9. Dobrynin AV (2008) Theory and simulations of charged polymers: from solution properties to polymeric nanomaterials. Curr Opin Colloid Int Sci 13:376–388. doi:10.1016/j.cocis.2008.03.006
10. Radeva T (ed) (2001) Physical chemistry of polyelectrolytes. Marcel Dekker, New York
11. Dobrynin AV, Rubinstein M (2001) Counterion condensation and phase separation in solutions of hydrophobic polyelectrolytes. Macromolecules 34:1964–1972. doi:10.1021/Ma001619o
12. Khokhlov AR (1980) Collapse of weakly charged poly-electrolytes. J Phys A-Math Gen 13:979–987
13. Khokhlov AR (1980) Swelling and collapse of polymer networks. Polymer 21:376–380
14. Muzzarelli RAA, Muzzarelli C (2005) Chitosan chemistry: relevance to the biomedical sciences. Adv Polym Sci 186:151–209
15. Makhlof A, Tozuka Y, Takeuchi H (2011) Design and evaluation of novel pH-sensitive chitosan nanoparticles for oral insulin delivery. Eur J Pharm Sci 42:445–451. doi:10.1016/j.ejps.2010.12.007
16. Shih I-L, Shen M-H, Van Y-T (2006) Microbial synthesis of poly(ε-lysine) and its various applications. Bioresour Technol 97:1148–1159. doi:10.1016/j.biortech.2004.08.012
17. Hiraki J, Ichikawa T, S-i N, Seki H, Uohama K, Seki H, Kimura S, Yanagimoto Y, Barnett JW Jr (2003) Use of ADME studies to confirm the safety of ε-polylysine as a preservative in food. Regul Toxicol Pharmacol 37:328–340. doi:10.1016/s0273-2300(03)00029-1
18. Dobrynin AV, Colby RH, Rubinstein M (2004) Polyampholytes. J Polym Sci, Part B: Polym Phys 42:3513–3538. doi:10.1002/polb.20207
19. Fuoss RM (1948) Viscosity function for polyelectrolytes. J Polymer Sci 3:603–604
20. Hara M (2001) Polyelectrolytes in nonaqueous solutions. In: Radeva T (ed) Polyelectrolytes in nonaqueous solutionsedn. Marcel Dekker, New York
21. Hara M (1993) Polyelectrolytes in nonaqueous solution. In: Hara M (ed) Polyelectrolytes in nonaqueous solutionedn. Marcel Dekker, New York
22. Sperber B, Schols HA, Stuart MAC, Norde W, Voragen AGJ (2009) Influence of the overall charge and local charge density of pectin on the complex formation between pectin and beta-lactoglobulin. Food Hydrocol 23:765–772. doi:10.1016/j.foodhyd.2008.04.008
23. Li C, Shen J, Peter C, van der Vegt NFA (2012) A chemically accurate implicit-solvent

coarse-grained model for polystyrenesulfonate solutions. Macromolecules 45:2551–2561. doi:10.1021/ma202490h

24. Vink H (2001) Conductance of polyelectrolyte solutions, anisotropy, and other anomalies. In: Radeva T (ed) Conductance of polyelectrolyte solutions, anisotropy, and other anomaliesedn. Marcel Dekker, New York

25. Tømmeraas K, Wahlund P-O (2009) Poly-acid properties of biosynthetic hyaluronan studied by titration. Carbohydr Polym 77:194–200. doi:10.1016/j.carbpol.2008.12.021

26. Manning GS (1969) Limiting laws and counterion condensation in polyelectrolyte solutions I. Colligative Properties. J Chem Phys 51:924–933

27. HaddadPR JPE (1990) Ion chromatography: principles and applications. Elsevier, Amsterdam

28. DA RusselWB S, Schowalter WR (1989) Colloidal dispersions. Cambridge University Press, Cambridge, UK

29. Delgado AV, Gonzalez-Caballero F, Hunter RJ, Koopal LK, Lyklema J (2007) Measurement and interpretation of electrokinetic phenomena. J Colloid Interface Sci 309:194–224. doi:10.1016/j.jcis.2006.12.075

30. Bohinc K, Kralj-Iglic V, Iglic A (2001) Thickness of electrical double layer. Effect of ion size. Electrochim Acta 46:3033–3040

31. von Smoluchowski M (1921) Elektrische endosmose und stroemungsstroeme. In: Greatz L (ed) Elektrische endosmose und stroemungsstroemeedn. Barth J.A., Leizig

32. Kunz W, Henle J, Ninham BW (2004) 'Zur Lehre von der wirkung der Salze' (about the science of the effect of salts): Franz Hofmeister's historical papers. Curr Opin Colloid Int Sci 9:19–37. doi:10.1016/j.cocis.2004.05.005

33. Hofmeister F (1887) About regularities in the protein precipitating effects of salts and the relation of these effects with the physiological behaviour of salts. Arch exp Path Pharm 24:247–260

34. Hofmeister F (1888) Zur lehre von der wirkung der salze. Naunyn-Schmiedeberg's Arch Pharmacol 25:1–30

35. Kunz W, Lo Nostro P, Ninham BW (2004) The present state of affairs with Hofffieister effects. Curr Opin Colloid Interface Sci 9:1–18. doi:10.1016/j.cocis.2004.05.004

36. Karlstrom G, Carlsson A, Lindman B (1990) Phase diagrams of nonionic polymer -water systems. Experimental and theoretical studies of the effects of surfactants and other cosolutes. J Phys Chem 94:5005–5015

37. Jungwirth P, Winter B (2008) Ions at aqueous interfaces: from water surface to hydrated proteins. Annu Rev Phys Chem 59:343–66

38. Livney YD, Portnaya I, Faupin B, Ramon O, Cohen Y, Cogan U, Mizrahi S (2003) Interactions between inorganic salts and polyacrylamide in aqueous solutions and gels. J Polym Sci, Part B: Polym Phys 41:508–519

39. Cacace MG, Landau EM, Ramsden JJ (1997) The hofmeister series: salt and solvent effects on interfacial phenomena. Q Rev Biophys 30:241–277. doi:10.1017/s0033583597003363

40. Zhang YJ, Cremer PS (2006) Interactions between macromolecules and ions: the hofmeister series. Curr Opin Chem Biol 10:658–663. doi:10.1016/j.cbpa.2006.09.020

41. Collins KD (2006) Ion hydration: implications for cellular function, polyelectrolytes, and protein crystallization. Biophys Chem 119:271–281. doi:10.1016/j.bpc.2005.08.010

42. Collins KD, Neilson GW, Enderby JE (2007) Ions in water: characterizing the forces that control chemical processes and biological structure. Biophys Chem 128:95–104. doi:10.1016/j.bpc.2007.03.009

43. Collins KD (1995) Sticky ions in biological systems. Proc Natl Acad Sci USA 92:5553–5557

44. Collins KD (1997) Charge density-dependent strength of hydration and biological structure. Biophys J 72:65–72

45. Collins KD (2004) Ions from the hofmeister series and osmolytes: effects on proteins in solution and in the crystallization process. Methods 34:300–311. doi:10.1016/j.ymeth.2004.03.021

46. Livney YD, Ramon O, Kesselman E, Cogan U, Mizrahi S, Cohen Y (2001) Swelling of dextran Gel and osmotic pressure of soluble dextran in the presence of salts. J Polym Sci, Part B: Polym Phys 39:2740–2750

47. Collins KD, Washabaugh MW (1985) The Hofmeister effect and the behaviour of water at interfaces. Quart Rev Biophys 18:323–422

48. von Hippel PH, Schleich T (1969) Ion effects on solution structure of biological macromolecules. Acc Chem Res 2:257–265

49. Hamabata A, von Hippel PH (1973) Model studies on the effects of neutral salts on the conformation stability of biological macromolecules. II. Effects of vicinal hydrophobic groups on the specificity of binding of ions to amide groups. Biochem J 7:1271

50. Zhang Y, Cremer PS (2009) The inverse and direct Hofmeister series for lysozyme. Proc Natl Acad Sci 106:15249–15253. doi:10.1073/pnas.0907616106

51. Dobrynin AV, Colby RH, Rubinstein M (1995) Scaling theory of polyelectrolyte solutions. Macromolecules 28:1859–1871. doi:10.1021/ma00110a021

52. de Gennes PG (1979) Scaling concepts in polymer physics. Cornell University Press, Ithaca, NY

53. Pfeuty P (1978) Conformation des polyelectrolytes ordre dans les solutions de polyelectrolytes. J Phys (Paris) 39:C2–149

54. Fuoss RM (1948) Viscosity function for polyelectrolytes. J Polym Sci 3:603–604

55. Katchalsky A, Eisenberg H (1951) Molecular weight of polyacrylic and polymethacrylic acid. J Polym Sci 6:145–154

56. Tolstoguzov V, Srinivasan D, Paraf A (1997) Protein-polysaccharide interactions. CRC Press, Boca Raton

57. Grinberg VY, Tolstoguzov VB (1997) Thermodynamic incompatibility of proteins and polysaccharides in solutions. Food Hydrocol 11:145–158

58. Dautzenberg H (2001) Polyelectrolyte complex formation in highly aggregating systems: methodical aspects and general tendencies. In: Radeva T (ed) Polyelectrolyte complex formation in highly aggregating systems: methodical aspects and general tendencies. Marcel Dekker, New York, NY

59. de Kruif CG, Weinbreck F, de Vries R (2004) Complex coacervation of proteins and anionic polysaccharides. Curr Opin Colloid Int Sci 9:340–349

60. Livney YD (2008) Complexes and conjugates of biopolymers for delivery of bioactive ingredients via food. In: Garti N (ed) Complexes and conjugates of biopolymers for delivery of bioactive ingredients via food, 1st edn. Woodhead, Cambridge, England

61. Kossel A (1896) Ueber die basischen stoffe des zellkerns. Hoppe-Seiler's Z Physiol Chem 22:176–187

62. Tiebackx FW (1911) Simultaneous coagulation of two colloids. Zeitschrift fuer Chemie und Industrie der Kolloide 8:198–201

63. Bungenberg de Jong HG, Kruyt HR (1929) Coacervation (partial miscibility in colloid systems). Proc Acad Sci Amsterdam 32:849–856

64. Michaels AS, Miekka RG (1961) Polycation–polyanion complexes: preparation and properties of poly(vinylbenzyltrimethylammonium) poly(styrenesulfonate). J Phys Chem 65:1765–1773

65. Schmitt C, Turgeon SL (2011) Protein/polysaccharide complexes and coacervates in food systems. Adv Colloid Interface Sci 167:63–70. doi:10.1016/j.cis.2010.10.001

66. McClements DJ (2006) Non-covalent interactions between proteins and polysaccharides. Biotechnol Adv 24:621–625

67. Turgeon SL, Beaulieu M, Schmitt C, Sanchez C (2003) Protein-polysaccharide interactions: phase-ordering kinetics, thermodynamic and structural aspects. Curr Opin Colloid Int Sci 8:401–414

68. Tolstoguzov V (2000) Compositions and phase diagrams for aqueous systems based on proteins and polysaccharides. Int Rev Cytol 192:3–31

69. Doublier JL, Garnier C, Renard D, Sanchez C (2000) Protein-polysaccharide interactions. Curr Opin Colloid Int Sci 5:202–214

70. Schmitt C, Sanchez C, Sobry-Banon S, Hardy J (1998) Structure and technofunctional properties of protein-polysaccharide complexes: a review. Crit Rev Food Sci Nutr 38:689–753

71. Thunemann AF, Muller M, Dautzenberg H, Joanny JFO, Lowen H (2004) Polyelectrolyte complexes. In: Schmidt M (ed) Polyelectrolytes with defined molecular architecture II. Springer, Berlin

72. Ulrich S, Seijo M, Stoll S (2006) The many facets of polyelectrolytes and oppositely charged macroions complex formation. Curr Opin Colloid Int Sci 11:268–272. doi:10.1016/j.cocis.2006.08.002

73. Sukhishvili SA, Kharlampieva E, Izumrudov V (2006) Where polyelectrolyte multilayers and polyelectrolyte complexes meet. Macromolecules 39:8873–8881. doi:10.1021/ma061617p

74. Hoda N, Larson RG (2009) Explicit- and implicit-solvent molecular dynamics simulations of complex formation between polycations and polyanions. Macromolecules 42:8851–8863. doi:10.1021/ma901632c

75. Jvd G, Spruijt E, Lemmers M, Cohen Stuart MA (2011) Polyelectrolyte complexes: bulk phases and colloidal systems. J Colloid Interface Sci 361:407–422. doi:10.1016/j.jcis.2011.05.080

76. da Silva FLB, Jonsson B (2009) Polyelectrolyte-protein complexation driven by charge regulation. Soft Matter 5:2862–2868. doi:10.1039/b902039j

77. de Vries R, Stuart MC (2006) Theory and simulations of macroion complexation. Curr Opin Colloid Int Sci 11:295–301

78. da Silva FL, Lund M, Joensson B, Aakesson T (2006) On the complexation of proteins and polyelectrolytes. J Phys Chem B 110:4459–4464

79. Cooper CL, Dubin PL, Kayitmazer AB, Turksen S (2005) Polyelectrolyte-protein complexes. Curr Opin Colloid Int Sci 10:52–78

80. Weinbreck F, de Kruif CG (2003) Complex coacervation of globular proteins and gum arabic. Roy Soc Chem 284:337–344, Special Publication

81. Harnsilawat T, Pongsawatmanit R, McClements DJ (2006) Characterization of b-lactoglobulin-sodium alginate interactions in aqueous solutions: a calorimetry, light scattering, electrophoretic mobility and solubility study. Food Hydrocol 20:577–585

82. Ron N, Zimet P, Bargarum J, Livney YD (2010) Beta-lactoglobulin-polysaccharide complexes as nanovehicles for hydrophobic nutraceuticals in non-fat foods and clear beverages. Int Dairy J 20:686–693

83. Zimet P, Livney YD (2009) Beta-lactoglobulin and its nanocomplexes with pectin as vehicles for omega-3 polyunsaturated fatty acids. Food Hydrocol 23:1120–1126. doi:10.1016/j.foodhyd.2008.10.008

84. Bertrand P, Jonas A, Laschewsky A, Legras R (2000) Ultrathin polymer coatings by complexation of polyelectrolytes at interfaces: suitable materials, structure and properties. Macromol Rapid Commun 21:319–348. doi:10.1002/(sici)1521-3927(20000401)21:7<319::aid-marc319>3.0.co;2-7

85. Decher G (1997) Fuzzy nanoassemblies: toward layered polymeric multicomposites. Science 277:1232–1237. doi:10.1126/science.277.5330.1232

86. Decher G, Hong JD, Schmitt J (1992) Buildup of ultrathin multilayer films by a self-assembly process.3. Consecutively alternating adsorption of anionic and cationic polyelectrolytes on charged surfaces. Thin Solid Films 210:831–835. doi:10.1016/0040-6090(92)90417-a

87. Sukhishvili SA (2005) Responsive polymer films and capsules via layer-by-layer assembly. Curr Opin Colloid Int Sci 10:37–44. doi:10.1016/j.cocis.2005.05.001

88. Sukhorukov GB (2001) Designed nano-engineered polymer films on colloidal particles and capsules. Stud Interface Sci 11:383–414

89. Ogawa S, Decker EA, McClements DJ (2004) Production and characterization of O/W emulsions containing droplets stabilized by lecithin-chitosan-pectin mutilayered membranes. J Agric Food Chem 52:3595–3600

90. Aoki T, Decker EA, McClements DJ (2005) Influence of environmental stresses on stability of O/W emulsions containing droplets stabilized by multi-layered membranes produced by a layer-by-layer electrostatic deposition technique. Food Hydrocol 19:209–220

91. Radtchenko IL, Sukhorukov GB, Leporatti S, Khomutov GB, Donath E, Mohwald H (2000) Assembly of alternated multivalent ion/polyelectrolyte layers on colloidal particles. Stability of the multilayers and encapsulation of macromolecules into polyelectrolyte capsules. J Colloid Interface Sci 230:272–280. doi:10.1006/jcis.2000.7068

92. Cohen Stuart MA, Kleijn JM (2001) Kinetics of polyelectrolyte adsorption. In: Radeva T (ed) Kinetics of polyelectrolyte adsorptionedn. Marcel Dekker, New York

93. Kotz J, Kosmella S, Beitz T (2001) Self-assembled polyelectrolyte systems. Prog Polym Sci 26:1199–1232. doi:10.1016/s0079-6700(01)00016-8

94. Amiel C, Sikka M, Schneider JW, Tsao YH, Tirrell M, Mays JW (1995) Adsorption of hydrophilic-hydrophobic block-copolymers on silica from aqueous-solutions. Macromolecules 28:3125–3134. doi:10.1021/ma00113a015

95. Torchilin VP (2001) Structure and design of polymeric surfactant-based drug delivery systems. J Control Release 73:137–172. doi:10.1016/s0168-3659(01)00299-1

96. Zana R (2005) Dynamics in micellar solutions of amphiphilic block copolymers. In: Zana R (ed) Dynamics in micellar solutions of amphiphilic block copolymersedn. CRC Press/Taylor & Francis, New York

97. Perrin P, Millet F, Charleux B (2001) Emulsions stabilized by polyelectrolytes. In: Radeva T (ed) Emulsions stabilized by polyelectrolytes. Marcel Dekker, New York

98. Forster S, Abetz V, Muller AHE (2004) Polyelectrolyte block copolymer micelles. In: Schmidt M (ed) Polyelectrolytes with defined molecular architecture II, vol 166. Springer, Berlin, pp 173–210. doi:10.1007/b10951

99. Horne DS (2002) Casein structure, self-assembly and gelation. Curr Opin Colloid Interface Sci 7:456–461

100. Livney YD, Schwan AL, Dalgleish DG (2004) A study of beta-casein tertiary structure by intramolecular crosslinking and mass spectrometry. J Dairy Sci 87:3638–3647

101. Livney YD (2010) Milk proteins as vehicles for bioactives. Curr Opin Colloid Interface Sci 15:73–83

102. Shapira A, Davidson I, Avni N, Assaraf YG, Livney YD (2012) β-casein nanoparticle-based oral drug delivery system for potential treatment of gastric carcinoma: stability, target-activated release and cytotoxicity. Eur J Pharm Biopharm 80:298–305. doi:10.1016/j.ejpb.2011.10.022

103. Kataoka K, Harada A, Nagasaki Y (2001) Block copolymer micelles for drug delivery: design, characterization and biological significance. Adv Drug Deliv Rev 47:113–131. doi:10.1016/s0169-409x(00)00124-1

104. Zimet P, Rosenberg D, Livney YD (2011) Re-assembled casein micelles and casein nanoparticles as nano-vehicles for [omega]-3 polyunsaturated fatty acids. Food Hydrocol 25:1270–1276. doi:10.1016/j.foodhyd.2010.11.025

105. Semo E, Kesselman E, Danino D, Livney YD (2007) Casein micelle as a natural nano-capsular vehicle for nutraceuticals. Food Hydrocol 21:936–942

106. Vriezema DM, Aragones MC, Elemans J, Cornelissen J, Rowan AE, Nolte RJM (2005) Self-assembled nanoreactors. Chem Rev 105:1445–1489. doi:10.1021/cr0300688

107. Michel AS, Mestdagh MM, Axelos MAV (1997) Physico-chemical properties of carrageenan gels in presence of various cations. Int J Biol Macromol 21:195–200. doi:10.1016/s0141-8130(97)00061-5

108. Grant GT, Morris ER, Rees DA, Smith PJC, Thom D (1973) Biological interactions between polysaccharides and divalent cations: the egg-box model. FEBS Lett 32:195–198. doi:10.1016/0014-5793(73)80770-7

109. Gombotz WR, Wee SF (1998) Protein release from alginate matrices. Adv Drug Deliv Rev 31:267–285. doi:10.1016/s0169-409x(97)00124-5

110. Wang LX, Bloomfield VA (1990) Osmotic-pressure of polyelectrolytes without added salt. Macromolecules 23:804–809. doi:10.1021/ma00205a018

111. Fuoss RM, Katchalsky A (1951) The potential of an infinite rod-like molecule and the distribution of the counter ions. Proc Natl Acad Sci USA 37:579–589

112. Katchalsky A (1971) Polyelectrolytes. Pure Appl Chem 26:327–373

113. Noda I, Kato N, Kitano T, Nagasawa M (1981) Thermodynamic properties of moderately concentrated solutions of linear polymers. Macromolecules 14:668–676. doi:10.1021/ma50004a042

114. Tombs MP, Peacocke AR (1974) The osmotic pressure of biological macromolecules. Clarendon, Oxford

115. Donnan FG (1933) Some considerations relating to membrane equilibria and the secondary swelling of protein gels. J Soc Leather Trade Chem 17:136–143

116. Hill TL (1956) A fundamental studies. On the theory of the donnan membrane equilibrium. Discussions of the Faraday Society 21:31–45. doi:10.1039/DF9562100031

117. Hill TL (1957) Electrolyte theory and the donnan membrane equilibrium. J Phys Chem 61:548–553

118. Flory PJ, Rehner J Jr (1943) Statistical mechanics of crosslinked polymer networks II. Swelling. J Chem Phys 11:521–526

119. Flory PJ (1979) Molecular theory of rubber elasticity. Polymer 20:1317–1320. doi:10.1016/0032-3861(79)90268-4

120. Flory PJ (1953) Principles of polymer chemistry. Cornell University Press, Ithaca

121. James HM, Guth E (1953) Statistical thermodynamics of rubber elasticity. J Chem Phys 21:1039–1049

122. Skouri R, Schosseler F, Munch JP, Candau SJ (1995) Swelling and elastic properties of polyelectrolyte gels. Macromolecules 28:197–210. doi:10.1021

123. Khokhlov AR, Starodubtzev SG, Vasilevskaya VV (1993) Conformational transitions in polymer gels – theory and experiment. Adv Polym Sci 109:123–175

124. Katchalsky A, Michaeli I (1955) Polyelectrolyte gels in salt solutions. J Polym Sci 15:69–86

125. Katchalsky A, Lifson S, Eisenberg H (1951) Equation of swelling for polyelectrolyte gels. J Polym Sci 7:571–574

126. Khokhlov AR, Khalatur PG (2005) Solution properties of charged hydrophobic/hydrophilic copolymers. Curr Opin Colloid Interface Sci 10:22–29. doi:10.1016/j.cocis.2005.04.003

127. Holm C, Joanny JF, Kremer K, Netz RR, Reineker P, Seidel C, Vilgis TA, Winkler RG (2004) Polyelectrolyte theory. In: Polyelectrolytes with defined molecular architecture II, vol 166. Springer, Berlin, pp 67–111. doi:10.1007/B11349

128. Liao Q, Dobrynin AV, Rubinstein M (2003) Molecular dynamics simulations of polyelectrolyte solutions: osmotic coefficient and counterion condensation. Macromolecules 36:3399–3410. doi:10.1021/ma0259968

129. Stevens MJ, Kremer K (1995) The nature of flexible linear polyelectrolytes in salt-free solution – a molecular-dynamics study. J Chem Phys 103:1669–1690. doi:10.1063/1.470698

130. Krul LP, Nareiko EI, Matusevich YI, Yakimtsova LB, Matusevich V, Seeber W (2000) Water super absorbents based on copolymers of acrylamide with sodium acrylate. Polym Bull 45:159–165. doi:10.1007/pl00006832

131. Zohuriaan-Mehr MJ, Kabiri K (2008) Superabsorbent polymer materials: a review. Iran Polym J 17:451–477

132. Kazanskii KS, Dubrovskii SA (1992) Chemistry and physics of agricultural hydrogels. Adv Polym Sci 104:97–133

133. Saunders JR, Abu-Salih S, Khaleque T, Hanula S, Moussa W (2008) Modeling theories of intelligent hydrogel polymers. J Comput Theor Nanosci 5:1942–1960. doi:10.1166/jctn.2008.1001

134. Sata T, Yang WK (2002) Studies on cation-exchange membranes having permselectivity between cations in electrodialysis. J Membr Sci 206:31–60. doi:10.1016/s0376-7388(01)00491-4

135. Mizutani Y (1990) Ion-exchange membranes with preferential permselectivity for monovalent ions. J Membr Sci 54:233–257. doi:10.1016/s0376-7388(00)80612-2

136. Morris ER, Nishinari K, Rinaudo M (2012) Gelation of gellan – a review. Food Hydrocol 28:373–411. doi:10.1016/j.foodhyd.2012.01.004

137. He CL, Kim SW, Lee DS (2008) In situ gelling stimuli-sensitive block copolymer hydrogels for drug delivery. J Control Release 127:189–207. doi:10.1016/j.jconrel.2008.01.005

138. Scranton AB, Rangarajan B, Klier J (1995) Biomedical applications of polyelectrolytes. In: Peppasand NA, Langer RS (eds) Biomedical applications of polyelectrolytesedn. Springer-Verlag Berlin, Berlin

139. Park TG, Hoffman AS (1992) Synthesis and characterization of Ph- and or temperature-sensitive hydrogels. J Appl Polym Sci 46:659–671. doi:10.1002/app.1992.070460413

Polyelectrolytes, Simulation

Barbara Hribar-Lee and Vojko Vlachy
Faculty of Chemistry and Chemical Technology, University of Ljubljana, Ljubljana, Slovenia

Introduction

Nature and synthetic chemistry have provided polyelectrolytes of different shapes: They can be rod-like as, for example, DNA, or flexible (chain-like) as are many of the synthetic polyelectrolytes. Moreover, they can change their conformation in solution and, under the influence of external conditions such as nature of the

solvent, salt content, pH, or temperature, undergo the transition from globular to extended state. In the simplest case, the polyelectrolyte solutions contain long and often highly charged polyions and the related number of counterions to render the systems electroneutral. Thermodynamic, transport, and structural measurements indicate that their properties are governed by the Coulomb interaction, as also by the short-range, solvent mediated, specific ion effects. The role of the hydrophobic interaction, especially in the systems containing benzene groups, or in conjugated polyelectrolytes, is also important. Altogether we deal with a complicated system where we need to treat accurately both, the long-range Coulomb interaction (hundred angstroms), as well as the short-range (few angstroms only) forces.

Cylindrical Cell Model

First computer simulations of simple rod-like model of polyion were performed in the cell model approximation [1–4]. In [1] the polyions were treated as rigid cylinders of finite length. The counterions were charged hard spheres embedded in the dielectric continuum within the cell. The osmotic coefficient was found to decrease with the decreasing degree of polymerization. The concentration dependence of this quantity exhibited minimum, shifted toward lower concentrations when the degree of polymerization increased. Later, in [2, 3], the distributions of mono- and divalent counterions around very long cylindrical polyion were simulated. Important conclusion was that the Poisson-Boltzmann equation provided semiquantitatively correct results for the osmotic coefficient. Inclusion of the ion-ion correlations through the modified Poisson-Boltzmann theory led to considerably better agreement between theory and simulations, especially when divalent counterions were present in solution. The computer simulations were also used to calculate osmotic coefficient via the contact theorem [4, 5]. The latter two studies demonstrated that neglecting of the interionic correlations by the mean field

approach leads to a partial compensation of the shortcomings of the Poisson-Boltzmann osmotic equation. In another contribution, Le Bret and Zimm [6] used Monte Carlo method to investigate the ion size effects on distribution of ions in solution of rod-like polyelectrolyte mimicking DNA. Extensive Monte Carlo simulations and comparison with the other polyelectrolyte theories were performed by Mills et al. [7, 8]. The grand canonical simulations of the rod-like polyelectrolyte were performed in [9, 10]. The mean activity coefficient of simple electrolyte in solution was calculated and, very interestingly, the results for divalent counterions indicated the "charge inversion" [9]. Extensive simulations of the rod-like polyions in the cell model and comparisons with the modified PB theory were performed by Das et al. [11, 12] and Piñero et al. [13]. In the latter study, the emphasis was on exploration of the catalytic effect on ions, caused by presence of rod-like polyions.

Flexible Polyelectrolytes Interacting via the Screened Coulomb Potential

Polyions are not fully extended in solution and those, containing hydrophobic groups, may collapse into the globule under certain conditions. Valleau simulated flexible polyelectrolyte (a constrained "necklace" model) in ionic solution [14]. Average conformations of the polyion immersed in a primitive-model aqueous electrolyte were studied for several model parameters. Similar studies were performed by Woodward and Jönsson using a bead-spring polyelectrolyte model [15]; they found the screened Coulomb potential between charged species (polyion monomers or ions) to be an excellent approximation for systems with low and moderate added salt concentrations of 1:1 electrolyte. For divalent counterions, this is not true anymore. Seidel [16] studied the persistence length for the same model potential and found an evident influence of the flexibility of the underlying neutral chain on properties of the charged chain.

Modeling Flexible Polyelectrolytes with Explicit Ions

Kremer and coworkers [17–19] performed very complete molecular dynamics simulations for multichain polyelectrolyte systems. The Coulomb interaction between the monomers (bead-spring model polyelectrolyte) and counterions was treated explicitly. Experimental results for the osmotic pressure and the structure factor were reproduced. In addition, the persistence length and end-to-end distance of polyelectrolyte chains were calculated. The authors showed that the chains exhibit significant departures from the fully extended conformation even at low chain densities. Furthermore, the chains contracted significantly before they overlapped. At high polymer density and poor solvent conditions [18], equivalent to strongly screened electrostatic interaction, the chains were found to be extremely collapsed. The pearl necklace conformations were observed [19] and analyzed in detail, as was also the position of the first peak of the structure factor with respect to the monomer density. To study the shift in the apparent dissociation constant, Monte Carlo simulations of linear weak polyacids have been performed in the cell model approximation [20]. Widom's particle-insertion method was utilized for the purpose. Simulation results were compared with experiments. Thermodynamic properties of a model solution with chain-like polyions and hard sphere counterions were, for the purpose of comparison with the integral equation theory, published in [21]. There were other studies in this direction. For example, conformational characteristics of single flexible polyelectrolyte chain of 150 univalent and negatively charged beads, connected by a harmonic-like potential in the presence of an equal number of positive counterions, were studied in molecular dynamics simulations by Jesudason et al. [22]. Extensive computer simulations of polyelectrolyte solutions were performed by Dobrynin and coworkers [23–26] (for review see [24–26]). In [23], they evaluated osmotic coefficients and counterion distribution functions of rod-like and flexible polyelectrolyte chains with explicit counterions by using

molecular dynamics approach. Osmotic pressure was studied also by Chang and Yethiraj [27], and very recently by Carrillo and Dobrynin [28]. In this last paper, the polyelectrolyte solution was modeled as an ensemble of bead-spring chains of charged Lennard-Jones particles with explicit counterions and salt ions. The simulations showed that in dilute and semidilute polyelectrolyte solutions, the electrostatic-induced chain persistence length scaled with the solution ionic strength as $I^{-\frac{1}{2}}$. This dependence is due to the counterion condensation on polyions. The simulations confirmed that the peak position in the polymer scattering function scaled with the polymer concentration c_p in dilute polyelectrolyte solutions as $c_p^{1/3}$. In semidilute polyelectrolyte solutions, and for low concentration of added salt, the position of this peak shifts toward the large values of the wave number. The paper contains important citations of previous relevant studies. The rheology of dilute salt-free polyelectrolyte solutions was studied by Stoltz and coworkers [29] using Brownian dynamics simulations and coarse-grained bead-spring polyelectrolyte model with explicit counterions. An overview of the simulation studies and theories of polyelectrolyte solutions was provided by Yethiraj [30].

Explicit Water Simulations of Polyelectrolyte Solutions

All-atom simulations of polyelectrolyte systems are less frequent and they only became emerging in last 5 years. Among the first such studies was the paper of Molnar and Rieger [31]. These authors studied the "like-charge attraction" between polyanions observed in the presence of multivalent cations on a fully atomistic scale. As a relevant example, they examined the interaction of negatively charged carboxylic groups of sodium polyacrylate molecules with divalent calcium ions in explicit water. They showed that Ca^{2+} ions initially associate with single chains of polyacrylates; strongly shielded polyanions approach each other and eventually precipitate. Chialvo and Simonson [32] examined the

solvation behavior of short-chain polystyrene sulfonate in aqueous electrolyte solutions by molecular dynamics simulation. The explicit atomistic picture of all species was used. The goal was to determine the hydration effects on the conformation of the polyelectrolyte with varying degree of sulfonation and varying the valence of counterions. Chang and Yethiraj [33] studied dilute salt-free solutions of charged flexible polymer molecules in poor solvents. The simulations suggest that the presence of explicit solvent molecules can be an important aspect of polyelectrolyte behavior in poor solvents. In another contribution, Ju and coworkers [34] simulated solution of poly-methacrylic acid in aqueous solutions at various degrees of charge density. They observed that water molecules may act as a bridging agent between two neighboring carboxylic groups. These bridged water molecules stabilize the rod-like chain conformation and display different dynamic properties from the bulk water. A similar study was recently published by Sulatha and Natarajan [35]. Druchok and coworkers [36–38] presented a molecular dynamics simulation in explicit water of a solution of aliphatic 3,3- and 6,6-ionene oligocations with sodium co-ions and fluorine, chlorine, bromine, and iodine counterions. The purpose of these studies was to investigate how the increasing number of methylene groups (increased hydrophobicity) affected the specific ion interaction between the counterions in solution and quaternary ammonium group on the ionene backbone. The results were able to explain some experimental observations in ionene solutions and weakly charged polyelectrolytes in general.

Simulations of Polyelectrolytes at Surfaces

The adsorption of polyelectrolytes to surfaces is a problem of growing interest stimulated by many industrial applications. Explicit and implicit solvent models were used in studying this problem via computer simulation [39, 40]. Using molecular and Brownian dynamics simulations and freely jointed models of polyelectrolytes, Reddy and Yethiraj [39] established that the solvent plays a dominant role in the adsorption of polyelectrolytes in poor solvents, and that the many-body effects qualitatively influence the adsorption characteristics and mechanism. The effects of surface charge density, charge distributions, solvent quality, and short-ranged interactions were studied by Carillo and Dobrynin by using the molecular dynamics simulations [25, 41].

Future Directions

The progress in this area of research is hampered by uncertainties in the current force fields, mixing rules, and other details of simulation protocols. In addition, some thermodynamic properties of solution like, the enthalpy or heat capacity of solution, cannot be simulated with sufficient accuracies to be tested against the experimental data for polyelectrolyte solutions. Further development of the force fields and methods to calculate solution thermodynamic parameters is needed to advance this area of science.

Cross-References

▶ Polyelectrolytes, Properties
▶ Specific Ion Effects, Theory

References

1. Vlachy V, Dolar D (1982) Monte Carlo studies of polyelectrolyte solution at low degrees of polymerization. J Chem Phys 76:2010–2014. doi:10.1063/1.443174
2. Bratko D, Vlachy V (1982) Distribution of counterions in the double layer around a cylindrical polyion. Chem Phys Lett 90:434–438. doi:10.1016/0009-2614(82)80250-9
3. Bratko D, Vlachy V (1985) Monte Carlo studies of polyelectrolyte solutions. Effect of polyelectrolyte charge density. Chem Phys Lett 115:294–298. doi:10.1016/0009-2614(85)80031-2
4. Vlachy V (1982) On the virial equation for the osmotic pressure of linear polyelectrolytes. J Chem Phys 77:5823–5825. doi:10.1063/1.443741

5. Piñero J, Bhuiyan LB, Reščič J, Vlachy V (2006) Coulomb correlation between counterions in the double layer around cylindrical polyions. Acta Chim Slov 53:316–323

6. Le Bret M, Zimm B (1984) Monte Carlo determination of the distribution of ions about a cylindrical polyelectrolyte. Biopolymers 23:271–285

7. Mills P, Anderson CF, Record MT Jr (1985) Monte-Carlo studies of counterion DNA interactions – comparison of the radial-distribution of counterions with predictions of other poly-electrolyte theories. J Phys Chem 89:3984–3994. doi:10.1021/j100265a012

8. Mills P, Paulsen MD, Anderson CF, Record MT Jr (1986) Monte-Carlo simulations of counterion accumulation near helical DNA. Chem Phys Lett 129:155–158. doi:10.1016/0009-2614(86)80188-9

9. Vlachy V, Haymet ADJ (1986) A grand canonical Monte Carlo simulation study of polyelectrolyte solutions. J Chem Phys 84:5874–5880. doi:10.1063/1.449898

10. Mills P, Anderson CF, Record MT Jr (1986) Grand canonical Monte-Carlo calculations of thermodynamic coefficients for a primitive model of DNA salt-solutions. J Phys Chem 90:6541–6548. doi:10.1021/j100282a025

11. Das T, Bratko D, Bhuiyan LB, Outwaite CW (1995) Modified Poisson-Boltzmann theory applied to polyelectrolyte solutions. J Phys Chem 99:410–418. doi:10.1021/j100001a061

12. Das T, Bratko D, Bhuiyan LB, Outwaite CW (1997) Polyelectrolyte solutions containing mixed valency ions in the cell model: a simulation and modified Poisson-Boltzmann study. J Chem Phys 107:9197–9207. doi:10.1063/1.475211

13. Piñero J, Bhuiyan LB, Reščič J, Vlachy V (2008) Ionic correlations in the inhomogeneous atmosphere surrounding cylindrical polyions. Catalytic effects of polyions. J Chem Phys 128:214904

14. Valleu JP (1989) Flexible polyelectrolyte in ionic solution: a Monte Carlo study. Chem Phys 129:163–174. doi:10.1016/0301-0104(89)80001-1

15. Woodward CE, Jönsson B (1991) Monte Carlo and mean field studies of a polyelectrolyte in salt solution. Chem Phys 155:207–219. doi:10.1016/0301-0104(91)87021-M

16. Seidel C (1996) Polyelectrolyte simulation. Ber Bunsenges-PCCP 100:757–763

17. Stevens MJ, Kremer K (1995) The nature of flexible linear polyelectrolytes in salt-free solution – a molecular-dynamics study. J Chem Phys 103:1669–1690. doi:10.1063/1.470698

18. Micka U, Holm C, Kremer K (1999) Strongly charged, flexible polyelectrolytes in poor solvents: molecular dynamics simulations. Langmuir 15:4033–4044. doi:10.1021/la981191a

19. Limbach HJ, Holm C, Kremer K (2002) Structure of polyelectrolytes in poor solvent. Europhys Lett 60:566–572. doi:10.1209/epl/i2002-00256-8

20. Ullner M, Woodward CE (2000) Simulations of the titration of linear polyelectrolytes with explicit simple ions: comparisons with screened coulomb models and experiments. Macromolecules 33:7144–7156

21. Bizjak A, Reščič J, Kalyuzhnyi YV, Vlachy V (2006) Theoretical aspects and computer simulations of flexible charged oligomers in salt-free solutions. J Chem Phys 125:214907. doi:10.1063/1.2401606

22. Jesudason CG, Lyubartsev AP, Laaksonen A (2009) Conformational characteristics of single flexible polyelectrolyte chain. Eur Phys J E 30:341–350. doi:10.1140/epje/i2009-10532-5

23. Liao Q, Dobrynin AV, Rubinstein M (2003) Molecular dynamics simulations of polyelectrolyte solutions: osmotic coefficient and counterion condensation. Macromolecules 36:3399–3410. doi:10.1021/ma0259968

24. Dobrynin AV (2004) Molecular simulations of charged polymers. In: Kotelyanskii M, Theodorou DN (eds) Simulation methods for polymers. Marcel Dekker, New York, pp 259–312

25. Dobrynin AV, Rubinstein M (2005) Theory of polyelectrolytes in solutions and at surfaces. Prog Polym Sci 30:1049–1118. doi:10.1016/j.progpolymsci.2005.07.006

26. Dobrynin AV (2008) Theory and simulations of charged polymers: from solution properties to polymeric nanomaterials. Curr Opin Coll Interface Sci 13:376–388. doi:10.1016/j.cocis.2008.03.006

27. Chang R, Yethiraj A (2005) Osmotic pressure of salt-free polyelectrolyte solutions: a Monte Carlo simulation study. Macromolecules 38:607–616. doi:10.1021/ma0486952

28. Carrillo YJ-M, Dobrynin AV (2011) Polyelectrolytes in salt solutions: molecular dynamics simulations. Macromolecules 44:5798–5816. doi:10.1021/ma2007943

29. Stoltz C, de Pablo JJ, Graham MD (2007) Simulation of nonlinear shear rheology of dilute salt-free polyelectrolyte solutions. J Chem Phys 126:124906. doi:10.1063/1.2712182

30. Yethiraj A (2009) Liquid state theory of polyelectrolyte solutions. J Phys Chem B 113:1539–1551. doi:10.1021/jp8069964

31. Molnar F, Rieger J (2005) "Like-charge attraction" between anionic polyelectrolytes: molecular dynamics simulations. Langmuir 21:786–789. doi:10.1021/la048057c

32. Chialvo AA, Simonson JM (2005) Solvation behavior of short-chain polystyrene sulfonate in aqueous electrolyte solutions: a molecular dynamics study. J Phys Chem B 109:23031–23042. doi:10.1021/jp053512e

33. Chang R, Yethiraj A (2006) Dilute solutions of strongly charged flexible polyelectrolytes in poor solvents: molecular dynamics simulations with explicit solvent. Macromolecules 39:821–828. doi:10.1021/ma051095y

34. Ju S-P, Lee W-J, Huang C-I, Cheng W-Z, Chung Y-T (2007) Structure and dynamics of water surrounding

the polymethacrylic acid. A molecular dynamics study. J Chem Phys 126:224901

35. Sulatha MS, Natarajan U (2011) Origin of the difference in structural behavior of poly(acrylic acid) and poly(methacrylic acid) in aqueous solution discerned by explicit-solvent explicit-ion MD simulations. Ind Eng Chem Res 50:11785–11796. doi:10.1021/ie2014845

36. Druchok M, Hribar–Lee B, Krienke H, Vlachy V (2008) A molecular dynamics study of short–chain polyelectrolytes in explicit water: toward the origin of ion–specific effects. Chem Phys Lett 450:281–285. doi:10.1016/j.cplett.2007.11.024

37. Druchok M, Vlachy V, Dill KA (2009) Computer simulations of ionenes, hydrophobic ions with unusual solution thermodynamic properties. The ion-specific effects. J Phys Chem B 113:14270–14276. doi:10.1021/jp906727h

38. Druchok M, Vlachy V, Dill KA (2009) Explicit − water molecular dynamics study of a short − chain 3,3 ionene in solution with sodium halides. J Chem Phys 130:134903-1–134903-8. doi:10.1063/1.3078268

39. Reddy G, Yethiraj A (2010) Solvent effects in polyelectrolyte adsorption: computer simulation with explicit and implicit solvent. J Chem Phys 132:074903. doi:10.1063/1.3319782

40. Reddy G, Chang R, Yethiraj A (2006) Adsorption and dynamics of a single polyelectrolyte chain near a planar charged surfaces: molecular dynamics simulation with explicit solvent. J Chem Theory Comput 2:630–636. doi:10.1021/ct050267u

41. Carillo J-MY, Dobrynin AV (2007) Molecular dynamics simulation of polyelectrolyte adsorption. Langmuir 23:2472–2482. doi:10.1021/la063079f

Polymer Electrolyte Fuel Cells (PEFCs), Introduction

Günther G. Scherer
Electrochemistry Laboratory, Paul Scherrer Institute, Villigen, Switzerland

Introduction

Novel highly efficient conversion technologies for mobility (electromobility) and combined heat and power systems (CHP) with independence on fossil fuels, in particular crude oil, are of utmost interest to face the energy challenges of the future [1, 2]. Fuel cell technology, based on the "cold" combustion of a fuel in an electrochemical cell, can fulfill these requirements. Another area of application for fuel cell technology is portable electric and electronic devices, where the argument of potentially higher energy density as compared to today's available battery technologies, hence, longer time of operation, is of prime interest [3].

The polymer electrolyte fuel cell concept, utilizing a thin ion-conducting polymer film, can fulfill the specifications of many of these applications. Typically operating at temperatures around 100 °C, this technology is the choice for many of these applications, due to their flexibility in start at ambient temperature, load following behavior, flexible power demand, etc. However, limitations exist for operation temperatures below 100 °C in the freedom of choice of fuel, limiting this essentially to hydrogen at high purity.

In this context, the installation of new supply infrastructures for alternative fuels, e.g., H_2, is an important additional economical and political factor, in particular for mobility applications. Dedicated well-to-wheel energy analysis has clearly shown that energy conversion in fuel cells has to be based on fuels derived from renewable sources, particularly when hydrogen is the fuel [4].

The Solid Polymer Electrolyte

The characteristics of any fuel cell technology are determined by specifics of the electrolyte chosen, e.g., low or high temperature, acidic or alkaline. However, general statements can be made, which hold for any electrolyte, due to its universal function it has to fulfill in an electrochemical cell.

This concerns the transport of charge in ionic form from one interface to the other within the cell. The ion conduction should be carried by an ion, which is produced at one electrode and consumed at the other to avoid losses caused by concentration gradients, hence minimize losses in the ionic circuit [5]. This majority ion should carry as much charge as possible through the

Polymer Electrolyte Fuel Cells (PEFCs), Introduction, Fig. 1 Specific conductivity versus temperature of different electrolytes interesting for fuel cell applications (Adopted from K. D. Kreuer)
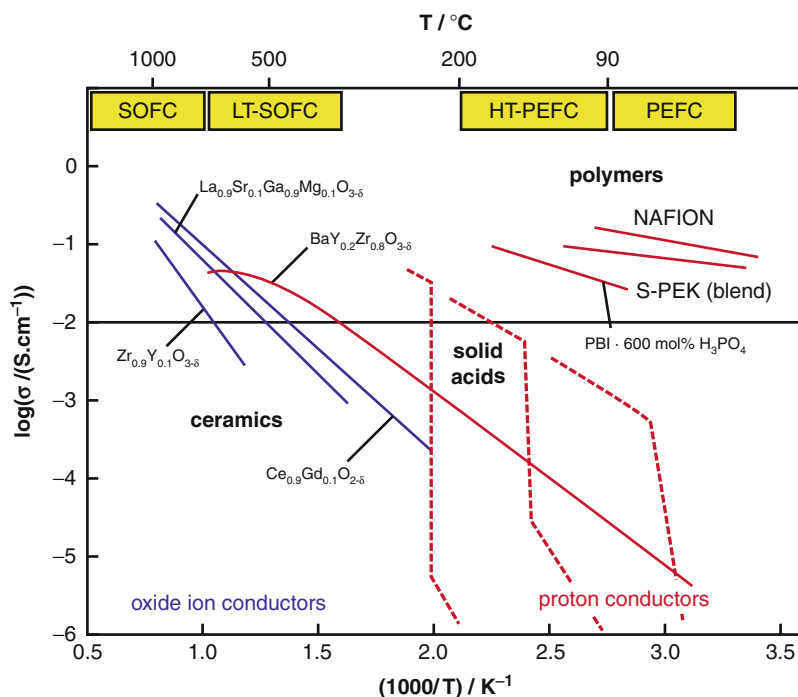

electrolyte; as a consequence, its transport number (Hittorf number) should be as high as possible, ideally one. For high power applications with an aqueous electrolyte, the concentration of this respective anion or cation must be high and exclusively responsible for conduction. Typically, a specific ionic conductivity in the range of 100 mS/cm is required, which at a current density of 1 A/cm^2 and an electrolyte gap of 100 μm would yield an ohmic voltage loss in the range of 100 mV. As seen in Fig. 1, the conductivities of various electrolytes are strongly temperature dependent and cover a wide temperature range, depending on the ion-conducting species in its respective environment (material). Again, electrolytes are of interest, which offer the opportunity that the ionic species is participating in the fuel cell reaction.

Further, the electrolyte material has to act as separator to (1) avoid crossover and, as a consequence, "hot" combustion of the fuel and the oxidant at the respective counter electrode and (2) to avoid touching of the electrodes by short circuiting the electronic pathway. Thereby, the electrolyte/separator gap should be as narrow

as possible to lower the ohmic contribution to the overall voltage loss. In case of a liquid electrolyte, it can be absorbed into an inert matrix, providing porosity high enough for an ionic conduction path with low tortuosity for the ion and at the same time a high enough bubble pressure to suppress gas crossover. An ideal concept is the one of a solid electrolyte, which fulfills the dual electrolyte and separator function at the same time, providing a transfer number of one for the current carrying ionic species, as in the case of solid polymer electrolytes (ion-exchange membranes), thereby excluding a contribution of electronic conduction.

One has to emphasize that the electrolyte has to sustain the potential window of the respective fuel cell reaction, given by the Gibbs free energy, at least over the device lifetime, specified for a certain application.

The idea to utilize a "solid ion-exchange membrane electrolyte" in a secondary cell employing metal electrodes was first published by Grubb in 1959 [6], reflecting the fact that a solid electrolyte acts in the dual function of ion conductor and separator. This concept was extended to H$_2$/O$_2$

$$-(CF_2-CF_2)_k-(CF_2-CF)_l-$$
$$| $$
$$O-(CF_2-CF-O)_m-CF_2-CF_2-SO_3H$$
$$| $$
$$CF_3$$
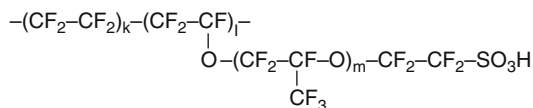
Polymer Electrolyte Fuel Cells (PEFCs), Introduction, Fig. 2 Generalized structure formula of Nafion®-type membranes (DuPont) with $m = 1$, $l = 1$, $k = 5-7$

fuel cells in 1960 [7]. The solid polymer electrolyte consisted of a heterogeneous membrane, where particles of sulfonated cross-linked polystyrene bonded into sheet form with an inert binder. Actually, the realization of this concept happened only a few years after the preparation of a free-standing synthetic polymeric ion-exchange membrane was described by Juda et al. for the first time [8].

Many different types of polymer membranes containing fixed ionic groups have been explored since. Up to today, the materials of choice are perfluoro sulfonic acid membranes of the Nafion-type (Fig. 2), for the first time described by Grot [9]. These materials, similar products have later been developed by other companies (Asahi Glass, Asahi Kasei, Solvay, 3M, Gore, etc.), have been continuously improved for their application in fuel cells. A comprehensive overview of membrane development can be found in [10].

The Concept of the Polymer Electrolyte Fuel Cells

The idea of using a thin ion-conducting polymer membrane, *solid polymer electrolyte*, as electrolyte and separator can lead to different concepts of cells. Firstly, when ionic charges, anions or cations, are chemically bound to the polymer (ionomer) network, the respective countercharge can move freely within the polymer volume, preconditioned a certain volumetric charge density within the polymer exists, which under uptake of, e.g., water, leads to phase separation into a hydrophobic polymer (backbone) and a hydrophilic, charge-containing phase [11]. As a consequence, the polymer morphology allows the continuous transport of this ion from one electrode interface to the other. One has to
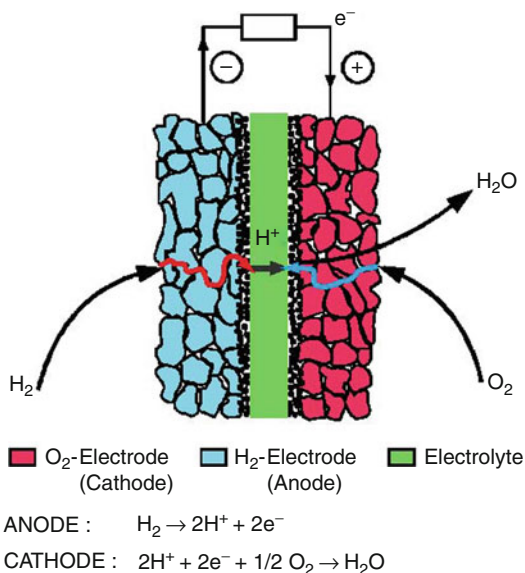
Polymer Electrolyte Fuel Cells (PEFCs), Introduction, Fig. 3 Simplified scheme with an acidic solid polymer electrolyte, e.g., the polymer electrolyte fuel cell (*PEFC*). Fuel, H_2; Oxidant, O_2. Only porous gas diffusion electrodes and electrolyte are shown; cell housing is not shown [12]

emphasize that ionic conductivity increases with water content. The optimization of the in situ water content of the solid electrolyte is of paramount importance for an optimal performance, whereby the visco-mechanical properties of the polymer sheet have to be balanced.

A simplified scheme of the electrochemical heart of a PEFC is displayed in Fig. 3, where the "central solid electrolyte" is contacted by two porous gas diffusion electrodes (GDLs), which are in intimate contact to the membrane surface (see below, three phase boundary). At the interface to the membranes, the GDLs contain nanoparticles of platinum (black dots) as electrocatalyst.

Depending on the fuel, H_2, MeOH (gas or liquid), or other, the solid polymer electrolyte properties have to be tailored, in particular for their properties towards separation of fuel and oxidant.

Generally speaking, the ion conduction in the electrolyte contributes to the losses (ohmic losses, see Fig. 3) in the cell voltage.

Hence, one of the major tasks in fuel cell development is the reduction of these losses in the ionic circuit part, because the work available in the external electronic circuit should be as high as possible. This concerns the reduction of the membrane thickness to as low values as possible, today down to a few microns, and the optimization of the specific conductivity at low water content (see water management).

In aqueous acidic electrolytes the ionic conduction is provided by an H^+ ion, respectively $H(H_2O)_n^+$. As mentioned above, H^+ is created by the anodic oxidation of H_2 as a fuel, and the conducting species is transported to the cathode, where it is consumed in the direct (ideally four electrons) cathodic reduction of molecular oxygen. Hereby, water as the reaction product appears at the cathode side of the cell.

In an anion exchange membrane (not shown), the ionic conduction is provided by OH^--ions, created by the ORR at the cathode. Principally, OH^- ions are carriers for the O^{2-} ions, produced as intermediate by the cathodic reduction reaction of molecular O_2 and the follow-up reaction with a water molecule. After conduction, OH^- reacts with the H^+ created at the anode and yields water as a product at the anode side.

Solid polymer electrolytes on the basis of a polymer cation exchange membrane in H^+-form or an anion exchange polymer membrane in OH^--form can be considered as quasi-aqueous electrolytes, whereby the water is absorbed in the phase separated ionic nano morphology of the respective material. This nano morphology forms ionic pathways through the polymeric membrane connecting the two fuel cell electrodes.

In cells operated at temperatures below 100 °C, liquid water will be the reaction product. For operation temperatures above the boiling point of water, a cell with an aqueous or quasi-aqueous electrolyte can be operated, however, at the expense of pressurizing it to avoid loss of the water and, as a consequence, concentration and conductivity changes in the electrolyte. Hence, water management of a PEFC operated at temperatures below 100 °C is an engineering issue and of utmost importance for many high power applications. Novel methods have been introduced to detect liquid water in PEFCs and to help understanding product water removal water [13].

## The Role of Electrocatalysis and the Electrode/Electrolyte Interface

Next to the voltage losses due to ionic conduction, voltage losses due to the activation overvoltages of the respective electrode reactions arise, as described by the Butler-Volmer, respectively the Tafel equation [14]. At the same value of current density the overvoltage for the HOR is much smaller than for the ORR, due to the simpler electron transfer kinetics. Overvoltage for an electrochemical reaction shows also a strong temperature dependency, as does activation energy, and decreases with increasing temperature.

Generally, for fuel cells with an acidic electrolyte, platinum is the electrocatalyst of choice at temperatures at these respective temperatures, due to stability requirements in this particular environment. High dispersion of the catalyst is required, taking into account its nature as a precious metal, to provide a high surface area to volume ratio. Platinum nanoparticles in the diameter range of a few nanometers, typically 2–5 nm, supported on carbon particles are utilized. Different carbons with different surface area (up to 800 m^2/g) are used. The amount of platinum in the catalyst powder is specified as weight % per g of carbon and further as mg loading per cm^2 geometric electrode area.

Platinum is prone to CO adsorption at temperatures of around 100 °C and below. For this reason, care has to be taken with respect to the purity of hydrogen, in particular for hydrogen liberated from a C-containing fuel by a reforming process (steam reforming, partial oxidation, autothermal reforming).

Alkaline electrolytes promise to allow cheaper, non-precious metal catalysts like nickel and its alloys.

There is a common problem to all material selections for the different fuel cell types,

(shown for cathode)
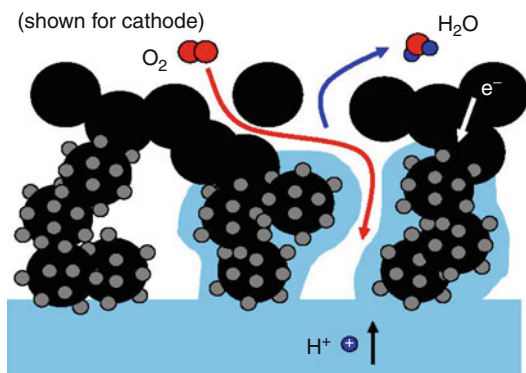
Polymer Electrolyte Fuel Cells (PEFCs), Introduction, Fig. 4 Electrode layer (interphase) with three phase boundary (schematic) of a polymer electrolyte fuel cell (cathode side). *Blue*, polymer electrolyte; *black*, carbon particles; *grey*, platinum nanoparticles (Adopted from L. Gubler)

namely, to generate an optimal electrolyte/electrode interface. One has to realize that gaseous molecular reactants are converted into ionic species, solvated/hydrated in their electrolyte medium, by exchanging electrons with the electrode material. This reaction occurs at the so-called triple phase boundary (triple point), where electron conducting, ion conducting, and gas phase (eventually dissolved in the electrolyte) join to each other. To allow a high surface area for current generation, the electrolyte/electrode interface is extended into a three-dimensional *interphase* with a thickness of a few μm. For a polymer electrolyte fuel cell, this *interphase* is drafted in Fig. 4 for the cathode (oxygen) side.

Types of PEFCs

Hydrogen is the preferred fuel for PEFCs. However, a PEFC can also be fed by liquid or gaseous methanol, called direct methanol fuel cell, DMFC. Other fuels based on alcohols, e.g., the direct ethanol fuel cell, DEFC, are subject to research.

In the past, most concepts for an alkaline fuel cell have been described with an aqueous alkaline electrolyte. Recently, also anion exchange membranes, alkaline solid polymer electrolytes, have been considered [15].

H$_2$-Fed PEFC

This type of H$_2$-fed fuel cell, due to its high achievable specific and volumetric power density (in the range of 1 kW/kg and 1 kW/l and above), its cold start behavior, and its fast load following properties, has found the interest of automotive industry and is under development by all major automotive companies.

A thin ion-conducting polymer sheet, typically in the range of 25 μm, is utilized as solid electrolyte, i.e., electrolyte and separator, in the PEFC (Fig. 3). For thermal stability reasons, only cation exchange membranes in the H$^+$-form have been considered up to today for technical applications (see also alkaline fuel cell). In comparison to cells with liquid electrolyte, this PEFC-concept offers the advantage that the "electrolyte" is chemically bound within the polymer matrix and only water as reactant, in addition to the gases, appears in the peripheral system components. Membranes are perfluorinated or partially fluorinated polymers, with side chains ending in pendant acid groups, e.g., the sulfonic acid group –SO$_3$H.

Under operation, the membrane has to contain some water, e.g., 15 water molecules per sulfonic acid group, to provide the necessary specific conductivity. This fact causes consequences for some of the system auxiliaries, as the gases, hydrogen and air, have to be humidified before flowing into the cell to sustain the hydration level in the membrane.

The acidic electrolyte asks for a precious metal catalyst; hence platinum supported on carbon particles serves as electrocatalyst, with typical Pt loadings of ca. 0.1 mg/cm^2 at the anode side and ca. 0.4 mg/cm^2 at the cathode side. Platinum nanoparticles, typically a few (3–5) nm in diameter, are deposited on various carbon substrates (e.g., 20–40 %Pt/C) by wet chemical processes and then further processed in combination with solubilized ionomer material and binder(s) (PTFE) to yield an ink, which then is applied either to the electrolyte membrane surface (CCM, catalyst coated membrane) or to the GDL to form the GDE.

Extensive characterization of these electrocatalysts for the fuel cell reactions has shown that the electrocatalytic activity of these nanoparticles is by a factor 10 lower than the activity of a polycrystalline platinum surface for the respective reactions, HOR or ORR [16]. This difference is not fully understood yet.

An interesting proprietary approach has been followed recently by the 3M Company, creating a continuous electrode area covered by nanoscale Pt-whiskers. Reactivity of these electrocatalytic layers is in the range of polycrystalline platinum surfaces [17].

Today, pure hydrogen is considered as the ideal fuel. Due to its CO-content, hydrogen derived from C-containing fuels (by steam reforming (SR), partial oxidation (POX), or autothermal reforming (ATR) followed by preferential oxidation (PROX)) would need specific measures in terms of electrocatalysis, e.g., PtRu as bifunctional electrocatalyst, to allow oxidation of CO. As an alternative, purification methods of the anode gas stream prior to entering the cell down to only a few ppm CO (depending on operation temperature) are necessary.

The electrocatalytic layers are contacted by gas diffusion layers (GDLs), allowing the gases, H_2 and O_2, as reactants to be passed to the interface and liquid H_2O as product removed from the interface. These GDLs consist of sheets of carbon cloth or paper with typically 100 μm thickness and 50 % porosity (Fig. 2). This arrangement of membrane, electrocatalytic layers, and gas diffusion layers is colloquially called membrane–electrode-assembly (MEA).

Most of the applications of this fuel cell type are developed for air operation, taking advantage of utilizing one reactant from the ambient environment. However, there exist also some applications in which pure oxygen is employed as oxidant. Due to the higher partial pressure of oxygen and the absence of electrochemically inert nitrogen as the majority component in the cathodic gas stream, humidification issues of the cell can be strongly simplified [18, 19].

Methanol-Fed Fuel Cell (PEFC-Type)

The same concept of combination of an acidic solid polymer electrolyte and acid stable precious metal electrocatalysts can also be applied to a methanol-fed fuel cell (Direct Methanol Fuel Cell, DMFC). Methanol can be fed in liquid or vapor form, mixed with water. The methanol molecule CH_3OH is electrochemically converted at the anode according to

$$\text{Anodic reaction}: CH_3OH + H_2O = 6\ H^+ 6e^-$$
$$+ CO_2 \quad (\text{Methanol Oxidation Reaction}, MOR)$$

$$\text{Cathodic reaction}: O_2 + 4H^+ + 4e^- = 2H_2O$$
$$(\text{Oxygen Reduction Reaction}, ORR)$$

$$\text{Overall reaction}: CH_3OH + H_2O + O_2$$
$$= CO_2 + 3H_2O$$
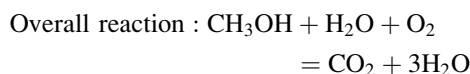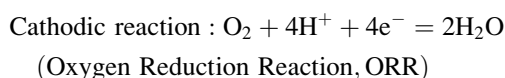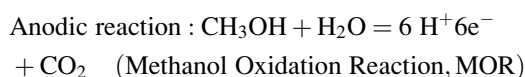
As seen from above, the MOR occurs under the consumption of one molecule of water, necessary to oxidize carbon in the CH_3OH molecule to CO_2, while potentially six protons are liberated. The ORR can be formulated the same way as in a hydrogen-fed cell.

The equilibrium potential for the anode reaction is at 0.02 V versus the Normal Hydrogen Electrode (NHE); hence, a theoretical cell voltage close to the H_2/O_2 fuel cell should be observed. In practice, the OCV is lower, for several reasons: Due to the similarity of methanol and water as solvents (e.g., solubility parameter), methanol also penetrates into the water-swollen polymer membrane and passes to the cathode (methanol crossover), causing a mixed potential at a lower value than the oxygen potential. Further, the anode reaction requires a binary or ternary bifunctional catalyst, containing next to platinum one metal component (or two) providing the splitting reaction of the water molecule involved to liberate oxygen for the carbon oxidation at lower potentials as compared to platinum. Examples would be Ru, Sn, Mo, others, or even combinations of two of these together with platinum as the hydrogen liberating catalyst part.

Intermediate oxidation species of the methanol molecule, e.g., –COH, may adsorb and poison the platinum catalyst surface, thereby impeding the full oxidation reaction.

These kinetic losses at the anode lead to a high anode overvoltage and, therefore, the cell voltage in the DMFC is lower at a respective value of current density as compared to a H_2-fed cell, as is the achievable power density.

Direct methanol fuel cell concepts with liquid electrolyte have also been considered in the past. One advantage of circulating liquid electrolytes is the option to cool the cell without additional cooling fluid.

Cross-References

▶ Fuel Cells, Principles and Thermodynamics
▶ Polymer Electrolyte Fuel Cells, Membrane-Electrode Assemblies
▶ Polymer Electrolyte Fuel Cells, Oxide-Based Cathode Catalysts

References

1. International Energy Agency (updated June 2011) Clean energy progress report, Paris
2. International Energy Agency (2004) Hydrogen and fuel cells, review of national R&D programs. OECD Publishing. ISBN 9789264108837
3. e.g., http://www.sfc.com/en/
4. http://www.roads2hy.com/pub_download.asp?PageIndex=1
5. Appleby AJ (1994) J Power Sources 49:15
6. Grubb WT (1959) J Electrochem Soc 106:275
7. Grubb WT (1960) J Electrochem Soc 107:131
8. Juda W, McRae WA (1953) US Patent 2,636,851
9. Grot WG (1972). Chem Ing Techn 44:163, 167
10. Scherer GG (ed) (2008) Fuel cells I. Adv Polym Sci 215. Springer, Berlin/Heidelberg. ISBN 978-3-540-69755-8; Fuel cells II (2008), Adv Polym Sci 216. Springer, Berlin/Heidelberg. ISBN 978-3-540-69763-3
11. Kreuer K-D (2007) Proton conduction in fuel cells. In: Limbach HH, Schowen RL, Hynes JT, Klinman JP (eds) Hydrogen-transfer reactions, vol 1. Wiley-VCH, Weinheim, pp 709–736, chap. 23
12. Scherer GG (1990) Ber Bunsenges Physik Chem 94:1008
13. Boillat P, Scherer GG (2012) Neutron imaging. In: Wang H, Yuan X-Z, Lui H (eds) PEM fuel cell diagnostic tools. CRC Press, Boca Raton, p 255
14. Schmickler W (1996) Grundlagen der Elektrochemie. Vieweg, Braunschweig
15. Merle G, Wessling M, Nijmeijer K (2011) J Membr Sci 377:1
16. Gasteiger HA, Kocha SS, Sompali B, Wagner FT (2005) Appl Catal B Environ 56:9
17. Debe M (2012) Nature 486:43
18. http://info.industry.siemens.com/data/presse/docs/m1-isfb07033403e.pdf
19. Büchi FN, Paganelli G, Dietrich P, Laurent D, Tsukada A, Varenne P, Delfino A, Kötz R, Freunberger SA, Magne P-A, Walser D, Olsommer D (2007) Fuel Cells 7:329

Polymer Electrolyte Fuel Cells, Mass Transport

Felix N. Büchi and Pierre Boillat
Paul Scherrer Institut, Villigen PSI, Switzerland

Introduction

Mass transport in electrochemical reactions is defined as the transport of reactants and products which does not include the transport of electric or ionic charges. In the case of polymer electrolyte fuel cells (PEFCs), mass transport includes the following phenomena:

1. The transport of gaseous reactants (hydrogen and oxygen) to the reaction sites
2. The transport of the product water away from the reaction sites.

Mass transport loss is defined as the loss in performance of the fuel cell due to limitations in mass transport processes. This performance loss is usually attributed to a reduction of the oxygen activity (associated to its partial pressure) at the electrode, in comparison to the oxygen partial pressure at the cell inlet. The accumulation of water in the transport pathways of the gaseous reactants can lead to increased mass transport losses and instability and can result in accelerated degradation.

The operation of fuel cells depends on mass transport on a variety of different scales, from the distribution of gas flow between different cells of

a stack down to transport on the nanometer scale inside the electrode.

At high current densities (>1 A/cm^2) required for the automotive application, or high humidity conditions, the mass transport losses can account for more than 100 mV of cell voltage losses [1]. Detailed understanding of the processes is therefore required to increase the electrochemical cell efficiency. In order to gain accurate insight into the complex mass transport processes, specific experimental methods and modeling approaches are developed.

Mass Transport on the Cell and Stack Level

In most PEFC designs, the reactant gases are actively supplied to the stack by feeding a given gas flow. The gas mass flow exceeds the quantity strictly needed for the electrochemical reaction, so that a sufficient concentration is present in the outlet section of the cell. Ideally, the gas flow should be distributed homogeneously to the flow channels of a cell and between the cells of a stack, but various processes can lead to inhomogeneous distributions as described below.

Channel-to-Channel Distribution of Gas Flow
A typical flow field consists of a number of flow channels running parallel to each other (see Fig. 1, top). The distribution between the different channels is determined by the flow resistance of each channel, which can vary from channel to channel due to the following reasons:
- Structural differences of the gas flow channel sections. Such differences can stem from manufacturing imprecision or inhomogeneous distribution of the compression force.
- The presence of liquid water in the flow channels and/or in the manifolds. As the gas flow velocity is an important parameter for water removal (c.f. below), this can lead to a "latching" effect: the gas flow is reduced in channels where liquid water appears, which in turns leads to less water removal in these sections.
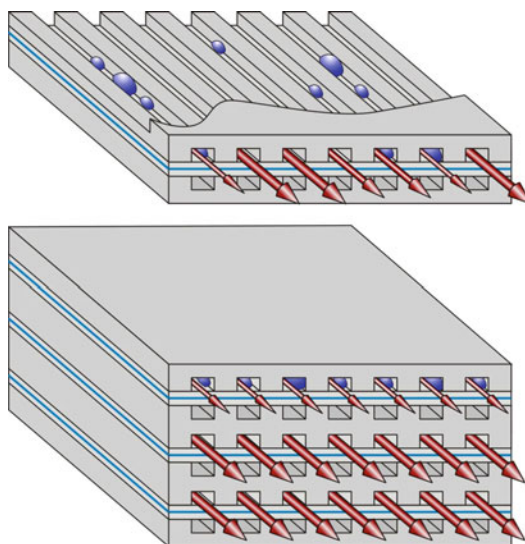
Polymer Electrolyte Fuel Cells, Mass Transport, Fig. 1 Accumulation of water in the flow channels can disturb the distribution of gas on the cell level (*channel to channel, see top*) and on the stack level (*cell to cell, see bottom*)

Different channels of the cell can be considered as placed in parallel, both concerning the gas flow and the electrical current flow. Thus, the complete absence of flow in one section of the cell will not lead to cell reversal, but to the absence of current production in this section. Nevertheless, long-term degradation effects can be expected, in particular in the absence of hydrogen.

Cell-to-Cell Distribution of Gas Flow
The distribution of gas flow between different cells of a stack can suffer from the same perturbations as described above between different channels (see Fig. 1 bottom). Again, both structural differences and accumulation of liquid water can be the cause of inhomogeneous distribution of gas flows.

The cells in a stack are connected in parallel with respect to the gas flow but in series with respect to the current. The implication is that in complete absence of gas flow in a cell, cell voltage reversal will occur which will induce a rapid damage (e.g., due to carbon corrosion). As a consequence, individual cell voltage

Polymer Electrolyte Fuel Cells, Mass Transport, Fig. 2 Mass transport through the cathode GDL, interconnecting the channel of the bipolar plate and the catalyst layer
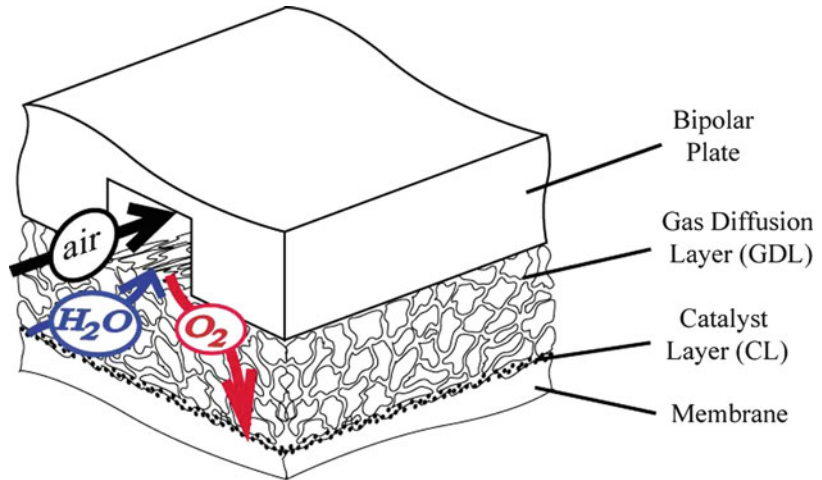
monitoring and effective purging strategies are essential for the durable operation of a stack.

Water Removal

A limited quantity of water can be removed as water vapor. This quantity is defined by the magnitude and relative humidity of the incoming gas flows. Water produced in excess of this quantity needs to be removed as a liquid. In the flow channels, water forms droplets which grow as they are fed by produced water transiting through the GDL. When the shear force produced by the gas flow is sufficient to offset the adhesion force of the droplet, it will detach and be carried away by the gas flow (or in some cases adhere to the wall or GDL in a downstream section of the flow channel). The typical size a droplet can grow until it detaches depends primarily on the velocity of the gas flow and on the gas viscosity. If the shear force is low (typically, for the hydrogen channels and/or for low flows), the droplets can grow large enough to form a "slug," meaning a complete filling with water of one fraction of the channel.

Transport in the Gas Diffusion Layer

The gas diffusion layer (GDL) connects the millimeter-scaled gas channels in the bipolar plate with the catalyst layer, where the electrochemical reaction takes place on the surface of nanometer-sized catalyst particles (see Fig. 2).

Gas diffusion layers are used to collect current over the channels and to provide access for the gases under the flow field ribs. Mass, charge, and heat are transported in and through the GDL in the respective pressure, concentration, potential, and temperature fields. The GDLs need to fulfill two antagonistic tasks: they need to be highly permeable for the reactant transport and highly conductive for charge and heat. The porous materials consist typically of carbon fibers with a diameter of 6–8 μm, in the form of either carbon papers or clothes. The maximum of the resulting pore size distribution usually lies in the range of tens of micrometers, and due to the orientation of the fibers, the pore and solid structures are often anisotropic. Porosities typically range in the order of 0.75–0.85 and the thickness is typically between 200 and 300 μm [2].

The main transport mechanism for the gaseous reactants through the GDL is diffusion in the concentration gradient between the gas channel and the surface of the catalyst layer and is described by Fick's first law:

$$N_{eff} = -D_{eff} \frac{\partial c}{\partial x} \qquad (1)$$

where N_{eff} is the effective flux, D_{eff} the effective diffusion coefficient, c the species concentration, and x the distance.

In the porous gas diffusion layer, the effective diffusion coefficient is different from the intrinsic

coefficient of the species in a gas mixture in free volume because (i) the solid structure of the GDL acts as a resistance which might be increased by (ii) the presence of liquid water in the pores of the GDL. The effect of multicomponent diffusion is described by the Stefan–Maxwell relation, which can be found in textbooks [3] and is not specific to fuel cells. This is therefore not discussed further here.

The effect of the solid obstructing the gas transport is determined by the porosity ε and tortuosity τ of the GDL. Tortuosity describes the elongation of the direct transport distance x by the solid structure of the GDL, and definition of the porosity is obvious. Liquid water may occupy part of the pore space, decreasing porosity and increasing tortuosity. This effect depends on the amount of liquid water present in the GDL, which is given as the saturation s, the fraction of the pore space occupied. The effective diffusion coefficient is therefore defined as:

$$D_{eff} = -D\frac{\varepsilon}{\tau}(1 - s)^n \qquad (2)$$

The effect of the saturation is not linear and described by the factor n in Eq. 2.

In the past years advanced characterization techniques such as synchrotron-based X-ray tomography have allowed to accurately determine the structure of the GDL materials including the effects of compression in the cell [4]. In combination with electrochemical methods [5, 6], this has lead to accurate determination of the effective diffusion coefficients as defined in Eq. 2. D_{eff} in dry GDL, depending on the compression and the direction (in- or through-plane), is in the range between 0.6 and 0.2 times the diffusion coefficient in the free volume (see Fig. 3).

Recently, the effect of liquid water has been quantified using tomographic techniques [7]. With liquid saturation reaching values up to 0.3–0.4 in the cathode, the effective diffusion coefficient D_{eff} drops considerably below 0.1 of the free volume value. This illustrates well that gas transport through the GDL can become a limiting factor at high current densities.
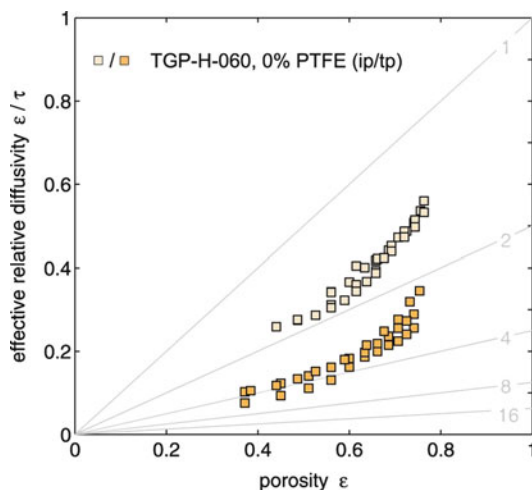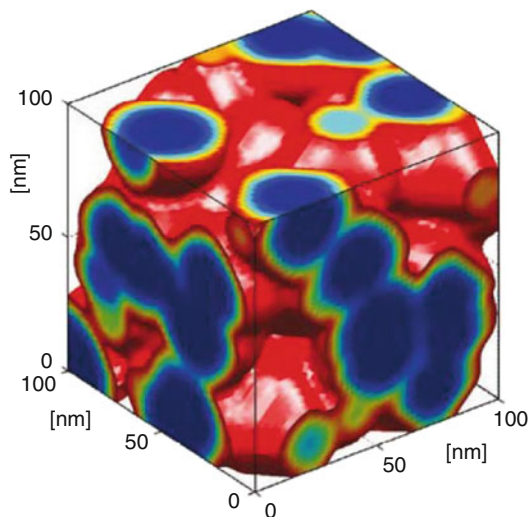

Polymer Electrolyte Fuel Cells, Mass Transport, Fig. 3 Effective relative diffusivity ε/τ as a function of the porosity of plain Toray 060 GDL (without PTFE) for different compressions (expressed in porosity). *ip* in-plane, *tp* through-plane. The *gray lines* indicate iso-tortuosity levels

The transport of liquid water through the GDL is not well understood at this point in time. Liquid water is transported by a pressure gradient between the catalyst layer and the gas channel, where it is removed from the cell. However, the buildup of the transportation paths depends on the local pore sizes and the surface properties (contact angle) of the GDL. Understanding has been gained in ex situ experiments by determining the liquid saturation as function of the capillary pressure [8, 9].

However, in operating cells the situation is more complicated, as the channel/rib structure of the flow field imposes inhomogeneous temperature and wetting boundary conditions. Further the local condensation/evaporation equilibrium strongly affects the liquid phase. The understanding of the transport of liquid water in the operating cell therefore also needs advanced in situ methods such as neutron radiography [10, 11] or X-ray tomography [12]; see section Experimental Methods for Mass Transport Analysis.

Transport of charge (as electrons) and heat in the GDL takes place in the solid part of the gas diffusion layer. As the fibers in usual materials are normally oriented in the in-plane direction,

Polymer Electrolyte Fuel Cells, Mass Transport, Fig. 4 Modeled catalyst layer cutout with a side length of 100 nm. The shown random structure includes 64 carbon particles with a diameter of 28 nm colored in blue. The ionomer coating has a thickness of 10 nm and is shown in colors from *green* to *red*

both heat and electric conduction show a high anisotropy, with in-plane conductivities up to ten times higher than the through-plane values.

Transport in the Catalyst Layer

The catalyst layer (CL) is also a porous structure. However, the pore size is much smaller (between 10 and few hundreds of nanometers) as compared to tens of micrometers in the GDL. Further, because the electrochemical conversion occurs here, charge is transported by both protons and electrons and the electrochemically interlinked charge transport becomes more complicated than the one in the GDL. Figure 4 shows a small schematic cutout of the CL showing the tortuous arrangement of the electronically (carbon) and ion-conducting (ionomer) phases. Reactants are predominantly transported in the pore space (void).

In the catalyst layer educts and water are transported in the void and the ionomer phases. Again, because of the porous and tortuous

structure, the effective transport parameters deviate substantially from the properties of the respective pure phases. However, in the case of the CL, due to the small scale and the thinness of the layer, it is experimentally difficult to accurately determine the geometry of the single phases. Also the compositions and structures of the CL, when using different preparation methods, have a higher variation than in the case of the GDL. Therefore, the effective transport properties are less well known. Generally, due to the relatively low porosity (typically 0.3–0.5) and high tortuosity of the CL, the effective transport parameters in all the phases are considerably lower (typically a factor of 0.05–0.2) than the one in the respective pure material.

In the catalyst layer, the presence of liquid water also complicates the mass transport processes. On the one hand, the liquid may fill part of the pore space, affecting the diffusional transport of the reactants in the pores. On the other hand, the relative humidity also strongly affects the ionic conductivity of the ionomer phase. As the humidity and/or presence of liquid water strongly varies with temperature and current density, the transport properties for gas and proton transport change significantly during operation.

Modeling

It has become obvious from the previous sections that transport of matter, heat, and charge on all scales of the cell is complex and interlinked and has a strong influence on the stationary and dynamic performance of the cell. As the experimental analysis is difficult and some of the parameters are poorly known, understanding of the important transport phenomena has also strongly relied on modeling of single components or cells.

Newman et al. [13] and De Levie [14] have developed the theoretical understanding of porous electrodes in the 1960s of the last century. Pioneering work for an entire cell (in 1D and isothermal conditions) has been done by Springer
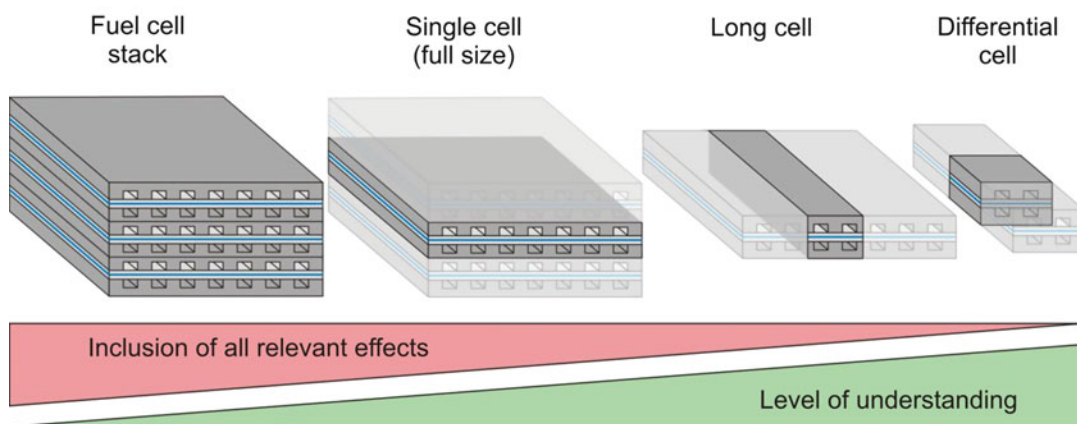
Polymer Electrolyte Fuel Cells, Mass Transport, Fig. 5 Illustration of the downscaling possibilities for experimental fuel cell studies

et al. [15] in the 1990s. Thereafter modeling efforts have seen an exponential growth till today with more and more sophisticated approaches being developed. With time models grew from one-dimensional to full three-dimensional treatment. The energy field and the complexity of two-phase flow (gaseous and liquid) in the different domains have been studied, and models for the time domain were developed, e.g., [16].

However, even with today's advanced computational capabilities, modeling is not able yet to capture the entire parameter space of a single cell without extensive experimental parameterization. In particular the two-phase transport in the catalyst layer and the GDL are still poorly understood. It will require a joint experimental and computational effort to close this important gap in the future.

Experimental Methods for Mass Transport Analysis

The most common analysis tool used for assessing PEFC performance is the recoding of current–voltage characteristics. However, the information obtained from such a characteristic is in most cases not sufficient to draw conclusions about mass transport processes. Therefore an insight into different possibilities of advanced analysis is given here.

Choices of Cell/Stack Design

As presented in the previous paragraphs, mass transport processes are relevant for different scales, from the processes inside the electrode up to the gas flow distribution in a complete stack. When performing experimental analysis of mass transport, the choice of cell/stack hardware will determine which transport processes will be included in the experiment. Some possible hardware designs (c.f. Fig. 5) are listed here:

- *Full-size stack*. The relevance for real operation is obvious, but analysis possibilities are limited.
- *Full-size single cell*. Some mass transport effect (cell-to-cell distribution) is not included but can be emulated by operating the cell with a constant differential pressure instead of a constant gas flow.
- "*Long cell*" (cell with a single channel or a few channels with technically relevant lengths). Channel-to-channel distribution effects may be reduced. On the contrary, the impact of a single channel blocking will be emphasized.
- "*Differential cell*" (cell with a few short parallel channels, operated with high stoichiometry to keep technically relevant gas velocities). The effect of gas consumption and water accumulation along the channels is not included.

The degree of understanding of the experimental results will usually increase when going

Polymer Electrolyte Fuel Cells, Mass Transport, Fig. 6 Illustration of in situ water visualization methods. *Top*: synchrotron 3D imaging of water in a differential cell. *Bottom*: neutron imaging of a long cell with an active area of 60 cm^2 for the H$_2$/air co- and counterflow arrangements
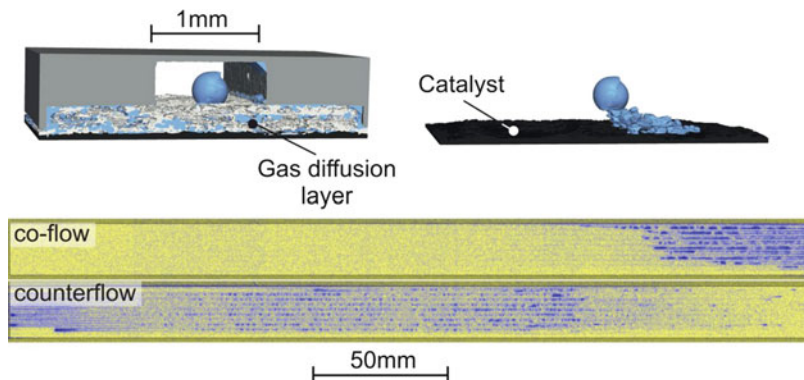
from a full technical stack to a differential cell, but the relevance for real stack operation becomes less obvious. Even on the scale of a differential cell, effects such as rib/channel distribution of reactants and current density make the interpretation of experimental results difficult, and experiments on further simplified cells are sometimes appropriate.

Visualization Methods

Because the occurrence of liquid water is a major factor for mass transport losses, visualization methods play an important role in the analysis of mass transport processes in PEFCs, in particular for the analysis of liquid water distribution.

- *Neutron imaging* [11] is used for the in situ analysis of the water distribution in the flow channels and GDLs (Fig. 6). Usual fuel cell construction materials including aluminum and, to some extent, steel are readily transparent for neutrons. Spatial resolution is limited, preventing the observation of single pores inside GDLs.
- *Synchrotron X-ray tomography* [12] is used for the in situ analysis of tridimensional water distribution in GDLs (Fig. 6). This method offers high spatial resolution. Limitations include the requisite of cell constructions transparent enough to X-rays and the issue of cell radiation damage. *Soft X-ray imaging* [17] has also been reported for the measurement of water in GDLs. Similarly to synchrotron X-ray imaging, strong limitations are set on the cell construction to make it transparent enough to X-rays.

- *Transparent fuel cells* [18] can be used to visualize the water inside flow channels. They have the advantage of allowing the use of inexpensive imaging equipment. The major drawback is the necessity of using transparent flow field and housing materials, which have different physical characteristics (contact angle, thermal properties) than commonly used materials.
- *Magnetic resonance imaging* [19] has been reported for observing the distribution of liquid water, in particular in the membrane. This method shares with neutron imaging the characteristic of being sensitive to different hydrogen isotopes, making labeling experiments possible. The drawbacks include a limited spatial resolution and the constraint of using nonconductive housing materials.

The visualization of gas flow or reactant distribution is scarcely used due to the limited possibilities of in situ measurements. For cells having a visual access to the flow channels, some optical methods have been reported:

- *Particle velocimetry* measurements for the analysis of the gas flow distribution [20]
- The use of *O$_2$-sensitive dyes* for the visualization of oxygen concentration distribution [21]

Electrochemical Analysis Methods

A few electrochemical analysis methods which can be used to characterize the impact of mass transport limitations on cell operation are listed here. These methods are sometimes used in combination with water visualization to draw

correlations between water accumulation and mass transport losses.

- **Electrochemical Impedance Spectroscopy (EIS)** consists in measuring the voltage response to sinusoidal current perturbation with different frequencies. This method can yield important information about mass transport limitations, but the interpretation of the results must be done very carefully. In particular, it has been shown that the cell global impedance spectrum is strongly affected by gas consumption along the channels [22]. Even on the scale of a differential cell, local effects on the rib/channel scale can dominate the resulting spectrum [23].

- The measurement of the **limiting current density** [24] can be used to obtain information about the diffusive structure of the cathode GDL. In most designs, it is necessary to use diluted oxygen (typ. 1–5 %) to lower the limiting current density within the reachable range.

- **Multiple gas analysis** consists in comparing the performance of the cell operated with different gases. Usually, the cathode gas is changed from air to pure O_2 and/or to helox (a mixture of helium and oxygen). The differences in performance can point out mass transport limitations. The use of different gases can induce parasitic effects (e.g., dry out when using helox), but these can be avoided by using only short periods of operation with O_2/helox [11].

Conclusions and Outlook

Mass transport in PEFC is a multi-scale issue ranging from the nanometer scale in the catalyst layer to the meter scale in the flow field channels. A reasonable understanding of the different processes exists, mainly based on the insight from specialized experimental setups. However, further mitigation of cell voltage and degradation losses associated with the different transport phenomena is required. This will need a combination of even more advanced experimental tools and model-based comprehension of the different processes to improve structures and materials.

Cross-References

▶ Polymer Electrolyte Fuel Cells (PEFCs), Introduction
▶ Polymer Electrolyte Fuel Cells, Membrane-Electrode Assemblies

References

1. Oberholzer P, Boillat P, Kaestner A, Lehmann EH, Scherer GG, Schmidt TJ, Wokaun A (2013) Characterizing local O_2 diffusive losses in GDLs of PEFCs using simplified flow field patterns. J Electrochem Soc 160:F659–F669
2. El-kharouf A, Mason TJ, Brett DJL, Pollet BG (2012) Ex-situ characterisation of gas diffusion layers for proton exchange membrane fuel cells. J Power Sources 218:393–404
3. Bird RB, Steward WE, Lightfoot EN (1960) Transport phenomena. Wiley, New York
4. Becker J et al (2009) Determination of material properties of gas diffusion layers: experiments and simulations using phase contrast tomographic microscopy. J Electrochem Soc 156:B1175–B1181
5. Flückiger R et al (2008) Anisotropic, effective diffusivity of porous gas diffusion layer materials for PEFC. Electrochim Acta 54:551–559
6. Kramer D et al (2008) Electrochemical diffusimetry of fuel cell gas diffusion layers. J Electroanal Chem 612:63–77
7. Rosén T et al (2012) Saturation dependent effective transport properties of PEFC gas diffusion layers. J Electrochem Soc 159:F536–F544
8. Fairweather JD, Cheung P, St-Pierre J, Schwartz DT (2007) A microfluidic approach for measuring capillary pressure in PEMFC gas diffusion layers. Electrochem Comm 9:2340–2345
9. Gostick JT, Ioannidis MA, Fowler MW, Pritzker MD (2008) Direct measurement of the capillary pressure characteristics of water–air–gas diffusion layer systems for PEM fuel cells. Electrochem Comm 10:1520–1523

10. Kramer D et al (2005) In situ diagnostic of two-phase flow phenomena in polymer electrolyte fuel cells by neutron imaging: part A. Experimental, data treatment, and quantification. Electrochim Acta 50:2603–2614

11. Boillat P et al (2012) Impact of water on PEFC performance evaluated by neutron imaging combined with pulsed helox operation. J Electrochem Soc 159:F210–F218

12. Eller J et al (2011) Progress in in situ X-ray tomographic microscopy of liquid water in gas diffusion layers of PEFC. J Electrochem Soc 158:B963–B970

13. Newman JS, Tobias CW (1962) Theoretical analysis of current distribution in porous electrodes. J Electrochem Soc 109:1183–1191

14. de Levie R (1963) On porous electrodes in electrolyte solutions: I. Capacitance effects. Electrochim Acta 8:751

15. Springer TE, Zawodzinski TA, Gottesfeld S (1991) Polymer elektrolyte fuel cell model. J Electrochem Soc 138:2334–2341

16. Zaglio M, Wokaun A, Mantzaras J, Büchi FN (2011) 1d-modelling and experimental study of the Pefc dynamic behaviour at load increase. Fuel Cells 11:526–536

17. Sasabe T, Deevanhxay P, Tsushima S, Hirai S (2011) Investigation on the effect of microstructure of proton exchange membrane fuel cell porous layers on liquid water behavior by soft X-ray radiography. J Power Sources 196:8197–8206

18. Zhang FY, Yang XG, Wang CY (2006) Liquid water removal from a polymer electrolyte fuel cell. J Electrochem Soc 153:A225–A232

19. Minard KR, Viswanathan VV, Majors PD, Wang L-Q, Rieke PC (2006) Magnetic resonance imaging (MRI) of PEM dehydration and gas manifold flooding during continuous fuel cell operation. J Power Sources 161:856–863

20. Martin J, Oshkai P, Djilali N (2005) Flow structures in a U-shaped fuel cell flow channel: quantitative visualization using particle image velocimetry. J Fuel Cell Sci Technol 2:70–80

21. Takada K et al (2011) Simultaneous visualization of oxygen distribution and water blockages in an operating triple-serpentine polymer electrolyte fuel cell. J Power Sources 196:2635–2639

22. Schneider IA, Kramer D, Wokaun A, Scherer GG (2007) Oscillations in gas channels. J Electrochem Soc 154:B770–B782

23. Schneider IA, Bayer MH, von Dahlen S (2011) Locally resolved electrochemical impedance spectroscopy in channel and land areas of a differential polymer electrolyte fuel cell. J Electrochem Soc 158:B343–B348

24. Baker DR, Caulk DA, Neyerlin KC, Murphy MW (2009) Measurement of oxygen transport resistance in PEM fuel cells by limiting current methods. J Electrochem Soc 156:B991–B1003
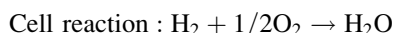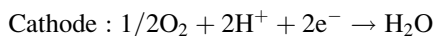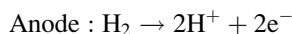
Polymer Electrolyte Fuel Cells, Membrane-Electrode Assemblies

Makoto Uchida
Fuel Cell Nanomaterials Center,
Yamanashi University, 6-43 Miyamaecho,
Kofu, Yamanashi, Japan

## The Electrode Structure and Electrochemical Reactions of MEAs (Membrane-Electrode Assemblies)

In general, a polymer electrolyte fuel cell (PEFC) consists of a polymer electrolyte membrane (proton exchange membrane) in contact with a porous anode and a porous cathode. The construction of a single cell of a PEFC is schematically shown in Fig. 1. Hydrogen and oxygen gases are supplied to the anode and cathode compartments, respectively, at which the hydrogen oxidation reaction (HOR) and oxygen reduction reaction (ORR) occur, thereby generating an electrical current:

$$\text{Anode}: H_2 \rightarrow 2H^+ + 2e^-$$

$$\text{Cathode}: 1/2O_2 + 2H^+ + 2e^- \rightarrow H_2O$$

$$\text{Cell reaction}: H_2 + 1/2O_2 \rightarrow H_2O$$

The MEA is composed of three main parts, e.g., polymer electrolyte membrane (PEM), gas diffusion medium, and catalyst layer (CL). The membrane, with hydrophilic proton-conducting channels embedded in a hydrophobic structural matrix, plays a key role in the operation of PEFCs. The PEMs for PEFCs commonly use perfluorosulfonic acid (PFSA) electrolytes such as Nafion®, with the chemical structure shown in Fig. 2, because of its high proton conductivity as well as chemical and thermal stability [1]. The gas diffusion medium (GDM), including both the microporous layer (MPL) and the gas diffusion layer (GDL), which typically is based on carbon fibers, is also an important component. The GDM is designed with three distinct

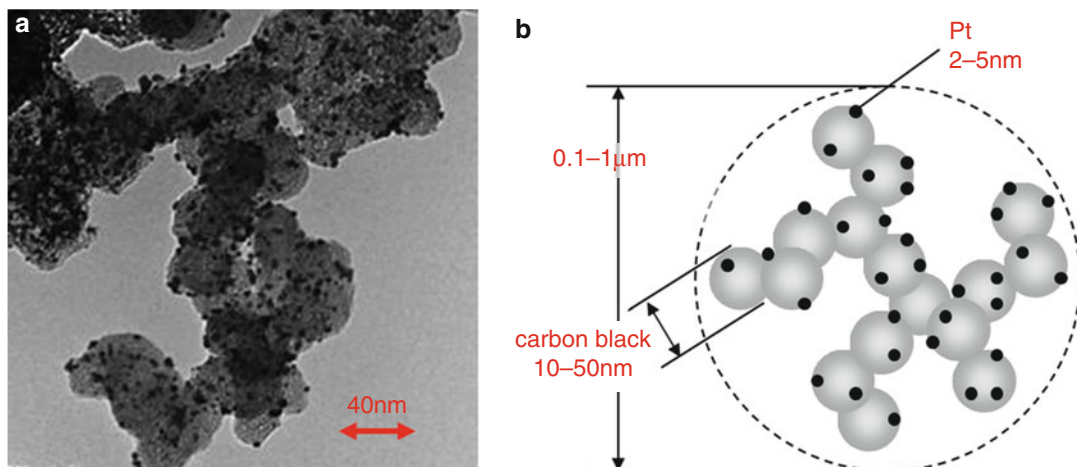**Polymer Electrolyte Fuel Cells, Membrane-Electrode Assemblies, Fig. 1** Schematic diagram of an MEA for a PEFC
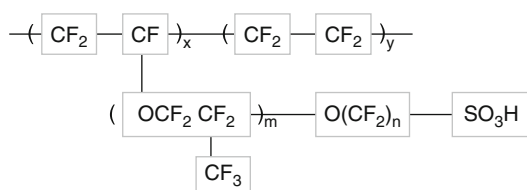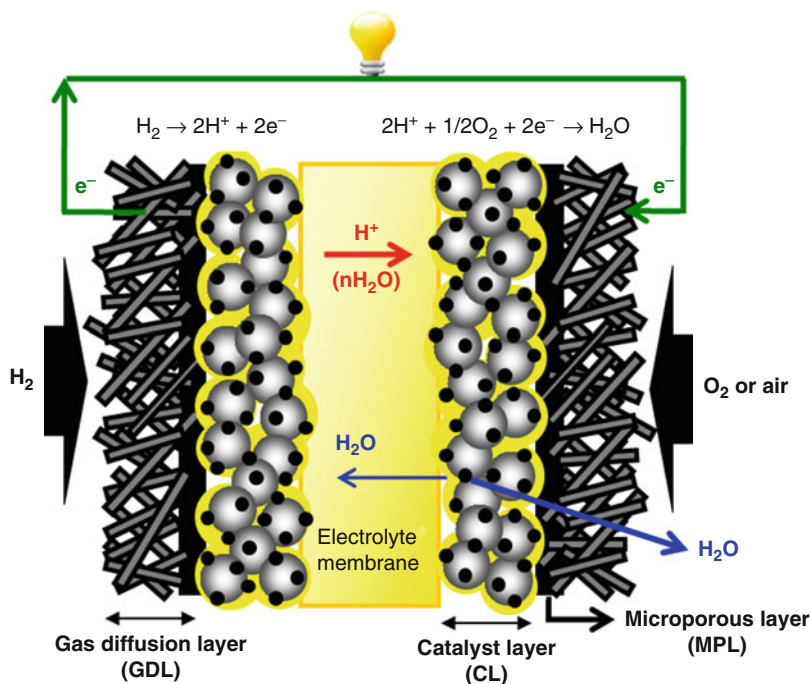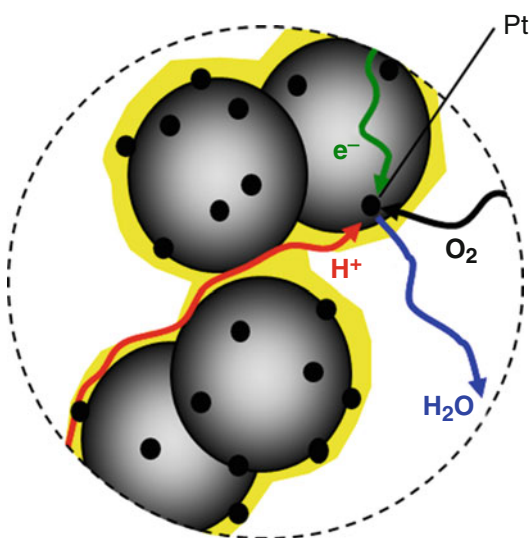

Polymer Electrolyte Fuel Cells, Membrane-Electrode Assemblies, Fig. 2 Chemical structure of perfluorosulfonic acid polymer

functions in mind: to transport reactant gases to the catalyst layers (CLs), to conduct electrons in or out of the CLs, and to exhaust product water from the cathode CL to the gas flow channel [2–7]. The CL consists of the electrocatalyst (Pt nanoparticles supported on carbon black, Pt/C) and a proton-conducting polymer electrolyte ionomer as a binder. In particular, the performance of the cathode CL controls the performance of the cell as a whole. The MEA, which consists of anode and cathode, each including their respective GDM and CL, is sandwiched on both sides of the membrane and placed between two bipolar plates, both containing gas flow channels, as well as coolant channels.

A typical transmission electron microscope image and schematic diagram of a Pt/C electrocatalyst are shown in Fig. 3a, b. The carbonaceous fine powder (carbon black), with a structure in which the 10–50 nm primary particles are connected together as in a string of beads, is generally used for the carbon support. The Pt nanoparticulates (2–5 nm in diameter) are supported on the surface of the carbon black. The Pt/C itself is coated with the PFSA ionomer. A proton generated by the HOR on the Pt/C in the anode CL is transported to the membrane through PFSA ionomer channels. A schematic depiction of the ORR on the Pt/C with an ideal PFSA film in the cathode CL is shown in Fig. 4. In the cathode CL, the proton from the membrane is transported to the Pt on the carbon support through the PFSA ionomer channels. The electrons generated simultaneously by the HOR in the anode are conducted to the gas diffusion medium connected with the bipolar plate through the carbon support network. The electrons in the cathode from the bipolar plate are conducted to the Pt on the carbon through the carbon support network and then react with oxygen (ORR) and the protons mediated via the PFSA. The gas transport, both of the

Polymer Electrolyte Fuel Cells, Membrane-Electrode Assemblies, Fig. 3 (**a**) Transmission electron microscope image. (**b**) Schematic diagram of the Pt/C

Polymer Electrolyte Fuel Cells, Membrane-Electrode Assemblies, Fig. 4 Schematic depiction of the ORR on the Pt/C with ideal PFSA film in the CL

hydrogen in the anode and the oxygen in the cathode, is mediated by the void channels existing in the carbon black network structure. If the catalyst layer needs to have more void volume for gas transport, extractable pore-forming materials can be used. The water generated in the cathode is exhausted from the MEA

through the gas channels or is returned to the membrane side through the PFSA ionomer channels.

The key point of the MEA development for the PEFC is how to promote the reactions on the surface of the platinum catalyst in the CLs, particularly at the cathode. To increase the reaction area that can contribute to the catalyst reduction, the supply channels of oxygen and hydrogen to the reactive sites, the conductive channels for protons, and the exit paths for the generated water all become important. In the present essay, mainly the development history and the current design for the reduction of Pt in the CL will be described.

Microscopic regions in which solid, gas, and liquid meet at a so-called three-phase boundary exist within the CL and are the locations at which the ORR proceeds. The properties and dimensions of these components control the performance of the fuel cell. In the PEFC, the reactant gases are transported through ionomer films that cover the electrocatalyst before they react at the latter. Thus, the film thickness must be small enough to avoid slowing down the gas diffusion. On the other hand, the film must be thick enough to avoid slowing down the ionic conduction (Fig. 1). Similarly, the support material must provide sufficient volume for electronic conduction yet provide enough void volume for effective

gas mass transport. Thus, it is clear that there will be dimensions at which gas transport, electronic conduction, and ionic conduction will be simultaneously optimized.

In the early stages of PEFC development, there was no concept of incorporating the polymer electrolyte in the interior of the CL. Although the PFSA membrane is used as the electrolyte, the membrane cannot make effective ionic contact deeply within the electrode as a liquid electrolyte can. The three-phase (gas/electrolyte/electrode) boundary as the reaction site therefore existed only at the interface between the membrane and the CL, with the result that the electrodes had low catalyst (platinum) utilization. Consequently, they required a high catalyst loading (4 mg/cm^2) [8]. Subsequently, PFSA solutions in alcoholic solvents were adopted as the most popular approach; these were soaked into the CLs to increase the contact area between the Pt particles and the PFSA. Thereby, the Pt loadings have so far been decreased to 0.35–0.5 mg/cm^2 [9–11]. Since the Pt utilization (U_{Pt}) values, defined as the percentage of possible Pt area that is electrochemically active, were still low (15–20 %), in spite of these approaches [9], many techniques were investigated to increase the interfacial area between Pt and PFSA. The PFSA solutions were impregnated into the CLs, thereby enabling the Pt loadings to decrease and at the same time U_{Pt} values to increase [12, 13]. It has been reported that the latter have reached 60 ∼ 80 %, calculated from the electrochemically active surface area (ECSA) measured by cyclic voltammetry (CV). These values represent a quite high-utilized Pt ratio in the CL. However, in the present state, the performance of the PEFC remains relatively low due to combined problems in the CL, even though the U_{Pt} shows almost the maximum possible.

Furthermore, for cost reduction, the amount of Pt used in the PEFC industry will be required to be reduced to one-tenth. In more detail, a conventional, present-day automobile is using a precious metal catalyst (Pt) in an amount of about 10 g as an exhaust gas catalyst. On the other hand, the prototypes of current fuel cell vehicles, with fuel cell stacks of about 100 kW, use ca. 100 g Pt per vehicle. Therefore, it is necessary to achieve a 0.1 g Pt/kW level of one-tenth, which is also the developmental goal for industry and the national project in order to achieve a cost close to the current vehicle level. However, the cell performance would be expected to decrease significantly, based on the reduction of the Pt amount in the CL. Therefore, the development of high-performance CLs is necessary to reduce the Pt amount without performance loss.

Design and Evaluation of Catalyst Layers with High Pt Effectiveness

An ideal CL requires the composition of the polymer electrolyte on the Pt/C surface to simultaneously optimize the gas diffusion and proton conductance, as shown in Fig. 4. However, the realization of an ideal CL is difficult; the polymer electrolyte in the actual CL does not distribute uniformly, as shown in Fig. 5. The Pt catalyst which is not covered by the polymer electrolyte cannot form a three-phase boundary and therefore does not contribute to the reaction. The Pt cannot be used effectively, and the utilization of Pt is low. Consequently, for the purpose of increasing the contact surface area between the polymer electrolyte and Pt, many research and development efforts have been conducted, for example, the method of using organic solvents with high boiling point [12] or the use of a colloidal polymer electrolyte [13]. Watanabe and coworkers [14, 15] characterized the microstructure of the hydrophobic gas diffusion electrode for phosphoric acid fuel cells. In their works, the CL was claimed to have two distinctive pore distributions, with a boundary of ca. 0.1 μm. The smaller pores (primary pores) were identified as the spaces between the primary particles of the carbon support and those connected together (aggregates) in their agglomerates, and the larger ones (secondary pores) were identified as the spaces between the agglomerates. Moreover, the effects of the microstructure on the carbon support in the CL on the performance of PEFCs were investigated in detail; the primary
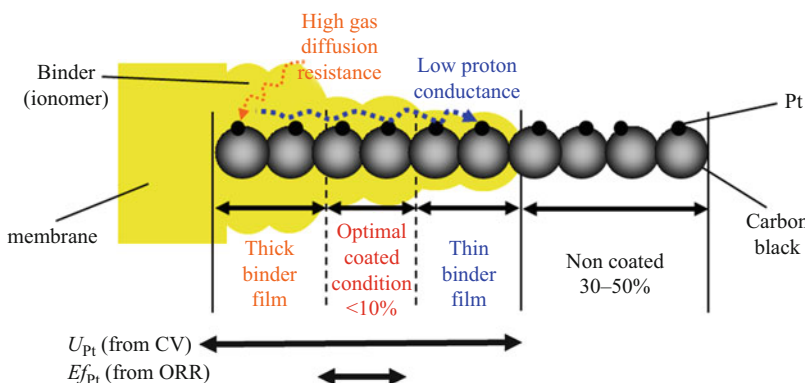
Polymer Electrolyte Fuel Cells, Membrane-Electrode Assemblies, Fig. 5 Schematic depiction of the ORR on the Pt/C with actual PFSA film in the CL
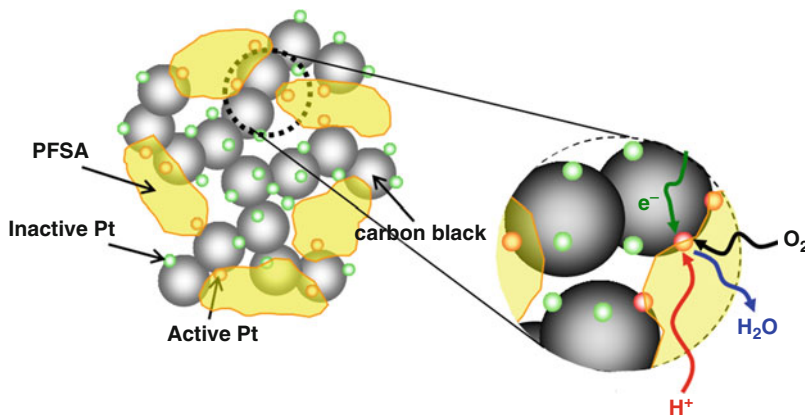
Polymer Electrolyte Fuel Cells, Membrane-Electrode Assemblies, Fig. 6 Schematic depiction of the variation of PFSA film thickness with depth within the CL

pores with distributed phosphoric acid mainly functioned as the reaction sites in the optimized CL structure due to the location of a large part of Pt particles (>80 %). The optimization of both the microstructure of the carbon support and the dispersion of the polymer electrolyte promoted the improvement of the effectiveness of Pt. Extending the design concept of CLs, the original design for the electrode model of the PEFC, as distinct from that of a liquid electrolyte system, was proposed by investigations of M. Uchida et al., e.g., reference [16]. Subsequently, various approaches for the optimization of the rheological properties of the CL ink by the use of improved solvent mixtures and associated procedures were examined. As a result, the U_{Pt} values calculated from the ECSA were improved to 70–97 % [17]. On the other hand, it has been shown that it is still necessary to reduce the Pt loading of MEAs, according to industry requirements, to about one-tenth, for cost reduction. It is

clear that there is little opportunity for reducing the Pt loading based on the results of the U_{Pt} values alone. However, it was realized that there were no clear indices to evaluate "the practical utilization" under the various actual operating conditions for PEFCs.

In recent research, a new evaluation method for the utilization under actual operating conditions was proposed as an "effectiveness of platinum (Ef_{Pt})" [18], based on the comparison of ORR mass activities for the MEA with those measured with the channel flow technique at the same temperature. The Ef_{Pt} value indicates the extent to which Pt particles exist in the CL in an optimal condition of binder coverage. A schematic depiction of the variation of PFSA film thickness with depth within the CL is shown in Fig. 6. In the case of U_{Pt}, the concept of Pt utilization can be rationalized from Fig. 6, because the U_{Pt} values are not affected by either proton conductance or the gas diffusion

resistance of the ionomer binder. The U_{Pt} value could in principle reach 100 %, if ionomer covers all of the Pt particles, based on the definition of U_{Pt}. In typical, conventional results, however, the U_{Pt} values of the MEA have indicated about 50–70 % under actual operating conditions.

On the other hand, in the case of Ef_{Pt} values evaluated for the important situation of air feed, or at higher current densities with O_2 feed, the optimal ionomer-coated condition was found to be the most effective for the ORR performance. Of course, both the thin and thick ionomer films also affected the ORR, but the contribution was relatively low, because the ionic path connectivity, proton conductance, and gas diffusion resistance all affected the cell performance loss. The values of Ef_{Pt} were found to be 10 % or less under actual operating conditions at the state-of-the-art CL structures. These values show that the ratio of catalyst existing in an effective reaction environment might be small during actual operation. Similar trends have also been observed from various other research efforts, including modeling studies [19]. Such results have indicated that we have much room for improvement for the design of the CL.

Future Directions

For the commercialization of PEFCs, in order to reduce the Pt loading without serious loss of cell performance and durability, it has been proposed that maximizing the Ef_{Pt} is necessary. In the relationship between the Pt catalyst powder and ionomer in a conventional CL, much of the Pt existing in mesopores of the carbon agglomerates cannot connect with the ionomer. Moreover, the primary particles of the carbon support contain many nanopores. The Pt in such nanopores also does not connect with the ionomer [16, 20]. Therefore, we must improve the Ef_{Pt} by improving the catalyst loading method, the support materials, and development of new ionomers. In addition, we should try to improve the ORR activity of the catalyst material itself. Of course, adequate durability of the MEA under practical conditions must also be secured.

The various challenges of the improvement in the ORR activity and the durability have been advancing by means of alloying, formation of Pt skin layers, and core-shell preparation methods. Approaches based on non-precious metals are proceeding as well. In addition, the further optimization of the thin CL structure by use of new, durable support materials (e.g., graphitized carbon blacks and conductive ceramic supports) should help to improve the effectiveness of Pt and the durability, as well as specific gas transport problems in the CL under high current density operating conditions.

Cross-References

▶ Hydrocarbon Membranes for Polymer Electrolyte Fuel Cells
▶ Platinum-Based Cathode Catalysts for Polymer Electrolyte Fuel Cells
▶ Polymer Electrolyte Fuel Cells, Oxide-Based Cathode Catalysts
▶ Polymer Electrolyte Fuel Cells (PEFCs), Introduction
▶ Polymer Electrolyte Fuel Cells, Perfluorinated Membranes

References

1. Yeager HL, Steck A (1981) Cation and water diffusion in Nafion ion exchange membranes: influence of polymer structure. J Electrochem Soc 128:1880–1884
2. Lim C, Wang CY (2004) Effects of hydrophobic polymer content in GDL on power performance of a PEM fuel cell. Electrochim Acta 49:4149–4156
3. Park GG, Sohn YJ, Yang TH, Yoon YG, Lee WY, Kim CS (2002) Effect of PTFE contents in the gas diffusion media on the performance of PEMFC. J Power Sources 131:182–187
4. Lin GY, Nguyen TV (2005) Effect of thickness and hydrophobic polymer content of the gas diffusion layer on electrode flooding level in a PEMFC. J Electrochem Soc 152:A1942–A1948
5. Park S, Lee JW, Popov BN (2008) Effect of PTFE content in microporous layer on water management in PEM fuel cells. J Power Sources 177:457–463
6. Wang ED, Shi PF, Du CY (2008) Treatment and characterization of gas diffusion layers by sucrose carbonization for PEMFC applications. Electrochem Commun 10:555–558

7. Gostick JT, Fowler MW, Ioannidis MA, Pritzker MD, Volfkovich YM, Sakars A (2006) Capillary pressure and hydrophilic porosity in gas diffusion layers for polymer electrolyte fuel cells. J Power Source 156:375–387

8. Appleby AJ, Yeager EB (1986) Solid polymer electrolyte fuel cells (SPEFCs). Energy 11:137–152

9. Ticianelli EA, Derouin CR, Srinivasan S (1988) Localization of platinum in low catalyst loading electrodes to attain high power densities in SPE fuel cells. J Electroanal Chem 251:275–295

10. Ticianelli EA, Derouin CR, Redondo A, Srinivasan S (1988) Methods to advance technology of proton exchange membrane fuel cells. J Electrochem Soc 135:2209–2214

11. Srinivasan S, Ticianelli EA, Derouin CR, Redondo A (1988) Advances in solid polymer electrolyte fuel cell technology with low platinum loading electrodes. J Power Sources 22:359–375

12. Wilson MS, Valerioand JA, Gottesfeld S (1995) Low platinum loading electrodes for polymer electrolyte fuel cells fabricated using thermoplastic ionomers. Electrochim Acta 40:355–363

13. Uchida M, Aoyama Y, Eda N, Ohta A (1995) New preparation method for polymer-electrolyte fuel cells. J Electrochem Soc 142:463–468

14. Watanabe M, Tomikawa M, Motoo S (1985) Experimental analysis of the reaction layer structure in a gas diffusion electrode. J Electroanal Chem 195:81–93

15. Watanabe M, Makita K, Usami H, Motoo S (1986) New preparation method of a high performance gas diffusion electrode working at 100 % utilization of catalyst clusters and analysis of the reaction layer. J Electroanal Chem 197:195–208

16. Uchida M, Fukuoka Y, Sugawara Y, Eda N, Ohta A (1996) Effects of microstructure of carbon support in the catalyst layer on the performance of polymer-electrolyte fuel cells. J Electrochem Soc 143:2245–2252

17. Gasteiger HA, Kocha SS, Sompalli B, Wagner FT (2005) Activity benchmarks and requirements for Pt, Pt-alloy, and non-Pt oxygen reduction catalysts for PEMFCs. Appl Catal Environ 56:9–35

18. Lee M, Uchida M, Yano H, Tryk DA, Uchida H, Watanabe M (2010) New evaluation method for the effectiveness of platinum/carbon electrocatalysts under operating conditions. Electrochim Acta 55:8504–8512

19. Xia Z, Wang Q, Eikerling M, Liu Z (2008) Effectiveness factor of Pt utilization in cathode catalyst layer of polymer electrolyte fuel cells. Can J Chem 86:657–667

20. Uchida M, Park YC, Kakinuma K, Yano H, Tryk DA, Kamino T, Uchida H, Watanabe M (2013) Effect of the state of distribution of supported Pt nanoparticles on effective Pt utilization in polymer electrolyte fuel cells. Phys Chem Chem Phys 15:11236–11247

Polymer Electrolyte Fuel Cells, Oxide-Based Cathode Catalysts

Akimitsu Ishihara
Yokohama National University, Hodogaya-ku, Yokohama, Japan

Introduction

Oxide-based cathode catalysts are entirely new non-precious metal cathode catalysts for low-temperature fuel cells such as polymer electrolyte fuel cells (PEFCs). These catalysts were developed from a viewpoint that high chemical stability was essentially required for the cathode for PEFCs. The cathode catalysts for PEFCs are exposed to an acidic and oxidative atmosphere, that is, a strong corrosive environment, therefore, even platinum nanoparticles dissolved during a long-time operation. This instability of electrocatalysts is one of the factors which hindered the wide commercialization of PEFCs.

Group 4 and 5 metal oxides, which are well known as valve metals, are expected to have high chemical stability even in acid electrolyte. Table 1 shows the solubility of platinum black powder and some oxide-based materials prepared by various methods in 0.1 M H_2SO_4 at 30 °C under atmospheric condition [1]. The solubility of the oxide-based materials was smaller than that of platinum black. Therefore, these oxide-based materials were chemically stable in acid electrolyte under atmospheric condition. However, these oxides were almost insulators. In addition, oxygen molecules hardly adsorb on a surface of the oxides with no defects. Therefore, the surface of group 4 and 5 metal oxides must be modified to have definite catalytic activity for oxygen reduction reaction (ORR). The surface modifications were classified into four [1]: (1) formation of complex oxide layer containing active sites, (2) substitutional doping of nitrogen, (3) creation of oxygen defects without using carbon and nitrogen, and (4) partial oxidation of compounds including carbon and nitrogen.
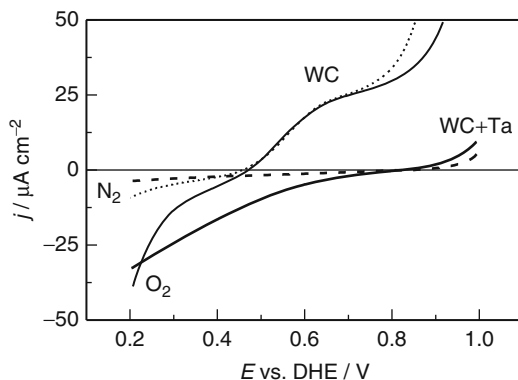
Polymer Electrolyte Fuel Cells, Oxide-Based Cathode Catalysts, Table 1 Solubility of platinum black powder and oxide-based materials prepared by various methods in 0.1 mol dm^{-3} H_2SO_4 at 30 °C under atmospheric condition

Catalysts	Preparation method	Solubility/μmol dm^{-3}
TaO_xN_y (powder)	Nitridation of Ta_2O_3 with NH_3	0.33
TaO_xN_y (thin film)	Reactive sputtering	0.20
ZrO_xN_y (thin film)	Reactive sputtering	0.041
TiO_{2-x} (plate)	Heat treatment	0.36 (50 °C)
Pt black (powder)	–	0.56

Surface Modifications of Oxides

Formation of Complex Oxide Layer Containing Active Sites

Tungsten carbide (WC) and molybdenum carbide have the platinum-like electronic structure. Therefore, these carbides are expected to be active for oxygen reduction reaction. However, tungsten and other carbides were unstable at the high potential region in an acid electrolyte. Tantalum (Ta) was added to tungsten carbide to form thin protective film. The pure WC corroded to form WO_3 and CO_2 at high potential region. However, the tantalum addition to tungsten carbide catalyst showed high electrochemical stability even at high potential region. Tungsten and tantalum formed complex hydroxide films, which had high corrosion resistance. The surface of the WC with Ta addition was covered by the complex hydroxide film. Figure 1 shows the potential–current curves for a Ta-added WC and a pure WC in N_2 and O_2 atmosphere [2]. The current observed under N_2 reflected electrochemical stability of the catalysts. The current difference under O_2 and N_2 corresponded to the ORR. The WC with Ta addition was stable, and the onset potential for the ORR was observed at about 0.8 V versus dynamic hydrogen electrode (DHE). XPS suggested that the surface of the WC with Ta addition was mainly consisted of complex hydroxide and there existed WC near the surface. Because the thin hydroxide film of
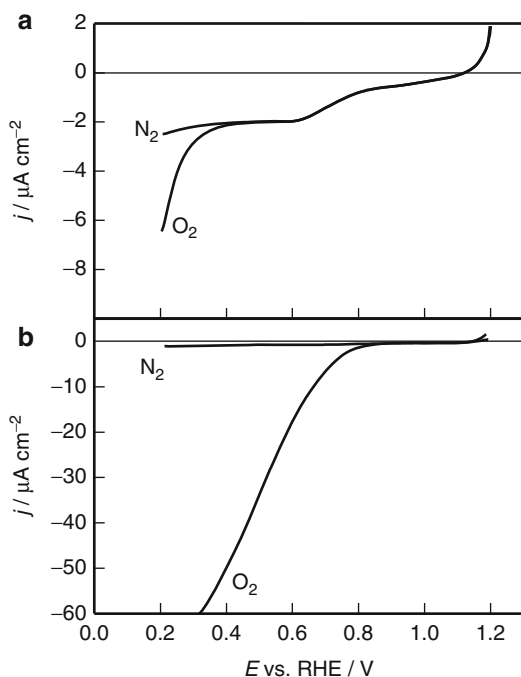

Polymer Electrolyte Fuel Cells, Oxide-Based Cathode Catalysts, Fig. 1 Potential–current curves for a Ta-added WC and a pure WC under N_2 and O_2 atmosphere in 0.1 M H_2SO_4 at 30 °C

W and Ta was formed on the WC, the catalytic activity was remained and the stability increased. However, long-term durability should be investigated.

Substitutional Doping of Nitrogen

In order to obtain a narrower band-gap of these oxides, the substitutional doping of N might be ineffective since its p states contribute to the band-gap narrowing by mixing with O $2p$ states.

Figure 2a, b show the potential–current curves of tantalum nitride (Ta_3N_5) and tantalum oxynitride ($TaO_{0.92}N_{1.05}$) under N_2 or O_2 in 0.1 M H_2SO_4 [3]. Ta_3N_5 had poor catalytic activity for the ORR. On the other hand, the ORR current with $TaO_{0.92}N_{1.05}$ started to flow at 0.8 V versus Reversible Hydrogen Electrode (RHE), indicating that $TaO_{0.92}N_{1.05}$ had definite catalytic activity for the ORR. Other nitrogen-doped oxides such as TaO_xN_y, NbO_xN_y, HfO_xN_y-C, and Zr_2ON_2 also have some catalytic activity for the ORR [4–7]. Because pure oxynitrides also have wide band-gap, it is predicted that pure oxynitrides might have poor catalytic activity for the ORR. These results indicate that the surface of these oxynitrides might have some defects which create the donor levels close to the edge level of the conduction band, that is, close to the Fermi level. The electrons in the donor level due to the surface defects probably participate in the ORR. Therefore, not only
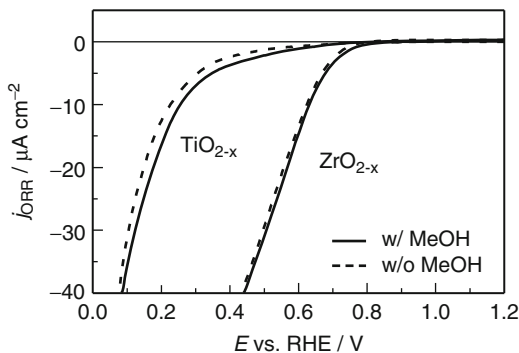
Polymer Electrolyte Fuel Cells, Oxide-Based Cathode Catalysts, Fig. 2 Potential–current curves of tantalum nitride (Ta_3N_5) and tantalum oxynitride ($TaO_{0.92}N_{1.05}$) under N_2 or O_2 in 0.1 M H_2SO_4 at 30 °C

Polymer Electrolyte Fuel Cells, Oxide-Based Cathode Catalysts, Fig. 3 Potential–current curves of ZrO_{2-x} and TiO_{2-x} in 0.1 M H_2SO_4 under O_2 with or without 0.1 M methanol at 30 °C

substitutional doping of N but also creating surface defects was required to enhance the catalytic activity for the ORR. Recently, the addition of carbon to TaON was found to be effective to increase the ORR current [4]. The additive carbon into oxynitride might form the electron conduction path. This result indicated that the suitable electron conduction path must be constructed to obtain larger ORR current.

Creation of Oxygen Defects Without Using Carbon and Nitrogen

Adsorption of oxygen molecules on the surface was required as the first step to proceed the ORR. The presence of the surface defects sites is required to adsorb the oxygen molecules on the surface of the oxides.

ZrO_{2-x} prepared by sputtering with ZrO_2 target under Ar atmosphere had clear catalytic activity for the ORR [8]. The onset potential of the sputtered ZrO_{2-x} for the ORR was observed

below 0.9 V versus RHE in 0.1 mol dm^{-3} H_2SO_4 at 30 °C. Other metal oxides such as Co_3O_{4-x}, TiO_{2-x}, SnO_{2-x}, and Nb_2O_{5-x} prepared by sputtering also showed ORR activity to some extent. In addition, these oxides were inactive for methanol oxidation. Figure 3 shows the potential–current curves of ZrO_{2-x} and TiO_{2-x} in 0.1 M H_2SO_4 under O_2 with or without 0.1 M methanol [8]. The presence of methanol did not affect the ORR activity of the oxides. Therefore, these oxides could be a possible candidate substituting the platinum cathode for direct methanol fuel cells.

TiO_x/Ti, $Ti_{0.7}Zr_{0.3}O_x$/Ti, $Ti_{0.3}Ta_{0.7}O_x$/Ti, ZrO_x/Ti, and TaO_x/Ti prepared by dip-coating method at 450 °C [9] and highly dispersed tantalum oxide prepared by electrodeposition in a nonaqueous solution [10] also showed high ORR activity. These oxides might have some oxygen defects on the surface. Therefore, there are various methods in preparing oxides with oxygen defects.

Partial Oxidation of Compounds Including Carbon and Nitrogen

The surface oxidation state would be changed by the control of a partial oxidation of non-oxides. Carbonitrides of group 4 and 5 elements were used as precursors for a partial oxidation. Carbonitrides form a complete solid solution of carbide and nitride. A partial
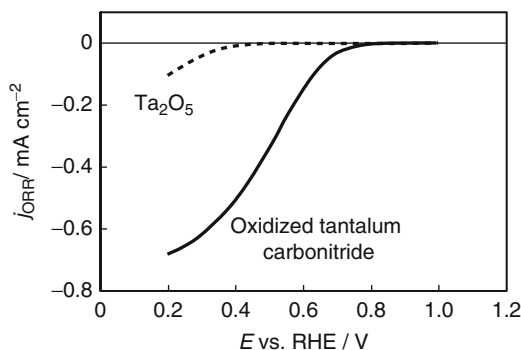
Polymer Electrolyte Fuel Cells, Oxide-Based Cathode Catalysts, Fig. 4 Potential–oxygen reduction current curves of oxidized tantalum carbonitride and commercial tantalum oxide in 0.1 M H_2SO_4 at 30 °C

oxidation of carbonitride, that is, the substitution for O atoms, brings an increase in ionic components among the chemical bonding, because the energy difference between the electron orbital of metal ion and O $2p$ orbital is higher than that between electron orbital of metal ion and C or N $2p$. The electronic state might be controlled by the control of the degree of the oxidation.

Figure 4 shows the potential–oxygen reduction current curves of oxidized tantalum carbonitride and commercial tantalum oxide [11]. Compared with commercial Ta_2O_5, the oxidized tantalum carbonitride had definite ORR activity. Oxidized tantalum carbonitride had Ta_2O_5 structure, and some deposited carbon was contained. A surface-sensitive conversion-electron-yield x-ray absorption spectroscopy analysis revealed that the oxidized tantalum carbonitride with high ORR activity contained oxygen-vacancy sites, providing both oxygen adsorption sites and local electron conduction paths [12]. The deposited carbon might form local micro electron conduction path and play an important role of the formation of the oxygen vacancies. In addition, it was found that nitrogen in precursors was essentially required to have high ORR activity. The nitrogen might concern the formation of the oxygen vacancies as active sites. Although it is necessary to clarify the role of

carbon and nitrogen, it is presumed that the oxygen vacancies act as active sites.

Catalyst Design

The four surface modifications provided the principle of the catalyst design of oxide-based cathodes. In order to increase the ORR current density, the following three points are required: (1) increase of density of oxygen defects such as vacancies as active sites, (2) preparation of highly dispersed fine particles to increase surface area, and (3) optimization of electron conduction path. It is considered that there are various methods to prepare the catalysts which satisfy these conditions.

Future Directions

Group 4 and 5 oxide-based cathodes have basically high chemical stability in acid electrolyte. In order to obtain larger ORR current, high dispersion of nano-sized oxides is one solution. The increase in surface area, the creation of oxygen defects, and the improvement of electronic conductivity are expected by becoming the oxides to be nano-sized. However, the surface energy of nano-sized oxides increases, indicating that the solubility may increase. It would be important to investigate the optimal size of the oxides.

Because carbon deteriorates in high potential, both carbon support and deposited carbon might become a key factor of catalyst degradation. In case of oxide-based cathode, the active sites are not related to the carbon. Therefore, carbon-free cathode would be possible in the future.

Cross-References

▶ Fuel Cells, Non-Precious Metal Catalysts for Oxygen Reduction Reaction
▶ Platinum-Based Cathode Catalysts for Polymer Electrolyte Fuel Cells

References

1. Ishihara A, Ohgi Y, Matsuzawa K, Mitsushima S, Ota K (2010) Progress in non-precious metal oxide-based cathode for polymer electrolyte fuel cells. Electrochim Acta 55(27):8005–8012
2. Lee K, Ishihara A, Mitsushima S, Kamiya N, Ota K (2004) Stability and electrocatalytic activity for oxygen reduction in WC+Ta catalyst. Electrochim Acta 49(21):3479–3485
3. Ishihara A, Lee K, Doi S, Mitsushima S, Kamiya N, Hara M, Domen K, Fukuda K, Ota K (2005) Tantalum oxynitride for a novel cathode of PEFC. Electrochem Solid-State Lett 8(4):A201–A203
4. Kikuchi A, Ishihara A, Matsuzawa K, Mitsushima S, Ota K (2009) Tantalum-based compounds prepared by reactive sputtering as a new non-platinum cathode for PEFC. Chem Lett 38(12):1184–1185
5. Ohnishi R, Katayama M, Takanabe K, Kubota J, Domen K (2010) Niobium-based catalysts prepared by reactive radio-frequency magnetron sputtering and arc plasma methods as non-noble metal cathode catalysts for polymer electrolyte fuel cells. Electrochim Acta 55(19):5393–5400
6. Chisaka M, Suzuki Y, Iijima T, Sakurai Y (2011) Effect of synthesis route on oxygen reduction reaction activity of carbon-supported hafnium oxynitride in acid media. J Phys Chem C 115:20610
7. Maekawa Y, Ishihara A, Mitsushima S, Ota K (2008) Catalytic activity of zirconium oxynitride prepared by reactive sputtering for ORR in sulfuric acid. Electrochem Solid-State Lett 11(7): B109–B112
8. Liu Y, Ishihara A, Mitsushima S, Kamiya N, Ota K (2007) Transition metal oxides as DMFC cathodes without platinum. J Electrochem Soc 154(7): B664–B669
9. Takasu Y, Suzuki M, Yang H, Ohashi T, Sugimoto W (2010) Oxygen reduction characteristics of several valve metal oxide electrodes in $HClO_4$ solution. Electrochim Acta 55(27):8220–8229
10. Seo J, Cha D, Takanabe K, Kubota J, Domen K (2012) Highly-dispersed Ta-oxide catalysts prepared by electrode position in a non-aqueous plating bath for polymer electrolyte fuel cell cathodes. Chem Commun 48:9074–9076
11. Ishihara A, Tamura M, Matsuzawa K, Mitsushima S, Ota K (2010) Tantalum oxide-based compounds as new non-noble cathodes for polymer electrolyte fuel cell. Electrochim Acta 55(26):7581–7589
12. Imai H, Matsumoto M, Miyazaki T, Fujieda S, Ishihara A, Tamura M, Ota K (2010) Structural defects working as active oxygen-reduction sites in partially oxidized Ta-carbonitride core-shell particles probed by using surface-sensitive conversion-electron-yield x-ray absorption spectroscopy. Appl Phys Chem 96:191905

Polymer Electrolyte Fuel Cells, Perfluorinated Membranes

Kohta Yamada
Asahi Glass Co. Ltd., Research Center, Kanagawa-ku, Yokohama, Japan

Introduction

Polymer electrolyte fuel cells (PEFCs) have attracted great interest for applications to automotive and residential cogeneration systems, because of their high power density and low operational temperature. One of the key materials for PEFCs is proton exchange membranes, which are electrolyte assembled between anode and cathode. The performance and the lifetime of membrane electrode assemblies (MEAs) for PEFCs depend on the properties of the membranes, which are chemical or electrochemical stability, mechanical strength in the form of membrane, proton conductivity in the range of operational temperatures, water transport between electrodes, and gas-barrier property to avoid fuel/oxidant crossover between electrodes. In addition, from the viewpoint of fabrication and commercialization of MEAs, the membranes should be requested appropriate properties for manufacture handling in the form thin film, low-cost, material reliability, and quality control. Although many types membranes have been developed to realize the above properties, the present essay will focus on perfluorinated sulfonic acid membrane (PFSA membrane), because they are extensively used in MEAs for PEFC systems due to high chemical stability compared with hydrocarbon membranes.

Development of Membranes

The concept of the usage of an ion exchange membrane as electrolyte in fuel cells dates back to the 1940s [1, 2]. Firstly, the development of ion

Polymer Electrolyte Fuel Cells, Perfluorinated Membranes,
Fig. 1 Chemical structure of PFSA polymers.
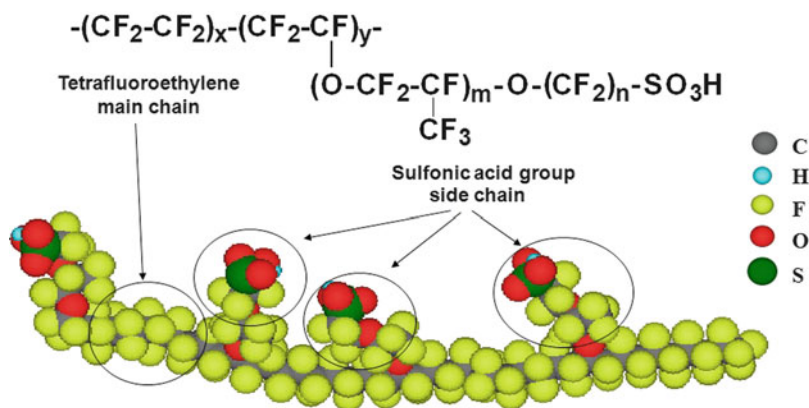
exchange membranes was eagerly performed using sulfonated poly(phenol-formaldehyde)- or sulfonated poly(styrene-divinylbenzene)-based polymers [3–6]. However these membranes were rapidly degraded by the hydroxyl radicals, which were thought to be by-products of the reaction on cathodes, oxygen reduction reaction [7, 8]. From the viewpoint of the chemical stability of electrolyte in MEA for a fuel cell, the PFSA membrane was firstly used by GE in 1966 for National Aeronautics and Space Administration (NASA) [9]. Although the stability problems of the electrolyte were alleviated in some extent by the use of the perfluorinated chemicals, there still were concerns about long-term stability of the electrolytes in electrochemical cells. Especially, long-term operations of fuel cells often require stable performance greater than 5,000 h for automobiles or 60,000 h for residential use under operating conditions. In the operations, the membranes are requested to be stable under severe conditions, simultaneously oxidizing, reducing and thermally circumstances [10].

Figure 1 describes the chemical structure of PFSA polymers, which was widely used as perfluorinated electrolytes for PEFCs. The structure is based on copolymers of tetrafluoroethylene (TFE) and perfluorovinyl ether monomers with a side chain of sulfonic acid group. While many acid groups have been examined in

ion exchange systems for several decades, the sulfonic acid group is still dominant due to high stability and proton conductivity. The ion exchange capacity of the polymers (IEC meq/g = 1,000/EW, EW: equivalent weight) can be controlled by changing the constituents x and y in the figure. As examples of these polymers, Nafion® from DuPont, Flemion® Asahi Glass Co. Ltd., and Aciplex® Asahi Kasei Chemicals are well known. Dow's short side chain monomer structure is also known, even though this polymer is no longer supplied commercially. As for durability test of these PFSA membranes in a fuel cell, Nafion (Nafion120 membranes) was demonstrated for approximately 60,000 h MEA operation at a cell temperature of 60 °C and 100 % RH [11]. However, under low humidity conditions, it has been clarified that even PFSA membranes significantly deteriorate in a short period of time [12–14]. The fuel cell operation under low humidity conditions is required especially for automotive applications to increase energy density of the PEFC systems.

In order to develop durable membranes under low humidity conditions, it was of utmost importance that the degradation mechanism was understood. It was commonly believed that the hydrogen peroxide formed in the catalyst layer diffuses into the membrane and subsequently the

Polymer Electrolyte Fuel Cells, Perfluorinated Membranes, Fig. 2 Schematic representation of apparatus for the accelerated degradation test.
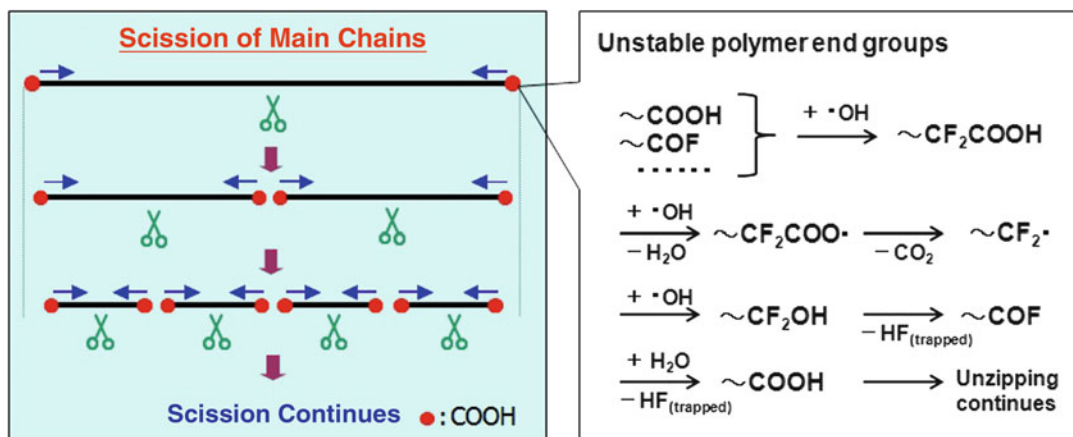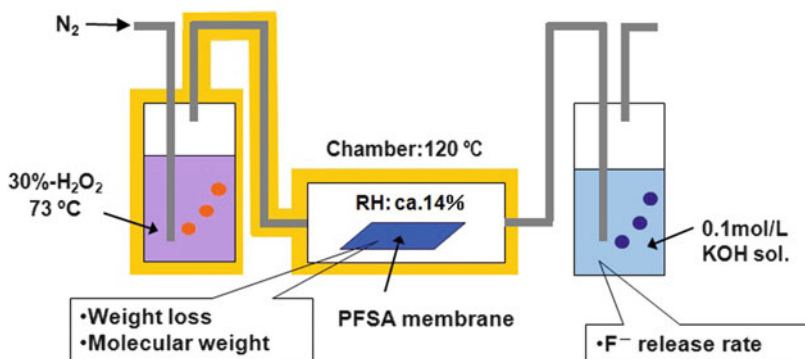
Polymer Electrolyte Fuel Cells, Perfluorinated Membranes, Fig. 3 Decomposition mechanism of PFSA polymer under low humidity conditions.

chemical degradation of the PFSA polymer proceeded via a peroxide radical attack. Therefore, to investigate the degradation mechanism of the PFSA membrane itself under low humidity conditions, an accelerated test method was developed, in which the membrane was exposed to a gas stream containing hydrogen peroxide [15]. The schematic representation of the apparatus for the accelerated test is shown in Fig. 2. As an indicator of the decomposition of the PFSA membrane, fluoride ion (F^-) in the effluent gas was trapped in a KOH solution and analyzed. As a result, membrane degradation was thought to proceed via the following two steps as shown in

Fig. 3. Hydrogen peroxide or presumably the hydroxyl radical decomposes the polymer by:

1. An unzipping reaction at the unstable polymer end groups
2. Scission of the main chains of the PFSA polymer

An unzipping reaction at the unstable polymer end groups was initially discussed by Curtin et al. [16]. Also, the scission of the main chains occurs, which produces new unstable end groups and allows for the unzipping reaction to continue [15].

Based on the analysis of degradation mechanism above, some durable membranes have been investigated recently in order to protect from
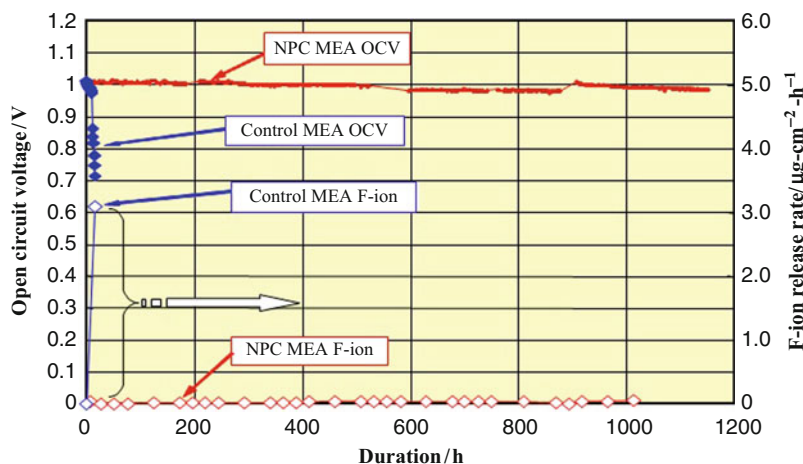
Polymer Electrolyte Fuel Cells, Perfluorinated Membranes, Fig. 4 Open circuit voltage durability of 25cm^2 MEAs at 120°C and 18%RH. Hydrogen and air was flowed at 50 and 200ml/min for anode and cathode, respectively. For NPC MEA, the thickness of NPC membrane was 40μm. For control MEA, Flemion®SH50 membrane of 50μm was used.

hydroxyl radical attack. As an example, cross-linking the polymer with a cationic radical quencher, which will protect the sulfonic acid group, was carried out [17]. The ionically cross-linking polymer membrane (new polymer composite membrane, NPC membrane) showed high chemical stability resistant to the degradation caused by the hydroxyl radical and has also improved mechanical properties at high temperatures and low humidity conditions. Figure 4 shows the OCV durability of MEAs with NPC membrane at 120 °C under low humidity. Open circuit voltage (OCV) durability tests are often used as an accelerated test of MEAs. The cell temperature was kept at 120 °C and the relative humidity of hydrogen and air was 18 %. The thickness of the NPC membrane was 40 μm. As a reference, MEA with Flemion SH 50 membrane was used. As shown in Fig. 4, the reference MEA failed within 10 h of operation, releasing a large amount of fluoride ion. In contrast, the MEA with NPC membrane showed excellent stability over 1,000 h, and the fluoride ion release rate was approximately 2×10^{-8} g (F$^-$) cm^{-2} h^{-1}, which was less than 1 % of the reference MEA and would predict a membrane-based MEA life of >6,000 h. This result demonstrates the exceptional chemical stability of the NPC membrane against the degradation caused by the hydroxyl radicals even at 120 °C and low humidity.

Future Directions

Although the highly durable PFSA membranes have been developed as mentioned above, significant cost reduction of MEA is also required for the widespread commercialization of PEFC systems for automotive and residential applications. Especially, the improvement of the MEA power density is thought to be indispensable for the purpose. Recently, in order to attain higher MEA performance, the PFSA ionomers for catalyst coating have been intensively investigated. Especially, to reduce overpotential for cathode reaction (oxygen reduction reaction), the improvement of conductivity by increasing IEC in the ionomers, the synthesis of high oxygen-permeable ionomers, and the control of hydrophobic properties in cathode layer by solvent-soluble perfluorinated polymers have been expected.

Cross-References

References

1. Grubb WT (1957) Proceedings of the 11th annual battery research and development conference, p 5
2. Grubb WT (1959) USP 2,913,511
3. Adams B et al (1935) J Soc Chem Ind 54
4. Adams B et al (1936) Br Pat 450:308
5. D'Alelio G (1944) USP 2,366,007
6. Abrams IM (1956) Ind Eng Chem 48:1469
7. LaConti AB (1977) Proceedings of the symposium on electrode materials and process for energy conversion and storage, vol 77, p 354
8. Stek AE et al (1995) Proceedings of the 1st international symposium on new materials for fuel cell systems, vol 74
9. Grot WG (1994) Macromol Symp 82:161
10. LaConti (2003) Mechanisms of membrane degradation. In: Handbook of fuel cells, vol 3. Wiley, p 647, England
11. St-Pierre J et al (2000) J New Mater Electrochem Syst 3:99
12. Endoh E et al (2004) Electrochem Solid State Lett 7:A209
13. Liu W, Cleghorn S (2005) Electrochem Soc Trans 1:263
14. Inaba M et al (2006) Electrochim Acta 51:5746
15. Hommura S et al (2008) J Electrochem Soc 155:A29
16. Curtin DE et al (2004) J Power Sources 131:41
17. Endoh E (2008) Electrochem Soc Trans 12:41

Potentiometric pH Sensors at Ambient Temperature

Metini Janyasupab[1], Ying-Hui Lee[2] and
Chung-Chiun Liu[1]
[1]Electronics Design Center, and Chemical
Engineering Department, Case Western Reserve
University, Cleveland, OH, USA
[2]Chemical Engineering Department, National
Tsing Hua University, Hsinchu, Taiwan

Introduction

Monitoring pH is performed countless times on a daily basis. This is especially true in clinical analysis, environmental monitoring, and the food industry, where potentiometric pH sensors have become necessary analytically routine. In spite of the well-established technology, pH sensors still encounter problems with long-term stability and poor selectivity from certain reducing agents and alkaline ions. In general, potentiometric pH sensors can be categorized in three classes: (i) glass, (ii) metal/metal oxides, and (iii) polymers. In this entry, we will discuss the fundamentals, demonstrate the mechanism, and provide advantages and limitations of each class, including the trends that recent studies have demonstrated in potentiometric pH sensors.

Glass electrodes were established nearly 100 years ago and have been widely employed for pH measurement in aqueous solutions. Typical construction for the pH measurement is shown in Fig. 1 [1]. The wall of the glass tube is relatively thick and strong, and the crucial glass membrane bulb underneath is made as thin as possible, separating the internal solution and the external solution (the solution to be determined) for the pH measurement. The surface of the glass membrane is protonated by the internal and the external solution until the equilibrium is reached. This leads to the potential difference between both sides of the glass membrane. The Nernst equation of the potentials on both sides of the glass membrane is

$$E_1 = E_{10} + \frac{RT}{F}\ln[H^+]_{in}$$
$$= E_{10} + 0.0591 \log[H^+]_{in}$$

$$E_2 = E_{20} + \frac{RT}{F}\ln[H^+]_{out}$$
$$= E_{20} + 0.0591 \log[H^+]_{out}$$

The potential inside, E_1, and outside, E_2, also depend upon standard reduction potential. E_{10}, and E_{20}. E_1, and, outside, E_2 have a logarithmic relationship to concentration of hydrogen ion with a scale factor of temperature (T) in Kelvin, Faraday's constant (F), and ideal gas constant (R). At ambient temperature ($\sim$298 K), the scale factor of ($RT.F^{-1}$). ln 10 can be simplified to

Potentiometric pH Sensors at Ambient Temperature, Fig. 1 Typical construction of the combination design for the glass electrode [1]

pH meter

filling hole
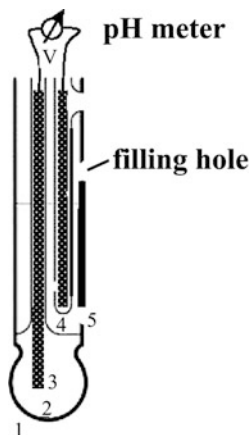
1: External solution
2: Glass elecctrode internal solution
3: Ag/AgCl reference electrode
4: Ag/AgCl reference electrode (internal solution)
5: Junction

0.0591 V/pH. Therefore, the potential difference across the glass membrane is

$$E = E_0 + 0.0591 \, \log \frac{[H^+]_{in}}{[H^+]_{out}}$$
$$= E_0 + 0.0591(pH_{out} - pH_{in})$$

Since the concentration of hydrogen ions is fixed, it can be incorporated in the constant

$$E = E_0' + 0.0591 pH_{out}$$

Accordingly, a small amount of H^+ can pass through liquid junction denoted by label (5) in Fig. 1. Consequently, the pH of the external solution can be determined through the potential difference. The constants in the above equations, E_{10}, E_{20}, and E_0, will change according to the composition of the glass membrane. The composition of the glass today is 21–33 % Li_2O, 2–4 % Cs_2O, 3–5 % La_2O_3 (Nd_2O_3, Er_2O_3), 2–4 % CaO (BaO), and SiO_2 (till 100 %) from most glass electrode manufacturers [2].

The glass electrodes are chosen due to their high selectivity, reliability, detection limit, long-term stability, independence of redox interferences, and ease of use [3]. However, longer response time is needed for the glass electrodes to reform a hydrated layer before use. Both acid error and alkali ion error exist in the glass electrode. The thickness of the hydrated layer will become thinner due to the acid stripping, causing the measured pH to remain higher than

the real value. Alkali ions, especially sodium ions, can replace proton, subsequently suppressing the proton activity. As a result, the pH value decreases. Furthermore, major disadvantages of the glass electrode are (i) high cost, (ii) large size, (iii) inflexibility, and (iv) mechanical fragility. Many factors (e.g., solution temperature, glass composition, glass thickness, and the shape of the glass tip) contribute to the high impedance of the glass electrodes. Among these factors, the temperature is highly considered since it affects the pH measurement in two ways. The temperature changes the dissociation degree of ions in solution; mean while, the resistance across the glass membrane is reduced with higher temperatures. Consequently, temperature compensation is required for the pH measurement [4]. In addition to the temperature instability, the presence of internal solution limits the use of glass electrodes in a vertical position [3]. pH glass microelectrodes are dedicated and fragile with a limited lifetime. The trade-off between resistivity and leakage is unpreventable. Therefore, the glass electrodes are impractical for the miniaturization of pH-sensing devices. Instead, an all-solid-state electrode is desirable for many specialized applications [5–7].

Metal/Metal Oxide Electrode

To determine pH in food and physiological processes, a pH electrode must be non-fragile,
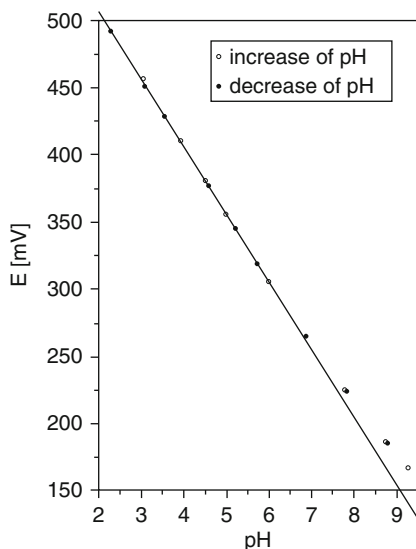
| Drink	pH(RuO$_2$)	pH(glass)
Coca-Cola	2.52 ± 0.02	2.49 ± 0.01
Fanta (12 % of lemon juice)	2.59 ± 0.03	2.63 ± 0.02
Red wine	3.65 ± 0.10	3.34 ± 0.01
Orange juice	4.30 ± 0.15	3.86 ± 0.02
Milk	6.73 ± 0.03	6.69 ± 0.02

Potentiometric pH Sensors at Ambient Temperature, Fig. 2 (*Left*) Potentiometric calibration curve of screen-printed RuO$_2$ in universal buffer and (*right*) comparison to a commercial glass electrode in some drink and beverages [18] (Reprinted from Analytica Chimica Acta, 1997. **351**(1–3): p. 143–149 with permission from Elsevier)

adequately small, and able to penetrate the tissue of samples. Due to the intrinsic properties of glass, pH measurement in microscale in these specialized systems by conventional glass electrode is impractical. Therefore, a new alternative for pH measurement uses metal/metal oxide, classified as one of solid-state pH electrodes. There are several metal/metal oxides, e.g., molybdenum [8], lead [9], iridium [10–12], cobalt [13], palladium [14], manganese [15], or ruthenium [16] oxide, exhibiting Nerstian behaviors at ambient temperature. In principle, a reversible metal/metal oxide electrode utilizes a change of electronic charge at the electrode-electrolyte interface, describing by an oxygen intercalation mechanism to hydrogen ion response as the following [17]:

$$MO_x + 2yH^+ + 2ye^- \leftrightarrow MO_{x-y} + yH_2O$$
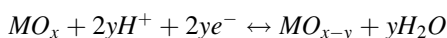
The electrode potential depends on the ion exchange on metal sites of the OH group on the surface which can be expressed as [16]

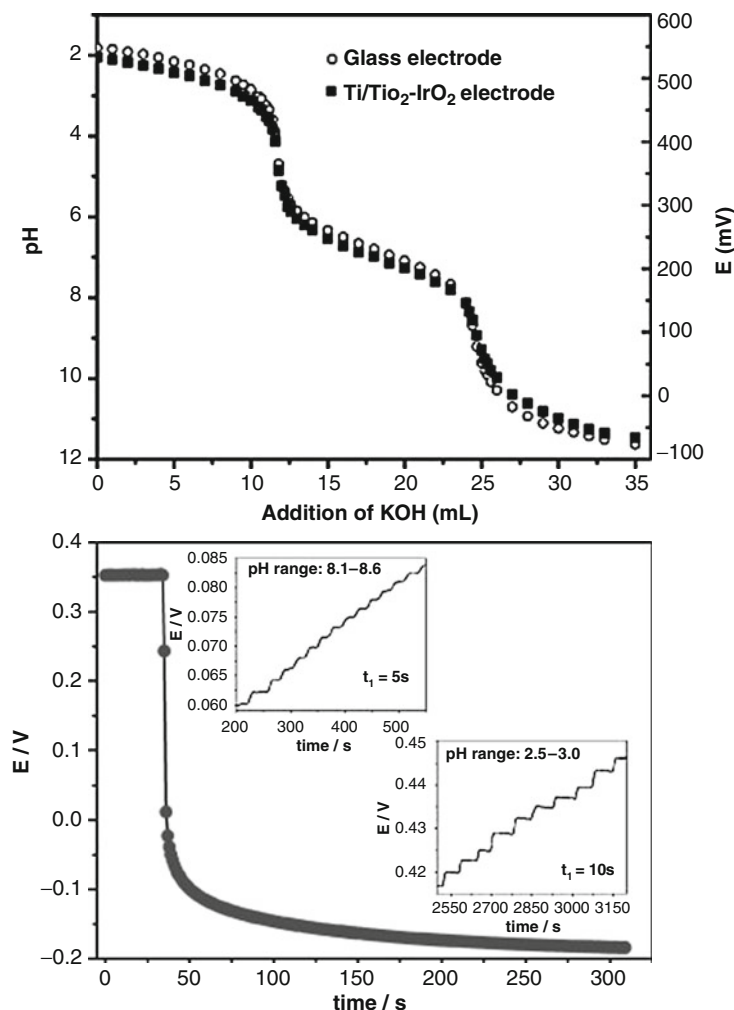$$MO_x(OH)_z + yH^+ + ye^- \leftrightarrow MO_{x-y}(OH)_{y+z}$$
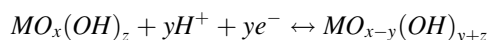
$$E = E_0' + 0.0591 \ \log\left[\frac{MO_x(OH)_z}{MO_{x-y}(OH)_{y+z}}\right] + 0.0591pH_{\text{out}}$$

The metal oxide must be sparingly soluble in tested solution and sufficiently resistive to strong corrosion in acidity or alkalinity. The intercalation equilibrium reaction must be reach as quickly to provide electron transfer to the working electrode, and it is contributed only by H$^+$ ions. As shown in Fig. 2, Koncki and Mascini demonstrated [18] a RuO$_2$ screen-printed pH sensor, successfully fabricated on a plastic platform which is flexible, sufficiently strong, and safe to test in food processing. In this work, the pH values of several beverages such as Coca-Cola and red wine were examined by RuO$_2$ in comparison to a commercial glass sensor. Since RuO$_2$ (and other metal oxides) rely on the proton/ion exchange mechanism, the potentiometric responses are not necessarily contributed by pH change. Therefore, the linear range of the sensor is limited (up to pH = 8); ruthenium encounters dissolution from alkaline ions beyond this point in potentiometric pH measurement.

In clinical analysis, Marzouk and coworkers [12] also reported the use of metal/metal oxide (IrO_2) pH sensor by monitoring ischemic rabbit heart muscle. However, the sensor had low sensitivities in the presence of Na^+, K^+, Li^+, NH_4^+, Ca^{2+}, Mg^{2+}, dissolved oxygen, lactate, ascorbate, and urate. In 2008, Da Silva et al. [19] showed promising results of IrO_2 design, incorporating 30 % mol. IrO_x and 70 % mol. TiO_2 in a binary system, which shows performance comparable to a commercial pH glass membrane electrode in Fig. 3 (linear range from pH 4 to 12). According to this experiment, the sensor does not exhibit hysteresis effect and is highly selective against alkaline ions: Li^+, Na^+, and K^+. The pH measurement by IrO_2 is nearly similar to the glass electrode; however, it still suffers interference by strong reducing agents such as ascorbic acid, H_2O_2, Fe^{2+}, I^-, or SO_3^{2-} [1]. Recently, Shim et al. [20] reported an improvement of Ru oxide pH sensor by using 3D nanoporous Ru oxide film on gold substrate. Facilitated by a reverse micelle nonionic surfactant, L_2, Ru oxide can be electrochemically deposited as shown by Fig. 4a, b, and the surface roughness is modified by Triton-X. In Fig. 4c, the potentiometric response is determined from pH 2 to 11 by adding NaOH and reversely titrated by HCl in comparison to the commercial pH glass electrode. The L_2-eRuO shows a reliable near Nerstian behaviors (sensitivity of −60.5 mV/pH, $r^2 = 0.9997$) at response time of 6–8 s in the pH range of 2–11. Controlling the oxide thickness and
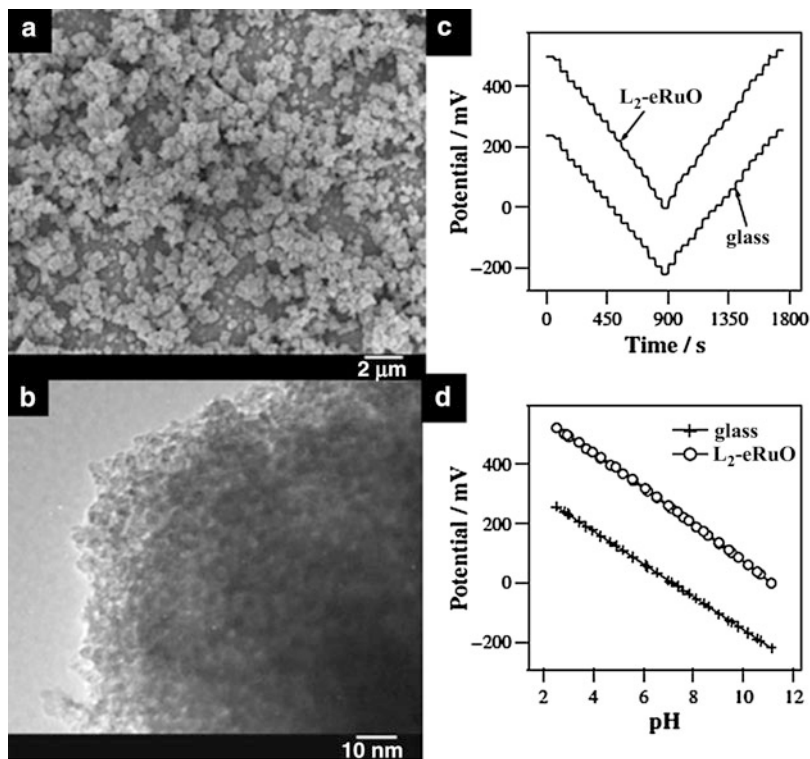
preventing parasite reactions involved in oxygen intercalation and ion exchange would overcome metal dissolution and provide better performance over the traditional pH glass electrode.

Polymeric pH Sensor

Because of the effect of severe interference by reducing agents and toxicity, metal/metal oxide pH sensors are less attractive in physiological measurements. Coexisting alkaline ions and long monitoring times are growing concerns for in vivo analysis using metal oxide. This leads to another class of pH sensor by selectively modifying pH electrode with polymers. In 1980, polymeric pH sensor, using poly (1,2-diaminobenzene) thick film coated on platinum electrode, was elaborated by Heineman et al. [21]. The sensor detected good potentiometric response (sensitivity of 57 mV/pH, $r^2 = 0.991$) from pH 4 to 10. In general, a pH-sensitive polymer network consists of a backbone polymer,

carrying weak acid or basic groups in order to obtain charge from ion exchange or protonation [22]. For example, polypropylenimine (PPI) [23, 24], polyethylenimine (PEI) [25], poly (vinyl chloride) (PVC) [26], polypyrrole (PPy), and polyaniline (PANI) [27, 28] exhibit in general Nerstian behaviors toward H^+ ions changes. Lakard et al. [29] reported a comparison of PPy, PPPD, PEI, and PANI for potentiometric polymer-based pH sensors. In Fig. 5 (left), surface morphology of each membrane is characterized by SEM images. As shown in Fig. 5 (right), all polymers exhibit near Nerstian response between pH 2 and 10. Among these polymers, PEI and PPI show the fastest response time within 15 s, whereas the others take a few minutes to reach steady state. On the other hand, PANI exhibits the highest sensitivity of 52 mV/pH with an acceptable correlation coefficient ($r^2 = 0.957$). PPPD maintains the optimum r^2 value of 0.995, implying a highly correlated response toward H^+ ions change. Furthermore, flexible thin film PANI coated on a carbon
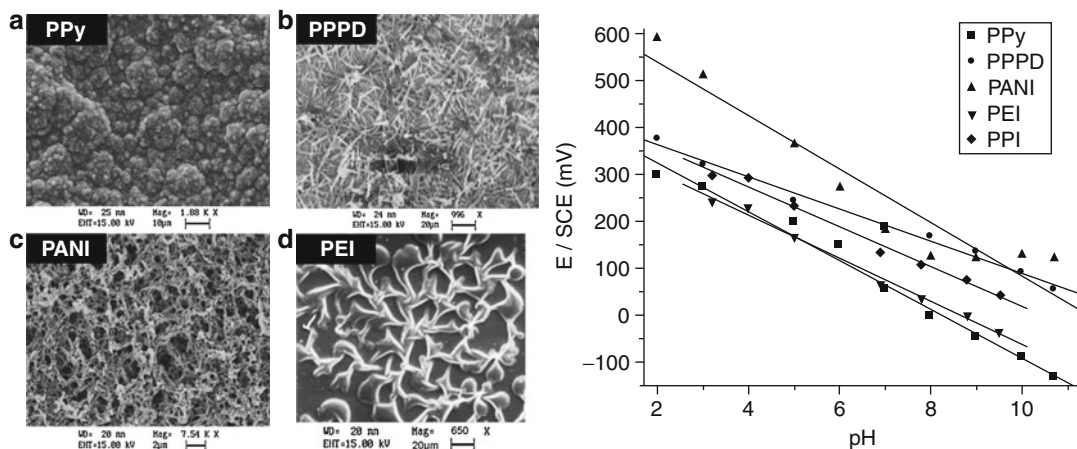
Potentiometric pH Sensors at Ambient Temperature, Fig. 5 SEM and calibration curves of PPy, PPPD, PANI, and PEI on Pt electrode [29] (Reprinted from Polymer, 2005. **46**(26): p. 12233–12239 with permission from Elsevier)
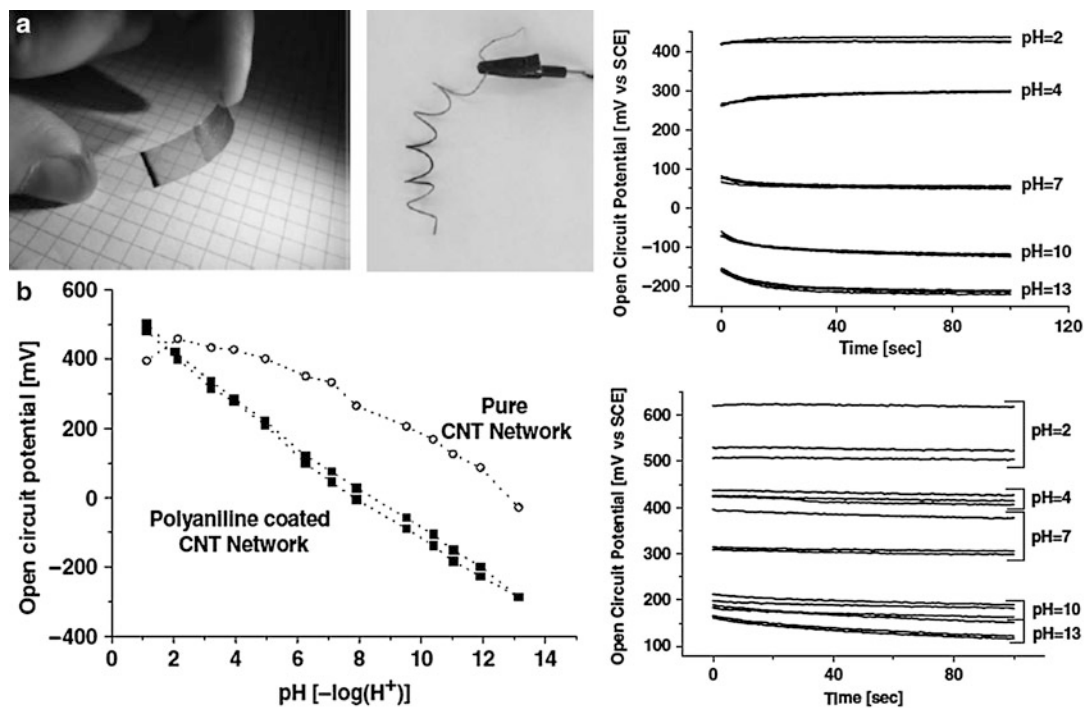
Potentiometric pH Sensors at Ambient Temperature, Fig. 6 Transparent and flexible CNT/PANI pH sensor (**a**), pH dependence of open circuit time of CNT/PANI in comparison to pure CNT network (**b**), and reproducibility (n = 3) of the sensor dipping in pH $2 \rightarrow 7 \rightarrow 13 \rightarrow 4 \rightarrow 10$ in sequence [30]

nanotube (CNT) pH sensor was elaborated by Kaempgen and Roth [30]. The CNT network has a high mechanical respect ratio, highly conductive to ions, and chemically stable. Figure 6 illustrates features of a plastic PANI/CNT film

and a simple wire for pH sensors. The novel electrode can detect from pH 1 to 13 and has a good linearity with excellent sensitivity of 58 mV/pH. The potential is stabilized within a few seconds and remains unchanged for a long
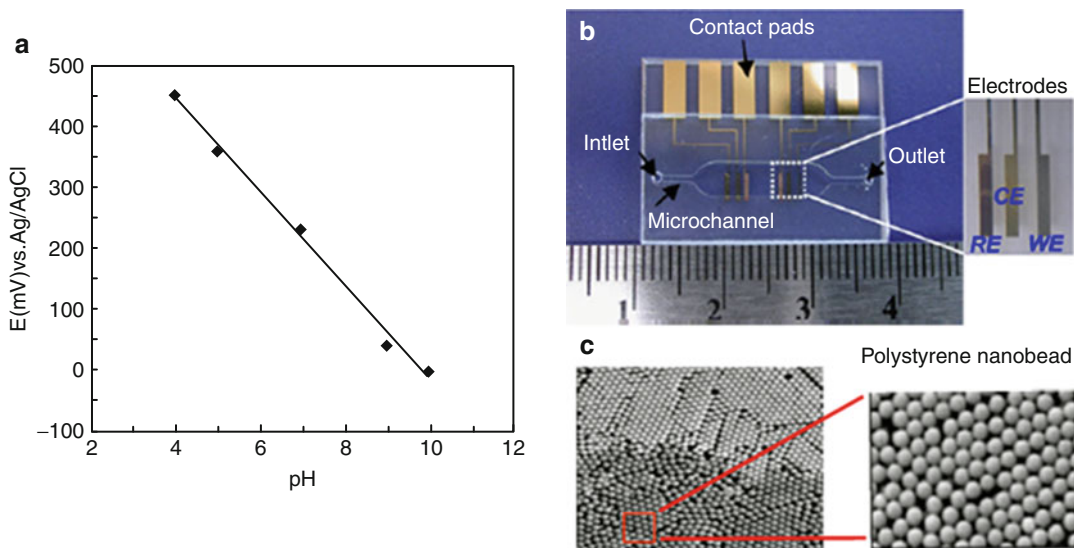
Potentiometric pH Sensors at Ambient Temperature, Fig. 7 (**a**) Potentiometric pH calibration curve, (**b**) disposable microelectrode lab chip sensor, and (**c**) SEM image of self-assembly polystyrene nanobead [32] (Reprinted from Talanta, 2010. **83**(1): p. 1–8 with permission from Elsevier)

period of time (5 min). Further stability testing was carried out and drift of 2 mV/pH was observed after 5 h and in extreme acidity and alkalinity (pH of 1 and 13, respectively). Nevertheless, PANI/CNT has shown highly reproducible results by measuring pH of $2 \rightarrow 7 \rightarrow 13 \rightarrow 4 \rightarrow 10$, accordingly in separate trials (Fig. 6, right). In comparison to pure CNT network, PANI-coated CNT clearly exhibit both higher sensitivity and reproducibility, providing a promising advancement to polymeric solid-state pH sensors.

Functionalizations of metal/metal oxide or carbon nanotechnology with polymers are reported in potentiometric pH designs. Li et al. [31] demonstrated a simple fabricated polybisphenol A (PBPA), electropolymerized on indium thin oxide (ITO) for pH sensing. The PBPA/ITO exhibits a sensitivity of 58.6 ± 1.4 mV/pH, near theoretical value, and can be stored for up to 12 days. Possible interferents such as Na^+, K^+, Cl^-, and SO_4^{2-} show no significant response. Jang and coworkers developed self-assembly nanobead polystyrene, deposited on Au/Bi in lab chip sensor. As shown in Fig. 7, the microfluid chip has two ion-selective membranes to H^+ and NO_3^- species.

The potentiometric response of the nanobead polystyrene is measured as shown Fig. 7a. This sensor has the sensitivity of 77.031 mV/pH, exhibiting super Nerstian behavior from pH range 4–10. However, interference by alkaline ions and reducing agent interference of pH electrode have not been reported in this study.

Taouil et al. [33] reported functionalized polypyrroles, poly(11-N-pyrrolylundecanoic acid) (PUPA), which shows enhancement in conductivity from PPy. Similar alkyl chain PPy, poly (N-undecypyrrole) (PUP), was synthesized containing non-protonatable group. Figure 8 (left) shows the presence of carboxylic acid group in PUPA and other identical chemical composition to PUP film, characterized by XPS spectrum. PUPA exhibits near Nerstian behavior in the range of pH 4–9 shown in Fig. 8 (right). In comparison, PUPA has an excellent sensitivity of 51 mV/pH ($r^2 = 0.995$), higher than that of PUP (33 mV/pH, $r^2 = 0.994$) and PPy (48 mV/pH, $r^2 = 0.996$). After 30 days, the PUPA shows a slight change in performance (sensitivity of 48 mV/pH, $r^2 = 0.996$), whereas, the sensitivity of PPy decreases to 33 mV/pH ($r^2 = 0.992$). Based on the result, the behavior of PUPA can be explained by the presence of carboxylic acid
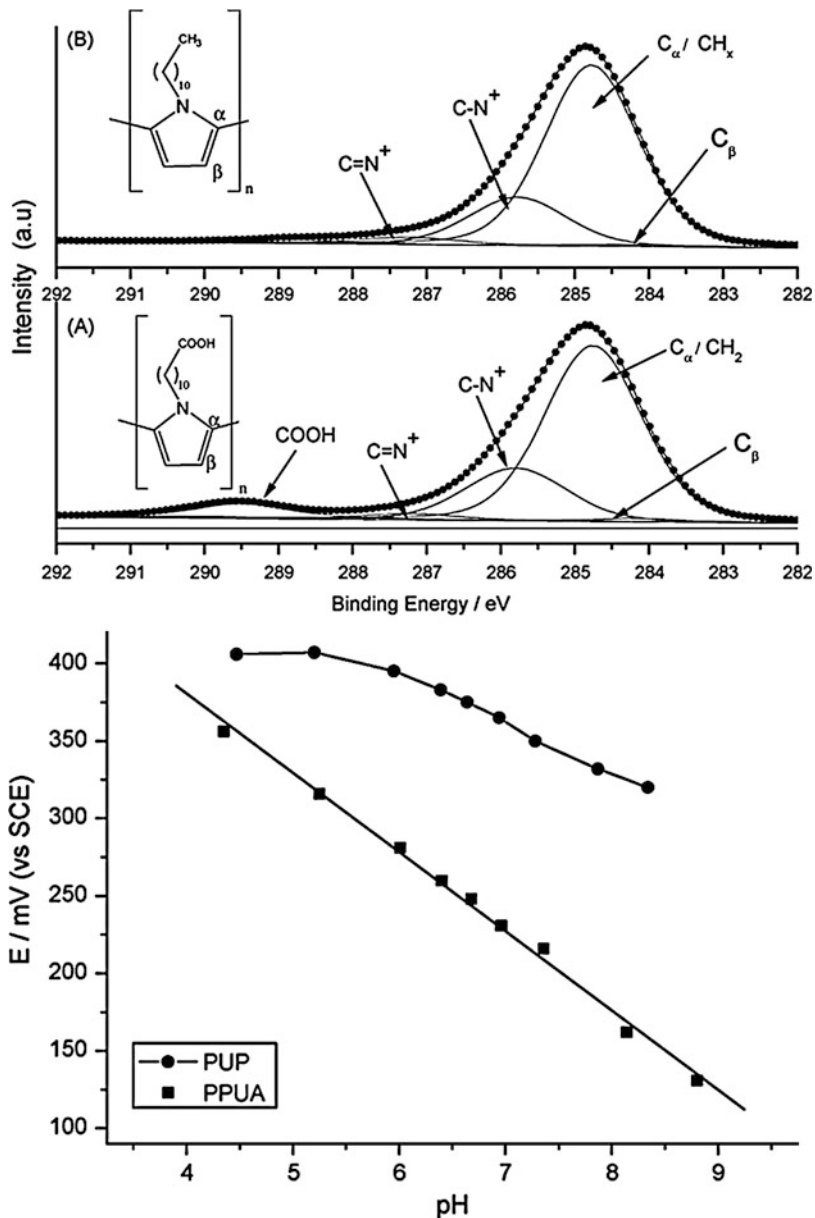
group that can be reversibly deprotonated according to the pH value. In contrast, PUP, which contains nitrogen from pyrrole, confirms that protonation is limited because these nitrogen atoms are sterically hindered [33]. For interference, a high concentration ($\sim$1 M) of several existing ions – Li^+, K^+, Na^+, Ca^{2+}, Cl^-, and SO_4^{2-} – shows no significant change in both PUPA and PUP. However, CO_3^{2-} severely affects the sensor showing an increase of

15 mV/pH on both films, indicating further improvement of polypyrrole potentiometric sensors.

This entry reviews the development of various pH sensors and provides assessment of these pH sensors for further development in order to meet the specific need. pH detection by metal/metal oxide sensors and polymer-based sensors involves in protonation or oxygen intercalation mechanism. Therefore, strong reducing agents or

alkaline ions are a major challenge to improve selectivity. Long-term stability from the film deterioration also needs to be addressed for practical use. Nevertheless, both classes can provide high mechanical strength, stiffness, and non-fragile materials, desirable for many practical uses. In view of replacing glass membrane pH sensor, hybridization in pH sensor designs of carbon nanotechnology, protonable group functionalization, or metal/metal oxide and polymer combination are expected to provide further improvements for potentiometric pH sensors.

Cross-References

▶ pH Electrodes - Industrial, Medical, and Other Applications
▶ Potentiometry

References

1. Kurzweil P (2009) Metal oxides and ion-exchanging surfaces as pH sensors in liquid: state-of-the-art and outlook. Sensors 9(6):4955–4985
2. Belyustin AA (2010) The centenary of glass electrode: from Max Cremer to F. G. K. Baucke. J Solid State Electrochem 15(1):47–65
3. Vonau W, Guth U (2006) pH Monitoring: a review. J Solid State Electrochem 10(9):746–752
4. Kohlmann FJ (2003) pH technical handbook. Hach Company
5. Zhang X, Ogorevc B, Wang J (2002) All solid-state pH nano-electrode based on polyaniline thin film electrodeposited onto ion-beam etched carbon fiber. Anal Chim Acta 452:1
6. Slim C et al (2008) Polyaniline films based ultramicroelectrodes sensitive to pH. J Electroanal Chem 612(1):53–62
7. Li J, Du Y, Fang C (2007) Developing an iridium oxide film modified microelectrode for microscale measurement of pH. Electroanalysis 19(5):608–611
8. Shuk P, Ramanujachary KV, Greenblatt M (1996) New metal-oxide-type pH sensors. Solid State Ionics 86–88, Part 2(0):1115–1120
9. Eftekhari A (2003) pH sensor based on deposited film of lead oxide on aluminum substrate electrode. Sens Actuators B Chem 88(3):234–238
10. Hitchman ML, Ramanathan S (1988) Evaluation of iridium oxide electrodes formed by potential cycling as pH probes. Analyst 113(1):35–39
11. VanHoudt P, Lewandowski Z, Little B (1992) Iridium oxide pH microelectrode. Biotechnol Bioeng 40(5):601–608
12. Marzouk SAM et al (1998) Electrodeposited iridium oxide pH electrode for measurement of extracellular myocardial acidosis during acute ischemia. Anal Chem 70(23):5054–5061
13. Meruva RK, Meyerhoff ME (1998) Catheter-type sensor for potentiometric monitoring of oxygen, pH and carbon dioxide. Biosens Bioelectron 13(2):201–212
14. Yun M et al (2004) Electrochemically grown wires for individually addressable sensor arrays. Nano Lett 4(3):419–422
15. Cherchour N et al (2011) pH sensing in aqueous solutions using a MnO2 thin film electrodeposited on a glassy carbon electrode. Electrochim Acta 56(27):9746–9755
16. Liao Y-H, Chou J-C (2008) Preparation and characteristics of ruthenium dioxide for pH array sensors with real-time measurement system. Sens Actuators B Chem 128(2):603–612
17. Głab S et al (1989) Metal-metal oxide and metal oxide electrodes as pH sensors. Crit Rev Anal Chem 21(1):29–47
18. Koncki R, Mascini M (1997) Screen-printed ruthenium dioxide electrodes for pH measurements. Anal Chim Acta 351(1–3):143–149
19. da Silva GM et al (2008) Development of low-cost metal oxide pH electrodes based on the polymeric precursor method. Anal Chim Acta 616(1):36–41
20. Shim JH et al (2012) A nanoporous ruthenium oxide framework for amperometric sensing of glucose and potentiometric sensing of pH. Microchimica Acta 177(1–2):211–219
21. Heineman WR, Wieck HJ, Yacynych AM (1980) Polymer film chemically modified electrode as a potentiometric sensor. Anal Chem 52(2):345–346
22. Richter A et al (2008) Review on hydrogel-based pH sensors and microsensors. Sensors 8(1):561–581
23. van Duijvenbode RC et al (1999) Synthesis and protonation behavior of carboxylate-functionalized poly (propyleneimine) dendrimers. Macromolecules 33(1):46–52
24. van Duijvenbode RC, Borkovec M, Koper GJM (1998) Acid–base properties of poly (propylene imine) dendrimers. Polymer 39(12):2657–2664
25. Herlem G et al (2001) pH sensing at Pt electrode surfaces coated with linear polyethylenimine from anodic polymerization of ethylenediamine. J Electrochem Soc 148(11):E435–E438
26. Liu X-J et al (2007) Potentiometric liquid membrane pH sensors based on calix[4]-aza-crowns. Sens Actuators B Chem 125(2):656–663
27. Gill EI et al (2008) Novel conducting polymer composite pH sensors for medical applications. In: Katashev A, Dekhtyar Y, Spigulis J (eds) 14th Nordic-Baltic conference on biomedical engineering and medical physics. Springer, Berlin/Heidelberg, p 225–228

28. Ansari R et al (2012) Solid-state Cu (II) ion-selective electrode based on polyaniline-conducting polymer film doped with copper carmoisine dye complex. J Solid State Electrochem 16(3):869–875

29. Lakard B et al (2005) Potentiometric pH sensors based on electrodeposited polymers. Polymer 46(26):12233–12239

30. Kaempgen M, Roth S (2006) Transparent and flexible carbon nanotube/polyaniline pH sensors. J Electroanal Chem 586(1):72–76

31. Li Q et al (2011) A novel pH potentiometric sensor based on electrochemically synthesized polybisphenol A films at an ITO electrode. Sens Actuators B Chem 155(2):730–736

32. Jang A et al (2010) Potentiometric and voltammetric polymer lab chip sensors for determination of nitrate, pH and Cd(II) in water. Talanta 83(1):1–8

33. Taouil AE et al (2010) Effects of polypyrrole modified electrode functionalization on potentiometric pH responses. Synth Met 160(9–10):1073–1080

Potentiometry

Winfried Vonau
Kurt-Schwabe-Institut fuer Mess- und Sensortechnik e.V. Meinsberg, Waldhein, Germany

Introduction

Potentiometry is an electrochemical measurement technique. The term was introduced in connection with potential determinations of electrochemical measuring chains by W. Ostwald [1]. Often instead of potentiometric measurement the measurement of galvanic voltages is spoken about. Mainly, the measuring setup consists of two electrodes (galvanic cell). These half cells are called indicator (or measuring) and reference electrode. Additionally, a high-impedance potential measuring device is necessary. Figure 1 shows a scheme of such an arrangement also called potentiometric measuring cell or chain. An important feature of the method is the fact that it is measured under the conditions of no current flow. The measurand may be used to determine the analytical quantity of interest, i.e., the activity of some components of an analyte solution or the partial pressure of

gases (see also high-temperature electrochemistry). The potential that develops in the electrochemical cell is the result of the free energy change that would occur if the chemical phenomena were to proceed until the equilibrium condition has been fulfilled.

For the potentiometric measurement, according to Eq. 1, the potential of the cell can be expressed in terms of the potential developed by the indicator electrode (E_{ind}) and the reference electrode (E_{ref}) under consideration of the junction potential (E_j):

$$E = (E_{ind} - E_{ref}) + E_j \qquad (1)$$

An important mathematical basis of the potentiometry also of high interest for practical measurements is formed by the Nernst Eq. 2. It allows the calculation of required analytical values, e.g., ion activity (a_i) as function of concentration, from the voltage E produced by any electrochemical cell (see Eq. 3):

$$E = E^{\ominus} - (RT/nF)lnQ \qquad (2)$$

$E^{\ominus}=$ standard electrochemical cell potential (voltage).

R = gas constant.

T = temperature in Kelvin.

n = number of moles of electrons transferred in the balanced equation or the charge/valency of the ion. In the case of the hydrogen ion, $n = 1$.

F = Faraday constant = 96.485 C mol^{-1}.

Q = mass-action expression (approximated by the equilibrium expression).

$$E = E^{\ominus} - (RT/nF)ln\, a_i \qquad (3)$$

A distinction is made between direct potentiometry and potentiometric titration. First mentioned is the method which makes use of the single measured electrode potential, for example, to determine ions using different ion-selective electrodes (ISE). While the potential of the reference electrode must be independent on the composition of the measurement medium, the indicator electrode should be fast responding and highly sensitive and selective for special

ions in a large concentration range. Figure 2 shows in principle the course of the curves for direct potentiometric determinations of a cation (i) and an anion (ii) at $T = 298$ K with pC and pA as negative logarithms of the cation a_C+ and anion activities a_A- which have to be recorded for the calibration of potentiometric chains before measuring.
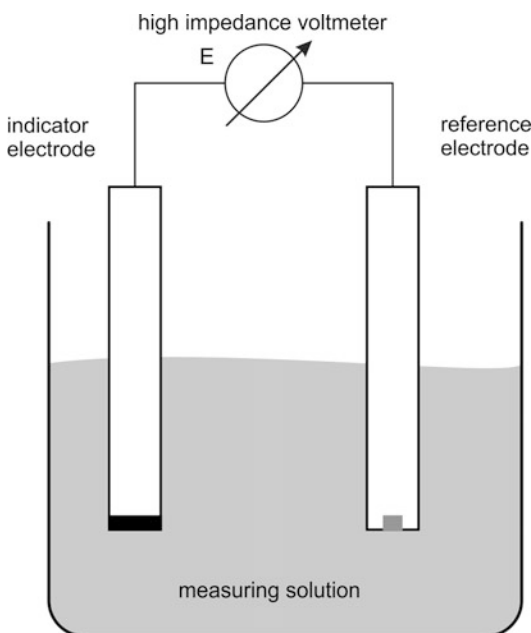
Potentiometry, Fig. 1 Scheme of a potentiometric measuring chain

Potentiometric titrations (neutralization titrations, oxidation–reduction titrations, precipitation titrations, complex formation titrations, differential titrations) provide information different from a direct potentiometric measurement. The equivalence point of the reaction (see Fig. 3) will be revealed by a sudden change in potential in the plot of potential readings against the volume of the titrating solution. One electrode has to be maintained at a constant (possibly unknown) reference potential. The other electrode must serve as an indicator of the changes in ionic concentration and has to respond rapidly. The solution should be stirred during the titration. Compared to direct potentiometric measurements, potentiometric titrations generally offer increased accuracy and precision because potentials are used to detect rapid changes in activity that occurs at the equivalence point of the titration. Furthermore, the influences of liquid junction potentials and activity coefficients are minimized.

In both, direct potentiometry and potentiometric titration redox reactions as well as equilibrium adjustments cause the function of the electrochemical cells.

Electrodes for Potentiometry

There are several possibilities to generate the reference potential in potentiometric measuring chains. Based on research results of Le Blanc [2] at first, the standard hydrogen electrode (SHE)
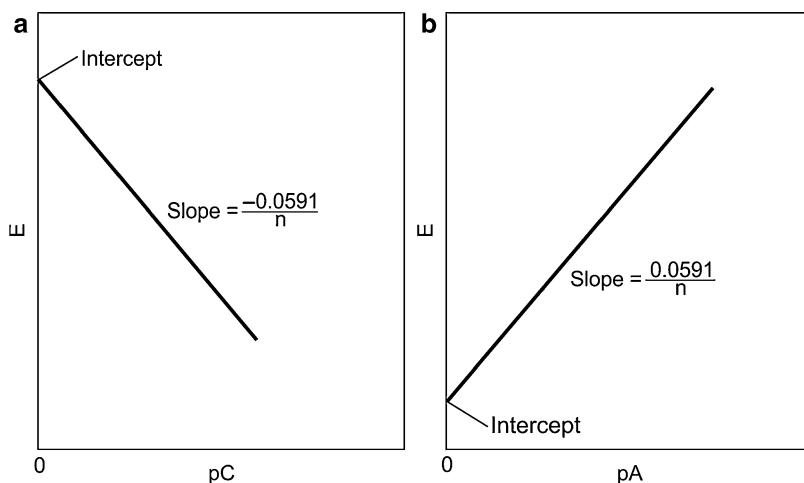
Potentiometry, Fig. 2 Potentiometric calibration curves for cations (**a**) and anions (**b**)
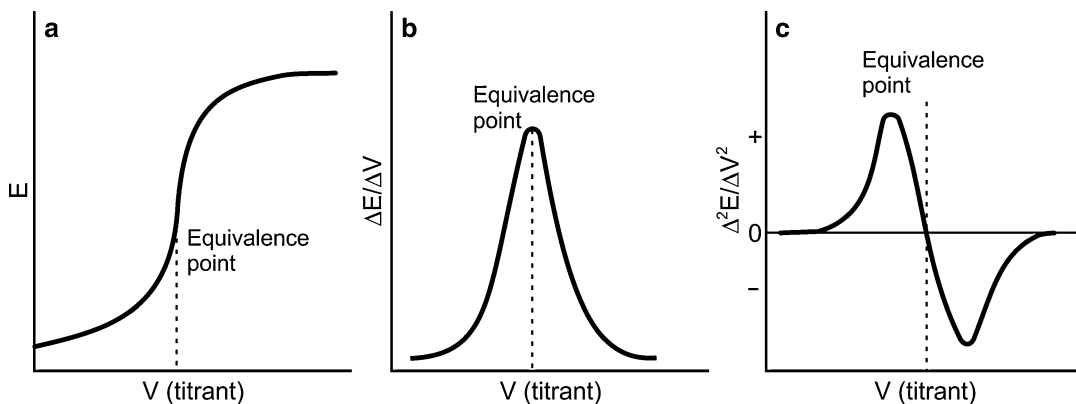
Potentiometry, Fig. 3 Potentiometric titration curves, (**a**) typical plot of E versus volume, (**b**) typical first derivative titration curve, (**c**) typical second derivative titration curve

was established for this purpose. Using the shorthand notation for electrochemical cells, the SHE can be described as follows:

$$Pt, H_2(g, \ 101.325 \, kPa)/H^+$$
$$(aq, a = 1.00)//2H^+(aq) + 2e^- \rightleftharpoons H_2(g)$$
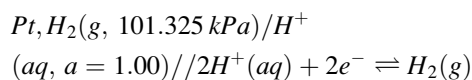
The potential of that electrode was defined as the origin of the electrochemical potential scale and was arbitrarily declared to be zero for all temperatures. Because of their complicated handling and some other disadvantages, the standard hydrogen electrode today is used only for very precise measurements, especially for the calibration and testing of pH buffer solutions. It is not trivial to realize exactly the experimental conditions that are necessary. Instead of the standard hydrogen electrode (SHE) more commonly the normal hydrogen electrode (NHE) is used, which contains an acid solution of the concentration 1 mol/L.

In practice, the so-called reference electrodes of the second kind, e.g., the Ag/AgCl, Cl^- electrode or the Hg/Hg_2Cl_2, Cl^- (calomel) electrode, are preferably applied because they are more convenient to use. Their potential is stable and well defined in relation to the potential of the SHE. Such electrodes are commercially available in a variety of chemical systems and embodiments for different applications [3]. A substantial drawback of conventional reference electrodes is their liquid electrolyte filling. The performance of such electrodes is position

dependence, and they are mechanically fragile and suitable to only a limited extend for miniaturization or for applications at high pressures and temperatures. In recent years several solutions for all solid-state arrangements were introduced, such as electrodes with solid polymer electrolyte, reference electrodes based on bronzes from the transition metals molybdenum and tungsten, or electrodes containing essentially an Ag/AgCl-reference element and a solid crystalline KCl melt. A current overview is given in [4].

Concerning the indicator electrodes often it is distinguished between metallic and membrane electrodes. The potential of a metallic electrode is determined by a redox reaction at the interphase electrode/solution. Basically there are three different kinds of metal-based indicator electrodes (Table 1):

Membranes as location for the potential determining reaction in indicator electrodes as part of potentiometric measuring chains can be divided in crystalline and noncrystalline membranes.

Noncrystalline membranes	Crystalline membranes
Silicate (i) and chalcogenide glasses (ii)	Single crystals (v)
Liquid–liquid ion exchanger (iii)	Separate or mixed polycrystals (vi)
Immobilized liquid–liquid/PVC matrix (iv)	

(i). Oxidic glasses with special compositions can be part of potentiometric sensors to

determine the activity of H^+, Na^+, K^+, NH_4^+, Cs^+, Rb^+, Li^+, Ag^+, and several other cations [5] as well as of the redox potential [6].

Examples. H^+ (more precise H_3O^+) activity 72 wt% SiO_2, 22 wt% Na_2O, 6 wt% CaO [7].

Redox potential 50 wt-% SiO_2, 39 wt% Fe_2O_3, 7 wt% Na_2O, 4 wt% Li_2O [8].

(ii). Using such materials leads to ISE for the determination of several heavy metals but also for anions such as F^- [9]. Besides compact sensors it is possible to fabricate chalcogenide glass electrodes in thin film technology [10].

**Example.** Fe^{3+} activity $Fe_2Se_{60}Ge_{28}Sb_{12}$ [11].

(iii). One of the most famous liquid membrane electrodes has been used for calcium determination. This electrode works by an ion-exchange process. The cation exchanger is an aliphatic diester of phosphoric acid, $(RO)_2PO_2^-$, where each R group is an aliphatic hydrocarbon chain containing between 8 and 16 carbons. The phosphate group can be protonated but has a strong affinity for Ca^{2+}. The cation exchanger is dissolved in an organic solvent and held in a porous compartment between the analyte solution and an internal reference calcium chloride solution. The ion exchanger uptakes Ca^{2+} into the membrane.

Example. $Ca^{2+}(aq) + 2(RO)_2PO_2^-$ (organic) $\rightleftharpoons \left[(RO)_2PO_2\right]_2Ca$(organic).

(iv). An alternative to liquid membrane electrodes is to use a polymer matrix-based membrane, which is composed of a polymer such as polyvinylchloride (PVC), a plasticizer, and the ion carrier or exchanger. The response of these electrodes is highly selective and they have replaced many liquid membrane electrodes.

Polymer-based electrodes are available, e.g., for the determination of K^+, NH_4^+, Ba^{2+}, Ca^{2+}, Cl^-, and NO_3^-.

Example.

K^+ activity [12]

Valinomicin
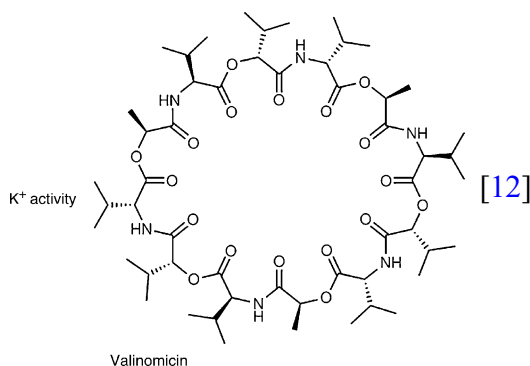
(v). It is also known to use membranes consisting of (doped) single crystals. At the inner phase boundary, the single crystals are in contact with other solids (all solid-state electrodes). In order to get reproducible and long-term stable potentials in these cases, it is necessary to create non-blocked (reversible) interfaces.

Example. Fluoride can be analyzed potentiometrically using the half cell F^-/LaF_3 (doped with Eu)/AgF/Ag [13].

(vi). Besides the usage of metals in contact with one of its hardly soluble salts (electrodes of the 2nd kind) for the potentiometric ion determination (Ag/AgCl membrane to monitor chloride, see above), sometimes mixed compositions are used. As a result, a lot of electrode properties can be improved (mechanical and light stability, lower detection limit).

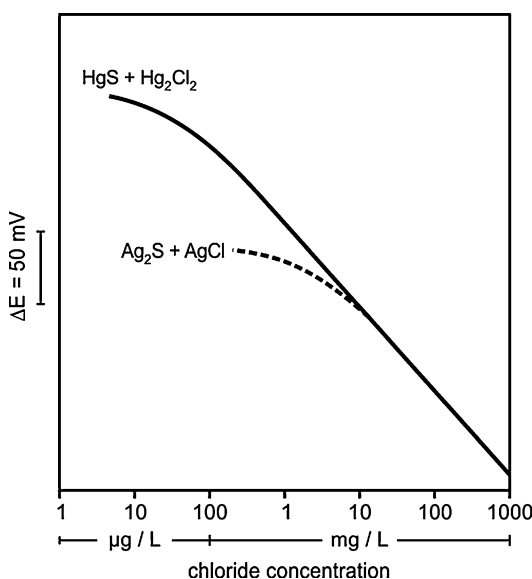**Example.** Potentiometric chloride determination with heterogeneous membranes (Fig. 4).

Cross Selectivity

Full selectivity for exactly one type of ion is never given. ISE have only a particular sensitivity for a special type of ion but often show interference with ions with similar chemical properties or a similar structure. For this reason the cross sensitivity to other ions that may be present in the

Potentiometry, Table 1 Kinds of metal based indicator electrodes

Electrodes of the 1st kind	Electrodes of the 2nd kind	Redox electrodes
	A metal is coated with one of its salt precipitate	
A metal is in contact with a solution containing its cation, e.g., Zn/Zn^{2+}, Ag/Ag^+, Cu/Cu^{2+}	An example is the Ag/AgCl electrode to measure the activity of chloride ions in a solution	An inert metal is in contact with a solution containing soluble oxidized and reduced forms of redox half-reactions
E is a function of the cation activity in the system metal/metal ion	E is a function of the anion activity	Electrode materials are often Au, Pt, or Pd
Example:	Example:	E is determined by the ratio of reduced and oxidized species
$Ag^+ + e^- \rightleftharpoons Ag$	$Ag^+ + e^- \rightleftharpoons Ag$ $Ag^+ + Cl^- \rightleftharpoons AgCl(\Downarrow)$ $AgCl(\Downarrow) + e^- \rightleftharpoons Ag + Cl^-$	Example: $Fe^{3+} + e^- \rightleftharpoons Fe^{2+}$

Potentiometry, Fig. 4 Measuring ranges for two different potentiometric chloride electrodes with heterogeneous membrane

sample solution must always be taken into consideration when selecting an ISE for a potentiometric determination. One of the best-known examples of such a cross sensitivity is the so-called alkali error of pH glass electrodes. Unfortunately, there are only very few ion-selective electrodes that have a linear range similar to that of pH glass electrodes. The use of an ISE is normally restricted to a concentration range of 4–5 powers. If an ISE is used for a measurement often the Nernst Eq. 3 must be

extended by the contribution made by the particular interfering ion for the evaluation of the measured potential. This leads to the Nikolskij Eq. 4:

$$E = E - (RT/nF) \ln \left(a_i + K_{j/i}a_j\right) \qquad (4)$$

$K_{j/i}$ is the selectivity coefficient of the ISE for an interfering ion S. This is a factor that describes the influence of the interfering ion in relationship to the ion to be measured (i). These selectivity coefficients are known for the most important interfering ions for an ISE, and therefore, a simple estimation can be made to estimate if an interfering ion present in the sample solution will influence the measured value or not.

Future Directions

Until today, there are still no satisfactory electrode membrane materials for the potentiometric determination of several important ions such as SO_4^{2-} and PO_4^{3-} so that here remains a need of research for the future.

For a lot of potentiometric indicator electrodes solid-state embodiments are available widely equivalent to the electrolyte containing systems concerning the electrode performance. Because this does not apply for all measuring electrodes (e.g., for pH glass electrodes) and for reference electrodes to the full extent, there is also still a need for development in this field.

Especially for medical applications it is often necessary to use miniaturized equipment. Due to this fact the engineers are faced with the task to develop new potentiometric electrodes by microtechnological methods, e.g., thin or thick film technology. This creates the opportunities to come to a number of miniaturized multisensors as part of lab on chip systems increasingly required in biotechnology and other areas.

Cross-References

▶ Potentiometric pH Sensors at Ambient Temperature
▶ Reference Electrodes

References

1. Drucker C (1943) Ostwald-Luther Hand- und Hilfsbuch zur Ausführung physikochemischer Messungen. Dover, New York
2. Le Blanc M (1893) Die elektromotorischen Kräfte der Polarisation II. Z Phys Chem 12:133–358
3. Lisdat F, Moritz W, Müller L (1990) Referenzelektroden für wässrige und geschmolzene Systeme. Zeitschrift für Chemie 30:427–433
4. Vonau W, Oelßner W, Guth U, Henze J (2010) An all-solid-state reference electrode. Sens Actuators B 144:368–373
5. Eisenman G (1967) The physical basis for the ionic specifity of the glass electrode. In: Eisenman G (ed) Glass electrodes for hydrogen and other cations, principles and practice. Marcel Dekker, New york
6. Nikolskij BP, Schulz MM (1971) US Patent US 3 773 642
7. MacInnes DA, Dole M (1930) The behavior of glass electrodes of different compositions. J Am Chem Soc 52:29–36
8. Nikolskij BP, Schulz MM, Pisarevskij AM, Beljustin AA, Bolchnzeva SK, Dolidse WA, Tarasova WM, Karatschenzeva JM, Dolmasowa LI (1973) German Patent DE 2 134 101
9. Vlassov Y, Bychkov E (1987) Ion-selective chalcogenide glass electrodes. Ion-Selective Rev 9:5–93
10. Kloock JP, Mourzina YG, Ermolenko Y, Doll T, Schubert J, Schöning MJ (2004) Inorganic thin-film sensor membranes with PLD-prepared chalcogenide glasses. Challenges and implementation. Sensors 4:156–162
11. König C (1993) Entwicklung und Charakterisierung einer Chalkogenidglaselektrode zur selektiven Detektion von Eisen(III)ionen. Dissertation. Goethe University Frankfurt/M., Germany
12. Pioda L, Stankova V, Simon W (1969) Highly selective potassium ion responsive liquid membrane electrode. Anal Lett 2:665–674
13. Fjedly TA, Nagy K (1980) Fluoride electrodes with reversible solid-state contacts. J Electrochem Soc 127:1299

Potentiostat

Manuel Lohrengel
University of Düsseldorf, Düsseldorf, Germany

Introduction

In the beginning, electrochemical experiments were reduced to potential measurements of systems, which were stationary or in equilibrium. But with time, scientists became interested in systems apart from equilibrium [1] or even in time-dependent reactions. This was realized by galvanostatic experiments (Potentiostat), which were by two reasons advantageous: They were easily realized and guaranteed a constant reaction rate, which was relevant in some cases. Moreover, time-dependent reactions could be monitored, if the potential was recorded vs. time. These charging curves were the main technique to follow electrode kinetics up to the sixties of the last century.

The potential, however, or more precise, the potential drop somewhere within the electrode interface, is said to be the cause of all electrochemical reactions. Therefore, scientists tried to control the potential of electrodes or cells.

Less effective was the use of a power supply and variable resistors, controlled by human intervention [2] or by slow electromechanical devices [3, 4]. More effective was the combination of a controlled power supply with an electronic control circuit, which worked fast and unattended. This was realized by *Hickling* [5], who called the instrument for the first time "potentiostat." The name is nowadays somewhat misleading as scientists do not want to keep the

potential constant but wish to vary it in a predetermined way in most cases.

Definition

A potentiostat is a controlled electric power supply, which adjusts the potential drop across an active or passive dipole to a desired value. To do this, the device has to measure the actual potential drop and to force currents through the dipole, until actual value and desired value become equal. In electrochemical systems, the interest to keep the potential drop across a complete cell is limited to rare cases, e.g., charging or discharging of batteries. More interesting are kinetics of single electrodes, which means an electric control of the interface electrode/electrolyte. An additional device is needed to measure the electrolyte potential, the so-called reference electrode. As a result, a three-electrode setup is obtained (working, counter, and reference electrodes). Reference electrodes include at least one interface *ionic conductor/ electronic conductor* with an additional potential drop which must be taken into account.

The popularity of potentiostats is reflected by a large number of publications discussing concepts, function, and applications [6–13].

Basic Circuit

Perfect combinations of control circuit and power source are operational amplifiers, which were built from discrete components in the fifties and become much more popular as integrated circuits from 1960 onward.

Most potentiostats are based on operational amplifiers. Figure 1 shows the fundamental setup. The output voltage U_{out} of an operational amplifier depends on the difference of the input voltages U_+ and U_- according to

$$U_{out} = A \cdot (U_+ - U_-) \qquad (1)$$

with an open-loop gain $A > 10^6$. A difference $U_+ - U_-$ causes an increasing output voltage
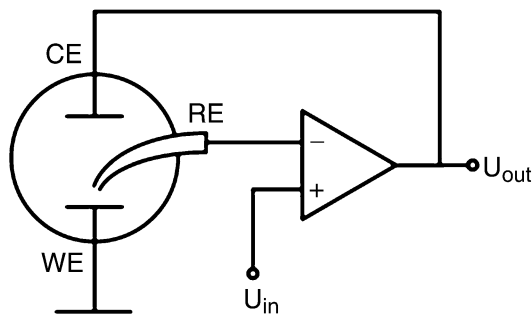
Potentiostat, Fig. 1 Fundamental potentiostat circuit with an operational amplifier

and, therefore, forces currents through the cell. This reduces the difference $U_+ - U_-$ close to zero due to the negative feedback of the output to U_-.

The limits of the output are controlled by the power supply and the particular circuit design. Typical values range from $\pm$ 5 V to $\pm$ 100 V and currents up to $\pm$ 100 mA. This value can be increased to some 10 A or even more by additional booster amplifiers. Input resistances from 10^9 Ω to 10^{12} Ω prevent notable current flow through the reference electrode.

The open-loop gain A decreases with increasing frequency, typically by a factor of 10 per decade of frequency and A comes close to 1 (unity gain) in the MHz region. This means the useful bandwidth is at least one or two orders of magnitude lower than at unity gain. This is especially important for pulse experiments or experiments at higher frequencies.

Another limitation is the slew rate, which describes the rate of change at the output in response to a large amplitude input step. Typical values such as 10^6 V/s are less informative as electrochemical cells mean capacitive loads. A potential step ΔU and an electrode capacitance ΔU yield a charge
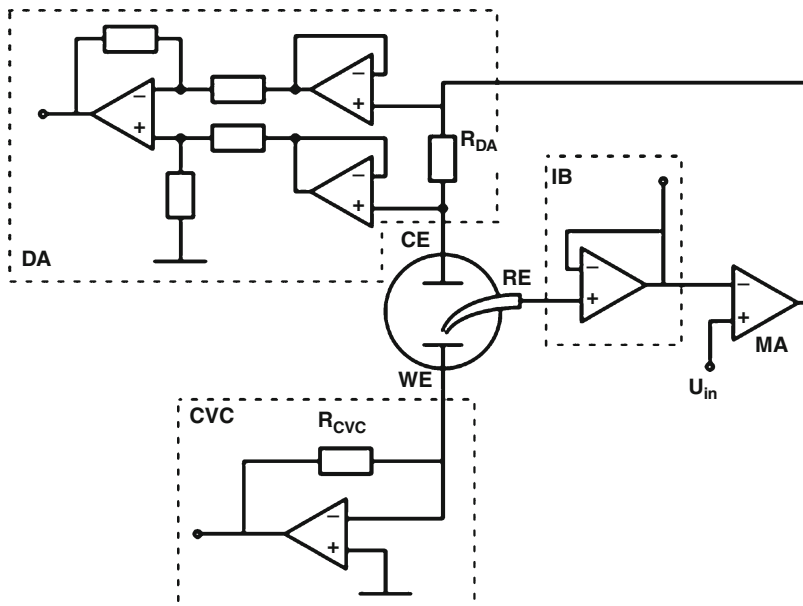
$$\Delta Q = C \cdot \Delta U \qquad (2)$$

which must be provided by the amplifier. This means at least a time interval Δt determined by the amplifier's maximum current i_{max}:

$$\Delta t = \frac{\Delta Q}{i_{max}} = \frac{C \cdot \Delta U}{i_{max}} \qquad (3)$$

Potentiostat,
Fig. 2 Potentiostat system
with main amplifier (*MA*),
impedance buffer (*IB*), and
two independent optional
current detection systems:
current-to-voltage
converter (*CVC*) and
differential amplifier (*DA*)

Accordingly, adjustment times of 30–100 μs
have to be expected in real systems for a potential
step of 1 V.

Potentiostat Systems

The basic setup controls the potential, but no
information is returned from the experiment.
A potentiostat system allows monitoring the
actual potential, recording the cell current, and
mixing different input signal such as potential
steps, sweeps, sinusoidal signals, and dc levels.
Figure 2 shows some concepts.

Potential Monitor
Reference electrodes are sensitive to current
flow, due to their large source resistance and/or
to small exchange currents of the redox system.
Therefore, reference electrodes are usually
connected via special high-impedance amplifiers
(voltage followers, IB in Fig. 2).

In thermodynamics the electrolyte is thought
to be at zero potential and the electrode potential
is given. In experiments, however, the
working electrode is at ground potential, and
therefore, the sign is inverted. This can cause
some confusion.

Current Monitor
Current-to-Voltage Converter
A current-to-voltage converter (CVC) is
connected to the working electrode in Fig. 2.
The cell current I flows also through R_{CVC}
because the input resistances of the amplifier are
extremely high. The negative feedback, however,
keeps the potential of the inverting input to the
same level as the non-inverting input, i.e., zero
potential (virtual ground). Therefore, the output
voltage of the CVC is given by

$$U_{CVC} = -R_{CVC} \cdot I \qquad (4)$$

and can be used to record the current. This con-
cept is also used for IR-drop elimination
(▶ iR-Drop Elimination).

This circuit is most often used, but some
disadvantages must be respected. The CVC
must be able to deliver at least the same (large)
currents as the main amplifier, and virtual ground
is not necessarily guaranteed for fast changing or
noisy signals.

Differential Amplifier
The potential drop across a resistor R_{DA} between
counter electrode and main amplifier output
can also be used for current monitoring.

The signal is buffered by a more complex differential amplifier [14] (preferentially an instrumentation amplifier, DA in Fig. 2). The cell current I is given by

$$I = -\frac{U_{DA}}{R_{DA}} \qquad (5)$$

The amplifiers maximum output current can be small as only recording devices must be supported. Disadvantageous is the limitation of the main amplifier output current by R_{DA}, especially if high values of R_{DA} are chosen to detect small currents.

It was useful in some cases to use both systems (CVC and DA) in parallel. The resistor R_{DA} was short-circuited in one direction to allow high currents, recorded by the current-to-voltage amplifier, and very small currents in the other direction, recorded by the differential amplifier. Moreover, the differential amplifier could be modified into an auto-ranging system to record current transients after large potential steps [15].

Alternative Concepts

The current-to-voltage amplifier is replaced in some concepts by other systems such as simple resistors between working electrode and ground potential [16, 17], negative resistances (gyrator circuits, [18, 19]), logarithmic current amplifiers, and current-photon-converters [20], often in context with IR-drop elimination (▶ iR-Drop Elimination).

Composition of Input Signals

An adder circuit is presented in Fig. 3. The output voltage U_{add} is the sum of all input signals according to

$$U_{\mathrm{add}} = -(U_1 + U_2 + U_3 + \ldots + U_n) \qquad (6)$$

if all resistors are equal. The output signal is connected to the non-inverting input of the main amplifier (MA) in Fig. 2. The advantage of this concept is the control of the composed signal at the adder output.

A modified popular concept is the adder potentiostat (Fig. 4) which combines summation
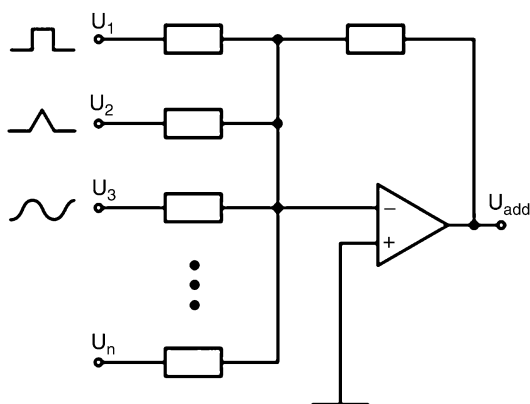
Potentiostat, Fig. 3 Adder circuit to compose an input signal from different sources U_1 to U_n
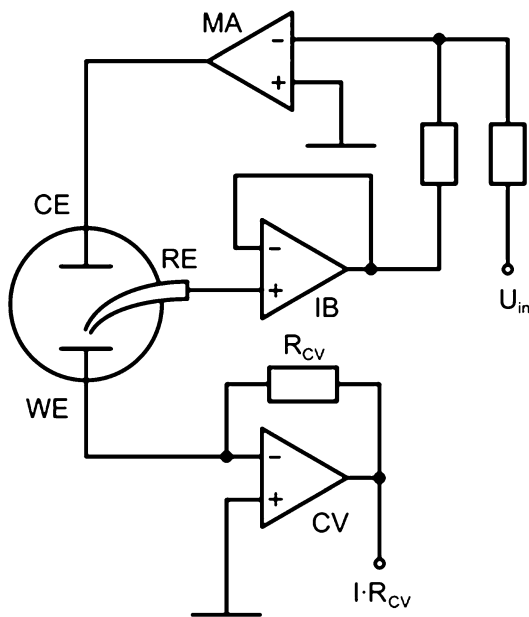
Potentiostat, Fig. 4 Adder potentiostat with main amplifier (*MA*), impedance buffer (*IB*), and current-to-voltage converter (*CV*)

and potential control in one amplifier. Due to resistor network, the circuit would draw currents from the reference electrode. To avoid this, an additional impedance buffer as in Fig. 4 must be added. The composed input signal cannot be monitored.

Digital Concepts

Modern potentiostats are equipped with computer interfaces (e.g., USB), at least to transfer experimental data such as potential and current. Optional is a complete control by the computer, e.g., current ranges (eventually auto-ranging), potential programs, and frequency response characteristics.

The main amplifier in Fig. 2 is substituted in completely digitized concepts by an analog-to-digital converter, a processor, and a digital-to-analog converter. The transfer function, especially the frequency-dependent amplification A, can be easily modified. Such concepts are more complex and not applicable for extremely fast applications.

Multi-electrode Concepts

Most electrochemical cells consist of three electrodes: working electrode, counter electrode, and reference electrode. In some applications, however, the working electrode is split into several separate electrodes, e.g., in rotating disc/ring systems (Rotating Disc Electrode). This requires an independent potential control of the working electrodes.

An early concept of a bipotentiostat was presented in [21] but suffered from interactions between the working electrodes. This was overcome by some modifications shown in [22]. More popular is a bipotentiostat based on the adder concept [12], which was presented for the first time in [23]. The circuit is very complex and cannot be extended to more than two working electrodes.

More flexible concepts are based on a counter electrode connected to ground (Fig. 5, [24, 25]). Some can be extended to more than two working electrodes, and every electrode can be equipped with an individual ▶ reference electrode to avoid interactions due to current flow in the electrolyte and to minimize IR drops (▶ iR-Drop Elimination).

Galvanostats

The introduction of operational amplifiers, starting after 1950, made galvanostatic setups
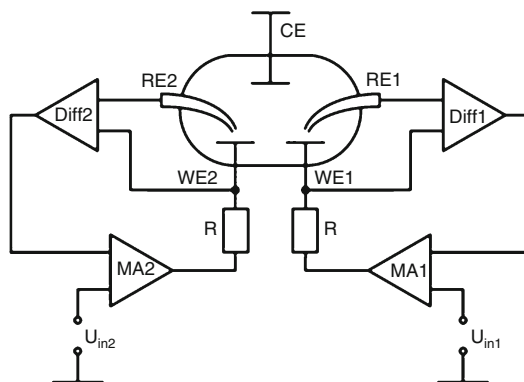
Potentiostat, Fig. 5 Concept of multipotentiostat with counter electrode (*CE*) connected to ground, 2 working electrodes (*WE*), 2 reference electrodes (*RE*), 2 main amplifiers (*MA*), and 2 differential amplifiers (Diff)

much less complex but potentiostats as well. Potentiostats seemed to be more versatile, and thus, galvanostatic mode was simply added as an option in many cases. Every potentiostat, however, can be changed into a galvanostat by simple modifications, see entry ▶ Galvanostat.

Future Directions

The quality of commercial potentiostat systems is nowadays almost perfect. The electrical performance, computer, and software support allow effective and convenient investigations of main-stream problems with minor efforts. But this is a risk, as *"...most students and many professional scientists adopt the "black box" approach to electrochemical instrumentation, and fail to appreciate the operation and limitations of various circuits employed."* [10].

Future challenges result from less common components, e.g., electrodes (microelectrodes, porous electrodes, scanning probes, reference electrodes with extremely high source resistances), cell geometry (thin film cells, capillary cells, industrial reactors), and special requirements such as noise reduction, high frequencies, high voltages, and extremely small or large currents.

Cross-References

References

1. Tafel J (1905) Polarisation during cathodic hydrogen development. Z Phys Chem 50:641–712
2. Lingane JJ, Kolthoff IM (1939) Fundamental studies with the dropping mercury electrode. I. The Ilkovic equation of polarographic diffusion currents. J Am Chem Soc 61:825–834. doi:10.1021/ja01873a016
3. Caldwell CW, Parker RC, Diehl H (1944) Apparatus for automatic control of electrodeposition with graded electrode potential. Ind Eng Chem 16:532–535
4. Lingane JJ (1945) Automatic apparatus for electrolysis at controlled potential. Ind Eng Chem 17:332–333
5. Hickling A (1942) Studies in electrode polarisation Part IV- The automatic control of the potential of a working electrode. Trans Faraday Soc 38:27–33
6. von Fraunhofer JA, Banks CH (1972) Potentiostat and its applications. Butterworths, London
7. Schroeden RR (1972) Operational amplifier instruments for electrochemistry. In: Mattson JS, Mark HB, MacDonald HC (eds) Computers in chemistry and instrumentation, vol 2. Marcel Dekker, New York
8. Gabe DR (1972) Bibliography of potentiostat design. Br Corros J 7:236–238
9. Harrar JE (1975) Techniques, apparatus, and analytical applications of controlled-potential coulometry. In: Bard AJ (ed) Electroanalytical chemistry, vol 8. Marcel Dekker, New York
10. Macdonald DD (1977) Transient techniques in electrochemistry. Plenum, New York
11. Greef R (1978) Instruments for use in electrode process research. J Phys E 11:1–15. doi:10.1088/0022-3735/11/1/001
12. Bard AJ, Faulkner LR (1980) Electrochemical methods: fundamentals and applications. Wiley, New York
13. McKubre MCH, MacDonald DD (1984) Electronic instrumentation for electrochemical studies. In: White RE, O'M Bockris J, Yeager E (eds) Comprehensive treatise of electrochemistry, vol 8, Experimental Methods in Electrochemistry. Plenum, New York
14. Mumby JE, Perone SP (1971) Potentiostat and cell design for the study of rapid electrochemical systems. Chem Instrum 3:191–227
15. Lohrengel MM, Schultze JW, Speckmann HD, Strehblow HH (1987) Growth, corrosion and capacity of copper oxide films investigated by pulse techniques. Electrochim Acta 32:733–742
16. Booman GL, Holbrook WB (1965) Electroanalytical controlled-potential instrumentation. Anal Chem 37:1793–1809
17. Brown ER, McCord TG, Smith DE, DeFord DD (1966) Some investigations on instrumental compensation of nonfaradaic effects in voltammetric techniques. Anal Chem 38:1119–1129. doi:10.1021/ac60241a004
18. Gabrielli C, Keddam M (1974) Progres recents dans la mesure des impedances electrochimiques en regime sinusoidal. Electrochim Acta 19:355–362
19. Lamy C, Herrmann CC (1975) A new method for ohmic-drop compensation in potentiostatic circuits: stability and bandpass analysis, including the effect of faradaic impedance. J Electroanal Chem 59:113–135
20. Faulkner LR (1987) In: Fleischmann MS, Pons S, Rolison DR, Schmidt PP (eds) Ultramicroelectrodes. Datatech Systems, Morganton
21. Anderson LB, Reilley CN (1965) Thin-layer electrochemistry: steady-state methods of studying rate processes. J Electroanal Chem 10:295–305
22. Gutwillinger P, Schade G (1979) Simplified bipotentiostat. Electrochim Acta 24:1135–1136
23. Napp DT, Johnson DC, Bruckenstein S (1967) Simultaneous and independent potentiostatic control of two indicator electrodes. Application to the copper (II)/copper(I)/copper system in 0.5M potassium chloride at the rotating ring-disk electrode. Anal Chem 39:481–485. doi:10.1021/ac60248a01
24. Kinza H, Lohse H (1975) Electrocatalytic reduction of the nitrate ion by a positive electrode potential. Z Phys Chem Leipzig 256:233–249
25. Burshtein RKH, Vilinskaya VS, Knots LL, Kushnev VV, Lentser BI, Tarasevich MR (1972) Apparatus for automatic control of ring-disk electrode potentials. Elektrokhimiya 8:1183–1187

Predominance-Zone Diagrams for Chemical Species

Ignacio Gonzalez and Alberto Rojas-Hernández
Department of Chemistry, Universidad Autónoma Metropolitana-Iztapalapa, México, Mexico

Determination of the Thermodynamic Equilibrium State of a Multicomponent and Multi-Reacting System

The study of processes involving several chemical species in solution (e.g., electrochemistry, geochemistry, biochemistry, hydrometallurgy, chemical analysis, and environmental chemistry)

generally requires a precise knowledge of the stability of the different species present in the system in each phase, as well as their coexistence.

The thermodynamic equilibrium of the components of the system provides a useful model to determine the stability of its species and phases. The law of mass action allows calculating the chemical composition of a given system at equilibrium [1].

For a large number of chemical species or equilibria, it is necessary to use iterative calculations in order to determine the thermodynamic equilibrium of the system, due to the set of nonlinear equations (e.g., mass or charge balance of each phase and the law of mass action of each of the independent equilibria).

Perrin [2] and Ingri et al. [3] proposed computational programs to calculate the chemical composition of a system with a limited number of components in thermodynamic equilibrium. Based on these, others have been proposed that apply different algorithms to solve the nonlinear set of equations involved in multicomponent and multi-reacting systems [2–8]. On the other hand, the algorithms based on Gibbs energy minimization of the system have been improved [9–12]. It has been demonstrated that the two types of algorithms are equivalent [13].

Graphic Representations of Systems in Thermodynamic Equilibrium

The study of multicomponent and multi-reacting systems involves many calculations, and it is common to give excessive importance to the mathematical problem, disregarding the chemical problem to be solved. For this reason, the application of several graphic representations and methods has been proposed; they help to consider a given set of thermodynamic equilibrium conditions with a better perspective.

The first type of graphic representation is that of distribution and logarithmic diagrams, representing species fractions (in linear or logarithmic form) as a function of composition variables of the system [14, 15]. The second class is that of the reaction prediction diagrams, and to

this class belong the Latimer [16, 17], Frost [18, 19], and Ellingham [20–22] diagrams. The third kind is that of the predominance-zone diagrams (PZD), and to this type belong Pourbaix [23] diagrams.

From this point to the end of the article, more information will be given for the PZD concerning algorithms, methods of construction, and applications.

Predominance-Zone Diagrams and their Construction Algorithms

PZD establish zones in a multidimensional space where generally one species has higher quantity or concentration with respect to others of a previously defined set (the condition of predominance). The mathematical problem is to find the boundaries from which this predominance is defined in that multidimensional space. The dimensions of the space are generally chemical composition variables, like pH, concentration or amount of species (in linear or logarithmic form), and electrode potential.

The Pourbaix diagrams (also known as potential-pH (Eh-pH) diagrams since this is the simplest representation proposed by Marcel Pourbaix) are the more famous PZD in electrochemistry. There are many papers in the scientific literature that describe their construction algorithms (Fig. 1).

The majority of these articles establish equations involving the Gibbs energy of the systems or the chemical potentials of species. Some of those papers have been compiled in recent works [24, 25] that furthermore describe construction for multicomponent and multi-reacting systems, where one of the axes of the diagram represents the potential of one electrode, while the others represent other chemical composition variables.

There are also few algorithms that use the law of mass action for independent equilibria instead of the chemical potentials of the species [26].

The Pourbaix diagrams are generally achieved as a final representation that is applied to describe or interpret several electrochemical problems;

Predominance-Zone Diagrams for Chemical Species, Fig. 1 Pourbaix diagram of americium species for $-\log[Am]_{Total} = 10.0$ [24]. *Dashed lines* represent the oxidation (*upper*) and reduction (*lower*) of water

Am (OECD-NEA update/FLASK-AQ)
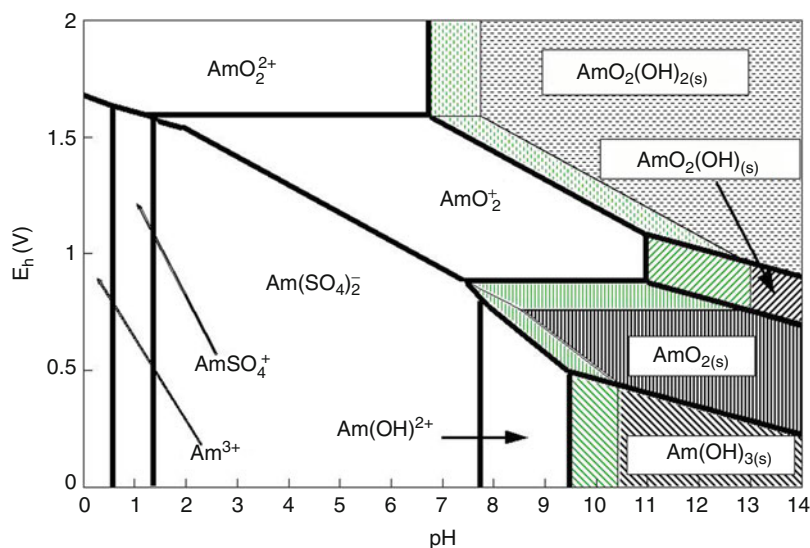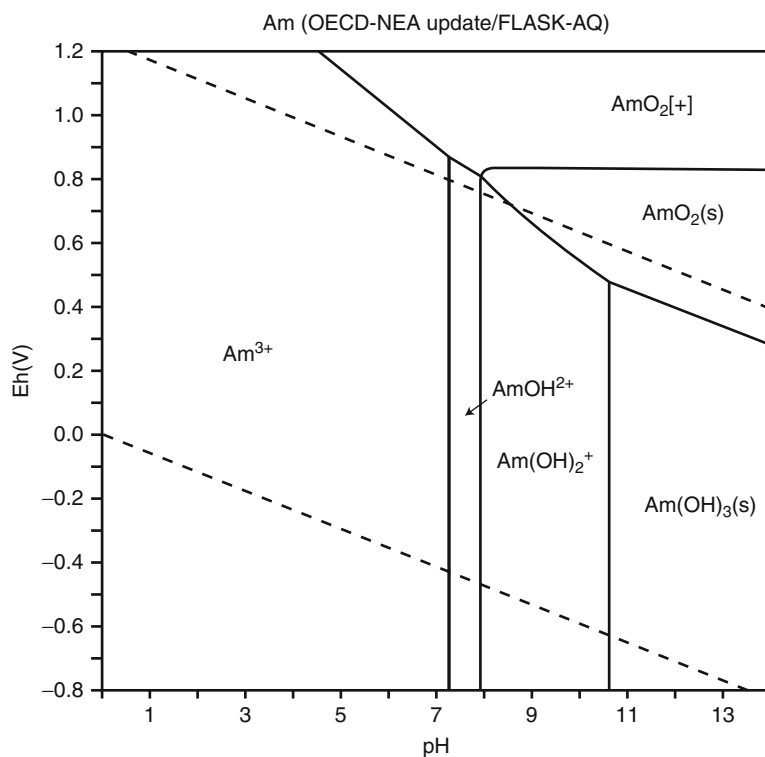
Predominance-Zone Diagrams for Chemical Species, Fig. 2 Pourbaix-type diagram of americium species at $-\log[SO_4{}'] = 0.523$ in the Eh/pH space, constructed with the MGSE. $SO_4{}' = HSO_4{}^- + SO_4{}^{2-}$. *Dashed black* zones represent the coexistence of condensed phases for a $-\log[Am]_{Total} = 8.0$, while *dashed black* and *green* zones represent the coexistence of condensed phases for a $-\log[Am]_{Total} = 6.0$ [29]. In this diagram, unlike that of Fig. 1, the formation of complexes of americium with sulfates in solution is considered

Predominance-Zone Diagrams for Chemical Species, Fig. 3 Different kinds of PZD for the Mg (II)-phosphates-ammonia-water system, constructed with the MGSE [29]. $PO_4'' = PO_4' = H_3PO_4 + H_2PO_4^- + HPO_4^{2-} + PO_4^{3-}$ and $NH_3' = NH_3 + NH_4^+$. (**a**) Predominance-zone diagram for Mg(II)-soluble species at $-\log[NH_3'] = -0.3$ and $-\log[PO_4''] = 1.0$ in the $-\log[Mg]_{Total}$/pH space. (**b**) Condensed phase diagram (CPD) for Mg(II)-insoluble species at $-\log[NH_3'] = -0.3$ in the $-\log[PO_4'']_{Total}$/pH space. (**c**) Predominance-existence diagram (PED) for all Mg (II) species at $-\log[NH_3'] = -0.3$ and $-\log[PO_4''] = 1.0$ in the $-\log[Mg]_{Total}$/pH space
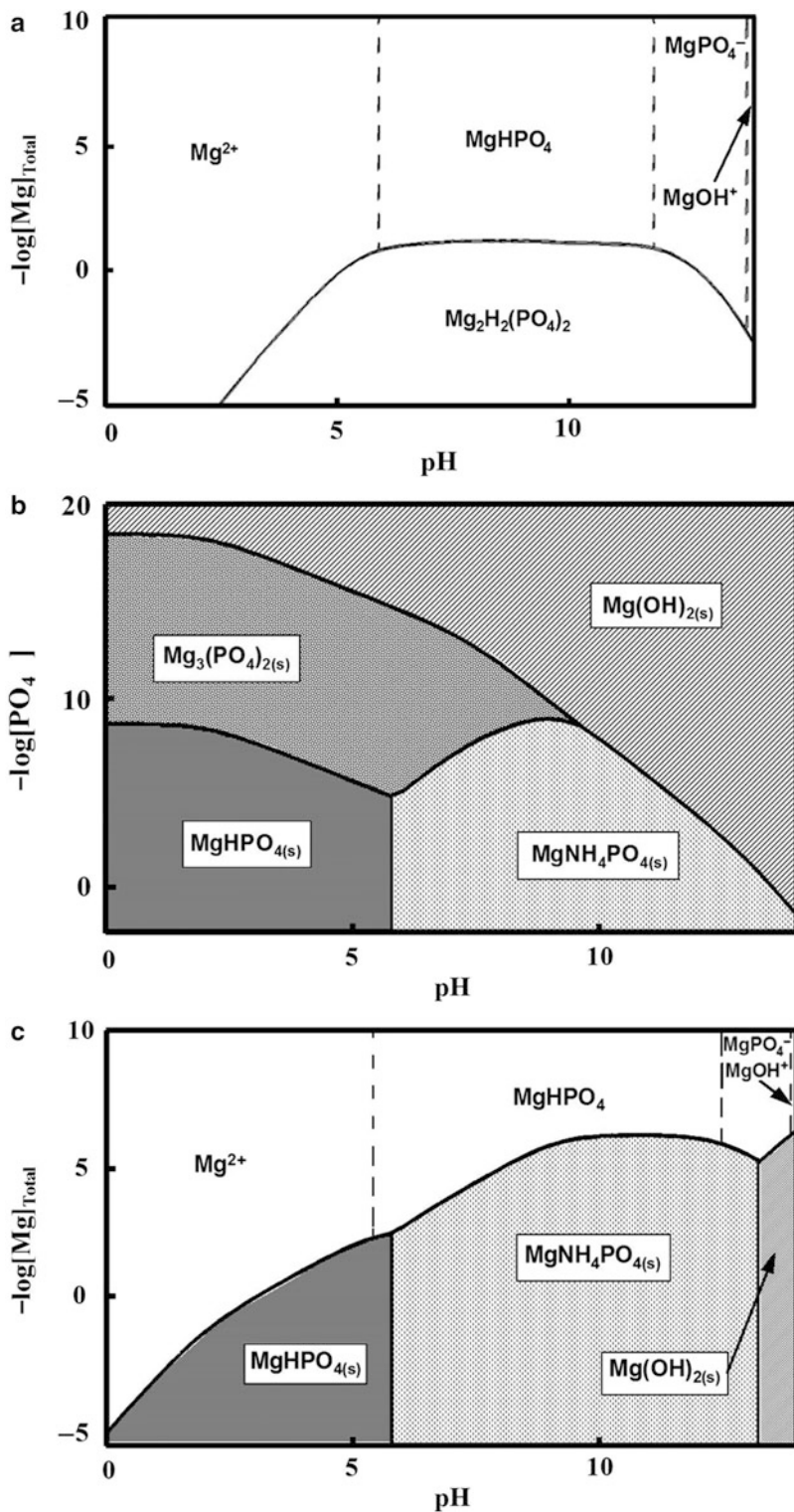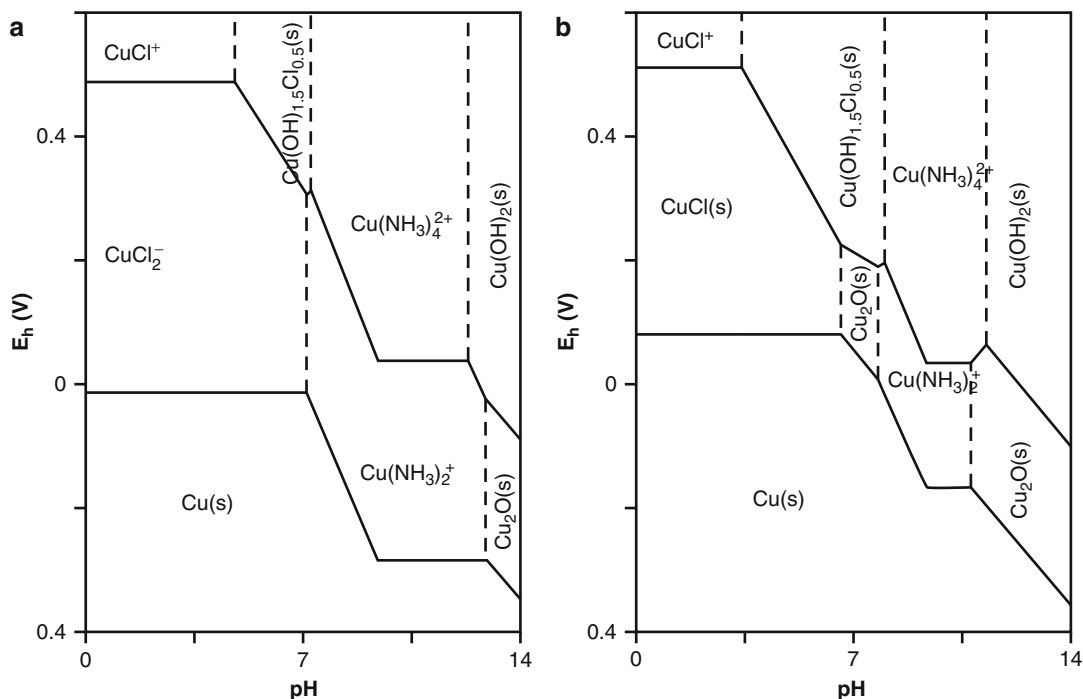
Predominance-Zone Diagrams for Chemical Species, Fig. 4 Pourbaix-type diagrams for copper species [49, 50] at $-\log[\text{NH}_3''] = -\log[\text{Cl}'] = 0$, constructed with the MGSE [26, 29]. $\text{NH}_3'' = \text{NH}_3' = \text{NH}_3 + \text{NH}_4^+$ and $\text{Cl}' = \text{Cl}^-$. (**a**) $-\log[\text{Cu}]_{\text{Total}} = 0.001$ M. (**b**) $-\log[\text{Cu}]_{\text{Total}} = 0.1$ M

nevertheless there are some papers that use them as an intermediate way of obtaining another graphic representation where there is no axis of electrode potential. One example of this is the paper of Osseo-Asare and Brown, used to describe some extraction processes for systems in hydrometallurgy [27].

It is true that there are many systems whose graphic representations do not require an electrode potential axis because the involved processes do not exchange electrons. It is thus unnecessary to use the Pourbaix diagram as an intermediate step because this type of diagram may be constructed directly, following construction algorithms completely analogous to those used to achieve the Pourbaix diagrams. Some examples of these algorithms can be found in the scientific literature [10, 28] (Fig. 2).

Remarkable inside the last kind of algorithms is the *method of generalized species and equilibria* (MGSE) [26, 29–36]. The MGSE extends the method of Gaston Charlot for the study of chemical equilibrium in solution [15, 37] through a definition of *conditional constant* (similar to a former concept proposed by Gerold Schwarzenbach [38] and developed further by Anders Ringbom [39, 40]). Its algorithms for PZD allows for the selection of the graphic representation spaces in terms of chemical composition variables of *generalized species* in order to relate the predominance boundaries in these spaces with *conditional constants of generalized equilibria*. The last feature gives the MGSE a great capability of prediction and interpretation of multicomponent and multi-reacting systems in thermodynamic equilibrium (Fig. 3).

Computational Methods for the Construction of Predominance-Zone Diagrams

There are many computational programs available nowadays to construct PZD. Some of these can be used online by Internet, covering the costs of services, like the Thermo-Calc [41] or

Predominance-Zone Diagrams for Chemical Species, Fig. 5 PZD for zinc-soluble species in the $-\log[NH_3']$/pH space, constructed with the MGSE [26, 29]. $NH_3' = NH_3 + NH_4^+$. (**a**) Without considering the ternary complexes $Zn(NH_3)_2(OH)_2$ and $Zn(NH_3)(OH)_3^-$ [52]. (**b**) Considering these ternary complexes [29], which model could better represent the reality?
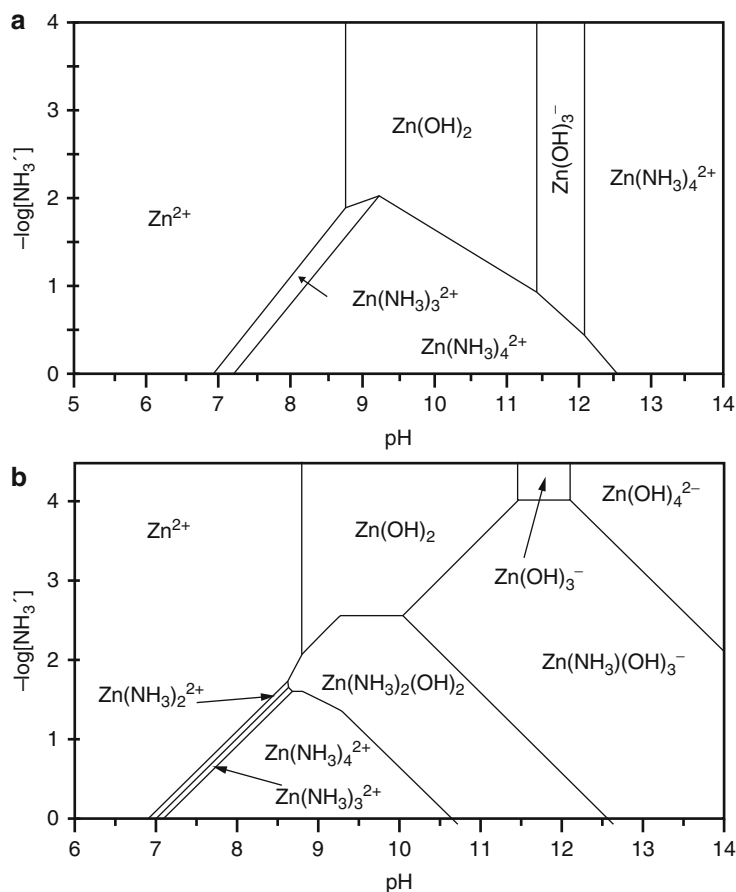
CSIRO Thermochemistry System [42]. Others, like STABCAL, have appeared in scientific literature references [43]. Nevertheless, possibly the more powerful computational set of programs available to construct PZD is the suite MEDUSA [44] that uses algorithms of the computational program SOLGASWATER [10].

Some Applications of Predominance-Zone Diagrams

One of the main applications of PZD is to evaluate the relative importance of species on systems in thermodynamic equilibrium for a set of given initial or imposed conditions. For this reason, some references that have applied PZD in different fields of electrochemistry are compiled in the final paragraphs of this essay.

Corrosion

Pourbaix diagrams have been proposed initially in order to explain corrosion phenomena, and for this reason the application of the PZD to study problems in this field may yet be found in electrochemical literature [45]. Nevertheless, other kinds of PZD have also been used to explain corrosion phenomena [46].

Electrocrystallization and Electrodeposition

There are many references that describe different applications of PZD to predict and interpret electrocrystallization and electrodeposition processes in multicomponent systems [47–65] (Fig. 4).

Pourbaix diagrams are used in many of these cases [47, 50, 63], but the application of other kinds of PZD is also common when the process requires it [47, 49, 52, 56, 60] (Fig. 5).

I= 0.010 M

$[CO_3^{2-}]_{TOT}$ = 3.90 mM $[Ca^{2+}]_{TOT}$ = 0.88 mM

$[UO_2^{2+}]_{TOT}$ = 53.40 μM $[Mg^{2+}]_{TOT}$ = 0.97 mM

Predominance-Zone Diagrams for Chemical Species, Fig. 6 Predominance-zone diagram of uranyl species for a soil water in the high plains of Mexico, constructed with MEDUSA software [44] in the $-\log$ $[PO_4^{3-}]_{Total}$/pH space. The formation equilibrium constants of all considered species (45 soluble and 26 insoluble, from 6 soluble components) were taken from the HYDRA database (included with MEDUSA), only slightly modified for UO_2CO_3 and $(UO_2)_2CO_3(OH)_3^-$ species and substituting $UO_2(H_2PO_4)_2$ for $UO_2(HPO_4)_2^{2-}$ in the input data file [70]. The selected concentration conditions for the different species take into account the experimental measurements as well as the temperature (T) and the ionic strength (I)

Environmental Chemistry and Electrochemistry

PZD have a great application potential to develop studies related to environmental chemistry and electrochemistry. In the first place, we want to illustrate this with some studies for the research and remediation of Cr(VI) [66–68]. Some other cases of environmental studies that apply PZD are metal recovery from wastes [69], mobility of ionic and neutral species in several systems [70], chemical and biochemical leaching processes [71], and characterization of species in natural systems [72] (Fig. 6).

Coagulation and Flocculation

Coagulation and flocculation processes are used to separate dissolved and suspended solids from waters, mainly to purify the waters [73, 74]. Coagulants with opposite electrical charges to those of the suspended solids are added to the water to neutralize the negative charges on dispersed non-settleable solids such as clay and color-producing organic substances. Aluminum and iron ions are commonly used as inorganic coagulants [74]. These ions are directly added from sacrificial electrodes for electrocoagulation and electroflocculation. The PZD should be used

$[SO_4^{2-}]_{TOT} = 1.70$ mM $[Cl^-]_{TOT} = 84.00$ mM $[SO_4^{2-}]_{TOT} = 0.00$ $[Cl^-]_{TOT} = 0.00$

Predominance-Zone Diagrams for Chemical Species, Fig. 7 Predominance-zone diagrams of aluminum species constructed with MEDUSA software [44], in the $-\log[Al^{3+}]_{Total}$/pH space. The formation equilibrium constants of all considered species (13 soluble and 5 insoluble, from 4 soluble components) were taken from the HYDRA database (included with MEDUSA). (**a**) PZD

obtained considering the mixed Al(III)-Sulfate-OH⁻ complexes and the insoluble amorphous hydroxide, Al $(OH)_{3(am)}$, at specific conditions of total sulfate and chloride concentrations. It may be that the coexistence zones of mixed insoluble complexes are overestimated due to the use of formation equilibrium constants of crystalline phases. (**b**) PZD obtained in the absence of sulfates and chlorides
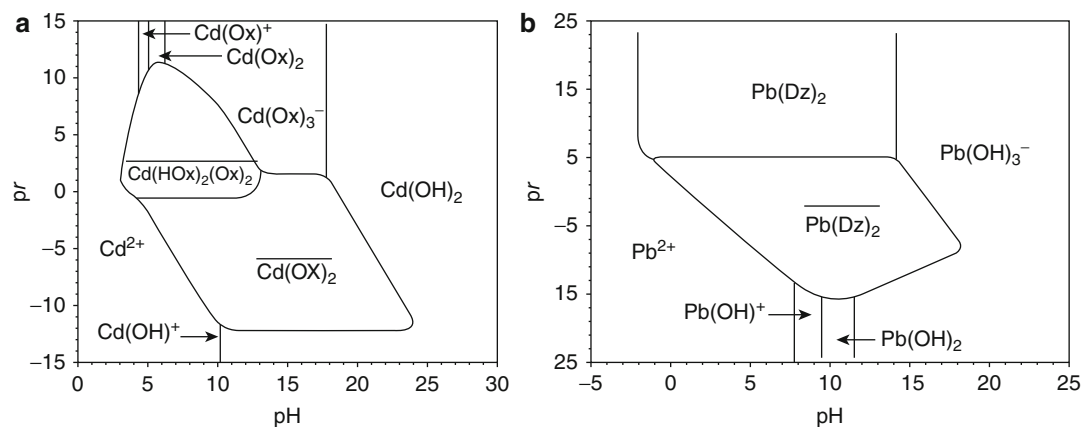
Predominance-Zone Diagrams for Chemical Species, Fig. 8 Predominance-zone diagrams in extraction (PZDE) [36], constructed with the MGSE [29], in the pr/ pH space. The nonaqueous phase is trichloromethane. pr $= -\log r$ where r represents the nonaqueous volume/aqueous volume ratio, the bar over the species takes into account the species dissolved in nonaqueous phase, HOx

represents oxine, and HDz represents dithizone. (**a**) PZD of Cd(II) species at a [oxine noncomplexed] $= 0.1$ M; this concentration considers the aqueous phase volume. (**b**) PZD of Pb(II) species at a [dithizone noncomplexed] $= 0.1$ M; this concentration considers the aqueous phase volume

to establish the optimal experimental conditions (i.e., concentration, pH) for the coagulation process. Soluble metallic hydroxyl complexes are required to separate suspended solids; meanwhile, insoluble metallic hydroxides are required for the separation of soluble chemical species (Fig. 7).

Future Directions

Pourbaix diagrams have been extensively used in corrosion studies, as well as for stability diagrams in geochemistry.

But the application of these and other PZD has practically not included other chemistry and electrochemistry fields (e.g., synthesis, separations, and characterizations), in spite of their great power to interpret results and predict operational conditions for several processes. Therefore, the application of PZD should be promoted as the powerful tools that they are.

Some fundamental developments should be undertaken to construct and interpret PZD in systems with a distribution of species between several phases (e.g., ionic exchange, adsorption, and spreading and growing of species on surfaces), as has been done for liquid-liquid extraction systems [36] (Fig. 8).

Finally, these kinds of representations should be developed to study chemical equilibria for chemical reactions taking place in soft matter (pastes, amorphous systems and polymers, among others).

Cross-References

▶ Activity Coefficients
▶ Anodic Reactions in Electrocatalysis - Oxidation of Carbon Monoxide
▶ Cell, Electrochemical
▶ Degradation of Organics, Use of Combined Electrochemical-Ultrasound
▶ Disinfection of Water, Electrochemical
▶ Electrolytes, Classification
▶ Electrolytes, Thermodynamics

▶ Environmentally Accepted Processes for Substitution and Reduction of Cr(VI)
▶ Metal Ion Removal by Cathodic Reduction
▶ Solvents and Solutions

References

1. Perrin DD, Sayce IG (1967) Computer calculation of equilibrium concentrations in mixtures of metal ions and complexing species. Talanta 14:833–842. doi:10.1016/0039-9140(67)80105-X
2. Perrin DD (1965) Multiple equilibria in assemblages of metal ions and complexing species: a model for biological systems. Nature 206:170–171. doi:10.1038/206170a0
3. Ingri N, Kakolowicz W, Sillén LG, Warnqvist B (1967) High-speed computers as a supplement to graphical methods – V: Haltafall, a general program for calculating the composition of equilibrium mixtures. Talanta 14:1261–1286. doi:10.1016/0039-9140(67)80203-0
4. Zeleznik FJ, Gordon S (1968) Calculation of complex equilibria. Ind Eng Chem 60:27–57. doi:10.1021/ie50702a006
5. Helgeson HC (1968) Evaluation of irreversible reactions in geochemical processes involving minerals and aqueous solutions – I. Thermodynamic relations. Geochim Cosmochim Acta 32:853–877. doi:10.1016/0016-7037(68)90100-2
6. Ting-Po I, Nancollas GH (1972) EQUIL. General computational method for the calculation of solution equilibriums. Anal Chem 44:1940–1950. doi:10.1021/ac60320a007
7. Dunsmore HS, Midgley D (1972) Computer calculatiodoi:10.1016/0039-9140(88)80166-8n of the composition of equilibrium mixtures in solution. Anal Chim Acta 72:121–126. doi:10.1016/S0003-2670(01)82955-X
8. Leung VW-H, Darvell VW, Chan AP-C (1988) A rapid algorithm for solution of the equations of multiple equilibrium systems – RAMESES. Talanta 35:713–718. doi:10.1016/0039-9140(88)80166-8
9. Karpov IK, Chudnenko KV, Kulik DA (1997) Modeling chemical mass transfer in geochemical processes: thermodynamic relations, conditions of equilibria, and numerical algorithms. Am J Sci 297:767–806. doi:10.2475/ajs.297.8.767
10. Eriksson G (1979) An algorithm for the computation of aqueous multi-component, multiphase equilibria. Anal Chim Acta 112:375–383. doi:10.1016/S0003-2670(01)85035-2
11. Gautam R, Seider WD (1979) Computation of phase and chemical equilibrium: Part I. Local and constrained minima in Gibbs free energy. AICHE J 25:991–999. doi:10.1002/aic.690250610

12. Smith WR (1980) The computation of chemical equilibria in complex systems. Ind Eng Chem Fundam 19:1–10. doi:10.1021/i160073a001
13. Smith WR, Missen RW (1982) Chemical reaction equilibrium analysis: theory and algorithms. Wiley, New York
14. Högfeldt E (1983) Graphic presentation of equilibrium data. In: Kolthoff IM, Elving PJ (eds) Treatise on analytical chemistry, Part I, Vol 2, Sect D, 2nd edn. Wiley, New York
15. Rojas-Hernández A, Ramírez MT, González I, Ibanez JG (1995) Predominance zone diagrams in solution chemistry: dismutation processes in two component systems (M-L). J Chem Educ 72:1099–1105. doi:10.1021/ed072p1099
16. Latimer WM (1952) The oxidation state of the elements and their potentials in aqueous solutions. Prentice-Hall, New York
17. Freiser H (1994) Enhanced Latimer potential diagrams via spreadsheets. J Chem Educ 71:786–788. doi:10.1021/ed071p786
18. Frost AA (1951) Oxidation potential-free energy diagrams. J Am Chem Soc 73:2680–2682. doi:10.1021/ja01150a074
19. Martínez-de-Ilarduya JM, Villafañe F (1994) A warning for Frost diagrams users. J Chem Educ 71:480–482. doi:10.1021/ed071p480
20. Ellingham HJT (1944) Reducibility of oxides and sulfides in metallurgical processes. J Soc Chem Ind 63:125–130
21. Gaskell DR (2001) Metal production: Ellingham diagrams. In: Buschow KHJ, Cahn R, Flemings MC, Ilschner B, Kramer EJ, Mahajan S, Veyssiere P (eds) Encyclopedia of materials: science and technology, vol 10. Elsevier, Oxford, pp 5481–5486. ISBN:0-08-0431526
22. Kishimoto H, Yamaji K, Brito ME, Horita T, Yokokawa H (2008) Generalized Ellingham diagrams for utilization in solid oxide fuel cells. J Min Metall Sect B 44B:39–48. doi:10.2298/JMMB0801039K
23. Pourbaix M (1966) Atlas of electrochemical equilibria in aqueous solutions (English edition). Pergamon, Oxford
24. Takeno N (2005) Atlas of Eh-pH diagrams: intercomparison of thermodynamic databases. Open File Report No.419. AIST Geological Survey of Japan, Tokyo. http://www.gsj.jp/GDB/openfile/files/no0419/openfile419e.pdf. Accessed 1 Jan 2012
25. Winston R (ed) (2000) Uhlig's corrosion handbook. 2nd edn. Chaps 6 and 7. Wiley, New York
26. Rojas-Hernández A, Ramírez MT, Ibáñez JG, González I (1991) Construction of multicomponent Pourbaix diagrams using generalized species. J Electrochem Soc 138:365–371. doi:10.1149/1.2085590
27. Osseo-Asare K, Brown TH (1979) A numerical method for computing hydrometallurgical activity-activity diagrams. Hydrometallurgy 4:217–232. doi:10.1016/0304-386X(79)90013-6
28. Garrels RM, Christ CL (1965) Solutions, minerals and equilibria. Freeman, San Francisco
29. Rojas-Hernández A (1996) The method of generalized species and equilibria for the study of chemical systems in equilibria with buffering conditions: theory and algorithms of predominance-zones diagrams (Spanish). PhD thesis. Universidad Autónoma Metropolitana, Unidad Iztapalapa, Mexico
30. Rojas A, González I (1986) Relationship of two-dimensional predominance-zone diagrams with conditional constants for complexation equilibria. Anal Chim Acta 187:279–285. doi:10.1016/S0003-2670(00)82919-0
31. Rojas-Hernández A, Ramírez MT, González I, Ibanez JG (1991) Relationship of multidimensional predominance-zone diagrams with multiconditional constants for complexation equilibria. Anal Chim Acta 246:435–442. doi:10.1016/S0003-2670(00)80983-6
32. Rojas-Hernández A, Ramírez MT, González I (1992) Multi-dimensional predominance-zone diagrams for polynuclear chemical species. Anal Chim Acta 259:95–104. doi:10.1016/0003-2670(92)85080-P
33. Rojas-Hernández A, Ramírez MT, González I (1993) Equilibria among condensed phases and a multi-component solution using the concept of generalized species. Part I. Systems with mixed complexes. Anal Chim Acta 278:321–333. doi:10.1016/0003-2670(93)85116-2
34. Rojas-Hernández A, Ramírez MT, González I (1993) Equilibria among condensed phases and a multi-component solution using the concept of generalized species. Part II. Systems with polynuclear species. Anal Chim Acta 278:335–347. doi:10.1016/0003-2670(93)85117-3
35. Rojas-Hernández A, Ramírez MT, González I (1996) Distribution of mononuclear chemical species in two-phase multicomponent systems using generalized species and equilibria. Quim Anal 15(Suppl.1):S4–S8. http://www.seqa.es/site/index.php?option=com_content&task=view&id=113&Itemid=112. Accessed 1 Jan 2012
36. Páez-Hernández ME, Ramírez MT, Rojas-Hernández A (2000) Predominance-zone diagrams and their application to solvent extraction techniques. Talanta 51:107–121. doi:10.1016/S0039-9140(99)00276-3
37. Charlot G (1969) Traité de chimie analytique générale, vol 1. Masson, Paris
38. Schwarzenbach G (1957) Complexometric titrations. Methuen, London
39. Ringbom A (1958) The analyst and the inconstant constants. J Chem Educ 35:282–288. doi:10.1021/ed035p282
40. Ringbom A (1963) Complexation in analytical chemistry. Wiley-Interscience, New York
41. http://www.calphad.com/thermo_calc.html. Accessed 1 Jan 2012
42. Zhang L, Sun S, Jahanshahi S, Chen C, Bourke B, Wright S, Somerville M (2002) CSIRO's multiphase

P

reaction models and their industrial applications. JOM 54:51–56. doi:10.1007/BF02709751

43. Wang HH, Young CA (1996) Mass-balanced calculations of Eh-pH diagrams using STABCAL. In: Woods R, Richardson P, Doyle FM (eds) Electrochemistry in minerals and metal processing IV, vol 96-6. The Electrochemical Society, Pennington

44. Puigdomenech I (2011) Making Equilibrium diagrams using sophisticated algorithms (MEDUSA). KTH Royal Institute of Technology. Department of Chemistry. http://www.kemi.kth.se/medusa/ Accessed 1 Jan 2012

45. Mouanga M, Ricq L, Douglade J, Berçot P (2007) Effects of some additives on the corrosion behaviour and preferred orientations of zinc obtained by continuous current deposition. J Appl Electrochem 37:283–289. doi:10.1007/s10800-006-9255-3

46. Arzola S, Palomar-Pardave ME, Genesca J (2003) Effect of resistivity on the corrosion mechanism of mild steel in sodium sulfate solutions. J Appl Electrochem 33:1233–1237. doi:10.1023/B:JACH.0000003855.95788.12

47. Becerril-Vilchis A, Meas Y, Rojas-Hernández A (1994) Electrodeposition of americium and physicochemical behavior of the solution. Radiochim Acta 64:99–105

48. Soto AB, Arce EM, Palomar-Pardavé M, González I (1996) Electrochemical nucleation of cobalt onto glassy carbon electrode from ammonium chloride solutions. Electrochim Acta 41:2647–2655. doi:10.1016/0013-4686(96)00088-6

49. Nila C, González I (1996) Thermodynamics of Cu-H2SO4-Cl–H2O and Cu-NH4Cl-H2O based on predominance-existence diagrams and Pourbaix-type diagrams. Hydrometallurgy 42:63–82. doi:10.1016/0304-386X(95)00073-P

50. Nila C, González I (1996) The role of pH and Cu(II) concentration in the electrodeposition of Cu(II) in NH4Cl solutions. J Electroanal Chem 401:171–182. doi:10.1016/0022-0728(95)04278-4

51. Trejo G, Ortega R, Meas Y, Ozil P, Chainet E, Nguyen B (1998) Nucleation and growth of zinc from chloride concentrated solutions. J Electrochem Soc 145:4090–4097. doi:10.1149/1.1838919

52. Rodríguez-Torres I, Valentin G, Lapicque F (1999) Electrodeposition of zinc-nickel alloys from ammonia-containing baths. J Appl Electrochem 29:1035–1044. doi:10.1023/A:1003610617785

53. Ibrahim MAM (2000) Copper electrodeposition from non-polluting aqueous ammonia baths. Plat Surf Finish 87:67–72

54. Rodríguez-Torres I, Valentin G, Chanel S, Lapicque F (2000) Recovery of zinc and nickel from electrogalvanisation sludges using glycine solutions. Electrochim Acta 46:279–287. doi:10.1016/S0013-4686(00)00583-1

55. Trejo G, Ruiz H, Borges RO, Meas Y (2001) Influence of polyethoxylated additives on zinc electrodeposition from acidic solutions. J Appl Electrochem 31:685–692. doi:10.1023/A:1017580025961

56. Mendoza-Huizar LH, Robles J, Palomar-Pardavé M (2002) Nucleation and growth of cobalt onto different substrates Part I. Underpotential deposition onto a gold electrode. J Electroanal Chem 521:95–106. doi:10.1016/S0022-0728(02)00659-9

57. Díaz-Arista P, Antaño-López R, Meas Y, Ortega R, Chainet E, Ozil P, Trejo G (2005) EQCM study of the electrodeposition of manganese in the presence of ammonium thiocyanate in chloride-based acidic solutions. Electrochim Acta 51:4393–4404. doi:10.1016/j.electacta.2005.12.019

58. Ortiz-Aparicio JL, Meas Y, Trejo G, Ortega R, Chapman TW, Chainet E, Ozil P (2007) Electrodeposition of zinc-cobalt alloy from a complexing alkaline glycinate bath. Electrochim Acta 52:4742–4751. doi:10.1016/j.electacta.2007.01.010

59. Ballesteros JC, Diaz-Arista P, Meas Y, Ortega R, Trejo G (2007) Zinc electrodeposition in the presence of polyethylene glycol 20000. Electrochim Acta 52:3686–3696. doi:10.1016/j.electacta.2006.10.042

60. Alonso Alejandro R, Lapidus Gretchen T, González I (2007) A strategy to determine the potential interval for selective silver electrodeposition from ammoniacal thiosulfate solutions. Hydrometallurgy 85:144–153. doi:10.1016/j.hydromet.2006.08.009

61. Ortiz-Aparicio JL, Meas Y, Trejo G, Ortega R, Chapman TW, Chainet E, Ozil P (2008) Effect of quaternary ammonium compounds on the electrodeposition of ZnCo alloys from alkaline gluconate baths. J Electrochem Soc 155:D167–D175. doi:10.1149/1.2823000

62. Poisot-Diaz ME, González I, Lapidus GT (2008) Electrodeposition of a silver-gold alloy (DORE) from thiourea solutions in the presence of other metallic ion impurities. Hydrometallurgy 93:23–29. doi:10.1016/j.hydromet.2008.02.015

63. Alonso Alejandro R, Lapidus GT, González I (2008) Selective silver electroseparation from ammoniacal thiosulfate leaching solutions using a rotating cylinder electrode reactor (RCE). Hydrometallurgy 92:115–123. doi:10.1016/j.hydromet.2008.02.001

64. Rios-Reyes CH, Granados-Neri M, Mendoza-Huizar LH (2009) Kinetic study of the cobalt electrodeposition onto glassy carbon electrode from ammonium sulfate solutions. Quim Nova 32:2382–2386. doi:10.1590/S0100-40422009000900028

65. Lin ZB, Xie BG, Chen JS, Sun JJ, Chen GN (2009) Nucleation mechanism of silver during electrodeposition on a glassy carbon electrode from a cyanide-free bath with 2-hydroxypyridine as a complexing agent. J Electroanal Chem 633:207–211. doi:10.1016/j.jelechem.2009.05.015

66. Barrera-Díaz C, Palomar-Pardavé M, Romero-Romo M, Martínez S (2001) A comparison between chemical and electrochemical methods for the reduction of hexavalent chromium in aqueous solution. Proceedings of the electrochemical society 2001. 23(Energy and electrochemical processes for a cleaner environment):486–495

67. Barrera-Díaz C, Palomar-Pardavé M, Romero-Romo M, Martínez S (2003) Chemical and electrochemical considerations on the removal process of hexavalent chromium from aqueous media. J Appl Electrochem 33:61–71. doi:10.1023/A:1022983919644

68. Lugo-Lugo V, Barrera-Díaz C, Bilyeu B, Balderas-Hernández P, Ureña-Nuñez F, Sánchez-Mendieta V (2010) Cr(VI) reduction in wastewater using a bimetallic galvanic reactor. J Hazard Mater 176:418–425. doi:10.1016/j.jhazmat.2009.11.046

69. Rodríguez-Torres I, Valentin G, Lapicque F (1999) Recovery of zinc and nickel species from electrogalvanization sludges. Hung J Ind Chem 1-(Conference Proceedings, Novel Chemical Reaction Engineering for Cleaner Technologies):62–67. Accessed 1 Jan 2012

70. Guzmán ETR, Regil EO, Gutiérrez LRR, Alberich MVE, Hernández AR, Regil EO (2006) Contamination of corn growing areas due to intensive fertilization in the high plane of Mexico. Water Air Soil Poll 175:77–98. doi:10.1007/s11270-006-9114-1

71. Núñez-López RA, Meas Y, Gama SC, Borges RO, Olguín EJ (2008) Leaching of lead by ammonium salts and EDTA from *Salvinia minima* biomass produced during aquatic phytoremediation. J Hazard Mater 154:623–632. doi:10.1016/j.jhazmat.2007.10.101

72. Bautista-Flores AN, Rodríguez de San Miguel E, de Gyves J, Jönsson JÅ (2010) Optimization, evaluation, and characterization of a hollow fiber supported liquid membrane for sampling and speciation of lead(II) from aqueous solutions. J Membrane Sci 363:180–187. doi:10.1016/j.memsci.2010.07.028

73. Bratby J (2006) Coagulation and flocculation in water and wastewater treatment. IWA Publishing, London. Accessed 1 Jan 2012

74. http://iwawaterwiki.org/xwiki/bin/view/Articles/CoagulationandFlocculationinWaterand Wastewater Treatment. Accessed 1 Jan 2012

Primary Batteries for Medical Applications

Prabhakar A. Tamirisa, Kaimin Chen and Gaurav Jain
MECC, Medtronic Inc., Minneapolis, MN, USA

Introduction

Primary or non-rechargeable batteries are used to power several major types of implanted medical devices such as pacemakers, implanted cardioverter defibrillators (ICDs), cardiac and hemodynamic monitors, cardiac resynchronization therapy (CRT) devices, neurostimulators (electrical stimulation in regions such as spinal cord, deep brain, sacral nerve, vagal nerve, cochlea, gastric nerve, phrenic nerve), and drug pumps. Examples of non-implanted medical devices that can be powered by primary batteries include hearing aids, external defibrillators, infusion pumps, transcutaneous electrical nerve stimulators (TENs), and monitors such as Holter monitors, pulse oximeters, heart rate monitors, blood pressure monitors, and blood glucose sensors. Batteries for implanted medical applications are subject to regulations of national agencies such as FDA in the United States.

Energy and power density (ratio of energy and power deliverable by a battery to its volume) of batteries determine their suitability for most electrical devices. Other important criteria for use in medical devices are safety and reliability in operation during lifetime of the device (up to 10 years or longer), predictability of battery performance characteristics, and provision of device replacement indicators based on battery depletion and mechanical design features such as shape and size to allow efficient packaging in the device and for patient comfort.

High energy density is an important feature for primary batteries since this minimizes battery size and maximizes service life. Consequently, lithium metal anode-based batteries, which possess high energy density due to the high electrochemical capacity (3,860 mAh/g) and oxidation potential (3.04 V vs. SHE) of lithium, constitute the vast majority of primary batteries used in medical applications, especially implanted medical devices. Non-implanted medical devices use commercially available batteries, including non-lithium-based primary batteries. A prominent example is the use of Zn/air batteries in hearing aids. Primary batteries used in implanted medical devices are often classified in terms of their power capabilities as low (10–100 μW), medium (100 μW–10 mW), and high-rate batteries (up to 10 W). Power capability of a battery is a function of the electrochemical characteristics of electrode

Primary Batteries for Medical Applications, Fig. 1 Ragone plots of medium (MR) and high-rate (HR) hybrid chemistries compared to SVO and I_2-based battery systems; ERI = elective replacement indicator, DSVO = decomposition SVO, CSVO = combination SVO (Reprinted from Ref. [8], Copyright (2006), with permission from Elsevier)
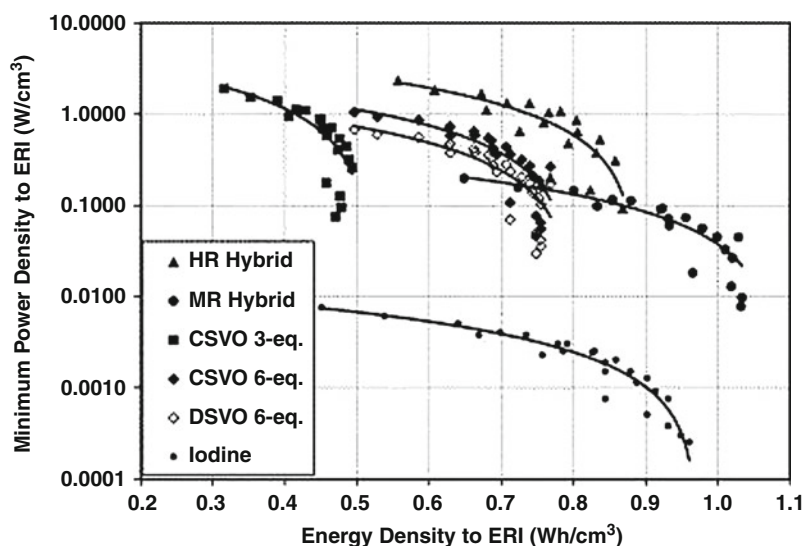
and electrolyte materials as well as mechanical design such as electrode and separator design. In the past decades, several battery chemistries and mechanical designs have been developed to meet the often stringent criteria for medical devices. This article will highlight the characteristics of these chemistries and mechanical designs.

Evolution of Primary Battery Chemistries in Implanted Medical Applications

The earliest primary battery used in implanted medical devices based on Zn/HgO [1] suffered from disadvantages such as hydrogen evolution during operation, sudden approach to depletion, and poor longevity due to high self-discharge. Alternative energy systems such as the rechargeable nickel-cadmium batteries and nuclear batteries were able to overcome the longevity issue but posed other challenges. In the case of rechargeable batteries, patients were faced with the burden of recharging the batteries, while nuclear batteries came with a regulatory burden to track the radioisotopes used in the batteries, especially after explant of the devices. Most of these challenges were overcome with the introduction of the lithium metal-based batteries in the early 1970s. The first lithium anode battery

(Li/I_2)-based pacemaker was implanted in 1972 [2–5]; the battery did not evolve gases during its operation, thus allowing hermetic encapsulation inside a device. As peak power demands increased in the 1980s and 1990s, due to the introduction of new medical devices such as neurostimulators, implanted drug pumps, and ICDs, new chemistries such as $Li/SOCl_2$, Li/MnO_2, and Li/SVO were developed to meet the demand [3, 6, 7]. With the introduction of devices with greater microprocessor power, memory, and communication systems, complex therapy algorithms and long-distance telemetry were introduced in medical devices. In order to maintain peak power characteristics of the Li/SVO system, but improve energy density to minimize device volume, hybrid chemistries based on CF_x-SVO cathode systems have been introduced recently [8]. Figure 1 showcases the improvements that are achieved with the hybrid chemistry in comparison to batteries with a non-hybrid cathode chemistry such as Li/SVO or Li/I_2.

Lithium Primary Battery Characteristics

Chemical Characteristics
Lithium batteries can be classified on the basis of the chemical identity of electrochemical couples and separators. Li/I_2 battery is based on a cathode

consisting of a charge-transfer complex of poly (vinyl pyridine) and iodine; the electrolyte and separator, LiI is formed in-situ upon contact between lithium metal and the cathode mixture, $Li/SOCl_2$ battery is based on a liquid cathode (containing a lithium salt for ionic conduction) coupled with a porous carbon support to deposit the solid discharge reaction products. Other commonly used battery chemistries consist of solid cathodes in combination with lithium anode and liquid electrolyte; anode and cathode are separated using a porous insulator. Lithium batteries for implanted medical devices have a well-defined operating temperature: the body temperature at 37 °C.

I. Li/I_2

Li/I$_2$ battery, first introduced as a power source for pacemakers in 1972, is a solid electrolyte battery with I_2 as the cathode [2]. To enhance cathode conductivity, I_2 is mixed with poly(vinyl pyridine) (PVP) to create an electronically conductive charge transfer complex. A thin layer of PVP is also applied on the lithium anode to improve cell resistance. One unique characteristic of Li/I_2 is that the discharge product, LiI, serves as a separator as well as the electrolyte. When I_2 is in contact with lithium during the construction of the battery, a layer of LiI is formed and serves as the separator. Being an ionic conductor, LiI also serves as the electrolyte. However, as discharge progresses, more LiI is formed and eventually leads to a large cell resistance increase and rapid decrease in cell operating voltage. Li/I_2 has an excellent volumetric energy density at 1 Wh/cc and has been a reliable power source for low-power applications such as implantable pacemakers for the past 40 years.

II. $Li/SOCl_2$

$Li/SOCl_2$ uses liquid $SOCl_2$ as the cathode; $LiAlCl_4$ which is used as the electrolyte salt is dissolved in the cathode. A porous carbon electrode serves as the cathode current collector. As discharge proceeds, nonconductive LiCl and S deposit inside the porous carbon electrode resulting in a significant increase in cell resistance and rapid voltage drop near the end of service. $Li/SOCl_2$ batteries have been used to power various implantable neurological devices such as deep brain stimulators (DBS) for reducing symptoms associated with Parkinson's disease, sacral nerve stimulators for bladder control issues, spinal cord stimulators for chronic back and leg pain, and gastric stimulators for relieving chronic nausea and vomiting symptoms associated with gastroparesis and for treating obesity.

III. Li/MnO_2

Li/MnO_2 uses heat-treated MnO_2 as the cathode and $LiClO_4$ in a mixed solvent system of propylene carbonate (PC) and dimethoxyethane (DME) as the electrolyte. The applicable capacity of MnO_2 corresponds to 1 electron equivalent per MnO_2. Li/MnO_2 was developed as a power source in cardio-myostimulators and has also been developed for use in pacemakers and ICDs [4].

IV. Li/SVO

Li/SVO was developed for powering implantable cardioverter defibrillators (ICDs) in 1980s [3, 7]. The majority of today's ICDs are powered by Li/SVO. The cathode in Li/SVO is a silver vanadium oxide with a stoichiometry of $Ag_2V_4O_{11}$ and the electrolyte is typically 1.0 M $LiAsF_6$ in PC/DME. The applicable capacity of SVO corresponds to six equivalent electrons per $Ag_2V_4O_{11}$. Two methods have been used to synthesize SVO: decomposition method ($2AgNO_3$ + $2V_2O_5 = Ag_2V_4O_{11}$ + 2 NO_2 + ½ O_2) and combination method (Ag_2O + $2V_2O_5 = Ag_2V_4O_{11}$) [9, 10]. The combination reaction produces a crystalline and phase pure SVO, which provides stable power capability in the second portion of the discharge curve over time [11]. Li/SVO has also been adopted to power implantable neurological devices such as deep brain, sacral nerve, and spinal cord stimulators.

Primary Batteries for Medical Applications, Table 1 Summary of primary lithium battery characteristics and their applications in implanted medical devices

Battery chemistry	Overall cell reaction	Operating voltage range	Common electrolyte	Common implantable applications
Li/I_2	$Li + I_2 = LiI$	2.8–2.2 V	LiI (the product)	Pacemakers
$Li/SOCl_2$	$4Li + 2SOCl_2 = 4LiCl + S + SO_2$	3.6–3.0 V	$SOCl_2/LiAlCl_4$	Neurostimulators
Li/MnO_2	$Li + MnO_2 = LiMnO_2$	3.0–2.2 V	$LiClO_4/PC/DME$	Pacemakers, ICDs
Li/SVO	$6 Li + Ag_2V_4O_{11} = 2Ag + Li_6V_4O_{11}$	3.2–2.2 V	$LiAsF_6/PC/DME$	ICDs, neurostimulators
Li/CF_x	$Li + CF = C + LiF$	3.0–2.2 V	$LiBF_4/GBL$ $LiBF_4/GBL/DME$	Pacemakers, drug pump, and neurostimulators
Li/CF_x-SVO	$Li + CF = C + LiF$ $6 Li + Ag_2V_4O_{11} = 2Ag + Li_6V_4O_{11}$	3.2–2.2 V	$LiBF_4/GBL/DME$ $LiAsF_6/PC/DME$	Pacemakers, drug pump, ICDs, and neurostimulators

V. Li/CF_x

Li/CF_x uses CF_x (typically, $x \sim 1.0$) as the cathode and $LiBF_4$ in GBL-based solvents as the electrolyte. CF_x is obtained through fluorination of carbon at elevated temperatures with F_2 gas diluted with N_2. The morphology of CF_x often takes the shape of its carbon precursor. The deliverable capacity of CF_x is affected by the degree of fluorination [12]. The discharge products of CF_x are carbon and LiF. Since Li/CF_x batteries have a rapid decrease in voltage near the end of service, a second cathode component with a slightly lower operating voltage may be added to CF_x to provide a voltage-based end of service indicator [13]. Li/CF_x batteries have found uses in pacemakers, drug pumps, and neurostimulators such as cochlear implants.

VI. Li/CF_x-SVO

Li/CF_x-SVO uses both CF_x and SVO ($Ag_2V_4O_{11}$) as the cathode [8]. The cathode can be prepared as a mixture of CF_x and SVO or as discrete CF_x and SVO layers bonded to the current collector [13, 14]. The ratio of CF_x to SVO can be tailored to suit specific applications. Electrolytes used in Li/CF_x-SVO are typically $LiBF_4$ in GBL-based electrolytes or $LiAsF_6$ in PC/DME-based electrolyte. The choice of electrolyte depends on the power requirement of the applications. Li/CF_x-SVO combines the energy density advantage of CF_x and the power capability of SVO to produce a unique cathode that is suitable for implanted applications with a wide range of power requirements. Li/CF_x-SVO has been developed to power pacemakers, ICDs, implantable drug pump, neurostimulator for treating chronic back and leg pain, and deep brain stimulator (DBS) for reducing symptoms associated with Parkinson's disease (Table 1).
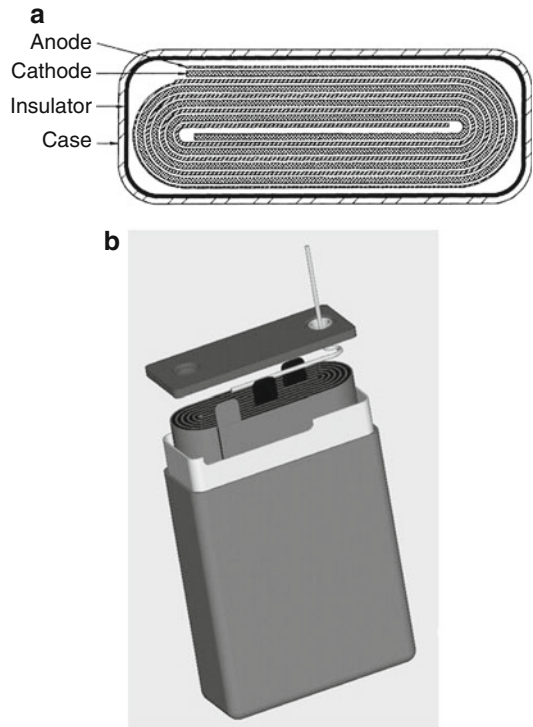
Mechanical Design

External shape and size constraints for batteries are typically dictated by the shape and the allocated internal volume of the medical device. Design of the internal components of batteries is guided by energy, power, and safety requirements. Energy and power densities of batteries are inversely correlated. Increased electrode area minimizes battery resistance and hence maximizes power density but at the expense of energy density since large electrode area is achieved through a larger fraction of inert materials in the battery such as current collectors, separators, spacers, and other insulators. Batteries for high-power applications such as ICDs use stacked or coiled designs wherein thin layers (100–300 μm) of electrode materials are applied to current collectors and either stacked or coiled to achieve
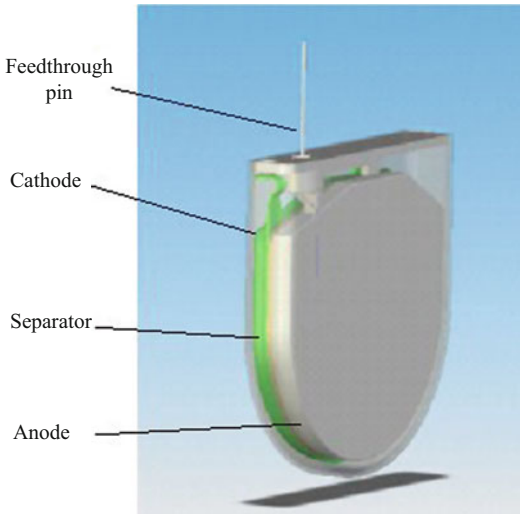
Primary Batteries for Medical Applications, Fig. 2 D-shaped monolithic battery with anode, separator, and cathode. Feedthrough pin connected to anode; case connected to cathode
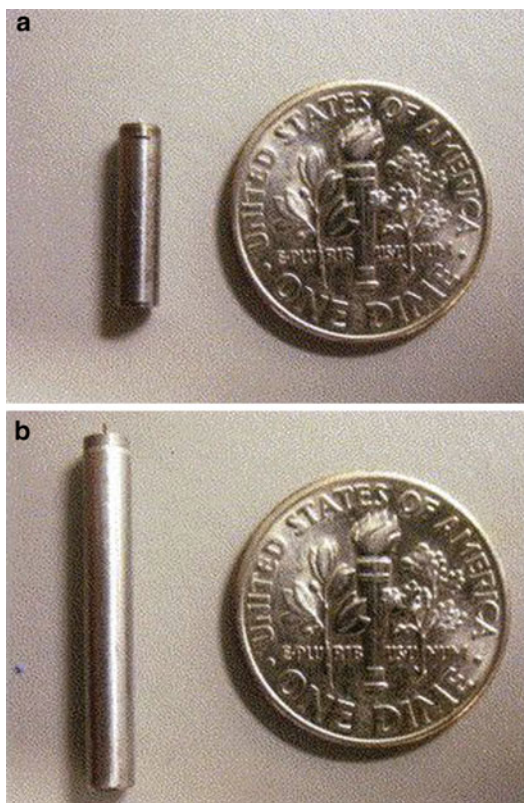

Primary Batteries for Medical Applications, Fig. 3 (**a**) Cross section view of a coiled electrode configuration used in high-rate designs; (**b**) assembly view of a coiled electrode configuration in insulator and battery case, showing attachment in the headspace (Reprinted from Ref. [7], Copyright (2001), with permission from Elsevier)

high electrode area (40–100 cm^2) and low resistance. Conversely, energy density is maximized by increasing the fraction of active materials relative to the inerts, by lowering electrode area (2–15 cm^2) and increasing electrode thickness (up to 8 mm). Low/medium rate batteries use thicker plate like electrodes and smaller areas seen in monolithic or single-plate designs. In general coiled electrodes are enclosed in prismatic cases (Fig. 2), while monolithic electrodes are used most commonly in D-shaped cases (see Fig. 3). Stacked electrodes are attractive from the standpoint of being able to provide additional shape flexibility that is generally unavailable to coiled electrodes. Cylindrical and coin shaped batteries are typically not common in implanted medical devices since they do not pack efficiently in the devices. However, cylindrical miniature batteries have been developed recently for use in injectable medical devices (see Fig. 4) [15].

Unlike batteries used in commercial and non-implanted medical devices, implanted medical device batteries are hermetically sealed in welded metal cases with glass-to-metal feedthroughs based on lithium-resistant glasses such as TA-23 and CABAL-12 to make connections to electrodes. To guarantee reliable containment of the electrodes and electrolyte and functionality of the feedthrough pins, materials for metal cases, covers, and feedthrough pins are selected by screening for materials degradation through pathways such as corrosion and chemical attack. Battery enclosures are designed to be compatible with volume changes due to expansion of electrodes and gas generation during service; typically gas generation is minimized or eliminated by design. Furthermore, medical device batteries are designed to possess high safety margins, often with redundant safety features such as multiple layers of separators that can shutdown in the event of an internal short circuit.

Primary Batteries for Medical Applications, Fig. 4 Photographs of cylindrical, pin-shaped batteries: (**a**) lithium-ion rechargeable battery, QL0003I, and (**b**) the lithium/CFx primary battery, QC0025B (Reprinted from Ref. [15], Copyright (2006), with permission from Elsevier)

Modeling for Design and Performance

Model-based predictions of battery performance and longevity are required to provide depletion indicators for batteries such as RRT (recommended replacement time), typically based on discharge voltage or resistance, to allow patients to schedule a replacement surgery before batteries reach EOS (end of service). Electrical characteristics of primary batteries used in medical applications have been modeled in a variety of ways including empirically or thermodynamics-based voltage curve models [16, 17], equivalent circuit models [18, 19], resistance models [11, 20], and more recently physics-based comprehensive models [17, 21–23] that can be used to predict pulse performance [24],

resistance characteristics, and, furthermore, medical device performance characteristics such as capacitor charge time in ICDs [25]. Statistical models developed by considering the distributions of the battery model parameters and device use conditions can be used to develop longevity predictions, which can be validated using real-time clinical/field performance data from the devices.

Design generation occurs early in the development cycle of batteries when energy/power requirements and shape/dimensional constraints are known and can also be based on models. Sizing of electrodes and consequently of the battery is guided by a balance of materials approach [6, 26], various design rules formulated for safety/reliability considerations (e.g., minimum values of separator thickness), and the intricacies of the chemistry such as incidence of parasitic reactions [26, 27] and expectations of energy/power density based on empirical performance data gathered from early prototypes.

Future Directions

Primary battery chemistries and mechanical designs for medical applications evolved to meet increasing power demands while attempting to maintain or exceed the high energy density achieved in the Li/I_2 battery. This trend is likely to continue due to interest in developing medical devices with long-range telemetry capabilities and newer therapy modalities that require higher currents. Simultaneously, the search for new cathode chemistries capable of higher energy density may be expected to continue. Platform technologies such as the CF_x-SVO hybrid cathodes [8], which achieve good performance over a much broader region of the energy-power density space in comparison to non-hybrid technologies, may become more common in the future resulting in reduced development cycle times and increased performance reliability. Depending on the use conditions of the devices, other types of hybrid technologies such as combinations of primary and rechargeable batteries may be developed. In the case of implanted medical devices,

materials selection for battery components may be guided by the need to make the devices MRI (magnetic resonance imaging) safe [28, 29].

Development of ultralow power electronics and advanced packaging technologies such as wafer-level packaging has begun to enable creation of leadless miniature devices that can be implanted near the site of therapy via minimally invasive procedures such as injection through a needle or a catheter [30, 31]. Miniature batteries with high energy densities and yet adequate power capabilities are required for such applications in order to achieve parity with the traditional implanted devices, especially in longevity and features that require high peak currents such as telemetry. Miniature batteries are being developed in new shapes, such as pin style or bobbin style [15], to enable integration with miniature, leadless devices. Thin-film solid-state batteries are attractive from the standpoint of integrating a minimally packaged battery into the device at the wafer or board level [32]. However, current designs of thin-film batteries which are produced using thin electrode and electrolyte layers (<5 μm) to minimize internal resistances are not sufficiently energy dense for many typical medical devices [33], which has prompted interest in three-dimensional battery electrode architectures to enhance energy and power density in solid-state and miniature batteries [34–37]. Since miniaturization results in increased inert material relative to the electrochemically active materials, energy and power density values are smaller in comparison to traditional medical device batteries. Therefore, innovations in packaging, mechanical design of electrodes, and development of new chemistries (electrodes and electrolyte materials) are required to achieve miniature batteries that exceed the current standard of 1 Wh/cc.

Use of predictive modeling can be expected to play an increasing role in the design and development phases of batteries for medical applications. Development of accelerated testing protocols and use of accelerated degradation models may become more prevalent to ensure highest levels of reliability in design and operation of batteries.

Cross-References

References

1. Ruben S (1947) Alkaline dry cell. US Patent 2422045
2. Holmes CF (2007) The lithium/iodine-polyvinylpyridine battery – 35 years of successful clinical use. ECS Trans 6(5):1–7. doi:10.1149/1.2790382
3. Holmes CF (2003) Electrochemical power sources and the treatment of human illness. Interface, vol 12. The Electrochemical Society, Pennington, NJ, USA
4. Root MJ (2008) Implantable cardiac rhythm device batteries. J Cardiovasc Transl Res 1(4):254–257. doi:10.1007/s12265-008-9054-9
5. Mallela VS, Ilankumaran V, Rao NS (2004) Trends in cardiac pacemaker batteries. Indian Pack Electrophysiol J 4(4):201–212
6. Skarstad PM (2004) Battery and capacitor technology for uniform charge time in implantable cardioverter-defibrillators. J Power Sources 136(2):263–267. doi:10.1016/j.jpowsour.2004.03.010
7. Crespi AM, Somdahl SK, Schmidt CL, Skarstad PM (2001) Evolution of power sources for implantable cardioverter defibrillators. J Power Sources 96:33–38
8. Chen K, Merritt DR, Howard WG, Schmidt CL, Skarstad PM (2006) Hybrid cathode lithium batteries for implantable medical applications. J Power Sources 162(2):837–840. doi:10.1016/j.jpowsour.2005.07.018
9. Liang CC, Bolster ME, Murphy RM (1982) Metal oxide composite cathode material for high energy density batteries. US Patent 4310609
10. Crespi AM (1993) Silver vanadium oxide cathode material and method of preparation. US Patent 5221453
11. Crespi A, Schmidt C, Norton J, Chen K, Skarstad P (2001) Modeling and characterization of the resistance of lithium/SVO batteries for implantable cardioverter defibrillators. J Electrochem Soc 148(1):A30–A37
12. Nakajima T, Groult H (2005) Fluorinated materials for energy conversion. Elsevier Science, p 592
13. Weiss DJ, Cretzmeyer JW, Crespi AM, Howard WG, Skarstad PM (1993) Electrochemical cells with end-of-service indicator. US Patent 5180642
14. Gan H, Takeuchi ES (2005) SVO/CFx parallel cell design within the same casing. US Patent 6926991
15. Nagata M, Saraswat A, Nakahara H, Yumoto H, Skinlo DM, Takeya K, Tsukamoto H (2005) Miniature pin-type lithium batteries for medical

applications. J Power Sources 146(1–2):762–765. doi:10.1016/j.jpowsour.2005.03.156

16. Root MJ (2010) Lithium–manganese dioxide cells for implantable defibrillator devices—discharge voltage models. J Power Sources 195(15):5089–5093. doi:10.1016/j.jpowsour.2009.12.083

17. Strange DA, Rayman S, Shaffer JS, White RE (2011) Physics-based lithium ion silver vanadium oxide cathode model. J Power Sources 196(22):9708–9718. doi:10.1016/j.jpowsour.2011.07.057

18. Schmidt CL, Skarstad PM (1997) Development of an equivalent-circuit model for the lithium/iodine battery. J Power Sources 65:121–128

19. Skarstad PM, Schmidt CL (1993) Modeling the discharge behavior of the lithium/iodine battery. J Power Sources 43–44:111–118

20. Root MJ (2011) Resistance model for lithium-silver vanadium oxide cells. J Electrochem Soc 158(12): A1347. doi:10.1149/2.049112jes

21. Davis S, Takeuchi ES, Tiedemann W, Newman J (2007) Simulation of the Li–CF[sub x] system. J Electrochem Soc 154(5):A477. doi:10.1149/1.2714323

22. Gomadam PM, Merritt DR, Scott ER, Schmidt CL, Skarstad PM, Weidner JW (2007) Modeling lithium/hybrid-cathode batteries. J Power Sources 174(2):872–876. doi:10.1016/j.jpowsour.2007.06.164

23. Gomadam PM, Merritt DR, Scott ER, Schmidt CL, Skarstad PM, Weidner JW (2007) Modeling Li/CF[sub x]-SVO hybrid-cathode batteries. J Electrochem Soc 154(11):A1058–A1064. doi:10.1149/1.2779963

24. Davis S, Takeuchi ES, Tiedemann W, Newman J (2008) Simulation of pulse discharge of the Li-CFx system. J Electrochem Soc 155(1):A24–A28. doi:10.1149/1.2800168

25. Gomadam PM, Brown JR, Scott ER, Schmidt CL (2007) Predicting charge-times of implantable cardioverter defibrillators. ECS Trans 6(5):15–23

26. Crespi AM, Skarstad PM (1993) Parasitic reactions and the balance of materials in lithium batteries for implantable medical devices. J Power Sources 43–44:119–125

27. Untereker DF (1978) The use of a microcalorimeter for analysis of load-dependent processes occurring in a primary battery. J Electrochem Soc 125(12):1907–1912

28. Levine GN, Gomes AS, Arai AE, Bluemke DA, Flamm SD, Kanal E, Manning WJ, Martin ET, Smith JM, Wilke N, Shellock FS (2007) Safety of magnetic resonance imaging in patients with cardiovascular devices. Circulation 116(24):2878–2891. doi:10.1161/CIRCULATIONAHA.107.187256

29. Faris OP, Shein M (2006) Food and drug administration perspective: magnetic resonance imaging of pacemaker and implantable cardioverter-defibrillator patients. Circulation 114(12):1232–1233. doi:10.1161/CIRCULATIONAHA.106.647800

30. McLaughlin BL, Smith B, Lachapelle J, Traviglia D, Sriram TS, O'Dowd D (2011) Ultra-high density packaging technology for injectable medical devices. In: 2011 annual international conference of the IEEE engineering in medicine and biology society, EMBC, Boston. IEEE, pp 2897–2900. doi:10.1109/IEMBS.2011.6090798

31. Miniaturization: Smaller, more efficient pacemakers, Medtronic Inc. http://www.medtronic.com/innovation/smarter-miniaturization.html. Accessed Sep. 17, 2013

32. Chen G, Fojtik M, Kim D, Fick D, Park J, Seok M, Chen M-T, Foo Z, Sylvester D, Blaauw D (2010) Millimeter-scale nearly perpetual sensor system with stacked battery and solar cells. Paper presented at the 2010 IEEE international solid-state circuits conference digest of technical papers (ISSCC)

33. Patil A, Patil V, Wook Shin D, Choi J-W, Paik D-S, Yoon S-J (2008) Issue and challenges facing rechargeable thin film lithium batteries. Mater Res Bull 43(8–9):1913–1942. doi:10.1016/j.materresbull.2007.08.031

34. Nathan M, Golodnitsky D, Yufit V, Strauss E, Ripenbein T, Shechtman I, Menkin S, Peled E (2005) Three-dimensional thin-fim Li-ion microbatteries for autonomous MEMS. J Microelectromechan S 14(5):879–885

35. Long JW, Dunn B, Rolison DR, White HS (2004) Three-dimensional battery architectures. Chem Rev 104:4463–4492. doi:10.1021/cr020740l

36. Zhang H, Yu X, Braun PV (2011) Three-dimensional bicontinuous ultra-fast and-discharge bulk battery electrodes. Nat Nanotechnol 6:277–281. doi:10.1038/nnano.2011.38

37. Baggetto L, Oudenhoven JFM, van Dongen T, Klootwijk JH, Mulder M, Niessen RAH, de Croon MHJM, Notten PHL (2009) On the electrochemistry of an anode stack for all-solid-state 3D-integrated batteries. J Power Sources 189(1):402–410. doi:10.1016/j.jpowsour.2008.07.076

Primary Batteries for Military Applications

George Blomgren
Blomgren Consulting Services, Lakewood, OH, USA

Introduction

There are many battery types that are in use for military applications. One of the most common is

Primary Batteries for Military Applications, Table 1 Lithium sulfur dioxide batteries in military applications

Designation	Nominal voltage (V)	Energy (Wh)	Weight (g)	Applications
BA-5093/U	23.4	77.3	635	Respirators
BA-5557A/U	16/13	54	410	Digital message devices
BA-5588A/U	13	35	290	Radios, respirators
BA-5590A/U	26/13	185	1,021	SINCGARS radios, chemical detectors, satellite radios, jammers, loudspeakers, range finders, countermeasures
BA-5598A/U	13	87	650	PRC-77 radios, direction finders, sensors
BA-5599A/U	7.8	50	450	Test sets, sensors

the standard batteries of commerce often found in consumer applications. This is an example of "dual use" which requires designers of military devices to accommodate batteries already in commerce to save costs. Since there are no unique features to the batteries used in this way, they will not be further discussed. Three other types of batteries are also used in military applications. Active batteries are designed for special military applications, but do not have special activation requirements. The second type is reserve batteries that require a physical or chemical step for activation. This type assures the military of very long shelf life since the activation usually involves introducing the electrolyte to the dry cell. Thus, the electrodes are maintained in a dry state prior to activation, and corrosion of the active materials does not occur in the shelf period. The third type of battery for military applications is thermally activated batteries. Again, a long shelf life is guaranteed since the electrolyte is present as a solid until thermal activation. The high temperature required to melt the electrolyte also allows very high currents since the kinetics and mass transport are greatly reduced at high temperature. These three types of applications and the battery types used will be discussed in turn.

Active Batteries

The most prominent among active batteries for military applications are lithium sulfur dioxide batteries, lithium manganese dioxide batteries, and lithium thionyl chloride batteries.

Lithium sulfur dioxide batteries have taken over from magnesium batteries as the main power source for communications batteries. Most of the applications involve multicell battery packs where the individual cells are larger than typical consumer cells, often of the F or DD size and have about 3 Ah capacity and are designed in a spirally wound configuration. Often a dual voltage is required for the application for different functions, which is accomplished by different wiring for the cells with concomitant switching. A list of typical battery sizes and designations is given in Table 1.

Lithium manganese dioxide batteries have become very prominent in recent years for military applications which are now widespread. Like sulfur dioxide batteries these are usually found in multicell packs often with dual voltage and cell sizes. The voltage of the system is similar to sulfur dioxide, so no major device changes are required. Typical batteries with their applications are given in Table 2 [1].

As is clear from Tables 1 and 2, the BA-5590 and BA-5390 batteries are the most widely used and deployed. All of the designations are from the US Department of Defense.

Lithium thionyl chloride batteries are not as numerous in production, but the applications are very widespread. This is mainly because of the very high specific energy and energy density of this battery type. Many different designs and form factors are used in the cells. The most

Primary Batteries for Military Applications, Table 2   Military applications for lithium manganese dioxide batteries

Designation	Nominal voltage (V)	Energy (Wh)	Weight (g)	Applications
BA-5312/U	10.8	41	275	PRC-112G survival radios
BA-5347/U	5	40	290	Thermal weapon sights, test sets
BA-5360/U	8.1	65	320	Digital communication devices
BA-5367/U	2.7	3.25	20	Night vision devices
BA-5368/U	10.8	12	140	Memory hold function, decoding devices
BA-5372/U	5.4	2.3	20	Memory hold function, encoding devices
BA-5380/U	5.4	45	230	Ground navigation sets, chemical agent monitors, respirators
BA-5390/U	27/13.5	250	1,350	SINCGARS radios, chemical agent detectors, satellite radios, jammers, loudspeakers, range finders, countermeasures

common type is the bobbin type in which the outer electrode is a thin sheet of lithium pressed against the stainless steel can. The next layer is a separator against the lithium foil. Next is the bobbin of highly porous carbon bonded into a bobbin by polytetrafluoroethylene fibers and pressed into a metal collector which is either a cylinder (for larger cells) or a pin for smaller cells. This arrangement gives very high energy to the system (among the highest energy density and specific energy for any system), although the current capability is only moderate. For high current cells, the electrodes are spirally wound in a similar fashion to the Li/SO_2 or Li/MnO_2 cells. The energy of this type is not as high as for the bobbin construction. A third geometry is the disc type which resembles a coin-type consumer battery in construction. Finally, a fourth type of construction is the large box cell, which holds many stacked electrodes and can have capacities as high as 16,500 Ah. This latter type is no longer in use, but was the main power supply for intercontinental ballistic missile silos for many years in the USA.

Reserve Batteries

This type of battery is noted for very long shelf life, often greater than 20 years. In the construction, the electrolyte is physically separated from the active materials of the electrodes until the cell is ready for use and is stored in a reservoir prior to activation [2]. The battery type is generally separated by the mode of activation. One type is activated by a force used to break a glass ampoule containing the electrolyte solution or forcibly breaking a diaphragm. This force may be handled manually or electrically. Single cells are generally activated by opening the ampoule, while multiple cells are usually activated by breaking a diaphragm and forcing the electrolyte into the cells, often with a bellows arrangement. This type of reserve cell is usually has a lithium anode with either a solid cathode or liquid cathode. The second type of reserve cell is generally spin activated. The spin is provided by the rotation of a projectile. The centripetal force on the spinning cell is used to open the electrolyte container as well as rapidly force the electrolyte into the interstices of the cells to complete the circuit. The chemistry of the cells may involve zinc alkaline battery chemistry, lithium battery chemistry, or in older versions lead fluoroborate cell chemistry. The latter involves a chemistry similar to rechargeable lead acid batteries, but utilizes a different electrolyte, fluoboric acid, rather than sulfuric acid. This along with the electrode design allows very high current capability to the cells. Typical applications for reserve batteries are fuzing of various kinds of munitions and projectiles as well as missile applications and even self-destruct mechanisms. The proximity fuze of World War II was made possible by the development of the lead fluoboric acid cell.

Thermal Reserve Batteries

This novel battery type utilizes solid inorganic salt electrolytes in a design which are present in the preactivated state as a simple pellet between electrodes [3]. There are also interspersed between electrodes a heat pellet which can be activated in a multielectrode design by a heat tape or bridge wire. Sometimes the activation is provided by a mechanical striking device or by an inertial device similar to the spin-activated reserve cells above. Thus when activation is called for, the ignitor is activated which in turn ignites the heat pellet which then melts the salt electrolyte which flows into the electrodes to complete the circuit. Again, they have multiple chemistries and may be single-cell- or multiple-cell construction. The salt pellet is usually a eutectic mixture of alkali metal salts, usually chlorides. The anodes may have lithium (as an alloy) or calcium metal. The lithium cells are most common and usually used FeS_2 cathodes, while calcium cells usually use calcium chromate cathodes. Typical applications are in missiles, bombs (munitions of all types), emergency escape systems, etc. They have very long shelf life (up to 25 years) and very fast activation. The activated stand time after activation may be very short, however, as little as 5 min or as long as an hour or so.

Cross-References

▶ Primary Batteries, Comparative Performance Characteristics
▶ Primary Batteries, Selection and Application

References

1. Reddy T (2011) Lithium primary batteries. In: Reddy T, Linden D (eds) Linden's handbook of batteries, 4th edn. McGraw Hill, New York
2. Chua D, Meyer B, Epply W, Swank J, Ding M (2011) Reserve military batteries. In: Reddy T, Linden D (eds) Linden's handbook of batteries, 4th edn. McGraw Hill, New York
3. Lamb C (2011) Thermal batteries. In: Reddy T, Linden D (eds) Linden's handbook of batteries, 4th edn. McGraw Hill, New York

Primary Batteries, Comparative Performance Characteristics

George Blomgren
Blomgren Consulting Services, Lakewood, OH, USA

Background

An electrochemical cell is a device which converts chemical energy into electrical energy. It has several requirements, namely, each chemically active material is confined to a single electrode; each electrode must have a means of conducting the electrical current generated to an external circuit, with one electrode acting as the positive pole and the other as the negative pole; the electrodes must be separated from each other by an electronically insulating but ionically conductive phase; and the entire assembly of electrodes, current leads, and insulating phase should be contained in a body which provides isolation from deleterious atmospheric effects (in general, air is harmful to metallic electrodes, and evaporation of liquid conductive phases will inactivate the cell). Such electrochemical cells are commonly called batteries, although strictly speaking, only an assemblage of cells should be called a battery or battery pack.

The electrochemical cells of interest here are primary batteries. They differ from rechargeable batteries in that they may only be used for one discharge and cannot be recharged (of course they may be partially discharged in a pulse mode may times until they are exhausted). They are of particular interest for applications that are infrequent or involve very small currents if they are continuous or frequent. They also must have adequate shelf life to fit the application, have reasonable energy content and sufficient power capability for the application, have a cost which is acceptable to the consumer, and have high reliability.

Primary batteries have a long history. The dominant cell type in use until World War II was the carbon-zinc cell also called the

Leclanche cell, with a zinc anode and a manganese dioxide cathode and a mildly acidic electrolyte. The chemistry dates back to the nineteenth century, but it was not fully developed for portable power until the dawn of the twentieth century. The war brought the alkaline battery onto the scene with a zinc anode, mercuric oxide cathode, and a concentrated alkaline electrolyte (KOH). In the 1950s the manganese oxide cathode was developed for the alkaline battery, and this system, also called the alkaline cell, began to take over from carbon-zinc cells in popularity among consumers because of its greater rate capability as well as its low leakage characteristics. The next major development in primary batteries was with lithium anode cells beginning in the 1970s. Li/CF_x cells, Li/MnO_2 cells, and Li/FeS_2 cells made their appearance at this time followed by liquid cathode cells starting with Li/SO_2 cells, then by $Li/SOCl_2$ and Li/SO_2Cl_2 cells. The development of lithium cells required the use of nonaqueous electrolytes. This development of lithium cells relied on methods of low moisture exposure and led to the use of dry rooms for development and manufacturing facilities. They also required a high level of cleanliness because of the sensitivity of the chemistry to small amounts of impurities. The major gain in energy density and specific energy were the main drivers for these advances. This gain was enabled by the very negative potential of the lithium anode giving rise to high-voltage cells and the concomitant increase in energy. Another feature of lithium cells was the need for tight sealing of the container to prevent the ingress of oxygen and moisture, but that was balanced by the low rate of gassing of the lithium anode in the presence of the specially chosen organic and inorganic solvents, in contrast to zinc anode cells in aqueous media. These details are discussed in depth in the articles describing the individual cells. Mention should be made that the use of liquid inorganic cathode electrolytes is only possible because of the thin, passivating layer of insoluble product which protects the lithium from aggressive reaction with the solvents. This type of protective layer is also developed on the lithium surface due to reaction with the organic solvents, such as propylene carbonate and dimethoxyethane, which are commonly used with the solid cathode materials.

Definitions

Convenient ways to compare primary batteries are the specific energy of the finished cell in watt hours per kilogram (Wh/kg), the energy density in watt hours per liter (Wh/l), and the voltage of the cell under open circuit or during a low current drain. The voltage is an intensive property and therefore is independent of the size of the battery as are the Wh/kg and Wh/l. In many batteries, the voltage is defined as sloping; that is, it declines steadily as the battery is discharged. In cases like this, the nominal voltage is usually selected as the starting voltage under low current drain or at open circuit. Because the voltage may also be affected by the corrosion/passivation properties of the anode, it may be most useful to measure the voltage under a low current drain. In selecting a battery type for an application, it is important to consider that if it is especially weight sensitive, the Wh/kg is most important and if it is especially volume sensitive, the Wh/l is most important. If the electronics within the device can be damaged by too high a voltage, then this property is most important. Of course, the rate capability (or current capability) is also quite important to the particular application. This is a more subtle property since the voltage behavior of a battery with increasing current is often highly nonlinear. Furthermore, the behavior of the voltage with time at a given current is often highly nonlinear. Therefore, a much more detailed consideration is usually appropriate in determining the suitability of a battery for a higher current application (at low currents, most batteries have a linear voltage current relationship defined by the internal resistance of the cell). Nevertheless, a property called the specific power (W/kg) and power density (W/l) is generally tabulated for primary batteries. Unfortunately, these properties are not well defined as noted above, so they are not of great use except as a very general guide to power capability. It would be better if the industry would standardize on

some definite definitions for these properties so that comparisons would be consistent, but they would not in any case be useful for a broad range of applications. A common designation of present-day aqueous batteries is "dry cell batteries." This term derives from much earlier technology in which many batteries were constructed with an excess quantity of electrolyte and the entire cell was contained in a box type of container. This type of battery was called a "wet cell battery." Because of the loss of energy density due to excess electrolyte, wet cells are no longer in common use as primary batteries.

Many battery sizes and dimensions have been standardized by electrical multinational organizations. The main organizations in this field are ANSI (American Standards Institute), IEC (International Electrotechnical Commission), and UL (Underwriters Laboratory). These organizations have also developed standardized tests for safety and performance in accordance with the most common applications for consumer batteries. For example, heavy and light flashlight tests, radio tests, and toy tests have been devised and are generally reported by the battery producers. For a comprehensive review of standardization of primary batteries, see [1].

Characteristics and Applications of Different Battery Systems

The common battery systems for consumers often have overlapping uses due to the design of the devices. For example, a flashlight with a tungsten bulb may be powered equally by carbon-zinc, alkaline, and in some cases lithium iron disulfide batteries. The circuit is simply a resistor (the tungsten filament). The resistance, however, is temperature dependent and thus it is sensitive to the voltage which controls the current of the battery – a higher voltage gives a higher current due to Ohm's Law – which results in a higher temperature of the filament as a quasi steady state is approached. If the current is too high, the temperature of the filament may exceed the stability limit of the filament, and the filament will separate or even melt if the temperature rise is too

fast. Therefore, if the filament is designed to accommodate the higher voltage of the lithium iron disulfide cell, it may also be used. In a LED flashlight, the color depends on the temperature which in turn depends on the voltage, while the light output depends on the power (voltage x current). For white light, the voltage needed is about 3.4 V, which may be obtained from almost any battery source, e.g., 2 alkaline cells, when a DC to DC converter is installed. It is important to use the recommended battery with the particular flashlight. For example, some flashlights recommend 2 or 3 AA alkaline batteries, while some recommend 2 or 3 lithium iron disulfide AA batteries. Some LED flashlights now operate on lithium manganese dioxide batteries, for example, CR123, while many are now designed for lithium ion or nickel-metal hydride rechargeable cells.

Many electronic devices such as wrist watches and clocks, remote controls, and electronic keys are operated by primary batteries. For small devices, alkaline or lithium button/coin cells are often utilized. These common miniature batteries are also used in very low drain devices such as electronic scales, clocks, and watches. The larger carbon-zinc cells are utilized in many clock devices because of the low drain rate needed for clock escapements. Children's toys are common applications for primary batteries. They are safe for children to handle, although parental supervision should be exercised with miniature batteries so that small children do not swallow them. Carbon-zinc and alkaline batteries are most commonly used in these applications. Lithium batteries are commonly used in photo applications – cameras and separate flash units. Their portability and easy replacement are advantages compared to some rechargeable batteries in these uses. In general, the highest drain devices can benefit from the use of lithium primaries, intermediate drain devices can benefit from alkaline batteries, while the lowest drain devices may use carbon-zinc batteries unless leakage and shelf life are problematic for the application. Smoke detectors and carbon monoxide detectors commonly use 9 V or AA batteries, and alkaline batteries are often the battery of choice because the alarms

Primary Batteries, Comparative Performance Characteristics, Table 1 Typical characteristics and applications of the most common types of primary batteries

System	Characteristics	Applications
Carbon-zinc (Leclanche or zinc chloride)	Common, low cost, widely available in different sizes	Flashlights, portable audio devices, toys, instruments
Alkaline (zinc-manganese dioxide – Zn/MnO_2)	Most popular general purpose battery with good low-temperature performance, medium rate capability, and low cost. Also found in many sizes	Many types of electronic instruments as well as toys and mechanical devices of all types
Mercury (Zn/HgO)	High capacity, flat discharge, good shelf life, but disposal problems due to mercury	Limited to devices that have controlled use and disposal. Has been widely employed in electronics in the past
Silver zinc (Zn/Ag_2O)	High capacity, flat discharge, good shelf life, but expensive. Usually made in miniature form	Hearing aids, watches, photography in small sizes. Military and aerospace in large sizes
Zinc air (Zn/O_2)	Very high energy density, low cost, very sensitive to environmental conditions and duty cycle	Hearing aids, pagers, medical devices, military electronics, and other special applications
Lithium liquid cathode	High to very high energy density, long shelf life, very good performance over wide temperature range but expensive	Utility meter readers, military electronics, aerospace uses. Toxic liquids inside require special protection
Lithium solid cathode	High to very high energy density, long shelf life, very good performance over wide temperature range and duty cycle. Lower cost than liquid cathode cells	Replacement for alkaline button cells and cylindrical applications. Different volt cathodes suit different applications
Lithium solid electrolyte	Very long shelf life but used only for low power applications	Medical electronics and implantable devices
Magnesium (Mg/MnO_2)	High capacity with long shelf life unless activated by discharge. Must be consumed in short period of time after activation	Formerly used in many military applications such as communications devices. Now mostly replaced by lithium batteries
Mercad (Cd/HgO)	Long shelf life and stable voltage. Low energy density and disposal problems	Limited to controlled applications requiring long shelf life and stable voltage

require substantial current over a fairly long time to ensure alerting everyone in the vicinity of the alarm. It is interesting that hearing aids are often best served by zinc air batteries because they are used in a continuous or near-continuous mode (e.g., for all awake hours) and have very high energy content for their size, thus giving good value. A disadvantage for this system is that the cells have a short shelf life after they are activated, so intermittent use is not recommended. Another factor to consider in selecting a battery type is how much damage to the device would be sustained if the battery leaks electrolyte. This is especially important in carbon-zinc cells which have the greatest tendency to leak, followed by alkaline cells, which leak very corrosive alkaline electrolyte when leakage does occur (e.g., when the device is accidentally left in the on condition

for a long time) and finally for lithium cells which are nearly hermetically sealed and very seldom display leakage. In summary, the best use of a given battery type is the one that best satisfies the use profile at the least cost and the least potential for damage [2].

Table 1 gives typical characteristics and applications of the most common types of primary batteries.

Carbon-Zinc Battery

This battery system has existed for over 100 years and still is a major battery particularly in the consumer market. It is still widely used for flashlights and portable radios as well as low drain devices such as digital clocks. It is widely available all over the world in most standard cell sizes. It has been supplanted in many consumer

electronic applications because of its low rate capability and leakage/reliability problems; however, it is still widely used in the developing world for a great many applications.

Alkaline Zinc-Manganese Dioxide Battery

Most of the industrialized world now uses the alkaline battery as the battery of choice for consumer electronics as well as many other electrical devices. The advantage over carbon-zinc cells is the higher rate capability, low leakage rate, long shelf life, and better reliability and low-temperature operation. It is intermediate in cost between carbon-zinc and lithium battery types. Like carbon-zinc, it is available in many standard sizes and types. It is commonly used in 9 V devices such as smoke detectors and carbon monoxide detectors, wherein six small cells are arranged in a rectangular metal container and leakage is minimal. This is important for expensive and safety-related devices because of the corrosive nature of the leakage liquid (KOH in most cases) which can ruin the device without the knowledge of the user. It has been available since the 1950s.

Mercury Battery

This battery type has been phased out in most applications because of the problems of disposal. The product of the reaction is liquid mercury which has a tendency to pool and can create a toxic hazard in landfills. Most countries have banned the use of mercury batteries in consumer applications for this reason. Other battery systems such as lithium primary batteries, zinc air, and alkaline batteries have to a large extent replaced mercury batteries.

Silver Zinc Battery

This battery is mainly produced in small-size (button) cells because of the cost of the cathode material (silver oxide). The battery has been produced in two forms, one using argentous oxide and the other argentic oxide or a mixture of argentous and argentic oxide. It has also been used in several military applications where the performance attributes are more important than the cost factor.

Zinc Air Battery

The fact that the cathode does not carry the weight of the active material (oxygen from the air) has given this battery outstanding energy per unit of weight and volume. It has lifetime issues, however, due to the difficulty of maintaining the correct moisture balance (high humidity results in battery flooding, while low humidity results in cathode drying) since it must be open to the air during operation. Schemes have been devised to limit the access of air during off periods, but these are cumbersome and are not in general use. The batteries are generally sealed with a pull-off tab that is to be removed on activation, and then the battery is used directly. Generally the lifetime is only a matter of a few weeks or months depending on the battery design, but for applications such as hearing aids, the much higher energy than other small cells makes this the battery of choice. The battery was used extensively at one time in railroad signaling applications but has now generally been replaced by sealed cells.

Lithium Liquid Cathode Battery

This battery type mainly involves the use of thionyl chloride or sulfuryl chloride liquid cathode electrolyte system. Because the liquid cathode electrolyte fills all the space usually taken up by the electrolyte (in the separator as well as in the pores of the cathode), the battery has very high energy density per unit weight and volume. The liquid cathodes are all toxic, so the cells are always hermetically sealed to prevent the escape of the toxic, corrosive vapors or liquids. Because of the construction, the cells are expensive. The main applications have been in industrial uses such as meter readers, counters of all kinds, in aerospace, and medical and military applications. The combination of high energy, long shelf life, and wide temperature range has allowed the field to develop substantially. The cells were even seen as having a wide service in downhole drilling rigs, where sensors need to be battery powered, at temperatures even exceeding the melting point of lithium. The voltage ranges from 3.5 to almost 4 V for the different liquid cathodes.

Lithium Solid Cathode Battery

This battery type has been designed with several cathode materials over the years, but the most common cathodes now are manganese dioxide (MnO_2), carbon monofluoride (CF_x), and iron disulfide (FeS_2). The first two operate around 3 V, while the last operates at 1.6 V and can therefore be used in place of carbon-zinc or alkaline zinc-manganese dioxide batteries. The first two types have been widely used in aerospace and medical and military applications in addition to consumer batteries. Because of the different voltages of the first two systems from aqueous batteries, they are made in special sizes so they cannot be used in place of a nominal 1.5 V battery and damage the electronic device. This is not true of the iron disulfide cathode cell, so it is made in conventional AA and AAA sizes. Because of restrictions on the amount of lithium in a single cell, larger sizes of iron disulfide batteries are not made for consumer applications. As in the liquid cathode batteries, the high energy (and power) as well as the long shelf life and wide temperature range of use have allowed many applications for these batteries. The use of silver vanadium oxide has seen wide use in medical applications because of its much higher rate capability and is widely implanted for cardiac defibrillator devices.

Lithium Solid Electrolyte Battery

A special lithium cell uses an iodine cathode with an in situ formed solid electrolyte which is very stable and used in implantable devices in medicine. These devices have been widely used in pacemakers.

Magnesium Manganese Dioxide Battery

This battery has seen applications in many military devices. Like the zinc air battery, the shelf life is very long in the unused state, in this case because magnesium is heavily passivated by the aqueous electrolyte. When the cell is used, however, the magnesium metal is exposed to fresh electrolyte and a strong corrosion reaction is initiated. This uses up much of the magnesium in wasteful reaction. For some military applications, the long shelf life is more important than the wasteful generation of hydrogen due to corrosion. Modern weapons generally use a variation of lithium batteries for most deployments now.

Mercad Battery

This system utilizes two toxic materials, mercuric oxide and cadmium metal. Because of its low voltage, however, it is thermodynamically stable, and if it is well sealed, it has a very long lifetime. It also has a very stable voltage and can be used as a voltage reference in electronic circuits. It is seeing less and less usage because of disposal issues and the availability of stable lithium cells with equivalent lifetime and voltage stability.

Other battery types which have been studied in some detail but are not in common use include aluminum air cells, magnesium air cells, and iron air cells.

Cross-References

▶ Primary Batteries, Selection and Application

References

1. Wicelinski S (2011) Battery standardization. In: Reddy T, Linden D (eds) Linden's handbook of batteries, 4th edn. McGraw Hill, New York
2. Linden D, Reddy T (2011) An introduction to primary batteries. In: Reddy T, Linden D (eds) Linden's handbook of batteries, 4th edn. McGraw Hill, New York

Primary Batteries, Selection and Application

George Blomgren
Blomgren Consulting Services, Lakewood, OH, USA

The selection of particular batteries for any given application is a complex decision based on operating and shelf life, power capability, sensitivity to hazards, and cost. Battery characteristics are tabulated in many sources [1]. It is important after

Primary Batteries, Selection and Application, Table 1 Qualitative comparison of primary battery types (1 to 7 where 1 is best)

System	Voltage	Wh.kg	W/kg	Profile flat?	Low temp.	High temp.	Shelf life	Cost
Carbon zinc	7	7	5	7	6	7	7	1
Alkaline	6	4	3	6	4	5	6	2
Zinc mercuric oxide	4	3	5	2	5	3	4	5
Zinc silver oxide	2	3	2	2	4	3	4	6
Zinc air	5	2	3	2	5	5	–	3
Lithium liquid cathode	1	1	1	1	1	2	1	5
Lithium solid cathode	1	1	1	2	2	3	2	3

examining these issues that the user or application developer makes measurements of the selected battery under the conditions of use of the application. The profile of current and voltage during operation and rest should be carefully documented, so the range of these properties during use under different conditions can be ascertained. Among these properties are ambient temperature and battery/device temperature during operation, maximum and minimum currents likely to be encountered, range of input impedance of the device as a function of frequency, as well as the frequency dependent impedance of the selected battery so that the impedance can be matched for optimum utilization of the battery. Part of the burden of the utilization of the battery rests with the application designer, who should be aware of battery characteristics so that optimum designs can be arrived at in parallel with battery selection. The device design often dictates the volume available for the battery as well as the voltage requirement. Sometimes the weight of the battery is very important for portability concerns, for example, with portable, handheld tools. In some cases, the criteria will favor choosing a secondary (rechargeable) battery over a primary one or primary over secondary. This is one of the most important decisions to be made. Cost of the battery is an important issue because cost may affect the acceptance of the ultimate consumer of the device. Users have much less freedom in making these selections since the voltage and current characteristics of the design greatly affect the suitability of the battery. It is often, but not always, desirable to accept the device manufacturer's recommendation for battery selection. For example, when a new version of a battery appears such as the lithium-iron sulfide battery or the nickel oxide additive to the zinc-manganese alkaline battery, it may be better to switch from a recommended standard alkaline cell to power the device.

Table 1 gives some general characteristic rankings of primary battery types that should be of help in narrowing the selection of a battery.

Obviously, these rankings are only semiquantitative and do not imply a linear relationship. However, for a first look at battery types, these can be useful. A more detailed study is necessary to make final selections as discussed above. Sometimes several battery types are selected and tested for optimum characteristics for the particular application under study.

An important area to be considered in battery selection is safety of the battery in combination with the device. Part of the safety consideration is the design of the battery compartment. In some cases, the battery compartment should be designed for maximum heat dissipation – in some cases, they should be designed for maximum electrical isolation. Electrical isolation can be important for devices which are not in waterproof containers and can result in battery short circuiting if the device is immersed in water. Small batteries such as miniature alkaline or lithium coin cells should be enclosed in the device in a way that is difficult for small children to access the battery. Many of these small cells have been swallowed by children with the result of serious medical complications. Considerations of battery design are complex, and the size, electrode configuration, and format of the cell are critical to the

energy content and power capability of the cell and should be part of the overall selection criteria.

Often, the consumer is confronted with the need to decide which battery is best to replace an expired battery. It is generally advisable to follow the device manufacturer's recommendation for the chemistry of the battery. For example, if a carbon zinc battery is chosen rather than an alkaline cell because of lower cost, the result may be very poor utilization of the battery if the application is not appropriate and opposes the recommendation of the manufacturer of the device. If a comparison among different battery manufacturers for a given type of battery is desired, there are many independent studies of different batteries available to the consumer.

Cross-References

▶ Primary Batteries, Comparative Performance Characteristics

References

1. Linden D, Reddy T (2011) An introduction to primary batteries. In: Reddy T, Linden D (eds) Linden's handbook of batteries, 4th edn. McGraw Hill, New York

Primary Battery Design

Jack Marple
Research and Development, Energizer Battery Manufacturing Inc, Westlake, OH, USA

Introduction

Effective battery design is a balance between the intended application, the required operating voltage, rate requirements, shelf life, operating temperature range, reliability, safety, and product costs. Each of these considerations must then be applied to the anode, cathode, separator, electrolyte, and other features such as pressure vents,

safety devices, and tolerance to abuse. Commercially, a few electrochemical systems have won out in the competitive field of primary batteries for general consumer use. These include Leclanche'(also known as carbon zinc) and its variant zinc chloride, alkaline zinc manganese dioxide, zinc nickel oxyhydroxide, zinc air, lithium iron disulfide, lithium manganese dioxide, lithium carbon mono-fluoride, lithium thionyl chloride, and lithium sulfur dioxide. Interestingly, in some cases, batteries may be referred to by the chemistry of the anode and cathode and in other cases, by the inventor, the appearance, the choice of electrolyte, or even the product size.

There are many references which provide details about the chemistry of each of these types of batteries [1]. But detail relative to product design considerations is more limited. It is the intent of this article to focus on material properties and how they impact product design, cell format, and application.

Battery Format

Primary batteries are generally available in two basic form factors, cylindrical and coin. Within these form factors, the arrangement of the working electrodes can vary considerably depending on the volumetric differences in anode and cathode materials, changes in the volume of these materials during electrochemical discharge, the application current, and the necessary interfacial surface area need to support the current. Additionally, factors such as material electronic conductivity, electrolyte ionic conductivity, separator requirements, and safety features of the battery need to be considered.

The following cross-sectional drawings provide a quick comparison as to how these considerations influence the final battery design and electrode configurations. Figures 1, 2, and 3 show the cross sections of the three most common cylindrical cell designs. Figure 1 is referred to as a "carbon zinc" construction where the center carbon electrode, which is used as a cathode current collector and gas vent, is most evident, and

Primary Battery Design, Fig. 1 (Carbon zinc) Zn can/anode with MnO_2 cathode and a porous carbon rod current collector and vent. Low rate – oldest construction
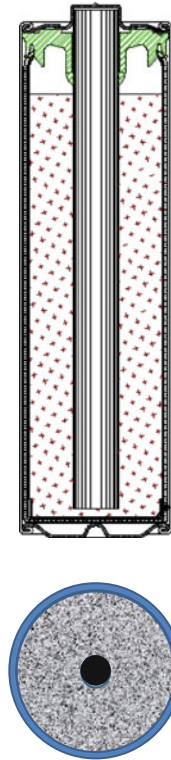
Primary Battery Design, Fig. 3 (Lithium) Wound layers of cathode coated onto a metal current collector with a solid Li foil anode which also serves as a current collector. High rate – newest construction
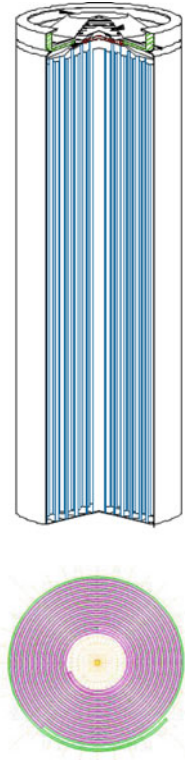
Primary Battery Design, Fig. 2 (Alkaline) Suspended Zn particle anode gel with a brass current collector and outer MnO_2 cathode with the container as current collector. Moderate rate
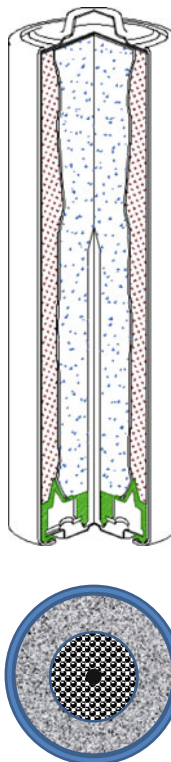
the zinc cell container also serves as the anode. Note that, volumetrically, the center of the cell is mostly cathode which is manganese dioxide.

Figure 2 is a typical alkaline cell construction which uses the same electrochemical couple as the "carbon zinc" cell. However, in this case the zinc is a powder, in the center of the cell, and the container is made of an inactive material, such as steel. Like carbon zinc cells, the cathode is manganese dioxide. The electrolyte is based on potassium hydroxide (or in some coin cells sodium hydroxide), which explains the use of the term "alkaline" to describe these cells.

Figure 3 represents a jelly roll construction most often used for lithium metal anode cells. The cathode can be made of manganese dioxide, carbon mono-fluoride, or iron disulfide. The use of lithium as an anode rather than zinc necessitates that the electrolyte be organic due to the extreme reactivity of lithium metal with water.

These three constructions represent products designed for increasing rate capability (Fig. 3 > Fig. 2 > Fig. 1). They also represent advances

over time in terms of commercial production, with Fig. 1 being older than Fig. 2 which is itself older than Fig. 3.

To better understand the differences in rate capability, application, and performance, it is necessary to look at each product in terms of its key components of anode, cathode, separator, and electrolyte.

Anode

In Figs. 1 and 2, each cell makes use of zinc metal as the anode half couple. However, when the anode also serves as the outer container it must be solid which limits the reaction surface area. For a carbon zinc cell, the surface area of the anode is limited to the interfacial area, creating a much longer diffusion path through the cathode than in Fig. 2 or 3. In the alkaline cell construction shown in Fig. 2, the zinc surface area has both an interfacial component and a contribution from particle size. However, limitations to increasing surface area, based on particle size, must be considered. These include zinc particle to particle contact, zinc oxidation, the need for cathode overbalance to prevent water decomposition and hydrogen gas generation during deep discharge, and stability of the zinc in this alkaline environment, which particularly in today's zero mercury cell design can contribute to gas generation and reduced shelf life.

Another means of achieving high interfacial surface area of the anode is shown in Fig. 3. In this case the anode is once again a solid metal, but a high surface area is achieved by winding together long, thin layers of cathode and anode. Using this configuration, electrode interfacial surface areas of approximately 200 cm^2 can be achieved in AA cells, which is at least 20 times higher than that of the other AA cell configurations.

These variations in cell and anode designs also increase the challenge of collecting the current from each electrode. In the case of carbon zinc cells shown in Fig. 1, the zinc container serves as its own current collector. In the case of Fig. 2, a brass nail often is positioned within the center of the zinc particle suspension thereby relying upon particle to particle contact for current collection. In Fig. 3, the lithium metal anode often serves as its own current collector with the aid of a small metal tab which connects the lithium metal foil to the outer cell container.

Anode Alloys

While the anode is referenced relative to its base metal composition, anodes are seldom pure metal. In the case of carbon zinc cells, lead is often added at about 0.5 % to help with the metal drawing and can manufacturing process. Alkaline cells today, with the removal of mercury from the gel formulations, rely upon a number of different elements to minimize hydrogen generation resulting from water decomposition. Common elements include In, Al, Bi, Sn, and Pb at about the 500 ppm level. Lithium cells often contain Al, at about 0.5 % level to increase the tensile strength and to control the formation of a passivation layer from the reaction of the lithium metal with the organic electrolyte components [2].

Cathode

Interestingly, commercial cells using MnO_2 as the cathode material are available in all three configurations. However, while the cathode has the same base composition, changes in purity and crystal structure are required for each system. Carbon zinc cells are normally based on raw ore, while alkaline cells require higher purity electrolytically plated MnO_2. Lithium cells require even higher purity material based on thermal treatment of the electrolytic MnO_2 in order to create a crystal structure which is more stable in organic electrolytes. In addition to MnO_2, lithium can also be coupled with other cathodes such as iron disulfide, carbon monofluoride, thionyl chloride, and SO_2. With the exception of iron disulfide, which is considered a 1.5 V system, all others are considered 3 V systems. To avoid damage to devices, these

**Primary Battery Design,
Fig. 4** Storage
maintenance based on
rating drain test at 20 C,
to 0.9 V
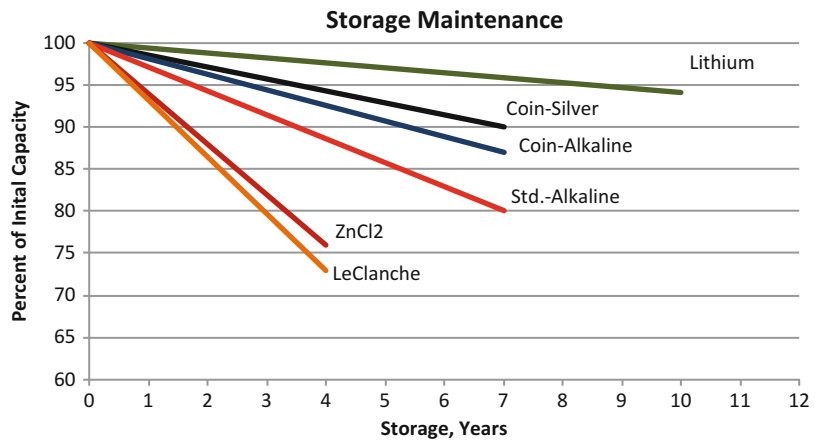
3 V systems are not available in standard 1.5 V formats such as AA cells.

Cathode design considerations include the conductivity of the active material; its stability relative to various forms of carbon conductors; volumetric changes of the reaction products; particle size influenced by electrode thicknesses and rate requirements; the use of processing aids such as polymers, surfactants, and rheology aids; and how the active materials will interface with a current collector. Additionally, in the case of lithium cells, it is critical to condition the cathode components prior to cell assembly to remove moisture and volatile process aids which can leach into the organic electrolyte and then react with lithium metal. Such reactions are almost always detrimental to cell impedance and product shelf life.

Figure 4 shows a comparison of storage maintenance as a function of product age for common primary systems. Actual shelf life varies by manufacturer and the cell's chemistry. Material purities, passivation additives, seal integrity, and temperature may further influence shelf life.

When discussing cathodes for primary cells, it is important to make a distinction between solid materials, mentioned above, and those in which the cathode electrochemical component is not in the physical electrode structure, but rather exist in a liquid or gas state. Examples include zinc air cells, lithium thionyl chloride cells, and lithium sulfur dioxide cells. In each case, the physical cathode structure serves as a catalytic reaction

site for a gas or liquid which is reduced most often on a high surface area carbon matrix. The polymeric binder in these structures is usually Teflon, and the carbon may be coated with a catalyst (e.g., MnO_2 in an air electrode). An important design consideration in each case is the stability of the carbon structure and the mobility of the cathode gas or liquid within this structure throughout the life of the battery.

Separators

For the most part, battery separators can be grouped into two categories: nonwovens and microporous membranes. The choice of a separator for each battery system must take into consideration such factors as cost, thickness, processibility, formability, pore size, tortuosity of pores, tensile strength, melt point, range of operating temperature stability, puncture resistance, dielectric strength, particle sizes of the anode and cathode materials, and stresses developed during product discharge.

Typically, carbon zinc and alkaline cells use nonwoven separators. In these cases, cost is an important design consideration, and the high conductivity of the electrolyte enables thicker separator materials. However, the thickness of the separator also defines the gap or distance between electrodes, which can impact the cell's ability to support high current densities. Pores are not well defined and are typically on the order of

several microns, while the thicknesses are often several hundreds of microns.

In contrast, lithium cells require thin microporous separators based on the low conductivity of organic electrolytes. These microporous separators more closely resemble membranes with a thickness of 25 μm or less with pore diameters in the hundredths of microns. They most often are polyolefins consisting of polyethylene or polypropylene. Despite their thinness, up to three layers of separately extruded films may be used.

In selecting a separator for a particular cell design, it is also important to consider its stability in the electrolyte, ability to wet out quickly by the electrolyte, ability to maintain electrolyte within its pore structure throughout the cell's life, and the impact it has on ionic mobility of the electrolyte salt. Since separator pores are seldom channels straight through the separator, the difference in true ion path versus the separator thickness is referred to as tortuosity. A certain amount of tortuosity is desired to prevent shorting, due to particle penetration and soft shorts from dendritic bridging between electrodes, while maintaining low tortuosity is often required to achieve the best high rate performance. Therefore, striking the right balance of pore size and structure is an important design consideration [3].

Electrolytes

The selection of the electrolyte formulation for a cell design is a critical decision, which impacts a wide range of cell characteristics, including operating temperature range, shelf life, rate capability, product safety, product application voltage range, solubility of impurities, and solubility of active components and reaction products. Optimized electrolytes are often more than just a solute in a solvent; they may contain other additives such as surfactants, voltage control agents, film formation components, and Le Chatelier's principle additives to control chemical equilibriums and solubility. In many battery systems, the anode and electrolyte need to form a stable passivation film on the surface of the anode. These films are referred to as the SEI or

solid electrolyte interfaces. SEI layers are highly important to controlling wasteful corrosion reactions while still allowing for unhindered ionic mobility through these passivation films.

Electrolyte conductivity provides the greatest impact of electrolyte on product design. As a reference point, the radically different product designs shown in Figs. 2 and 3 are, in fact, driven by the conductivity of the electrolytes. Alkaline cells have high concentrations of KOH in water, yielding conductivities of approximately 500 S/cm [4]. However, lithium cells must utilize organic solvents with low ionic salt concentrations because of the incompatibility of lithium metal with water-based electrolytes. Such organic electrolytes are more typically 10 S/cm [5], a factor of 50 times less conductive. To counter this large difference in conductivity, a lithium cell designer must dramatically increase the interfacial surface area of the electrodes and additionally minimize the gap or distance between the electrodes. As a result, an alkaline AA size battery typically has an interfacial electrode area of 10 cm^2, while an AA lithium cell is approximately 200 cm^2. Additionally, the distance between electrodes may be 200 μm in an alkaline cell but only 20 μm for a lithium cell. By increasing the interfacial electrode area by a factor of 20 and decreasing the distance between electrodes by a factor of 10, the disadvantage of lower electrolyte conductivity by a factor of 50 can be offset such that the lithium cell significantly outperforms the alkaline cell on high rate applications.

Figure 5 shows a comparison of service and operating voltage on a typical application drain of 200 mA for $ZnCl_2$, alkaline, and $LiFes_2$, AA cells. The differences in both rate capability and energy delivered are evident for these product design evolutions.

Total Product Design: Container and Format

Battery systems are often compared based on energy per weight or energy per volume. A plot of these two energy densities is referred to as
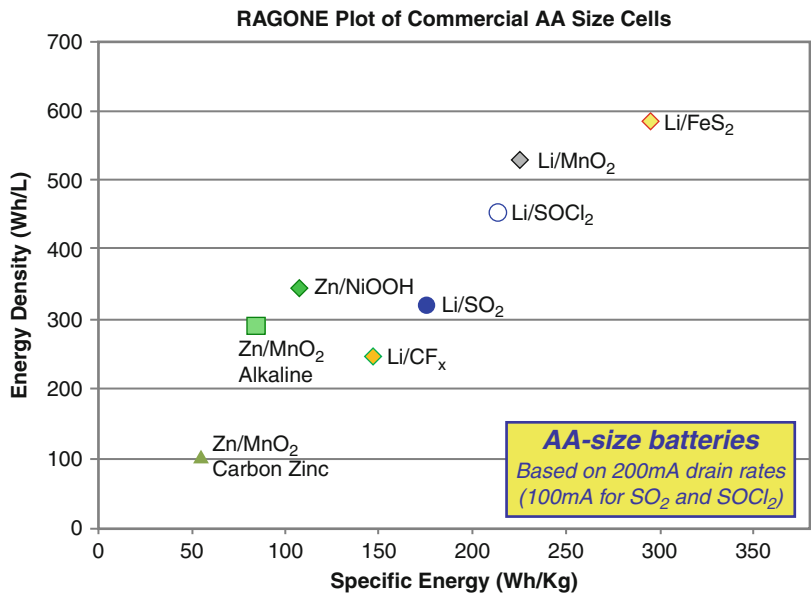
Primary Battery Design, Fig. 5 Comparison of operating voltage and service on a 200 mA, AA battery rating drain
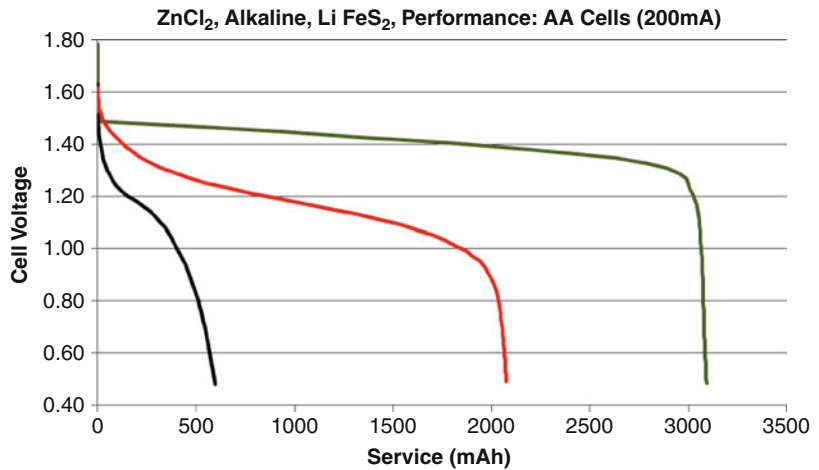
Primary Battery Design, Fig. 6 Ragone plot of primary AA cells

a Ragone plot. Figure 6 is a Ragone plot for commercial, primary, AA cells based on a common drain rate of 200 mA, consistent with many of today's device requirements. Figure 6 clearly shows the energy differences for the three products shown in Figs. 1, 2, and 3. While other systems have been developed, these systems have not found wide acceptance outside of the military or niche markets such as photo applications, high-end flashlights, remote meter sensors, and the medical industry.
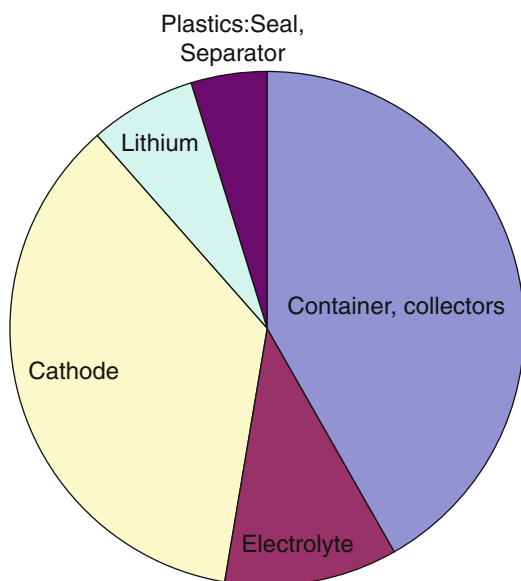
From a battery design standpoint, the challenge is to maximize active components and their utilization while minimizing non-active components such as the cell container, current collectors, seals, head space, separators, conductors, and void required for reaction products. The percent of both volume and weight that these non-active components contribute to any given battery system is dependent on format and size; the larger the battery, the greater the percentage of active components. Electrolyte is of

course needed for any system but can take on a more important role when it is also involved in the discharge reaction. This is particularly true for alkaline cells.

For many consumer applications, the focus is more on Wh/cc versus Wh/Kg. On a volume basis, the anode and cathode volumes account for 18 %, 34 %, and 38 % of the total AA cell volume for carbon zinc, alkaline, and lithium iron disulfide, respectively. These values change

Primary Battery Design, Fig. 7 Contributions of materials to total weight of a LiFeS$_2$ cell

considerably when electrolyte is included: 56 %, 43 %, and 56 % respectively. In general, these systems possess less than 40 % active volume percentages without electrolyte and less than 60 % with electrolyte. These active material utilization design limitations still exist despite having the benefit of more than 100, 50, and 20 years in product optimization respectively. Thus, when considering the potential energy of an electrochemical couple, it is important to realize that these values need to be reduced by as much as 60 % for defining the practical energy.

In addition to volumetric optimization, weight optimization is also important in today's ever decreasing in size portable devices. Figure 7 shows a breakdown of the components in percentage of total cell weight for one of the highest gravimetric systems, lithium iron disulfide. Note that close to 50 % of the cell's weight consist of non-electrochemically active materials with the majority of this weight associated with the battery container.
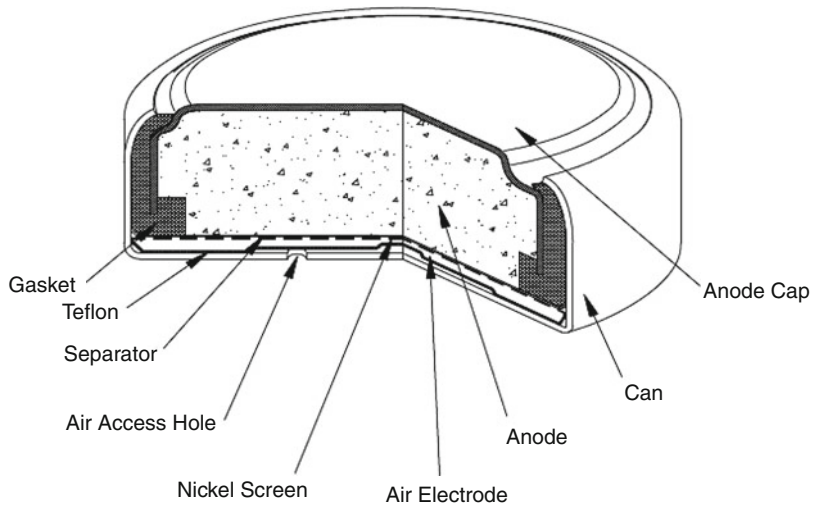
Coin Cells

Most of the above discussion on primary battery design has focused on cylindrical cells. While the design considerations are, for the most part, similar for coin cells, the increase in container
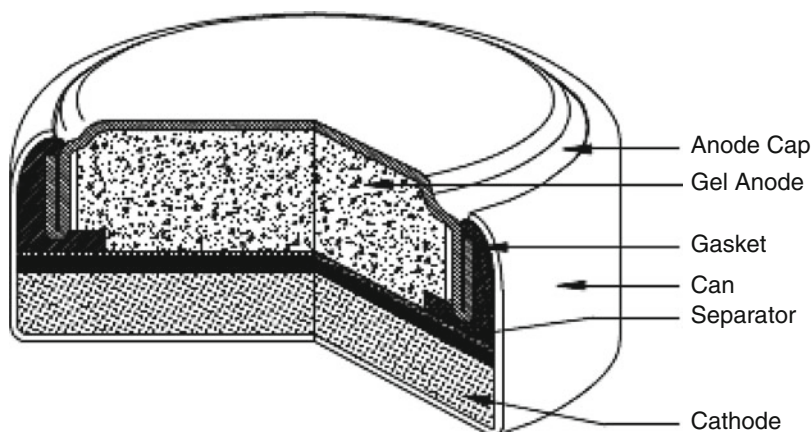
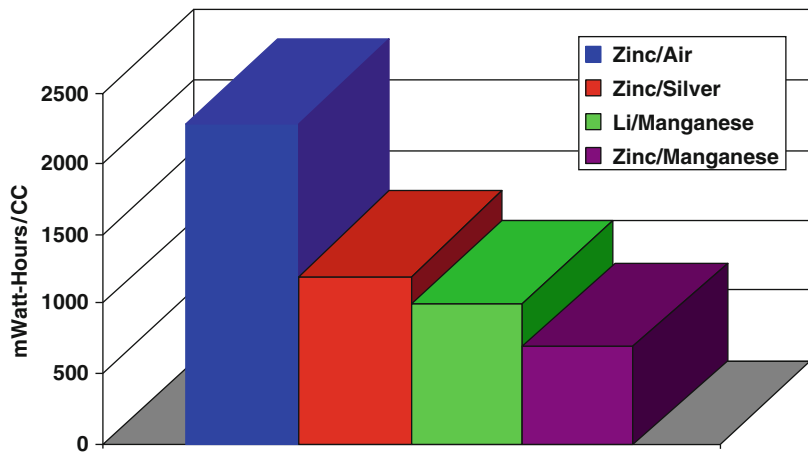**Primary Battery Design, Fig. 8** Cross section of a silver oxide cell

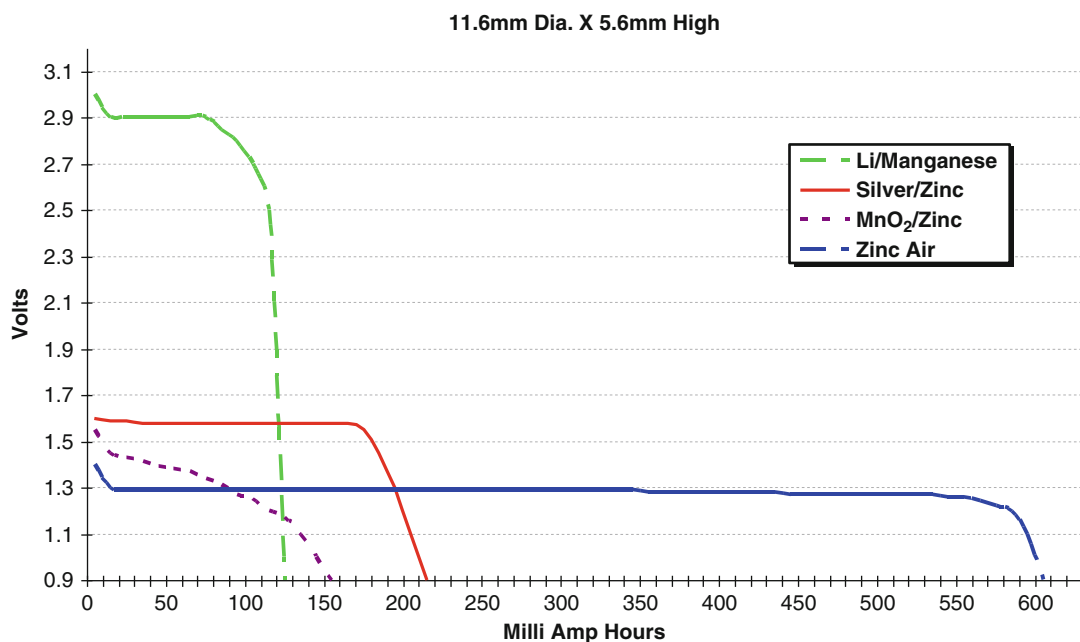**Primary Battery Design, Fig. 9** Cross section of a zinc air cell

Gasket

Teflon

Separator

Air Access Hole

Nickel Screen

Air Electrode

Anode

Can

Anode Cap

Primary Battery Design, Fig. 10 Volumetric energy densities for common coin cells

mWatt-Hours/CC

Zinc/Air
Zinc/Silver
Li/Manganese
Zinc/Manganese

2500

2000

1500

1000

500

0

interfaces, container volume, and decreased container strength place increased demand on volumetric or internal void considerations. Figures 8 and 9 show the cross-sectional profiles of two common coin cell chemistries.

The zinc air cell design is unique in that the cathode active material is supplied by oxygen in the air and, other than a thin reactive electrode sites for absorption and reduction of oxygen, the cells internal volume is primarily occupied by zinc anode. However, void volume must be reserved to account for the volumetric expansion of zinc to zinc oxide upon discharge.

Figures 10 and 11 provide a comparison of the volumetric energy densities in the various commercial coin cell chemistries. While zinc air cells by far exceed the other systems, on a watt-hour per cc basis, its application has been mostly limited to hearing aid applications. This application limitation is in part because the path way for oxygen into the cell also allows moisture in and out of the cell, as well as carbon dioxide which may cause wasteful carbonation of the anode components. As a result, the zinc air chemistry has been limited to applications with duration of a month or less.

11.6mm Dia. X 5.6mm High

Primary Battery Design, Fig. 11 Discharge profiles of various coin cell chemistries

Future Direction

Future designs of primary batteries will be strongly influenced by both shifts in applications and material science. A review of device applications by NPD [6] shows the following growth areas from 2005 to 2010 for primary batteries: wireless game controllers, wireless sensors, garage door openers, remote controls, and games/toys, while emerging market segments include LED lights, remote sensors, 3-D glasses, medical devices, ultralow power sensors, and military applications like night vision, GPS, and laser sights.

Rapid changes in material science such as nanomaterials, graphene, conductive polymers (both ionic and electronic), and ionic liquids will open battery designs to new formats such as thin printed and battery on board, non-replaceable primary batteries [7, 8]. These trends, further coupled with the rise in popularity of low-power applications, may transition some of today's secondary electrochemistries into primary applications without the added cost of charge control systems required for secondary batteries.

Cross-References

▶ Primary Batteries, Comparative Performance Characteristics
▶ Primary Batteries, Selection and Application

References

1. Linden D (2002) Handbook of batteries, 3rd edn. McGraw-Hill, New York
2. Marple WJ (2005) Nonaqueous electrochemical cell with improved energy density. US Patent No 6849360
3. Marple WJ (1994) Separator/electrolyte combination foe a nonaqueous cell. US Patent No. 5290414
4. Dow Website (2012) Form No 609-02127-804, Conductivity of solutions. http://msdssearch.dow.com/PublishedLiteratureDOWCOM/dh_003c/0901b8038003ccb2.pdf?filepath=liquidseps/pdfs/noreg/609-02127.pdf&fromPage=GetDoc
5. Blomgren G (1983) Properties of electrolytes. In: Gabano J-P (ed) Lithium batteries. Academic, New York
6. NPD (2010) Consumer battery usage. US Market, Commissioned by Energizer Battery Company
7. Sapru V (2011) Opportunities in the primary lithium battery market, battery power. Frost & Sullivan Webcom Communications, Greenwood Village, CO 80111
8. Svastano D (2011) Advancements in printed battery technology are driving growth, printed electronics now. http://www.printedelectronicsnow.com/articles/2011/01/advancements-in-printed-battery-technology-are-dri

Probe Beam Deflection Method

Cesar Alfredo Barbero
Department of Chemistry, National University of
Rio Cuarto, Rio Cuarto, Cordoba, Argentina

Introduction

Different techniques can be used to study electrochemical phenomena. Classic electrochemical studies are based on the study of electron fluxes at the electrode/electrolyte interface [1]. Using different ways of system perturbation and/or to measure the current-potential response of electrochemical systems, together with studies on the effect of electrolyte media (e.g., pH), it has been possible to obtain some information about electrochemical mechanisms. However, it has become clear that purely electrochemical techniques have significant limitations. To overcome those deficiencies, a plethora of in situ spectroscopic techniques has been developed in recent years. In those techniques, spectroscopies have been combined with electrochemical perturbations to help to understand complex electrochemical phenomena. Most of those techniques have been applied to study the electrode/electrolyte interface [2], by measuring changes occurring at the interface itself [3] or on the whole electrode [4]. On the other hand, the reaction occurring at the electrode necessarily created fluxes of solution species (ions, neutrals, solvent) from/to the electrode/ electrolyte interface. The study of such fluxes has been less common, inasmuch that fluxes could control the electrochemical systems, such as batteries, sensors, fuel cells, or supercapacitors. One reason is that few techniques are able to measure concentration gradients coupled to electrochemical reactions. The classical technique is optical interferometry. It has low sensitivity and slow response and both complex experimental setup and analysis. It has been mainly used to study electroplating cells and similar systems [5]. Some other techniques are able to detect ion fluxes in solution: radiotracer

detectors, pH sensors, fluorescence or absorption measurement on grid electrodes, scanning electrochemical microscopy, ring-disk voltammetry, surface plasmon resonance, confocal microscopy, and diffraction spectroelectrochemistry. They have been seldom used to study electrochemical systems. Probe beam deflection is a technique which allows fast monitoring of concentration gradients related to electrochemical phenomena and has been used to study a wide range of electrochemical phenomena [6]. The mechanism of detection in PBD involves deflection (refraction) of the probe beam by the refractive index gradient. While PBD techniques could be used to measure any electrochemical phenomena, it is difficult to relate the observed signal with electrochemical reactions when there are reactions in solution or several ions are exchanged. On the other hand, the ion exchange coupled to electrochemical reactions, between an electrode surface and a film confined at it, and the electrolyte solution is quite straightforward to be studied by PBD techniques.

Basic Principles

The usual scheme of a probe beam deflection experiment is depicted in Fig. 1. A solid/electrolyte is set up and a laser beam is set up to travel parallel to the surface. The interface is usually planar; however, spherical or cylindrical solids can be used. The only difference is the geometry of the interaction between probe beam and the interface. The deflection of a probe beam, which travels close to an electrode along a path length l, in an electrolyte of refractive index n (Fig. 1) could be understood as a distortion in the wave front of the beam. The wave speed increases according to $v = c/n$. In conditions of small deflection, the geometric optic approximation could be used [6]:

$$\theta(x,t) = \left(\frac{L}{n}\frac{\partial n}{\partial C}\right)\left(\frac{\partial C(x,t)}{\partial x}\right) \qquad (1)$$

where C is the concentration, l is the interaction path length, n is the refractive index of the bulk, and dn/dC is the variation of refractive index with
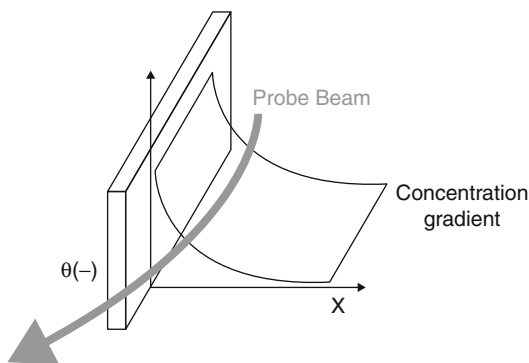
Probe Beam Deflection Method, Fig. 1 Probe beam deflection in a concentration gradient

concentration. The sign of the deflection depends on the change of refractive index with concentration (dn/dc).

The dn/dc constant is positive for liquids or solids dissolved in a solvent because the refractive index increases with concentration. Therefore, an increase of concentration at the electrode surface will be accompanied by a negative deflection (Fig. 1). On the other hand, when gases are dissolved in a liquid phase, the refractive index decreases; therefore, dn/dc has negative values. This has to be taken into account when the PBD data of electrochemical systems with gaseous reactants/products (e.g., hydrogen fuel cell) is analyzed. One way to make both signals proportional is to make the beam-electrode distance close to zero. However, the beam waist cannot be zero. From laser beam optics [7], it is known that a beam can be focused to a small spot, but there is a relationship between the waist ($w(x)$) and the path length (b) of the beam in front of the electrode. Since the interaction between the probe beam and the concentration gradient assumes that the beam is nearly cylindrical with a fixed waist, the electrode width has to be smaller than b. Otherwise, the waist at the extremes will be very different from the waist at the center of the electrode and the probe beam will sample different concentration gradients.

The possible perturbations (controlled potential or current) used in PBD could be all the usually used in electrochemistry. To obtain the equations governing the PBD signal for different electrochemical techniques, the concentration gradient has to be obtained. An electrochemical system could be modelled as a planar electrode of width w in contact with a semi-infinite fluid layer where diffusion occurs (being the diffusion layer several times thinner than w). The latter condition implies that border effects could be neglected and that interaction path length is $l = w$.

Using the mass transport equations and the boundary conditions, the variation of concentration gradient with time and distance could be obtained. Therefore, the calculation could use the methods developed previously in electrochemistry to calculate the concentration gradients in front of the electrode. In general, to obtain the equations to simulate the PBD response, the following steps have to be carried out: (i) obtain the concentration profile at distance x, for the technique under study, $C(x, t)$; (ii) differentiate with respect to x, to obtain $dC(x,t)/dx$; (iii) combine with Eq. 1 to obtain the dependence of deflection with time and space $\theta(x, t)$.

One characteristic of the technique, shared with purely electrochemical techniques where only electron fluxes are monitored, is its lack of specificity. That is, not individual concentration gradients but the sum of all concentration gradients is detected. This could be an advantage because it allows measuring all possible ion exchange not only of some ions (e.g., massive ions for EQCM) like other techniques. In the case of surface and film species, only concentration gradients due to ion exchange will be detected. Moreover, if the measurements are carried out in the presence of binary electrolytes that is electrolyte containing only one anion and one cation (e.g., ClNa), the diffusion of ions and its migration are necessarily coupled [8]. In that way, the diffusion of one ion is coupled to the other and a single gradient will be measured. A different situation exists when redox reactions in solution are monitored (e.g., $Fe(CN)_6^{-4}$ oxidation). There, the gradient of reactants, products, and supporting electrolyte (if present) has to be considered. Therefore, the interpretation of the PBD signal in terms of electrode reactions becomes difficult or impossible.

Following such procedure, the PBD signal ($q(x, t)$) could be calculated, when a potential pulse (from a potential where no reaction occurs to a potential where all the reactant is converted) is applied to the electrode and an electrode reaction occurs during the whole measurement. The profile follows Eq. 2:

$$\theta(x,t) = \left(\frac{l}{n}\frac{\partial n}{\partial C}\right)\frac{C_o}{\sqrt{\pi Dt}}e^{-x^2/4Dt} \quad (2)$$

where D is the diffusion coefficient and C_0 is the concentration of the redox species. As it can be seen, the PBD signal depends both on the time (t) and the beam-electrode distance (x). The PBD signal is zero at $t = 0$ (unlike the current which has an infinite value) and reaches a maximum value at a finite time (t_{max}):

$$\sqrt{t_{max}} = \frac{(x - x_0)}{\sqrt{2D}} \quad (3)$$

Equation 3 could be used to measure the diffusion coefficient of the species because x could be set up experimentally. Equation 2 can be used to simulate the PBD signal of a continuous electrochemical reaction. That is, when the redox species are transformed during the whole time span of the measurement. This is the case of redox reactions in solutions (e.g., Fe^{+2} electrochemically oxidized to Fe^{+3}), but in such cases, several concentration gradients have to be considered and interpretation is difficult. A simpler system involves metal deposition by reduction of a metal ion (e.g., Ag^+) to metal (Ag^0), where only one concentration gradient have to be considered.

A more interesting case deals with discontinuous reactions, where the reaction takes place in a short time span which is negligible compared with the duration of the measurement. An example is a monolayer of metal (e.g., Ag) which dissolves by oxidation giving short pulse of metal ions. The PBD signal profile follows Eq. 4:

$$\theta(x,t) = \left(\frac{l}{n}\frac{\partial n}{\partial C}\right)\frac{C_s}{\sqrt{\pi Dt}}\frac{x}{2Dt}e^{-x^2/4Dt} \quad (4)$$

where D is the diffusion coefficient of the mobile species and C_s is the surface concentration of the redox species. Equation 4 is similar to Eq. 2 but the time profiles are sharper and the time for the maximum PBD signal (t_{max}) obeys Eq. 5:

$$\sqrt{t_{max}} = (x - x_0)/\sqrt{6D} \quad (5)$$

The discontinuous reaction with a binary electrolyte is completely described by Eq. 4. Discontinuous reactions occur in electroactive films, adsorbed redox monolayers, ion desorption in double layers, stripping of underpotential metal deposit, stripping of metals in Hg amalgams, etc.

The experimental setup allows measuring the PBD signal along with the current and potential; therefore, the data analysis involves comparison of both kinds of data, since the absolute value of beam-electrode distance (x) cannot be set experimentally and could be measured by fitting the experimental measurement with simulation. In that sense, experimental PBD data can be postprocessed to extrapolate the data to $x = 0$ (electrode surface), therefore making it comparable with current. Another way to perform such comparison involves the so-called sampled deflection voltammetry. If the potential is pulsed between two oxidation states, C_0 (or C_s) will follow a potential-concentration relationship (e.g., Nernst equation). Therefore, the PBD signal at each extreme potential measures the effect of such relationship on the ion exchange. Since the related sampled current voltammetry technique gives the changes of electronic charge with potential, both data can be compared and the relationship between electron and ion exchange ascertained. Analytical equations similar to Eqs. 2 and 4 have been obtained for different electrochemical techniques, including constant current and alternating current or potential. On the other hand the important case when the potential is cyclically scanned at constant rate between different potentials (cyclic voltadeflectometry, CVD), which is directly related to cyclic voltammetry, cannot be solved analytically. Therefore, numerical calculation techniques have been devised, mainly based
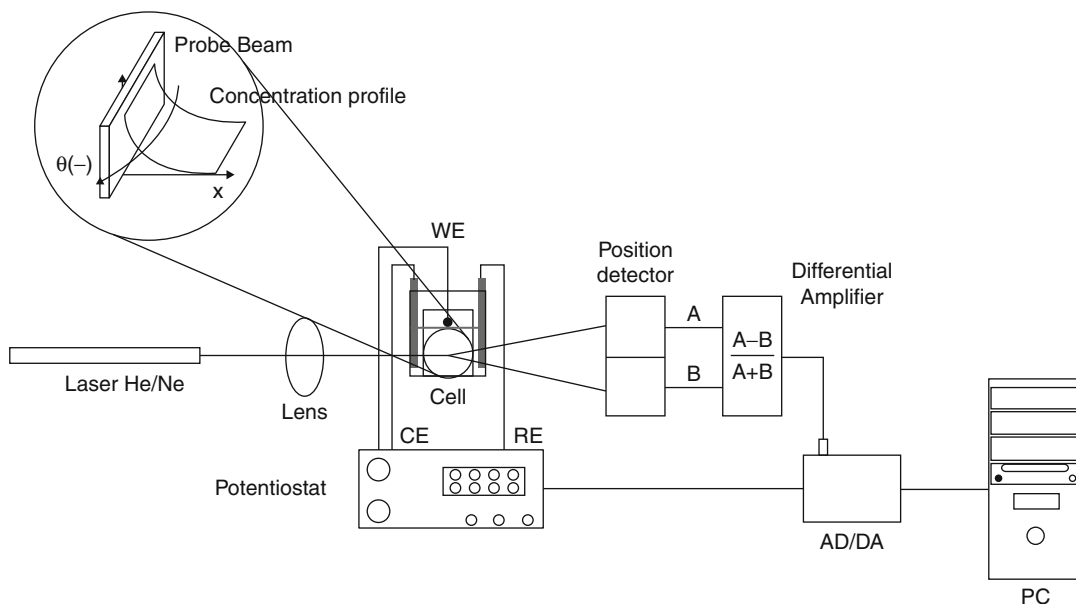
Probe Beam Deflection Method, Fig. 2 Experimental setup for probe beam deflection techniques

on finite differences [6]. Additionally, the semi-integration numerical procedure has been used both to simulate the CVD signal and to post-process the experimental data [6].

Experimental Details

The application of PBD techniques to study electrochemical phenomena requires integrating an optical setup to the electrochemical cell (Fig. 2).

A laser (usually a high pointing stability He-Ne laser) is loosely collimated by a lens to pass parallel to planar working electrode. The electrode is placed inside a rectangular optical cell where counter and reference electrodes are placed outside the beam path. The refracted laser beam impinges onto a lateral position detector, usually a spliced photodiode. The signal of each half of the photodiode is fed into a differential amplifier which ratios the difference of signal to its sum. In that way, intensity fluctuations in the laser are cancelled out. The differential signal is then digitized by an A/D converter and fed into a computer. The computer, trough a D/A converter, also provides the signal used to control the potentiostat and input the actual current and potential signals. The measurement speed is determined by the amplifier bandwidth, which is in the tens of kHz range. Therefore, millisecond time resolution is easily achieved. The cell is mounted onto an X-Y stage which allows adjusting the cell tilt to make the electrode surface parallel to the laser beam. The X-Y stage has an additional micrometric screw which allows moving the surface in the direction perpendicular to the beam direction. In that way, the beam-electrode distance (x) could be adjusted in relative way with micrometric resolution. The usual electrode surface is a flat conductive material (e.g., glassy carbon). An electroactive film can be deposited onto the surface as a thin film. In the case of porous electrodes, the powdered materials can be mixed with a binder (e.g., Nafion) into an ink and dip coated onto a flat surface.

Applications

The mainstream application of PBD techniques has been the study of redox coupled ion exchange of electroactive films [9]. The electroactive material could be redox polymers (e.g., polyvinylferrocene [10]), conductive polymers

(e.g., polyaniline [11]), redox oxides (e.g., cobalt oxide [12]), or inorganic solid complexes (e.g., Prussian blue [13]). Using binary electrolytes (e.g., HCl), the observed PBD signal can be directly related to the actual ion fluxes occurring between the film and solution. The signal/noise ratio could be always improved by forming thicker films (increasing C_s in Eq. 4). The method was used in aqueous and nonaqueous electrolytes [9]. The techniques allowed detecting ion exchange not predicted by simple models of charge electroneutrality. An interesting film was built by layer-by-layer self-assembly. In this case, the film is anisotropic and PBD gives unique information on the influence of the outer layer charge on the ion exchange kinetics [14].

A related system involves thin (one or few monolayers) of surface species either covalently bonded or adsorbed onto the solid substrate. Since the effective surface concentration (C_s) is quite smaller than for thicker films, the PBD signal can be too weak to measure. One way to overcome this problem involves increasing the active area of the electrode while maintaining the geometrical area, by using porous electrodes. In that way, the adsorption of redox intermediates (e.g., CO) of methanol fuel cells on mesoporous metal electrodes have been studied successfully [15]. Double/layer charging of conductive surfaces involves the exchange of ions with the electrolyte solution. Highly porous electrode materials are applied in supercapacitors and deionizers. The large active area makes them easy to study the specific ion adsorption by PBD [16] and the potential of zero charge to be determined [17]. PBD techniques have also been used to study other electrochemical systems, such as metal deposition/dissolution, hydrogen adsorption, underpotential deposition, silicon dissolution, graphite intercalation, and oscillating oxidation of formic acid [6].

Advantages and Disadvantages

PBD techniques' biggest advantage is to be a simple and fast way to ascertain the ion exchange of surface confined species, including electroactive films, surface redox species, and double layer on porous electrodes. Cyclic voltadeflectometry techniques could be used in an exploratory way, equivalent to cyclic voltammetry, to study the ion exchange. Then, chonodeflectometry could be used to obtain quantitative data on the ion exchange.

The main disadvantage of PBD techniques is its lack of specificity. The deflection signal is related with the sum of all concentration gradients present in the experiment. Therefore, the understanding of a PBD measurement of a soluble redox system, where several concentration gradients (due to reduced and oxidized species, summed to those of the supporting electrolyte) could be present, is quite difficult.

Future Directions

A future application of PBD techniques would be the study of ion exchange across liquid/liquid interfaces like those found in ITIES (interface between two immiscible electrolyte solutions) systems. Similarly, the effect of potential on the ion transfer across artificial or natural membranes could be studied by PBD.

The PBD techniques' usefulness could be significantly extended by making it more specific. This can be achieved by measuring the photothermal signal due to the optical absorption of colored ions. Using modulated laser or LED sources and phase-sensitive detectors, it is possible to measure the individual ion concentration gradients.

Cross-References

▶ Electrochemical Quartz Crystal Microbalance
▶ Ion Mobilities
▶ Radiotracer Methods
▶ Scanning Electrochemical Microscopy (SECM)
▶ UV–Vis Spectroelectrochemistry

References

1. Bard AJ, Faulkner L (1984) Electrochemical methods. Wiley, New York
2. Abruña HD (1991) Electrochemical Interfaces. Modern techniques for in-situ interface characterization. VCH, Weinheim
3. Gale RJ (1988) Spectroelectrochemistry. Theory and practice. Plenum Press, New York
4. Buttry DA (1991) Applications of the quartz crystal microbalance in electrochemistry. In: Bard AJ (ed) Electroanalytical chemistry. M. Dekker, New York, p 17
5. Shaposhnik VA, Vasileva VI, Praslov DB (1995) Concentration fields of solutions under electrodialysis with ion-exchange membranes. J Membr Sci 101:23–30
6. Lang GG, Barbero CA (2012) Laser techniques for the study of electrode processes (Monographs in electrochemistry). Springer, Berlin
7. Alda J (2003) Laser and gaussian beams propagation and transformation. In: Encyclopedia of optical engineering. Marcel Dekker, New York
8. Newman JS, Thomas-Alyea KE (2004) Electrochemical systems. Wiley-IEEE, New York
9. Barbero CA (2005) Ion exchange at the electrode/electrolyte interface studied by probe beam deflection techniques. Phys Chem Chem Phys 7:1875–1884
10. Barbero C, Calvo EJ, Miras MC, Koetz R, Haas O (2002) A probe beam deflection study of ion exchange at poly(vinylferrocene) films in aqueous and nonaqueous electrolytes. Langmuir 18:2756–2764
11. Barbero C, Miras MC, Haas O, Kötz R (1991) Direct in situ evidence for proton/anion exchange in polyaniline films by means of probe beam deflection. J Electrochem Soc 138:669–672
12. Barbero C, Planes GA, Miras MC (2001) Redox coupled ion exchange in cobalt oxide films. Electrochem Comm 3:113–116
13. Plichon V, Besbes S (1990) Mirage detection of counter-ion flux between Prussian blue films and electrolyte solutions. J Electroanal Chem 284:141–153
14. Grumelli DE, Wolosiuk A, Forzani E, Planes GA, Barbero C, Calvo EJ (2003) Probe beam deflection study of ion exchange in self-assembled redox polyelectrolyte thin films. Chem Commun 3014–3015
15. García G, Bruno MM, Planes GA, Rodriguez JL, Barbero CA, Pastor E (2008) Probe beam deflection studies of nanostructured catalyst materials for fuel cells. Phys Chem Chem Phys 10:6677–6685
16. Bruno MM, Cotella NG, Miras MC, Barbero CA (2005) Porous carbon–carbon composite replicated from a natural fibre. Chem Commun 5896–5898
17. Planes GA, Miras MC, Barbero CA (2005) Double layer properties of carbon aerogel electrodes measured by probe beam deflection and AC impedance techniques. Chem Commun 2146–2148
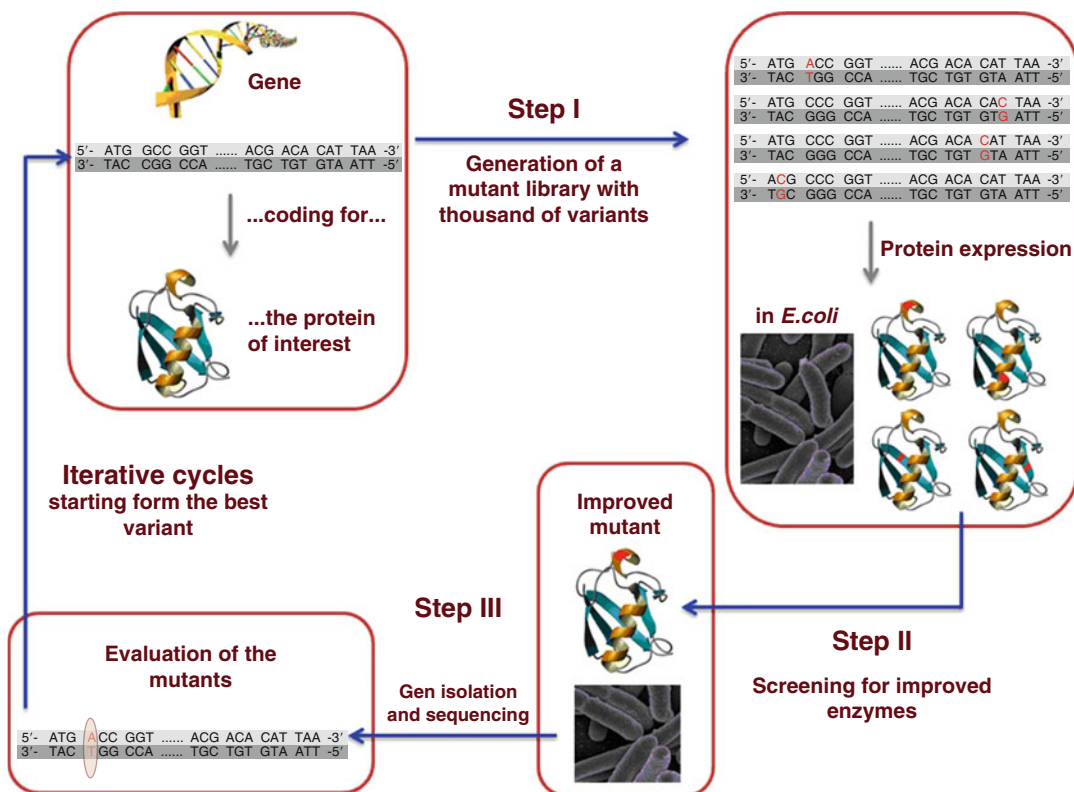
Protein Engineering for Electrochemical Applications

Anna Joëlle Ruff and Ulrich Schwaneberg
Lehrstuhl für Biotechnologie, RWTH Aachen University, Aachen, Germany

Introduction

Enzymes are molecular machines to sustain life in organisms through chemical reactions. Enzymes are by natural design not engineered to be driven efficiently by electrical current since redox-active centers, which catalyze chemical reaction, are often deeply buried inside of an enzyme. The protein shell that surrounds a catalytic center functions often as an isolator and prevents "loss of electrons." The latter would lead to formation of reactive radical species which could harm organisms and futile consumption of "energy" by wasting reduction equivalents such as NADH or NADPH. Enzymes have therefore usually sophisticated electron transfer pathways and control mechanism for oxidation/reduction and reduction reactions. Furthermore, the optimal reaction conditions of enzymes in their natural environment (low substrate/product concentrations, neutral pH, viscosity, salt concentration, ambient temperature) differ from application conditions in bioelectrocatalysis, for instance, in diagnostics (e.g., glucose determination [1]; enzymatic biofuel cells [2]), fine chemical production [3–5], or applications in bleaching or biofuel production [6]. Especially attractive are applications in which cost-effective electrical current from renewable sources can directly be used to drive enzymes.

Protein engineers have developed methods for rational and evolutive protein engineering which empowers them to design enzymes that are tailored for electrochemical applications ("bioelectrozymes"). Bioelectrozymes are usually optimized in specific properties such as stability (e.g., oxidative, thermal) and electron transfer rates (higher activity, mediator acceptance/specificity). An emphasis is often

Protein Engineering for Electrochemical Applications, Fig. 1 Directed evolution scheme. Step I: Diversity generation on DNA level. Step II: Screening for improved variants on protein level. Step III: Isolating gene(s) that encode for improved variant(s) and used for the next round of evolution, starting with Step I [5]

given to the design of the interface between the electrode and enzyme to ensure an efficient electrical communication. These design principles are described in the following two paragraphs: Protein Engineering Principles and Design of Bioelectrozymes.

Protein Engineering Principles

Protein engineers can redesign enzymes by rational design and/or directed evolution. Rational design strategies are much less time consuming compared to directed evolution campaigns which require the screening of thousands of variants in iterative round of diversity generation and screening. Rational design requires however a deep molecular and structural understanding based on crystal structures or a reliable homology model to rationally reengineer properties of bioelectrozymes. Focused enzyme properties such as activity, selectivity, thermal resistance, shift of pH profiles [7, 8]. Modifications for oriented immobilization are more successfully improved by using rational design strategies and designed enzyme variants can simply be ordered as synthetic genes. Rationally not understood properties are generally tackled by directed evolution which does not require any structural information. Enzyme properties improved by directed evolution comprise stabilities toward pH, temperature, salt, organic solvent, tolerance toward high concentrations of substrate or product, and acceptance of alternative cofactor systems like mediators that shuttle electrons between electrode and enzyme. Figure 1 shows the standard directed evolution scheme in three steps (Step I: Diversity generation on the gene level,

Step II: Screening for improved variants on the protein level, and Step III: Isolating gene(s) that encode for improved variant(s) followed by subsequent iterative rounds to improve enzyme properties). Iterative rounds are important for the success of a directed evolution experiments since enzyme properties are gradually improved, for instance, activities are usually improved by a factor of 1.5–2.5 per round of evolution [3]. A standard directed evolution campaign takes usually 12–24 months and allows within physical constrains to reengineer all kind of enzyme properties that can be reflected in a screening systems. Library sizes of 1,200–2,000 variants proved often to be sufficient to find improved variants [9] despite the size of the protein sequence space. For instance, 64 Mio different peptides are available with a peptide length of six amino acids since nature provides 20 amino acid building blocks per amino acid position (20^6 different variants). Limitations in diversity generation and high throughput screening technologies that arise from the combinatorial complexity of the protein sequence space are discussed in recent reviews [3, 10]. Time requirements of 12–24 months for tailored enzymes are often still too long to fit into timelines of process developments. Notably directed enzyme evolution and natural evolution (Charles Darwin in the seventeenth century [11]) are very different in their nature: (A) Direct evolution selects on the enzyme level, natural evolution on the organism level, and (B) Directed evolution mutates *one* gene with a mutation rate of 1–5 mutations per gene and selects usually for improved variants; natural evolution can exchange and recombine genes or accumulate mutations which are not beneficial (natural drift); additionally natural mutation rates are less than 1 per 10^{6-7} bp.

Recently unifying protein engineering concepts with combined evolutive and rational design approaches are emerging in which directed evolution is used to identify hot spots or regions that are responsible for the targeted property and subsequent computational studies are used to identify and direct focus mutagenesis studies on residues in close proximity [12, 23]

with a high likelihood to target residues that influence the targeted property.

Prominent oxidoreductases in bioelectrocatalysis are glucose oxidase and glucose dehydrogenase (e.g., applications in diabetes diagnostics), mono-oxygenases (e.g., important roles in synthesis of steroids and secondary metabolites), laccases (e.g., applications in textile bleaching and lignin treatment), bilirubin oxidase (e.g., biofuel cells), and peroxidases (e.g., general analytic applications). Applications of oxidoreductases in enzymatic biofuel cells are summarized comprehensively in reviews [5, 13].

Design of Bioelectrozymes

The main challenge in bioelectrozymes design is to ensure an efficient electrical communication between the electrode and the catalytic redox center of an enzyme. The glucosylation shell and/or amino acids surrounding an active-site can act as an isolator and effectively prevent an electrical communication between an electrode and a catalytic redox center. Strategies for efficient electrical communication comprise direct wiring of electrodes to the catalytic redox center through a conducting polymer [14], employment of mediators (small molecules) as electron shuttles which can come in close proximity to redox centers or electron pathways in enzymes [15, 16], and protein engineering strategies that are governed by the principle to reduce the distance between an electrode and the catalytic center or an electron transfer pathway within an enzyme [2]. Discovered engineering principles for efficient electrical communication comprise: I. Truncating enzymes at the N-, C-terminus or shortening of a loop in a protein to expose redox-active catalytic sites so that a conducting support can be positioned in close proximity (examples are a microperoxidase and a laccase [5]. II. Amino acid substitutions in close proximity to the active-site affect interactions that alter specificities (e.g., through sterical demands) or electrical communication with a mediator (potentials, charged interactions [23]). An alternative are specific binding sites that are generated at the protein surface in close proximity
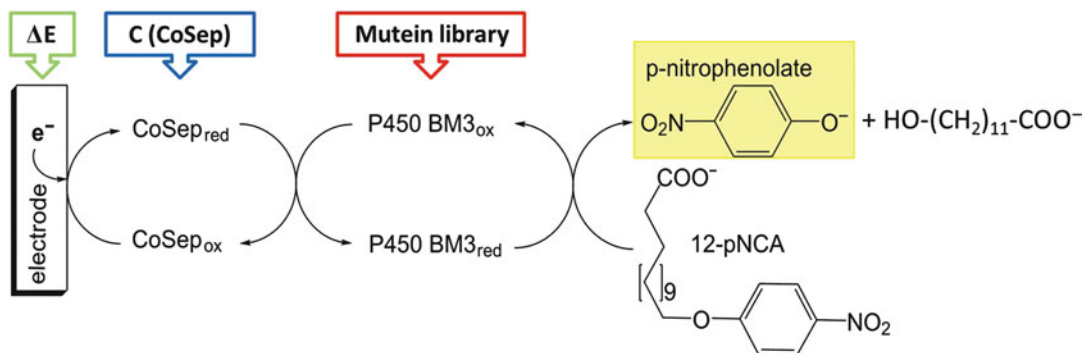
Protein Engineering for Electrochemical Applications, Fig. 2 Example of a reaction scheme of an electrochemical-driven conversion in microtiter plate format [18] of the model substrate 12-pNCA [21] by P450 BM3 with CoSep as mediator. Catalytic activity is monitored through a yellow color development due to para-nitrophenolate formation at 410 nm

to electron pathways Mediator [15]. III. Amino acid exchanges at exposed surface regions by genetic engineering for oriented immobilization of enzymes with one or multiple contact points that are located opposite of a catalytic center [17]. Oriented immobilization on electrodes surface ensures often an efficient communication resulting in high power outputs [2, 5]. Especially the reengineering of the mediator-enzyme interface offers promising avenues for identifying in mutant libraries improved bioelectrozymes and to match application demands, for instance, in drug metabolite detection by using an electrochemical microtiter plates ([18, 19]; see Fig. 2) or in fine chemical production [20].

Structural and molecular understanding of mediated electron transfer enables a paradigm shift from a mediator acceptance screening to a rational mediator design which considers only stability and electron transfer performance parameters. The rational mediator design would employ a subsequent enzyme engineering step to ensure an efficient electron transfer between mediator and enzyme which would open novel and exciting opportunities for enzymes in bioelectrocatalysis.

Outlook/Future Perspective

Bioelectrozymes will very likely have a bright future in diagnostics (employed in miniaturized electrochemical devices), fine chemical production using cost-efficient electrochemical reactors with low down-stream processing costs, and switchable interactive materials [22]. Fundamental design principles in reengineering enzymes (see section Design of Bioelectrozymes) and designing the interface between electrode and enzyme for efficient electrical communication have been discovered in the last decade. A molecular understanding of the interface between mediator and enzyme will likely allow in the near future to develop ideal enzyme/mediator couples and overcome current strategies in which a variety of mediators are synthesize from a mediator "lead structure" that was found experimentally to drive the wild-type enzyme. A combined approach to rationally construct ideal mediators (from an application point of view) and to reengineer efficiently the interface to the interacting enzyme will ensure a rapid development of the field due to the economic benefit that tailor-made bioelectrozymes will offer in the above-mentioned application. The combinatorial complexity of the protein sequence combined with the sophisticated genetic engineering methods renders it very likely that exciting bioelectrozymes wait to be discovered in the upcoming decade.

Cross-References

▶ Biofilms, Electroactive

References

1. Yu EH, Prodanovic R, Güven G, Ostafe R, Schwaneberg U (2011) Electrochemical oxidation of glucose using mutant glucose oxidase from directed protein evolution for biosensor and biofuel cell applications. Appl Biochem Biotechnol 165:1448–1457

2. Wong TS, Schwaneberg U (2003) Protein engineering in bioelectrocatalysis. Curr Opin Biotechnol 14:590–596

3. Ruff AJ, Dennig A, Schwaneberg U (2013) To get what we aim for: progress in diversity generation methods. FEBS J 280(13):2961–2978

4. Hollmann F, Arends IWCE, Buehler K, Schallmey A, Buehler B (2011) Enzyme-mediated oxidations for the chemist. Green Chem 13:226–265

5. Güven G, Prodanovic R, Schwaneberg U (2010) Protein engineering – an option for enzymatic biofuel cell design. Electroanalysis 22:765–775

6. Liu H, Zhu L, Bocola M, Chen N, Spiess AC, Schwaneberg U (2013) Directed laccase evolution for improved ionic liquid resistance. Green Chem 15:1348–1355

7. Jakob F, Martinez R, Mandawe J, Hellmuth H, Siegert P, Maurer K-H, Schwaneberg U (2013) Surface charge engineering of a Bacillus gibsonii subtilisin protease. Appl Microbiol Biotechnol 97(15):6793–6802

8. Martinez R, Jakob F, Tu R, Siegert P, Maurer K-H, Schwaneberg U (2013) Increasing activity and thermal resistance of *Bacillus gibsonii* alkaline protease (BgAP) by directed evolution. Biotechnol Bioeng 110:711–720

9. Tee KL, Schwaneberg U (2007) Directed evolution of oxygenases: screening systems, success stories and challenges. Comb Chem High Throughput Screen 10:197–217

10. Agresti JJ, Antipov E, Abate AR, Ahn K, Rowat AC, Baret J-C, Marquez M, Klibanov AM, Griffiths AD, Weitz DA (2010) Ultrahigh-throughput screening in drop-based microfluidics for directed evolution. Proc Natl Acad Sci USA 107:4004–4009

11. Campbell NA, Reece JB (2006) Biologie 6. überarbeitete Auflage. Pearson Studium 503–520

12. Vojcic L, Despotovic D, Maurer K-H, Zacharias M, Bocola M, Martinez R, Schwaneberg U (2013) Reengineering of subtilisin Carlsberg for oxidative resistance. Biol Chem 394:79–87

13. Zhu Z, Momeu C, Zakhartsev M, Schwaneberg U (2006) Making glucose oxidase fit for biofuel cell applications by directed protein evolution. Biosens Bioelectron 21:2046–2051

14. Katz E, Willner I (2003) A biofuel cell with electrochemically switchable and tunable power output. J Am Chem Soc 125:6803–6813

15. Shehzad A, Panneerselvam S, Linow M, Bocola M, Roccatano D, Mueller-Dieckmann J, Wilmanns M, Schwaneberg U (2013) P450 BM3 crystal structures reveal the role of the charged surface residue Lys/Arg184 in inversion of enantioselective styrene epoxidation. Chem Commun (Camb Engl) 49:4694–4696

16. Ströhle FW, Cekic SZ, Magnusson AO, Schwaneberg U, Roccatano D, Schrader J, Holtmann D (2013) A computational protocol to predict suitable redox mediators for substitution of NAD(P)H in P450 monooxygenases. J Mol Catal B: Enzym 88:47–51

17. Abian O, Grazú V, Hermoso J, González R, García JL, Fernández-Lafuente R, Guisán JM (2004) Stabilization of penicillin G acylase from *Escherichia coli*: site-directed mutagenesis of the protein surface to increase multipoint covalent attachment. Appl Environ Microbiol 70:1249–1251

18. Ley C, Schewe H, Ströhle FW, Ruff AJ, Schwaneberg U, Schrader J, Holtmann D (2013) Coupling of electrochemical and optical measurements in a microtiter plate for the fast development of electro enzymatic processes with P450s. J Mol Catal B: Enzym 92:71–78

19. Ley C, Zengin Çekiç S, Kochius S, Mangold K-M, Schwaneberg U, Schrader J, Holtmann D (2013) An electrochemical microtiter plate for parallel spectroelectrochemical measurements. Electrochim Acta 89:98–105

20. Holtmann D, Mangold K-M, Schrader J (2009) Entrapment of cytochrome P450 BM-3 in polypyrrole for electrochemically-driven biocatalysis. Biotechnol Lett 31:765–770

21. Schwaneberg U, Schmidt-Dannert C, Schmitt J, Schmid RD (1999) A continuous spectrophotometric assay for P450 BM-3, a fatty acid hydroxylating enzyme, and its mutant F87A. Anal Biochem 269:359–366

22. Van Rijn P, Tutus M, Kathrein C, Zhu L, Wessling M, Schwaneberg U, Böker A (2013) Challenges and advances in the field of self-assembled membranes. Chem Soc Rev 42:6578–6592

23. Arango Gutierrez E, Mundhada H, Meier T, Duefel H, Bocola M, Schwaneberg U (2013) Reengineered glucose oxidase for amperometric glucose determination in diabetes analytics. Biosensors and Bioelectronics 50:84–90

Pulse and Step Methods

Manuel Lohrengel
University of Düsseldorf, Düsseldorf, Germany

Introduction

If one physical parameter is suddenly changed in an electrochemical system, which is stationary or

**Pulse and Step Methods,
Fig. 1** Schematic
representation of a potential
step (*left*) and the
corresponding current
transient (*right*). The
increasing part of the
current transient is
dominated by the electronic
setup (typically $<<100\,\mu s$)
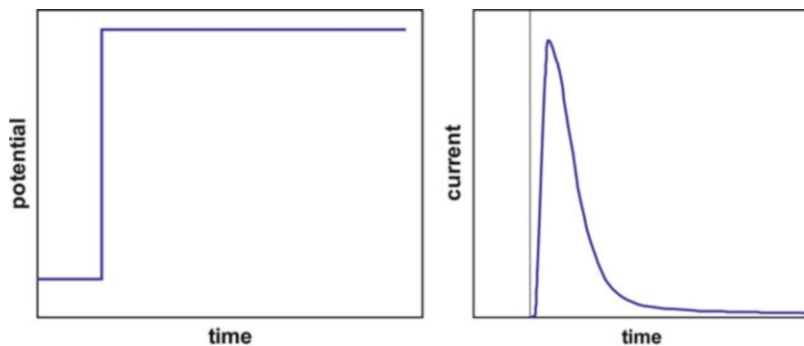
in equilibrium, the system will respond with
a relaxation process to return to more stable con-
ditions. The physical parameter may be random,
such as pressure, temperature, current density,
magnetic field, light intensity, electrolyte con-
centration, or electrode area, but in most cases
the potential will be stepped because interface
processes are fundamentally controlled by the
potential.

In a double-step experiment the second step is
often of same amplitude but inverse direction and
can compensate, at least in part, effects of the first
one. Such experiments are usually called pulse
experiments. The intention behind step or pulse
experiments will focus on two aspects:

• Analysis of the electrolyte, such as determina-
  tion of components and their concentration, of
  concentration gradients, and, especially, of
  their changes with time [1–4]. Most tech-
  niques were developed for and used in
  polarography.
• Analysis of material and charge transport
  through the interface electrode/electrolyte,
  such as dissolution and deposition, especially
  adsorption, corrosion, passivation, galvanics,
  shaping, and polishing [4].

The response to a potential step is a current
transient, a time-dependent current density
(Fig. 1). These experiments are classified as
chronoamperometry. Potential transient as
a response to current step experiments, formerly
also called charging curves [5], is related to
chronopotentiometry. These transients are
recorded and interpreted. Step experiments are
large signal, time domain experiments and inves-
tigate processes far from equilibrium; they are

not limited to special conditions, e.g., a linear
response as in frequency domain techniques
(impedance spectroscopy). Most restrictions
come from the limits of the experimental setup,
such as maximum output values and slew rates of
potentiostats or galvanostats or dynamics of the
recording systems.

Analysis in the Electrolyte

Chronoamperometry

The current density of a redox reaction will
change, if the potential is changed. Chronoam-
perometry usually starts at potentials without far-
adaic processes. The response to a potential step,
the current transient, contains the re-arrangement
of the electrode interface, mainly double-layer
charging, which is indicated by a current peak
and can be reduced to some 10 μs in a suitable
potentiostatic setup. Assuming a simple reaction

$$O + ne^- \rightarrow R \qquad (1)$$

no product R in the beginning and a planar elec-
trode with the area A, a time-dependent faradaic
current I will be observed after the peak, which
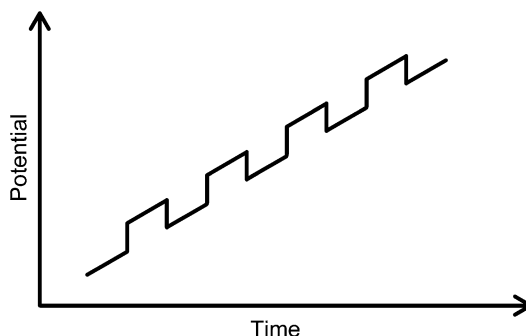can be expressed by the Cottrell equation [6]

$$I = \frac{nFAc_\infty\sqrt{D_O}}{\sqrt{\pi \cdot t}} \qquad (2)$$

with the initial concentration c_∞ and the diffusion
coefficient D_O of O.

Deviations will occur for long times due to
convection, for especially shaped electrodes
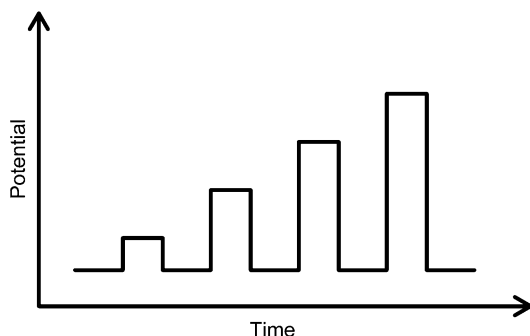
Pulse and Step Methods, Fig. 2 Schematic pulse program of normal-pulse voltammetry

Pulse and Step Methods, Fig. 3 Schematic pulse program of differential-pulse voltammetry

(spherical or microelectrodes) and, of course, for more complex reactions.

The electrode reaction can be inverted by a second potential step of different sign and same amplitude at $t = \tau$ (double potential step or pulse chronoamperometry). The first transient follows Eq. 2 and the second one, however, is given by [7, 8]:

$$I = nFAc_\infty \sqrt{D_O} \left[\frac{1}{\sqrt{\pi(t - \tau)}} - \frac{1}{\sqrt{\pi \cdot t}} \right] \quad (3)$$

Pulse Voltammetry
Pulse voltammetry is a subset of chronoamperometry with special pulse sequences. Pulse voltammetry was introduced as *square wave polarography* [9] to increase sensitivity in polarography.

Normal-pulse voltammetry consists of a series of rectangular pulses with increasing amplitude (Fig. 2). The potential between the pulses is chosen so that no reaction occurs. The currents are measured just before the end of the pulses to suppress effects of interface charging. The analysis follows the Cottrell equation.

Series of rectangular pulses (typical length some 10 ms) with constant amplitude ΔE are superimposed to linear potential ramp in *differential-pulse voltammetry* (Fig. 3). The currents are detected twice per pulse, just before the pulse and before the end of the pulse. The differences are plotted versus potential of the linear sweep. Current peaks will be observed for reversible systems with heights:

$$I = \frac{nFAc\sqrt{D}}{\sqrt{\pi \cdot t}} \left[\frac{1 - \exp\left(\frac{nF\Delta E}{2RT}\right)}{1 + \exp\left(\frac{nF\Delta E}{2RT}\right)} \right] \quad (4)$$

Staircase voltammetry is similar to linear sweep techniques. The current is detected at the end of each step and, thus, suppresses interface charging effects, just as in the other techniques. The resulting current-potential curve is similar to the corresponding sweep but excludes charging currents.

Chronocoulometry
Chronocoulometry is very similar to chronoamperometry. The charge transient is recorded, which is yielded by electronic integration in analog setups or by numeric integration in digital systems. Advantages are noise reduction, as integration suppresses higher frequencies, and a more obvious separation of double-layer charging and faradaic current.

Chronopotentiometry
In chronopotentiometry, the potential responses (potential transient) to current steps are recorded. If the system is initially stationary or close to equilibrium, the potential will change rapidly due to charging of the electrode interface. This fast step corresponds to the current peak in chronoamperometry. After electrode charging, the potential becomes dominated by the reaction of electroactive species, the faradaic part.
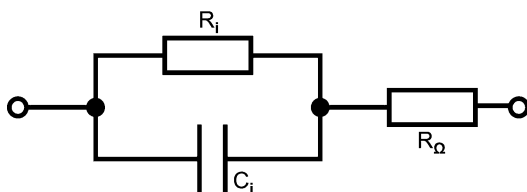
Pulse and Step Methods, Fig. 4 Simplified impedance between reference electrode and working electrode: electrolyte resistance R_Ω, interface resistance R_i, and interface capacitance C_i

Analysis of the Interface Electrode/Electrolyte

Diffusion-controlled processes in the electrolyte were investigated and analyzed by solving Fick's laws of diffusion. Effects of the impedance of the interface, e.g., charging of the electrode interface, were eliminated.

A simplified equivalent of this impedance is shown in Fig. 4. Investigations are usually carried out by impedance spectroscopy [10]. Step experiments, however, are advantageous in some cases: they are much faster (μs to ms instead of some 100 s) and are not limited to linear response (equilibrium or stationary conditions, small amplitudes).

Determination of Electrolyte Resistance
The electrolyte resistance R_Ω (Fig. 4) between reference and working electrode can be determined by short current pulses [5]. This is necessary for some concepts of *iR* compensation (▶ iR-Drop Elimination).

Determination of Interface Capacitance
The interface capacitance can be measured by short pulses [11–13]. The current transient of a potential step ΔU is dominated by capacitive charging of the electrode interface for short times. The interface capacitance C_i in Fig. 5 has to be charged via R_Ω with a time constant $R_\Omega \cdot C_i$. This charge Δq_i and the interface capacitance C_i are obtained from simultaneous integration of the current density i_i according to

$$C_i = \frac{\Delta q_i}{\Delta U} = \frac{\int i_i \partial t}{\Delta U} \tag{5}$$
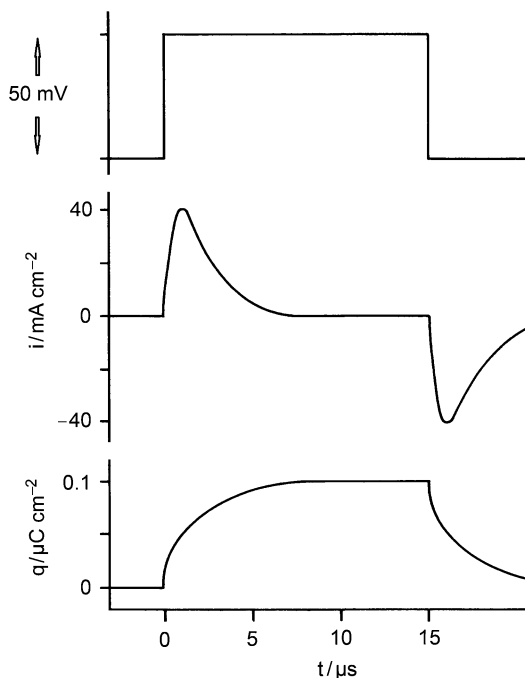
Pulse and Step Methods, Fig. 5 Measurement of interface capacitance by short pulses. From *top*: potential, current density and charge density

Typical time constants and, thus, pulse lengths are around 20 μs (Fig. 5).

An interpretation of the potential dependent capacitance (Mott-Schottky analysis [14]) yields information about semiconducting properties of the electrode. The corresponding experiment requires a modified technique in non-stationary systems, because the complete function must be measured in extremely short times to avoid fundamental system changes. This was done by superimposing small pulse to each step of a potential staircase (Fig. 6). With this technique, the complete analysis requires less than 500 μs [15].

Determination of Random Reactions
Surface reactions on the electrode are extremely complex. The current transient after a potential step can include:
- Dielectric phenomena (double-layer charging, dielectric relaxation [16])
- Adsorption (physisorption, chemisorption, ordered sublayers)
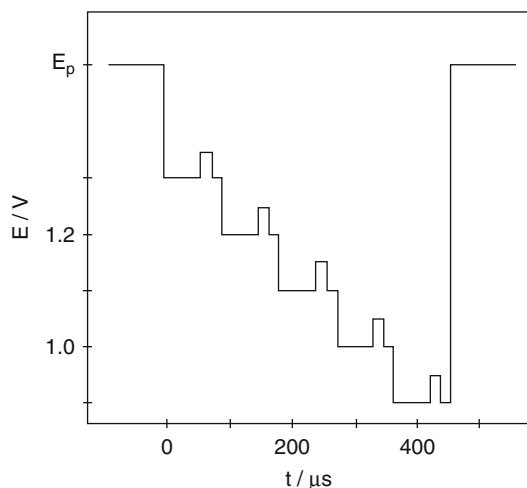
Pulse and Step Methods, Fig. 6 Example of pulse measurements of the potential dependent capacitance for Mott-Schottky analysis. The electrode was pre-polarized to E_p

- Formation of new phases (passivation, galvanic deposition, including kinetic phenomena such as nucleation [17], and charge and material transport such as solid-state diffusion, migration, tunneling of electrons or holes)
- Electrode dissolution (corrosion, electropolishing, shaping by anodic dissolution [18], often accompanied by formation of supersaturated product films).

The current density i will often follow a "universal law" [16] (well known as Curie-von Schweidler law in dielectric systems [19])

$$i \propto t^{-1} \qquad (6)$$

Less common is a current increasing with time, which is observed in autocatalytic systems, e.g., if a kinetic hindrance is overcome by the potential pulse. A description in these cases is often possible by a modified law

$$i \propto t^n \qquad (7)$$

An analysis of current transients according to Eq. 7 becomes easy in a double-logarithmic plot. The slope of linear parts yields the exponent n, as

$$\frac{\partial \log i}{\partial \log t} = n \qquad (8)$$

The size of n classifies the process: self-inhibiting processes for $n < 0$, stationary processes for $n = 0$, and autocatalytic processes for $n > 0$. Typical examples of n and corresponding reactions are [20]:

$n = -1$	High-field oxide growth; dielectric relaxation
$n = -0.5$	Diffusion
$n = 0$	Stationary corrosion; 1-dim. growth of nuclei (whisker) at a constant number of nuclei
$n = 1$	1-dim. progressive nucleation (whisker) or 2-dim. at constant number
$n = 2$	2-dim. progressive nucleation (hemisphere, dendrites) or 3-dim. at constant number
$n = 3$	3-dim. progressive nucleation

Several mechanisms may be superimposed in real systems. In this case, Eq. 2 becomes more complex:

$$i = A + B \cdot t^n + C \cdot t^m + \dots \qquad (9)$$

Identification of single processes according to Eq. 9 requires data acquisition over one or two decades in time and current density. Therefore, the complete transient has to cover many orders of magnitude, e.g., current densities from 1 A/cm^2 to 10 nA/cm^2 and a time scale from 1 μs to 10^3 s. This requires especially designed electronic devices and strategies to handle the numerous data [21].

Future Directions

Step and pulse techniques for investigations of redox reactions in the electrolyte are well developed for many years. Future research will focus on faster and more complex reactions.

Investigations of random processes by pulse experiments, which are not limited by diffusion in the electrolyte, are much less common. The increasing interest of industry to introduce pulse techniques, such as pulse plating [22], formation of gradient layers, or pulse electrochemical machining (PECM) [23], will help making these techniques more popular.

Cross-Reference

▶ iR-Drop Elimination

References

1. Wang J (2006) Analytical Electrochemistry. Wiley-VCH, New York
2. Brett CMA, Brett AMO (1998) Electrochemistry principles methods and applications. Oxford Science, Oxford
3. Bard AJ, Faulkner LR (1980) Electrochemical methods: fundamentals and applications. Wiley, New York
4. Macdonald DD (1977) Transient techniques in electrochemistry. Plenum, New York
5. Vetter KJ (1967) Electrochemical kinetics theoretical and experimental aspects. Academic, New York
6. Cottrell FG (1903) Residual current in galvanic polarization regarded as a diffusion problem. Z Phys Chem 42:385–431
7. Smit NM, Wijnen MD (1960) Square-wave electrolysis I cyclic potential-step method. Rec Trav Chim 79:5–21
8. Kimmerle F, Chevalet J (1969) The determination of heterogeneous rate constants by double-step potentiostatic method. J Electroanal Chem 21:237–255
9. Barker GC, Jenkin IL (1952) Square-wave polarography. Analyst 77:685–696
10. Macdonald JR (1987) Impedance spectroscopy. Wiley, New York
11. Wagner C (1950) Determination of the concentrations of cation and anion vacancies in solid potassium chloride. J Electrochem Soc 97:72–74. doi:10.1063/1.1747460
12. Gilman S (1964) Electrochemical surface oxidation of platinum. Electrochim Acta 9:1025–1046. doi:10.1016/0013-4686(64)85049-0
13. Krischer CC, Osteryoung RA (1965) A method for the dynamic measurement of capacity at electrode interfaces. J Electrochem Soc 97:735–739. doi:10.1149/1.2423677
14. Stimming U, Schultze JW (1976) The capacity of passivated iron electrodes and the band structure of the passive layer. Ber Bunsenges Physik Chem 80:1297–1302
15. König U, Lohrengel MM, Schultze JW (1987) Computer supported pulse measurements of current and capacity during fast oxide formation on iron. Ber Bunsenges Physik Chem 91:426–431
16. Jonscher AK (1983) Dielectric relaxation in solids. Chelsea Dielectric Press, London
17. Schultze JW, Lohrengel MM, Roß D (1983) Nucleation and growth of anodic oxide films. Electrochim Acta 28:973–984
18. Olsson COA, Landolt D (2003) Passive films on stainless steels- chemistry structure and growth. Electrochim Acta 48:1093–1104. doi:10.1016/S0013-4686(02)00841-1
19. von Schweidler E (1907) Studien über die Anomalien im Verhalten der Dielektrika. Ann Phys 24:711–770
20. Lohrengel MM (1993) Pulse measurements for the investigation of fast electronic and ionic processes at the electrode/electrolyte interface. Ber Bunsenges Physik Chem 112:440–447
21. Lohrengel MM (1993) Thin anodic oxide layers on aluminum and other valve metals: high field regime. Mater Sci Eng R11:243–294
22. Chandrasekar MS, Pushpavanam M (2008) Pulse and pulse reverse plating- conceptual advantages and applications. Electrochim Acta 53:3313–3322. doi:10.1016/j.electacta.2007.11.054
23. Lohrengel MM (2005) Pulsed electrochemical machining of iron in $NaNO_3$ fundamentals and new aspects. Mater Manufact Proc 20:1–9

P